TECHNISCHE UNIVERSITÄT MÜNCHEN

Lehrstuhl für Numerische Mechanik

Stabilized Cut Finite Element Methods for Complex Interface Coupled Flow Problems

Benedikt Schott

Vollständiger Abdruck der von der Fakultät für Maschinenwesen der Technischen Universität München zur Erlangung des akademischen Grades eines

Doktor-Ingenieurs (Dr.-Ing.)

genehmigten Dissertation.

Vorsitzender:	Univ.-Prof. dr.ir. Daniel J. Rixen
Prüfer der Dissertation:	
	1. Univ.-Prof. Dr.-Ing. Wolfgang A. Wall
	2. Prof. Erik Burman, Ph.D. University College London / UK

Die Dissertation wurde am 23. Mai 2016 bei der Technischen Universität München eingereicht und durch die Fakultät für Maschinenwesen am 15. März 2017 angenommen.

ABSTRACT

Novel computational methodologies for complex interface coupled flow problems are developed in this thesis. Computational models for incompressible single-phase flow and interactions between fluid and solid phases rely on the framework of cut finite element methods which allow domains and computational meshes to be chosen geometrically unfitted.

A broad range of multiphysics problems arising from various engineering and scientific fields are dominated by interactions of fluid phases with each other as well as with structural bodies. For complex practical problem configurations, involved computational domains are often subjected to large deformations or even undergo topological changes. Most if not all established existing computational approaches are limited in their applicability for such scenarios. Cut finite element methods (CUTFEMs) are promising discretization techniques and allow for a sharp representation of the solution fields based on computational grids which are not forced to be aligned with the respective subdomain geometry. This way, such approaches provide powerful simulation tools to substantially simplify mesh generation for complex geometries. While highly increasing versatility, decoupling of the finite dimensional approximation spaces from the physical domains entails additional complexity for such numerical approaches which manifests in numerical instabilities arising in boundary and interface zones.

The main contribution of this thesis is to theoretically analyze the sources of encountered instabilities, to support the made statements by comprehensive numerical studies and, as a consequence, to introduce novel stabilization mechanisms to counteract these issues. The central focus is directed to the development of numerical approaches which guarantee inf-sup stability and allow to establish spatially optimal *a priori* error estimates for flow problems governed by the non-linear incompressible Navier-Stokes equations. All novel computational methods developed throughout this work utilize weak variational constraint enforcement of boundary and interface coupling conditions based on the well-established Nitsche method. The enhancement of different so-called ghost-penalty stabilization techniques for velocity and pressure solutions is of decisive importance to ensure stability for transient low- and high-Reynolds-number flows independent of the boundary position within the computational grid. Besides a sound mathematical proof of stability and optimality for a linear auxiliary problem governed by the Oseen equations, comprehensive numerical convergence studies and the simulation of transient single-phase flows through complex-shaped non-moving as well as moving fluid domains demonstrate accuracy, robustness and the high capabilities of the developed CUTFEM flow solver.

A further major contribution of the present thesis constitutes in the extension of theoretical analyses from single-phase flows to coupled flow problem configurations. In a first step, overlapping unfitted discretization concepts for fluid domain decomposition are considered. A Nitsche-type coupling strategy, which is able to sufficiently control convective mass transport across interfaces, is introduced and validated for challenging test examples: two- and three-dimensional cylinder benchmarks and the turbulent recirculating flow in a lid-driven cavity at $\mathrm{Re} = 10000$. In a second step, adaption of this computational methodology to different modelings of incom-

pressible two-phase flow is elaborated. Special emphasis is put on the accurate representability of solutions in topologically degenerated situations and on the robustness of coupling methods for interacting fluids which exhibit strong differences in the numerical resolution of their respective physics. These can be characterized in terms of involved fluid viscosities related to respective mesh sizes. Predicting exponential growth rates for a Rayleigh–Taylor instability as well as investigation of damping effects due to surface tension demonstrates excellent performance. As an outlook, to illustrate the extensibility of the proposed flow solvers to more sophisticated incompressible two-phase flows and to point out the major improvements made in this work, the simulation of the temporal evolution of a separating flame front for a flame-vortex interaction serves as test example.

Having developed computational methods for the simulation of interactions between fluid phases, extensions to different geometrically unfitted discretizations for fluid-structure interaction (FSI) can be made. Fundamentals on interface modeling for FSI and a standard Galerkin formulation for solid mechanics are reviewed. Numerically stabilized coupled systems of fluids and solids are set up and tailored non-linear solution strategies are proposed which allow for changing approximation spaces during iterative procedures. Finally, highly dynamic FSI problems show the high capabilities of the developed monolithic FSI solvers and highlight their superiority over a multitude of other computational approaches.

Concluding, the diversity of already successfully realized single-phase and coupled flow problem settings demonstrates the high versatility of CUTFEMs. These achievements give rise to hope for further extensibility of the framework of unfitted cut finite element discretizations as well as of developed stabilization techniques to other challenging multiphysics problems.

ZUSAMMENFASSUNG

In der vorliegenden Arbeit werden neuartige numerische Verfahren zur Berechnung komplexer Interface-gekoppelter Strömungsprobleme entwickelt. Die Berechnungsmodelle für inkompressible Einphasenströmungen sowie für Wechselwirkungen zwischen fluiden Phasen und Festkörpern verwenden schnittbasierte Finite-Elemente-Methoden, die es erlauben, dass physikalische Gebiete und Berechnungsgitter geometrisch nicht passend zueinander gewählt werden.

Eine große Bandbreite an Multiphysics-Anwendungen aus unterschiedlichen Bereichen der Ingenieurswissenschaften und anderen Wissenschaftsbereichen werden durch Interaktionen zwischen verschiedenen Fluiden sowie deren Wechselwirkungen mit Strukturkörpern beschrieben. In komplexen praktischen Problemstellungen unterliegen die entsprechenden Teilgebiete oftmals großen Deformationen oder sind sogar topologischen Änderungen unterworfen. Die meisten, wenn nicht sogar alle etablierten rechnergestützten Berechnungsverfahren sind für solche Problemstellungen nicht geeignet. Finite-Elemente-Methoden, die auf dem Schneiden von Berechnungsnetzen basieren (CUTFEM), stellen dabei leistungsfähige Diskretisierungsansätze dar, die eine genaue Darstellung der Lösungsfelder ermöglichen und dabei nicht erfordern, dass das Berechnungsnetz und das Gebiet aneinander angepasst sind. Auf diese Art und Weise stellen solche Ansätze effektive Simulationswerkzeuge dar, welche die Netzerstellung für komplexe Geometrien maßgeblich vereinfachen. Während das Entkoppeln endlich-dimensionaler Ansatzfunktionenräume von physikalischen Gebieten die Vielseitigkeit solcher Berechnungsverfahren stark erhöht, so zieht dies jedoch auch weitere Schwierigkeiten in Form von numerischen Instabilitäten nach sich, welche sich in den Randbereichen und Phasengrenzflächen ausbilden.

Der wichtigste Beitrag dieser Arbeit liegt in der theoretischen numerischen Analyse von Ursachen für auftretende Instabilitäten sowie deren umfassende Untersuchung mithilfe von numerischen Studien und in Folge dessen in der Einführung von neuartigen Stabilisierungsmechanismen, um diesen Instabilitäten entgegen zu wirken. Dabei liegt das Hauptaugenmerk auf der Entwicklung von numerischen Verfahren, die inf-sup-Stabilität und räumlich optimale *a priori*-Fehlerabschätzungen für Strömungsprobleme garantieren, denen die nichtlinearen inkompressiblen Navier-Stokes Gleichungen zugrunde liegen. Die in dieser Arbeit entwickelten neuartigen numerischen Verfahren verwenden ein schwaches, variationelles Aufbringen von Rand- und Interface-Kopplungsbedingungen mithilfe der etablierten Nitsche-Methode. Um für zeitabhängige Strömungen mit niedrigen wie auch mit hohen Reynolds-Zahlen numerische Stabilität unabhängig von der Interface-Position zu gewährleisten, spielt die Weiterentwicklung von verschiedenen sogenannten Ghost-Penalty-Stabilisierungen, angewandt auf Geschwindigkeits- und Drucklösungen, eine entscheidende Rolle. Neben dem mathematischen Beweis von numerischer Stabilität und Optimalität für ein lineares Hilfsproblem, welches durch die Oseen-Gleichungen beschrieben ist, weisen umfassende numerische Konvergenzstudien sowie die Simulation von zeitabhängigen Einphasenströmungen durch komplex geformte unbewegte wie auch bewegte Fluid-Berechnungsgebiete die Genauigkeit und Robustheit des entwickelten CUTFEM-Fluid-Lösers nach und zeigen dessen großes Potenzial auf.

Ein weiterer wichtiger Beitrag der vorliegenden Arbeit besteht in der Erweiterung theoretischer Analysen von Einphasenströmungen auf Problemstellungen gekoppelter Strömungen. In einem ersten Schritt werden Konzepte für Fluid-Gebietszerlegungen basierend auf überlappenden, nicht zueinander passenden Diskretisierungen betrachtet. Eine Nitsche-artige Kopplungsmethode, die es erlaubt konvektiven Massentransport über Interfaces hinweg zu kontrollieren, wird hierzu eingeführt und mithilfe anspruchsvoller Testbeispiele validiert: Dazu dienen zwei- und dreidimensionale Zylinder-Benchmarks sowie eine turbulente Strömung in einer sogenannten „lid-driven cavity“ ($\mathrm{Re} = 10000$). In einem zweiten Schritt werden Anpassungen dieses Berechnungsverfahrens auf verschieden geartete inkompressiblen Zweiphasenströmungen erörtert. Besonderes Augenmerk liegt dabei zum einen auf der exakten Darstellbarkeit von Lösungen in topologisch entarteten Situationen, und zum anderen auf der Robustheit der Kopplungsmethoden für wechselwirkende fluide Phasen, die starke Unterschiede in der numerischen Auflösung deren jeweiliger Physik aufweisen. Diese lassen sich anhand der Verhältnisse von Viskositäten zu Netzweiten beschreiben. Herausragende Ergebnisse wurden bei der Bestimmung von exponentiellen Wachstumsraten für Rayleigh-Taylor-Instabilitäten sowie von Dämpfungseffekten in Folge von Oberflächenspannung erzielt. Um als Ausblick die Erweiterungsmöglichkeiten des vorgestellten Fluid-Lösers auf anspruchsvollere inkompressible Zweiphasenströmungen aufzuzeigen und dabei die wichtigsten Verbesserungen, die in dieser Arbeit erzielt wurden, zu verdeutlichen, wird beispielhaft die zeitliche Entwicklung der Phasengrenze einer Flammen-Wirbel-Interaktion simuliert.

Die Weiterentwicklung numerischer Verfahren für die Simulation von Wechselwirkungen fluider Phasen ermöglicht Anpassungen auf verschiedene, geometrisch nicht zusammenpassende Diskretisierungen, die auf die Simulation von Fluid-Struktur-Interaktionen (FSI) anwendbar sind. Hierfür werden Grundlagen zu Grenzschicht-Modellierungen für FSI sowie eine Standard-Galerkin Formulierung für Strukturmechanik erörtert. Es werden numerisch stabilisierte gekoppelte Systeme, bestehend aus Fluiden und Strukturkörpern, formuliert und maßgeschneiderte, nichtlineare Lösungsstrategien vorgestellt, die es erlauben, dass sich Ansatzfunktionenräume während des iterativen Verfahrens verändern. Abschließend zeigen hochdynamische FSI-Probleme die besonderen Fähigkeiten der entwickelten FSI-Löser auf und verdeutlichen deren Überlegenheit gegenüber einer Vielzahl anderer numerischer Ansätze.

Zusammenfassend zeigen sich die enormen Einsatzmöglichkeiten schnittbasierter Finite-Elemente-Methoden in der Vielzahl der bereits erfolgreich umgesetzten Einphasenströmungen wie auch gekoppelter Strömungsprobleme. Diese geben Anlass zur Hoffnung auf Weiterentwicklungen von schnittbasierten Finite-Elemente-Diskretisierungsansätzen sowie entwickelter Stabilisierungstechniken für weitere anspruchsvolle Mehrfeldprobleme.

TABLE OF CONTENTS

NOMENCLATURE

Domains, Observers and Frames of Reference

$\mathbb{N}$	integers
$\mathbb{R}$	real numbers
$(\cdot)^d$	dimension of vector-valued quantity
$f, g\ \boldsymbol{f}, \boldsymbol{g}$	scalar and vector-valued quantities
$\boldsymbol{e}_1, \boldsymbol{e}_2, \boldsymbol{e}_3$	orthonormal basis of Euclidean space $\mathbb{R}^3$
$\mathscr{R}_{\boldsymbol{X}}, \mathscr{R}_{\boldsymbol{x}}, \mathscr{R}_{\boldsymbol{\chi}}$	material, spatial, referential domains
$\boldsymbol{X}, \boldsymbol{x}, \boldsymbol{\chi}$	material, spatial, referential coordinates
$(\cdot)_{\boldsymbol{X}}, (\cdot)_{\boldsymbol{x}}, (\cdot)_{\boldsymbol{\chi}}$	quantities with respect to material, spatial, referential coordinates
$\boldsymbol{I}$	identity mapping
$\boldsymbol{\varphi}$	bijective mapping from material to spatial domain
$\boldsymbol{\Phi}$	bijective mapping from referential to spatial domain
$\boldsymbol{\Psi}$	bijective mapping from referential to material domain
$J_{\boldsymbol{X}\mapsto\boldsymbol{x}}$	Jacobian of bijective mapping from material to spatial domain
$J_{\boldsymbol{\chi}\mapsto\boldsymbol{x}}$	Jacobian of bijective mapping from referential to spatial domain
$\boldsymbol{u}$	convective velocity
$\boldsymbol{w}$	velocity of a fixed particle $\boldsymbol{X}$ in referential coordinate system
$\hat{\boldsymbol{u}}$	grid velocity
$\boldsymbol{c}$	ALE convective velocity
$V_{\boldsymbol{X}}, V_{\boldsymbol{x}}, V_{\boldsymbol{\chi}},$	observed material control volume, mapped to spatial and referential domains
$\nabla_{\boldsymbol{X}}, \nabla_{\boldsymbol{x}}, \nabla_{\boldsymbol{\chi}}$	material, spatial, referential gradient operators
$\nabla_{\boldsymbol{X}}\cdot, \nabla_{\boldsymbol{x}}\cdot, \nabla_{\boldsymbol{\chi}}\cdot$	material, spatial, referential divergence operators
$M(t)$	time-dependent mass of a continuum
$P(t)$	time-dependent linear momentum of a continuum
$\rho_{\boldsymbol{X}}, \rho_{\boldsymbol{x}}, \rho_{\boldsymbol{\chi}}$	density of a continuum in material, spatial, referential coordinates
$\rho^0_{\boldsymbol{X}}, \rho_{\boldsymbol{x}}, \rho^G_{\boldsymbol{\chi}}$	material, spatial, referential density of a continuum
$\boldsymbol{f}$	external volumetric body forces
$\boldsymbol{t}, \boldsymbol{t}_{\boldsymbol{x}}$	external surface tractions in spatial coordinates
$\boldsymbol{t}_{\boldsymbol{X}}$	pseudo surface traction in material coordinates
$\boldsymbol{\sigma}_{\boldsymbol{x}}$	two-point spatial stress tensor, Cauchy stress tensor
$\boldsymbol{\sigma}_{\boldsymbol{X}}, \boldsymbol{P}$	material stress tensor, first Piola–Kirchhoff stress tensor

Domains, Boundaries and Interfaces

d	spatial dimension of domain
$\Omega, \Omega^i, \Omega^j$	domain, subdomains
$\partial\Omega, \partial\Omega^i$	domain and subdomain boundary
$\Gamma, \Gamma^{ij}, \Gamma^i$	interface (between Ω^i and Ω^j), exterior subdomain boundary $\Gamma^i \subset \partial\Omega$
N_{dom}	number of subdomains
$\boldsymbol{n}, \boldsymbol{n}^i, \boldsymbol{n}^{ij}$	outward-pointing unit normal vector at boundaries and interfaces

Boolean Set Operators and Level-Set Method

ϕ	scalar level-set function
d	signed distance function
$()^c$	complementary operator for subdomains
$\cap$	Boolean intersection operator for level-set represented subdomains
$\cup$	Boolean union operator for level-set represented subdomains
$\setminus$	Boolean difference operator for level-set represented subdomains
$\triangle$	Boolean symmetric difference operator for level-set represented subdomains

Mathematical Operators

$[\![\cdot]\!]$	jump operator over discontinuous functions across interface or interior faces
$\{\cdot\}, \langle\cdot\rangle$	weighted average operators over discontinuous functions
w^i, w^j	weights for averaging
$\{\cdot\}_{\text{m}}$	mean average operator over discontinuous functions
$\lim$	limit
sign	sign function
$(\cdot) \circ (\cdot)$	concatenation of operations
$\frac{\mathrm{d}\cdot}{\mathrm{d}t}$	total time derivative
$\frac{\partial\cdot}{\partial t}, \frac{\partial\cdot}{\partial x}$	partial time derivative and derivative with respect to x
abs	absolute value
span	linear span of a set, closed subspace spanned by a set
$\delta_{r,s}$	Kronecker-δ
$\oplus$	operator for composing function spaces associated with several subdomains
$\times$	operator for product spaces associated with a single subdomain
supp	support of a function
const	constant function
∇	spatial gradient
$\nabla\cdot$	divergence operator
Δ	Laplace operator
$\operatorname{tr}()$	trace operator
$\partial^j_{\boldsymbol{n}} v$	j-th normal derivative of function v
α	multi-index $\alpha = (\alpha_1, ..., \alpha_d)$ for derivatives
$a \lesssim b$	equivalent to $a \leqslant Cb$ with a generic positive constant C
$\operatorname{card}(x)$	cardinality (number) of elements in the set x

Finite Element Spatial Discretization

$\widehat{\mathcal{T}}_h$	set of finite elements with mesh size parameter h, the computational mesh
$\mathcal{T}_h$	active part of a finite element mesh, subset of $\widehat{\mathcal{T}}_h$
T	finite element of mesh $\mathcal{T}_h$
$\hat{T}$	d-simplicial, d-rectangular or d-wedge-shaped reference element
$\text{nnod}_{\hat{T}}$	number of nodes of element $\hat{T}$
S_T	bijective mapping from element parameter space to current coordinates
$\boldsymbol{\xi} = (\xi_1, \ldots, \xi_d)$	d-dimensional parameter space of reference finite elements
$\hat{N}_s(\boldsymbol{\xi})$	Lagrange interpolation function defined at node s of reference element $\hat{T}$
N_s	global basis function, hat function, at node s
$\mathcal{N}$	set of nodes of computational mesh
s	node $s \in \mathcal{N}$
h_T, h	characteristic element length, piecewise constant mesh size function
Ω_h, Γ_h	mesh dependent domain and interface approximations
$\boldsymbol{X}, \boldsymbol{x}_h, \boldsymbol{d}_h$	material coordinates, spatial coordinates and displacements
$\boldsymbol{X}_s, \boldsymbol{x}_s, \boldsymbol{d}_s$	node-wise material coordinates, spatial coordinates and displacements
$\mathcal{F}_h$	set of interior and boundary faces of computational mesh $\mathcal{T}_h$
$\mathcal{F}_i$, $\mathcal{F}_e$	set of interior inter-element faces and set of exterior boundary faces of mesh
F	face of finite element mesh
$\hat{F}$	reference face in $(d-1)$-dimensional parameter space $\boldsymbol{\eta}$
$\text{nnod}_{\hat{F}}$	number of nodes of face $\hat{F}$
$\boldsymbol{\eta} = (\eta_1, \ldots, \eta_d)$	$(d-1)$-dimensional trace parameter space for faces of reference elements
$\hat{N}_l(\boldsymbol{\eta})$	Lagrange interpolation function defined at node l of reference face $\hat{F}$
$\mathcal{E}_i$	set of interior edges of computational mesh $\mathcal{T}_h$
E	edge of finite element mesh
k	polynomial degree of finite element interpolation
$\mathbb{V}^k(\hat{T})$	set of polynomials on d-simplices, d-rectangles, d-wedges of order at most k
$\mathbb{P}^k(\hat{T})$	set of polynomials on d-simplices $\hat{T}$ of order at most k
$\mathbb{Q}^k(\hat{T})$	set of polynomials on d-rectangles $\hat{T}$ of order at most k
$\mathbb{W}^k(\hat{T})$	set of polynomials on d-wedges $\hat{T}$ of order at most k
$\dim$	dimension of finite dimensional space

Terminology and Notation on Extended and Cut Finite Element Spatial Discretizations

$\widehat{\mathcal{T}}_h$	background finite element mesh/triangulation with mesh size parameter h
$\mathcal{T}_h$	active part of cut finite element mesh/triangulation $\widehat{\mathcal{T}}_h$
$\mathcal{T}_\Gamma$	set of finite elements intersected by the interface
$\mathcal{F}_\Gamma$	set of faces adjacent to cut elements in the interface zone
Ω_h^*	fictitious domain
$\mathcal{X}_h$	continuous finite element function space consisting of piecewise polynomials
$\mathcal{X}_h^{\mathrm{dc}}$	discontinuous function space consisting of piecewise polynomials
$()^i$	superscripts indicating association of mesh quantities to subdomain Ω^i
Γ_T	interface within element T
F	face between two elements
T_F^+, T_F^-	two elements which share the face F
f	facet, polygonal segment of a face F or an interface segment of Γ_T
V	volume-cell, polyhedral part of finite element due to intersection
Ω_T	physical volume of element T consisting of sets of polyhedral volume-cells
$\mathcal{N}'$	subset of enriched nodes in the XFEM
s'	enriched node in the XFEM
$\tilde{N}_{s'}$	global enriched basis function for node s' in the XFEM
$\psi_{s'}$	node enrichment function in the XFEM
$\mathcal{I}$	*abs*-enrichment function in the XFEM
$\mathcal{S}$	Heaviside-enrichment function in the XFEM
$\mathcal{X}_h^\Gamma$	extended function space for two subdomains enriched at the interface
$\tilde{\mathcal{X}}_h$	composed discontinuous function space for multidomain problem settings
C	volume-cell connection within the support of a nodal shape function
$\mathcal{C}_s$	set of volume-cell connections C_i around a node s
$\mathrm{numdof}\,(s)$	number of DOFs per node s for a scalar cut function space
$\mathrm{PATH}_C(V, \tilde{V})$	path between $V, \tilde{V}$ consisting of volume-cells $V_i \in C$ and connecting facets f

Function Spaces, Inner Products and Norms

$C^0(U)$	space of continuous functions on U
m	order of function space
$W^{k,p}(U)$	Sobolev space up to order k based on $L^p(U)$-semi-norms on U
$H^m(U)$	standard Sobolev space of order $m \in \mathbb{R}$ on U
$L^2(U)$	Sobolev space of order $m = 0$ on U
$H^{div}(U)$	Sobolev space of L^2-functions on U for which their divergence is in $L^2(U)$
$(\cdot,\cdot)_{m,U}$	inner product associated with $H^m(U)$ defined in a domain U
$\langle\cdot,\cdot\rangle_{m,U}$	inner product associated with $H^m(U)$ defined on a face or an interface U
$(\cdot,\cdot)_U$	inner product associated with $L^2(U)$ defined in a domain U
$\langle\cdot,\cdot\rangle_U$	inner product associated with $L^2(U)$ defined on a face or an interface U
$\lVert\cdot\rVert_{k,p,U}$	norm associated with $W^{k,p}(U)$
$\lVert\cdot\rVert_{m,U}, \lvert\cdot\rvert_{m,U}$	norms and semi-norms associated with $H^m(U)$
$\lVert\cdot\rVert_U$	norm associated with $L^2(U)$
$\lVert\cdot\rVert_{\pm 1/2,h,\Gamma}$	discrete h-scaled semi-norms on $H^{1/2}(\Gamma)$ and $H^{-1/2}(\Gamma)$

Numerical Analysis - Weak Enforcement of Constraints and Oseen's Problem

$\mathscr{B}, \mathscr{B}_h, \mathscr{L}, \mathscr{L}_h$	left- and right-hand sides of continuous/discrete variational formulations
$\mathscr{S}_h$	discrete stabilization operator
f, g	scalar external volumetric loads, Dirichlet boundary data
$\mathscr{V}, \mathscr{V}_{\boldsymbol{g}_\mathrm{D}}, \mathscr{V}_{\mathbf{0}}$	variational trial/test function spaces (including Dirichlet conditions)
$\mathscr{V}_h, \mathscr{V}_{\boldsymbol{g}_\mathrm{D}}, \mathscr{V}_{\mathbf{0}}$	discrete trial/test function spaces (including Dirichlet conditions)
u, u_h, v, v_h	continuous/discrete trial and test functions
$\vert\vert\vert \cdot \vert\vert\vert, \vert\vert\vert \cdot \vert\vert\vert_*$	continuous energy norm w.r.t the domain, discrete energy norm w.r.t the mesh
c_s,C_cons,C_cont	lower bound stability and upper bound consistency/continuity constants
$\partial_{\boldsymbol{n}}^j$	normal derivative of order j
D^j	total derivative of order j
E	extension operator for functions in $W^{k,p}(\Omega)$ to fictitious domain Ω^*
I_h, I_h^*	interpolation operator and its extension into fictitious domain
$\pi_h^*, \boldsymbol{\pi}_h^*, \Pi_h^*$	Clément interpolation operator for scalars, vectors, products
$\mathscr{O}_h$	Oswald interpolation operator
C_P	Poincaré constant
$\boldsymbol{\Phi}_p$	pressure L^2-norm scaling constant
ω_h	norm scaling constant
Λ, Λ_h	continuous and discrete Lagrange-multiplier function space
λ_h, μ_h	trial and test function boundary Lagrange-multiplier
$\vert\vert\vert(\cdot,\cdot)\vert\vert\vert$	triple norm for product space of bulk field and Lagrange multiplier
$h_{\mathscr{V}_h}, h_{\Lambda_h}$	characteristic element lengths of bulk and boundary discretizations $\mathscr{V}_h, \Lambda_h$
$\mathscr{B}_h^\mathrm{BH}, \mathscr{L}_h^\mathrm{BH}$	left- and right-hand side operator for method by Barbosa and Hughes
$\vert\vert\vert \cdot \vert\vert\vert^\mathrm{BH}$	triple norm for method by Barbosa and Hughes
$\mathscr{B}_h^\mathrm{NIT}, \mathscr{L}_h^\mathrm{NIT}$	left- and right-hand side operator for Nitsche's method
$\vert\vert\vert \cdot \vert\vert\vert^\mathrm{NIT}$	triple norm for Nitsche's method
$\mathscr{B}_h^\mathrm{MHS}, \mathscr{L}_h^\mathrm{MHS}$	left- and right-hand side operator for mixed/hybrid stress-based method
$\vert\vert\vert(\cdot,\cdot)\vert\vert\vert^\mathrm{MHS}$	triple norm for mixed/hybrid stress-based method
Σ, Σ_h	continuous/discrete function space for stress-based Lagrange-multiplier
$\boldsymbol{\sigma}_h, \boldsymbol{\tau}_h$	stress-based trial and test function Lagrange-multipliers
$\boldsymbol{U}, \boldsymbol{\Sigma}$	finite-dimensional vectors of nodal values for u_h and $\boldsymbol{\sigma}_h$
$\boldsymbol{K}_{xy}, \boldsymbol{G}_{xy}$	volume/boundary coupling matrices between fields $x, y \in \{\boldsymbol{u}, \boldsymbol{\sigma}\}$ for MHS
Π_h	face-wise L^2-projection
$\delta, \delta_2, \delta_3, n$	stabilization parameters for BH method and MHS method
γ	non-dimensional stabilization parameters for Nitsche's method
C_T	non-dimensional constant resulting from trace inequality
f_T	dimensional scaling function resulting from trace inequality
α	dimensional scaling function for the Nitsche penalty term
ρ_T^max	maximum eigenvalue of generalized eigenvalue problem for estimating f_T^2
ϵ	scaling for Young's inequality
$\vert\vert\vert \cdot \vert\vert\vert$	energy norms according to various methods for weak constraint enforcement
$\kappa(\boldsymbol{A})$	L^2-norm condition number of matrix $\boldsymbol{A}$
$\boldsymbol{v}_h, \boldsymbol{V}, v_s$	discrete function, finite-dimensional vector of nodal values, nodal values

Time Discretization

t, T_0, T_i, T	time, initial time, intermediate time levels, final time
Δt	time-step length
t^n	discrete time levels for time stepping
J^n	time interval $(t^{n-1}, t^n]$
$()^n, ()^{n-1}, ()^{n-2}$	superscripts indicating current and previous time levels
$()^{n-\alpha_f}, ()^{n-\alpha_m}$	generalized mid-point quantities in generalized-α scheme
$\gamma, \beta, \alpha_f, \alpha_m, \rho_\infty$	parameters for generalized-α time-stepping scheme
θ	parameter for one-step-θ time-stepping scheme
N	number of discrete time intervals
$\sigma, \sigma_\theta, \sigma_{\mathrm{BDF2}}$	pseudo-reaction scalings resulting from discretizing time derivatives
$H, H_\theta, H_{\mathrm{BDF2}}$	operator comprising history terms of discrete form of previous time levels
Υ	test function operator for discrete time derivative
F	operator comprising right-hand side of variational formulation in ODE form
$\mathcal{V}^n, \mathcal{Q}^n, \mathcal{W}^n$	function spaces for velocity and pressure and its product space at t^n
$\mathcal{X}_h^n, \mathcal{V}_h^n, \mathcal{Q}_h^n, \mathcal{W}_h^n$	discrete cut finite element function spaces associated with discrete time t^n
$\boldsymbol{u}_h^n, p_h^n, \boldsymbol{a}_h^n$	discrete time-level approximations on velocity, pressure, acceleration at t^n
$\tilde{\boldsymbol{u}}_h^{n-1}, \tilde{p}_h^{n-1}, \tilde{\boldsymbol{a}}_h^{n-1}$	projected approximations between discrete function spaces from t^{n-1} to t^n
$\boldsymbol{P}^n$	projection operator between function spaces of different time levels t^{n-1}, t^n
$\boldsymbol{E}^*$	extension operator for newly activated ghost-DOFs
$\mathcal{E}_h^n$	face-jump penalty-based operator for linear extension system at t^n
$\bar{\mathcal{X}}_h^n, \bar{\mathcal{X}}_{h,0}^n$	discrete trial/test function space for extension systems at t^n
u_Γ	interface normal velocity

Dimensionless Quantities

Re	Reynolds number
Re_T	element Reynolds number
Re_τ	wall Reynolds number
Co	Courant number
Co_T	element Courant number
At	Atwood number
CFL	Courant–Friedrichs–Lewy number

Fluid - Governing Equations and Variational Formulation

$(\cdot)^{\mathrm{f}}$	superscript denoting fluid quantity
ρ	density of fluid
ν, μ	kinematic and dynamic viscosity of fluid
$\boldsymbol{\sigma}, \boldsymbol{\sigma}(\boldsymbol{u}, p)$	Cauchy stress tensor
$\boldsymbol{\tau}$	symmetric deviatoric viscous stress part of Cauchy stress tensor
$\boldsymbol{\epsilon}$	symmetric strain rate tensor
$\boldsymbol{u}, \boldsymbol{u}_h$	fluid velocity and discrete finite element approximation
p, p_h	dynamic fluid pressure and discrete finite element approximation
U_h, V_h	product of velocity and pressure solution or test functions
$\boldsymbol{c}$	relative convective velocity
$\hat{\boldsymbol{u}}$	grid velocity
$\mathscr{A}, \mathscr{L}, \mathscr{A}_h, \mathscr{L}_h$	left- and right-hand sides of continuous/discrete variational formulations
c, a, b, c_h, a_h, b_h	continuous/discrete operators comprising terms of variational formulations
l, l_h	right-hand side linear forms including loads and Neumann terms
$\boldsymbol{u}_0$	initial condition for transient initial boundary value problems
$\boldsymbol{g}_{\mathrm{D}}, \boldsymbol{g}_{\mathrm{D}}^i$	Dirichlet boundary data for velocity field (for fluid phase i)
$\boldsymbol{h}_{\mathrm{N}}, \boldsymbol{h}_{\mathrm{N}}^i$	Neumann boundary data (for fluid phase i)
$\boldsymbol{f}$	external body force load acting on fluid volume
$\mathcal{V}, \mathcal{V}_{\boldsymbol{g}_{\mathrm{D}}}, \mathcal{V}_{\mathbf{0}}$	trial/test function spaces for velocity (including Dirichlet conditions)
$\mathcal{Q}$	trial/test function space for pressure
$\mathcal{W}, \mathcal{W}_{\boldsymbol{g}_{\mathrm{D}}}, \mathcal{W}_{\mathbf{0}}$	trial/test velocity-pressure product spaces (including Dirichlet conditions)
$\mathcal{V}_h$,$\mathcal{V}_{h,\boldsymbol{g}_{\mathrm{D}}}$,$\mathcal{V}_{h,\mathbf{0}}$	discrete trial/test function spaces for velocity
$\mathcal{Q}_h$	discrete trial/test function space for pressure
$\mathcal{W}_h$,$\mathcal{W}_{h,\boldsymbol{g}_{\mathrm{D}}}$,$\mathcal{W}_{h,\mathbf{0}}$	discrete trial/test velocity-pressure product spaces

Coupled Flow Problems

M	mass flow rate across interfaces
$\boldsymbol{n}^{ij}, \boldsymbol{t}_r^{ij}$	interface normal/tangential unit vectors
u_Γ	interface velocity in its normal direction
$\boldsymbol{g}_\Gamma^{ij}, \boldsymbol{h}_\Gamma^{ij}$	abstract jump conditions for interface velocities and tractions
κ	interface curvature
ι_{st}	surface-tension coefficient for two-phase flows
s_{L}	laminar flame speed for premixed combustion
$\mathscr{A}_h^{X_i}, \mathscr{L}_h^{X_i}$	left- and right-hand sides of discrete subdomain fluid formulations
$\mathscr{C}_h^{ij}, \mathscr{L}_h^{ij}$	left- and right-hand sides of Nitsche-type coupling terms
φ	scaling function for average weights
γ_{upw}	upwinding stabilization parameter
l	number of fluid subdomains

Fluid - Stabilized Formulations

$\boldsymbol{u}_h^{\text{sgs}}, p_h^{\text{sgs}}$	velocity and pressure sub-grid scale components for RBVM method
$\boldsymbol{r}_{\text{M}}, r_{\text{C}}$	linear momentum/incompressibility strong residual part for RBVM method
$\tau_{\text{M}}, \tau_{\text{C}}$	SUPG/PSPG and LSIC stabilization scaling functions for RBVM method
$\boldsymbol{G}$	second rank covariant metric tensor for RBVM method
C_I	inverse estimate constant for RBVM method
c_h, a_h, b_h	discrete stabilized operators comprising terms of Nitsche formulation
l_h	right-hand side linear forms including loads and Neumann terms
$\mathscr{A}_h^{\text{RBVM}}, \mathscr{L}_h^{\text{RBVM}}$	left- and right-hand sides of discrete RBVM fluid formulation
$\boldsymbol{\beta}, \boldsymbol{\beta}^*, \boldsymbol{\beta}_h$	advective velocity, its extension and discrete interpolated counterpart
$\boldsymbol{n}_F, \boldsymbol{t}_i$	unit normal vector and orthonormal tangential vectors on inter-element faces
$\mathscr{A}_h^{\text{CIP}}$,$\mathscr{L}_h^{\text{CIP}}$	left- and right-hand sides of discrete CIP fluid formulation
$\mathscr{S}_h^{CIP}$	comprised CIP fluid stabilization operator
s_β, s_u, s_p	CIP operators for streamline derivative, incompressibility and pressure
$\underset{\sim}{\phi}_\beta, \underset{\sim}{\phi}_u, \underset{\sim}{\phi}_p$	element-wise scaling functions for CIP/GP stabilizations
$\tilde{\phi}_\beta, \tilde{\phi}_u, \tilde{\phi}_p$	smoothed stabilization parameter scaling functions for CIP/GP stabilizations
$\gamma_\beta, \gamma_u, \gamma_p$	non-dimensional stabilization parameters for CIP/GP stabilizations
ϕ, c_ν, c_σ	scalings and constants for weighting different regimes in CIP/GP method
$g, \tilde{g}$	face-jump-based and L^2-projection-based ghost-penalty stabilizations
γ_g	dimensionless ghost-penalty-stabilization parameter
π_P, P	patch-wise L^2-projection and patches for projection-based ghost penalties
$\mathscr{G}_h, \mathscr{G}_h^{\text{GP}}$	comprised GP stabilization operator
$\alpha, \alpha_\nu, \alpha_u$	different Nitsche penalty term scaling functions
$\gamma_\nu, \gamma_\sigma$	dimensionless stabilization parameter for viscous/reactive ghost penalties
g_β, g_u, g_p	CIP related GP operators
g_ν, g_p	viscous and (pseudo-)reactive GP operators
$\mathscr{A}_h^{\text{CIP,GP}}$	left-hand side of discrete CIP/GP-CutFEM fluid formulation
$\mathscr{L}_h^{\text{CIP,GP}}$	right-hand side of discrete CIP/GP-CutFEM fluid formulation
$\mathscr{A}_h^{\text{RBVM,GP}}$	left-hand side of discrete RBVM/GP-CutFEM fluid formulation
$\mathscr{L}_h^{\text{RBVM,GP}}$	right-hand side of discrete RBVM/GP-CutFEM fluid formulation

Solid - Governing Equations and Variational Formulation

$(\cdot)^{\mathrm{s}}$	superscript denoting solid quantity
$\rho^{\mathrm{s}}, \rho^0_{\boldsymbol{X}}$	material density of structure defined in initial referential configuration
$\boldsymbol{d}, \boldsymbol{d}_h$	displacement field and discrete approximation
$\boldsymbol{u}, \boldsymbol{u}_h$	velocity field and discrete approximation
$\boldsymbol{a}, \boldsymbol{a}_h$	acceleration field and discrete approximation
D_h, W_h	product of discrete displacement and velocity solution or test functions
$\boldsymbol{F}$	deformation gradient tensor
$J_{\boldsymbol{X}\mapsto\boldsymbol{x}}$	determinant of deformation gradient tensor
$\boldsymbol{R}, \boldsymbol{U}$	rigid body rotation and stretch part of polar decomposition of $\boldsymbol{F}$
$\boldsymbol{C}$	symmetric right Cauchy-Green tensor
$\boldsymbol{E}$	Green-Lagrange strain tensor
$\boldsymbol{P}$	non-symmetric first Piola–Kirchhoff stress tensor
$\boldsymbol{S}$	symmetric second Piola–Kirchhoff stress tensor
$\Psi, \tilde{\Psi}$	strain-energy function depending on $\boldsymbol{E}$ and $\boldsymbol{C}$
$\lambda^{\mathrm{s}}, \mu^{\mathrm{s}}$	Lamé parameters
$E^{\mathrm{s}}, \nu^{\mathrm{s}}$	Young's modulus and Poisson's ratio
$\boldsymbol{f}$	external body force load acting on structural volume
$\boldsymbol{g}_{\mathrm{D}}, \boldsymbol{g}^i_{\mathrm{D}}$	Dirichlet boundary data for displacement field (for body i)
$\boldsymbol{h}_{\mathrm{N}}, \boldsymbol{h}^i_{\mathrm{N}}$	Neumann boundary data (for body i)
$\boldsymbol{d}_0, \dot{\boldsymbol{d}}_0$	initial conditions for displacement and velocity
$\mathscr{A}, \mathscr{L}, \mathscr{A}_h, \mathscr{L}_h$	left- and right-hand sides of continuous/discrete variational formulations
a, a_h	continuous/discrete operators comprising terms of variational formulations
l, l_h	right-hand side linear forms including loads and Neumann terms
$\mathscr{D}_{\boldsymbol{g}_{\mathrm{D}}}, \mathscr{D}_{\boldsymbol{0}}$	trial/test function spaces for displacement (including Dirichlet conditions)
$\mathscr{L}$	trial/test function spaces for velocity
$\mathscr{W}$	product space of discrete displacements and velocities
$\mathscr{D}_{h,\boldsymbol{g}_{\mathrm{D}}}, \mathscr{D}_{h,\boldsymbol{0}}$	discrete trial/test function spaces for displacements
$\mathscr{L}_h$	discrete trial/test function space for velocities
$\mathscr{W}_{h,\boldsymbol{g}_{\mathrm{D}}}, \mathscr{W}_{h,\boldsymbol{0}}$	trial/test product function space of discrete displacements and velocities
$\boldsymbol{D}, \boldsymbol{U}, \boldsymbol{A}$	vectors of nodal values for displacement, velocity and acceleration
$\boldsymbol{M}, \boldsymbol{F}_{\mathrm{int}}, \boldsymbol{F}_{\mathrm{ext}}$	mass matrix, internal and external force vectors
$\boldsymbol{C}, c_M, c_K$	Rayleigh-damping matrix, linear scaling parameters

Fluid-Structure Interaction

$\Omega^{\mathrm{s}}, \Omega_h^{\mathrm{s}}$	solid domain and discrete approximation
$\Omega^{\mathrm{f}}, \Omega_h^{\mathrm{f}}, \Omega_h^{\mathrm{f}*}$	fluid domain, discrete approximation and fictitious fluid domain
$\mathscr{A}_h^{\mathrm{f}}, \mathscr{A}_h^{\mathrm{s}}, \mathscr{L}_h^{\mathrm{f}}, \mathscr{L}_h^{\mathrm{s}}$	operators comprising discrete formulations for fluids and structures
$\mathscr{C}_h^{\mathrm{fs}}$	Nitsche-coupling terms at fluid-structure interface
$\boldsymbol{R}^{\mathrm{f}}, \boldsymbol{R}^{\mathrm{s}}$	fluid and structural non-linear residuals without interface terms
$\boldsymbol{H}^{\mathrm{f}}, \boldsymbol{H}^{\mathrm{s}}$	history terms occurring in fluid and structural residuals
$\boldsymbol{F}^{\mathrm{f}}, \boldsymbol{F}^{\mathrm{s}}$	boundary and interfacial force terms on fluid and structural side
$\boldsymbol{C}^{\mathrm{fs}}, \boldsymbol{C}^{\mathrm{sf}}$	matrix notation of Nitsche-coupling terms for fluid and structural blocks
$\boldsymbol{R}^{\mathrm{fs}}$	global non-linear residual for coupled fluid-structure system
$\boldsymbol{R}_U, \boldsymbol{R}_P, \boldsymbol{R}_D$	residual blocks for fluid velocity and pressure and structural displacements
$\boldsymbol{L}^{\mathrm{fs}}$	global system matrix resulting from (pseudo-)linearization of FSI residual
$\boldsymbol{L}_{xy}$	(pseudo-)linearization of residual $\boldsymbol{R}_x$ with respect to vector y
$\boldsymbol{U}_\Gamma$	structural interface velocity

Numerical Examples

$c_{\mathrm{lift}}, c_{\mathrm{drag}}$	lift and drag coefficients
Δp	pressure difference
$(\cdot)^{\max}$	maximum value
$(\cdot)^{\min}$	minimum value
$(\cdot)_{\mathrm{in}}$	inflow quantity
$(\cdot)_{\mathrm{eff}}$	effective quantity
$(\cdot)^{\mathrm{mean}}$	mean value
$\boldsymbol{f}_l^{\mathrm{s}}$	nodal forces at structural node l
H, B	height, thickness
$\boldsymbol{R}, \vartheta, \omega$	rotation matrix, rotation angle, angular velocity
d	diameter
r	radius
a_0, a	(initial) amplitude
α^*, α	(non-dimensioned) growth rate
k^*, k	(non-dimensioned) wave number
Ψ	stream-function
$\boldsymbol{u}^{\mathrm{vort}}$	vortex induced velocity

Abbreviations

ALE	Arbitrary Lagrangean–Eulerian
AMG	Algebraic MultiGrid
BACI	Bavarian Advanced Computational Initiative
BB	Babuška–Brezzi
BDF	Backward Differentiation Formula
BH	Barbosa–Hughes
CAD	Computer-Aided Design
CIP	Continuous Interior Penalty
CUTFEM	Cut Finite Element Method
DD	Domain Decomposition
DFS	Depth-First-Search
DG	Discontinuous Galerkin
DNS	Direct Numerical Simulation
DOF	Degree Of Freedom
FEM	Finite Element Method
FSI	Fluid-Structure Interaction
GFEM	Generalized Finite Element Method
GMR	Generalized Mid-point Rule
GMRES	Generalized Minimal RESidual
GP	Ghost Penalty
GTR	Generalized Trapezoidal Rule
IB	Immersed Boundary method
IBVP	Initial Boundary Value Problem
LSIC	Least-Squares Incompressibility Constraint
MHS	Mixed/Hybrid Stress-based method
NH	Neo-Hookean
NIT	NITsche's method
ODE	Ordinary Differential Equation
OST	One-Step-Theta
PDE	Partial Differential Equation
PUFEM	Partition of Unity Finite Element Method
PUM	Partition of Unity Method
PSPG	Pressure-Stabilizing/Petrov–Galerkin
RBVM	Residual-Based Variational Multiscale
SGFEM	Stable Generalized Finite Element Method
SUPG	Streamline Upwind/Petrov–Galerkin
SVK	Saint Venant–Kirchhoff
XFEM	eXtended Finite Element Method

Chapter 1

Introduction

Physical phenomena which are dominated by fluids and structures in motion have always fascinated mankind. A glance into nature shows the greatest variety of complex interactions between liquids, gases and solids. Continuous materials, which naturally occur, range from viscous slow-moving liquids to chaotic and highly turbulent flows of gases and from rigid bodies to highly compressible and largely non-linearly deforming structural materials. Now, as ever, humans try to reproduce and realize what the laboratories of nature have already done over thousands of years. Observing and studying the environment build the basis to acquire new levels of knowledge and experience. For instance, the impressive ability of birds to fly through the air or of fishes to perform elegant and fast swim maneuvers in the water excited people to attempt constructing aircrafts and hot air balloons or boats and sailing vessels - technical inventions that later made a great advance in mobility.

1.1 Motivation

Interfacial mutual interactions of different gas, liquid and solid phases are omnipresent phenomena in nature and science and cover a wide range of multiphysics problems in continuum mechanics. To a large extent urged on the ongoing technological development in science and engineering, the necessity for a profound understanding of complex coupled flow problems highly increased in the last century. Fluid dynamics in general find a huge field of relevant applications in different scientific fields like engineering, geophysics, astrophysics, meteorology or medicine. Even if the investigation of isolated single-phase flows already enables to grasp a large amount of transport phenomena, most if not all physical flow phenomena require to take interactions with other involved phases into account.

Gas-liquid combinations, which are very often air-water systems and exhibit a large contrast in the physical parameters like density and viscosity, play an important role in meteorology for predicting the formation of clouds and a reliable weather forecast. Air-water interactions occur also for falling raindrops, the formation of water droplets owing to condensation and for rising bubbles in surrounding liquid columns. These often come along with capillary and surface-tension effects at the separating phase boundaries. Moreover, the formation of ocean waves, water sloshing or combustion of liquids are examples for gas-liquid interactions in nature.

In engineering, such phenomena are of great importance in the development of, for example, pipeline systems for oil-gas mixtures, boilers, condensers, air-conditioning and refrigeration plants, ink-jet printers or spin-stabilization of satellites in orbit, to name just a few. An example for liquid-liquid interaction in nature is the tremendous impact of oil spill extent after oil-platform or oil-tanker accidents.

The range of interface-coupled multiphysics flow phenomena present in nature and science highly widens when considering occurrences of gas-solid and liquid-solid combinations. Both phenomena are summarized under the term fluid-structure interaction (FSI). Examples of frequent prevalences in nature, which are known to everyone, are leaves of a deciduous tree floating in the wind, a flag fluttering in the wind or slender branches floating down a stream. In general, FSI is often designated as one-sided, if fluid flow dominates the structural motion whose response to the flow is low resulting in a stable behavior. This is mostly the case if the structural material is relatively stiff and flow can be characterized by a low Reynolds number. In contrast, if the flow highly excites the structural body such that it largely deforms or even vibrates, this, in return, can strongly impact the flow pattern in the sense of an oscillatory FSI. Such mutual interactions between fluids, gases and solids have a ubiquitous presence in nature and, particularly, find widespread applications in science and engineering.

Whether by land, sea or air, FSI plays a decisive role in aero- or hydrodynamics of most vehicles. Tire hydroplaning or aerodynamic fluttering of flexible components in the automotive sector, the flow-induced vibration of airplane wings or the drag acting on vessels are important aspects which need to be well understood to allow for continuous advancements and optimization. Interactions of fluids with rotating structural components gained great attention, as they occur in rotating turbine blades of jet aircraft engines or propellers, the rotor system and engines of helicopters and vessels. A further important application area for such types of fluid-structure interaction is given by the energy sector. In the field of renewable energies, electricity can be extracted from rotating turbines of wind power plants and hydroelectric power stations, which are driven by wind or falling water. Further potential applications in industrial engineering are pumps, seals, flaps, membrane valves or hydromounts. Many of these are not dominated by only two interacting phases, but rather define even three- or multifield problems incorporating several gas, liquid and solid phases. As such examples, one could think about oil and gas pipelines where there might be a significant fraction of solids or swimming structures, like sailing boats, which mutually interact with air and water simultaneously.

For a very long period of time, the investigation of such complex interface coupled multiphysics phenomena mainly relied on comprehensive experimentation or prototyping. Owing to the rapid advances in computer technology, the enormous increase in computing capacity and further enhancements of complex numerical algorithms, the development of computational approaches towards the simulation of such phenomena has become an important research field in science and engineering. Computational modeling of complex effects allows for faster and more cost-effective developments of engineering products. Moreover, due to the complexity of multiphysics and the expense of setups, experiments on interactions are limited and reliable predictions of the studied behavior often fail. Computational approaches are thus often superior and allow for more effective investigations and more accurate analyses of physical or calculated quantities of interest.

Moreover, the advantages of simulation tools go much beyond the aspect of cost-effectiveness. Over the recent years, computational modelings reap significant benefits in fields of environment protection and medicine, two of the probably most important research fields for humankind. As

an example, modeling of so-called biofilms became an active research area [28, 29, 96, 204]. Focus is thereby directed to get a deeper understanding of their macro-scale dynamics to allow for reliable predictions of their interaction with surrounding flow environments [77, 242, 249, 250]. Biofilm structures are communities of microorganisms surrounded by an extracellular self-secreted polymer matrix. Their formation is desirable in some applications, while being completely penalizing in other cases. Great success has been already achieved in the targeted use of biofilms to aid improving the biological treatment of wastewater. This allows to make effective steps to save water - one of the most important natural resources on this planet. In contrast, biofilms are also involved in a wide variety of microbial infections in the human body [92, 238]. They can cause venous catheter infections, middle-ear infections and the formation of dental plaque. Besides delayed wound healing, their growth can even result in lethal processes such as infective endocarditis and infections of permanent indwelling devices such as joint prostheses or heart valves. One of the major aims of applying advanced computational models for FSI is to study short- and long-time consequences without the need of performing often ethically questionable experiments, which could damage the sensitive natural environment or even cause the loss of human life. The use of computational modeling for advanced multiphysics applications involving FSI is of greatest interest for research in medicine and the development of medical devices [83, 169]. A deep understanding of blood flow through veins or the human heart including the opening and closing of valves as the heart contracts and relaxes are important for the development of stents and prosthetic heart valves. An active research field is the computational prediction of the rupture risk for so-called abdominal aortic aneurysms [177, 251], which are among the most common causes of death in western countries. Strokes can be most often traced back to the rupture of an atherosclerotic plaque in the carotid bifurcation, which provides a further application area for FSI. First attempts have been even made on research on the respiratory system [261, 269, 273]. The huge impact of computational FSI offers a better understanding of respiratory mechanics and in that way can contribute to protect human health and save lives in future.

This overview shows a great variety of different research areas which require deeper understandings of multiphysics in which different gas, fluid and solid phases mutually interact and thereby exhibit complex and highly dynamic behavior. Most of these physical relevant phenomena can be modeled by coupled non-linear governing partial differential equations (PDEs), which are defined on the variety of mentioned complex geometries. A powerful framework for the computational approximation of the topologies and the respective solution fields is provided by the finite element method (FEM). Its ability to simulate single-phase problems and selected coupled problems has been impressively demonstrated over the recent decades. Nowadays, the rapidly increasing complexity of multiphysics configurations, however, takes them often to the limit of their capabilities. Most severe limitations arise from their inability to deal with topological changes of the computational geometry as omnipresent in many of the above-mentioned applications. For instance, breaking up and merging of fluid and gas phases or contacting and detachment processes of solid phases are challenging situations computational approaches are currently faced with. Moreover, now and in future, novel computational methods need to be able to flexibly combine different approximation techniques, which are best-suited for the respective single phases.

A powerful discretization technique, which provides an extension of classical finite element approaches to deal with such shortcomings, are so-called geometrically unfitted finite element

methods. These rely on the fundamental idea of choosing FEM-based approximations of the physical fields independently of, or more precisely, unfitted to the actual physical geometry. Cutting-off finite elements and their associated discrete approximations at boundaries and interfaces gives rise for the naming cut finite element method (CUTFEM) [63]. It needs to be pointed out, that this computational technology has its origin in the famous extended finite element method (XFEM) [21, 188] - two designations which are often used as synonyms owing to their close relation. Even though their high capabilities have been already demonstrated by means of highly complex multiphysics applications, with certain respects these methods are still in their infancy. In fact, many computational algorithms based on these methodologies exhibit severe fundamental issues. Their elucidation and further advancements with regard to fundamental properties of numerical stability and their application to complex interface coupled flow problems constitute the major objective of the present thesis.

1.2 Research Objectives and Accomplishments

The overall objective of this thesis lies in the substantial improvement of cut/extended finite element methods existing so far with regard to a multitude of various aspects. Emphasis is put on single-phase flow as well as on coupled multiphysics flow problems, even though in certain respects the actual physics plays only a subordinate role rather than the type of partial differential equation (PDE) to be approximated. Resuming the previous elaborations, incompressible flows especially as part of multiphysics interactions show an enormous complexity from a physical point view and, moreover, exhibit a multitude of characteristic numerical issues which need to be dealt with. Besides their undisputed importance, such multiphysics are perfectly suited to demonstrate methodological refinements and developments.

1.2.1 Specification of Requirements

In a large number of earlier works on related topics preceding this thesis, it was indicated that, to a large extent, it is crucial to strike new paths to make further progress in the applicability of geometrically unfitted finite element methods to advanced problem settings. Most restrictive limitations and unresolved issues so far, which need to be lifted, are summarized next.

Accuracy of Cut Finite Element Approximations. Geometrically unfitted cut finite element methods feature an extreme variability of potential discretization concepts. Mainly the fact of approximating geometry independent from computational meshes and associated solution approximations allows for a multitude of novel computational approaches. In particular their maintenance of applicability in topologically challenging scenarios, that is largely changing and deforming physical domains including topological changes, renders this computational framework highly attractive. Accurate solution approximations based on the underlying computational grid are crucial for their practical applicability. As one of the major issues of most enrichment strategies available for extended finite element methods so far, a lack of representability of solutions for high curvature interfaces has been pointed out, e.g., in the work by Henke [147]. Due to the rapidly increasing complexity of multiphysics problem settings, generalizations and refinements of intersection-based approximation techniques are essential.

Numerical Stability and Optimality Requirements. Over the last decade, the framework of cut finite element methods gained great attention and a multitude of applications to complex multiphysics problems have been developed. However, due to the major emphasis on complex application fields, the fundamental development of robust and accurate unfitted schemes was given scant consideration, even though severe issues have been frequently observed and reported in literature. Two major challenges could be identified: First, due to the intersection of finite elements and integration of variational formulations on the actual physical geometry, resulting finite-dimensional systems exhibit severe conditioning issues rendering in almost singular linearized matrix systems and, as a result, in poor solution accuracy and deteriorated linear iterative solver efficiency. Second, numerical accuracy and stability behavior of most existing formulations show severe dependencies on the boundary/interface location within computational meshes. In particular for highly sensitive applications like incompressible flows, this lack of robustness significantly decreases performance of such algorithms. Concerning weak constraint enforcement of boundary and coupling conditions, even though being well-suited for some interface-fitted discretizations, Lagrange-multiplier-based mortar methods (see, e.g., Popp [209] and Béchet *et al.* [18]) lost importance caused by strong difficulties to ensure inf-sup stability. Even many stabilized approaches like mixed/hybrid stress-based Lagrange-multiplier methods (see, e.g., Gerstenberger [123]) or straightforward attempts of the usage of the Nitsche method [196] lack optimality or even stability in topologically pathological situations. From a numerical point of view, fundamental requirements of guaranteeing inf-sup stability and establishing *a priori* error estimates, which are crucial for all computational approaches, require further consideration. Techniques for the weak constraint enforcement and for sufficiently controlling solutions in the vicinity of the interface are of greatest importance. Fundamentals for these research objectives have been laid by the development of so-called *ghost-penalty* stabilizations (see the pioneering works by Burman [50] and Burman and Hansbo [44, 45, 60]) which in combination with Nitsche's method constitute the theoretical basis for all computational approaches proposed throughout this thesis.

Suitability for Interface Coupled Flow Problems. Unfitted finite element methods have demonstrated their high capabilities for single-phase flows and particularly for important challenging interface coupled flow problems. Over the recent years, many different computational approaches have been developed towards different applications, however, many of them exhibit severe issues with regard to robustness of the interface couplings. Depending on involved physics in each subdomain and their numerical resolution, different aspects are crucial for the performance of such methodologies and require adaption and refinement to obtain optimal suitability for different settings. Specific requirements which are of great importance for different flow problems are discussed below.

Single-phase flows: Approximating single-phase flows on geometries, whose boundaries are unfitted to the mesh, demand stabilization techniques to account for different sources of numerical instabilities. Due to the unfittedness, Dirichlet boundary conditions need to be enforced weakly. Nitsche-type techniques, as exclusively used throughout this thesis, require specific adaption to account for accurate constraint enforcement in low- and high-Reynolds-number flows and to thereby guarantee inf-sup stability and retain optimality of the approximation independent of the interface location. Moreover, three well-known fluid instabilities need to be controlled

for continuous Galerkin approximations and require specific adaption in the boundary zone: Convective effects need to be controlled, inf-sup stability is to be guaranteed due to the use of equal-order approximations for velocity and pressure and further control on the incompressibility is crucial for highly convective flows.

Extensibility to Single-Phase Domain Decomposition: The capability of unfitted domain decomposition techniques for single fluid phases has been indicated in a first work by Shahmiri *et al.* [236] on an overlapping mesh technique applied to mainly laminar viscous flows. Its significance for the development of novel approaches towards fluid-structure interaction has been demonstrated by Shahmiri [235]. Nevertheless, if the flow in the vicinity of the interface is characterized by convective mass transport across the interface or even turbulence occurs, the interface coupling demands further adaption. Different applicable techniques to establish further control on the coupling are drawn in the framework of Discontinuous Galerkin (DG) methods (see, e.g., works by Di Pietro and Ern [85]). Moreover, focus needs to be turned to the development of methods which allow to retain stability and optimality properties if meshes with highly different resolutions are coupled at interfaces. This is crucial to fully exploit the high capability of domain decomposition.

Coupling of Fluids with High Material Contrast. Highly different material properties in two-phase flows often cause further difficulties for interface coupling methods. Weak constraint enforcement appeals with considerable advantages in numerically under-resolved regions, as the case, for instance, in turbulent flows (see, e.g., works by Burman and Zunino [61], Burman and Zunino [62] and Bazilevs and Hughes [15]). Accuracy in the vicinity of boundaries and interfaces gets improved when weakening the constraint enforcement. This way, spurious oscillations as often arising from strong enforcement techniques can be avoided, while the strength of imposition can be automatically regularized depending on the resolution of physical effects measured in terms of density, viscosity and the characteristic element size. Guaranteeing these requirements uniformly, that is, independent of the intersection of the mesh, can be achieved by specific flux averaging strategies for Nitsche's method, supported by individual sets of ghost-penalty operators for all involved fluid phases. Such techniques will be theoretically discussed in this work.

Interaction of Fluids and Solids. Unfitted XFEM-based approaches for fluid-structure interaction have been originally considered in works by Gerstenberger and Wall (see, e.g., in [124]). This promising discretization strategy gave rise to many further developments on unfitted finite-element based FSI methodologies. Recent developments have been made by, e.g., Burman and Fernández [58] and Alauzet *et al.* [1]. One of the major difficulties consists in developing robust couplings for a large variety of material combinations consisting of viscous or convective flows with almost rigid or strongly compressible structures incorporating non-linear constitutive relations. Moreover, the need for different temporal discretizations of the distinct physical fields demands further consideration. Another issue arises from the strong non-linearities in fluid and solid fields. These put high demands on the non-linear solution techniques and on the robustness of the coupling over time. Refinements of previously mentioned approaches to highly convective flows in three spatial dimensions require robust geometric treatment of the mesh intersection and efficient solution techniques of the full-implicitly coupled systems as well as implementations of algorithms in a fully parallelized code framework.

Requirements regarding Treatment of Moving and Topologically Changing Domains. As indicated by the aforementioned coupled multiphysics flow problems, the development of unfitted computational approaches aims at their application to problems in which domains largely deform and are allowed to topologically change. Moreover, even if approaches indicate spatial robustness, its full evidence is constituted for problems in which physical domains are subjected to large changes over time. For such purposes, different methodologies have been investigated (see, e.g., works by Fries and Zilian [117], Codina *et al.* [76], Henke *et al.* [148], Zunino [279]). Nevertheless, to the best of the author's knowledge, all of these methods are limited to first-order accuracy in time. Major issues arise from the use of finite-difference based temporal time stepping schemes. Higher-order approximations could be achieved, for instance, by the use of very costly discontinuous space-time approximations (see, e.g., a recent work by Lehrenfeld [174]). This topic is of active current research and raises many outstanding issues as will be elaborated throughout this work. However, the development of satisfactory higher-order accurate solution strategies goes beyond the scope of this thesis. Moreover, a full-implicit coupling of non-linear multiphysics problems arise further issues with respect to the use of changing unfitted approximation spaces within non-linear solution procedures. Its necessity, in particular for fluid-structure interaction and more advanced application fields of fluid-structure-contact interaction or fluid-structure-fracture interaction (as addressed in parts by Mayer *et al.* [184] and Sudhakar [244]), is undisputed and needs further consideration.

Flexibility and Extensibility to Multiphysics Applications. Requirements which go beyond the theoretical development of computational methods and algorithms consist in their implementation in a flexible and efficient code environment. Particularly the framework of unfitted methods and their versatility with regard to combinations with other fitted or unfitted approximations, which are best-suited for the respective single-fields, enables to develop powerful coupled multiphysics solvers. Such algorithms demand efficiency and flexibility in the computational set-up of such problem settings. Highest flexibility with regard to combinability of approximations for several fluid phases and structural bodies, the ability to incorporate domain decomposition techniques and enabling the usage of unfitted boundaries within one implementation framework are desirable aspects. These would allow to fully exploit the advantages of geometrically unfitted discretizations.

1.2.2 Contribution of this Work

The present Ph.D. thesis summarizes scientific results accomplished within the project "Interdisciplinary Modeling of Biofilms"[1] of the International Graduate School for Science and Engineering (IGSSE) at the Institute for Computational Mechanics headed by Prof. Dr.-Ing. Wolfgang A. Wall of the Technical University of Munich. Some aspects with regard to numerical analysis of computational approaches proposed in this work have been achieved in collaboration with Ph.D. André Massing during a three month research stay at the Center for Biomedical Computing headed by Ph.D. Marie E. Rognes hosted by Simula Research Laboratory in Oslo, Norway.

[1] Support via the International Graduate School for Science and Engineering (IGSSE) of the Technical University of Munich (TUM) is gratefully acknowledged.

Concerning the previously elaborated requirements on future cut/extended finite element methods and unfitted discretization concepts for coupled multiphysics applications, the following major scientific contributions of the present thesis can be summarized:

A Face-Oriented Stabilized XFEM Approach for Incompressible Navier-Stokes Equations: This approach (see Schott and Wall [230]) constitutes, to the best of the authors' knowledge, the first stable extended finite-element-based computational approach for the simulation of low- and higher-Reynolds-number single-phase flows governed by the non-linear incompressible Navier-Stokes equations. It utilizes a Nitsche-type method for the weak enforcement of boundary conditions and so-called continuous interior penalty (CIP) stabilizations to counteract instabilities in the interior of the fluid domain (see Burman *et al.* [48]). To overcome issues of ill-conditioning due to bad intersections of finite elements and to stabilize fluid and pressure solutions in the vicinity of the boundary, the technique of so-called ghost-penalty (GP) stabilizations (see Burman and Hansbo [60]) has been expanded to the incompressible Navier-Stokes equations. Comprehensive numerical studies show optimal error convergence and demonstrate the superiority of this novel methodology in the vast field of unfitted finite-element-based approaches for flow problems existing so far. The main outcomes can be summarized as follows: A substantial improvement of accuracy and system conditioning has been achieved. The approach exhibits optimal error convergence behavior and highly reduced sensitivity with respect to the positioning of the boundary. Stability for low- and high-Reynolds-number flows in two- and three spatial dimensions can be guaranteed. Moreover, a generalized framework for setting up cut finite element approximation spaces has been developed to overcome the issue with low representability of solutions in domains which exhibit high curvature boundaries or interfaces.

A Stabilized Nitsche Cut Finite Element Method for the Oseen Problem: The previously introduced approach is proven to be inf-sup stable and allows to establish optimal *a priori* error estimates in an energy norm for a linearized auxiliary problem governed by the so-called Oseen equations (see Massing *et al.* [183]). All stability and error estimates hold uniformly, that is, independent of the positioning of the boundary within the computational mesh. A substantial contribution compared to earlier related numerical analyses (see Burman *et al.* [48]), constitutes in the extension of a CIP-stabilized Nitsche-type method to geometrically unfitted approximations by incorporating a set of ghost-penalty operators for velocity and pressure in the vicinity of the boundary. The proposed analysis provides a novel framework for ghost-penalty stabilizations involving non-constant coefficients. Moreover, the ghost-penalty technique guarantees stability and optimality also for higher-order spatial approximations provided that the geometry approximation ensures the required order of accuracy. Besides corroborating theoretical statements by numerical convergence studies for the Oseen problem, extensibility to the transient incompressible Navier-Stokes equations is confirmed by simulations of challenging three-dimensional low- and high-Reynolds-number single-phase flows through complex geometries.

An Extended Embedding Mesh Approach for 3D Low- and High-Reynolds-Number flows: This approach (see Schott and Shahmiri *et al.* [232]) constitutes an extended domain decomposition approach for single-phase flows based on overlapping fluid meshes. Embedding an arbitrary fluid patch, whose mesh boundary defines the interface, into a fixed background fluid mesh

renders in a discretization concept which is highly beneficial when it comes to computational grid generation for complex domains (see Hansbo *et al.* [139] for the conceptual idea). It allows for locally increased resolutions independent from size and structure of the background mesh and is best-suited to efficiently resolve boundary-layers in complex fluid-structure interaction problems (see Shahmiri [235]). A residual-based variational multiscale (RBVM) formulation in the interior of the fluid subdomains is supported by interface-zone ghost-penalty stabilizations to overcome issues related to cutting finite element meshes. Nitsche's method is extended by techniques known from Discontinuous Galerkin methods (see, e.g., Di Pietro and Ern [85]) to sufficiently account for discontinuous approximation spaces and to control convective mass transport across the interface.

A Stabilized Nitsche-type Extended Variational Multiscale Method for Two-Phase Flow: This novel methodology (see Schott and Rasthofer *et al.* [231]) utilizes the RBVM technique to stabilize immiscible fluid phases in incompressible two-phase flows. A Nitsche-type interface coupling is adapted to account for high contrast in material properties. Emphasis is put on the definition of the flux-averaging strategy incorporated in Nitsche's method (see Burman and Zunino [62]) to fully reap the benefits of weak constraint enforcement for numerically under-resolved fluid phases. Independent sets of supporting ghost-penalty terms (see Schott and Wall [230]) ensure stability with respect to the interface location. For capturing the evolution of the interface, a level-set method is applied.

In summary, the present thesis marks a decisive step in the development of geometrically unfitted cut/extended finite element methods and makes substantial progress towards novel methodologies for the simulation of interface coupled problems in computational fluid dynamics (CFD). Different fields of computational mathematics, computer sciences and engineering are brought together in this work. Comprehensive simulation problem studies and a sound mathematical numerical analysis of existing approaches build the basis for developing new fundamental concepts and computational approaches in this research area. The development of novel stabilization techniques for transient low- and higher-Reynolds-number single-phase flows in complex non-moving as well as moving domains are the basis for establishing numerically stable and optimally convergent simulation tools. Due to the highly improved accuracy and stability, it allows for the first time to fully exploit the high capabilities of unfitted discretization concepts and provides application to multiphysics flow problems like domain decomposition, incompressible two-phase flow and fluid-structure interaction. This work lays the foundation for extensibility to further coupled multiphysics problems in different fields of computational science and engineering.

Besides the theoretical developments, the implementation of all computational methods and algorithms proposed throughout this work is a further major contribution of this thesis. All methods are implemented in the in-house software environment BACI (see Wall *et al.* [262]), developed at the Institute for Computational Mechanics of the Technical University of Munich. At this stage, the contribution of Dipl.-Ing. Christoph Ager, Dipl.-Ing. Michael Hiermeier, Dr.-Ing. Yogaraj Sudhakar and Dr.-Ing. Ulrich Küttler to the development of a Geometric CUT Library is gratefully acknowledged. As indicated, major parts of the thesis have been already published in peer-reviewed journals.

1.3 Outline of the Thesis

All conceptual ideas, computational methods and algorithms devised in the present work and their application to a variety of flow problems are presented with increasing complexity. The remainder of this thesis is organized as follows.

Chapter 2 is devoted to basic concepts of classical finite element discretizations and to the presentation of the high capabilities of geometrically unfitted finite element methods. After reviewing fundamentals of continuum mechanics, different common strategies for approximating boundaries, interfaces and subdomains in multiphysics problems are discussed. Closely connected to this topic is **Appendix A**. It provides an overview of level-set representations of basic geometric objects whose combinations allow for easily setting up highly complex geometries. Afterwards, different concepts of domain decomposition in the framework of classical FEMs are compared and severe limitations are drawn. This builds the basic motivation for developing different composed unfitted strategies for complex multifield problems discussed subsequently. As a major contribution, in this chapter, novel strategies to guarantee accurate representability of solution fields in topologically challenging geometric situations are proposed.

Establishing stabilized CUTFEMs for incompressible single-phase flows throughout **Chapter 3** constitutes the major contribution of this work and serves as theoretical basis for all further extensions to multiphysics flow problems in the subsequent chapters. After reviewing well-established fluid formulations for classical fitted-mesh FEMs, preliminary mathematical results required for numerical analyses of CUTFEMs are recalled. The weak constraint enforcement of boundary conditions for fitted mesh approximation is analyzed in very detail and major differences to unfitted approximations and arising issues from that are pointed out. This allows to develop a precise understanding of issues of most CUTFEMs existing so far, as observed in comprehensive numerical studies. On this basis, novel Nitsche-type CUTFEMs for incompressible single-phase flows have been developed. Adding so-called ghost-penalty stabilizations in the vicinity of the intersected boundary allows to establish uniform inf-sup stability and optimal *a priori* energy norm error estimates independent of the mesh intersection. Numerical convergence studies, simulations of transient flows through complex geometries and extensions to setups in moving domains finalize this chapter.

Extensions of introduced fluid formulations to various unfitted composed discretizations for coupled flow problems are provided in **Chapter 4**. Main focus is turned to domain decomposition for single-phase flows, based on the concept of overlapping interface-fitted meshes with non-interface-fitted background meshes, as well as to interactions of different fluid phases at temporally evolving interfaces. Theoretical refinements on Nitsche-type couplings are made with emphasis on stability and optimality in presence of high contrast in material parameters or highly different mesh resolutions. Concluding, various challenging two- and three-dimensional simulations validate these computational approaches.

Chapter 5 demonstrates the successful application of proposed interface coupling methods beyond pure flow problems. Unfitted monolithic approaches to fluid-structure interaction, even incorporating techniques of fluid domain decomposition, are devised and algorithms to deal with non-linearities inherent in the description of interacting fluids and solids are discussed. Numerical tests for highly dynamic FSI support the theoretical explanations.

Finally, **Chapter 6** summarizes major results and developments achieved in this thesis and gives perspectives of potential and promising research fields for CUTFEMs in the future.

Chapter 2

Spatial Discretization Techniques for Multiphysics using Cut Finite Elements

Coupled multiphysics problem configurations governed by partial different equations (PDEs) put highest demands on computational approaches. Different involved physical fields and modeling approaches at common interfaces often require highly different approximation properties regarding computational grids and discrete function spaces used for representing the field solutions. Finite element methods (FEMs), which build the basis for all numerical schemes developed and analyzed throughout this thesis, provide a multitude of approximation properties that can be appropriately chosen for the considered problem. While for single-field problems, different well-suited FEM-based numerical approximation techniques have been developed over the last decades, the design of FEMs for interface coupled multiphysics configurations remains further challenging. The necessity of taking into account specific requirements for the different involved physics highly increases the complexity of constructing well-suited computational approaches for the entire coupled configuration. In particular, when domains and computational grids are moving or are even topologically changing over time, classical FEMs are strictly limited in their applicability.

Complex physical configurations build the motivation for developing advanced composite finite-element-based approaches, which are simple in their construction and, in particular, highly versatile for a wide range of applications. For a long time, the use of interface-fitted meshes for respective subdomains, while retaining the nodal connectivity at interfaces, was standard in computational science and engineering. The natural idea of decomposing the overall computational domain into physically reasonable subregions, which are of specific interest and put special demands on their spatial approximation, opened a new era in the development of computational methods. Using well-suited computational grids for each subdomain individually together with appropriate techniques to connect the solution fields, provide highly competitive approaches. However, such techniques are often still limited when meshes largely move or domains undergo topological changes.

Motivation of the present work is to develop FEM-based computational methods which are not subjected to such limitations anymore and in that way deliver new levels of flexibility in composing discretization techniques for multiphysics configurations. Fundamental idea for realizing this purpose is to choose fixed computational grids which do not account for the interface

motion between the physical subdomain. Even if grid motion is allowed, it does not need to be adapted to the movement of the physical subdomains anymore. However, to retain consistency with the underlying physics, such FEMs, which are designated to be *geometrically unfitted*, then require the geometric subdivision of computational meshes into active and inactive parts, sharply separated by the phase boundary within finite elements. Moreover, discrete function spaces defined on cut meshes have to be constructed appropriately to enable complex topological situations. In general, such novel composite unfitted mesh techniques are not limited to any specific combination of physical fields, however, require thoroughly studied discrete variational formulations according to the governing PDEs. The development of finite element methods on cut meshes require special consideration in particular in view of numerical stability and optimality, as will be elaborated in detail for incompressible flows in Chapter 3. Although all techniques proposed in this chapter are not limited to any specific physics or governing equations, the algorithmic methods and methodologies are elaborated by means of single-phase and coupled multiphysics flow problems; special consideration is given to different composite discretization techniques for fluid-structure(-contact) interactions and couplings of fluid phases as they occur in different configurations of single-phase and multiphase flows.

The present chapter, on the one hand, reviews fundamentals on finite element discretizations and computational domains. On the other hand, it addresses a multitude of general aspects regarding domain decomposition and cut finite element approximation spaces. The outline is given as follows: After introducing basics on computational domains, their decomposition into subregions and on different techniques for interface representation, fundamentals on reference frames are recalled. An overview of existing domain decomposition techniques and a discussion of the high capabilities of novel cut-finite-element-based approaches finalize Section 2.1. A comprehensive survey on different enrichment strategies for standard finite element function spaces will be given in Section 2.2. Moreover, novel strategies to manage multiple sets of degrees of freedom (DOFs) for improved representability of solutions in topologically complex configurations will be proposed. Notes on implementation aspects of cut finite element methods conclude this chapter.

2.1 Domain Decomposition - General Aspects and an Overview of Concepts

Decomposing the overall computational domain into subregions provides a powerful technique to combine well-suited approximation technique specifically adapted for each physical subdomain. FEM-based approximations, which are the basis for all numerical techniques developed and analyzed throughout this thesis, provide a high number of properties that can be individually chosen for the subproblems. Approximation properties like polynomial orders or the choice between continuous and element-wise discontinuous Galerkin schemes, the possibility of locally adapted grids or the variety of options between different element shapes and technologies form the basis of all advanced FEMs. Combining different approximations for the respective subdomains opens a broad variety of computational approaches which show their flexibility particularly in constructing finite-dimensional approximations of the computational domains on the one hand and of the physical quantities on the other hand. Such composite techniques are

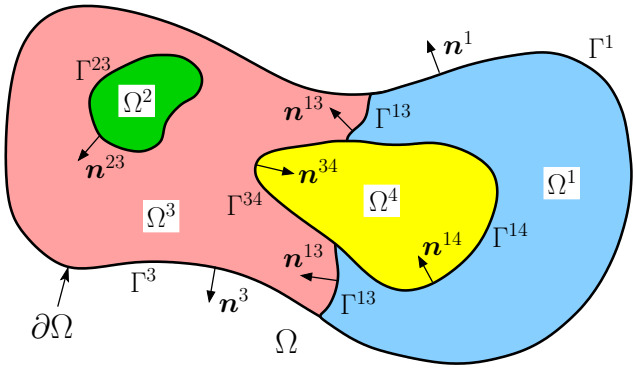

Figure 2.1: Example of a multifield problem setting $(d = 2)$ consisting of subdomains Ω^i, $i = 1 \dots 4$, exterior boundaries Γ^1, Γ^3 and interfaces $\Gamma^{13}, \Gamma^{14}, \Gamma^{23}, \Gamma^{34}$ with respective unit normal vectors.

well-suited for coupled multiphysics problems, like for instance fluid-structure interaction or the coupling of incompressible flows involving high contrast in the material properties or even combinations of such coupled problems - applications that are in the main focus of this work.

In the following sections, first, an abstract domain decomposition problem setting including general notation is introduced and fundamentals of continuum mechanics regarding different frames of references are reviewed. Second, interface representation techniques commonly used for discretization approaches which are based on the idea of cutting finite elements are discussed. Afterwards, an overview of classical FEM-based domain decomposition approaches with particular focus on their capabilities and limitations for different coupled flow problems is given. Finally, different aspects of geometrically unfitted domain decomposition techniques, which use cut finite elements, are worked out to highlight the potential of these numerical schemes for various coupled multiphysics configurations.

2.1.1 Abstract Domain Decomposition Problem Setting

Let $\Omega \overset{\text{def}}{=} \cup_{1 \leqslant i \leqslant N_{\text{dom}}} \Omega^i$ be the physical domain consisting of a partition into $N_{\text{dom}} \geqslant 1$ disjoint subdomains $\Omega^i \subset \mathbb{R}^d$, $1 \leqslant i \leqslant N_{\text{dom}}$, with $d = 2, 3$ and $\Gamma^{ij} \overset{\text{def}}{=} \overline{\Omega^i} \cap \overline{\Omega^j}$ $(i < j)$ the interfaces, respectively. For the subdomain boundaries $\partial\Omega^i$, which are assumed as $(d-1)$-manifolds, partitions $\partial\Omega^i = \Gamma^i \cup (\bigcup_{j \neq i} \Gamma^{ij})$ with exterior boundaries $\Gamma^i \subset \partial\Omega$ are considered. Outward-pointing unit normal vectors defined on the manifolds are denoted with $\boldsymbol{n}^i$ for boundaries and with $\boldsymbol{n}^{ij} \overset{\text{def}}{=} \boldsymbol{n}^i = -\boldsymbol{n}^j$ for interfaces, respectively. This generalized multifield setting is depicted in Figure 2.1.

For scalar quantities $f : \Omega \to \mathbb{R}$, which may exhibit a discontinuity between subdomains Ω^i and Ω^j, like for instance material parameters, weighted average operators and a jump operator are defined at all points $\boldsymbol{x} \in \Gamma^{ij}$ as

$$\{f(\boldsymbol{x})\} = \lim_{t \to 0^+} (w^i f(\boldsymbol{x} - t\boldsymbol{n}^{ij}) + w^j f(\boldsymbol{x} + t\boldsymbol{n}^{ij})), \tag{2.1}$$

$$\langle f(\boldsymbol{x}) \rangle = \lim_{t \to 0^+} (w^j f(\boldsymbol{x} - t\boldsymbol{n}^{ij}) + w^i f(\boldsymbol{x} + t\boldsymbol{n}^{ij})), \tag{2.2}$$

$$[\![f(\boldsymbol{x})]\!] = \lim_{t \to 0^+} (f(\boldsymbol{x} - t\boldsymbol{n}^{ij}) - f(\boldsymbol{x} + t\boldsymbol{n}^{ij})) \tag{2.3}$$

with positive weights $w^i, w^j \in [0,1]$ and $w^i = 1 - w^j$. These weights are specified later depending on the subdomain problems. Furthermore, it can be easily shown that for two scalar quantities f, g the following relationship holds

$$[\![fg]\!] = [\![f]\!]\,\{g\} + \langle f \rangle [\![g]\!]. \tag{2.4}$$

Vector-valued equivalences can be defined component-wise. These notations and conventions serve as a basis for all considered multiphysics problems considered throughout this thesis.

2.1.2 Fundamentals of Continuum Mechanics

The purpose of this section is to review basic kinematic descriptions mainly used in continuum mechanics. Depending on the problem setting, for each physical field defined on temporally moving domains, an appropriate description of motion has to be chosen. In general, three different frames of reference can be distinguished: the *Lagrangean frame of reference*, the *Eulerian frame of reference* and the *Arbitrary Lagrangean-Eulerian (*ALE*) description*.

In the following, the conceptual ideas of these different kinematic descriptions are elaborated and mathematical notations are introduced that are necessary to develop more generalized domain decomposition techniques for general multifield settings. Afterwards, fundamental conservation laws for continua are derived. The explanations in this section are kept short. For a more comprehensive overview, the interested reader is referred to, e.g., the textbook by Donéa and Huerta [91].

2.1.2.1 Introducing Domains, Observers and Frames of Reference

Descriptions of Motion. The most general case, the *Arbitrary Lagrangean-Eulerian (*ALE*)* description of motion is presented first, from which the Lagrangean and the Eulerian viewpoints can be deduced as particular cases afterwards. For the considered description, three domain configurations are introduced: a *material domain* $\mathscr{R}_{\boldsymbol{X}} \subset \mathbb{R}^d$, a *spatial domain* $\mathscr{R}_{\boldsymbol{x}} \subset \mathbb{R}^d$ and a *referential domain* $\mathscr{R}_{\boldsymbol{\chi}} \subset \mathbb{R}^d$.

The material domain $\mathscr{R}_{\boldsymbol{X}}$ is made up of material particles $\boldsymbol{X} \in \mathbb{R}^d$ which are under consideration, often defined at starting time $t = T_0$. Following these particles in their motion along time-dependent paths $\boldsymbol{x}(\boldsymbol{X}, t)$ for times $t \in (T_0, T)$, the *spatial domain* $\mathscr{R}_{\boldsymbol{x}}(t)$ is formed. The motion of particles with material coordinates $\boldsymbol{X}$ to spatial coordinates $\boldsymbol{x}(\boldsymbol{X}, t)$ can be tracked and mathematically expressed in terms of a bijective mapping

$$\boldsymbol{\varphi}(\boldsymbol{X}, t) : \begin{cases} \mathscr{R}_{\boldsymbol{X}} \times (T_0, T) & \to \mathscr{R}_{\boldsymbol{x}} \times (T_0, T), \\ (\boldsymbol{X}, t) & \mapsto \boldsymbol{\varphi}(\boldsymbol{X}, t) = (\boldsymbol{x}_{\boldsymbol{X}}(\boldsymbol{X}, t), t), \end{cases} \tag{2.5}$$

provided that $J_{\boldsymbol{X} \mapsto \boldsymbol{x}} \overset{\text{def}}{=} \det(\partial \boldsymbol{x}_{\boldsymbol{X}}(\boldsymbol{X}, t)/\partial \boldsymbol{X}) > 0 \,\forall\, (\boldsymbol{X}, t) \in \mathscr{R}_{\boldsymbol{X}} \times (T_0, T)$, i.e. no singularities along the particle paths.

To define the region of interest to be observed, together with its computational approximation, it is required to introduce an independent *referential domain* $\mathscr{R}_{\boldsymbol{\chi}}(t)$ and reference coordinates $\boldsymbol{\chi}$, with respect to which physical quantities, like for example mass and momentum in fluid and structural mechanics, are measured by the *observer*. Note that in general the referential configuration is arbitrary and independent of the material or spatial configurations. In particular, the

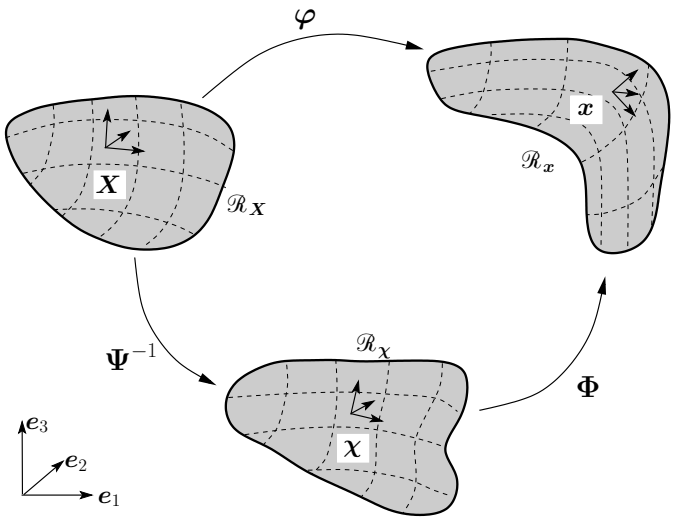

Figure 2.2: Different reference configurations: a material domain $\mathscr{R}_{\boldsymbol{X}} \subset \mathbb{R}^d$, a spatial domain $\mathscr{R}_{\boldsymbol{x}} \subset \mathbb{R}^d$ and a referential domain $\mathscr{R}_{\boldsymbol{\chi}} \subset \mathbb{R}^d$. Bijective mappings $\boldsymbol{\varphi}, \boldsymbol{\Phi}, \boldsymbol{\Psi}^{-1}$ allow transformations between different descriptions.

observer can move independently of the particles under consideration. In classical finite element methods, it is common to fit the computational grid to the referential domain at any time t. In that way, the grid points follow the observer in its motion, which finally enables classical one- or multistep time-integration schemes for the temporal discretization of often resulting systems of ordinary differential equations (ODEs). Application of non-geometry-fitted discretizations is one of the main aspects to be addressed throughout this thesis.

The referential configuration is commonly defined such that it coincides with the material configuration and the spatial configuration at initial time T_0, i.e. $\mathscr{R}_{\boldsymbol{\chi}}(T_0) \stackrel{\text{def}}{=} \mathscr{R}_{\boldsymbol{x}}(T_0) = \mathscr{R}_{\boldsymbol{X}}$. Then, a second bijective mapping between reference and spatial domain, which describes the motion of grid points in the spatial configuration, can be defined as

$$\boldsymbol{\Phi}(\boldsymbol{\chi}, t) : \begin{cases} \mathscr{R}_{\boldsymbol{\chi}} \times (T_0, T) & \to \mathscr{R}_{\boldsymbol{x}} \times (T_0, T), \\ (\boldsymbol{\chi}, t) & \mapsto \boldsymbol{\Phi}(\boldsymbol{\chi}, t) = (\boldsymbol{x}_{\boldsymbol{\chi}}(\boldsymbol{\chi}, t), t). \end{cases} \tag{2.6}$$

Combining the two mappings $\boldsymbol{\varphi}$ and $\boldsymbol{\Phi}$ enables to define a bijective mapping $\boldsymbol{\Psi}^{-1} \stackrel{\text{def}}{=} \boldsymbol{\Phi}^{-1} \circ \boldsymbol{\varphi}$ relating material and referential configuration as

$$\boldsymbol{\Psi}^{-1}(\boldsymbol{X}, t) : \begin{cases} \mathscr{R}_{\boldsymbol{X}} \times (T_0, T) & \to \mathscr{R}_{\boldsymbol{\chi}} \times (T_0, T), \\ (\boldsymbol{X}, t) & \mapsto \boldsymbol{\Psi}^{-1}(\boldsymbol{X}, t) = (\boldsymbol{\chi}_{\boldsymbol{X}}(\boldsymbol{X}, t), t). \end{cases} \tag{2.7}$$

The different configurations $\boldsymbol{X}, \boldsymbol{x}, \boldsymbol{\chi}$ including the mappings $\boldsymbol{\varphi}, \boldsymbol{\Phi}, \boldsymbol{\Psi}^{-1}$ are visualized in Figure 2.2.

Time Derivative Relations for Physical Quantities. In the following, relationships between material time derivative and time derivatives in the referential configuration are deduced, which are the basis for conservation laws to be expressed in a general ALE frame of reference.

A quantity f to be observed carries equal values independent of the viewpoint, expressed by $f_{\boldsymbol{X}}, f_{\boldsymbol{x}}, f_{\boldsymbol{\chi}}$ with respect to the different reference systems as indicated by the subscripts $\boldsymbol{X}, \boldsymbol{x}, \boldsymbol{\chi}$, respectively. Making use of the mappings $\boldsymbol{\Psi}^{-1}, \boldsymbol{\varphi}$ and of $f_{\boldsymbol{X}} = f_{\boldsymbol{\chi}} \circ \boldsymbol{\Psi}^{-1} = f_{\boldsymbol{x}} \circ \boldsymbol{\varphi}$ yields

$$f_{\boldsymbol{X}}(\boldsymbol{X}, t) = f_{\boldsymbol{\chi}}(\boldsymbol{\chi}_{\boldsymbol{X}}(\boldsymbol{X}, t), t) \quad \forall (\boldsymbol{X}, t), \tag{2.8}$$

$$f_{\boldsymbol{X}}(\boldsymbol{X}, t) = f_{\boldsymbol{x}}(\boldsymbol{x}_{\boldsymbol{X}}(\boldsymbol{X}, t), t) \quad \forall (\boldsymbol{X}, t). \tag{2.9}$$

Calculating the total derivative of (2.8) relates time derivatives in the material and in the referential frame of reference

$$\frac{\mathrm{d} f_{\boldsymbol{X}}}{\mathrm{d} t}(\boldsymbol{X}, t) = \frac{\partial f_{\boldsymbol{\chi}}}{\partial t}(\boldsymbol{\chi}_{\boldsymbol{X}}(\boldsymbol{X}, t), t) + \frac{\partial f_{\boldsymbol{\chi}}}{\partial \boldsymbol{\chi}}(\boldsymbol{\chi}_{\boldsymbol{X}}(\boldsymbol{X}, t), t) \cdot \boldsymbol{w}_{\boldsymbol{X}}(\boldsymbol{X}, t), \tag{2.10}$$

where $\boldsymbol{w}_{\boldsymbol{X}}(\boldsymbol{X}, t) \overset{\text{def}}{=} \frac{\partial \boldsymbol{\chi}_{\boldsymbol{X}}}{\partial t}(\boldsymbol{X}, t)$ is the velocity of a fixed particle $\boldsymbol{X}$ in the referential coordinate system.

Depending on the considered conservation law it can be advantageous to rewrite (2.10) in terms of spatial gradients $\frac{\partial f_{\boldsymbol{x}}}{\partial \boldsymbol{x}}$ instead of referential gradients $\frac{\partial f_{\boldsymbol{\chi}}}{\partial \boldsymbol{\chi}}$, as it is common for fluids for example,

$$\frac{\mathrm{d} f_{\boldsymbol{X}}}{\mathrm{d} t}(\boldsymbol{X}, t) = \frac{\partial f_{\boldsymbol{\chi}}}{\partial t}(\boldsymbol{\chi}_{\boldsymbol{X}}(\boldsymbol{X}, t), t) + \frac{\partial f_{\boldsymbol{x}}}{\partial \boldsymbol{x}}(\boldsymbol{x}_{\boldsymbol{X}}(\boldsymbol{X}, t), t) \cdot \boldsymbol{c}_{\boldsymbol{X}}(\boldsymbol{X}, t) \tag{2.11}$$

with

$$\boldsymbol{c}_{\boldsymbol{X}}(\boldsymbol{X}, t) \overset{\text{def}}{=} \frac{\partial \boldsymbol{x}_{\boldsymbol{\chi}}}{\partial \boldsymbol{\chi}}(\boldsymbol{\chi}_{\boldsymbol{X}}(\boldsymbol{X}, t), t) \cdot \boldsymbol{w}_{\boldsymbol{X}}(\boldsymbol{X}, t). \tag{2.12}$$

Here, the total derivative of $\boldsymbol{\varphi} = \boldsymbol{\Phi} \circ \boldsymbol{\Psi}^{-1}$ yields the relationship

$$\boldsymbol{u}_{\boldsymbol{X}}(\boldsymbol{X}, t) \overset{\text{def}}{=} \frac{\partial \boldsymbol{x}_{\boldsymbol{X}}}{\partial t}(\boldsymbol{X}, t) = \frac{\partial \boldsymbol{x}_{\boldsymbol{\chi}}}{\partial \boldsymbol{\chi}}(\boldsymbol{\chi}_{\boldsymbol{X}}(\boldsymbol{X}, t), t) \cdot \boldsymbol{w}_{\boldsymbol{X}}(\boldsymbol{X}, t) + \frac{\partial \boldsymbol{x}_{\boldsymbol{\chi}}}{\partial t}(\boldsymbol{\chi}_{\boldsymbol{X}}(\boldsymbol{X}, t), t) \tag{2.13}$$

such that

$$\boldsymbol{c}_{\boldsymbol{X}}(\boldsymbol{X}, t) = \boldsymbol{u}_{\boldsymbol{X}}(\boldsymbol{X}, t) - \hat{\boldsymbol{u}}_{\boldsymbol{\chi}}(\boldsymbol{\chi}_{\boldsymbol{X}}(\boldsymbol{X}, t), t) \tag{2.14}$$

is the relative velocity between particle velocity $\boldsymbol{u}_{\boldsymbol{X}}$ and grid velocity

$$\hat{\boldsymbol{u}}_{\boldsymbol{\chi}}(\boldsymbol{\chi}_{\boldsymbol{X}}(\boldsymbol{X}, t), t) \overset{\text{def}}{=} \frac{\partial \boldsymbol{x}_{\boldsymbol{\chi}}}{\partial t}(\boldsymbol{\chi}_{\boldsymbol{X}}(\boldsymbol{X}, t), t). \tag{2.15}$$

Combining (2.11) and (2.14), the total time variation of a quantity f for a fixed particle $\boldsymbol{X}$ in material coordinates is equal to the local time variation in the referential system plus an additional convective effect accounting for the relative movement of referential system and material reference system. On the basis of the introduced *Arbitrary Lagrangean-Eulerian* framework, classical observer viewpoints can be easily deduced.

In the *Lagrangean* description, the observer follows material particles $\boldsymbol{X}$ in their motion, resulting in previously defined mappings $\boldsymbol{\Psi}^{-1} = \boldsymbol{I}$, where $\boldsymbol{I}$ denotes the trivial identity mapping, and $\boldsymbol{\Phi} = \boldsymbol{\varphi}$ such that $\boldsymbol{\chi} \equiv \boldsymbol{X}$. As there is no relative motion between material configuration and reference system, no convective effects occur resulting in $\boldsymbol{c} = \boldsymbol{0}$ and $\boldsymbol{u} = \hat{\boldsymbol{u}}$. For a physical quantity measured in material coordinates it holds

$$\frac{\mathrm{d} f_{\boldsymbol{X}}}{\mathrm{d} t}(\boldsymbol{X}, t) = \frac{\partial f_{\boldsymbol{X}}}{\partial t}(\boldsymbol{X}, t). \tag{2.16}$$

In particular in structure mechanics with moderate material deformations of the bodies, the Lagrangean description is commonly used as it easily enables describing boundaries and allows for history-dependent materials. In contrast, for instance, for fluid flows incorporating strong vortices, the mesh cannot follow the complex motion of Lagrangean particles, otherwise the mesh distorts.

For this purpose, the *Eulerian* viewpoint, in which the referential configuration is fixed and non-varying in time, is an appropriate choice and it holds $\boldsymbol{\chi} = \boldsymbol{x}$. In this description, at a given spatial point of a fixed non-moving computational domain, the observer measures a physical quantity associated with the material particle passing through this point at the current time. Due to the fact that material particle and spatial point do not belong to each other, convective effects occur when observing the deforming material in a fixed computational frame. The previously introduced mappings then simplify to $\boldsymbol{\Phi} = \boldsymbol{I}$, $\boldsymbol{\varphi} = \boldsymbol{\Psi}^{-1}$ and the grid velocity vanishes, i.e. $\hat{\boldsymbol{u}} = \boldsymbol{0}$ and $\boldsymbol{c} = \boldsymbol{u}$. For a physical quantity measured in spatial coordinates it holds

$$\frac{\mathrm{d}f_{\boldsymbol{X}}}{\mathrm{d}t}(\boldsymbol{X},t) = \frac{\partial f_{\boldsymbol{x}}}{\partial t}(\boldsymbol{x}_{\boldsymbol{X}}(\boldsymbol{X},t),t) + \frac{\partial f_{\boldsymbol{x}}}{\partial \boldsymbol{x}}(\boldsymbol{x}_{\boldsymbol{X}}(\boldsymbol{X},t),t) \cdot \boldsymbol{u}_{\boldsymbol{X}}(\boldsymbol{X},t) \tag{2.17}$$

with $\boldsymbol{u}_{\boldsymbol{X}}$ the velocity of a particle $\boldsymbol{X}$ passing the spatial point $\boldsymbol{x}$ at time t.

2.1.2.2 Deducing Conservation Laws

Fundamentals of continuum mechanics state the conservation of mass and the balance of linear and angular momentum. These quantities are commonly formulated in terms of volume integrals. Deriving conservation laws for these mechanical quantities requires the observation of their temporal change in relationship with the mechanical action of external volumetric and surface loads. In the following, conservation laws are deduced for the most general case, that is the ALE description of motion, which serves as starting point for the different kinematics and specific constitutive laws commonly used for scalar quantities, fluids and solids as considered in this work; see Section 2.1.3.2, Section 3.1.1 and Section 5.1.1 for the field specific derivations. The subsequent elaborations are kept very short and only recall the statements required throughout the thesis. More detailed explanations can be found in textbooks by Gurtin [137] and by Truesdell and Noll [254] or in the theses by Klöppel [163] and Gamnitzer [119].

The Reynolds Transport Theorem. Conservation of quantities holds for control volumes $V_{\boldsymbol{x}}(t)$ which can be tracked via their particle motion as $(V_{\boldsymbol{x}}(t),t) = \boldsymbol{\varphi}(V_{\boldsymbol{X}}(t),t)$ or equivalently expressed in referential coordinates as $(V_{\boldsymbol{x}}(t),t) = \boldsymbol{\Phi}(V_{\boldsymbol{\chi}}(t),t)$ for all $t \in (T_0,T)$. In the following a volumetric integral over a physical quantity f, which is defined as

$$F(t) \overset{\text{def}}{=} \int_{V_{\boldsymbol{x}}(t)} f_{\boldsymbol{x}}(\boldsymbol{x},t)\,\mathrm{d}\boldsymbol{x} = \int_{V_{\boldsymbol{X}}(t)} \underbrace{(f_{\boldsymbol{X}} J_{\boldsymbol{X}\to\boldsymbol{x}})(\boldsymbol{X},t)}_{\overset{\text{def}}{=} f^0_{\boldsymbol{X}}(\boldsymbol{X},t)}\,\mathrm{d}\boldsymbol{X} = \int_{V_{\boldsymbol{\chi}}(t)} \underbrace{(f_{\boldsymbol{\chi}} J_{\boldsymbol{\chi}\to\boldsymbol{x}})(\boldsymbol{\chi},t)}_{\overset{\text{def}}{=} f^G_{\boldsymbol{\chi}}(\boldsymbol{\chi},t)}\,\mathrm{d}\boldsymbol{\chi}, \tag{2.18}$$

is considered.

The temporal change of $F(t)$ can be mathematically described by the ALE *transport theorem by Reynolds* (see, e.g., [119])

$$\frac{\mathrm{d}F(t)}{\mathrm{d}t} = \int_{V_{\boldsymbol{\chi}}(t)} \frac{\partial f_{\boldsymbol{\chi}}^G}{\partial t}(\boldsymbol{\chi},t) + \underbrace{\frac{\partial f_{\boldsymbol{\chi}}^G}{\partial \boldsymbol{\chi}}(\boldsymbol{\chi},t)\cdot \boldsymbol{w}_{\boldsymbol{\chi}}(\boldsymbol{\chi},t) + f_{\boldsymbol{\chi}}^G(\boldsymbol{\chi},t)(\nabla_{\boldsymbol{\chi}}\cdot \boldsymbol{w}_{\boldsymbol{\chi}})(\boldsymbol{\chi},t)}_{=(\nabla_{\boldsymbol{\chi}}\cdot(f_{\boldsymbol{\chi}}^G \boldsymbol{w}_{\boldsymbol{\chi}}))(\boldsymbol{\chi},t)} \,\mathrm{d}\boldsymbol{\chi}, \tag{2.19}$$

where $\nabla_{\boldsymbol{\chi}}\cdot(\cdot)$ denotes the divergence operator with respect to referential coordinates $\boldsymbol{\chi}$ and $\boldsymbol{w}_{\boldsymbol{\chi}}(\boldsymbol{\chi},t) = \boldsymbol{w}_{\boldsymbol{X}}(\boldsymbol{X}_{\boldsymbol{\chi}}(\boldsymbol{\chi},t),t) = \frac{\partial \boldsymbol{\chi}_{\boldsymbol{X}}}{\partial t}(\boldsymbol{X}_{\boldsymbol{\chi}}(\boldsymbol{\chi},t),t)$ the domain velocity. The divergence part in (2.19) can be alternatively expressed as the flux over the moving boundary $\partial V_{\boldsymbol{\chi}}(t)$, when applying Gauss' divergence theorem. Utilizing (2.11) and following elaborations in [119], the ALE transport theorem can be equivalently written in spatial coordinates

$$\frac{\mathrm{d}F(t)}{\mathrm{d}t} = \int_{V_{\boldsymbol{x}}(t)} \frac{\partial f_{\boldsymbol{\chi}}}{\partial t}(\boldsymbol{\Phi}^{-1}(\boldsymbol{x},t)) + \frac{\partial f_{\boldsymbol{x}}}{\partial \boldsymbol{x}}(\boldsymbol{x},t)\cdot \boldsymbol{c}_{\boldsymbol{x}}(\boldsymbol{x},t) + f_{\boldsymbol{x}}(\boldsymbol{x},t)(\nabla_{\boldsymbol{x}}\cdot \boldsymbol{u}_{\boldsymbol{x}})(\boldsymbol{x},t)\,\mathrm{d}\boldsymbol{x} \tag{2.20}$$

with $V_{\boldsymbol{x}}(t)$ the spatial coordinates of the control volume as previously defined.

In a *Lagrangean* description, i.e. $\boldsymbol{\Psi}^{-1} = \boldsymbol{I}$ and $\boldsymbol{\chi} = \boldsymbol{X}$, the Reynolds transport theorem (2.19) simplifies with $f_{\boldsymbol{\chi}}^G \equiv f_{\boldsymbol{X}}^0 = f_{\boldsymbol{X}} J_{\boldsymbol{X}\mapsto\boldsymbol{x}}$ to

$$\frac{\mathrm{d}F(t)}{\mathrm{d}t} = \int_{V_{\boldsymbol{X}}(t)=V_{\boldsymbol{X}}(T_0)} \frac{\partial f_{\boldsymbol{X}}^0}{\partial t}(\boldsymbol{X},t)\,\mathrm{d}\boldsymbol{X} = \int_{V_{\boldsymbol{X}}(t)=V_{\boldsymbol{X}}(T_0)} \frac{\partial (f_{\boldsymbol{X}} J_{\boldsymbol{X}\mapsto\boldsymbol{x}})}{\partial t}(\boldsymbol{X},t)\,\mathrm{d}\boldsymbol{X} \tag{2.21}$$

due to the vanishing domain velocity of the referential coordinate system ($\boldsymbol{w}_{\boldsymbol{X}} \equiv \boldsymbol{0}$), as the observed control volume contains the same material particles all the time.

In an *Eulerian* setting, i.e. $\boldsymbol{\Psi}^{-1} = \boldsymbol{\varphi}$ and $\boldsymbol{\Phi} = \boldsymbol{I}$ with $\boldsymbol{\chi} = \boldsymbol{x}$ and $\boldsymbol{c}_{\boldsymbol{x}} = \boldsymbol{u}_{\boldsymbol{x}}$, the Reynolds transport theorem emerges as

$$\frac{\mathrm{d}F(t)}{\mathrm{d}t} = \int_{V_{\boldsymbol{x}}(t)} \frac{\partial f_{\boldsymbol{x}}}{\partial t}(\boldsymbol{x},t) + \underbrace{\frac{\partial f_{\boldsymbol{x}}}{\partial \boldsymbol{x}}(\boldsymbol{x},t)\cdot \boldsymbol{u}_{\boldsymbol{x}}(\boldsymbol{x},t) + f_{\boldsymbol{x}}(\boldsymbol{x},t)(\nabla_{\boldsymbol{x}}\cdot \boldsymbol{u}_{\boldsymbol{x}})(\boldsymbol{x},t)}_{=(\nabla_{\boldsymbol{x}}\cdot(f_{\boldsymbol{x}}\boldsymbol{u}_{\boldsymbol{x}}))(\boldsymbol{x},t)} \,\mathrm{d}\boldsymbol{x}. \tag{2.22}$$

For classical finite element based approximation techniques of fluids, for instance, the observed control volume is often chosen being fixed over time, i.e. $V_{\boldsymbol{x}}(t) = V_{\boldsymbol{x}}(T_0)$, however, then contains different particles $V_{\boldsymbol{X}}(t)$ at different time levels, which causes convective effects.

Conservation of Mass. Mass of a continuum defined by a spatial control volume $V_{\boldsymbol{x}}(t)$ can be written in integral form with respect to different frames of reference as

$$M(t) = \int_{V_{\boldsymbol{x}}(t)} \rho_{\boldsymbol{x}}(\boldsymbol{x},t)\,\mathrm{d}\boldsymbol{x} = \int_{V_{\boldsymbol{X}}(t)} \underbrace{(\rho_{\boldsymbol{X}} J_{\boldsymbol{X}\mapsto\boldsymbol{x}})(\boldsymbol{X},t)}_{\stackrel{\text{def}}{=}\rho_{\boldsymbol{X}}^0(\boldsymbol{X},t)}\,\mathrm{d}\boldsymbol{X} = \int_{V_{\boldsymbol{\chi}}(t)} \underbrace{(\rho_{\boldsymbol{\chi}} J_{\boldsymbol{\chi}\mapsto\boldsymbol{x}})(\boldsymbol{\chi},t)}_{\stackrel{\text{def}}{=}\rho_{\boldsymbol{\chi}}^G(\boldsymbol{\chi},t)}\,\mathrm{d}\boldsymbol{\chi}, \tag{2.23}$$

where $\rho_{(\cdot)}$ denotes the spatial density of the volume with a subscript indicating the different coordinate systems and $\rho_{\boldsymbol{X}}^0, \rho_{\boldsymbol{\chi}}^G$ the material and referential densities. Using the ALE transport

theorem to express the change of this volumetric quantity, mass conservation in a general ALE formulation emerges as

$$0 = \frac{\mathrm{d}M(t)}{\mathrm{d}t} = \int_{V_{\boldsymbol{\chi}}(t)} \frac{\partial \rho_{\boldsymbol{\chi}}^G}{\partial t}(\boldsymbol{\chi}, t) + \frac{\partial \rho_{\boldsymbol{\chi}}^G}{\partial \boldsymbol{\chi}}(\boldsymbol{\chi}, t) \cdot \boldsymbol{w}_{\boldsymbol{\chi}}(\boldsymbol{\chi}, t) + \rho_{\boldsymbol{\chi}}^G(\boldsymbol{\chi}, t)(\nabla_{\boldsymbol{\chi}} \cdot \boldsymbol{w}_{\boldsymbol{\chi}})(\boldsymbol{\chi}, t)\, \mathrm{d}\boldsymbol{\chi}, \tag{2.24}$$

$$0 = \frac{\mathrm{d}M(t)}{\mathrm{d}t} = \int_{V_{\boldsymbol{x}}(t)} \frac{\partial \rho_{\boldsymbol{\chi}}}{\partial t}(\boldsymbol{\Phi}^{-1}(\boldsymbol{x}, t)) + \frac{\partial \rho_{\boldsymbol{x}}}{\partial \boldsymbol{x}}(\boldsymbol{x}, t) \cdot \boldsymbol{c}_{\boldsymbol{x}}(\boldsymbol{x}, t) + \rho_{\boldsymbol{x}}(\boldsymbol{x}, t)(\nabla_{\boldsymbol{x}} \cdot \boldsymbol{u}_{\boldsymbol{x}})(\boldsymbol{x}, t)\, \mathrm{d}\boldsymbol{x}, \tag{2.25}$$

expressed with respect to referential coordinates ($\boldsymbol{\chi}$) and spatial coordinates ($\boldsymbol{x}$), respectively. This can be derived from (2.19) and (2.20) with $f_{\boldsymbol{\chi}}^G = \rho_{\boldsymbol{\chi}}^G$ and $f_{\boldsymbol{x}} = \rho_{\boldsymbol{x}}$.

Based on (2.24), *mass conservation in a Lagrangean description* simplifies to

$$0 = \int_{V_{\boldsymbol{X}}(t)=V_{\boldsymbol{X}}(T_0)} \frac{\partial \rho_{\boldsymbol{X}}^0}{\partial t}(\boldsymbol{X}, t)\, \mathrm{d}\boldsymbol{X} = \int_{V_{\boldsymbol{X}}(t)=V_{\boldsymbol{X}}(T_0)} \frac{\partial (\rho_{\boldsymbol{X}} J_{\boldsymbol{X}\mapsto\boldsymbol{x}})}{\partial t}(\boldsymbol{X}, t)\, \mathrm{d}\boldsymbol{X} \tag{2.26}$$

similarly to (2.21), which can be written even in local form as

$$0 = \frac{\partial \rho_{\boldsymbol{X}}^0}{\partial t}(\boldsymbol{X}, t) = \frac{\partial (\rho_{\boldsymbol{X}} J_{\boldsymbol{X}\mapsto\boldsymbol{x}})}{\partial t}(\boldsymbol{X}, t) \quad \forall\, (\boldsymbol{X}, t). \tag{2.27}$$

Based on (2.25) with $\boldsymbol{c}_{\boldsymbol{x}} \equiv \boldsymbol{u}_{\boldsymbol{x}}$, *mass conservation in an Eulerian description* simplifies to

$$0 = \int_{V_{\boldsymbol{x}}(t)} \frac{\partial \rho_{\boldsymbol{x}}}{\partial t}(\boldsymbol{x}, t) + \frac{\partial \rho_{\boldsymbol{x}}}{\partial \boldsymbol{x}}(\boldsymbol{x}, t) \cdot \boldsymbol{u}_{\boldsymbol{x}}(\boldsymbol{x}, t) + \rho_{\boldsymbol{x}}(\boldsymbol{x}, t)(\nabla_{\boldsymbol{x}} \cdot \boldsymbol{u}_{\boldsymbol{x}})(\boldsymbol{x}, t)\, \mathrm{d}\boldsymbol{x}, \tag{2.28}$$

which in local form can be rewritten similar as done in (2.22) as

$$0 = \frac{\partial \rho_{\boldsymbol{x}}}{\partial t}(\boldsymbol{x}, t) + \nabla_{\boldsymbol{x}} \cdot (\rho_{\boldsymbol{x}} \boldsymbol{u}_{\boldsymbol{x}})(\boldsymbol{x}, t) \quad \forall\, (\boldsymbol{x}, t). \tag{2.29}$$

Balance of Linear Momentum. Following Newton's second law, in continuum mechanics the change of linear momentum of a transported control volume $V_{\boldsymbol{x}}(t)$ is balanced by external forces which act on the volume and on its boundary $\partial V_{\boldsymbol{x}}(t)$. Thereby, the body forces are denoted by $\boldsymbol{f}_{(\cdot)}$ and surface tractions by $\boldsymbol{t}_{(\cdot)}$ with subscripts denoting the coordinate system. The linear momentum $P(t)$ in global form is given as a volume integral

$$P(t) = \int_{V_{\boldsymbol{x}}(t)} (\rho_{\boldsymbol{x}} \boldsymbol{u}_{\boldsymbol{x}})(\boldsymbol{x}, t)\, \mathrm{d}\boldsymbol{x} = \int_{V_{\boldsymbol{X}}(t)} (\rho_{\boldsymbol{X}}^0 \boldsymbol{u}_{\boldsymbol{X}})(\boldsymbol{X}, t)\, \mathrm{d}\boldsymbol{X} = \int_{V_{\boldsymbol{\chi}}(t)} (\rho_{\boldsymbol{\chi}}^G \boldsymbol{u}_{\boldsymbol{\chi}})(\boldsymbol{\chi}, t)\, \mathrm{d}\boldsymbol{\chi}. \tag{2.30}$$

Combining the ALE variant of the Reynolds transport theorem (2.19), the product rule and mass conservation (2.24) or their equivalences in spatial coordinates (2.20) and (2.25), the material time derivative of linear momentum emerges as

$$0 = \frac{\mathrm{d}P(t)}{\mathrm{d}t} = \int_{V_{\boldsymbol{\chi}}(t)} \rho_{\boldsymbol{\chi}}^G(\boldsymbol{\chi}, t) \left(\frac{\partial \boldsymbol{u}_{\boldsymbol{\chi}}}{\partial t}(\boldsymbol{\chi}, t) + \frac{\partial \boldsymbol{u}_{\boldsymbol{\chi}}}{\partial \boldsymbol{\chi}}(\boldsymbol{\chi}, t) \cdot \boldsymbol{w}_{\boldsymbol{\chi}}(\boldsymbol{\chi}, t) \right) \mathrm{d}\boldsymbol{\chi}, \tag{2.31}$$

$$0 = \frac{\mathrm{d}P(t)}{\mathrm{d}t} = \int_{V_{\boldsymbol{x}}(t)} \rho_{\boldsymbol{x}}(\boldsymbol{x}, t) \left(\frac{\partial \boldsymbol{u}_{\boldsymbol{\chi}}}{\partial t}(\boldsymbol{\Phi}^{-1}(\boldsymbol{x}, t)) + \frac{\partial \boldsymbol{u}_{\boldsymbol{x}}}{\partial \boldsymbol{x}}(\boldsymbol{x}, t) \cdot \boldsymbol{c}_{\boldsymbol{x}}(\boldsymbol{x}, t) \right) \mathrm{d}\boldsymbol{x}, \tag{2.32}$$

expressed with respect to referential and spatial coordinates, respectively. For further elaborations, see derivations in [119, 163]. The existence of a unique *Cauchy stress tensor* $\boldsymbol{\sigma}_{\boldsymbol{x}}$ for given surface traction $\boldsymbol{t}_{\boldsymbol{x}}$ which satisfies

$$\boldsymbol{\sigma}_{\boldsymbol{x}}(\boldsymbol{x},t)\cdot\boldsymbol{n}_{\boldsymbol{x}}(\boldsymbol{x},t)=\boldsymbol{t}_{\boldsymbol{x}}(\boldsymbol{x},t) \tag{2.33}$$

is stated by Cauchy's fundamental lemma. This allows to apply Gauss' divergence theorem to the surface traction.

Balancing the time derivative (2.32) with external loads, the ALE *balance of linear momentum* in spatial representation results in

$$\begin{aligned}0=\int_{V_{\boldsymbol{x}}(t)}\rho_{\boldsymbol{x}}(\boldsymbol{x},t)\left(\frac{\partial\boldsymbol{u}_{\chi}}{\partial t}(\boldsymbol{\Phi}^{-1}(\boldsymbol{x},t))+\frac{\partial\boldsymbol{u}_{\boldsymbol{x}}}{\partial\boldsymbol{x}}(\boldsymbol{x},t)\cdot\boldsymbol{c}_{\boldsymbol{x}}(\boldsymbol{x},t)\right)\mathrm{d}\boldsymbol{x}\\ -\int_{V_{\boldsymbol{x}}(t)}(\rho_{\boldsymbol{x}}\boldsymbol{f}_{\boldsymbol{x}}+\nabla_{\boldsymbol{x}}\cdot\boldsymbol{\sigma}_{\boldsymbol{x}})(\boldsymbol{x},t)\,\mathrm{d}\boldsymbol{x}.\end{aligned} \tag{2.34}$$

The *Eulerian version of linear momentum balance* simplifies to

$$\begin{aligned}0=\int_{V_{\boldsymbol{x}}(t)}\rho_{\boldsymbol{x}}(\boldsymbol{x},t)\left(\frac{\partial\boldsymbol{u}_{\boldsymbol{x}}}{\partial t}(\boldsymbol{x},t)+\frac{\partial\boldsymbol{u}_{\boldsymbol{x}}}{\partial\boldsymbol{x}}(\boldsymbol{x},t)\cdot\boldsymbol{u}_{\boldsymbol{x}}(\boldsymbol{x},t)\right)\mathrm{d}\boldsymbol{x}\\ -\int_{V_{\boldsymbol{x}}(t)}(\rho_{\boldsymbol{x}}\boldsymbol{f}_{\boldsymbol{x}}+\nabla_{\boldsymbol{x}}\cdot\boldsymbol{\sigma}_{\boldsymbol{x}})(\boldsymbol{x},t)\,\mathrm{d}\boldsymbol{x}.\end{aligned} \tag{2.35}$$

The *Lagrangean version of linear momentum balance* expressed in material coordinates is

$$0=\int_{V_{\boldsymbol{X}}(T_0)}\rho^0_{\boldsymbol{X}}(\boldsymbol{X},t)\frac{\partial\boldsymbol{u}_{\boldsymbol{X}}}{\partial t}(\boldsymbol{X},t)\,\mathrm{d}\boldsymbol{X}-\int_{V_{\boldsymbol{X}}(T_0)}(\rho^0_{\boldsymbol{X}}\boldsymbol{f}_{\boldsymbol{X}}+\nabla_{\boldsymbol{X}}\cdot\boldsymbol{\sigma}_{\boldsymbol{X}})(\boldsymbol{X},t)\,\mathrm{d}\boldsymbol{X}, \tag{2.36}$$

where $\nabla_{\boldsymbol{X}}\cdot(\cdot)$ denotes the material divergence operator and $\boldsymbol{\sigma}_{\boldsymbol{X}}$ a material stress tensor which emerges to $(\boldsymbol{\sigma}_{\boldsymbol{X}}\cdot\boldsymbol{n}_{\boldsymbol{X}})(\boldsymbol{X},t)=\boldsymbol{t}_{\boldsymbol{X}}(\boldsymbol{X},t)$, the pseudo surface traction in material configuration at the boundary $\partial V_{\boldsymbol{X}}(T_0)$. The material stress tensor $\boldsymbol{\sigma}_{\boldsymbol{X}}$ is also called *first Piola–Kirchhoff stress tensor* and is often notated with $\boldsymbol{P}$. Commonly used constitutive laws for the stress tensors will be proposed in the respective sections, see Section 3.1.1 for fluids and Section 5.1.1 for structures. For the sake of completeness, the balance of linear momentum is also called *Cauchy's first equation of motion*.

Remarks on Balance of Angular Momentum. A law for the balance of angular momentum can be deduced analogously to the balance of linear momentum. This finally results in a symmetry requirement for the Cauchy stress tensor $\boldsymbol{\sigma}_{\boldsymbol{x}}$ defined with respect to spatial coordinates in (2.33). While the first Piola–Kirchhoff stress tensor $\boldsymbol{P}$ in material coordinates is non-symmetric due to the mapping between spatial and material coordinates, balance of angular momentum demands symmetry for the Cauchy stress tensor $\boldsymbol{\sigma}_{\boldsymbol{x}}$

$$\boldsymbol{\sigma}_{\boldsymbol{x}}=\boldsymbol{\sigma}_{\boldsymbol{x}}^{T}. \tag{2.37}$$

This result is designated as *Cauchy's second equation of motion*.

2.1.3 Representation and Approximation of Boundaries and Interfaces

Over the past years different powerful numerical interface representation techniques and related temporal evolution algorithms have been devised for a host of complex problem settings. Such methods find their application in different application fields ranging from computational geometry, computer vision through to challenging setups in computational fluid mechanics. For the latter one, several numerical techniques like Particle Methods, as proposed, e.g., by Sethian [233] or Volume-of-fluid (VOF) approaches, see early works by Hirt and Nichols [151] and by Noh and Woodward [197] on a former technique, the Simple Line Interface Calculation (SLIC) method, have been developed to simulate temporally evolving interfaces in flows - to name but a few. For a more comprehensive overview, the interested reader is referred to, e.g., the textbook by Sethian [234]. Having in mind the major coupled flow problems to be addressed in the present work - the simulation of interactions between fluid phases with different material properties and the interaction between fluids and solids - focus is directed to the following two widely used techniques.

As a first approach, explicitly parametrized interfaces are considered. Tracking evolving interfaces using trace mesh approximations belongs to the class of so-called *front-tracking* methods. As a second technique, an implicit *front-capturing* method for evolving interfaces is introduced: the well-established *Level-Set Method*, as described, e.g., in the textbook by Sethian [234]. In the subsequent paragraphs the aforementioned approaches are introduced in some more detail and differences regarding the view of geometric perspective are elaborated. Moreover, the applicability to different flow problems with focus on the time-dependent evolution of boundaries, which the respective approaches entail, are discussed.

2.1.3.1 Explicit Front-Tracking using a Trace Mesh Representation

One of the most natural approaches to moving interface representations is the *Lagrangean interface tracking*. In the following, the evolving interface $\Gamma(t)$ is assumed to be the boundary of a moving domain $\Omega(t)$. Under the assumption of moderate deformations of the domain during $t \in (T_0, T)$, a Lagrangean description of the kinematics is an appropriate choice, see explanations in Section 2.1.2. Then, the motion from reference configuration $\Omega(T_0)$ defined at the initial time $t = T_0$ to the current configuration $\Omega(t)$ can be expressed in terms of the bijective mapping $\boldsymbol{\varphi}$, as described in (2.5). Alternatively, for a material particle $\boldsymbol{X}$ given in the referential configuration, which is equal to the initial configuration for this viewpoint, total displacements can be defined as

$$\boldsymbol{d}(\boldsymbol{X}, t) \stackrel{\text{def}}{=} \boldsymbol{x}_{\boldsymbol{X}}(\boldsymbol{X}, t) - \boldsymbol{X} \quad \forall\, \boldsymbol{X} \in \Omega(T_0). \tag{2.38}$$

The initial configuration $\Omega(T_0)$ is approximated geometrically as $\Omega_h(T_0)$ with a computational grid $\mathcal{T}_h$ consisting of a family of isoparametric finite elements $T \in \mathcal{T}_h$ such that

$$\Omega(T_0) \approx \Omega_h(T_0) \stackrel{\text{def}}{=} \bigcup\nolimits_{T \in \mathcal{T}_h} T, \tag{2.39}$$

where for each possibly curvilinear element $T \in \mathcal{T}_h$ a bijective mapping $S_T : \hat{T} \mapsto T$ from a referential d-simplex or a d-rectangle $\hat{T}$ exists. While an affine mapping S_T is assumed as a polynomial that is linear in all coordinates $\boldsymbol{\xi} = (\xi_1, \ldots, \xi_d)$ spanning the parameter space of the reference element $\hat{T}$, isoparametric mappings S_T are based on interpolation functions

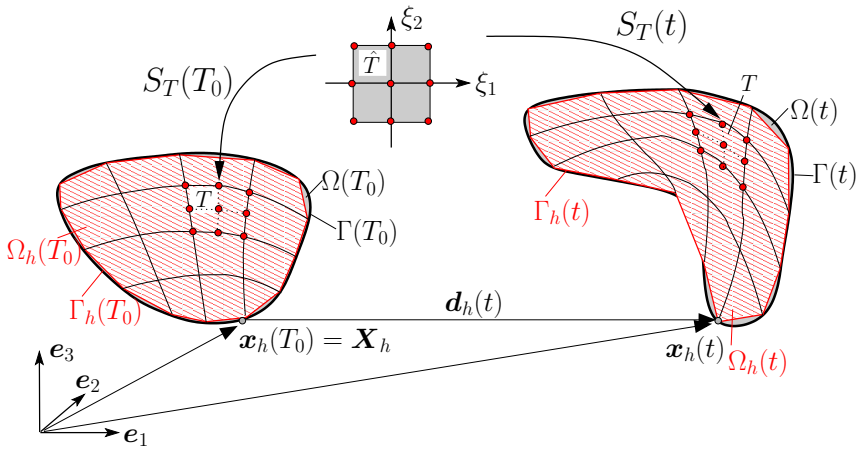

Figure 2.3: Basic notation for kinematic relations described in a Lagrangean frame of reference for a two-dimensional ($d = 2$) moving body approximated with a family of isoparametric finite elements.

$\hat{N}_s(\boldsymbol{\xi}) \in \mathbb{V}^k(\hat{T})$ ($s = 1, \ldots, \text{nnod}_{\hat{T}}$) of the reference element, which are often referred to as *shape functions*. The set of nodes in element $\hat{T}$ is denoted with $\mathcal{N}(\hat{T})$, the number of nodes with $\text{nnod}_{\hat{T}}$. For the element-wise interpolation in the parameter space $\boldsymbol{\xi}$, Lagrangean polynomials of order at most $k \geqslant 1$ are used. These constitute a basis of the polynomial function spaces $\mathbb{V}^k(\hat{T})$, i.e. $\mathbb{P}^k(\hat{T}), \mathbb{Q}^k(\hat{T}), \mathbb{W}^k(\hat{T})$ for simplices, rectangles or wedges $\hat{T}$, respectively. Domain approximations can then be composed of element-wise descriptions with respect to the element parameter spaces $\boldsymbol{\xi}$ as

$$\boldsymbol{X}_h|_T(\boldsymbol{\xi}) = \sum_{s=1}^{\text{nnod}_{\hat{T}}} \hat{N}_s(\boldsymbol{\xi}) \boldsymbol{X}_s, \tag{2.40}$$

$$\boldsymbol{x}_h|_T(\boldsymbol{\xi}, t) = \sum_{s=1}^{\text{nnod}_{\hat{T}}} \hat{N}_s(\boldsymbol{\xi}) \boldsymbol{x}_s(t) \quad t \in (T_0, T), \tag{2.41}$$

where $\boldsymbol{X}_s, \boldsymbol{x}_s(t)$ denote the location of the grid nodes in referential and spatial configurations. Defining node displacements $\boldsymbol{d}_s(t) \overset{\text{def}}{=} \boldsymbol{x}_s(t) - \boldsymbol{X}_s$, the time-dependent displacement field $\boldsymbol{d}$ can be approximated and parametrized element-wise by $\boldsymbol{\xi}$ as

$$\boldsymbol{d}_h|_T(\boldsymbol{\xi}, t) = \sum_{s=1}^{\text{nnod}_{\hat{T}}} \hat{N}_s(\boldsymbol{\xi}) \boldsymbol{d}_s(t). \tag{2.42}$$

In a non-element-wise context, notations $\boldsymbol{d}_h(\boldsymbol{X}_h, t)$ and $\boldsymbol{x}_h(\boldsymbol{X}_h, t)$ for $\boldsymbol{X}_h \in \Omega_h(T_0)$ are commonly used. A visualization of the isoparametric domain approximation is given in Figure 2.3. Finally, based on this concept, continuous isoparametric function spaces for piecewise polynomial approximations can be formulated in spatial coordinates as

$$\mathscr{X}_h(t) \overset{\text{def}}{=} \left\{ x_h \in C^0(\overline{\Omega_h}(t)) : x_h|_T = v_{\hat{T}} \circ S_T^{-1}(t) \text{ with } v_{\hat{T}} \in \mathbb{V}^k(\hat{T}) \, \forall \, T \in \mathscr{T}_h \right\}, \tag{2.43}$$

where $S_T^{-1}(t)$ denote mappings of spatial coordinates of $\Omega_h(t)$ at time t to the respective element parameter spaces $\boldsymbol{\xi}$.

Having introduced an approximation of the moving domain $\Omega(t)$, an approximate interface $\Gamma_h(t)$ can be easily defined. Based on the domain approximation $\Omega_h(t)$ with isoparametric

elements $T \in \mathcal{T}_h$, for elements T sharing faces with the boundary Γ, the d-dimensional element parameter spaces $\boldsymbol{\xi}$ can be restricted to $(d-1)$-dimensional trace parameter spaces $\boldsymbol{\eta}$. Thereby, a trace parameter space defines a parametrization of the facet of a d-dimensional reference element $\hat{T}$, which is a face for $d = 3$ and an edge for $d = 2$. Denoting the set of all faces of the computational mesh $\mathcal{T}_h$ with $\mathcal{F}_h$ and the set of exterior faces which are aligned with the boundary of domain $\Omega_h(t)$ with $\mathcal{F}_e$, an approximation of the interface $\Gamma(t)$ is

$$\Gamma(t) \approx \Gamma_h(t) \stackrel{\text{def}}{=} \bigcup\nolimits_{F \in \mathcal{F}_e} F. \tag{2.44}$$

Alternatively, considering an interface Γ as $(d-1)$-manifold independent of a domain Ω, an interface approximation can be defined directly, provided a unique orientation is given. Assuming an isoparametric family of $(d-1)$-dimensional faces $\mathcal{F}_e$ embedded into the d-dimensional coordinate space, face-wise descriptions of coordinates and displacements with respect to the underlying face parameter space $\boldsymbol{\eta}$ can be expressed as

$$\boldsymbol{X}_h|_F(\boldsymbol{\eta}) = \sum\nolimits_{l=1}^{\text{nnod}_{\hat{F}}} \hat{N}_l|_{\hat{F}}(\boldsymbol{\eta}) \boldsymbol{X}_l, \tag{2.45}$$

$$\boldsymbol{x}_h|_F(\boldsymbol{\eta}, t) = \sum\nolimits_{l=1}^{\text{nnod}_{\hat{F}}} \hat{N}_l|_{\hat{F}}(\boldsymbol{\eta}) \boldsymbol{x}_l(t) \quad t \in (T_0, T), \tag{2.46}$$

$$\boldsymbol{d}_h|_F(\boldsymbol{\eta}, t) = \sum\nolimits_{l=1}^{\text{nnod}_{\hat{F}}} \hat{N}_l|_{\hat{F}}(\boldsymbol{\eta}) \boldsymbol{d}_l(t) \quad t \in (T_0, T), \tag{2.47}$$

where $\boldsymbol{X}_l, \boldsymbol{x}_l(t)$ are the d-dimensional coordinates of the $\text{nnod}_{\hat{F}}$ interfacial grid nodes in referential and spatial configurations. It can be defined further $\boldsymbol{d}_l(t) \stackrel{\text{def}}{=} \boldsymbol{x}_l(t) - \boldsymbol{X}_l$. Note that the parameter space $\boldsymbol{\eta}$ is $(d-1)$-dimensional. The manifold, however, carries d-dimensional coordinates. Interface/domain approximations and their according face/element parameter spaces are exemplarily shown for $d = 3$ in Figure 2.4.

This explicit front-tracking technique is useful in particular for problem situations where the interface evolves naturally as the boundary of a subdomain which is geometrically approximated with a fitted mesh and where kinematic relations are described in moving reference systems $\boldsymbol{\chi}$, as it is the case for Lagrangean and Arbitrary-Lagrangean-Eulerian methods. Prerequisite for such an interface tracking technique, as well as for the underlying kinematic descriptions, is a moderate deformation of the computational grid preserving the mesh quality during the simulation. Promising application areas within the scope of complex coupled flow problems are discussed in Section 2.1.4 and applied to different flow problem settings in Chapters 4 and 5.

2.1.3.2 Implicit Front-Capturing Level-Set Method

Level-set methods are based on an implicit description of an evolving $(d-1)$-dimensional manifold by embedding its initial position as a zero-level-set of a scalar function, which is denoted by $\phi(\boldsymbol{x}, t)$ in the present work. This function is defined in a d-dimensional domain Ω enclosing the interface. At any time, Lagrangean particles $\boldsymbol{X}$ follow the moving interface front $\Gamma^{ij}(t)$ along time-dependent paths $\boldsymbol{x}(\boldsymbol{X}, t) \in \Omega$, which allows to describe the interface as

$$\Gamma^{ij}(t) \stackrel{\text{def}}{=} \{\boldsymbol{x} \in \Omega \mid \phi(\boldsymbol{x}, t) = 0\}. \tag{2.48}$$

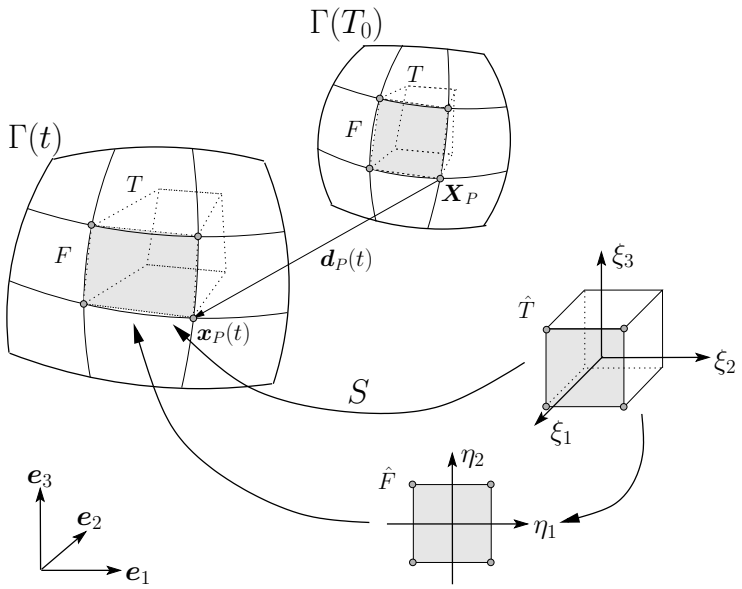

Figure 2.4: Explicit front-tracking based on a trace mesh approximation of a 2-manifold embedded into the three-dimensional space ($d = 3$). Isoparametric family of 4-node face-elements $F \in \mathscr{F}_e$ with reference faces $\hat{F}$ parametrized with $(d-1)$-dimensional parameter space $\boldsymbol{\eta}$ constructed as the trace of reference elements $\hat{T}$ with corresponding element parameter coordinates $\boldsymbol{\xi}$.

For such a level-set function ϕ, the following sign convention holds at any time $t \in (T_0, T)$ which enables to separate two subdomains Ω^i, Ω^j $(i < j)$ in a univocal manner

$$\phi(\boldsymbol{x}, t) \begin{cases} > 0 & \forall\, \boldsymbol{x} \in \Omega^j(t), \\ = 0 & \forall\, \boldsymbol{x} \in \Gamma^{ij}(t), \\ < 0 & \forall\, \boldsymbol{x} \in \Omega^i(t). \end{cases} \tag{2.49}$$

Following the explanations in Section 2.1.2, particles $\boldsymbol{X}$ moving with the interface front require that $\phi_{\boldsymbol{x}}(\boldsymbol{x}(\boldsymbol{X}, t), t) = \phi_{\boldsymbol{X}}(\boldsymbol{X}, t)\ \forall\, t \in (T_0, T)$, which implies an initial value formulation for its temporal evolution

$$\left.\frac{\partial \phi}{\partial t}\right|_{\boldsymbol{x}} + \boldsymbol{u} \cdot \nabla \phi = 0 \quad \forall\, (\boldsymbol{x}, t) \in \Omega \times (T_0, T), \tag{2.50}$$

$$\left.\frac{\partial \phi}{\partial t}\right|_{\boldsymbol{\chi}} + \boldsymbol{c} \cdot \nabla \phi = 0 \quad \forall\, (\boldsymbol{x}, t) \in \Omega \times (T_0, T), \tag{2.51}$$

written in an Eulerian and an ALE-frame of reference, respectively. Note that all gradients denote spatial derivatives, i.e. $\nabla(\cdot) = \nabla_{\boldsymbol{x}}(\cdot)$. Initially, the solution of these transport equations has to satisfy the initial condition $\phi(t = T_0) = \phi_0$. Assuming a moving reference system in an ALE description, the relative transport velocity occurring in (2.51) is defined as $\boldsymbol{c} \overset{\text{def}}{=} \boldsymbol{u} - \hat{\boldsymbol{u}}$, where $\hat{\boldsymbol{u}}$ is the velocity of the moving reference system. This simplifies to $\boldsymbol{c} \overset{\text{def}}{=} \boldsymbol{u}$ for a fixed Eulerian configuration in (2.50). When dealing with moving boundaries, the advective transport velocity $\boldsymbol{u}$ can be predefined externally, can depend on the geometrical description itself or can

be the solution of a surrounding flow field. The latter is the case, for instance, when the front is transported as separating interface between two fluid phases. For an overview about possible discretization techniques of equations (2.50) and (2.51), the reader is referred to textbooks by, e.g., Sethian [234] or Donéa and Huerta [91].

The level-set function ϕ is assumed to be a signed-distance function and is initially defined as

$$\phi(\boldsymbol{x}, T_0) = \min_{\tilde{\boldsymbol{x}} \in \Gamma^{ij}(T_0)} \left(\operatorname{sign}\left((\boldsymbol{x} - \tilde{\boldsymbol{x}}) \cdot \boldsymbol{n}^{ij} \right) \|\boldsymbol{x} - \tilde{\boldsymbol{x}}\| \right) \quad \forall\, \boldsymbol{x} \in \Omega, \tag{2.52}$$

implying $\|\nabla \phi(\boldsymbol{x}, T_0)\| = 1$. Due to different transport velocities near the interface front, when the interface evolves, the signed-distance property can get lost. To guarantee accurate approximations of the zero-isocontour and to avoid mass loss, interface-preserving re-distancing measures have to be performed periodically; for an introduction to this topic, see the textbook by Sethian [234]. Recent applications to advanced multiphase-flow settings can be found in works by, e.g., Henke [147] or Rasthofer [215] and references therein.

Due to the implicit representation of the interface, geometric quantities like interface unit normal vector $\boldsymbol{n}$ and interface curvature κ can be computed $\forall\, \boldsymbol{x} \in \Gamma(t)$ as

$$\boldsymbol{n}(\boldsymbol{x}) = \frac{\nabla \phi(\boldsymbol{x})}{\|\nabla \phi(\boldsymbol{x})\|} \qquad \text{and} \qquad \kappa(\boldsymbol{x}) = -\nabla \cdot \left(\frac{\nabla \phi(\boldsymbol{x})}{\|\nabla \phi(\boldsymbol{x})\|} \right), \tag{2.53}$$

where $\nabla \cdot (\cdot)$ denotes the spatial divergence operator.

For the numerical discretization, let $\{\mathcal{T}_h\}_{h>0}$ be a family of meshes with mesh size parameter $h > 0$, which approximate the entire open and bounded domain Ω. Continuous finite element spaces used for the approximation of the level-set function ϕ_h are defined as

$$\mathcal{S}_h \overset{\text{def}}{=} \left\{ \phi_h \in C^0(\overline{\Omega_h}) : \phi_h|_T \in \mathbb{V}^k(T)\, \forall\, T \in \mathcal{T}_h \right\}, \tag{2.54}$$

based on piecewise polynomials of order $k \geqslant 1$ on tetrahedral, hexahedral or wedge-shaped ($\mathbb{V} \in \{\mathbb{P}, \mathbb{Q}, \mathbb{W}\}$) elements $T \in \mathcal{T}_h$. The extension to isoparametric finite element discretizations would be straightforward.

For the approximation of the smooth zero-isocontour Γ a piecewise planar surface Γ_h consisting of linear triangles ($d = 3$) or lines ($d = 2$) is assumed. Depending on the finite elements and the polynomial degree k, continuous piecewise linear function approximations $\mathcal{I}(\phi_h)$ of ϕ_h on regular refinements and subdivisions of non-planar interface segments are required, as proposed, e.g., by Groß and Reusken [135]. If not stated otherwise, in the present work, affine linear elements ($k = 1$) are used exclusively. The interface approximation is then given as

$$\Gamma_h(t) \overset{\text{def}}{=} \{ \boldsymbol{x} \in \Omega \mid \mathcal{I}(\phi_h)(\boldsymbol{x}, t) = 0 \}. \tag{2.55}$$

Note that, in particular for higher-order approximations $\mathcal{S}_h$, the geometric approximation of Ω_h and Γ_h needs to be computed sufficiently accurate to retain optimal error convergence properties in the overall *a priori* error estimates; see, e.g., recent works by Lehrenfeld [175], Fries and Omerović [116] and Burman *et al.* [65] on related topics. As an example, the implicit representation of a complex torus-shaped manifold together with a potential interface approximation and its construction within one finite element is shown in Figure 2.5.

In particular for multifield problem settings, as introduced in Section 2.1.1, the level-set framework for embedded interfaces and boundaries provides a powerful tool. As one decisive feature,

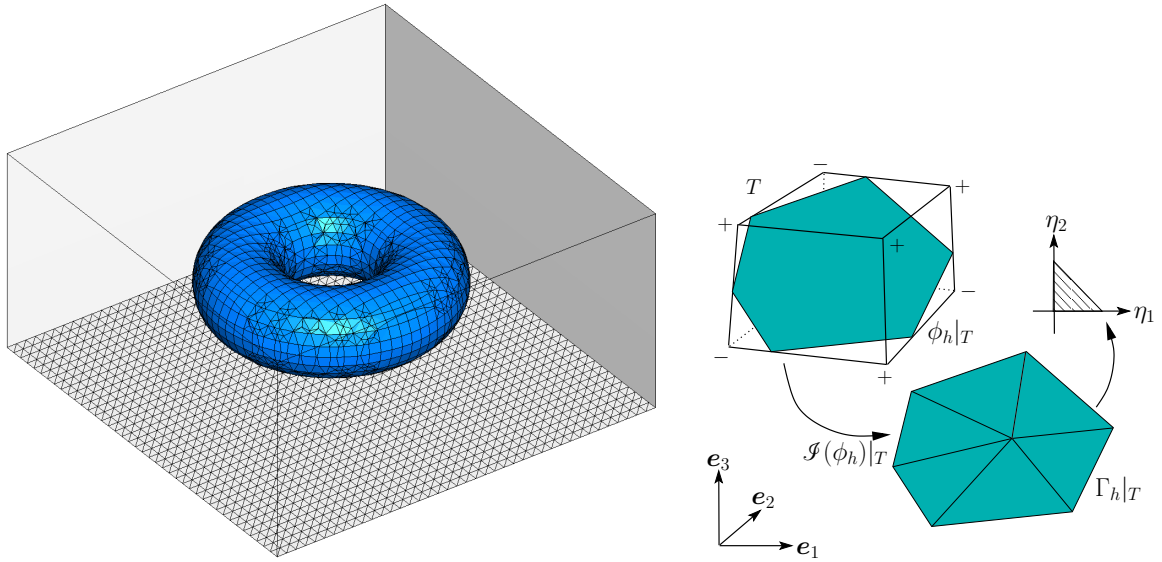

Figure 2.5: Approximation of a torus-shaped manifold which is defined as the zero-isocontour of the level-set function $\phi(x_1, x_2, x_3)^2 = (\sqrt{x_1^2 + x_2^2} - R)^2 + x_3^2 - r^2$, see (A.9), with $r = 0.05, R = 0.2$ (left). Element-wise approximation of discrete level-set field ϕ_h and subdivision into simple shaped triangular elements, defining Γ_h within one element $T \in \mathcal{T}_h$ (right).

the evolution of fronts $\Gamma^{ij}(t)$ can be dealt with quite naturally by solving a transport partial differential equation (PDE) as stated in (2.50), which enables an accurate transport of interfaces which separate different phases. However, not only its ability to simply compute geometric quantities, as proposed in (2.53), but, in particular, the attractive feature of naturally handling topological changes as breaking and merging of evolving fronts, level-set representations reach their full potential in complex multiphase-flow situations. For such problems settings, even when the interface undergoes very large changes, frequent time-consuming remeshing of the computational domain can be avoided. How to benefit from level-set methods in the context of a Nitsche-type extended variational multiscale method for incompressible two-phase flow has been recently proposed by Schott and Rasthofer *et al.* [231]; its further application to premixed combustion has been discussed by Henke [147].

As a further important advantage, logical combinations of various level-set functions ϕ^i can drastically simplify mesh generation on complex geometries. Boolean set operations for implicit surfaces have been provided by Sethian [234]. Assuming two subregions Ω^1, Ω^2 represented by negative values of respective level-set functions ϕ^1, ϕ^2, different set operations can be realized easily

$$\Omega^{1,c} \quad \Leftrightarrow \quad \phi = -\phi^1, \tag{2.56}$$

$$\Omega^1 \cap \Omega^2 \quad \Leftrightarrow \quad \phi = \max\left\{\phi^1, \phi^2\right\}, \tag{2.57}$$

$$\Omega^1 \cup \Omega^2 \quad \Leftrightarrow \quad \phi = \min\left\{\phi^1, \phi^2\right\}, \tag{2.58}$$

$$\Omega^1 \setminus \Omega^2 \quad \Leftrightarrow \quad \phi = \max\left\{\phi^1, -\phi^2\right\}, \tag{2.59}$$

$$\Omega^1 \triangle \Omega^2 \quad \Leftrightarrow \quad \phi = \min\left\{\max\left\{\phi^1, -\phi^2\right\}, \max\left\{\phi^2, -\phi^1\right\}\right\}, \tag{2.60}$$

where $(\cdot)^c$ denotes the complementary set and $\triangle$ the symmetric difference of two sets. Concatenation of Boolean operations for an arbitrary number of subregions can be used then to easily create complex regions by simply replacing the set operators with $\min/\max$-operations on the respective level-set functions. It is assumed thereby that all level-set fields ϕ^{ij} are discretized on the same approximation space $\mathscr{S}_h$. Otherwise, additional projections between different grids have to be introduced. Note that even combinations with evolving interfaces can be performed. The signed-distance properties of each level-set field are preserved by these operations, the accuracy of the approximation, however, is limited to the mesh size h of the underlying grid.

Recently, Burman *et al.* [63] proposed some examples based upon logical combinations of level-set functions describing basic geometric forms. An overview of implicit descriptions of most common geometric objects up to more advanced shapes, like a helical pipe, is given in Appendix A. An example for a complex-shaped computational domain exclusively described by Boolean combinations of several level-set functions is shown in Figure A.2; its defining composed level-set function is provided in Appendix A.3. This example of a composed geometry will be later utilized for flow simulations in Section 3.6.2.3.

2.1.4 General Concepts of Domain Decomposition Techniques

Multiphysics problems typically put highest demands on their discretization spaces. Coupled problems consisting of several physics like, e.g., fluids, solids, transport phenomena of scalar quantities or many others, require different specific mesh qualities for the involved single fields. The field solutions strongly dependent on material laws and properties as well as on given data and the governing equations. Depending on the physical field, well-suited finite-element-based discretizations have been developed which often make use of individual mesh features, like size, shape and polynomial degree of finite elements, or differ in the choice between a continuous and a discontinuous Galerkin scheme. Several approaches are also based on specific finite element families. Such range from spectral elements to enriched function spaces and others are designed to directly incorporate certain approximation features, as they arise, e.g., from the div- and curl-operators. For an overview of the enormous variety of finite element technologies, the interested reader is referred to, e.g., [3, 37, 78, 195, 216, 217].

In that way, it seems a logical conclusion to make the attempt to combine optimal single field discretizations within a domain decomposition approach and to couple the different approximation spaces at common interfaces. The domain of a multiphysics problem setting, as introduced in Section 2.1.1, can be thereby either composed of subdomains associated with different physics, or a domain, which belongs to one physical field, can be artificially decomposed into subregions in order to compose several specific meshes. As the meaning of the term *domain decomposition* changes in literature depending on the context it is used, it needs to be pointed out that throughout the present thesis this naming solely designates the split of the physical domain into subregions, which comes along with interface couplings governed by certain coupling constraints. In the following, an overview of finite-element-based domain decomposition strategies is given and general concepts are introduced. Focus is directed to their applicability to multiphysics problems, which involve, among others, incompressible flows. Further emphasis is put on their ability to deal with time-dependent phase boundaries.

Considering a single domain Ω, the basic concept of FEMs consists in a decomposition of the approximated computational domain Ω_h into simple-shaped finite elements, as introduced

in (2.39). Throughout this thesis, low-order two- and three-dimensional finite elements based on Lagrangean interpolation functions of degree $k = 1, 2$ are exclusively used. Their element-wise polynomial finite element spaces are denoted by $\mathbb{P}^k$ for simplices, by $\mathbb{Q}^k$ for hexahedral and by $\mathbb{W}^k$ for wedge-shaped elements. For simplices, the index k denotes the total degree of the polynomial. In contrast, for hexahedral elements, k specifies the polynomial degree in each coordinate direction. Accordingly, the notation holds for wedge-shaped elements. In the present work, these different element types are also referred to as 3-node triangular (*tri3*), 6-node triangular (*tri6*), 4-node quadrilateral (*quad4*), 8-node quadrilateral (*quad8*) and 9-node quadrilateral (*quad9*) in 2D and as 4-node tetrahedral (*tet4*), 10-node tetrahedral (*tet10*), 8-node hexahedral (*hex8*), 20-node hexahedral (*hex20*) and 27-node hexahedral (*hex27*) in 3D. The three-dimensional wedge-shaped elements are called 6-node wedge (*wedge6*) and 15-node wedge (*wedge15*).

2.1.4.1 Notation and Terminology on Computational Domains and Meshes

First of all, terminology and notation frequently used in the context of domain decomposition techniques are introduced. In literature, some terms describing the mesh location with respect to the physical domain and the positioning of different meshes relative to each other often differ. Their meanings often depend on the considered application and on the specific utilized numerical scheme. To avoid misunderstandings, the following terminology on computational domains and meshes is used throughout this thesis:

Let $\widehat{\mathcal{T}}_h$ be a background mesh with mesh size parameter $h > 0$ which covers an open and bounded physical domain Ω. The *active* part of this mesh is defined as

$$\mathcal{T}_h = \{T \in \widehat{\mathcal{T}}_h : T \cap \Omega \neq \emptyset\} \tag{2.61}$$

consisting of all elements in $\widehat{\mathcal{T}}_h$ which intersect Ω. Denoting the union of all elements $T \in \mathcal{T}_h$ by Ω_h^*, then $\mathcal{T}_h$ is called a *(geometrically) fitted* or more precisely a *boundary-fitted* mesh if $\overline{\Omega_h} = \overline{\Omega_h^*}$ and an *unfitted* or *non-boundary-fitted* mesh if $\overline{\Omega_h} \subsetneq \overline{\Omega_h^*}$. In the latter case it is referred to Ω_h^* as *fictitious domain*. To each mesh, the subset of elements that intersect the boundary Γ

$$\mathcal{T}_\Gamma = \{T \in \mathcal{T}_h : T \cap \Gamma \neq \emptyset\} \tag{2.62}$$

is associated, which plays a particular role for unfitted meshes. Notations related to fitted and unfitted computational meshes are depicted in Figure 2.6. For a given mesh $\mathcal{T}_h$, the space

$$\mathscr{X}_h \overset{\text{def}}{=} \left\{v_h \in C^0(\Omega_h^*) : v_h|_T \in \mathbb{V}^k(T) \,\forall\, T \in \mathcal{T}_h\right\} \tag{2.63}$$

denotes the finite element approximation space consisting of continuous piecewise polynomials of order $k \geqslant 1$ and

$$\mathscr{X}_h^{\text{dc}} \overset{\text{def}}{=} \left\{v_h \in L^2(\Omega_h^*) : v_h|_T \in \mathbb{V}^k(T) \,\forall\, T \in \mathcal{T}_h\right\} \tag{2.64}$$

the space of discontinuous piecewise polynomials. In contrast to the continuous space, where degrees of freedom at common nodes of neighboring elements are shared by all adjacent elements, in a discontinuous function space, each element $T \in \mathcal{T}_h$ carries own degrees of freedom for all its nodes. The concept of element-wise continuous and discontinuous function spaces can be analogously transferred when domains are decomposed into subregions, which is referred to as *domain decomposition* in this work.

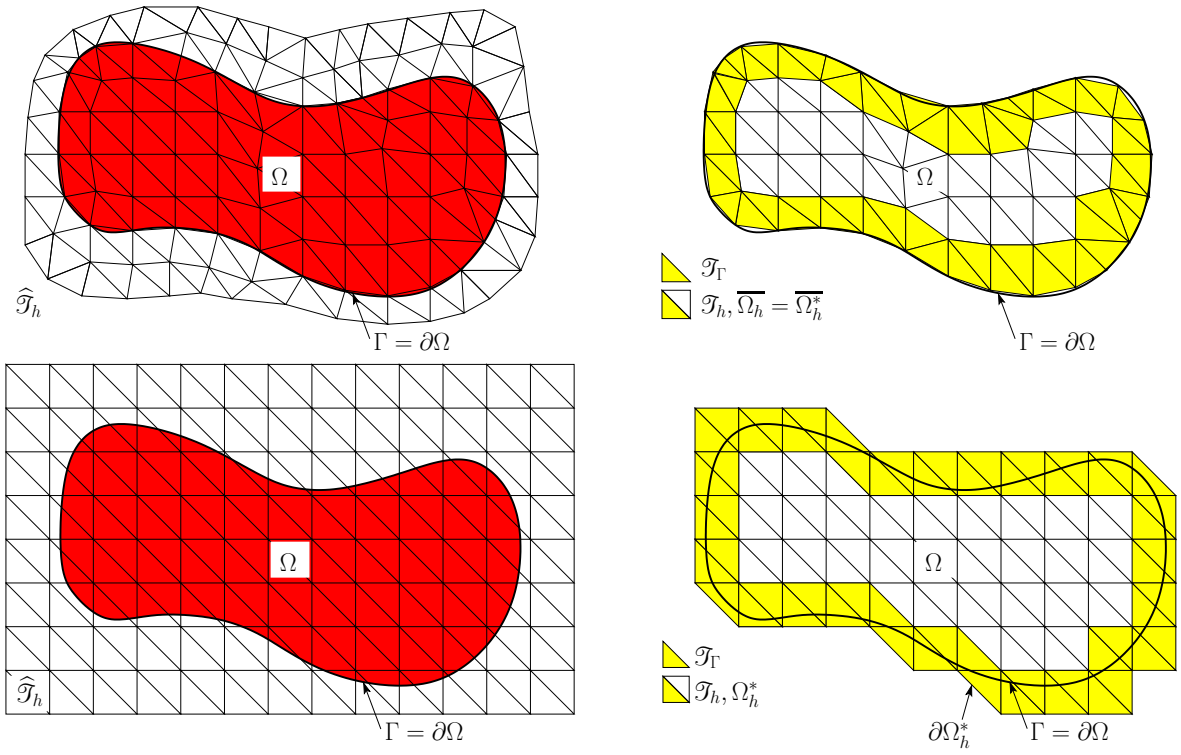

Figure 2.6: Boundary-fitted versus non-boundary-fitted meshes: A computational grid $\widehat{\mathcal{T}}_h$ is (geometrically) fitted to the boundary Γ of a physical domain Ω (upper left) and its active part $\mathcal{T}_h$ fits to the domain such that $\overline{\Omega_h} = \overline{\Omega_h^*}$ (upper right). The physical domain Ω is defined as the interior of a given boundary Γ embedded into an unfitted background mesh $\widehat{\mathcal{T}}_h$ (lower left), the fictitious domain Ω_h^* is the union of the minimal subset $\mathcal{T}_h \subset \widehat{\mathcal{T}}_h$ covering Ω (lower right).

2.1.4.2 Limitations of Fitted Mesh Discretization Techniques

Considering a domain Ω decomposed into two disjoint subdomains Ω^1, Ω^2, as introduced in Section 2.1.1, two covering meshes $\mathcal{T}_h^1, \mathcal{T}_h^2$ which are assumed to be fitted to the common interface Γ^{12} are called *matching* or *node-matching* whenever all nodes located at the interface are shared by both meshes. This, however, does not necessarily imply that the two meshes even have to carry identical sets of degrees of freedom associated with these nodes. If additionally all interfacial degrees of freedom are shared by both discretizations, a natural continuity condition is built in the discrete finite element function space $\mathcal{X}_h$. In contrast, having two independent sets of interface DOFs, the composed space $\mathcal{X}_h = \mathcal{X}_h^1 \oplus \mathcal{X}_h^2$ is discontinuous by construction and, in that way, allows for capturing sharp discontinuities in the physical fields across the interface. Then, however, additional measures are required to impose interface coupling conditions. For this purpose, different techniques will be elaborated in detail and examined carefully with focus on stability and optimality properties in Chapters 3–5.

Computational grids which are all fitted to the interface, however, non-node-matching to each other, are denoted as *non-matching* meshes. Different possible domain decomposition concepts based upon interface-fitted matching and non-matching meshes are depicted in Figure 2.7. Note that all domain decomposition methods considered in this work are based on continuous subdomain functions spaces $\mathcal{X}_h^i$.

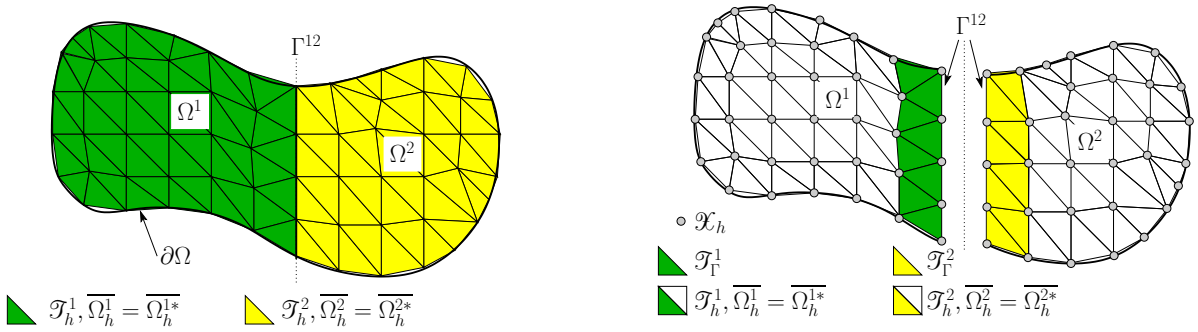

(a) Subdomain meshes are node-matching. The finite element function space $\mathscr{X}_h$ is strongly continuous across the interface Γ^{12} as all interfacial DOFs are shared by the two meshes.

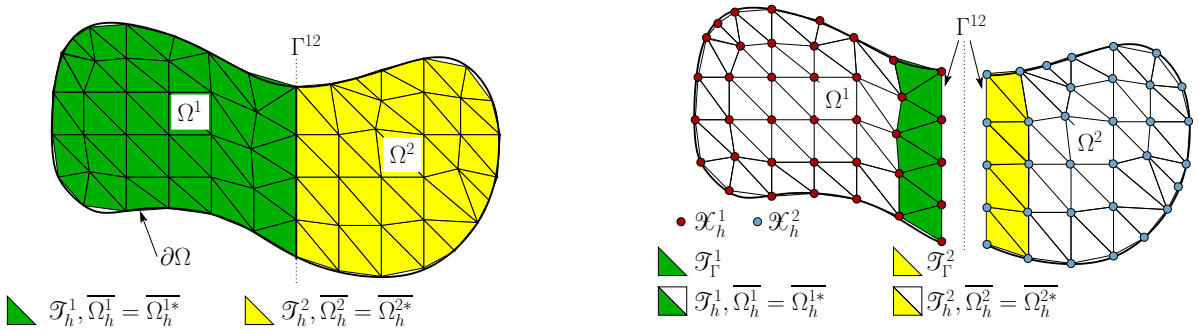

(b) Fitted domain decomposition with node-matching subdomain meshes $\mathscr{T}_h^1, \mathscr{T}_h^2$ at the interface Γ^{12}. Discrete composed function space $\mathscr{X}_h = \mathscr{X}_h^1 \oplus \mathscr{X}_h^2$ allows for strong discontinuities across Γ^{12}.

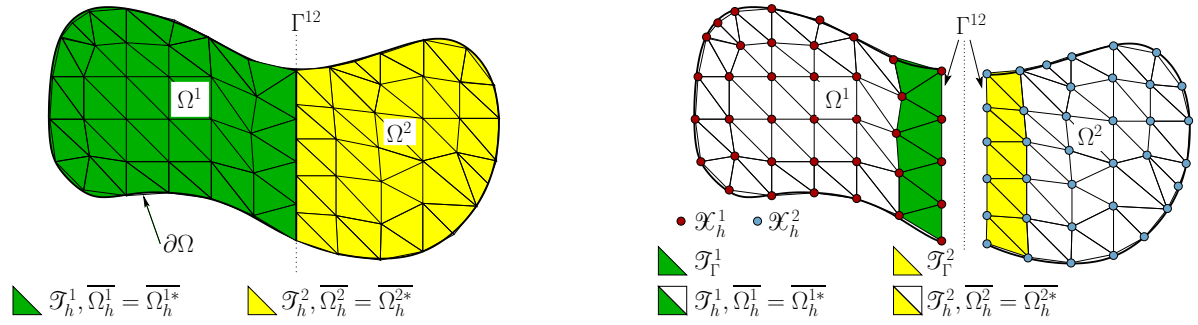

(c) Fitted domain decomposition with non-node-matching subdomain meshes $\mathscr{T}_h^1$ and $\mathscr{T}_h^2$ at the interface Γ^{12}. Discrete composed function space $\mathscr{X}_h = \mathscr{X}_h^1 \oplus \mathscr{X}_h^2$ allows for strong discontinuities across Γ^{12} and different mesh sizes.

Figure 2.7: Domain decomposition strategies for $\Omega_h = \Omega_h^1 \dot{\cup} \Omega_h^2$ based upon interface-fitted meshes, i.e. $\overline{\Omega_h^1} = \overline{\Omega_h^{1*}}$ and $\overline{\Omega_h^2} = \overline{\Omega_h^{2*}}$.

To demonstrate the capabilities and limitations of interface-fitted domain decomposition strategies in the following, the example of fluid-structure interaction (FSI), which is one of the primary coupled multiphysics applications considered in the present work, is predestined. In fact, the use of a single *matching* continuous finite element function space for the entire domain Ω, for which the continuity of the fields is strongly incorporated in the discrete space, is one of the most easiest and feasible finite element discretization methods. Regarding stability no additional measures are required at the interface and continuity requirements are automatically fulfilled. This choice, however, comes along with very restrictive limitations for transient problems with moving domains. For instance for fluid-structure interaction, where the fluid is classically described with an ALE moving mesh approach and the solid is formulated in a Lagrangean frame of reference (see, e.g., works by Küttler [168] and Mayr *et al.* [185] for such approaches), the temporal motion and deformation of the solid is strictly limited. Otherwise, the fluid mesh can distort and time consuming remeshing and projection steps have to be performed regularly. Limitations of matching approximations for moving domain problems are indicated in Figure 2.8.

Using *non-matching* fluid and structural meshes instead, already extends the applicability of FSI algorithms to a greater multitude of problem settings, as also shown in Figure 2.8. Relaxation of the strong node-matching constraint allows for independent mesh movements in interface-tangential directions and thus enables for instance large structural rotations in an embedded fluid and thereby allows for different mesh sizes. Such a technique has been considered, e.g., by Klöppel *et al.* [164] in combination with an inf-sup stable dual mortar Lagrange-multiplier approach to weakly impose the required continuity of the field solutions. For flow problems, non-matching mesh methods rather show their high potential in situations when mass transport across the interface is allowed. This is the case for mesh-tying problems when an interface is introduced to artificially separate a single physical domain into different phases carrying the same material. Such problem settings will be considered in more detail in Section 4.3. However, when phase change across the interface is not physically motivated due to mass conservation constraints, as it would be the case for fluid-structure interaction or immiscible two-phase flow, the interface is naturally largely driven in interface-normal direction following the material particles in their motion. In that way, approaches which utilize interface-fitted meshes are still limited in domain motions and deformations. As already indicated in Figure 2.8, a powerful strategy to overcome such limitations consists in decoupling computational meshes from the geometries.

2.1.4.3 Capabilities of Unfitted Mesh Techniques for Multiphysics

The main focus in this thesis is to develop computational approaches to multiphysics problems that involve incompressible flows and thereby reduce restrictions on the interface location and its temporal movement. The fundamental idea is to construct finite-element-based computational grids, which serve as basis for the discrete function spaces used for the approximation of the solutions, however, may be independent of the location of the separating phase boundary. Due to the temporal interface motion, which may be prescribed by given data or be naturally computed from the field solutions, the overall domain Ω_h gets separated into time-dependent subregions $\Omega_h^1(t)$ and $\Omega_h^2(t)$. The background meshes $\widehat{\mathcal{T}}_h^1$ and $\widehat{\mathcal{T}}_h^2$ associated with the subdomains, however, are now assumed to be non-fitted to the moving interface $\Gamma(t)$. Each

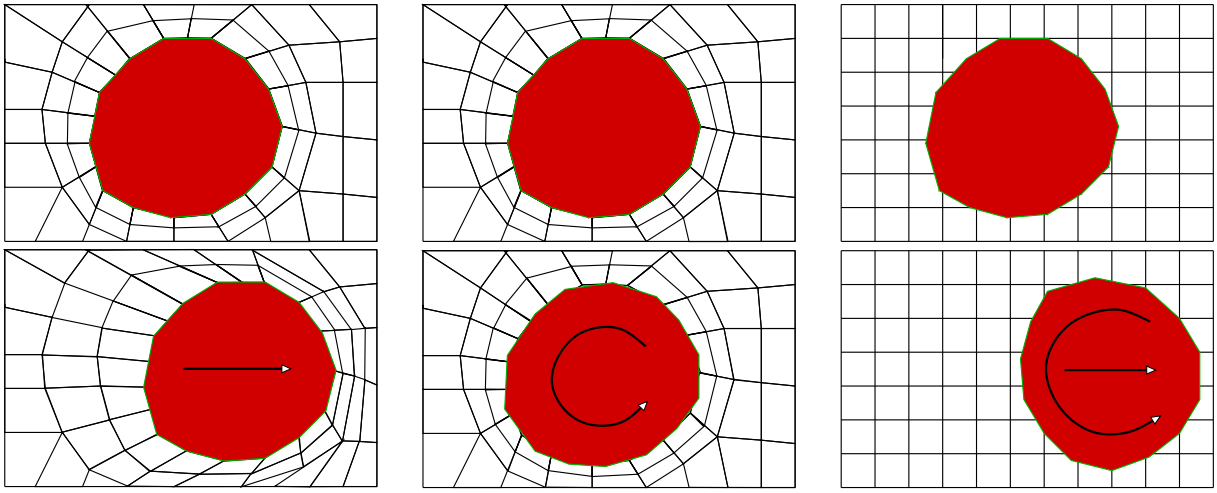

Figure 2.8: Multiphysics with moving domains: (Left) *Node-matching moving meshes* are subjected to strict limitations regarding their interface motion and deformation, otherwise the meshes can distort. (Middle) *Interface-fitted non-node-matching meshes* enable mesh motion in interface-tangential directions, but can fail for large mesh movement in interface-normal directions. (Right) *Unfitted non-matching meshes* allow for arbitrary motion of the meshes relative to each other.

mesh can be either fixed in space or even moving over time, if a general ALE-framework is applied, as introduced in Section 2.1.2. Thereby, interface and mesh motions can be treated fully decoupled from each other. It has to be remarked that for time-dependent domains the active parts $\mathcal{T}_h^1, \mathcal{T}_h^2$ of the respective background meshes are changing over time, see definition (2.61). As introduced in (2.62), respective sets of elements intersected by the interface are given by $\mathcal{T}_\Gamma^1 = \{T \in \mathcal{T}_h^1 : T \cap \Gamma \neq \emptyset\}$ and $\mathcal{T}_\Gamma^2 = \{T \in \mathcal{T}_h^2 : T \cap \Gamma \neq \emptyset\}$. Related fictitious subdomains $\Omega_h^{1*}, \Omega_h^{2*}$ are defined accordingly. This serves as starting point for specific strategies considered subsequently. A visualization of this generalized unfitted domain decomposition discretization strategy is shown in Figure 2.9.

While interface-fitted approaches are often also referred to as *non-overlapping* mesh methods in literature, numerical schemes where the boundary of the finite element grid does not fit to the interface include terms like *overlapping mesh method*. Throughout this work, this classification is only used to describe the positioning of the meshes relative to each other. Moreover, in literature, the term *overlapping meshes* often automatically implies that weak formulations related to the field governing equations are evaluated not only in the physically meaningful part of the respective active mesh, namely $\Omega^i \cap \mathcal{T}_h^i$, but twice in the overlap region of the two meshes. This implication, however, is expressly not desired for all formulations presented in this work.

Treating interface motions independent of the computational grids now widens the range of feasible interface-coupled multiphysics problems. In this thesis, focus is put on applications where incompressible flows are involved in one or two subdomains. In the following, some examples for coupled flow problems, which will be considered in more detail later in this work, are sketched in view of the applicability of different geometrically unfitted mesh approaches. More detailed elaborations on these problem settings, stabilized weak formulations, numerical examples as well as discussions with regard to their placement within a more general context of other related methods are provided in respective paragraphs in Chapters 3–5.

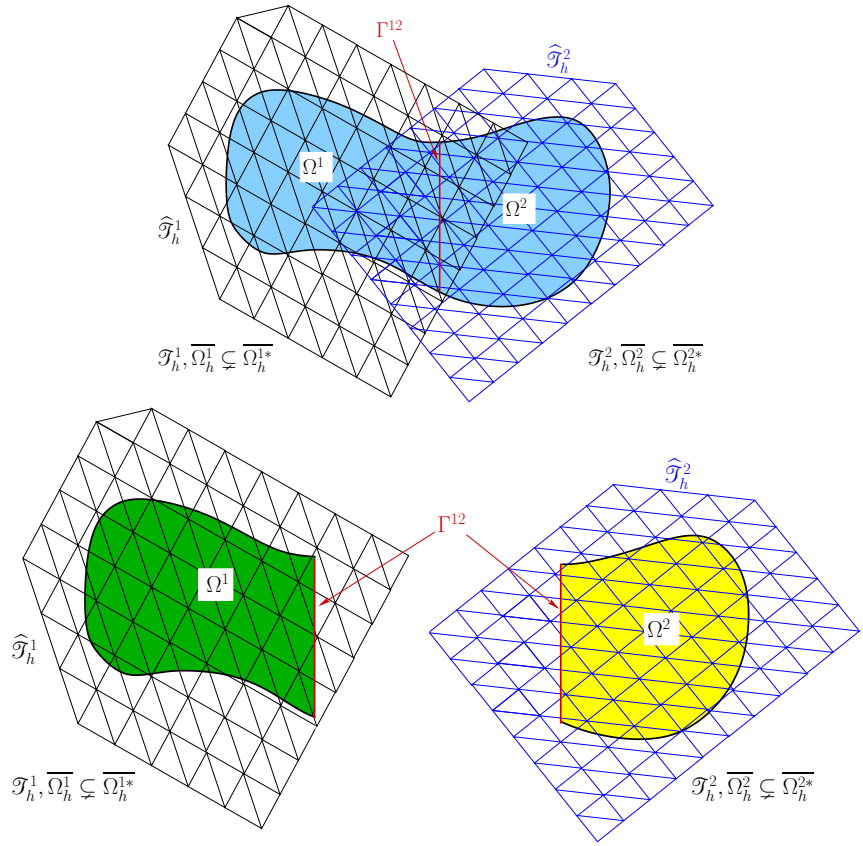

Figure 2.9: Generalized unfitted domain decomposition technique based on computational meshes which do not necessarily need to fit to the interface Γ^{12}. In that way, restrictions on the interface location and its temporal movement are highly reduced.

Unfitted Boundaries. Considering a single fluid phase, enforcing different essential and natural constraints of Dirichlet-, Neumann- or Robin-type on boundaries which do not fit to the underlying background mesh $\widehat{\mathcal{T}}_h$ defines the starting point for developing unfitted finite element methods for coupled multiphysics flow problems. For complex three-dimensional fluid domains, generating high quality computational grids which are conform with the domain boundary can often get time-consuming and difficult. This becomes particularly cumbersome and costly for geometries given by, for instance, CAD data from industrial applications or by image data from, e.g., geological or biological sources. For this purpose, utilizing finite element methods that compute the solution to the problem on the active part $\mathcal{T}_h$ of mostly fixed grids, which are intersected by the boundary, can drastically simplify meshing of the computational domain, as shown in Figure 2.10a. Special measures are required to impose the different types of boundary conditions in a consistent weak sense. However, ensuring robustness, stability and accuracy of the numerical scheme becomes more challenging due to the intersection of elements. As one major issue, depending on the interface location, small parts of intersected elements are often not sufficiently controlled by the weak formulation, which for consistency reasons is defined only on the physical domain Ω_h. To overcome this issue, inf-sup stable and optimally convergent methods need to be developed, analyzed and studied, as done in very detail throughout Chapter 3.

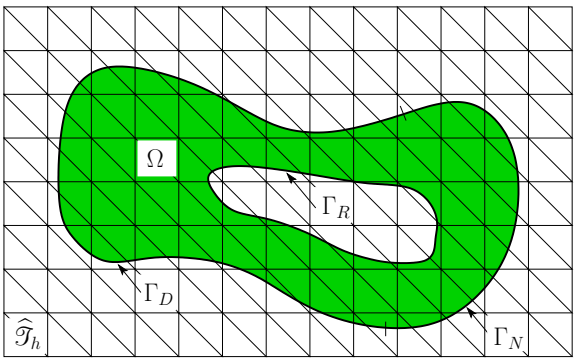

(a) Using computational meshes $\widehat{\mathcal{T}}_h$ which are unfitted to the fluid domain boundary can drastically simplify mesh generation. Dirichlet-, Neumann- and Robin-type boundary conditions at $\Gamma_{\mathrm{D}}, \Gamma_{\mathrm{N}}, \Gamma_{\mathrm{R}} \subset \partial\Omega$ need to be imposed weakly.

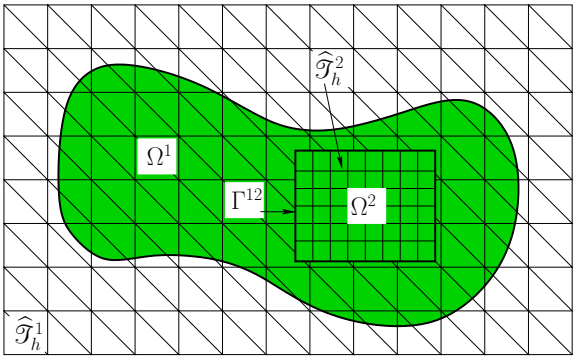

(b) Overlapping mesh fluid domain decomposition for a single fluid phase: a fine resolved mesh $\mathcal{T}_h^2 = \widehat{\mathcal{T}}_h^2$ is embedded into an unfitted background mesh $\widehat{\mathcal{T}}_h^1$. Mass transport across the artificial interface is allowed while the embedded mesh can arbitrarily move.

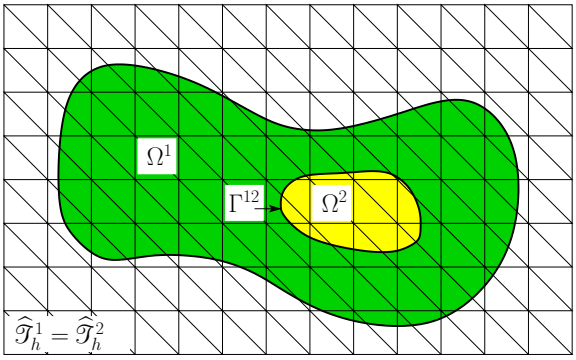

(c) Unfitted approach to incompressible two-phase flow based upon the same underlying meshes $\widehat{\mathcal{T}}_h^1 = \widehat{\mathcal{T}}_h^2$, however, different non-interface-fitted active mesh parts $\mathcal{T}_h^1, \mathcal{T}_h^2$. No restriction on the movement of the phase-separating interface due to the possibility of respective time-varying active mesh parts.

Figure 2.10: Discretization strategies for coupled flow problems based upon non-interface-fitted meshes associated with the subdomains.

Fluid Mesh Tying - Unfitted Overlapping Mesh Domain Decomposition. Complex fluid domains require appropriate mesh qualities in certain subregions for the spatial discretization of the problem specific characteristics. In particular high-Reynolds-number flows, which may exhibit near-wall turbulent boundary layers, put highest demands on the mesh quality. Local high mesh resolutions are important to capture steep gradients in the solution fields. Mesh adaptivity techniques are often used for such scenarios, however, are computationally very expensive due to iterative procedures in the construction of well-suited meshes and thus their application to time-dependent moving domains is of limited use; see, for instance, the publication by Oden and Demkowicz [199] for a survey on early works.

Overlapping mesh domain decomposition techniques are highly beneficial in such situations. In general, any combination of unfitted active overlapping meshes $\mathcal{T}_h^1, \mathcal{T}_h^2$, which cover the subregions Ω_h^1, Ω_h^2 of the overall fluid domain Ω_h, can be used. In this work, one specific setting of composite grids is investigated in more detail. Embedding a boundary-fitted fluid patch $\mathcal{T}_h^2$ such that $\Omega_h^2 = \Omega_h^{2*}$ into an unfitted background mesh $\mathcal{T}_h^1$ with $\Omega_h^1 \subsetneq \Omega_h^{1*}$, as depicted in Figure 2.10b, exhibits many powerful features for complex fluid domains, as will be explained in the following.

When it comes to computational grid generation for a complex region, for which a boundary description is given, constructing a boundary-fitted layer of fluid elements elongated in wall-normal direction is an easy task in general. Overlapping such a patch with a background mesh and coupling them in an unfitted non-node-matching manner even allows for the use of locally increased resolutions within the fluid patch independent of the background mesh properties. Adapted to the specific problem situation, mesh properties like grid size, shape and polynomial degree of finite elements and the structuring of the meshes can be chosen independently. Such an overlapping domain decomposition technique comes to its full extent when domain boundaries start to move. Then, the embedded fluid patch is able to follow the boundary independent of its location within the background mesh. The fundamental idea of this technique in the context of finite element methods traces back to a work by Hansbo *et al.* [139], which has been adapted to flows in a publication by Shahmiri *et al.* [236]. Further developments regarding interface stabilizations, which ensure inf-sup stability and optimal convergence properties for low- and high-Reynolds-number flows, have been proposed by Schott and Shahmiri *et al.* [232]. Stabilization techniques and a numerical analysis with particular emphasis on issues related to interface stability and mass transport across the introduced artificial interface will be presented in detail in Section 4.2, supported by various challenging numerical simulations in Section 4.3.

Incompressible Two-Phase Flow. Considering immiscible two-phase flows with high contrast in the material properties of the fluid phases, a method of choice could be to use two unfitted meshes $\mathcal{T}_h^1$ and $\mathcal{T}_h^2$, which overlap in the interface region. The underlying background meshes can thereby be chosen identically for both subdomains, i.e. $\widehat{\mathcal{T}}_h^1 = \widehat{\mathcal{T}}_h^2$. To preserve mass conservation of the immiscible fluid phases, the interface, which can be defined implicitly by a level-set field, moves in interface-normal direction following the fluid particles in their motion. Thereby, the interface is not restricted in its movement and function spaces for each fluid phase are defined on time-changing active sets of the underlying finite element grid. A visualization of this unfitted scheme is shown in Figure 2.10c. Based on this discretization technique, a stabilized Nitsche-type extended variational multiscale method has been proposed

by Schott and Rasthofer *et al.* [231]. Stability requirements in case of high material contrast in conjunction with the interface coupling scheme and particular interface-zone stabilization techniques are addressed in Section 4.2. Moreover, an outlook to its applicability to classical two-phase flow including surface tension and to an advanced premixed-combustion application is given in Section 4.4.

Fluid-Structure Interaction. For the numerical simulation of mutual interactions of fluids and solids, different competitive approaches are considered in the current work. While for solids a Lagrangean description together with boundary-fitted meshes is the most reasonable choice, for flows, an Eulerian or a more general ALE description is preferable. The use of non-interface-fitted approximations for the fluid allows for various overlapping mesh strategies between fitted structural meshes and unfitted fluid meshes, which show their capabilities in several different situations.

In a first approach, similar to the embedded fluid-fluid overlapping mesh approach described previously, now a structural mesh $\mathcal{T}_h^{\mathrm{s}}$ fitted to the boundary of the solid overlaps with an unfitted background fluid mesh $\mathcal{T}_h^{\mathrm{f}}$ such that

$$\overline{\Omega_h^{\mathrm{s}}} = \overline{\Omega_h^{\mathrm{s}*}}, \qquad \overline{\Omega_h^{\mathrm{f}}} \subsetneq \overline{\Omega_h^{\mathrm{f}*}}, \qquad \Omega_h^{\mathrm{s}*} \cap \Omega_h^{\mathrm{f}*} \neq \emptyset, \tag{2.65}$$

as visualized in Figure 2.11a. Such an overlapping mesh technique enables arbitrary solid motions and interactions with the surrounding fluid, whose mesh is not subjected to any distortion. Moreover, this technique even allows for additional interactions between several structural bodies in a surrounding fluid. Contact of submersed structures, as considered in algorithms developed by Mayer *et al.* [184], is supported in general. Such problem settings, however, go beyond the scope of this thesis. Based on these mesh configurations, different coupling schemes for fluid-structure interaction have been considered. To name just a few, Burman and Fernández [58] developed a Nitsche-type coupling for viscous Stokes' flow coupled to linear elastic material or Gerstenberger [123] developed fluid-structure coupling schemes based on stress-based Lagrange-multiplier interface methods in combination with partitioned solution algorithms. A comprehensive overview of related works will be given in Chapter 5. In Section 5.3, a full-implicit Nitsche-type fluid-structure coupling for low- and high-Reynolds-number flows governed by the incompressible Navier-Stokes equations and interacting with non-linear structural materials will be proposed.

Nevertheless, in some cases the previously introduced unfitted technique is not perfectly suited. As regular background fluid meshes are usually used to simplify meshing, for many applications the mesh resolution can be very high even in regions far from the fluid-structure interface. This might result in enormous computational costs, in particular, for simulations in three spatial dimensions. Otherwise, when using a coarser mesh in the overall fluid domain, the quality of the solution next to the fluid-structure interface would decrease considerably. For this reason, a second expanded domain decomposition approach is proposed. It provides a powerful simulation tool and combines capabilities of the overlapping fluid-structure coupling and the aforementioned unfitted overlapping fluid-fluid mesh-tying technique. Approximating the vicinity of the solid with a finer mesh resolution and the far-field with a coarser mesh can be easily realized as depicted in Figure 2.11b and explained in the following: In a first step, the fitted solid mesh $\mathcal{T}_h^{\mathrm{s}}$ overlaps with a high resolution background mesh $\mathcal{T}_h^{\mathrm{f}_2}$. This is usually

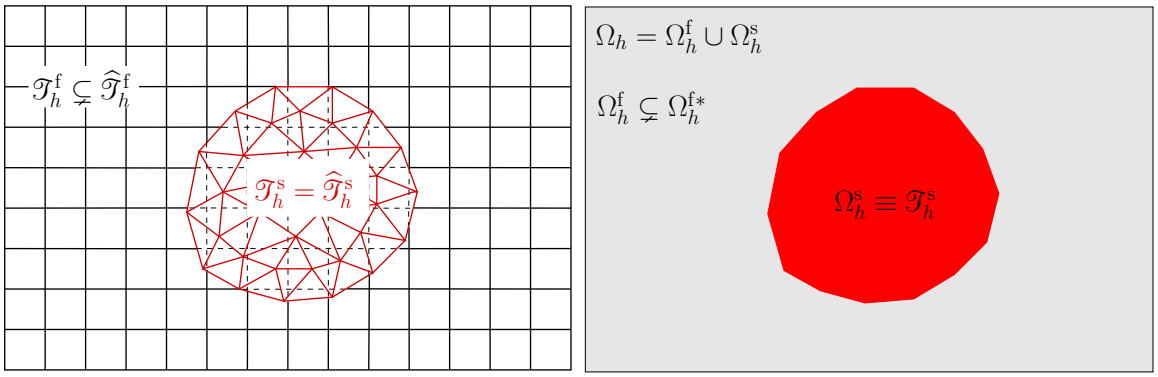

(a) Using an unfitted fluid mesh $\mathcal{T}_h^{\mathrm{f}}$ overlapped by an interface-fitted structural mesh $\mathcal{T}_h^{\mathrm{s}}$ allows for simulating fluid-structure interaction where the solid can undergo large deformations and motions; even contact of submersed bodies and topological changes are supported.

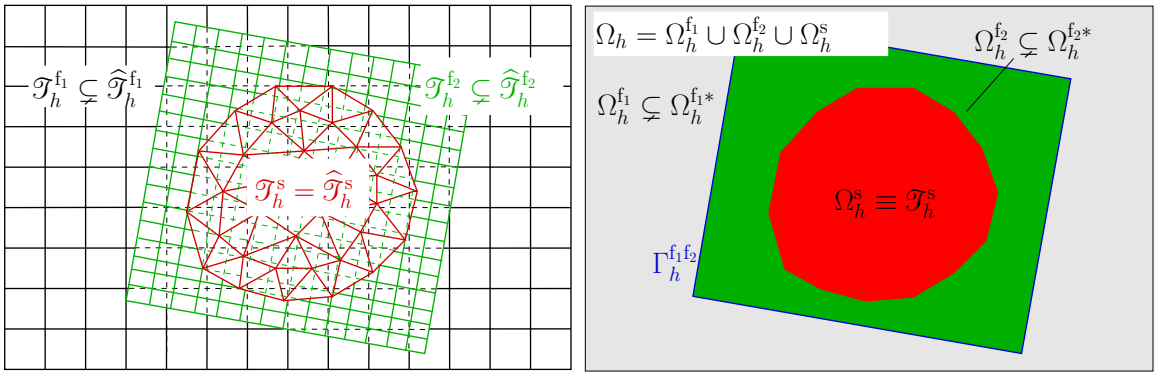

(b) Combination of an unfitted overlapping fluid-structure coupling with an overlapping fluid-fluid domain decomposition technique. This technique enables different mesh resolutions in the vicinity of the solid $\mathcal{T}_h^{\mathrm{s}}$ with a finer fluid grid $\mathcal{T}_h^{\mathrm{f}_2}$ and a coarser fluid discretization $\mathcal{T}_h^{\mathrm{f}_1}$ far form the fluid-solid interface.

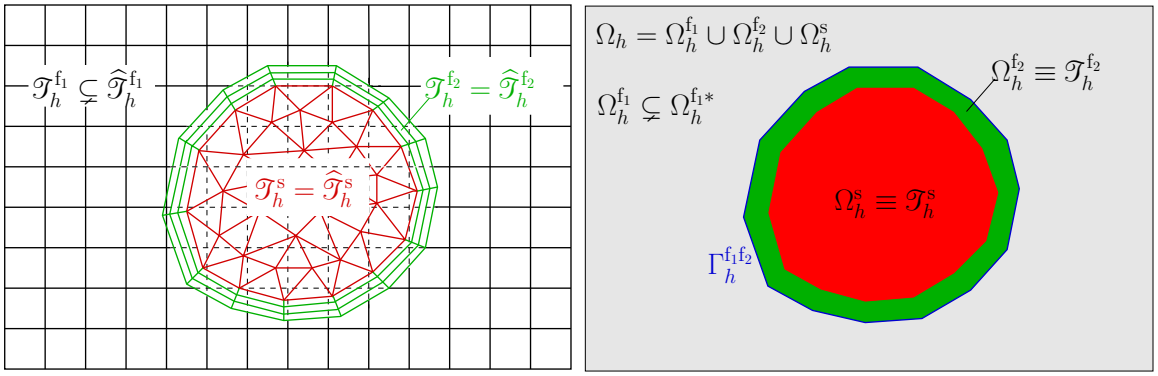

(c) Fitting a surrounding patch of fluid elements to the fluid-structure interface $\Gamma^{\mathrm{f}_2\mathrm{s}}$ and embedding it unfitted into a background fluid mesh $\mathcal{T}_h^{\mathrm{f}_1}$ with the help of overlapping mesh domain decomposition techniques provides a powerful simulation tool. It drastically simplifies meshing of complex geometries and allows to perfectly capture steep near-wall gradients in the boundary layer region around the solid. ALE-techniques allow the embedded mesh to follow the solid in its movement.

Figure 2.11: Different fluid-structure-interaction domain decomposition approaches based upon the use of unfitted overlapping meshes (left) with according decomposition of the entire domain (right).

defined in a region of expected structural motion. In second step, this fluid mesh is embedded into a coarse background fluid mesh $\mathcal{T}_h^{\mathrm{f}_1}$ using unfitted overlapping mesh techniques. This results in the following domain and mesh configurations

$$\overline{\Omega_h^{\mathrm{f}_1}} \subsetneq \overline{\Omega_h^{\mathrm{f}_1 *}}, \qquad \overline{\Omega_h^{\mathrm{f}_2}} \subsetneq \overline{\Omega_h^{\mathrm{f}_2 *}}, \qquad \overline{\Omega_h^{\mathrm{s}}} = \overline{\Omega_h^{\mathrm{s}*}} \tag{2.66}$$

with

$$\Omega_h^{\mathrm{f}_1 *} \cap \Omega_h^{\mathrm{f}_2 *} \neq \emptyset \qquad \Omega_h^{\mathrm{f}_2 *} \cap \Omega_h^{\mathrm{s}*} \neq \emptyset. \tag{2.67}$$

This approach will be considered in more detail in Section 5.4. Such composed techniques highly increase efficiency and accuracy of computational algorithms and still retain the capability with respect to dealing with large structural motions. The major limitation, which has been newly introduced by incorporating a priori knowledge on the expected structural motion, can be relaxed by enabling moving mesh techniques to allow the inner embedded fluid patch to follow the structure in its motion. This could be easily realized by applying ALE concepts and is part current research.

For fluid-structure interactions, in which (self-)contact of structural bodies or even topological changes do not have to be supported, the aforementioned overlapping fluid-fluid-structure coupling can be adapted, resulting in a third powerful approach: Instead of using an unfitted overlapping mesh approach at the fluid-solid interface $\Gamma^{\mathrm{f}_2\mathrm{s}}$, one can also use interface-fitted meshes $\mathcal{T}_h^{\mathrm{s}}$ and $\mathcal{T}_h^{\mathrm{f}_2}$. They may be chosen either non-node-matching or node-matching at $\Gamma^{\mathrm{f}_2\mathrm{s}}$. The latter variant is considered in this work. The usually finer resolved fluid patch $\mathcal{T}_h^{\mathrm{f}_2}$ is thereby embedded into a coarser background grid $\mathcal{T}_h^{\mathrm{f}_1}$ in an unfitted way, based upon the introduced overlapping fluid domain decomposition approach. This setup results in

$$\overline{\Omega_h^{\mathrm{f}_1}} \subsetneq \overline{\Omega_h^{\mathrm{f}_1 *}}, \qquad \overline{\Omega_h^{\mathrm{f}_2}} = \overline{\Omega_h^{\mathrm{f}_2 *}}, \qquad \overline{\Omega_h^{\mathrm{s}}} = \overline{\Omega_h^{\mathrm{s}*}} \tag{2.68}$$

with

$$\Omega_h^{\mathrm{f}_1 *} \cap \Omega_h^{\mathrm{f}_2 *} \neq \emptyset \qquad \Omega_h^{\mathrm{f}_2 *} \cap \Omega_h^{\mathrm{s}*} = \emptyset. \tag{2.69}$$

A visualization of this approach is given in Figure 2.11c. Applying an ALE-framework to the embedded fluid patch, the solid-fitted fluid mesh $\mathcal{T}_h^{\mathrm{f}_2}$ can follow the body in its movement. This enables to accurately capture effects at the fluid-structure interface independent of the fluid patch location within the background mesh $\mathcal{T}_h^{\mathrm{f}_1}$. This renders such approaches highly attractive, e.g., for interactions of solids with turbulent incompressible flows, in which capturing boundary layer effects in the vicinity of solids is a crucial task. Successful application of this technique to FSI has been already shown by Shahmiri [235]. The contribution of present thesis to this topic mainly consists in the further enhancement of the required stabilization techniques for the incorporated fluid-domain decomposition technique. Theoretical aspects will be discussed in Section 4.2 and examples will be provided in Section 4.3 to demonstrate the high capabilities of this method.

This presented overview indicates the high flexibility of novel discretization techniques which make use of non-interface-fitted computational meshes. The various number of feasible mesh configurations for different physical fields in combination with the possibility to incorporate

artificial domain decomposition for single fields allow for easily constructing mesh composites which are appropriately designed for the respective multiphysics problem setting. This is mainly thanks to the fact that meshes can be chosen independent of the respective subdomains, provided that stable weak formulations are available for the physical fields. To allow to approximate incompressible low- and high-Reynolds number flows on unfitted meshes, accurate, inf-sup stable and optimally convergent discrete formulations are developed throughout Chapter 3 of this thesis. One of the main difficulties consists in the fact that strongly consistent subdomain weak formulations are evaluated only in the respective physical regions, i.e. in $\Omega^i \cap \mathcal{T}_h^i$. As this is only a part of the respective active computational mesh, this can result in inf-sup instabilities, in loss of optimality and in a potential ill-conditioning due to the intersection of elements in the interface zone - issues that have to specifically treated by appropriate stabilization techniques.

It needs to be highlighted that such domain decomposition methods are no longer limited to multiphysics applications where incompressible flows are involved, as exclusively considered in this work. Enhancements to, for instance, the solution of any transport phenomena of scalar quantities like heat transfer, chemical concentration processes or many others is straightforward. Considering such problem settings, however, goes beyond the scope of this thesis.

All unfitted non-matching discretization approaches introduced in this section require the representation of discrete solutions based upon finite element spaces whose underlying computational grids do not fit to the respective subdomain boundaries in a classical node-wise manner. For this purpose, before introducing techniques for imposing boundary or coupling conditions, in the subsequent section, general concepts of so-called *cut finite element function spaces* are introduced.

2.2 Finite-Dimensional Cut Finite Element Approximations

The fundamental idea of applying finite-element-based methods which allow to sharply take care of boundaries and interfaces that do not fit to computational grids and intersect finite elements, is twofold. On the one hand, as pointed out in previous sections, decoupling of physical subdomains from their respective computational meshes widens the flexibility of coupling schemes for many multiphysics problems. On the other hand, physical models often assume solutions being discontinuous when local length scales at phase boundaries are not fully resolved by the mesh. Thus, an accurate representation of non-smooth features with the numerical approach is desirable for a multitude of coupled physical models. For this purpose, FEM-based approximations using cut elements will be introduced.

First, an overview about different numerical techniques to incorporate discontinuities into the discrete function spaces is given. Emphasis is put on enriching classical finite element spaces with the *eXtended Finite Element Method* (XFEM) and to a specific class of related methods which are often referred to as *Cut Finite Element Methods* (CUTFEM). Quantities related to element intersections are introduced and techniques for enriching finite elements are briefly elaborated. Afterwards, a generalized concept for constructing cut finite element function spaces to sharply approximate discontinuous fields on complex geometries is presented. As motivating applications, advanced fluid-solid interactions or multiphase flow configurations are considered.

2.2.1 An Overview of eXtended and Cut Finite Element Methods

From a macroscopic point of view, solution fields to physical phenomena which involve highly different length scales within subdomains or near phase boundaries are often predestined to be modeled being discontinuous. Non-smooth material characteristics and steep gradients in the transition zone then require being sharply approximated by discrete functions. Potential applications range from dislocations and cracks in solid mechanics to boundary layers, phase boundaries, shocks and flame fronts in fluid mechanics. In fluids, separated liquid and gas phases often exhibit high contrast in their material properties and come along with strong surface-tension effects, which motivates to model fields as discontinuous. In that way, interactions between those fluids, solids or even porous media are potential application areas.

Classical FEMs can represent discontinuous fields only when meshes associated with subdomains fit to the interface. This, however, limits interfaces in their motion as discussed for various multiphysics problems in previous sections. In contrast, enriching classical polynomial finite spaces by functions that are able to represent desired discontinuities within finite elements allows to sharply capture non-smooth characteristics of the physical problem. Thereby, the desired discontinuity is assumed to be known *a priori* from modeling to get incorporated into the extended finite element function space depending on the interface location within the computational grid. In a review article by Fries and Belytschko [115] such methods are called enriched methods. When constructing enriched function spaces, it is desirable to guarantee the so-called partition-of-unity property, which ensures that an enrichment function ψ, which mimics the discontinuity, can be trivially recovered by means of enriched nodal shape functions $N_s\psi$, whenever $\sum_s N_s(\boldsymbol{x}) = 1$. A method featuring this property with compact support of the shape functions is the Partition of Unity Method referred to as PUM and PUFEM in the works by Melenk and Babuška [186] and Babuška and Melenk [6], respectively. A few years after establishing this concept, the PUM was referred to as Generalized Finite Element Method (GFEM) (see, e.g., Duarte *et al.* [94] and Strouboulis *et al.* [243]). Almost one decade later, Babuška and Banerjee [5] picked up the fundamental methodology of GFEMs and proposed an adaption to get rid of ill-conditioning of the resulting global stiffness matrices and so to improve severe loss of accuracy depending on the interface position; the proposed technique was called Stable Generalized Finite Element Method (SGFEM). Parallel to the development of the GFEM, the partition-of-unity concept based on hat-functions was also used in fracture mechanics by Belytschko and Black [21] and Moës *et al.* [188] to predict crack propagation. They introduced different enrichments to represent the discontinuity along the crack and at the crack tip. In the context of fracture mechanics, for the latter partition-of-unity methods the naming eXtended Finite Element Method (XFEM) was introduced by Dolbow *et al.* [88]. This designation became a synonym whenever function spaces are enriched by specific shape functions that exhibit compact support.

Over the last years, XFEMs became very popular and were adapted to a wide area of application fields. A survey on XFEMs in the context of material modeling was proposed by Belytschko *et al.* [24]. Solidification processes involving moving interfaces were considered, e.g., by Chessa *et al.* [72] and Ji *et al.* [159]. In particular in the field of multiphase flows the XFEM became a competitive numerical method. Originally proposed for two-phase flows by Chessa and Belytschko [71], different enrichment strategies were investigated to capture pressure jumps caused by surface tension effects as well as kinks in the velocity solution which arise due to a discontinuity in the material properties; see, e.g., Groß and Reusken [133], Diez *et al.*

[86], Sauerland and Fries [225], Rasthofer *et al.* [214] and Schott and Rasthofer *et al.* [231] for different combinations of enrichments for velocity and pressure approximations. For premixed combustion, which requires to additionally account for a jump in the velocity field across the flame front, the XFEM was adapted by van der Bos and Gravemeier [255] and Henke [147]. Enriched function spaces for the flow field in fluid-structure interactions have been utilized, e.g., by Zilian and Legay [278], Gerstenberger and Wall [125], Legay *et al.* [173] and Burman and Fernández [58]. Moreover, embedding mesh techniques for resolving boundary layers in fluid-solid interaction configurations which are based on fluid domain decomposition techniques were developed by Shahmiri *et al.* [236], Massing *et al.* [182] and Schott and Shahmiri *et al.* [232]. Approximating two-phase Darcy flows with the XFEM was considered by Fumagalli and Scotti [118] and a mixed finite element method for Darcy flow in fractured porous media using non-matching grids was proposed by D'Angelo and Scotti [97]. Duddu *et al.* [95] introduced an XFEM-based approach towards modeling of growth of biofilms.

Over the recent years, FEM-based discretization techniques utilizing fixed background grids which are non-fitting to embedded boundaries or interfaces to represent approximate solutions of governing PDEs were summarized under the term *Cut Finite Element Method* (CUTFEM), see, e.g., Burman *et al.* [63] and references therein. These methods utilize finite elements which are cut by the boundary or interface similar to the XFEM. There, for the solution approximation, most often a classical continuous or discontinuous polynomial finite element function space is used which is then simply cut-off at the interface. This procedure is equivalent to multiplying the classical finite element function space by a Heaviside enrichment function in the XFEM. This equivalence explains the parallel usage of both designations for such enriched or cut finite element techniques - XFEMs and CUTFEMs.

References and a comprehensive overview of the multitude of different techniques with regard to enforcing boundary or coupling constraints will be first given for boundary-fitted meshes in Section 3.3. Enhancement of the imposition of boundary conditions in the XFEM or CUTFEM is made in Sections 3.4–3.6. Further developments for coupling constraints in fluid-coupled problems will be proposed later in Sections 4.2 and 5.3.

2.2.2 Cutting Finite Elements - Notation and Fundamentals of Cut-Entities

Suitable CUTFEMs for the sharp representation of discontinuities within cut finite elements of unfitted meshes require a unique belonging of physical points and their material properties to active and inactive parts of the computational mesh. For this purpose, subdivision of finite elements, which are intersected by the boundary or interface, into physical parts associated with the different subdomains and into according non-physical parts is required.

Cut-related mesh entities and according notation for intersected elements will be introduced in the following. All proposed terms remain valid, however, simplify for the case when elements are not bisected, but the interface "touches" one of the element surfaces; this recovers the usage of interface-fitted meshes. Subsequent elaborations are strongly based on the publications by Schott and Wall [230] and Massing *et al.* [183]. Without limiting generality, explicit interface representations are used for visualization exclusively in the following.

Based on notation for computational meshes introduced in Section 2.1.4.1, let $\widehat{\mathcal{T}}_h$ be an interface-fitted or a non-interface-fitted background mesh such that the domain Ω is covered by the

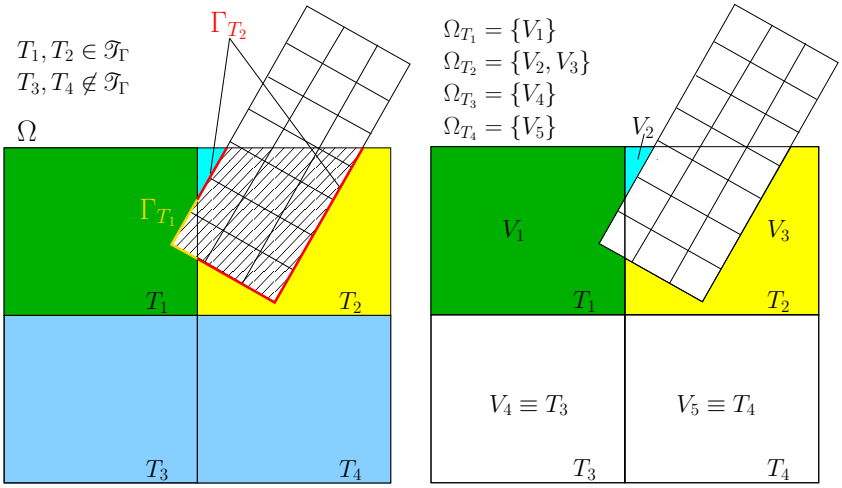

Figure 2.12: Polyhedral representation of domain Ω_h with so-called *volume-cells*: (a) Cut situation, subdivision of Γ into element-wise parts $\Gamma_{T_i} = \Gamma \cap T_i$ associated with background elements T_i. (b) Partition of physical domain Ω into volume-cells V_i.

mesh $\overline{\Omega} \subset \widehat{\mathcal{T}}_h$. Recalling definitions on the active mesh part $\mathcal{T}_h$, the fictitious domain Ω_h^* and the set of all intersected finite elements T of the underlying background mesh $\mathcal{T}_\Gamma \subset \mathcal{T}_h$, the part of the interface Γ which lies in an element $T \in \mathcal{T}_\Gamma$ is called *interface segment* and is denoted by $\Gamma_T \overset{\text{def}}{=} \Gamma \cap T$, as shown in Figure 2.12a.

For inter-element faces in $\mathcal{T}_h$ in three spatial dimensions ($d = 3$), i.e. for edges in two spatial dimensions ($d = 2$), let $\mathcal{F}_i$ be the set of *interior faces* F which are shared by exactly two elements, denoted by T_F^+ and T_F^-. Furthermore, introduce the notation $\mathcal{F}_\Gamma$ for the set of all interior faces belonging to elements intersected by the boundary Γ,

$$\mathcal{F}_\Gamma = \{F \in \mathcal{F}_i \mid T_F^+ \cap \Gamma \neq \emptyset \vee T_F^- \cap \Gamma \neq \emptyset\}. \tag{2.70}$$

If an interface Γ intersects elements $T \in \mathcal{T}_\Gamma$ of a non-interface-fitted mesh, it subdivides them into several arbitrary formed polyhedra. In this work, such polyhedra are called *volume-cells* and are notated with V_i. Volume-cells can be either associated with the physical volume Ω or to the ghost domain $\widehat{\mathcal{T}}_h \backslash \Omega$. Cells which are part of the physical volume Ω are denoted as *physical volume-cells*. The physical volume for an element T is then given by

$$\Omega_T = \{ \text{ polyhedra } V_i \subseteq (T \cap \Omega) \mid V_i \cap V_j = \emptyset \text{ for } i \neq j\} \tag{2.71}$$

and consists of only volume-cells V_i, V_j which are not connected within $T \cap \Omega$, as depicted in Figure 2.12b. Otherwise, two volume-cells would conflate to one single volume-cell. All polyhedra that are not contained in Ω lie within the ghost domain and are not considered for CutFEMs anymore. For uncut elements $T \in \mathcal{T}_h \backslash \mathcal{T}_\Gamma$, a unique volume-cell can be identified with the element itself, i.e. $V_T \equiv T$.

Based on this volume-cell representation the physical volume can now be rewritten as

$$\overline{\Omega}_h = \bigcup_{T \in \mathcal{T}_h} \bigcup_{V \in \Omega_T} V. \tag{2.72}$$

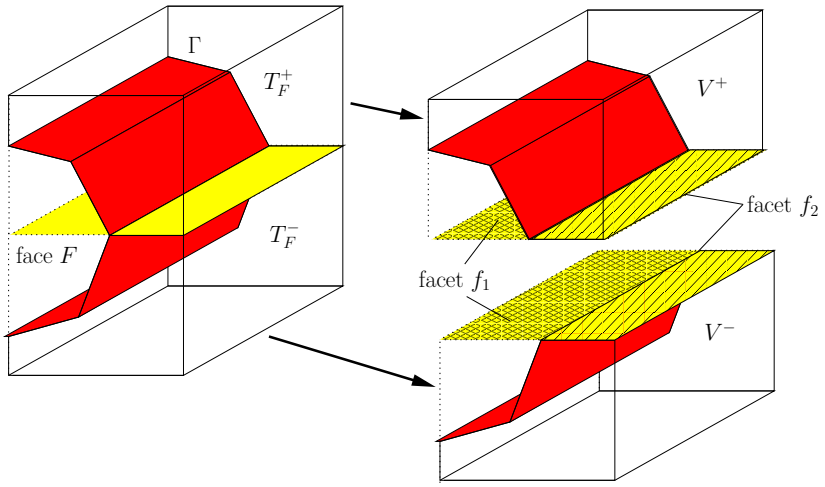

Figure 2.13: Facets of a face $F \in \mathcal{F}_i$ between two three-dimensional intersected elements T_F^+, T_F^- with respective volume-cells V^+, V^-: Intersecting surface Γ (red), facets f_1, f_2 (yellow). Facets f_i between three-dimensional elements are arbitrary formed two-dimensional polygons which form disjoint segments of the two-dimensional face F.

Similarly, boundaries and interfaces Γ can be composed of segments associated with the element's volume-cells

$$\Gamma_h = \bigcup_{T \in \mathcal{T}_\Gamma} \bigcup_{V \in \Omega_T} (\Gamma_T \cap V). \tag{2.73}$$

Disjoint segments of a face $F \in \mathcal{F}_i$ which is intersected by Γ are called *facets* f throughout this work. Facets belonging to the physical domain Ω_h and to the ghost domain $\widehat{\mathcal{T}}_h \backslash \Omega_h$ are visualized in Figure 2.13.

Cut-related geometric objects are constructed in consecutive steps. In a first step, *intersection points* between all faces F of the background mesh and all interface segments are identified. For a level-set representation, intersection points can be simply computed by interpolating nodal level-set values (see, e.g., Burman *et al.* [63] or Groß and Reusken [134]). Afterwards, intersection points together with nodes of background and interface representations are connected to *lines*, i.e. edge segments of the intersecting meshes, respectively. Closed polygons consisting of lines then build up *facets* f and are associated with either faces F of the background mesh or with interface segments in Γ_T. Finally, facets which are connected to each other via lines and belong to the same side with respect to the interface form the boundary of three-dimensional polyhedra. There are *active physical volume-cells* V and *inactive volume-cells*. The latter ones are located in the ghost part of the computational mesh. For details with regard to algorithms related to the intersection and construction of intersection-related geometric objects, the interested reader is referred to, e.g., textbooks by de Berg *et al.* [82] and Schneider and Eberly [228] or the article by Massing *et al.* [179] and references therein.

For implicit interface descriptions, the positioning of volume-cells with respect to the interface orientation can be simply determined by the sign of level-set values. Otherwise, a predefined orientation of the interface mesh by means of a unit normal vector is assumed. In the latter case, for a node of the background mesh which is located next to the interface, the angle between interface normal vector and a cut-line of the background mesh which connects the

node with a point on Γ allows to determine the positioning. Once positioning with respect to the interface of a single node is known, this information can be propagated through the intersected computational mesh for all geometric entities associated to one subdomain. This can be efficiently realized using a "DEPTH-FIRST-SEARCH (DFS)"-algorithm applied to an abstract graph consisting of geometric volume-cells V and pairwise connecting facets f utilized as graph-nodes and graph-edges (see, e.g., the textbook by Goodrich and Tamassia [128] for an introduction). The depth-search is stopped at a certain level whenever an interface-aligned facet $f \subset \Gamma$ is reached. Otherwise, positioning information would be incorrectly propagated across interfaces. For remaining nodes with undetermined positioning, the algorithm can be restarted at another node which is located next to the interface.

2.2.3 Strategies for Enriching Function Spaces in the XFEM

The fundamental idea of the XFEM is to extend, or enrich, a standard finite element function space with additional functions which enable to accurately represent desired features within finite elements $T \in \mathcal{T}_\Gamma$ in the boundary or interface zone. These are usually problem dependent and can be, for example, discontinuities, singularities or logarithmic functions to name just a few. Focusing on interface coupled flow problems in this thesis, the desired features to be represented are discontinuous fields in the interface zone. The conceptual idea can be described as follows.

Principle for Interface Problems. Considering the finite element space

$$\mathscr{X}_h = \left\{ v_h \in C^0(\widehat{\mathcal{T}}_h) : v_h|_T \in \mathbb{P}^k(T) \,\forall\, T \in \widehat{\mathcal{T}}_h \right\} \tag{2.74}$$

consisting of continuous piecewise approximations of order $k \geqslant 1$, a nodal basis $\mathscr{B} \overset{\text{def}}{=} \{N_s\}_{s \in \mathcal{N}}$ can be defined, where $\mathcal{N} = \{s = 1, \ldots, \dim(\mathscr{X}_h)\}$ is an index-set and $\dim(\mathscr{X}_h)$ denotes the dimension of the discrete space. The nodal basis functions N_s satisfy *partition-of-unity* and it holds $N_s(\boldsymbol{x}_r) = \delta_{r,s}$ for $r, s \in \mathcal{N}$ at all nodes $\boldsymbol{x}_r \in \mathbb{R}^d$ of the computational mesh $\widehat{\mathcal{T}}_h$, where $\delta_{r,s}$ is the Kronecker-δ. Then, a classical finite element space can be written as $\mathscr{X}_h = \operatorname{span}\{N_s\}_{s \in \mathcal{N}}$.

The original function space $\mathscr{X}_h$ can now be enriched with additional basis functions $\tilde{N}_{s'}$ which are constructed of multiplying nodal basis functions $N_{s'}$ with so-called *enrichment functions* $\psi_{s'}$

$$\tilde{N}_{s'}(\boldsymbol{x}, t) \overset{\text{def}}{=} N_{s'}(\boldsymbol{x}) \cdot \psi_{s'}(\boldsymbol{x}, t) \tag{2.75}$$

for a subset of nodes $s' \in \mathcal{N}' \subset \mathcal{N}$. Thereby, $\mathcal{N}'$ usually denotes the set of all nodes of elements $T \in \mathcal{T}_\Gamma$ intersected by Γ. Note that for evolving interfaces or boundaries this subset may change over time t. The enrichment function $\psi_{s'}$ introduces the desired sharp discontinuity to the function space and depends on the interface location and on point coordinates $\boldsymbol{x} \in \mathbb{R}^d$. The enriched function space can be defined as

$$\mathscr{X}_h^\Gamma \overset{\text{def}}{=} \operatorname{span}\{N_s\}_{s \in \mathcal{N}} \cup \operatorname{span}\{\tilde{N}_{s'}\}_{s' \in \mathcal{N}'}. \tag{2.76}$$

Different types of *strong* and *weak discontinuities* can be represented by appropriate choices for the enrichment function. An overview of common strategies can be found, e.g., in Fries [114].

An example for an enrichment type to capture a *weak discontinuity*, namely the jump in derivatives of the solution field across Γ, is the so-called *abs*-enrichment. Assuming a signed-distance function $d : \Omega \to \mathbb{R}$ based on the interface Γ, the enrichment function is defined as

$$\psi_{s'}(\boldsymbol{x}, t) \overset{\text{def}}{=} \mathscr{I}(\boldsymbol{x}, t) - \mathscr{I}(\boldsymbol{x}_{s'}, t) \tag{2.77}$$

with

$$\mathscr{I}(\boldsymbol{x}, t) \overset{\text{def}}{=} \sum\nolimits_{s \in \mathcal{N}} \operatorname{abs}(d_s(t)) N_s(\boldsymbol{x}) - \operatorname{abs}(\sum\nolimits_{s \in \mathcal{N}} d_s(t) N_s(\boldsymbol{x})), \tag{2.78}$$

where $\operatorname{abs}(z) = |z|$ is the absolute value and d_s denotes nodal values of the signed-distance level-set field for $s \in \mathcal{N}$. As by construction the discontinuity occurs only in the derivative but not in the field itself, no additional measures are required to ensure continuity of functions across the interface.

Discontinuities in the primal variable itself are called *strong discontinuities*. Modeling jumps across the interface can be realized by means of an enrichment function which involves a piecewise constant step function

$$\psi_{s'}(\boldsymbol{x}, t) \overset{\text{def}}{=} \mathscr{S}(\boldsymbol{x}, t) - \mathscr{S}(\boldsymbol{x}_{s'}, t) \tag{2.79}$$

with

$$\mathscr{S}(\boldsymbol{x}, t) \overset{\text{def}}{=} \begin{cases} -1 & \text{if } d(\boldsymbol{x}, t) < 0, \\ +1 & \text{if } d(\boldsymbol{x}, t) \geqslant 0. \end{cases} \tag{2.80}$$

For both enrichment functions ψ, (2.77) and (2.79), the respective first parts introduce the desired discontinuity, whereas the second parts are constant shifts which do not introduce new basis functions into the function space, however, guarantee that the enrichment function vanishes at grid nodes, i.e. $\psi(\boldsymbol{x}_s, t) = 0$. On the one hand, this simplifies the strong incorporation of Dirichlet conditions into the function space as well as post-processing, as no reinterpretation of nodal degrees of freedom v_s for $s \in \mathcal{N}$ is necessary. On the other hand, in doing so, enrichment functions contribute just locally to elements $T \in \mathcal{T}_\Gamma$ intersected by Γ.

Single-Phase Problems and Extension to Multifield Problems. For single-phase problems, the terminology of *extending* or *enriching* function spaces, as intended by the naming XFEM, is often misleading. Function spaces for single phase problems are rather modified or, more precisely, cut-off at the interface. Therefore, the designation *cut finite element method* (CUTFEM) is utilized with growing frequency whenever non-interface-fitted meshes are used to represent discrete solutions and intersected elements are subdivided for purposes of weak form integration. This naming is preferred and used throughout this work.

Note that performing integration just on the physical domain is equivalent to cutting-off the standard function space at the boundary or interface. This technique even allows to easily recover the previously introduced step-enriched function space $\mathscr{X}_h^\Gamma$, which is based on a single background mesh $\widehat{\mathcal{T}}_h$ to represent solutions associated with two subdomains Ω_h^1 and Ω_h^2. Utilizing notation from Section 2.1.4.1, this space can be rewritten equivalently and, furthermore, easily

expanded to several subdomains Ω_h^i, $1 \leqslant i \leqslant N_{\text{dom}}$. A function space composed of subspaces associated with each subdomain can be constructed as

$$\tilde{\mathscr{X}}_h = \mathscr{X}_h^1 \oplus \mathscr{X}_h^2 \oplus \ldots \oplus \mathscr{X}_h^{N_{\text{dom}}}, \tag{2.81}$$

where $\mathscr{X}_h^i = \text{span}\{N_s\}_{s \in \mathcal{N}^i}$ is the cut finite element space of subdomain Ω_h^i. All subspaces are defined on identical meshes $\widehat{\mathscr{T}}_h^1 = \widehat{\mathscr{T}}_h^2 = \ldots = \widehat{\mathscr{T}}_h^{N_{\text{dom}}}$, however, have different index sets $\mathcal{N}^i$ which include only nodes of active elements $T \in \mathscr{T}_h^i$ for $i = 1, \ldots, N_{\text{dom}}$, respectively. Note that a discrete function $v_h \in \tilde{\mathscr{X}}_h$ then satisfies $v_h|_{\Omega_h^i} = v_h^i|_{\Omega_h^i}$ with $v_h^i \in \mathscr{X}_h^i$ for all $i = 1, \ldots, N_{\text{dom}}$. By construction, v_h exhibits the desired discontinuity across Γ_h^{ij}.

Multiphysics settings, as introduced in Section 2.1.1, which incorporate several subdomains Ω_h^i separated by interfaces Γ_h^{ij} and utilize composite function spaces $\tilde{\mathscr{X}}_h$ for discretization, require special consideration. The representability of solutions on complex geometries, incorporating, for instance, thin-shaped structural bodies in fluid-structure interaction or complex-shaped two-phase-flow interfaces which undergo topological changes, have to be carefully thought out. Within the next section, a general strategy for flexibly managing multiple sets of nodal degrees of freedom (DOFs) will be presented. In a first step, single-phase problems are considered and afterwards, in a second step, an extension to multifield settings is proposed. Numerical examples will demonstrate the capabilities of this technique for composite discrete cut function spaces.

2.2.4 CutFEM-based DOF-Management for Complex Domains

To obtain accurate cut finite element approximations for arbitrary-shaped embedded interfaces, in the following, a general technique to manage multiple DOFs associated with nodes of the underlying computational mesh $\widehat{\mathscr{T}}_h$ in the interface zone will be proposed. Multiple cuts within finite elements and special topological cases will be supported as well. The subsequent elaborations are based on work published by Schott and Wall [230].

Expanded Cut Finite Element Function Space. Accurate cut finite element function spaces which account for topological changes and multiple element intersections are based on the volume-cell partitioning (2.72) of the domain Ω_h. A continuous function space expanded by volume-cell information can be written as

$$\mathscr{X}_h \overset{\text{def}}{=} \left\{ v_h \in C^0(\overline{\Omega_h}) : v|_V \in \mathbb{Q}^k(T) \; \forall V \in \Omega_T, \forall T \in \mathscr{T}_h \right\}. \tag{2.82}$$

Approximations restricted to an elemental volume-cell $V \in \Omega_T$ are based on standard polynomial shape functions N_s of the underlying element T

$$v_h|_V = \sum_{s=1}^{\text{nnod}_T} N_s|_V \cdot v_s. \tag{2.83}$$

In order to enable independent solution approximations on two sides of the interface within one finite element, as depicted in Figure 2.14, it is necessary to take into account independent sets of DOFs, respectively. Using continuous approximations, the decision whether two volume-cells share one nodal DOF depends on their physical connectivity. For sharing a DOF, a physical connection of two volume-cells within the support of the DOF's nodal shape function N_s needs

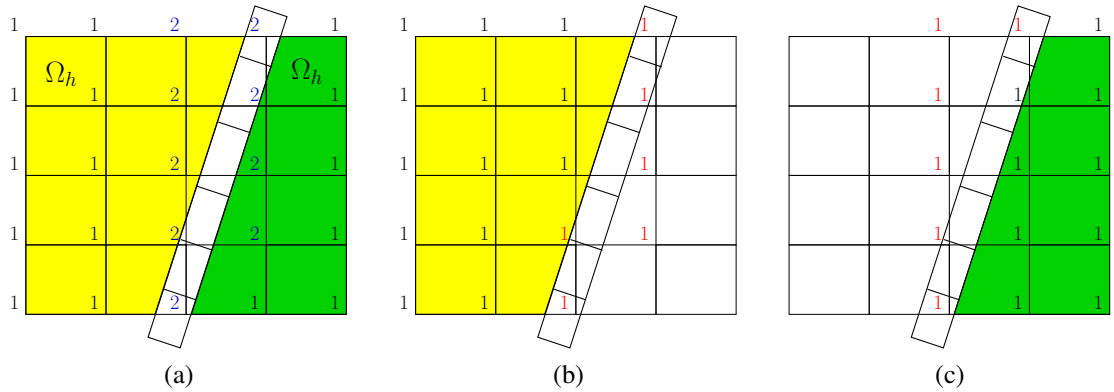

Figure 2.14: Enrichment strategy: (a) Number of required nodal DOFs to represent independent solutions on different sides of the interface. (b) Continuous solution on left side of the interface represented with one set of DOFs (standard-DOFs in black, ghost-DOFs in red). (c) Continuous solution on right side of the interface represented with a second set of DOFs (standard-DOFs in black, ghost-DOFs in red).

to exist. To approximate a solution accurately when the support of N_s ($\mathrm{supp}\,(N_s)$) is subdivided into more than one physical volume-cell, multiple sets of DOFs have to be used at those nodes, as indicated in Figures 2.14a–2.14c. Then, for the volume-cell-based approximation of a solution in (2.83), respective DOFs v_s, $s = 1, ..., \mathrm{nnod}_T$, which represent the solution in the volume-cell V, have to be used. The algorithmic procedure is described in detail in the following.

The Algorithmic Setup. Considering continuous scalar approximations $v_h \in \mathscr{X}_h$, in a first step (PHASE I), the required number of DOFs per node has to be determined. The influence region of a DOF, assigned to a node s, and of its nodal shape function N_s is defined by its support $\mathrm{supp}\,(N_s)$. For continuous Galerkin approximations, the support of a nodal shape function N_s is given by all elements sharing node s. Thus, all the physical volume-cells covered by $\mathrm{supp}\,(N_s)$ can be influenced by an associated nodal DOF, see Figure 2.15a.

In order to determine the total number of required DOFs for a single node $s \in \mathcal{N}$, volume-cells which are connected within its shape function support $(\mathrm{supp}\,(N_s))$ have to be found. Such connections between volume-cells $V \subset \mathrm{supp}\,(N_s)$ are identified with common, delimiting facets f. Note that three-dimensional volume-cells which share only vertices or edges are classified as non-connected, since such connections do not reflect the physical connectivity required for a continuous solution. Mathematically, disjoint connections of volume-cells are defined as

$$C \overset{\text{def}}{=} \left\{ V \subset \mathrm{supp}\,(N_s) \cap \Omega_h \mid \forall \tilde{V} \in C : \exists\, \mathrm{PATH}_C(V, \tilde{V}) \right\}, \tag{2.84}$$

where $\mathrm{PATH}_C(V, \tilde{V})$ denotes a path consisting of volume-cells and common connecting facets

$$\begin{aligned} \mathrm{PATH}_C(V, \tilde{V}) &\overset{\text{def}}{=} (V = V_0, V_1, ..., V_{k-1}, V_k = \tilde{V}) \\ \text{with facets} f_j = V_j \cap V_{j+1},\ &\text{where } V_i \in C\ \forall\, i = 0, ..., k. \end{aligned} \tag{2.85}$$

Note that a connection can even consist of only a single volume-cell. Furthermore, $\mathscr{C}_s$ denotes all determined connections C covered by $\mathrm{supp}\,(N_s)$. For the example of a thin structure shown in Figure 2.15b, two disjunct volume-cell connections (C_1 and C_2) within the support of node s

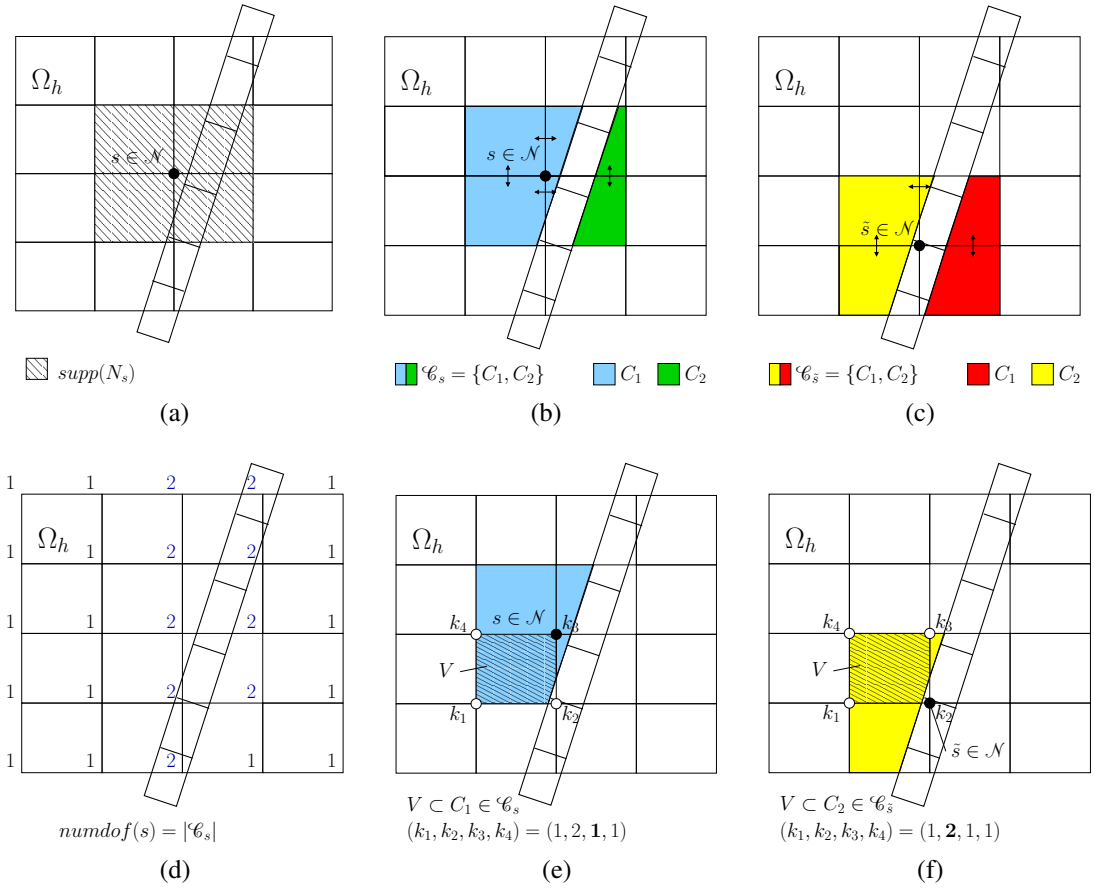

Figure 2.15: DOF-management: (a) Elements cut by a thin structure and support of shape function N_s at node s. (b) Identified volume-cell connections $\mathscr{C}_s = \{C_1, C_2\}$ around node s. (c) Identified volume-cell connections $\mathscr{C}_{\tilde{s}} = \{C_1, C_2\}$ around node $\tilde{s}$. (d) Determined number of nodal DOFs $\mathrm{numdof}(s) = |\mathscr{C}_s|$. (e) Assignment of DOF with index $k_3 = 1$ to volume-cell V for node s. (f) Assignment of DOF with index $k_2 = 2$ to volume-cell V for node $\tilde{s}$.

could be determined, i.e. $\mathscr{C}_s = (C_1, C_2)$. As a further example, volume-cell connections belonging to a second node $\tilde{s}$ are visualized in Figure 2.15c.

Finally, each volume-cell connection $C \in \mathscr{C}_s$ comes along with either a physical DOF or a ghost-DOF at the respective node. Thus, each node $s \in \mathcal{N}$ carries at most one physical DOF and potentially several ghost-DOFs. The total number of DOFs for each node $s \in \mathcal{N}$ is then defined as $\mathrm{numdof}(s) \overset{\text{def}}{=} |\mathscr{C}_s|$, see visualization in Figure 2.15d.

In a second step (PHASE II), to each volume-cell, respective DOF indices for all of the cell's elemental nodes have to be assigned. In the preceding PHASE I, DOFs have been already assigned to connections of volume-cells $C \in \mathscr{C}_s$, which could be identified in the vicinity of the respective nodes. Note, for each element node $s \in \mathcal{N}(T)$, a volume-cell $V \in \Omega_T$ is contained in exactly one connection $C_k \in \mathscr{C}_s$, $1 \leqslant k \leqslant |\mathscr{C}_s|$. As a direct consequence, for each node $s \in \mathcal{N}(T)$, to a volume-cell $V \in C_k$ the respective volume-cell connection index k gets assigned. This assignment procedure of DOF indices is visualized for a certain volume-cell V and two adjacent nodes s and $\tilde{s}$ in Figure 2.15e and Figure 2.15f. Finally, a volume-cell-based tuple of DOF indices $(k_1, k_2, ..., k_{\mathrm{nnod}_T})$ can be used during the assembly procedure of volume-cell-based

element stiffness matrices when evaluating the discrete variational formulation. Algorithm 2.1 gives an overview of the different steps of the proposed DOF-management technique.

Algorithm 2.1 CutFEM-based DOF-management algorithm

1: INPUT: volume-cells V for all elements $T \in \mathcal{T}_h$.
2: PHASE I (build volume-cell connections in $\text{supp}\,(N_s)$ and determine number of required DOFs per node)
3: **for** each node $s \in \mathcal{N}$ **do**
4: Connect volume-cells $V \subset \text{supp}\,(N_s)$ between elements via common facets f: $C \overset{\text{def}}{=} \{V \subset \text{supp}\,(N_s) \cap \Omega \mid \forall \tilde{V} \in C : \exists\, \text{PATH}_C(V, \tilde{V})\}$ with $\text{PATH}_C(V, \tilde{V}) \overset{\text{def}}{=} (V = V_0, V_1, ..., V_{k-1}, V_k = \tilde{V})$ where $V_j \cap V_{j+1} = f$ are facets, $V_i \in C, i = 0, ..., k$.
5: Connections around node s: $\mathscr{C}_s \overset{\text{def}}{=} \big(C_1, C_2, ..., C_{|\mathscr{C}_s|}\big)$.
6: Get number of DOFs: $\text{numdof}(s) \overset{\text{def}}{=} |\mathscr{C}_s|$.
7: Assign DOFs to the volume-cell connections $C_k \in \mathscr{C}_s$, $1 \leqslant k \leqslant |\mathscr{C}_s|$.
8: **end for**
9: PHASE II (assign DOFs to volume-cells)
10: **for** all elements $T \in \mathcal{T}_h$ **do**
11: **for** each volume-cell $V \in \Omega_T$ **do**
12: **for** all $s \in \mathcal{N}(T)$ (nodes of element T where $\text{nnod}_T \overset{\text{def}}{=} |\mathcal{N}(T)|$) **do**
13: Find $V \in C_k$ where $C_k \in \mathscr{C}_s \overset{\text{def}}{=} \big(C_1, C_2, ..., C_{|\mathscr{C}_s|}\big)$, $1 \leqslant k \leqslant |\mathscr{C}_s|$ to get index k.
14: Assign the determined DOF-index k of this volume-cell connection to the volume-cell V as the respective DOF for its element node s.
15: **end for**
16: **end for**
17: **end for**
18: OUTPUT: $\text{numdof}(s) \overset{\text{def}}{=} |\mathscr{C}_s|$ and $(k_1, k_2, ..., k_{\text{nnod}_T})$ set of DOF-indices for each volume-cell V.

Without loss of generality, all visualizations in Figures 2.14 and 2.15 use 4-node quadrilateral elements in two dimensions. However, the proposed technique summarized in Algorithm 2.1 is applicable to any spatial dimension and element type $\mathbb{P}^k, \mathbb{Q}^k, \mathbb{W}^k$ of order $k \geqslant 1$.

Moreover, piecewise discontinuous volume-cell-based cut finite element function spaces could be defined as well. As no nodal connectivity has to be accounted for in such cases, independent sets of elemental DOFs can be created for each physical volume-cell $V \in \Omega_T$. Nevertheless, the facet-volume-cell connectivity is though required for weak coupling strategies of the elemental domain parts. Piecewise discontinuous functions spaces, however, are not further considered within the scope of this thesis.

In the following, the necessity of an expanded function space $\mathscr{X}_h$ as defined in (2.82) is exemplarily shown for the flow around multiple structure.

A Numerical Example - Flow around Multiple Structures. The intention of this example is to demonstrate the applicability of the proposed method to complex-shaped domains build up of different embedded structural obstacles. A computed two-dimensional flow around different

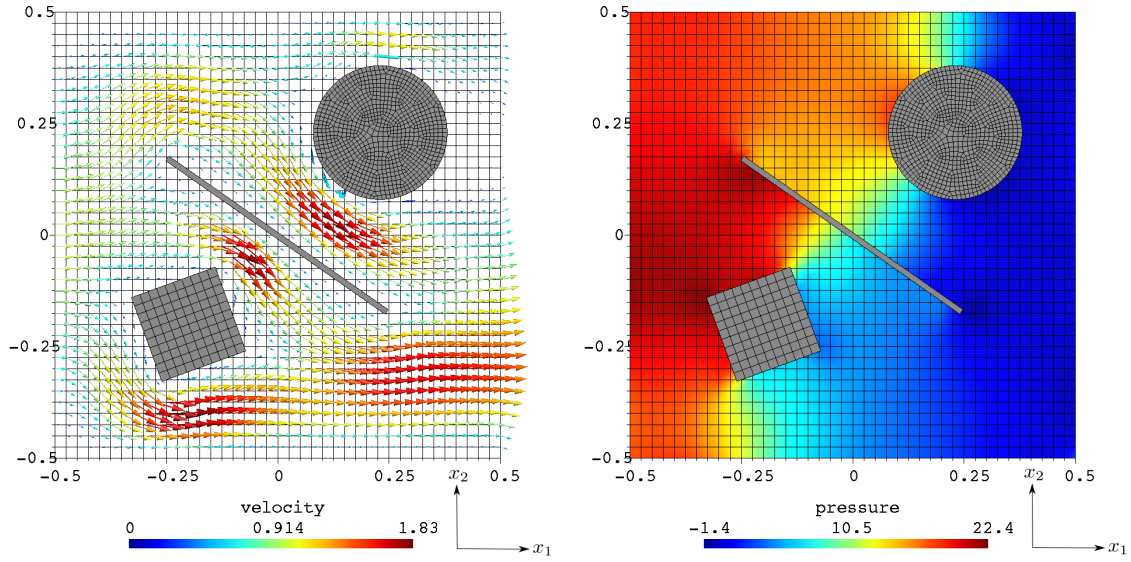

Figure 2.16: Flow around multiple structures: velocity solution (left) and pressure solution (right).

structures serves for the validation of the DOF-management strategy for unfitted cut approximation spaces in different topological situations.

For the fluid field a square domain of dimensions $(-0.5, 0.5)^2$ is discretized with a relatively coarse 40×40 background mesh consisting of linearly interpolated hexahedral $\mathbb{Q}^1$ elements as shown in Figure 2.16. Three different rigid obstacles are located within the fluid domain: a rectangular block with sharp corners discretized with a similar mesh size compared to the background mesh, a rotated thin plate approximated with only one hexahedral element and a fine meshed cylinder. In x_1-direction, a quadratic inflow is enforced strongly and zero Dirichlet boundary conditions for velocity are set at the top and bottom walls. The velocity at the inflow is given as $u_1(x_1, x_2) = 4(0.5 + x_2)(0.5 - x_2)$ and $u_2 = 0$. At the outflow, a zero-traction Neumann boundary condition is applied. The resulting velocity and pressure approximations $\boldsymbol{u}_h, p_h$ around the three obstacles are visualized in Figure 2.16 for a fluid with kinematic viscosity $\nu = 0.1\, m^2/s$. For further details on the discrete stabilized flow field formulation, the reader is referred to Sections 3.5 and 3.6.

A close-up view of the vicinity of the left upper tip of the embedded thin structure in Figure 2.17 depicts the number of DOFs determined by Algorithm 2.1. To represent independent solutions on different sides of this thin obstacle, several DOFs are required for nodes located next to the interface, as there the structural surface splits the support of respective nodal shape functions into independent non-connected volume-cells. Numbers of nodal volume-cell connections, which determine the number of DOFs per node ($\mathrm{numdof}(s) \overset{\text{def}}{=} |\mathfrak{C}_s|$), are shown in Figure 2.17a.

As a foresight, in Figure 2.17b the number of physical facets f per intersected face $F \in \mathfrak{F}_i$ is depicted. In the interface region, faces are subdivided into several polygonal segments. These will play an important role for different stabilization techniques later. Further elaborations with regard to the stabilization topic and the current numerical example will be provided in Section 3.4.3 and Section 3.4.4.1.

The resulting pressure solution approximation p_h in the vicinity of the thin structural body is presented in Figure 2.17c. Its smoothness near the structural tip, indicated by the pressure

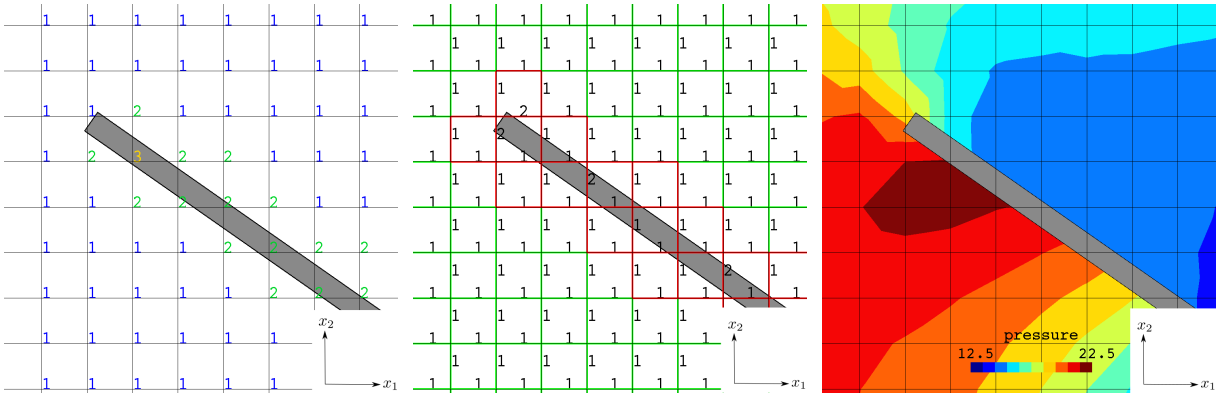

(a) (b) (c)

Figure 2.17: Flow around the tip of a thin structure: (a) Number of DOFs $\mathrm{numdof}(s) = |\mathscr{C}_s|$. (b) Uncut faces $F \in \mathscr{F}_i \backslash \mathscr{F}_\Gamma$ (green), number of facets f for faces $F \in \mathscr{F}_\Gamma$ which are located within the physical domain next to intersected elements (red). This classification of facets is required for different continuous interior penalty CIP and ghost penalty GP stabilization techniques proposed in Section 3.1.3.2 and Section 3.4.3. (c) Pressure contours around the tip of an embedded thin structure.

contour lines, has to be highlighted. This is, first, due to the sufficient number of DOFs, which allows to accurately represent the solution and, second, due to the use of appropriate stabilization techniques for cut finite elements, as will be elaborated in detail in Section 3.4.3.

2.2.5 Expansion of Cut Finite Element Function Spaces to Multiphysics Settings

The CUTFEM-based DOF-management handling proposed in Algorithm 2.1 can be easily extended from one physical subdomain to multidomain settings with two or more subdomains Ω_h^i and respective solution field approximations v_h^i, $i = 1, ..., N_{\mathrm{dom}}$, which are defined on a single background mesh, i.e.

$$\widehat{\mathscr{T}}_h \overset{\mathrm{def}}{=} \widehat{\mathscr{T}}_h^1 = ... = \widehat{\mathscr{T}}_h^{N_{\mathrm{dom}}}, \tag{2.86}$$

as introduced in Section 2.1.1, on the basis of a composed function space (2.81).

Assuming unique positioning information for all volume-cells associated with a certain subdomain Ω_h^i, PHASE I of Algorithm 2.1 can be enhanced to construct volume-cell connections only between physical volume-cells with equal positioning. Once PHASE I is finished with a set of connections $\mathscr{C}_s = (C_1, C_2, ..., C_{|\mathscr{C}_s|})$ for all nodes $s \in \mathcal{N}$, where connections C_k can now be associated with possibly different subdomains Ω_h^i, PHASE II can be run in an unchanged way.

When integrating weak formulations on a specific volume-cell $V \subset \Omega_h^i$, respective sets of DOFs $(k_1, k_2, ..., k_{\mathrm{nnod}_T})$, which are associated with the subdomain function space $\mathscr{X}_h^i$ (2.81) of Ω_h^i the volume-cell belongs to, are used for the assembly process. A possible setting with several subdomains $\Omega_h^1, \Omega_h^2, \Omega_h^3$ including the construction of volume-cell connections for each subdomain Ω_h^i is exemplarily depicted in Figure 2.18 for a single node s.

This strategy has been already successfully applied to two-phase flow by Schott and Rasthofer *et al.* [231], where several advantages over classical XFEM-based enrichment strategies originally used, e.g., in the work by Chessa and Belytschko [71], could be shown. Classical strategies

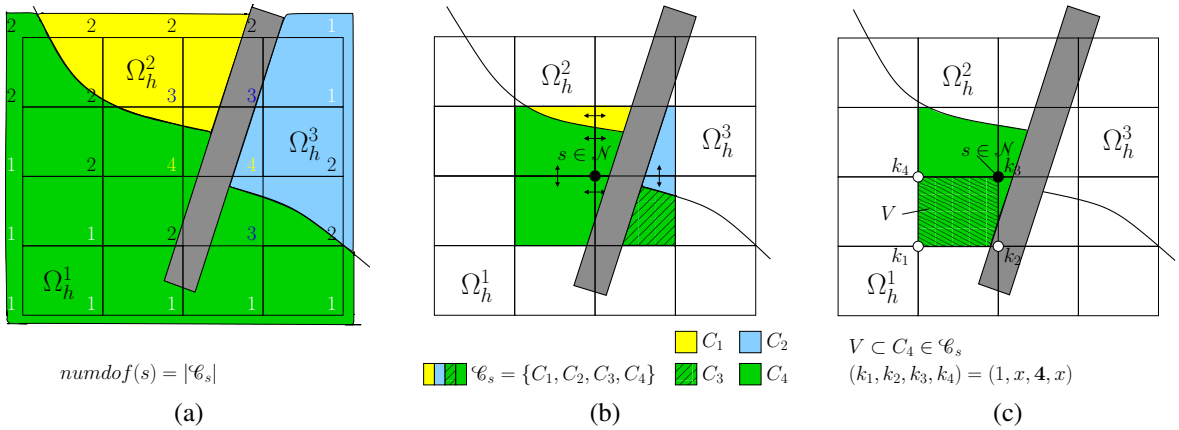

Figure 2.18: Multidomain DOF-management: (a) Multidomain setting with subdomains $\Omega_h^1, \Omega_h^2, \Omega_h^3$ and determined number of nodal DOFs $\mathrm{numdof}(s) = |\mathfrak{C}_s|$. (b) Identified volume-cell connections $\mathfrak{C}_s = \{C_1, C_2, C_3, C_4\}$ around node s, built individually for each subdomain Ω_h^i. Connections C_3 and C_4 belong to the same subdomain Ω_h^1. (c) Assignment of DOF with index $k_3 = 4$ to volume-cell V for node s; x denote DOF indices which cannot be seen from the visualization.

often show severe limitations in situations of complex topological changes, like merging and breaking of fluid phases. Moreover, this framework allows for configurations which involve an arbitrary number of subdomains Ω_h^i. Possible applications might be, for example, immiscible multiphase flows and interactions of those with arbitrary shaped solids. Enhancements to problem settings involving different complex-shaped phases and demanding physics are straightforward to realize.

Reduced Volume-Cell-Composite Multifield Enrichment. While independent nodal DOFs for different physical fields in Ω_h^i are essential to accurately represent solutions v_h^i that belong to different physics, also the use of slightly reduced subdomain approximation spaces $\mathcal{X}_h^i$ can be advantageous in some specific situations, as will be elaborated in the following.

For continuous approximations, all nodes located within one specific subdomain Ω_h^i carry one unique physical DOF to represent the solution field v_h^i inside the domain. However, following Algorithm 2.1, nodes which are located outside this subdomain often carry several DOFs, so-called *ghost*-DOFs, to accurately represent the solution in the interface region. Algorithmically, this is caused by non-connected volume-cells. This strategy is reasonable and essential for situations where topological changes occur or complex-shaped interfaces are not well-resolved by the background mesh, as discussed before. More precisely, the necessity of multiple ghost-DOFs associated with one physical subdomain depends on the approximation of highly curved interfaces by the mesh. Large changes in the direction of unit normal vectors associated with interface segments between non-connected cells can be used as an indicator for that. Otherwise, whenever interfaces are well-resolved, it might be advantageous to avoid frequent changes of approximation spaces and as a result strongly varying numbers of ghost-DOFs when interfaces evolve in time. In such cases, ghost-DOFs can be merged by formally constructing *composites of volume-cells* within the shape function support, which are in fact not connected by facets f, but belong to the same subdomain and exhibit only small variations in the direction of interface

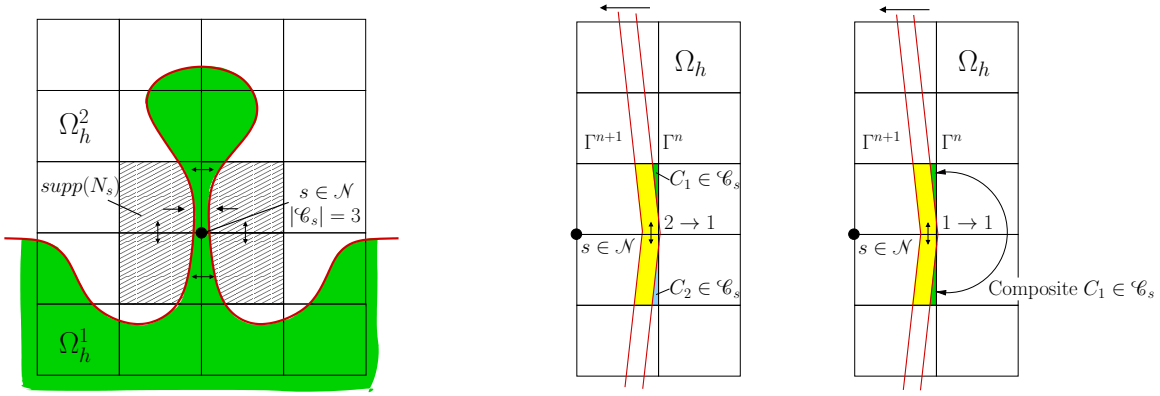

(a) (b)

Figure 2.19: Comparison of different enrichment strategies: (a) Volume-cell based enrichment strategy: Insufficiently resolved high-curvature interfaces in a premixed combustion setting shortly before the flame-front (parallel approaching interfaces) breaks up and the outer fluid phase Ω_h^2 merges; in addition to the physical DOF for phase Ω_h^1, two ghost-DOFs are necessary to accurately approximate the flow in Ω_h^2. (b) Reduced volume-cell-composite enrichment strategy: Frequent changes of approximation spaces and varying number of ghost-DOFs for an interface with almost zero curvature (left) and reduced enrichment strategy which uses a volume-cell-composite for volume-cells of the same subdomain (right).

normals. The representability for multifield problems can be thereby retained, as still different ghost-DOFs are used when belonging to distinct subdomains. In Figure 2.19, two different setups visualize the advantages of the two proposed enrichment strategies: the *volume-cell-based strategy* and the *reduced volume-cell-composite multifield enrichment*.

2.2.6 Notes on Numerical Quadrature on Cut Meshes

Owing to the fact that the computational mesh $\mathcal{T}_h$ is non-fitted to the domain Ω_h, the approximation of discrete formulations require special quadrature techniques. The major challenge therein is to develop schemes which are robust in their construction, ensure a sufficiently accurate approximation and at the same time minimize the number of quadrature points to retain efficiency. Stabilized formulations developed in this thesis require the approximation of volumetric integrals in subdomains Ω_h^i, on the interface Γ_h and on interior faces $F \in \mathcal{F}_i$ of the computational mesh. In the following, a brief introduction to the different integration techniques used in this thesis is given.

Quadrature Schemes for Arbitrary Polyhedra. Following the concept of cutting finite elements introduced in Section 2.2.2, domain integrals are composed of integrals in volume-cells V, which for $d = 3$ are arbitrarily shaped three-dimensional polyhedra in the interface region. For uncut finite elements $V \equiv T$, in this work, classical Gaussian cubature rules are applied as provided, e.g., by third-party software environments like the open-source library INTREPID of the Trilinos project conducted by Sandia National Laboratories (see Heroux *et al.* [149]).

The evaluation of terms on cut polyhedra, in contrast, requires special techniques. Early approaches to integration in XFEMs and CUTFEMs are based on subdividing the volume of a

polyhedron into simple-shaped cells, like tetrahedra or hexahedra, for which again cubature rules for polynomials are existing. Such techniques are often referred to as *subtetrahedralization* or *tessellation* in literature and have been suggested, e.g., by Sukumar *et al.* [247]. These procedures are easy to implement whenever the interface is represented implicitly by a level-set field defined on the underlying finite element mesh. In such cases, a limited number of differently shaped polyhedra exists for which a tessellation can be explicitly constructed (see, e.g., in Burman *et al.* [63] and references therein).

Things can become more sophisticated for overlapping mesh methods. Intersecting background mesh with trace meshes can render in an unlimited number of intersection scenarios depending on mesh locations and, in particular, depending on the different grid sizes. In such cases, decomposition techniques often lack robustness for concave polyhedra, as reported, e.g., by Sudhakar and Wall [245]. Moreover, for fine-resolved intersecting trace meshes this often renders in high numbers of sub-cells and makes integration on polyhedra an expensive task, as discussed, e.g., by Mousavi *et al.* [191]. In the meanwhile, different other types of quadrature schemes have been developed.

For so-called *moment-fitting methods*, cubature rules are constructed on the basis of predefined locations of integration points, for which respective integration weights are computed by fitting them in a way such that single monomials are integrated in a best-approximation sense. As a major drawback of such methods, least-squares systems with non-sparsity patterns have to be solved and their conditioning can deteriorate depending on the distribution of integration points within the polyhedra. For such techniques, see the works by, e.g., Mousavi *et al.* [191], Mousavi and Sukumar [190] and Müller *et al.* [193].

Various novel strategies make use of the *divergence theorem* to perform integration on polyhedra. A detailed overview of different techniques based on this idea can be found in Sudhakar *et al.* [246]. The approach devised in the latter publication is used for all simulations proposed in this thesis. Fundamental idea is to convert critical volumetric integrals into quadrature problems defined on polygonal facets f which delimit the volumes. Surface integrals on facets can be easily dealt with by subdividing them into planar two-dimensional triangular cells, a task for that the complexity is highly reduced compared to three-dimensional decompositions. Utilizing this procedure renders in a competitive integration method with highly reduced complexity. For further theoretical and algorithmic details and comparisons to other techniques, the reader is referred to the original publication [246].

Quadrature on Interface Segments. When constructing volume-cell based cubature rules by transforming them into surface integrals, as discussed before, interface-segment quadrature rules for $\Gamma_T \cap V$ related to a polyhedra V within a finite element T are simultaneously built. Facets of volume-cells which are aligned with the interface are then split into simple-shaped planar cells for which Gaussian cubature rules are given. Concerning details on required transformations between parameter and physical coordinate systems of elements and the triangulated sub-cells, the interested reader is referred to, e.g., the theses by Henke [147] or Gerstenberger [123].

Quadrature on Faces. Evaluating discrete operators along entire faces $F \in \mathcal{F}_i$, related integrals can be approximated with standard Gaussian quadrature rules defined on respective reference faces as provided by the open-source library INTREPID (see Heroux *et al.* [149]).

Chapter 3

Developing Stabilized Cut Finite Element Methods for Incompressible Flow

Resuming Chapter 2, the high versatility and the great benefit of cut finite element methods (CUTFEMs) for approximating solutions to multiphysics problems which incorporate fluid flows is undisputed. The possibility of approximating laminar and turbulent flows with non-boundary-fitted finite element meshes expands the potential of such discretization techniques to a wide range of biomedically and industrially relevant applications. In particular, their capabilities with regard to moving boundaries and interfaces without having to deal with potential mesh distortion simplifies grid generation substantially.

Before developing unfitted finite element methods for coupled flow problems, this chapter is devoted to a detailed numerical analysis of some issues of CUTFEMs in general, and to the development of stabilized CUTFEMs for incompressible single-phase flows with stationary and moving boundaries in particular. When approximating Navier-Stokes equations on boundary-fitted finite element meshes, depending on the choice of function spaces and the flow regime, discrete variational formulations often require additional stabilization techniques to guarantee existence and uniqueness of approximative solutions and their optimal convergence to the exact solution with mesh refinement. The price to be paid for the flexibility provided by unfitted mesh techniques is the additional effort that has to be put on developing stable and optimal convergent numerical schemes. Besides well-established stabilization techniques known from classical continuous finite element approximation, additional measures are required on cut elements. As the computational meshes are non-fitted to the domain boundary, boundary conditions have to be imposed in a weak variational form. Most if not all cut finite element methodologies which have been developed over the last decade suffer from a lack of inf-sup stability and suboptimal convergence rates that often strongly depend on the location of the boundary within finite elements. Furthermore, such discretization techniques are often accompanied by a negative side effect of rendering in ill-conditioned global system matrices which deteriorates the accuracy of these methods as well as the efficiency of iterative solution techniques for related systems. Such characteristics are undesirable and have to be taken into consideration for the design of CUTFEMs.

This chapter is organized as follows: After reviewing the governing equations and stabilization techniques applicable to classical fitted-mesh finite element approximations in Section 3.1, an

overview of useful mathematical tools and concepts required for numerically analyzing cut finite element methods is given in Section 3.2. A survey of weakly imposing boundary conditions on boundary-fitted meshes is given in Section 3.3. Therein, focus is directed towards stability properties of different techniques as well as on analogies and differences between those, which serves as starting point for developing CUTFEMs for incompressible flows. General numerical issues inherent in cut finite element approximations are numerically analyzed and discussed in Section 3.4. Derived theoretical results will be verified by several numerical simulations and studies. A so-called *ghost penalty* interface zone stabilization technique is introduced which provides the basis for robust and accurate CUTFEMs. In Section 3.5, a novel stabilized discrete formulation is proposed for a linear auxiliary problem to the Navier-Stokes equations, the so-called Oseen problem. Inf-sup stability and optimal *a priori* error estimates will be mathematically proven and corroborated by comprehensive convergence studies. Extensions of stabilized formulations to single-phase flows with stationary as well as moving boundaries governed by the transient incompressible Navier-Stokes equations are proposed in Section 3.6. Extensive numerical simulations demonstrate accuracy and robustness of the stabilized CUTFEMs. The great potential of unfitted approximation techniques for fluid flows will have been shown already for single-phase problems before extensions are made to coupled flow problems. Domain decomposition for single- and multiphase flows are considered in Chapter 4 and unfitted discretization techniques for fluid-structure interaction problems are proposed in Chapter 5. The present chapter is based on work published by Schott and Wall [230] and Massing *et al.* [183].

3.1 Finite Element Formulations for Incompressible Flow

In this section, fundamentals on governing equations for laminar and turbulent low-Mach-number flows, the incompressible Navier-Stokes equations, are addressed. Furthermore, well-established stabilization techniques applicable to classical boundary-fitted finite element discretization methods utilizing continuous approximation spaces for velocity and pressure will be reviewed.

3.1.1 Governing Equations for Fluid Mechanics

Throughout this thesis, all considered flows are assumed as incompressible flows of Newtonian fluids. Based on fundamental conservation laws for continua proposed in Section 2.1.2.2, governing equations are derived in the following and an initial boundary value problem (IBVP) for incompressible Navier-Stokes equations is formulated. Independent of the kinematic description, all flow equations are described in spatial coordinates; for respective quantities the indicating subscript $(\cdot)_{\boldsymbol{x}}$ will be omitted.

Incompressibility Constraint. For low Mach number flows, a reasonable assumption on the density of continua is to not change in space and time such that $\rho(\boldsymbol{x}, t) = \text{const}$. Mathematically, the ALE form of conservation of mass (2.25) expressed in spatial coordinates then reduces to an incompressibility constraint for the flow field

$$\nabla \cdot \boldsymbol{u} = 0. \tag{3.1}$$

Constitutive Law for Newtonian Fluids. Recalling Cauchy's fundamental lemma, the Cauchy stress tensor $\boldsymbol{\sigma}$ defined in the balance of linear momentum (2.33) is composed of a hydrostatic and a viscous stress state as

$$\boldsymbol{\sigma} = -p\boldsymbol{I} + \boldsymbol{\tau}. \tag{3.2}$$

Thereby, $p = -\operatorname{tr}(\boldsymbol{\sigma})/d$ is called the *dynamic fluid pressure*, which can be considered as Lagrange multiplier enforcing the incompressibility constraint, and $\boldsymbol{\tau}$ is the deviatoric viscous stress part satisfying $\operatorname{tr}(\boldsymbol{\tau}) = 0$. For Newtonian fluids, viscous stresses are modeled being linearly related to the velocity gradient which, combined with the symmetry requirement resulting from the balance of angular momentum (2.37) and the assumption of isotropic material, results in the constitutive relation

$$\boldsymbol{\tau} = 2\mu\boldsymbol{\epsilon}(\boldsymbol{u}). \tag{3.3}$$

Therein, $\boldsymbol{\epsilon}(\boldsymbol{u}) \overset{\text{def}}{=} 1/2\left(\nabla\boldsymbol{u} + (\nabla\boldsymbol{u})^T\right)$ denotes the symmetric *strain rate tensor*. The unique material parameter which linearly relates stress and strain is the *dynamic viscosity* $\mu > 0$. It can be expressed in terms of a *kinematic viscosity* ν as $\mu = \nu\rho$.

Incompressible Navier-Stokes Equations in ALE Form. Combining the constitutive law with the ALE form of balance of linear momentum (2.34) and the incompressibility (3.1), the ALE version of the transient incompressible Navier-Stokes equations emerges to

$$\rho\frac{\partial \boldsymbol{u}_\chi}{\partial t} \circ \boldsymbol{\Phi}^{-1} + \rho(\boldsymbol{c}\cdot\nabla)\boldsymbol{u} + \nabla p - 2\mu\nabla\cdot\boldsymbol{\epsilon}(\boldsymbol{u}) = \rho\boldsymbol{f} \qquad \forall\,(\boldsymbol{x},t) \in \Omega\times(T_0,T], \tag{3.4}$$

$$\nabla\cdot\boldsymbol{u} = 0 \qquad \forall\,(\boldsymbol{x},t) \in \Omega\times(T_0,T], \tag{3.5}$$

where $\boldsymbol{f}$ is an external body force load and $((\boldsymbol{c}\cdot\nabla)\boldsymbol{u})_i \overset{\text{def}}{=} \sum_j \boldsymbol{c}_j \cdot \frac{\partial \boldsymbol{u}_i}{\partial x_j}$ with the ALE convective velocity $\boldsymbol{c}$, see (2.14). Assuming the fluid domain boundary $\partial\Omega$ to be split into disjunct Dirichlet and Neumann parts at all times t, i.e. Γ_{D} and Γ_{N}, conditions for the flow can be prescribed as

$$\boldsymbol{u} = \boldsymbol{g}_{\mathrm{D}} \qquad \forall(\boldsymbol{x},t) \in \Gamma_{\mathrm{D}}\times(T_0,T], \tag{3.6}$$

$$\boldsymbol{\sigma}\cdot\boldsymbol{n} = \boldsymbol{h}_{\mathrm{N}} \qquad \forall(\boldsymbol{x},t) \in \Gamma_{\mathrm{N}}\times(T_0,T]. \tag{3.7}$$

Here, $\boldsymbol{n}$ denotes the outward pointing unit normal on the boundary and $\boldsymbol{g}_{\mathrm{D}}$ and $\boldsymbol{h}_{\mathrm{N}}$ are given velocity field and surface traction on corresponding boundary parts. An initial flow field

$$\boldsymbol{u}(\boldsymbol{x},0) = \boldsymbol{u}_0(\boldsymbol{x}) \qquad \forall\,\boldsymbol{x} \in \Omega(T_0) \tag{3.8}$$

is defined in the initial domain and closes the IBVP for incompressible flow.

3.1.2 Variational Fluid Problem

Deriving a weak formulation for incompressible flow requires the definition of appropriate functional spaces. For any time $t \in (T_0,T]$ and $U \in \{\Omega(t),\Gamma(t)\}$, let $H^m(U)$ and $[H^m(U)]^d$ be the standard Sobolev space of order $m \in \mathbb{R}$ and their $\mathbb{R}^d$-valued equivalents. Their corresponding

inner products are denoted by $(\cdot,\cdot)_{m,\Omega}$ for the domain and by $\langle\cdot,\cdot\rangle_{m,\Gamma}$ for the boundary. Norms and semi-norms are notated with $\|\cdot\|_{m,U}$ and $|\cdot|_{m,U}$, respectively. If unmistakable, it is occasionally written $(\cdot,\cdot)_U$, $\langle\cdot,\cdot\rangle_U$ and $\|\cdot\|_U$ for the inner products and norms associated with $L^2(U)$, with U being a Lebesque-measurable subset of $\mathbb{R}^d$. For $m > 1/2$, the notation $[H^m_{\boldsymbol{g}}(\Omega)]^d$ is used to designate the set of all functions in $[H^m(\Omega)]^d$ whose $\mathbb{R}^d$-valued boundary traces are equal to $\boldsymbol{g}$. Later in the numerical analysis simplified problem settings with only Dirichlet boundaries will be considered, i.e. $\Gamma_{\mathrm{N}} = \emptyset$, for those the pressure is determined only up to a constant. For this purpose, let $L^2_0(\Omega)$ be the function space which consists of functions in $L^2(\Omega)$ with zero average.

The functional space for admissible fluid velocities is $\mathcal{V}_{\boldsymbol{g}_{\mathrm{D}}} \overset{\text{def}}{=} [H^1_{\Gamma_D,\boldsymbol{g}_{\mathrm{D}}}(\Omega(t))]^d \subset [H^1(\Omega(t))]^d$ which satisfies the Dirichlet boundary condition (3.6). The related space of admissible test functions $\mathcal{V}^{\mathrm{f}}_{\mathbf{0}}$ exhibits zero trace on Γ_{D}. For the pressure field the trial and test function space is given by $\mathcal{Q} = L^2(\Omega(t))$ if $\Gamma_{\mathrm{N}} \neq \emptyset$ and by $\mathcal{Q} = L^2_0(\Omega(t))$ if $\Gamma_{\mathrm{N}} = \emptyset$. The non-linear variational formulation for incompressible flow then reads as follows: for all $t \in (T_0, T]$, find fluid velocity and pressure $U(t) = (\boldsymbol{u}(t), p(t)) \in \mathcal{V}_{\boldsymbol{g}_{\mathrm{D}}} \times \mathcal{Q}$ such that for all $V = (\boldsymbol{v}, q) \in \mathcal{V}_{\mathbf{0}} \times \mathcal{Q}$

$$\mathcal{A}(U, V) = \mathcal{L}(V), \tag{3.9}$$

where

$$\mathcal{A}(U,V) \overset{\text{def}}{=} (\rho\frac{\partial \boldsymbol{u}_{\chi}}{\partial t} \circ \boldsymbol{\Phi}^{-1}(t), \boldsymbol{v})_{\Omega(t)} + c(\boldsymbol{u} - \hat{\boldsymbol{u}}; \boldsymbol{u}, \boldsymbol{v}) + a(\boldsymbol{u}, \boldsymbol{v}) + b(p, \boldsymbol{v}) - b(q, \boldsymbol{u}), \tag{3.10}$$

$$\mathcal{L}(V) \overset{\text{def}}{=} l(\boldsymbol{v}) \tag{3.11}$$

with the following trilinear, bilinear and linear forms c, a, b and l to shorten the presentation

$$c(\boldsymbol{\beta}; \boldsymbol{u}, \boldsymbol{v}) \overset{\text{def}}{=} (\rho(\boldsymbol{\beta} \cdot \nabla)\boldsymbol{u}, \boldsymbol{v})_{\Omega(t)}, \tag{3.12}$$

$$a(\boldsymbol{u}, \boldsymbol{v}) \overset{\text{def}}{=} (2\mu\boldsymbol{\epsilon}(\boldsymbol{u}), \boldsymbol{\epsilon}(\boldsymbol{v}))_{\Omega(t)}, \tag{3.13}$$

$$b(p, \boldsymbol{v}) \overset{\text{def}}{=} -(p, \nabla \cdot \boldsymbol{v})_{\Omega(t)}, \tag{3.14}$$

$$l(\boldsymbol{v}) \overset{\text{def}}{=} (\rho\boldsymbol{f}, \boldsymbol{v})_{\Omega(t)} + \langle \boldsymbol{h}_{\mathrm{N}}, \boldsymbol{v}\rangle_{\Gamma_{\mathrm{N}}(t)}. \tag{3.15}$$

Therein, $\hat{\boldsymbol{u}}$ denotes the grid velocity as introduced in (2.15) for formulations in an ALE frame.

3.1.3 Stabilized Discrete Formulations for Boundary-Fitted Meshes

The discrete functional space for the velocity field is defined by $\mathcal{V}_{h,\boldsymbol{g}_{\mathrm{D}}} = [\mathcal{X}_h]^d \cap \mathcal{V}_{\boldsymbol{g}_{\mathrm{D}}}$ and for the pressure field by $\mathcal{Q}_h = \mathcal{X}_h \cap \mathcal{Q}$, where $\mathcal{X}_h$ is the isoparametric finite element space as defined in (2.43). In this work, for the spatial discretization with fitted as well as unfitted meshes, continuous approximations of equal order $k \geqslant 1$ are considered exclusively. The velocity-pressure trial and test product spaces are defined as $\mathcal{W}_{h,\boldsymbol{g}_{\mathrm{D}}} = \mathcal{V}_{h,\boldsymbol{g}_{\mathrm{D}}} \times \mathcal{Q}_h$ and $\mathcal{W}_{h,\mathbf{0}} = \mathcal{V}_{h,\mathbf{0}} \times \mathcal{Q}_h$.

Different flow regimes, that is dominating advection or diffusion, can be specified by the so-called *Reynolds number* which in its global and local element-wise form is defined as

$$\mathrm{Re} \overset{\text{def}}{=} \frac{\|\boldsymbol{\beta}\|_{0,\Omega,\infty} \cdot L}{\nu} \qquad \text{and} \qquad \mathrm{Re}_T \overset{\text{def}}{=} \frac{\|\boldsymbol{\beta}\|_{0,T,\infty} \cdot h_T}{\nu} \tag{3.16}$$

with a flow characteristic global length scale L and approximation specific element lengths h_T for all elements $T \in \mathcal{T}_h$. Therein, $\boldsymbol{\beta}$ denotes a characteristic advective or convective flow velocity. While the Reynolds number is physically motivated and quantifies the ratio of inertia forces to viscous forces, an additional space and time approximation related characteristic number quantifies the ratio of advection to (pseudo-)reaction arising from temporal discretization, the so-called *Courant number*. In the context of finite element discretizations with characteristic element lengths h_T and a temporal approximation with a time-step length $\Delta t \propto \sigma^{-1}$, the Courant number is defined as

$$\mathrm{Co}_T \overset{\text{def}}{=} \frac{\|\boldsymbol{\beta}\|_{0,\Omega,\infty} \cdot \Delta t}{h_T} \propto \frac{\|\boldsymbol{\beta}\|_{0,\Omega,\infty}}{\sigma \cdot h_T}. \tag{3.17}$$

It is well-known that the standard Galerkin formulation (3.9) for the incompressible Navier-Stokes equations approximated with finite-dimensional subspaces suffers from different sources of instabilities:

- Due to the saddle-point structure and the use of equal-order interpolation spaces in the definition of $\mathcal{W}_h = \mathcal{V}_h \times \mathcal{Q}_h$, the resulting approximation violates the discrete inf-sup condition and thus is not stable in the sense of Babuška–Brezzi [36].
- Numerical solutions exhibit unphysical oscillations and sub-optimal error estimates in case of locally convection-dominant flow, i.e. if $\mathrm{Re}_T \gg 1$ for certain elements $T \in \mathcal{T}_h$. On the one hand, this is due to insufficient control on the convective term compared to the elliptic viscous term. On the other hand, in the limit case $\mu \to 0$, the velocity function space changes from $H^1(\Omega)$ to $H^{div}(\Omega)$, that is the space of $L^2(\Omega)$-functions whose divergence is also in $L^2(\Omega)$, and further control on the incompressibility needs to be recovered.
- When Dirichlet boundary conditions need to be enforced weakly, consistent stabilization terms at the boundary Γ are required to guarantee stability and optimal error convergence for low and high Reynolds numbers.

To counteract these numerical effects, the variational form (3.9) needs to be stabilized. The aforementioned instability arising from the weak imposition of boundary conditions will be considered separately in Section 3.3. Within this section, Dirichlet boundary conditions are assumed to be enforced strongly via the discrete function space.

A recent overview of various stabilization techniques to account for the first and second instability can be found in Braack *et al.* [31]. Throughout this thesis, two different classes of fluid stabilizations are used for fitted and unfitted finite-element-based approximations:

- the well-known *residual-based variational multiscale* framework, which combines a streamline upwind/ Petrov–Galerkin (SUPG) method and a pressure-stabilizing/Petrov–Galerkin (PSPG) method, supported by a least-squares incompressibility constraint (LSIC, grad-div) stabilization, and
- the class of *continuous interior penalty* (CIP) stabilizations, which controls the discrete convective derivative, the pressure gradient and the discrete divergence operator across inter-element faces in the interior of the computational mesh.

Both techniques can be used to control the same sources of instabilities introduced before. However, the methods are based on different discrete control mechanisms and provide desirable aspects from different perspectives, as will be discussed below. First, the two techniques are introduced for the fitted mesh case and can be finally combined and extended to obtain stable and accurate numerical approximations schemes for unfitted meshes as will be shown later in Section 3.6.

3.1.3.1 The Residual-based Variational Multiscale (RBVM) Method

One of the most frequently used stabilization techniques of the Galerkin scheme (3.9) is the well-known residual-based technique. All required element-wise stabilization terms of the well established SUPG/PSPG/LSIC approach can be derived from the variational multiscale framework. Velocity and pressure $(\boldsymbol{u}, p) \in \mathcal{W}_{\boldsymbol{g}_\mathrm{D}}$, as well as the corresponding weighting functions $(\boldsymbol{v}, q) \in \mathcal{W}_{\boldsymbol{0}}$, can be decomposed in the weak formulation as $\boldsymbol{u} = \boldsymbol{u}_h + \boldsymbol{u}_h^{\mathrm{sgs}}$, $p = p_h + p_h^{\mathrm{sgs}}$ into resolved components $\boldsymbol{u}_h, p_h$ and subgrid-scale components $\boldsymbol{u}_h^{\mathrm{sgs}}, p_h^{\mathrm{sgs}}$. As explained in, e.g., the textbook by Gresho and Sani [131], the latter two can be approximated as element-wise discrete residuals of momentum and continuity equation (3.4) and (3.5) as

$$\boldsymbol{u}_h^{\mathrm{sgs}} \overset{\mathrm{def}}{=} -\tau_{\mathrm{M}}(\rho \frac{\partial \boldsymbol{u}_{\boldsymbol{\chi},h}}{\partial t} \circ \boldsymbol{\Phi}^{-1}(t) + \boldsymbol{r}_{\mathrm{M}}(\boldsymbol{u}_h, p_h) - \rho \boldsymbol{f}) \qquad \text{and} \qquad p_h^{\mathrm{sgs}} \overset{\mathrm{def}}{=} -\tau_{\mathrm{C}} r_{\mathrm{C}}(\boldsymbol{u}_h) \tag{3.18}$$

with element-wise defined functions

$$\boldsymbol{r}_{\mathrm{M}}(\boldsymbol{u}_h, p_h) \overset{\mathrm{def}}{=} \rho((\boldsymbol{u}_h - \hat{\boldsymbol{u}}_h) \cdot \nabla)\boldsymbol{u}_h + \nabla p_h - 2\mu \nabla \cdot \boldsymbol{\epsilon}(\boldsymbol{u}_h), \tag{3.19}$$

$$r_{\mathrm{C}}(\boldsymbol{u}_h) \overset{\mathrm{def}}{=} \nabla \cdot \boldsymbol{u}_h, \tag{3.20}$$

and appropriate piecewise constant stabilization scaling functions

$$\tau_{\mathrm{M},T} = \frac{1}{\sqrt{\left(\frac{2\rho}{\Delta t}\right)^2 + (\rho(\boldsymbol{u}_h - \hat{\boldsymbol{u}}_h)) \cdot \boldsymbol{G}(\rho(\boldsymbol{u}_h - \hat{\boldsymbol{u}}_h)) + C_{\mathrm{I}}\mu^2 \boldsymbol{G} : \boldsymbol{G}}}, \tag{3.21}$$

$$\tau_{\mathrm{C},T} = \frac{1}{\tau_{\mathrm{M,T}} \mathrm{tr}\,(\boldsymbol{G})}, \tag{3.22}$$

as defined in Taylor *et al.* [252] and Whiting and Jansen [267] for all elements $T \in \mathcal{T}_h$. Hereby, the stabilization parameters take into account the definition of the relative convective velocity $(\boldsymbol{u}_h - \hat{\boldsymbol{u}}_h)$ and the second rank covariant metric tensor $G_{kl}(\boldsymbol{x}) = \sum_{i=1}^{d} (\partial \xi_i / \partial x_k\big|_{\boldsymbol{x}})(\partial \xi_i / \partial x_l\big|_{\boldsymbol{x}})$ is related to the mapping of the parent element domain to its reference element with local coordinate system $\boldsymbol{\xi}$. This tensor serves as a measure for the characteristic element length required to guarantee stable and optimal convergent schemes for low- and high-Reynolds-number flows. The time-step length of the temporal discretization is denoted by Δt and C_{I} is set to 36.0 for (tri-)linearly and to 60.0 for (tri-)quadratically interpolated hexahedral finite elements. For more detailed elaborations on the parameter scaling between convective and diffusive limit in terms of the inverse estimate constant C_{I} for different element types and polynomial orders, the interested reader is referred to Franca and Frey [112] and Whiting [266].

The combined SUPG/PSPG/LSIC stabilized discrete formulation for the incompressible Navier-Stokes equations then reads as follows: for all $t \in (T_0, T]$, find fluid velocity and pressure $U_h(t) = (\boldsymbol{u}_h(t), p_h(t)) \in \mathcal{V}_{h,\boldsymbol{g}_\mathrm{D}} \times \mathcal{Q}_h$ such that for all $V_h = (\boldsymbol{v}_h, q_h) \in \mathcal{V}_{h,\boldsymbol{0}} \times \mathcal{Q}_h$

$$\mathcal{A}_h^{\mathrm{RBVM}}(U_h, V_h) = \mathcal{L}_h^{\mathrm{RBVM}}(U_h, V_h), \tag{3.23}$$

where

$$\begin{aligned}
\mathcal{A}_h^{\mathrm{RBVM}}(U_h, V_h) &\stackrel{\mathrm{def}}{=} \mathcal{A}(U_h, V_h) \\
&+ \sum\nolimits_{T\in\mathcal{T}_h} \left(\rho\frac{\partial \boldsymbol{u}_{\boldsymbol{\chi},h}}{\partial t} \circ \boldsymbol{\Phi}^{-1}(t) + \boldsymbol{r}_\mathrm{M}(\boldsymbol{u}_h, p_h), \tau_{\mathrm{M,u}}(\rho(\boldsymbol{u}_h - \hat{\boldsymbol{u}}_h)\cdot\nabla)\boldsymbol{v}_h + \tau_{\mathrm{M,p}}\nabla q_h\right)_T \\
&+ \sum\nolimits_{T\in\mathcal{T}_h} \left(r_\mathrm{C}(\boldsymbol{u}_h), \tau_\mathrm{C}\nabla\cdot\boldsymbol{v}_h\right)_T, \qquad (3.24) \\
\mathcal{L}_h^{\mathrm{RBVM}}(U_h, V_h) &\stackrel{\mathrm{def}}{=} \mathcal{L}(V_h) \\
&+ \sum\nolimits_{T\in\mathcal{T}_h} \left(\rho\boldsymbol{f}, \tau_{\mathrm{M,u}}(\rho(\boldsymbol{u}_h - \hat{\boldsymbol{u}}_h)\cdot\nabla)\boldsymbol{v}_h + \tau_{\mathrm{M,p}}\nabla q_h\right)_T \qquad (3.25)
\end{aligned}$$

with $\tau_{\mathrm{M,u}} = \tau_{\mathrm{M,p}} = \tau_\mathrm{M}$. The first term in (3.24) and (3.25) contains the standard Galerkin formulation, respectively. In the second line of those equations, an SUPG term which accounts for stability issues in convection-dominated flows by adding artificial diffusion is combined with a PSPG term which makes the formulation inf-sup stable for equal-order-interpolated approximations for velocity and pressure. The last term in (3.24) ensures sufficient control over discrete mass conservation for convection-dominated flows with $\mu \to 0$. Fundamental idea of the strongly consistent residual-based techniques is to add element-wise semi-norm control over uncontrolled parts of the standard Galerkin formulation. The combination of SUPG/PSPG/LSIC stabilizations ensures additional control over

$$\sum\nolimits_{T\in\mathcal{T}_h} \|\tau_\mathrm{M}^{\frac{1}{2}}(\rho(\boldsymbol{\beta}_h\cdot\nabla)\boldsymbol{v}_h + \nabla q_h)\|_{0,T}^2 + \sum\nolimits_{T\in\mathcal{T}_h} \|\tau_\mathrm{C}^{\frac{1}{2}}\nabla\cdot\boldsymbol{v}_h\|_{0,T}^2, \tag{3.26}$$

with $\boldsymbol{\beta}_h = (\boldsymbol{u}_h - \hat{\boldsymbol{u}}_h)$ the advective velocity (see, e.g., Braack *et al.* [31] or the textbook by Roos *et al.* [222]). A more detailed derivation of the proposed stabilization terms and its interpretation in the context of the residual-based variational multiscale concept can be found, e.g., in the textbook by Hughes *et al.* [156].

3.1.3.2 The Continuous Interior Penalty (CIP) Method

One promising stabilization technique for incompressible flow approximated with continuous equal-order interpolations for velocity and pressure is the CIP technique. Compared to the RBVM technique which adds terms in the bulk and is consistent with respect to the strong residual of the Navier-Stokes equations, this method uses weakly consistent least squares stabilization of the gradient jumps across inter-element boundaries, i.e. edges in two and faces in three spatial dimensions. Thus, such operators are often referred to as *edge/face-based/oriented* stabilizations. The methodology has its origin in the early work by Douglas and Dupont [93] where it was used as an improvement for elliptic and parabolic Galerkin approximations by adding jump-penalty least squares terms. Burman and Hansbo [46] picked up this idea and used such a term to stabilize advection–diffusion problems. In the following years, this technique

gained great importance and was further developed for different problem fields. A general hp-framework was proposed by Burman and Ern [54]. CIP stabilizations for the generalized Stokes problem were proposed by Burman and Hansbo [47] and for Stokes and Darcy equations by Burman and Hansbo [42]. For incompressible high-Reynolds number flows, adaption was made by Burman *et al.* [48] for the Oseen equations and by Burman and Fernández [41] for the time-dependent Navier-Stokes equations. Considerations and investigations on this stabilization technique in the context of variational multiscale methods for turbulent flows were proposed in Burman [49]. Many further theoretical work on specific numerical aspects of this technique is available in literature. More details on existing literature with regard to different specific aspects of this class of stabilizations will be proposed in corresponding sections later in this work.

The CIP method for fitted meshes employed in this thesis is based on the publications [41, 48]. Symmetric stabilization terms penalize the jump of the velocity and pressure gradients over inter-element faces. More precisely, the jump over an interior face $F \in \mathscr{F}_i$ is defined by

$$[\![f(\boldsymbol{x})]\!] = \lim_{t \to 0^+} (f(\boldsymbol{x} - t\boldsymbol{n}_F) - f(\boldsymbol{x} + t\boldsymbol{n}_F)), \tag{3.27}$$

where $\boldsymbol{n}_F$ is a unit normal vector on F and $\boldsymbol{x} \in F$, with the natural component-wise extension to vector-valued functions. The main idea in the CIP method is to augment the discrete variational form (3.9) with the stabilization form

$$\mathscr{S}_h^{CIP}(U_h, V_h) = s_\beta(\boldsymbol{u}_h - \hat{\boldsymbol{u}}_h; \boldsymbol{u}_h, \boldsymbol{v}_h) + s_u(\boldsymbol{u}_h - \hat{\boldsymbol{u}}_h; \boldsymbol{u}_h, \boldsymbol{v}_h) + s_p(\boldsymbol{u}_h - \hat{\boldsymbol{u}}_h; p_h, q_h), \tag{3.28}$$

consisting of the (weakly) consistent symmetric jump-penalty stabilization operators

$$s_\beta(\boldsymbol{\beta}; \boldsymbol{u}_h, \boldsymbol{v}_h) \overset{\text{def}}{=} \gamma_\beta \sum\nolimits_{F \in \mathscr{F}_i} \phi_{\beta,F} \rho h \langle [\![(\boldsymbol{\beta}_h \cdot \nabla)\boldsymbol{u}_h]\!], [\![(\boldsymbol{\beta}_h \cdot \nabla)\boldsymbol{v}_h]\!] \rangle_F, \tag{3.29}$$

$$s_u(\boldsymbol{\beta}; \boldsymbol{u}_h, \boldsymbol{v}_h) \overset{\text{def}}{=} \gamma_u \sum\nolimits_{F \in \mathscr{F}_i} \phi_{u,F} \rho h \langle [\![\nabla \cdot \boldsymbol{u}_h]\!], [\![\nabla \cdot \boldsymbol{v}_h]\!] \rangle_F, \tag{3.30}$$

$$s_p(\boldsymbol{\beta}; p_h, q_h) \overset{\text{def}}{=} \gamma_p \sum\nolimits_{F \in \mathscr{F}_i} \phi_{p,F} \rho^{-1} h \langle [\![\nabla p_h]\!], [\![\nabla q_h]\!] \rangle_F \tag{3.31}$$

with non-dimensional stabilization parameters $\gamma_\beta, \gamma_u, \gamma_p > 0$, element-wise scaling functions

$$\phi_T = \nu + c_u(\|\boldsymbol{\beta}\|_{0,\infty,T} h_T) + c_\sigma(\sigma h_T^2), \qquad \phi_{\beta,T} = \phi_{p,T} = h_T^2 \phi_T^{-1}, \qquad \phi_{u,T} = \phi_T, \tag{3.32}$$

and the according face averages $\phi_{\beta,F}, \phi_{u,F}, \phi_{p,F}$ at interior faces $F \in \mathscr{F}_i$. For $\boldsymbol{\beta}_h \overset{\text{def}}{=} \boldsymbol{u}_h - \hat{\boldsymbol{u}}_h$ the ALE convective velocity is used, which further introduces a non-linearity into the stabilization form. The mesh size parameter h measures the maximal distance of points $\boldsymbol{x}$ in adjacent elements T_F^+, T_F^- to the face F. Furthermore, σ denotes a pseudo-reactive scaling resulting from temporal discretization and is defined as $\sigma_\theta = (\theta \Delta t)^{-1}$ for a one-step-θ time-stepping scheme and as $\sigma_{\text{BDF2}} = (2/3\Delta t)^{-1}$ for a BDF2 scheme; for fluids, these time integration schemes are exclusively used in this work and will be further considered in Section 3.6.1.3. For details on the temporal discretization of CIP stabilizations, the reader is referred to extensive numerical analyses by Burman and Fernández [40, 55], D'Angelo and Zunino [81] and Burman *et al.* [67]. The parameter scaling shifts for convective and reactive limits are set to $c_u = 1/6$ and $c_\sigma = 1/12$ as suggested in [231, 232]. For more detailed elaborations on scalings for different element types and polynomial orders, the interested reader is referred to Braack *et al.* [31] and Burman

and Ern [54]. The CIP scalings are set to $\gamma_\beta = \gamma_p = 0.05$ for hexahedral and wedge elements and to 0.01 for tetrahedral elements. Furthermore, it is chosen $\gamma_u = 0.05\gamma_\beta$. For the sake of completeness, it should be mentioned that also weighting strategies of the edge stabilization applicable to conservation equations with non-smooth data have been investigated by Ern and Guermond [102], however, are not applied for the simulations in the present work.

The principal stabilization mechanism of CIP operators consists in penalizing fluctuations. Note that for the aforementioned discrete derivatives it holds that

$$(\boldsymbol{\beta}_h \cdot \nabla)\boldsymbol{u}_h \notin [\mathscr{X}_h]^d, \quad \nabla \cdot \boldsymbol{u}_h \notin \mathscr{X}_h, \quad \nabla p_h \notin [\mathscr{X}_h]^d. \tag{3.33}$$

These polynomials are not fully controlled in the underlying continuous finite element approximation space $\mathscr{X}_h$, since they exhibit discontinuities across inter-element faces due to the incorporated spatial gradients. Control on these discontinuities can be retained by stabilizing fluctuations between the discontinuous polynomials and certain interpolation functions which again are contained in the finite element approximation space. Such control can be recovered by jump-penalties (3.29)–(3.31). The role of these stabilization operators in terms of controlling certain fluctuations will be elucidated by Lemma 3.1 and Corollary 3.2 in Section 3.2.2.2 and by a detailed analysis in Section 3.5.

Remark 3.1 *It has to be pointed out that the stabilization parameters* (3.32) *are scaled differently in Burman* et al. *[48]. The present choice corresponds to the scaling proposed by Codina [75] for the orthogonal sub-scale method and Knobloch and Tobiska [165] for the local projection scheme. Compared to [48], a reactive scaling is added to the stabilization parameters which has two effects. First, it allows us to establish stability and approximation properties using norms with contributions which are more typical for residual-based stabilization methods, see* (3.224)*. Second, for* $\|\boldsymbol{\beta}\|, \mu \to 0$*, inf-sup condition and the* a priori *estimates do not degenerate as they formally would do in [48]. A numerical analysis of this* CIP *method based on the proposed scalings will be proposed in Section 3.5 in the context of unfitted approximations.*

Remark 3.2 *Note that similar to the definition of stabilization parameters for the residual-based variational multiscale method* (3.21)*, the sum over different scalings in* (3.32) *reflects which term of the governing* PDE *is dominating others. Therein, the first sum, i.e.* $\nu + c_u(\|\boldsymbol{\beta}\|_{0,\infty,T} h_T)$*, is related to the Reynolds number and characterizes the ratio between resolved convection and diffusion in a local element-wise sense. The second sum, i.e.* $c_u(\|\boldsymbol{\beta}\|_{0,\infty,T} h_T) + c_\sigma(\sigma h_T^2)$*, corresponds to the Courant number and relates convection to (pseudo-)reaction, where the latter one can be alternatively expressed in terms of the time-step length* Δt*.*

Remark 3.3 *Note that for the classical* CIP *method on fitted meshes it is sufficient to penalize only the discontinuities of first-order derivatives of the mentioned polynomials, independent of the polynomial order of the approximation space, see the definitions in* (3.29)–(3.31)*. The need for penalizing also the higher-order derivatives in the vicinity of the boundary will be one of the major adaption of the* CIP *method for unfitted meshes. An analysis is given in Section 3.5.*

The final CIP stabilized discrete formulation for the incompressible Navier-Stokes equations reads as follows: for all $t \in (T_0, T]$, find fluid velocity and pressure $U_h(t) = (\boldsymbol{u}_h(t), p_h(t)) \in \mathcal{V}_{h,\boldsymbol{g}_\mathrm{D}} \times \mathcal{Q}_h$ such that for all $V_h = (\boldsymbol{v}_h, q_h) \in \mathcal{V}_{h,\boldsymbol{0}} \times \mathcal{Q}_h$

$$\mathcal{A}_h^{\mathrm{CIP}}(U_h, V_h) = \mathcal{L}_h^{\mathrm{CIP}}(V_h), \tag{3.34}$$

where

$$\mathcal{A}_h^{\mathrm{CIP}}(U_h, V_h) \overset{\mathrm{def}}{=} \mathcal{A}(U_h, V_h) + \mathcal{S}_h^{\mathrm{CIP}}(U_h, V_h) \quad \text{and} \quad \mathcal{L}_h^{\mathrm{CIP}}(V_h) \overset{\mathrm{def}}{=} \mathcal{L}(V_h) \tag{3.35}$$

in which the classical variational formulation is augmented by the CIP form $\mathcal{S}_h^{\mathrm{CIP}}$. The right-hand side remains unchanged.

Remarks on Alternative Formulations. In the following, some useful equivalent and alternative formulations for the jump penalty terms for continuous interpolation spaces are reviewed, see also Burman [38].

Due to the continuity of discrete functions in $\mathcal{X}_h$, inter-element jumps in face-tangential directions $\boldsymbol{t}_1, \dots, \boldsymbol{t}_{d-1}$ vanish and normal derivative jumps are equivalent to full-gradient jumps, i.e. for scalar functions it holds

$$[\![\partial_{\boldsymbol{n}}^1 p_h]\!][\![\partial_{\boldsymbol{n}}^1 q_h]\!] = [\![\boldsymbol{n} \cdot \nabla p_h]\!][\![\boldsymbol{n} \cdot \nabla q_h]\!] = [\![\nabla p_h]\!] \cdot [\![\nabla q_h]\!], \tag{3.36}$$

where $\boldsymbol{n} = \boldsymbol{n}_F$ denotes the normal vector with respect to the face F. Furthermore, the j-th normal derivative $\partial_{\boldsymbol{n}}^j v$ is given by $\partial_{\boldsymbol{n}}^j v = \sum_{|\alpha|=j} D^\alpha v(\boldsymbol{x}) \boldsymbol{n}^\alpha$ for multi-index $\alpha = (\alpha_1, \dots, \alpha_d)$, $|\alpha| = \sum_i \alpha_i$ and $\boldsymbol{n}^\alpha = n_1^{\alpha_1} n_2^{\alpha_2} \cdots n_d^{\alpha_d}$. Analogously, for vector-valued functions it holds

$$[\![\partial_{\boldsymbol{n}}^1 \boldsymbol{u}_h]\!][\![\partial_{\boldsymbol{n}}^1 \boldsymbol{v}_h]\!] = [\![\boldsymbol{n} \cdot \nabla \boldsymbol{u}_h]\!][\![\boldsymbol{n} \cdot \nabla \boldsymbol{v}_h]\!] = [\![\nabla \boldsymbol{u}_h]\!] : [\![\nabla \boldsymbol{v}_h]\!]. \tag{3.37}$$

Furthermore, velocity gradient jumps can be split component-wise as

$$\langle [\![\nabla u_h]\!], [\![\nabla v_h]\!] \rangle_F = \langle [\![(\boldsymbol{e}_\beta \cdot \nabla) u_h]\!], [\![(\boldsymbol{e}_\beta \cdot \nabla) v_h]\!] \rangle_F + \langle [\![(\boldsymbol{e}_{\beta,j}^{\mathrm{orth}} \cdot \nabla) u_h]\!], [\![(\boldsymbol{e}_{\beta,j}^{\mathrm{orth}} \cdot \nabla) v_h]\!] \rangle_F \tag{3.38}$$

with $\boldsymbol{e}_\beta = \frac{\boldsymbol{\beta}_h}{\|\boldsymbol{\beta}_h\|}$ and respective orthonormal vectors $\boldsymbol{e}_{\beta,j}^{\mathrm{orth}}$. The first term reflects a *streamline* part and the second part represents a *crosswind* part. As for stability only the streamline direction (3.29) needs to be sufficiently controlled, the crosswind part can be usually neglected. However, the latter part can be used in the context of variational multiscale modeling of unresolved scales in turbulent flows. Otherwise, it can be utilized to increase accuracy near interior layers as discussed by [38]; see also references therein.

Note that due to the continuity of $\boldsymbol{\beta}_h$, for streamline derivative jumps, by decomposing $\boldsymbol{\beta}_h$ and ∇u_h on a face $F \in \mathcal{F}_i$ in tangential and normal directions one can deduce

$$[\![(\boldsymbol{\beta}_h \cdot \nabla) u_h]\!] = (\boldsymbol{\beta}_h \cdot \boldsymbol{n}) [\![\boldsymbol{n} \cdot \nabla u_h]\!] \tag{3.39}$$

such that for the advective derivative jump penalty (3.29) holds

$$[\![(\boldsymbol{\beta}_h \cdot \nabla) \boldsymbol{u}_h]\!][\![(\boldsymbol{\beta}_h \cdot \nabla) \boldsymbol{v}_h]\!] = (\boldsymbol{\beta}_h \cdot \boldsymbol{n})^2 [\![\boldsymbol{n} \cdot \nabla \boldsymbol{u}_h]\!][\![\boldsymbol{n} \cdot \nabla \boldsymbol{v}_h]\!]. \tag{3.40}$$

To reduce the non-linearity in the definition of the stabilization parameter scaling (3.32), the scalings $(\boldsymbol{\beta}_h \cdot \boldsymbol{n})^2 / \|\boldsymbol{\beta}_h\|$ can be replaced by $|\boldsymbol{\beta}_h \cdot \boldsymbol{n}|$ or further by the maximum value at the face,

i.e. $\beta_{\boldsymbol{n},\infty,F} \overset{\text{def}}{=} \|\boldsymbol{\beta}_h \cdot \boldsymbol{n}\|_{0,\infty,F}$. Finally, the streamline character of this term is still incorporated in terms of the face-normal velocity $|\boldsymbol{\beta}_h \cdot \boldsymbol{n}|$. As a consequence, the following alternative CIP stabilization term can be used

$$s_\beta(\boldsymbol{\beta}; \boldsymbol{u}_h, \boldsymbol{v}_h) = \gamma_\beta \sum\nolimits_{F \in \mathcal{F}_i} \phi_{\beta,F} \rho \beta^2_{\boldsymbol{n},\infty,F} h \langle [\![\nabla \boldsymbol{u}_h]\!], [\![\nabla \boldsymbol{v}_h]\!] \rangle_F. \tag{3.41}$$

Note that the divergence jump penalty can be controlled by a stronger full-velocity-gradient jump penalty as suggested, e.g., by Burman [49]. In contrast to streamline control given by (3.40), which scales with $|\boldsymbol{\beta}_h \cdot \boldsymbol{n}|$, full control in terms of a scaling with $|\boldsymbol{\beta}_h|$ of ϕ_u is required. The combined velocity CIP stabilization can be then defined as

$$\overline{s}_\beta(\boldsymbol{\beta}; \boldsymbol{u}_h, \boldsymbol{v}_h) \overset{\text{def}}{=} \sum\nolimits_{F \in \mathcal{F}_i} \rho \overline{\phi}_{\beta,F} h \langle [\![\nabla \boldsymbol{u}_h]\!], [\![\nabla \boldsymbol{v}_h]\!] \rangle_F \text{ with} \tag{3.42}$$

$$\overline{\phi}_{\beta,F} \overset{\text{def}}{=} \gamma_\beta \phi_{\beta,F} \beta^2_{\boldsymbol{n},\infty,F} + \gamma_u \phi_{u,F} \lesssim \gamma_\beta \beta_{\boldsymbol{n},\infty,F} + \gamma_u \phi_{u,F}. \tag{3.43}$$

The advantage of this alternative control is a reduced matrix pattern and number of non-zero entries in the global system matrix for the full-velocity-gradient operator compared to the divergence operator (3.30). Note that the latter one introduces additional couplings between different velocity components arising from the divergence term multiplication. Using the velocity-jump control instead of the divergence operator and utilizing equality (3.40), all CIP stabilization operators are of the same matrix type for pressure and all single velocity components. The different operators then only differ in their scaling functions. This aspect can be exploited for efficient implementations.

For an comprehensive survey on advantages and drawbacks of these two introduced stabilization techniques, the reader is referred to an overview article by Braack *et al.* [31]. In the latter publication, different aspects like strong versus weak consistency of the stabilization operators, symmetry and decoupling of velocity and pressure stabilizations for the CIP technique, increased computational costs due to the enlarged matrix bandwidth or due to extra evaluation routines for inter-element-face terms are discussed. Further interesting investigations with regard to behavior for small time-step lengths or artificially induced boundary or interfacial conditions for the low-order RBVM method are addressed in references therein. Some of these aspects are recalled and discussed later in this work in the context of unfitted CUTFEMs.

3.2 Preliminaries to Numerical Analysis

In this section, analytical tools are collected which will be used in the forthcoming numerical analysis of cut finite element methods and are required to develop inf-sup stability and *a priori* error estimates. First, assumptions on computational meshes and functional spaces are introduced. Second, a number of useful trace and inverse inequalities are collected before the interpolation operators are presented which are suitable for establishing the approximation properties of cut finite element schemes. Finally, a brief overview of general concepts of numerical analyses and key ideas of inf-sup stability and *a priori* error estimates are given.

3.2.1 Assumptions on Computational Domains, Meshes and Function Spaces

Numerical analyses of all fitted and unfitted finite element methods considered throughout this chapter are based on the notation and terminology on computational domains and meshes introduced in Section 2.1.4.1. Cut-related entities which are used in the context of unfitted discretizations have been provided in Section 2.2.2. However, to simplify the analysis of cut finite element methods and to shorten its presentation, the subsequent sections rely on the following mesh assumptions.

The boundary Γ needs to be ensured being reasonably resolved by the (possibly) unfitted active mesh part $\mathcal{T}_h \subseteq \widehat{\mathcal{T}}_h$. Therefore, the mesh $\mathcal{T}_h$ is assumed to be quasi-uniform and the boundary Γ has to satisfy the following geometric conditions:

- G1: The intersection between Γ and a face $F \in \mathcal{F}_i$ is simply connected; that is, Γ does not cross an interior face multiple times.
- G2: For each element T intersected by Γ, there exists a plane S_T and a piecewise smooth parametrization $\Phi : S_T \cap T \to \Gamma \cap T$.
- G3: We assume that there is an integer $N > 0$ such that for each element $T \in \mathcal{T}_\Gamma$ there exists an element $T' \in \mathcal{T}_h \setminus \mathcal{T}_\Gamma$ and at most N elements $\{T_j\}_{j=1}^N$ such that $T_1 = T$, $T_N = T'$ and $T_j \cap T_{j+1} \in \mathcal{F}_i,\ j = 1, \ldots, N-1$. In other words, the number of faces to be crossed in order to "walk" from a cut element T to a non-cut element $T' \subset \Omega$ is bounded.

Similar geometric assumptions were made in works by Burman and Hansbo [45], Hansbo and Hansbo [138], Massing *et al.* [181]; Figure 3.1 illustrates this for a potential configuration.

In this work, for all solution fields only continuous finite element function spaces or vector-valued equivalents are used. In the subsequent elaborations, let $\mathcal{X}_h^k$ denote the standard finite element spaces consisting of continuous piecewise polynomials of order $k \geqslant 1$ on elements T

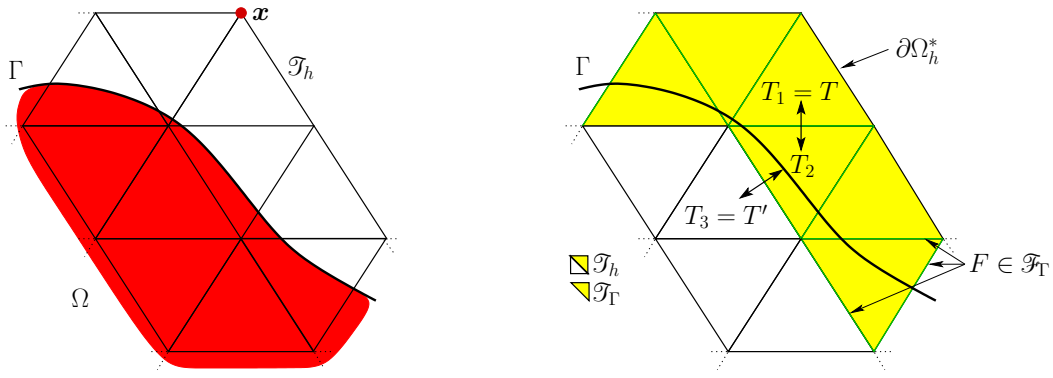

Figure 3.1: The boundary zone of the computational domain. (Left) A physical domain Ω embedded into a background mesh $\mathcal{T}_h$. Observe that for the elements associated with the node $\boldsymbol{x}$, only a small fraction resides inside the domain Ω. (Right) Elements colored in yellow are intersected by the boundary and therefore part of the mesh $\mathcal{T}_\Gamma$. Interior faces belonging to elements intersected by the boundary, i.e. $\mathcal{F}_\Gamma$, are marked in green. Shortest "walk" from cut element T to an uncut element T' ($\{T_1 = T, T_2, T_3 = T'\}$).

of a given active mesh $\mathcal{T}_h$, as introduced in (2.74). Extensions to expanded cut finite element functions spaces as considered in Section 2.2.4 may be realized with slightly weakened geometric assumptions G1–G3. Due to the highly increased technicality of resulting analyses, only the standard continuous discrete cut finite element spaces $\mathscr{X}_h^k$ under aforementioned assumptions are considered:

$$\mathscr{X}_h^k \overset{\text{def}}{=} \left\{ v_h \in C^0(\Omega_h^*) : v_h|_T \in \mathbb{V}^k(T) \, \forall \, T \in \mathcal{T}_h \right\} \tag{3.44}$$

with $\mathbb{V} \in \{\mathbb{P}, \mathbb{Q}, \mathbb{W}\}$ for simplices, quadrilaterals and wedge-shaped elements. For flow problems, velocity and pressure are assumed to be interpolated with equal order, i.e.

$$\mathscr{V}_h \overset{\text{def}}{=} [\mathscr{X}_h^k]^d, \qquad \mathscr{Q}_h \overset{\text{def}}{=} \mathscr{X}_h^k, \qquad \mathscr{W}_h \overset{\text{def}}{=} \mathscr{V}_h \times \mathscr{Q}_h. \tag{3.45}$$

3.2.2 Approximation Properties

In the following, fundamental approximation properties for continuous finite element function spaces are presented. Important trace inequalities and inverse estimates which will be instrumental in the stability and *a priori* error analysis of cut finite element methods are introduced and interpolation estimates for boundary-fitted meshes and their extension to cut finite element discretizations are recalled. The subsequent estimates are heavily used throughout this chapter.

3.2.2.1 Trace Inequalities and Inverse Estimates

Throughout this work, the notation $a \lesssim b$ is used for $a \leqslant Cb$ for some generic positive constant C which varies with the context but is always independent of the mesh size h and the position of the boundary or interface Γ relative to the mesh $\mathcal{T}_h$.

For discrete functions $v_h \in \mathscr{X}_h$, the following generalized inverse and trace inequalities are well-known

$$\|D^j v_h\|_T \lesssim h^{i-j} \|D^i v_h\|_T \qquad \forall \, T \in \mathcal{T}_h, \quad 0 \leqslant i \leqslant j, \tag{3.46}$$

$$\|\partial_{\boldsymbol{n}}^j v_h\|_{\partial T} \lesssim h^{i-j-1/2} \|D^i v_h\|_T \qquad \forall \, T \in \mathcal{T}_h, \quad 0 \leqslant i \leqslant j \tag{3.47}$$

with their counterparts for elements T arbitrarily intersected by the boundary Γ

$$\|\partial_{\boldsymbol{n}}^j v_h\|_{\Gamma \cap T} \lesssim h^{i-j-1/2} \|D^i v_h\|_T \qquad \forall \, T \in \mathcal{T}_h, \quad 0 \leqslant i \leqslant j \tag{3.48}$$

proven in the publications by Hansbo and Hansbo [138] and Burman *et al.* [66].

For functions $v \in H^1(\Omega_h^*)$, it will be made use of trace inequalities of the form

$$\|v\|_{\partial T} \lesssim h^{-1/2} \|v\|_T + h^{1/2} \|\nabla v\|_T \qquad \forall \, T \in \mathcal{T}_h, \tag{3.49}$$

$$\|v\|_{\Gamma \cap T} \lesssim h^{-1/2} \|v\|_T + h^{1/2} \|\nabla v\|_T \qquad \forall \, T \in \mathcal{T}_h, \tag{3.50}$$

see [66, 138] for a proof of the second one. Finally, the well-known Poincaré and Korn inequalities (see Brenner and Scott [34]) are recalled, which state that

$$\|\boldsymbol{v}\|_{0,\Omega} \lesssim C_P \|\nabla \boldsymbol{v}\|_{0,\Omega} \qquad \forall \, \boldsymbol{v} \in [H_0^1(\Omega)]^d, \tag{3.51}$$

$$\|\nabla \boldsymbol{v}\|_{0,\Omega} \lesssim \|\boldsymbol{\epsilon}(\boldsymbol{v})\|_{0,\Omega} \qquad \forall \, \boldsymbol{v} \in [H_0^1(\Omega)]^d \tag{3.52}$$

with the following variants if the boundary trace of $\boldsymbol{v}$ is not vanishing

$$\|\boldsymbol{v}\|_{0,\Omega} \lesssim C_P(\|\nabla \boldsymbol{v}\|_{0,\Omega} + \|\boldsymbol{v}\|_{\Gamma}), \quad \forall\, \boldsymbol{v} \in [H^1(\Omega)]^d, \tag{3.53}$$

$$\|\boldsymbol{v}\|_{1,\Omega} \lesssim \|\boldsymbol{\epsilon}(\boldsymbol{v})\|_{0,\Omega} + \|\boldsymbol{v}\|_{0,\Omega} \quad \forall\, \boldsymbol{v} \in [H^1(\Omega)]^d, \tag{3.54}$$

$$\|\boldsymbol{v}\|_{1,\Omega} \lesssim \|\boldsymbol{\epsilon}(\boldsymbol{v})\|_{0,\Omega} + \|\boldsymbol{v}\|_{0,\Gamma} \quad \forall\, \boldsymbol{v} \in [H^1(\Omega)]^d. \tag{3.55}$$

The hidden constants in (3.52)–(3.55) depend on the domain Ω and the boundary $\partial\Omega$. The constant C_P is called the Poincaré constant and scales as the diameter of the domain Ω.

3.2.2.2 Interpolation Operators

Subsequently, common interpolation operators for boundary-fitted finite element approximations and their extensions to cut finite element approximations are introduced.

Extension Operator for Sobolev Spaces. To construct an appropriate interpolation operator $L^2(\Omega) \to \mathscr{X}_h$, that is from the space of $L^2(\Omega)$-functions into the finite element function space defined on the active (background) mesh $\mathscr{T}_h$, first an extension from Ω to an enlarged domain Ω^* is required. This domain is assumed to be fixed and Lipschitz, containing all fictitious domains $\Omega_h^* \subset \Omega^*$ for $h \lesssim 1$. For Sobolev spaces $W^{k,p}(\Omega)$ which are defined with respect to the physical domain, $0 \leqslant k < \infty$, $1 \leqslant p \leqslant \infty$, an extension operator can be defined

$$E : W^{k,p}(\Omega) \to W^{k,p}(\Omega^*) \tag{3.56}$$

which is bounded as

$$\|Ev\|_{k,p,\Omega^*} \lesssim \|v\|_{k,p,\Omega}, \tag{3.57}$$

see the work by Stein [240] for a proof. Occasionally, it is written $v^* \overset{\text{def}}{=} Ev$. Utilizing this extension operator, for any interpolation operator $\pi_h : H^s(\Omega_h^*) \to \mathscr{X}_h$, i.e. $k = s$ and $p = 2$, its "fictitious domain" variant $\pi_h^* : H^s(\Omega) \to \mathscr{X}_h$ can be defined by simply requiring that

$$\pi_h^* u \overset{\text{def}}{=} \pi_h(u^*) = \pi_h(Eu) \tag{3.58}$$

for functions $u \in H^s(\Omega)$.

Clément Interpolant. Choosing π_h to be the *Clément operator* (see for instance Ern and Guermond [101] for an introduction), for $v \in H^r(\Omega^*)$ and $s, t \in \mathbb{N}$, $m \overset{\text{def}}{=} \min\{r, k+1\}$ the following interpolation estimates hold:

$$\|v - \pi_h v\|_{s,T} \lesssim h_T^{t-s} \|v\|_{t,\omega(T)}, \qquad \forall\, T \in \mathscr{T}_h, \quad 0 \leqslant s \leqslant t \leqslant m, \tag{3.59}$$

$$\|v - \pi_h v\|_{s,F} \lesssim h_T^{t-s-1/2} \|v\|_{t,\omega(T)}, \quad \forall\, F \in \mathscr{F}_i, \quad 0 \leqslant s \leqslant t - 1/2 \leqslant m - 1/2. \tag{3.60}$$

Here, $\omega(T)$ is the set of elements in $\mathscr{T}_h$ sharing at least one vertex with T (for (3.59)) and sharing at least one vertex with $F \in \mathscr{F}_i$ (for (3.60)), respectively. Due to the boundedness of the extension operator (3.57), it can be observed that the extended Clément interpolant π_h^* satisfies

$$\|v^* - \pi_h^* v\|_{s,\mathscr{T}_h} \lesssim h^{t-s} \|v\|_{t,\Omega}, \qquad 0 \leqslant s \leqslant t \leqslant m, \tag{3.61}$$

$$\|v^* - \pi_h^* v\|_{s,\mathscr{F}_i} \lesssim h^{t-s-1/2} \|v\|_{t,\Omega}, \quad 0 \leqslant s \leqslant t - 1/2 \leqslant m - 1/2. \tag{3.62}$$

In particular, use is made of the stability property

$$\|\pi_h^* v\|_{s,\mathcal{T}_h} \lesssim \|v\|_{s,\Omega}, \qquad 0 \leqslant s \leqslant m. \tag{3.63}$$

To shorten the notation, it is written $\|v\|_{s,\mathcal{T}_h}^2 \overset{\text{def}}{=} \sum_{T\in\mathcal{T}_h} \|v\|_{s,T}^2$ for the sum over elements and similarly $\|v\|_{s,\mathcal{F}_i}^2 \overset{\text{def}}{=} \sum_{F\in\mathcal{F}_i} \|v\|_{s,F}^2$ for the sum over faces. The Clément interpolant is denoted by $\boldsymbol{\pi}_h^*$ for vector-valued functions $\boldsymbol{v}$ and by Π_h^* for functions in a product space.

Oswald Interpolant. A main ingredient in the analysis of the continuous interior penalty method (see for instance the works by Burman *et al.* [48] and Burman and Ern [54]) was the use of the *Oswald interpolation operator*. By construction, the Oswald interpolation operator defines a mapping $\mathcal{O}_h : \mathcal{X}_h^{\mathrm{dc},k}(\mathcal{T}_h) \to \mathcal{X}_h^k(\mathcal{T}_h)$, with $\mathcal{X}_h^{\mathrm{dc},k}(\mathcal{T}_h)$ and $\mathcal{X}_h^k(\mathcal{T}_h)$ denoting the space of discontinuous and continuous piecewise polynomials of order k on meshes $\mathcal{T}_h$, see definitions (2.63) and (2.64). More precisely, for $v_h \in \mathcal{X}_h^{\mathrm{dc},k}(\mathcal{T}_h)$, the function $\mathcal{O}_h v_h \in \mathcal{X}_h^k(\mathcal{T}_h)$ is constructed in each interpolation node $\boldsymbol{x}_s$ by the average value

$$\mathcal{O}_h v_h(\boldsymbol{x}_s) = \frac{1}{\operatorname{card}(\mathcal{T}_h(\boldsymbol{x}_s))} \sum\nolimits_{T\in\mathcal{T}_h(\boldsymbol{x}_s)} v_h|_T(\boldsymbol{x}_s), \tag{3.64}$$

where $\mathcal{T}_h(\boldsymbol{x}_s)$ is the set of all elements $T \in \mathcal{T}_h$ sharing the node $\boldsymbol{x}_s$. In particular, it was shown in [54] that for $v_h \in \mathcal{X}_h^{\mathrm{dc},k}$, the fluctuation $v_h - \mathcal{O}_h v_h$ between the element-wise discontinuous polynomial v_h and its Oswald interpolation $\mathcal{O}_h v_h$ can be controlled in terms of jump-penalties:

Lemma 3.1 *Let ϕ be a piecewise constant function and $v_h \in \mathcal{X}_h^{\mathrm{dc},k}$. Then, the fluctuation between v_h and its Oswald interpolant $\mathcal{O}_h v_h$ can be bounded by face-jump penalty terms*

$$\|\phi^{\frac{1}{2}}(v_h - \mathcal{O}_h v_h)\|_T^2 \lesssim \sum\nolimits_{F\in\mathcal{F}_i(T)} \phi_T h \|[\![v_h]\!]\|_F^2 \quad \forall\, v_h \in \mathcal{X}_h^{\mathrm{dc},k}, \tag{3.65}$$

where $\mathcal{F}_i(T)$ denotes the set of all faces $F \in \mathcal{F}_i$ with $F \cap T \neq \emptyset$, and the hidden constant depends only on the shape-regularity of the mesh, the order k of the finite element space and the dimension d.

For a proof and a more precise statement which exhibits the dependency on the polynomial order, the interested reader is referred to the work by Burman and Ern [54].

The previous lemma elucidates the role of the continuous interior penalty stabilization operators (3.29)–(3.31) (see Section 3.1.3.2). Recalling the fact that the advective derivative, the divergence of the velocity and the pressure gradient are discontinuous polynomials, see (3.33), their fluctuation to the respective Oswald interpolation can be controlled by face-jump penalty terms:

Corollary 3.2 *Under the assumptions of Lemma 3.1 it holds that*

$$\|\phi_\beta^{\frac{1}{2}}((\boldsymbol{\beta}_h\cdot\nabla)\boldsymbol{v}_h - \mathcal{O}_h((\boldsymbol{\beta}_h\cdot\nabla)\boldsymbol{v}_h))\|_T^2 \lesssim \sum_{F\in\mathcal{F}_i(T)} \phi_{\beta,T} h \|[\![(\boldsymbol{\beta}_h\cdot\nabla)\boldsymbol{v}_h]\!]\|_F^2, \tag{3.66}$$

$$\|\phi_u^{\frac{1}{2}}(\nabla\cdot\boldsymbol{v}_h - \mathcal{O}_h(\nabla\cdot\boldsymbol{v}_h))\|_T^2 \lesssim \sum_{F\in\mathcal{F}_i(T)} \phi_{u,T} h \|[\![\nabla\cdot\boldsymbol{v}_h]\!]\|_F^2, \tag{3.67}$$

$$\|\phi_p^{\frac{1}{2}}(\nabla q_h - \mathcal{O}_h(\nabla q_h))\|_T^2 \lesssim \sum_{F\in\mathcal{F}_i(T)} \phi_{p,T} h \|[\![\nabla q_h]\!]\|_F^2, \tag{3.68}$$

with piecewise constant scaling functions $\phi_\beta, \phi_u, \phi_p$ and restrictions to elements $\phi_{\beta,T}, \phi_{u,T}, \phi_{p,T}$.

The role of the CIP stabilization terms s_β, s_u, s_p is to control these discontinuities between neighboring elements.

3.2.3 Concepts of Stability Analysis in a Nutshell

The following section is primarily aimed at mathematically unexperienced readers who are not that familiar with fundamental concepts of *inf-sup stability* analysis and mathematical techniques which are commonly used for deriving optimal *a priori* error estimates. The following elaborations are intended to provide readers with knowledge required to allow them to follow the major steps through the analysis and to understand most important aspects resulting from that. Readers who are familiar with these concepts may skip this section.

Many issues of numerical cut finite element approximations of PDE's already occur in the linear elliptic case. For this reason, Poisson's problem serves as model problem to introduce properties of numerical approximation, like *consistency, Galerkin orthogonality, continuity and inf-sup stability* which are fundamental for deriving stability and *a priori* error estimates.

Definition 3.1 (Variational and discrete formulation for Poisson's problem)
Let $\Omega \subset \mathbb{R}^n$ be an open bounded domain, $f \in L^2(\Omega)$ and $g \in H^{1/2}(\Gamma)$ given right-hand side and boundary data. The second-order elliptic Poisson problem reads: Find $u : \Omega \mapsto \mathbb{R}$ such that

$$-\Delta u = f \quad \text{in } \Omega \qquad \text{and} \qquad u = g \quad \text{on } \Gamma \tag{3.69}$$

with its variational continuous and discrete form

$$\mathscr{B}(u, v) = \mathscr{L}(v) \qquad \forall\, v \in \mathscr{V}_0 = H_0^1(\Omega), \tag{3.70}$$
$$\mathscr{B}_h(u_h, v_h) = \mathscr{L}_h(v_h) \quad \forall\, v_h \in \mathscr{V}_h = \mathscr{X}_h \cap \mathscr{V}_0, \tag{3.71}$$

where $u \in \mathscr{V}_g = H_g^1(\Omega)$ and $u_h \in \mathscr{V}_{h,g} = \mathscr{X}_h \cap \mathscr{V}_g$ with

$$\mathscr{B}(u, v) = \mathscr{B}_h(u, v) = (\nabla u, \nabla v) \quad \text{and} \quad \mathscr{L}(v) = \mathscr{L}_h(v) = (f, v). \tag{3.72}$$

Note that in general continuous and discrete forms are not identical, i.e. $\mathscr{B} \neq \mathscr{B}_h$ and $\mathscr{L} \neq \mathscr{L}_h$. For stabilized discrete formulations, $\mathscr{B}_h$ and $\mathscr{L}_h$ often include additional (weakly) consistent stabilization forms $\mathscr{S}_h$ such that, for instance, $\mathscr{B}_h = \mathscr{B} + \mathscr{S}_h$.

Definition 3.2 (Consistency of discrete formulation)
For a discrete formulation $\mathscr{B}_h = \mathscr{L}_h$ to be (strongly) consistent*, it is required that the solution $u \in \mathscr{V}$ of the continuous problem $\mathscr{B} = \mathscr{L}$ is also solution of the discrete problem*

$$\mathscr{B}_h(u, v_h) - \mathscr{L}_h(v_h) = 0 \quad \forall\, v_h \in \mathscr{V}_h \quad \textit{(strongly consistent)}. \tag{3.73}$$

Weak consistency requires the error introduced by the modified Galerkin scheme to converge with optimal order for $h \to 0$

$$\lim_{h \to 0} \left(\mathscr{B}_h(u, v_h) - \mathscr{L}_h(v_h)\right) = 0 \quad \forall\, v_h \in \mathscr{V}_h \quad \textit{(weakly consistent)}. \tag{3.74}$$

Note that the standard Galerkin approximation of the Poisson problem based on continuous approximations does not require additional terms and thus is strongly consistent.

Definition 3.3 (Galerkin orthogonality of a formulation)
Related to the definition of consistency, a discrete variational formulation is said to satisfy a (weak) Galerkin orthogonality *property if the error $u - u_h$ is $\mathscr{B}_h$-orthogonal on the discrete trial space $\mathscr{V}_h$*

$$\mathscr{B}_h(u - u_h, v_h) = 0 \quad \forall\, v_h \in \mathscr{V}_h \quad \textit{(strongly orthogonal)}, \tag{3.75}$$

$$\lim_{h\to 0} \left(\mathscr{B}_h(u - u_h, v_h)\right) = 0 \quad \forall\, v_h \in \mathscr{V}_h \quad \textit{(weakly orthogonal)}. \tag{3.76}$$

To guarantee *existence* and *uniqueness* of a solution of a discrete variational formulation, it is required that the bilinear form satisfies a discrete inf-sup condition on the discrete space $\mathscr{V}_h$, see the textbooks by Braess [33] and Boffi *et al.* [25] for details. Furthermore, the definition of an energy-norm $|||\cdot|||$ on the discrete space is required, which most often is closely related to the discrete bilinear form. In many simpler cases, it is possible to prove a stronger *coercivity* condition which implies inf-sup stability.

Definition 3.4 (Inf-sup stability and coercivity)
A discrete variational formulation satisfies an inf-sup condition if there exists a positive lower bounded constant $c_s \geqslant c > 0$ that is independent of the mesh size h such that

$$c_s \leqslant \inf_{v_h \in \mathscr{V}_h\backslash 0} \sup_{w_h \in \mathscr{V}_h\backslash 0} \frac{\mathscr{B}_h(v_h, w_h)}{|||v_h||| |||w_h|||} \tag{3.77}$$

with $|||v_h|||$ an energy norm on $\mathscr{V}_h$ that is related to the discrete form $\mathscr{B}_h$. For inf-sup stability it is sufficient to prove the bilinear form of being coercive*, i.e. $\exists c_s \geqslant c > 0$ such that*

$$c_s |||v_h|||^2 \leqslant \mathscr{B}_h(v_h, v_h) \quad \forall\, v_h \in \mathscr{V}_h. \tag{3.78}$$

Coercivity directly implies an inf-sup condition. It clearly ensures: $\exists c_s \geqslant c > 0$ such that

$$c_s |||v_h||| \leqslant \frac{\mathscr{B}_h(v_h, v_h)}{|||v_h|||} \leqslant \sup_{w_h \in \mathscr{V}_h\backslash 0} \frac{\mathscr{B}_h(v_h, w_h)}{|||w_h|||} \quad \forall\, v_h \in \mathscr{V}_h\backslash 0, \tag{3.79}$$

which remains also valid for the infimum over $v_h \in \mathscr{V}_h\backslash 0$, since c_s is independent of v_h and h.

Definition 3.5 (Continuity of a discrete variational formulation)
The $\mathscr{V}_h$-continuity (upper boundedness) of $\mathscr{B}_h$ is given provided that

$$\mathscr{B}_h(v_h, w_h) \leqslant C_{cont} |||v_h||| \cdot |||w_h||| \quad \forall v_h, w_h \in \mathscr{V}_h. \tag{3.80}$$

with a constant $C_{cont} \geqslant 0$ independent of h.

Note that for the standard Galerkin discrete formulation of the Poisson problem (3.69), an energy norm is defined by the bilinear form itself, i.e. $|||v_h||| \stackrel{\text{def}}{=} (\mathscr{B}_h(v_h, v_h))^{1/2}$. Then, $\mathscr{B}_h$ is coercive, inf-sup stable and continuous by definition with constants $c_s = C_{\text{cont}} = 1$, which ensures uniqueness and existence of a solution u_h, respectively.

Among uniqueness and existence of a solution to the discrete problem, it is desired to ensure optimal convergence of the error between continuous and discrete solution without knowing

both solutions *a priori*. Using introduced properties of satisfying an inf-sup condition, (weak) Galerkin orthogonality and continuity in combination with optimal estimates for interpolation or projection errors between solution u and an appropriate projection $\Pi_h u \in \mathcal{V}_h$ into the discrete space enables to derive an *a priori* error estimate measured in the energy norm of the form

$$|||u - u_h||| \leqslant Ch^r \|u\|_s \quad (\textit{a priori} \text{ energy norm error estimate}) \tag{3.81}$$

The optimal order r depends on the polynomial order of the approximation space and the regularity s of the solution $u \in H^s(\Omega)$. This can be proven for the Poisson problem as follows:

Proof. The error between discrete solution u_h and any other discrete function $v_h \in \mathcal{V}_h$ can be estimated by combining inf-sup stability, continuity and Galerkin orthogonality of the form

$$\mathcal{B}_h(u - u_h, w_h) = \mathcal{R}_h(u, w_h) \quad \text{with} \quad |\mathcal{R}_h(u, w_h)| \leqslant C_{\text{cons}} h^r \|u\|_s |||w_h||| \tag{3.82}$$

such that the consistency error $\mathcal{R}_h$ does not deteriorate the optimal convergence; it holds $\mathcal{R}_h \equiv 0$ in case of strong consistency. Let $\tilde{w}_h$ be the discrete function that takes the supremum in the inf-sup condition (3.77) for given $u_h - v_h$, then

$$\begin{aligned} |||u_h - v_h||| &\leqslant \frac{1}{c_s} \sup_{w_h \in \mathcal{V}_h \setminus 0} \frac{\mathcal{B}_h(u_h - v_h, w_h)}{|||w_h|||} = \frac{1}{c_s} \frac{\mathcal{B}_h(u_h - v_h, \tilde{w}_h)}{|||\tilde{w}_h|||} \\ &= \frac{1}{c_s} \left(\frac{\mathcal{B}_h(u - v_h, \tilde{w}_h) - \mathcal{R}_h(u, \tilde{w}_h)}{|||\tilde{w}_h|||} \right) \\ &\leqslant \left(\frac{C_{\text{cont}}}{c_s} |||u - v_h||| + \frac{C_{\text{cons}}}{c_s} h^r \|u\|_s \right) \frac{|||\tilde{w}_h|||}{|||\tilde{w}_h|||}. \end{aligned} \tag{3.83}$$

Splitting the error $|||u - u_h|||$ using triangle inequality into an interpolation/projection error for $u - v_h \notin \mathcal{V}_h$ and a discrete error for $v_h - u_h \in \mathcal{V}_h$ results in

$$|||u - u_h||| \leqslant |||u - v_h||| + |||v_h - u_h||| \leqslant (1 + \frac{C_{\text{cont}}}{c_s})|||u - v_h||| + \frac{C_{\text{cons}}}{c_s} h^r \|u\|_s. \tag{3.84}$$

It is assumed that for interpolation/projection errors $u - \Pi_h u$ optimal error estimates can be established based on estimates as proposed in Section 3.2.2, such that $|||u - \Pi_h u||| \leqslant C_{\text{I}} h^r \|u\|_s$. Thanks to this optimality, by choosing $v_h \overset{\text{def}}{=} \Pi_h u$, an *a priori* error estimate in the energy norm is obtained

$$|||u - u_h||| \leqslant \left((1 + \frac{C_{\text{cont}}}{c_s}) C_{\text{I}} + \frac{C_{\text{cons}}}{c_s} \right) h^r \|u\|_s. \tag{3.85}$$

This estimate clearly shows the dependency of error estimates on the stability, continuity and consistency constants which have to be ensured being independent of h to not deteriorate the optimality $\mathcal{O}(h^r)$.

□

3.3 Weak Imposition of Boundary Conditions for Boundary-Fitted Meshes

Weak enforcement of boundary conditions for PDEs in the context of finite element methods became an active research field over the last decades. Methodologies have been developed for different problem settings ranging from a single-phase elliptic Poisson problem up to coupling techniques for several phases in complex time-dependent multiphysics settings governed by often non-linear parabolic PDEs. In particular the variety of application fields and their adaption to various discretization concepts as, for instance, extensions from boundary-fitted to non-boundary-fitted computational meshes, highly increased the number of different techniques and related variants.

Neumann boundary conditions can be naturally enforced within a standard Galerkin formulation without introducing further sources of instabilities. However, additional constraints on the primal variable in terms of Dirichlet- or mixed Robin-type boundary conditions require special measures to control induced boundary instabilities. In particular for highly convective-dominated problems, for that not all physically meaningful length scales can be always resolved appropriately by the mesh, a weak constraint enforcement may be superior to strongly enforced conditions. Spurious currents, which in flow problems often arise near boundaries, can get highly reduced by weakening the fulfillment of constraints depending on the mesh resolution. For an example, steep near-wall gradients in boundary layer regions of turbulent flows require finest mesh resolution, on the one hand, to capture the physics and, on the other hand, not to suffer from artificial numerical effects arising from under-resolved flow characteristics; for further discussion on the capabilities of such techniques in that context, see, e.g., the work by Bazilevs and Hughes [15] or the thesis by Gamnitzer [119].

The complexity and difficulties in the design of accurate, stable and optimally convergent schemes, however, become more severe for unfitted discretizations. This section is aimed at giving an overview of different fundamental principles of weak constraint enforcement in the context of continuous Galerkin approximations. To examine strengths and weaknesses of a multitude of different techniques developed over the last decades, a survey on techniques regarding weak constraint enforcement will be given. Having in mind the need for a stable and optimally convergent weak enforcement technique for cut finite elements, the subsequent review on well-established methods shall give a clear understanding of capabilities and limitations of the considered methods. Many of these methods are closely related to each other and exhibit only a slight difference. Analogies between the considered methods will be elaborated by means of the linear elliptic Poisson problem. Adaption of these techniques and their usability to unfitted finite element methods are discussed later in Section 3.4. Further considerations are made throughout this chapter for single-phase flows and in Chapter 4 for single-phase mesh-tying problems and incompressible two-phase flows. Weak constraint enforcement techniques for fluid-structure interaction will be addressed in Chapter 5.

3.3.1 Poisson Problem with Weak Dirichlet Boundary Conditions

For investigations on techniques for weak Dirichlet constraint enforcement, Poisson's equation serves as linear model problem. The weak Dirichlet problem formulation in its strong and weak variational formulation is stated as follows:

Definition 3.6 (Strong and variational formulation of Poisson's boundary value problem) *Let $\Omega \subset \mathbb{R}^n$ be an open bounded domain with $\Gamma = \partial\Omega$. Right-hand side and boundary data are given by $f \in L^2(\Omega)$ and $g \in H^{1/2}(\Gamma)$. The Poisson problem governed in strong form is: find $u : \Omega \mapsto \mathbb{R}$ such that*

$$-\Delta u = f \quad \text{in } \Omega \qquad \text{and} \qquad u = g \quad \text{on } \Gamma. \tag{3.86}$$

Its variational continuous form reads: find $u \in \mathcal{V} = H^1(\Omega)$ and $\lambda \in \Lambda = H^{-1/2}(\Gamma)$ such that

$$\mathcal{B}(u, \lambda; v, \mu) = \mathcal{L}(v, \mu) \qquad \forall\, (v, \mu) \in \mathcal{V} \times \Lambda \tag{3.87}$$

$$\text{with} \quad \mathcal{B}(u, \lambda; v, \mu) \overset{def}{=} (\nabla u, \nabla v) - \langle \lambda, v \rangle - \langle u, \mu \rangle, \tag{3.88}$$

$$\mathcal{L}(v, \mu) \overset{def}{=} (f, v) - \langle g, \mu \rangle. \tag{3.89}$$

Note that by applying Green's formula one obtains $\lambda - \nabla u \cdot \boldsymbol{n} = 0$. Concerning well-posedness as well as existence and uniqueness of this problem, the reader is referred to, e.g., Babuška [4].

3.3.2 A Survey on Weak Dirichlet Constraint Enforcement

In this section, different methodologies for the weak constraint enforcement of Dirichlet boundary conditions are proposed. The most straightforward technique is the classical method of Lagrange multipliers by Babuška [4] and Brezzi [35]. It consists of choosing appropriate inf-sup stable pairs $\mathcal{V}_h \times \Lambda_h \subset \mathcal{V} \times \Lambda$ for discretizing the mixed formulation (3.87), which becomes a non-trivial task on unfitted meshes, as will be discussed later. Another class of methods consists of choosing specific Lagrange-multiplier spaces accompanied by adding stabilization terms to the variational form. In doing so, limiting constraints on the choice of pairs for discrete function spaces can be circumvented. The following stabilized methods are discussed within this section:

- a minimally stabilized method based on residual techniques proposed by Barbosa and Hughes [12, 13] and modified by Stenberg [241],
- a stabilized mixed/hybrid stress-based Lagrange-multiplier technique by Gerstenberger and Wall [125] and Baiges *et al.* [10], and
- variants of the classical Nitsche method, originally introduced by Nitsche [196].

Subsequently, these methods are introduced and reviewed regarding stability and optimality of error estimates. Differences between those will be identified and analogies will be drawn for boundary-fitted approximations. Limitations and capabilities of the different techniques for the unfitted mesh case will be discussed and further elaborated in Section 3.4.

3.3.2.1 Babuška's Classical Method of Lagrange Multipliers - The Issue of Violating Inf-Sup Conditions

The theoretical basis for the weak enforcement of Dirichlet boundary conditions is laid down in the early work by Babuška [4]. The *classical method of Lagrange multipliers*, proposed in that work, consists of choosing appropriate discrete subspaces in (3.87) for the primal field $\mathcal{V}_h \subset \mathcal{V}$ in the domain and for the multiplier field $\Lambda_h \subset \Lambda$ on the boundary:

Definition 3.7 (Discrete form of Babuška's method of Lagrange multipliers)
For $f \in L^2(\Omega)$ and $g \in H^{1/2}(\Gamma)$, the discrete form reads: find $(u_h, \lambda_h) \in \mathcal{V}_h \times \Lambda_h$ such that

$$\mathscr{B}(u_h, \lambda_h; v_h, \mu_h) = \mathscr{L}(v_h, \mu_h) \quad \forall\, (v_h, \mu_h) \in \mathcal{V}_h \times \Lambda_h. \tag{3.90}$$

For stability of this discrete problem, an *inf-sup*-condition similar to (3.77) needs to be satisfied, which strongly restricts the choice of admissible pairs of discrete subspaces. This condition is also known as Babuška–Brezzi (BB) condition, named after the pioneering works by Babuška [4] and Brezzi [35]. A closer look at these restrictions was given in the work by Pitkäranta [205, 206]. In [205] a discrete inf-sup condition based on mesh-dependent norms was formulated and proven being equivalent to the original inf-sup condition with respect to norms of the continuous Sobolev spaces as originally formulated in [4]. Following [205], existence and uniqueness relies on a discrete inf-sup condition as summarized in the following theorem:

Theorem 3.3 (Existence and uniqueness of a discrete solution; see, e.g., [4, 35, 206, 241])
Suppose that the finite element subspaces satisfy the so-called inf-sup *condition or* Babuška–Brezzi *(*BB*) condition for the off-diagonal term*

$$\sup_{v_h \in \mathcal{V}_h \setminus 0} \frac{\langle \mu_h, v_h \rangle}{(|v_h|^2_{1,\Omega} + \|v_h\|^2_{1/2,h,\Gamma})^{1/2}} \geqslant c_s \|\mu_h\|_{-1/2,h,\Gamma} \quad \forall\, \mu_h \in \Lambda_h \tag{3.91}$$

with $c_s > 0$ independent of h and

$$|v_h|^2_{1,\Omega} \geqslant C(|v_h|^2_{1,\Omega} + \|v_h\|^2_{1/2,h,\Gamma}) \quad \forall\, v_h \in \{v_h \in \mathcal{V}_h \mid \langle \mu_h, v_h \rangle = 0 \,\forall\, \mu_h \in \Lambda_h\}\,. \tag{3.92}$$

Therein, the mesh-dependent boundary norms are defined as

$$\|\mu_h\|_{\pm 1/2,h,\Gamma} \overset{def}{=} \|h^{\mp 1/2} \mu_h\|_{0,\Gamma}. \tag{3.93}$$

For the solution (u_h, λ_h) to (3.90) it then holds the following a priori *error estimate in the energy norm $|||v, \mu||| \overset{def}{=} (|v|^2_{1,\Omega} + \|v\|^2_{1/2,h,\Gamma} + \|\mu\|^2_{-1/2,h,\Gamma})^{1/2}$*

$$|||(u - u_h), (\lambda - \lambda_h)||| \leqslant C(h^k \|u\|_{k+1} + h^{l+3/2} \|\lambda\|_{l+1,\Gamma}), \tag{3.94}$$

provided that $u \in H^{k+1}(\Omega)$ and $\lambda \in H^{l+1}(\Gamma)$.

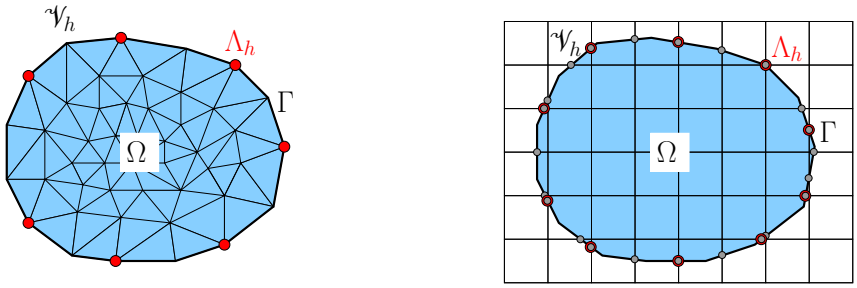

(a) (b)

Figure 3.2: Classical method of Lagrange multipliers for the weak imposition of Dirichlet constraints: (a) Satisfying an inf-sup condition for boundary-fitted meshes requires the boundary discretization Λ_h to be coarser than the primal field discretization $\mathcal{V}_h$, (b) Constructing stable Lagrange-multiplier spaces for unfitted meshes is based on a selection of intersection points which serve as a function basis.

Remark 3.4 (Inf-sup condition for fitted and unfitted meshes)

- *For boundary-fitted meshes, inf-sup stability requires the Lagrange-multiplier space Λ_h to be approximated coarser than the space $\mathcal{V}_h$ to ensure stability and optimal convergence:*

$$h_{\Lambda_h} \geqslant C h_{\mathcal{V}_h} \tag{3.95}$$

  with $h_{\Lambda_h}, h_{\mathcal{V}_h}$ the mesh size parameters of the boundary and bulk discretizations Λ_h and $\mathcal{V}_h$. As shown in the work by Pitkäranta [205, 206], the constant $C > 1$ required to guarantee the inf-sup condition (3.91) depends on Ω and is not straightforward to determine. A possible discretization for $\mathcal{V}_h$ and Λ_h is visualized in Figure 3.2a.

- *For non-boundary-fitted meshes, Ji and Dolbow [158] showed that a Lagrange-multiplier basis constructed of intersection points between boundary Γ_h and mesh $\mathcal{T}_h$ might result in oscillations of the multiplier field. Instabilities arise due to a violated inf-sup condition as the Lagrange-multiplier space might be too rich depending on the element intersection. Constructing stable Lagrange-multiplier spaces relies on counter criteria to guarantee an inf-sup condition and thereby requires preserving reasonable rates of convergence. Algorithms have been proposed, e.g., by Moës* et al. *[189] and Béchet* et al. *[18] for two-dimensional problems with extensions to three spatial dimensions by Hautefeuille* et al. *[146]. A visualization of this Lagrange-multiplier technique for an unfitted mesh is given in Figure 3.2b.*

As discussed above, most convenient choices of Lagrange-multiplier spaces are not stable in general. Moreover, the design of stable Lagrange-multiplier spaces becomes more challenging when boundary conditions or interfacial constraints need to be enforced on unfitted meshes. To circumvent limiting constraints on the function spaces stated by the Babuška–Brezzi condition (3.91), *stabilized Lagrange-multiplier methods* are often preferable.

Among the class of residual-based stabilization techniques, which will be discussed in more detail subsequently, different stabilization types have been developed for boundary and interface problems over the recent years. An extensive overview about Lagrange-multiplier methods for interface problems in the context of domain decomposition is given by Wohlmuth [271]. To enable choosing the discretization of the interface multiplier field independent of the two bulk discretizations, which can be advantageous to increase accuracy in particular for corner cases, Burman and Hansbo [43] proposed interior-penalty-stabilized Lagrange-multiplier methods for elliptic interface problems. This stabilization technique has been extended for the weak imposition of boundary conditions on unfitted meshes by Burman and Hansbo [44]. One drawback of these techniques, however, might be that Lagrange multipliers can not be condensed from the global system anymore, even though when discretized discontinuously. This is due to the stabilizing inter-element coupling. Recently, Burman [53] reviewed projection stabilization applied to Lagrange-multiplier methods and discussed its relation to classical residual-based methods, like the method by Barbosa and Hughes or Nitsche's method, a class of stabilization techniques which will be elaborated in more detail within the next sections.

3.3.2.2 Residual-based Stabilized Lagrange Multipliers - Circumvent the Babuška–Brezzi Condition

The idea of the original residual-based stabilized method by Barbosa and Hughes [12, 13] was to provide stability to the multiplier independent of the combination of discrete function spaces by adding terms to the original Galerkin formulation constructed from residuals of the Euler-Lagrange equations. Thereby, consistency of the discrete formulation is to be preserved. In the mentioned works, several stabilization operators were derived for the Poisson problem resulting in a symmetric discrete form: one term enforces the interface normal flux equality $\lambda_h - \nabla u_h \cdot \boldsymbol{n} = 0$, a second term accounts for the boundary condition $u_h - g = 0$ and a third term for the strong residual within the domain. As analyzed by Stenberg [241], this formulation exhibits an over-stabilization in general. Only the first part, the interface flux stabilization, is required to obtain a minimally stabilized inf-sup stable and optimal convergent scheme.

Definition 3.8 (Residual-based stabilized formulations)
The original method by Barbosa and Hughes [12, 13] reads: find $(u_h, \lambda_h) \in \mathcal{V}_h \times \Lambda_h$ *such that*

$$\mathcal{B}_h^{\mathrm{BH}}(u_h, \lambda_h; v_h, \mu_h) = \mathcal{L}_h^{\mathrm{BH}}(v_h, \mu_h) \quad \forall\, (v_h, \mu_h) \in \mathcal{V}_h \times \Lambda_h, \tag{3.96}$$

where

$$\mathcal{B}_h^{\mathrm{BH}}(u_h, \lambda_h; v_h, \mu_h) \overset{def}{=} \mathcal{B}\,(u_h, \lambda_h; v_h, \mu_h) + \mathcal{B}_h^{\delta}(u_h, \lambda_h; v_h, \mu_h) \tag{3.97}$$

with residual-based stabilizations $\mathcal{B}_h^{\delta}$ *for interface normal flux, boundary condition and strong residual* $R(u_h) - f = 0$*, where* $R(v_h) = -\Delta v_h$ *and* r_i *indicate optimally chosen powers of* h*,*

$$\begin{aligned}
\mathcal{B}_h^{\delta}(u_h, \lambda_h; v_h, \mu_h) &\overset{def}{=} -\delta h \langle \lambda_h - \nabla u_h \cdot \boldsymbol{n}, \mu_h \mp \nabla v_h \cdot \boldsymbol{n} \rangle \\
&\quad + \delta_2 h^{2r_2} \langle u_h, v_h \rangle + \delta_3 h^{2r_3} (R(u_h), R(v_h))_\Omega, \\
\mathcal{L}_h^{\mathrm{BH}}(v_h, \mu_h) &\overset{def}{=} \mathcal{L}\,(v_h, \mu_h) \\
&\quad + \delta_2 h^{2r_2} \langle g, v_h \rangle + \delta_3 h^{2r_3} (f, R(v_h))_\Omega.
\end{aligned} \tag{3.98}$$

Here, $\delta > 0$ *and* $\delta_2, \delta_3 \geqslant 0$ *are user-defined stabilization parameters. For a reduced stabilization suggested by Stenberg [241], the second and third residual terms are dropped, i.e.* $\delta_2 = \delta_3 = 0$*.*

Remark 3.5 (Symmetric versus non-symmetric formulations)
Characteristic stability and optimality properties of different variants can be reviewed as follows:

- *Residual-based stabilized methods are strongly consistent by construction.*
- *The different signs* $(\mp)$ *in* $\mathscr{B}_h^\delta$ *considerably affect inf-sup stability*

$$\sup_{(z,\eta)\in\mathscr{V}_h\times\Lambda_h\setminus 0}\frac{\mathscr{B}_h^{\mathrm{BH}}(z,\eta;v,\mu)}{|||(z,\eta)|||^{\mathrm{BH}}}\geqslant c_s|||(v,\mu)|||^{\mathrm{BH}}\quad\forall\,(v,\mu)\in\mathscr{V}_h\times\Lambda_h \tag{3.99}$$

with $|||(v,\mu)|||^{\mathrm{BH}}\overset{def}{=}(|v|^2_{1,\Omega}+\|v\|^2_{1/2,h,\Gamma}+\|\mu\|^2_{-1/2,h,\Gamma})^{1/2}$ *the energy norm controlling the bulk, the boundary condition and the Lagrange multiplier (see, e.g., in Stenberg [241]).*

- *The* symmetric variant *of* $\mathscr{B}_h^\delta$ *obtained by testing with* $\mu_h-\nabla v_h\cdot\boldsymbol{n}$ *in* (3.98) *yields* ***conditional inf-sup stability*** *provided that the stabilization parameter is positive and sufficient small, i.e.* $0<\delta\leqslant 1/(2C_T^2)$ *with* C_{T} *the constant resulting from a trace inequality*

$$\|\nabla v_h\cdot\boldsymbol{n}\|_{\Gamma\cap T}\leqslant C_{\mathrm{T}}h_T^{-1/2}\|\nabla v_h\|_T, \tag{3.100}$$

see also (3.47)*, relating the normal derivative of* v_h *on the element boundary to its gradient within the element* T*. This constant strongly depends on the shape, type and polynomial degree of the finite element* T*. Further elaborations in Section 3.4.2 will elucidate its important role in the context of unfitted meshes.*

- *Testing with* $\mu_h+\nabla v_h\cdot\boldsymbol{n}$ *in* $\mathscr{B}_h^\delta$ *makes the discrete formulation* $\mathscr{B}_h^{\mathrm{BH}}$ non-symmetric. *This, however, ensures* ***unconditional inf-sup stability*** *for all positive* δ*, i.e.* $\forall\,\delta>0$.
- *Compared to the classical method by Babuška, under the aforementioned assumptions on* δ*, the stabilized methods [12, 13, 241] are stable without constraints on the choice of* Λ_h *with respect to* $\mathscr{V}_h$ *and allows for natural definitions of* Λ_h *as visualized in Figure 3.3a.*
- *The symmetric variant is* adjoint-consistent *and ensures optimal* L^2*-error estimates compared to the* adjoint-inconsistent *non-symmetric form.*

3.3.2.3 A Stabilized Mixed/Hybrid Stress-based Formulation

Another class of stabilized techniques to circumvent the Babuška–Brezzi condition has been proposed by Gerstenberger and Wall [125]. In contrast to Stenberg's modification of the method by Barbosa and Hughes, an additional independent bulk stress field was introduced in the sense of a mixed/hybrid formulation. This stress field takes over the role of the trace Lagrange multipliers used in the methods proposed in [12, 13, 241]. In [125] such a technique has been originally used to impose Dirichlet conditions on unfitted meshes for incompressible flows governed by the Navier-Stokes equations. While the original method was non-symmetric even for symmetric problems, Baiges *et al.* [10] developed a variant which preserves symmetry in the discrete form for symmetric problems as, for instance, Stokes' problem. An adaption of those methods to large-eddy simulations for turbulent flows approximated on boundary-fitted meshes has been made by Gamnitzer [119]. Different variants for incompressible flow have been developed and studied by Kruse [167]. It has to be mentioned that all of these variants provide identical discrete forms for the linear elliptic Poisson equation.

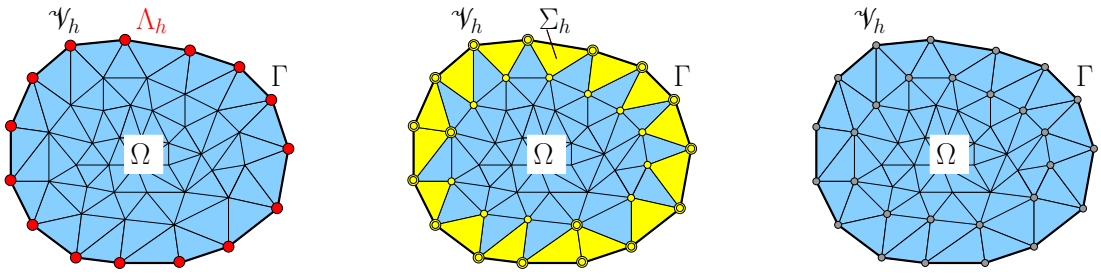

(a) (b) (c)

Figure 3.3: Stabilized Lagrange-multiplier methods for the weak imposition of Dirichlet boundary conditions on boundary-fitted meshes: (a) Residual-stabilized Lagrange-multiplier techniques by Barbosa and Hughes [12, 13] and Stenberg [241] circumvent the Babuška–Brezzi condition by adding stabilization terms on Γ and so allow to define Λ_h on the trace of $\mathcal{V}_h$. (b) The mixed/hybrid stress-based formulation by Gerstenberger and Wall [125] utilizes an additional element-wise discontinuous stress field Σ_h as a multiplier which is stabilized using additional volumetric balance equations. The space Σ_h can be defined either only for elements T near the boundary Γ or for all elements of the mesh $\mathcal{T}_h$. Note, the double-circled markers indicate discontinuous approximations of Σ_h. (c) Nitsche's method [196] uses the element-wise discontinuous gradients of the continuous function space $\mathcal{V}_h$ as multiplier space which is stabilized by an additional symmetric penalty term to guarantee inf-sup stability.

Definition 3.9 (Stabilized mixed/hybrid stress-based formulation by [123, 125])
Let $\mathcal{V}_h \subset \mathcal{V}$ and $\Sigma_h \subset [L^2(\Omega)]^d$ be the discrete function space for approximating the stress field ∇u_h. Then, the discrete stabilized mixed/hybrid formulation by Gerstenberger and Wall [125] reads as follows: find $(u_h, \boldsymbol{\sigma}_h) \in \mathcal{V}_h \times \Sigma_h$ such that

$$\mathcal{B}_h^{\mathrm{MHS}}(u_h, \boldsymbol{\sigma}_h; v_h, \boldsymbol{\tau}_h) = \mathcal{L}_h^{\mathrm{MHS}}(v_h, \boldsymbol{\tau}_h) \quad \forall\, (v_h, \boldsymbol{\tau}_h) \in \mathcal{V}_h \times \Sigma_h, \tag{3.101}$$

where

$$\mathcal{B}_h^{\mathrm{MHS}}(u_h, \boldsymbol{\sigma_h}; v_h, \boldsymbol{\tau_h}) \overset{def}{=} \mathcal{B}\left(u_h, \boldsymbol{\sigma}_h \cdot \boldsymbol{n}; v_h, \boldsymbol{\tau}_h \cdot \boldsymbol{n}\right) + \mathcal{B}_h^n(u_h, \boldsymbol{\sigma}_h; v_h, \boldsymbol{\tau}_h) \tag{3.102}$$

with a stabilization operator $\mathcal{B}_h^n$ and standard Galerkin operators $\mathcal{B}, \mathcal{L}$ from (3.88)–(3.89), i.e.

$$\mathcal{B}\left(u_h, \boldsymbol{\sigma}_h \cdot \boldsymbol{n}; v_h, \boldsymbol{\tau}_h \cdot \boldsymbol{n}\right) = (\nabla u_h, \nabla v_h) - \langle \boldsymbol{\sigma}_h \cdot \boldsymbol{n}, v_h \rangle - \langle u_h, \boldsymbol{\tau}_h \cdot \boldsymbol{n} \rangle, \tag{3.103}$$

$$\mathcal{B}_h^n(u_h, \boldsymbol{\sigma}_h; v_h, \boldsymbol{\tau}_h) \overset{def}{=} -\frac{1}{n} \sum\nolimits_{T \in \mathcal{T}_h} (\boldsymbol{\sigma}_h - \nabla u_h, \boldsymbol{\tau}_h \mp \nabla v_h)_{\Omega \cap T}, \tag{3.104}$$

$$\mathcal{L}_h^{\mathrm{MHS}}(v_h, \boldsymbol{\tau}_h) \overset{def}{=} \mathcal{L}\left(v_h, \boldsymbol{\tau}_h \cdot \boldsymbol{n}\right) = (f, v_h) - \langle g, \boldsymbol{\tau}_h \cdot \boldsymbol{n} \rangle. \tag{3.105}$$

Here, n is a stabilization factor that has to be chosen sufficiently large which, however, depends only on the sign $\mp$ in $\mathcal{B}_h^n$, as will be discussed below.

Remark 3.6 (Theoretical results)
The following theoretical inf-sup stability and optimality results can be summed up as follows:

- *The mixed/hybrid formulation ensures strong consistency.*
- *Note that the different signs* $(\mp)$ *in* $\mathscr{B}_h^n$ *affect inf-sup stability*

$$\sup_{(z,\boldsymbol{\eta})\in\mathscr{V}_h\times\Lambda_h\setminus 0}\frac{\mathscr{B}_h^{\mathrm{MHS}}(z,\boldsymbol{\eta};v,\boldsymbol{\tau})}{|||(z,\boldsymbol{\eta})|||^{\mathrm{MHS}}}\geqslant c_s|||(v,\boldsymbol{\tau})|||^{\mathrm{MHS}}\quad\forall\,(v,\boldsymbol{\tau})\in\mathscr{V}_h\times\Sigma_h \tag{3.106}$$

  with $|||(v,\boldsymbol{\tau})|||^{\mathrm{MHS}}\overset{def}{=}(|v|_{1,\Omega}^2+\|v\|_{1/2,h,\Gamma}^2+\sum_{T\in\mathscr{T}_h}\|\boldsymbol{\tau}\|_{0,h,T}^2)^{1/2}$ *the energy norm related to the mixed/hybrid discrete formulation.*
- *Note that in contrast to most residual-stabilized methods, the stabilization parameter* n *is independent of any trace inequality and independent of the polynomial order and element shape of the underlying finite element mesh* $\mathscr{T}_h$*; see Baiges* et al. *[10] as well as the related work by Barbosa and Hughes [13] for a stability analysis.*
- *The* symmetric variant *of* $\mathscr{B}_h^n$ *with testing* $\boldsymbol{\tau}_h-\nabla v_h$ *yields* ***conditional inf-sup stability*** *provided that* $2<n<\infty$*. By fixing* n*, this method is often interpreted of being free of any user-defined penalty or stabilization parameters. A more important aspect which needs to be highlighted, however, is the inherently contained information of trace estimates due to the volumetric stress-field projection.*
- *Testing with* $\boldsymbol{\tau}_h+\nabla v_h$ *in* $\mathscr{B}_h^n$ *makes the formulation* ***unconditionally inf-sup stable*** *for any choice of* $n>0$*, however, results in a* non-symmetric *discrete system even for symmetric variational formulations.*
- *Note that the additional stress field* $\boldsymbol{\sigma}$ *is not required to be defined on the entire domain* Ω*. In particular the choice of element-wise discontinuous approximations for* Σ_h *allows to restrict its definition to boundary-aligned elements* $T\in\mathscr{T}_\Gamma$*, see* (2.62)*. A visualization of a potential choice of function spaces is given in Figure 3.3b.*

For a profound understanding of limitations and issues of different types of stabilized methods for unfitted meshes, outlining similarities and differences of the methods for fitted meshes seems helpful. In a first step, analogies between the mixed/hybrid method and Stenberg's variant of the method by Barbosa and Hughes will be identified and drawn. In a second step, further relations between these two techniques and the well-established method by Nitsche [196] will be derived. Afterwards, considerations for the unfitted mesh case will be made.

Remark 3.7 (Analogies between the stabilized methods [125] and [12, 13, 241])
Symmetric and non-symmetric variants of the two methodologies for Poisson's problem can be directly opposed to each other

$$\begin{aligned}(\nabla u_h,\nabla v_h)-\langle\boldsymbol{\sigma}_h\cdot\boldsymbol{n},v_h\rangle-\langle u_h,\boldsymbol{\tau}_h\cdot\boldsymbol{n}\rangle-\frac{1}{n}\sum_{T\in\mathscr{T}_\Gamma}(\boldsymbol{\sigma}_h-\nabla u_h,\boldsymbol{\tau}_h\mp\nabla v_h)_{\Omega\cap T}\\ =(f,v_h)-\langle g,\boldsymbol{\tau}_h\cdot\boldsymbol{n}\rangle,\end{aligned} \tag{3.107}$$

$$\begin{aligned}(\nabla u_h,\nabla v_h)-\langle\lambda_h,v_h\rangle-\langle u_h,\mu_h\rangle-\delta\sum_{T\in\mathscr{T}_\Gamma}h_T\langle\lambda_h-\nabla u_h\cdot\boldsymbol{n},\mu_h\mp\nabla v_h\cdot\boldsymbol{n}\rangle_{\Gamma\cap T}\\ =(f,v_h)-\langle g,\mu_h\rangle.\end{aligned} \tag{3.108}$$

All subsequent statements can be proven using tools presented in [10, 12, 13, 241], however, are not presented in this work to shorten the presentation. Analogies and differences can be summarized as follows:

- *The used volumetric multiplier field in (3.107) can be identified as $\boldsymbol{\sigma}_h = \nabla u_h$, whereas the multiplier used in (3.108) approximates the normal stress $\lambda_h = \nabla u_h \cdot \boldsymbol{n}$ on the trace. Alternatively, also a vector-valued multiplier $\boldsymbol{\lambda}_h$ approximating $\boldsymbol{\lambda}_h \cdot \boldsymbol{n} = \nabla u_h \cdot \boldsymbol{n}$ could be introduced into (3.108) without changing stability and optimality properties.*
- *Both stabilized approaches enable the choice of piecewise discontinuous multiplier approximations. Element-wise condensation of the multiplier is then possible, resulting in a system without additional unknowns.*
- *Both methods are stabilized by filling the diagonal block of the saddle-point formulation with $\langle \lambda_h, \mu_h \rangle$ and $(\boldsymbol{\sigma}_h \cdot \boldsymbol{n}, \boldsymbol{\tau}_h \cdot \boldsymbol{n})$ in a strongly consistent way.*
- *The dimensionality gap between stabilizing terms on the bulk Ω_Γ in (3.107) and on the boundary Γ in (3.108) is compensated by the additional h-scaling in the latter form.*
- *The respective stabilization parameters are directly linked via $\delta \propto 1/n$.*
- *Both non-symmetric approaches ($(-)$-signs) are unconditionally stable under equivalent restrictions $0 < n = 1/\delta < \infty$.*
- *Both symmetric variants ($(+)$-signs) are conditional stable. While (3.107) requires that $2 < n < \infty$, where n is independent of element shape and polynomial order of the approximation space $\mathcal{V}_h$, the choice of δ in (3.108) depends on the constant C_T of a generalized trace inequality $0 < \delta < 1/(2C_T^2)$. In contrast, for (3.107) this mesh related information is incorporated in the element-wise L^2-projection between stress-field and gradient of the primal variable followed by its restriction to Γ. The projection automatically accounts for shape and polynomial order of the element and its approximation space. This makes this technique superior in particular for approximation spaces with higher-order polynomial degrees and for elements with irregular shape.*

In the following, one specific choice of function spaces $\mathcal{V}_h \times \Lambda_h$ for Stenberg's variant of the method by Barbosa and Hughes is considered which allows element-wise condensation of the multiplier variable. Note that a similar procedure allows for element-wise condensation in the mixed/hybrid stress-based formulation.

Condensation of Lagrange Multipliers on Element Level. Let $\mathcal{V}_h$ be a continuous finite element space of order $k \geqslant 1$. Furthermore, let Λ_h be a discontinuous space of piecewise polynomials of order l for all boundary elements such that $v_h|_{\Gamma_h} \in \Lambda_h$ and $\nabla v_h \cdot \boldsymbol{n} \in \Lambda_h$ for all $v_h \in \mathcal{V}_h$. Assuming element-wise constant normal vectors $\boldsymbol{n}$ in the following, this holds whenever $l \geqslant k$.

Following the elaborations by Stenberg [241], for each boundary-aligned element T specific functions $(v_h, \mu_h) = (0, \tilde{\mu}_h)$ are selected, whose boundary test function vanishes outside the current boundary segment, i.e. $\tilde{\mu}_h \equiv 0$ for $x \notin \Gamma_T = \Gamma \cap T$. Inserting this into (3.108), for each

element $T \in \mathcal{T}_\Gamma$ in the boundary zone one obtains

$$-\langle u_h, \tilde{\mu}_h \rangle + \sum\nolimits_{T \in \mathcal{T}_\Gamma} \delta h_T \langle \frac{\partial u_h}{\partial n}, \tilde{\mu}_h \rangle_{\Gamma_T} - \sum\nolimits_{T \in \mathcal{T}_\Gamma} \delta h_T \langle \lambda_h, \tilde{\mu}_h \rangle_{\Gamma_T} = -\langle g, \tilde{\mu}_h \rangle \tag{3.109}$$

$$\text{s.t.} \qquad \lambda_h|_{\Gamma_T}(u_h) = \Pi_h \left(\frac{\partial u_h}{\partial n}|_{\Gamma_T} - \frac{1}{\delta h_T}(u_h - g)|_{\Gamma_T} \right) \quad \forall T \in \mathcal{T}_\Gamma, \tag{3.110}$$

where Π_h denotes a face-wise L^2-projection on boundary segments Γ_T for which holds $\Pi_h v_h = v_h$ and $\Pi_h(\frac{\partial v_h}{\partial n}) = \frac{\partial v_h}{\partial n}$. Inserting this into (3.108), the condensed formulation reads

$$\begin{aligned} (\nabla u_h, \nabla v_h) &- \sum\nolimits_{T \in \mathcal{T}_\Gamma} \langle \Pi_h \left(\frac{\partial u_h}{\partial n}|_{\Gamma_T} - \frac{1}{\delta h_T}(u_h - g)|_{\Gamma_T} \right), v_h \rangle_{\Gamma_T} \\ &\mp \sum\nolimits_{T \in \mathcal{T}_\Gamma} \delta h_T \langle \frac{\partial u_h}{\partial n}, \frac{\partial v_h}{\partial n} \rangle_{\Gamma_T} \\ &\pm \sum\nolimits_{T \in \mathcal{T}_\Gamma} \delta h_T \langle \Pi_h \left(\frac{\partial u_h}{\partial n}|_{\Gamma_T} - \frac{1}{\delta h_T}(u_h - g)|_{\Gamma_T} \right), \frac{\partial v_h}{\partial n} \rangle_{\Gamma_T} = (f, v_h). \end{aligned} \tag{3.111}$$

Resorting and exploiting the aforementioned properties of Π_h for v_h and $\frac{\partial v_h}{\partial n}$ yields

$$\begin{aligned} (\nabla u_h, \nabla v_h) \mp \langle u_h, \frac{\partial v_h}{\partial n} \rangle - \langle \frac{\partial u_h}{\partial n}, v_h \rangle + \langle 1/(\delta h) u_h, v_h \rangle \\ = (f, v_h) + \langle 1/(\delta h) g, v_h \rangle \mp \langle g, \frac{\partial v_h}{\partial n} \rangle, \end{aligned} \tag{3.112}$$

which is the classical *Nitsche method* proposed in [196]. This method will be investigated in more detail in the next section and further throughout this thesis. A visualization of the multiplier function space given in terms of $\mathcal{V}_h$ is shown in Figure 3.3c. Note that due its close relation to the method by Barbosa and Hughes also the mixed/hybrid method (3.107) can serve as starting point to derive Nitsche's method by an analogous procedure as shown by Baiges *et al.* [10].

3.3.2.4 Nitsche's Method

Over the last decades, Nitsche's method has gained great attention and adaption to different problem settings regarding weak enforcement of boundary or interface coupling constraints has been made for various application fields. Originally applied to weakly impose Dirichlet conditions on boundaries by Nitsche [196], the method has been reviewed by Stenberg [241] in the context of the stabilized method by Barbosa and Hughes and by Baiges *et al.* [10] in the context of the mixed/hybrid stress-based Lagrange-multiplier method. Further extensions to enforce constraints for elliptic interface problems were introduced by Hansbo and Hansbo [138] for unfitted non-matching meshes and on composite overlapping grids by Hansbo *et al.* [139]. A survey on Nitsche techniques to enforce interfacial constraints on unfitted meshes including contrast in the material parameters was published by Burman and Zunino [62]. An extensive overview of literature about Nitsche's method and related topics addressing various aspects for boundary or interfacial constraint enforcement will be given throughout this thesis; for instance in Section 3.4.2 in the context of unfitted boundaries, in Section 4.2 for interfacial constraint techniques in flow problems and in Chapter 5 in the context of fluid-structure applications. For the sake of completeness, besides classical Dirichlet-type boundary and interfacial constraints,

Nitsche's method can be also adapted to treat generalized boundary/interfacial conditions of Robin-type; see, e.g., the work by Juntunen and Stenberg [161].

Main reasons for the great success and popularity are its simplicity and the advantage to not introduce further unknowns into the system, as it is the case for Lagrange-multiplier-based techniques with non-condensable multiplier function spaces. Moreover, the method is variational consistent and ensures fundamental requirements like inf-sup stability and optimal *a priori* estimates. As derived in the previous section, Nitsche's method can be characterized as a stabilized Lagrange-multiplier method for which the multiplier variable is replaced by its physical representation, the boundary flux, or more precisely its numerical approximation. Nevertheless, an often criticized characteristic of this approach is the fact that, at least for the symmetric variant, a user-defined parameter has to be specified to ensure stability; this aspect will be examined in more detail within this section. The classical Nitsche method for Poisson's problem with weak Dirichlet constraints is reviewed in the following.

Definition 3.10 (Nitsche's method for Poisson's problem)
Let be $\mathcal{V}_h \subset \mathcal{V}$, then Nitsche's method [196] reads as follows: find $u_h \in \mathcal{V}_h$ such that

$$\mathcal{B}_h^{\mathrm{NIT}}(u_h, v_h) = \mathcal{L}_h^{\mathrm{NIT}}(v_h) \quad \forall\, v_h \in \mathcal{V}_h, \tag{3.113}$$

where

$$\mathcal{B}_h^{\mathrm{NIT}}(u_h, v_h) \overset{def}{=} (\nabla u_h, \nabla v_h) - \langle \nabla u_h \cdot \boldsymbol{n}, v_h \rangle_\Gamma \mp \langle u_h, \nabla v_h \cdot \boldsymbol{n} \rangle_\Gamma + \langle (\gamma/h) u_h, v_h \rangle_\Gamma, \tag{3.114}$$

$$\mathcal{L}_h^{\mathrm{NIT}}(v_h) \overset{def}{=} (f, v_h) \mp \langle g, \nabla v_h \cdot \boldsymbol{n} \rangle_\Gamma + \langle (\gamma/h) g, v_h \rangle_\Gamma. \tag{3.115}$$

The first term in (3.114) corresponds to the standard Galerkin formulation and the second term results from integration by parts as $v_h|_\Gamma \neq 0$. The latter one is therefore called standard consistency term*. The third term is consistently added to the discrete form to enforce the Dirichlet constraint $u_h - g$. According to the choice of the signs $(\mp)$, two variants are commonly used: a* symmetric adjoint-consistent Nitsche method $(-)$ *and a* non-symmetric adjoint-inconsistent Nitsche method $(+)$*. The non-symmetric Nitsche-method further is called* penalty-free *if the fourth term in (3.114), the so-called* penalty term*, is omitted, i.e. $\gamma = 0$.*

Stability and Optimality for (Non-)symmetric and Penalty-free Nitsche Methods. Subsequently, advantages and drawbacks of different variants of Nitsche's method are discussed. While all variants are variationally consistent, they exhibit major differences regarding inf-sup stability. Theoretical results being reviewed in the following are based on Burman's work on a penalty-free non-symmetric Nitsche method [52] and on a recent article about stabilization techniques for Lagrange multipliers [53]. Fundamentals on stability of Nitsche's method will be discussed after providing coercivity statements which form the basis for further developments on unfitted cut finite element methods.

The symmetric method: The classical Nitsche method proposed in [196] exhibits a symmetric structure and so preserves symmetry of the underlying elliptic Poisson problem; an aspect which may be desirable from the iterative solvers point of view, but also for L^2-optimality reasons. Stability of that variant is obtained thanks to the penalty term for which a user-defined penalty parameter γ has to exceed a lower bound to ensure coercivity and thus inf-sup stability of the

formulation. This lower bound depends on a constant resulting from the trace inequality (3.100) which incorporates information about the polynomial degree and shape of the elements of the underlying finite element mesh. Inf-sup stability can be guaranteed by proving coercivity. An appropriate energy-norm can be defined as

$$|||v_h|||^{\mathrm{NIT}} \overset{\mathrm{def}}{=} (|v_h|^2_{1,\Omega} + \|v_h\|^2_{1/2,h,\Gamma})^{1/2}, \tag{3.116}$$

which controls the standard Galerkin formulation within the domain and on the boundary. For the definition of the mesh-dependent boundary norm, see (3.93). Note that the superscript $(\cdot)^{\mathrm{NIT}}$ is omitted for the rest of this section. Coercivity can be recalled as follows:

Proof.

$$\begin{aligned}
\mathscr{B}_h(v_h, v_h) &= |v_h|^2_{1,\Omega} - 2\langle v_h, \nabla v_h \cdot \boldsymbol{n}\rangle + \gamma\|v_h\|^2_{1/2,h,\Gamma} \\
&\geqslant |v_h|^2_{1,\Omega} - 2\|v_h\|_{1/2,h,\Gamma}\|\nabla v_h \cdot \boldsymbol{n}\|_{-1/2,h,\Gamma} + \gamma\|v_h\|^2_{1/2,h,\Gamma} \\
&\geqslant |v_h|^2_{1,\Omega} - 1/\epsilon\|\nabla v_h \cdot \boldsymbol{n}\|^2_{-1/2,h,\Gamma} + (\gamma - \epsilon)\|v_h\|^2_{1/2,h,\Gamma} \\
&\geqslant (1 - C_T^2/\epsilon)|v_h|^2_{1,\Omega} + (\gamma - \epsilon)\|v_h\|^2_{1/2,h,\Gamma} \\
&\geqslant \min\{1 - C_T^2/\epsilon, \gamma - \epsilon\}|||v_h|||^2 \\
&\geqslant c_s|||v_h|||^2.
\end{aligned} \tag{3.117}$$

In a first step, uncontrolled boundary inner products, which arise from the standard and adjoint consistency terms, are split via the Cauchy-Schwarz inequality. Next, an ϵ-scaled Young's inequality $(2ab \leqslant a^2/\epsilon + \epsilon b^2, \text{for } a, b \in \mathbb{R}, \epsilon > 0)$ is applied to the product of norms. Now, utilizing the trace inequality (3.100) enables to compensate the negative amount of the boundary flux by the bulk gradient, provided ϵ is chosen large enough such that $(1 - C_T^2/\epsilon) \geqslant c_s > 0$ with c_s independent of h. This limits the choice of ϵ to $\epsilon > C_T^2$ to preserve control on the H^1-semi-norm. Finally, the larger ϵ needs to be, which depends on C_T, the larger the stabilization parameter γ has to be chosen to recover control on v_h on the boundary. As a result, one obtains that inf-sup stability for the symmetric variant is guaranteed with a constant c_s provided that

$$\gamma \geqslant \epsilon > 2C_T^2, \tag{3.118}$$

which clearly indicates the dependency of γ on the trace inequality and thus on the shape and polynomial degree of the finite element mesh. Concluding, the symmetric Nitsche method is *conditionally stable* equivalent to the symmetric method by Barbosa and Hughes, see [12, 13].

□

Note that if precise statements for boundary flux errors with respect to the boundary semi-norm $\|\nabla v_h \cdot \boldsymbol{n}\|^2_{-1/2,h,\Gamma}$ have to be made, which is an important measure for coupled problems like, for instance, fluid-structure interaction, one can recover such control by utilizing the trace inequality again. By applying (3.100), the following norm equivalences hold

$$|v_h|^2_{1,\Omega} \leqslant |v_h|^2_{1,\Omega} + \|\nabla v_h \cdot \boldsymbol{n}\|^2_{-1/2,h,\Gamma} \leqslant (1 + C_T^2)|v_h|^2_{1,\Omega}, \tag{3.119}$$

$$|||v_h|||^2 \leqslant |v_h|^2_{1,\Omega} + \|\nabla v_h \cdot \boldsymbol{n}\|^2_{-1/2,h,\Gamma} + \|v_h\|^2_{1/2,h,\Gamma} \leqslant (2 + C_T^2)|||v_h|||^2, \tag{3.120}$$

which remain bounded as long as C_T does not deteriorate and is independent of h. Furthermore, coercivity can be extended to an energy-norm which additionally accounts for the flux control

$$\begin{aligned}\mathscr{B}_h(v_h, v_h) &\geqslant (1 - C_T^2/\epsilon)|v_h|_{1,\Omega}^2 + (\gamma - \epsilon)\|v_h\|_{1/2,h,\Gamma}^2 \\ &\geqslant (1 - 2C_T^2/\epsilon)|v_h|_{1,\Omega}^2 + C_T^2/\epsilon|v_h|_{1,\Omega}^2 + (\gamma - \epsilon)\|v_h\|_{1/2,h,\Gamma}^2 \\ &\geqslant \min\{1 - 2C_T^2/\epsilon, \gamma - \epsilon, 1/\epsilon\}(|||v_h|||^2 + \|\nabla v_h \cdot \boldsymbol{n}\|_{-1/2,h,\Gamma}^2) \\ &\geqslant \tilde{c}_s(|||v_h|||^2 + \|\nabla v_h \cdot \boldsymbol{n}\|_{-1/2,h,\Gamma}^2).\end{aligned} \tag{3.121}$$

Remark 3.8 (Stability and error dependency on the trace inequality) *From the last estimate the strong dependency of the stability constant c_s on the constant C_T is clearly visible. As recalled in (3.85), the smaller the stability constant, the larger the error in the final* a priori *error estimate. The constant C_T, which is a measure of the quality of elements T in the underlying mesh, in that way directly influences the error in the boundary region. Expecting a uniform control in the bulk with, for instance, $\tilde{c}_s = 1/2$, requires to choose $\epsilon = 4C_T^2$ and $\gamma \geqslant 4C_T^2$ to provide sufficient control on the boundary condition. While control on the boundary condition can be regularized by adapting γ, the quality of the interface fluxes directly correlates to the trace inequality constant C_T. In summary, large constants C_T decrease control over the boundary fluxes and require high penalty scalings in terms of γ to ensure stability. This, however, can further negatively affect the conditioning of the discrete system matrix. More detailed elaborations and graphical interpretations on the role of trace inequalities as well as numerical estimation techniques will be provided in the next section in the context of unfitted cut finite elements.*

The non-symmetric method with penalty parameter $\gamma > 0$: The strong dependency of the penalty parameter γ for the symmetric formulation is greatly reduced for a non-symmetric Nitsche method. Non-symmetric methods with $\gamma > 0$ were first considered by Stenberg [241] as variants of the method by Barbosa and Hughes. In Oden *et al.* [200] a non-symmetric Discontinuous Galerkin (DG) method was proposed and analyzed by Riviere *et al.* [220] with regard to stability and optimality of *a priori* error estimates.

Provided that $\gamma > 0$, i.e. $\gamma \neq 0$, the coercivity proof proposed above can be simplified. Due to the skew-symmetry of the consistency and adjoint consistency terms, these consistency terms cancel out when testing diagonally. As a result, no split via Young's inequality needs to be performed and coercivity directly results as

$$\mathscr{B}_h(v_h, v_h) = |v_h|_{1,\Omega}^2 + \gamma\|v_h\|_{1/2,h,\Gamma}^2 \geqslant \min\{1, \gamma\}|||v_h|||^2 \geqslant c_s|||v_h|||^2. \tag{3.122}$$

Similar to the symmetric version in (3.121), control over boundary fluxes can be recovered depending on the constant C_T of the trace inequality such that

$$\begin{aligned}\mathscr{B}_h(v_h, v_h) &= 1/2|v_h|_{1,\Omega}^2 + 1/2|v_h|_{1,\Omega}^2 + \gamma\|v_h\|_{1/2,h,\Gamma}^2 \\ &\geqslant \min\{1/2, \gamma, 1/(2C_T^2)\}(|||v_h|||^2 + \|\nabla v_h \cdot \boldsymbol{n}\|_{-1/2,h,\Gamma}^2) \\ &\geqslant \tilde{c}_s(|||v_h|||^2 + \|\nabla v_h \cdot \boldsymbol{n}\|_{-1/2,h,\Gamma}^2).\end{aligned} \tag{3.123}$$

In summary, the non-symmetric method is unconditionally stable for arbitrary positive $\gamma > 0$. This stability result is equivalent to that for the non-symmetric method by Barbosa and Hughes.

For the present work on incompressible flows, the loss of symmetry seems to be non-detrimental in a first view, since, due to the presence of the convective term in the incompressible Navier-Stokes equations, symmetry is not given anyway. Besides the symmetry, the adjoint-inconsistency seems to be a more important aspect, as it negatively affects the L^2-optimality, see discussion below and Remark 3.24 in Section 3.5. Bazilevs and Hughes [15] compared a symmetric and a non-symmetric Nitsche method for the incompressible Navier-Stokes equations. In their work, they observed that the adjoint-inconsistent non-symmetric method exhibits a non-monotonous error behavior and slightly reduced convergence rates with respect to the L^2-norm.

The penalty-free non-symmetric method with $\gamma = 0$: When considering the non-symmetric variant of Nitsche's method, which guarantees stability and optimality as long as $\gamma > 0$ is strictly positive, the natural question arises whether stability and optimality are preserved even in the limit case $\gamma = 0$. Burman [53] worked on a penalty-free non-symmetric method. Such a method can be interpreted as a Lagrange-multiplier method where the multiplier is replaced by the normal derivative $\nabla u_h \cdot \boldsymbol{n}$. While for classical Lagrange-multiplier approaches the spaces of bulk and multiplier field are decoupled, here, both spaces are strongly coupled as the trace of the bulk approximation is used for the multiplier. Whenever it is chosen $\gamma = 0$, the coercivity argumentation does not hold anymore, as diagonally testing only recovers control of the bulk semi-norm $|u_h|_{1\Omega}$. Control on the trace of u_h, usually introduced by the penalty term, is not obvious anymore. However, Burman [53] proved inf-sup stability of the penalty-free method with respect to the same energy-norm $|||v_h|||$ as defined in (3.116) together with the same optimal convergence in the H^1-norm. However, the convergence rate proven in the L^2-norm is suboptimal with half a power of h. On the other hand, numerical studies showed that even the penalty-free non-symmetric method converges optimally in the L^2-norm. Only the absolute error was observed being larger for the non-symmetric variant compared to the symmetric one. This, however, would be just a larger constant in the *a priori* result. This mismatch between numerical analysis and observations in simulation results has not been fully understood yet (see, e.g., [53] for discussions on this topic). Further studies on penalty-free non-symmetric Nitsche-type methods have been proposed by Schott and Shahmiri *et al.* [232] for fluid mesh-tying applications governed by the incompressible Navier-Stokes equations; see also Chapter 4 for such problem settings. Recently, analyses of penalty-free Nitsche methods have been proposed by Boiveau and Burman [27] for the weak the imposition of boundary conditions in compressible and incompressible elasticity and by Boiveau [26] for fitted and unfitted domain decomposition approximations of the Poisson problem.

3.4 CutFEM - An Analysis of General Stability Issues

As already discussed in Chapter 2, discretizing variational formulations on non-boundary- or non-interface-fitted meshes via intersecting grids and defining associated approximation spaces renders cut finite element approaches particularly promising for coupled multiphysics problems. Even though already the approximation of incompressible flows with fitted meshes requires different stabilization techniques in the bulk, as shown in Section 3.1.3, and further techniques to weakly impose constraints at boundaries, as discussed in Section 3.3.2, the difficulty of ensuring stability and optimal error estimates becomes more severe for unfitted meshes.

In particular pathological intersections of the finite element mesh result in conditioning issues and in intersection-dependent instabilities and suboptimal error estimates. Most if not all issues already occur for linear elliptic boundary-value or interface-coupled Poisson problems. These serve as model problems to mathematically analyze different aspects. Sources of instabilities will be illuminated and effective counteracting measures will be proposed. At the end of this section, numerical investigations will corroborate the theoretical statements for incompressible flow examples, which serve as preliminary studies for the next sections. The subsequent explanations are the basis for developing a stable and optimally convergent cut finite element method for incompressible flows, which will be then introduced and analyzed in Sections 3.5 and 3.6.

3.4.1 Conditioning and Stability Issues of Cut Approximation Spaces

Ill-Conditioning Issue of Global System Matrix. For standard boundary-fitted finite element approximations of second-order linear elliptic problems, it is expected that the condition number $\kappa(\boldsymbol{A})$ of the resulting global system matrix $\boldsymbol{A}$ is bounded from above by $\kappa(\boldsymbol{A}) \leqslant Ch^{-2}$, provided that the meshes are quasi-uniform. Proofs on that can be found in works by, e.g., Bank and Scott [11] or Ern and Guermond [101]. The relation between a discrete finite element formulation and its global system matrix can be summarized as follows: For a discrete function $v_h \in \mathcal{V}_h$, let $\boldsymbol{V} \in \mathbb{R}^n$ be the vector of nodal values v_s such that $v_h = \sum_{s=1}^{n} N_s v_s$ for a nodal basis $\mathcal{B} = \{N_s\}_{s=1}^{n}$ associated with the discrete finite element space $\mathcal{V}_h$. Furthermore, $|\boldsymbol{V}|$ denotes the Euclidean norm of the vector $\boldsymbol{V}$ and $|\boldsymbol{A}| = \sup_{\boldsymbol{V}\in\mathbb{R}^n\setminus\boldsymbol{0}} |\boldsymbol{A}\cdot\boldsymbol{V}|/|\boldsymbol{V}|$ its induced matrix norm. The associated condition number is defined as

$$\kappa(\boldsymbol{A}) = |\boldsymbol{A}||\boldsymbol{A}^{-1}|. \tag{3.124}$$

For estimating $\kappa(\boldsymbol{A})$ it is common to use the following relation between L^2-norm of a function $v_h \in \mathcal{V}_h$ on the computational mesh Ω_h^* and its n-dimensional vector representation $\boldsymbol{V}$

$$c_1 h^{d/2}|\boldsymbol{V}| \leqslant \|v_h\|_{0,\Omega_h^*} \leqslant c_2 h^{d/2}|\boldsymbol{V}| \tag{3.125}$$

with c_1, c_2 positive constants that only depend on the mesh uniformness and the polynomial degree in $\mathcal{V}_h$ (see, e.g., Massing *et al.* [180]). Bounded conditioning in the aforementioned sense can now be guaranteed when the discrete variational formulation controls the mesh-related L^2-norm $\|v_h\|_{0,\Omega_h^*}$. Such control can be deduced in terms of mesh-related inf-sup stability and continuity. Note that for this purpose stability estimates are needed to be established with respect to energy norms $|||v_h|||_*$ defined on the entire computational mesh Ω_h^*. Such a relation then links discrete stability to the matrix stability. For details on such proofs, the reader is referred to aforementioned literature. Extensions to cut finite element methods can be found in the work by Burman and Hansbo [45] and Massing *et al.* [180]. Establishing mesh-related energy norm estimates for a CUTFEM for the Oseen problem will be further discussed in Section 3.5.

Cut finite element methods without any additional measures do not ensure such estimates in general and the conditioning of the matrix system becomes strongly dependent on the location of the boundary within the computational mesh. Such dependencies have been often reported in literature, see, e.g., in [218, 225]. As a result, the loss of performance of iterative solution techniques can get significantly and the solution becomes sensitive to perturbations in the data.

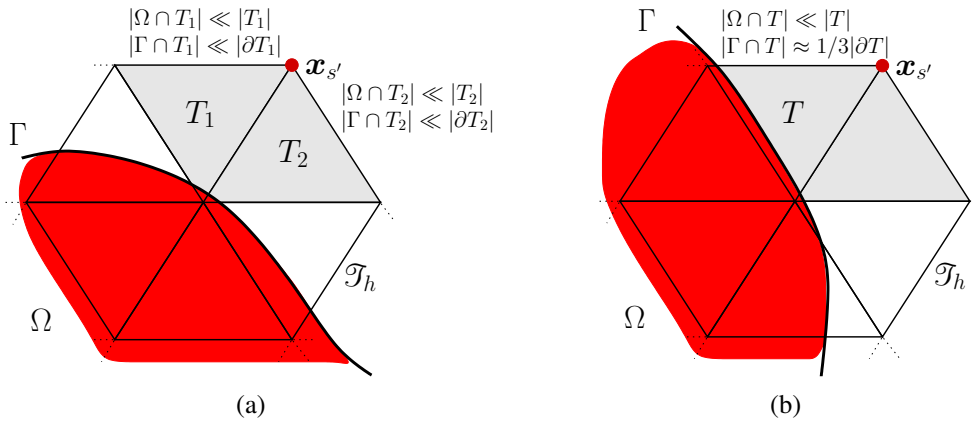

Figure 3.4: Pathological intersection scenarios: Only a small fraction of the intersected support of the basis function $N_{s'}$ (gray colored regions) associated with node s' remains inside the physical volume, i.e. $|\operatorname{supp}(N_{s'}) \cap \Omega| \ll |\operatorname{supp}(N_{s'})|$. (a) The "dotted cut" case with vanishing physical volume $|\Omega \cap T|$ and vanishing physical boundary $|\Gamma \cap T|$ in an element $T \in \mathcal{T}_h$ leads to poor conditioning of the linear matrix system. (b) The "sliver cut" situation with vanishing physical volume $|\Omega \cap T|$, however, non-vanishing physical boundary $|\Gamma \cap T|$ may lead to stability issues in the boundary region. Blocking or stabilizing the DOF associated with node s' with vanishing physical support can improve these issues.

The reason for ill-conditioning of CUTFEM matrix systems can be explained as follows: For non-boundary-fitted meshes, i.e. $\mathcal{T}_h \subset \widehat{\mathcal{T}}_h$, the domain Ω_h is only a subset of the active computational mesh $\mathcal{T}_h$. Then, in the interface region different pathological intersection scenarios may occur. In particular, two specific interface locations play an important role for conditioning and stability in cut finite element methods:

- the "dotted cut" case, for that the element's physical volume $|\Omega \cap T|$ and its physical boundary $|\Gamma \cap T|$ are much smaller compared to the entire element volume $|T|$ and its boundary $|\partial T|$, i.e. $|\Omega \cap T| \ll |T|$ and $|\Gamma \cap T| \ll |\partial T|$, as visualized in Figure 3.4a, and
- the "sliver cut" situation, in that the element's physical volume is smaller than the element, however, the boundary $\Gamma \cap T$ is of comparable magnitude to the element boundary, i.e. $|\Omega \cap T| \ll |T|$ and $|\Gamma \cap T| \approx |\partial T|$, see visualization in Figure 3.4b.

For "dotted cuts", the contribution of inner products of classical discrete formulation, which are defined within the physical domain Ω and on the physical boundary Γ, may drastically decrease. Such cases directly imply poor conditioning of the linear system. This is due to the fact that only a small portion of the volume and boundary integrals remain within the support of some shape functions associated with nodes in the ghost domain $\mathcal{T}_h \backslash \Omega_h$, as shown in Figure 3.4. In contrast, element intersections which produce small "sliver"-type fractions do not automatically cause ill-conditioning. Depending on whether polynomials v_h or their gradients are integrated along the boundary, the effect on the conditioning is different. As for elliptic problems, standard consistency terms of the form $\nabla u_h \cdot \boldsymbol{n}$ are contained in the discrete formulation, integrals over gradients usually contribute significantly to ghost-DOFs. In contrast, when integrating Lagrangean shape functions N_s itself, the polynomials tend to be zero near

the boundary of the support, i.e. $\partial(\text{supp}(N_s))$, and conditioning gets worse again. Sliver cuts play an even more critical role from the stability point of view, as will be elaborated further in Section 3.4.2.1.

Different strategies have been developed to deal with the conditioning issue arising for cut finite element spaces. Among classical preconditioning strategies to improve bad conditionings, as for example diagonal scaling of the global system matrix, an additional effective measure to obtain L^2-stable function spaces is to remove basis functions which exhibit small physical support from the function space. Reusken [218] introduced a strategy to block ill-conditioned basis functions. The key idea is to design a blocking criterion such that conditioning for the reduced space is improved and best approximation properties of the modified function space are thereby preserved. The main difficulty of that technique is to achieve a satisfactory balance between conditioning improvement and loss of accuracy caused by the reduced function space. For interface problems, so-called stable XFEM-enrichments have been introduced by Babuška and Banerjee [5]. This modified enrichment strategy has been compared to classical preconditioning strategies in the context of incompressible two-phase flow by Sauerland and Fries [226]. However, as could be shown by Henke [147], the approximation space defined by Babuška's Stable Generalized Finite Element Method (SGFEM) [5] is not able to accurately approximate strong discontinuities. While decoupling of two field solutions is possible, gradients of subdomain solutions are artificially coupled and cannot be adjusted independently. Other highly advantageous and promising strategies to circumvent the problem of ill-conditioning with the CUTFEM is to use specific stabilization operators in the interface region. Such a technique will be introduced in Section 3.4.3 and, later in this work, extended to different single- and multiphase problems for the incompressible Navier-Stokes equations.

On Mesh-dependent Stability and A Priori Error Estimates. As mentioned in the context of the conditioning issue, when deducing bounds for the matrix conditioning, special focus has to be directed towards establishing stability and continuity estimates. For such purposes, inf-sup stability and continuity estimates demand to be derived with respect to energy norms defined on the entire computational mesh Ω_h^*, instead of only on the physical domain Ω_h. In contrast, estimates for pure inf-sup stability and *a priori* error purposes could be also derived based on norms defined only on the physical domain. Nevertheless, it is of utmost importance that all constants involved in stability and *a priori* estimates are independent of the location of the boundary or interface Γ_h within the computational mesh $\mathcal{T}_h$. Otherwise, for a family of meshes $\{\mathcal{T}_h\}_h$ all constants would vary with the mesh size parameter h and so possibly worsen the optimality of the error estimates. This dependency can be clearly seen from the exemplary estimate (3.85). Further attention has to be paid in defining energy-norms and incorporated dependencies on the cut configuration have to be avoided. Otherwise, the weighting of different parts in the energy-norm, in particular interface error measures like the traces or interface fluxes, may lead to suboptimal rates, which often strongly vary depending on the different cut scenarios. Many if not all existing CUTFEMs developed over the last decade lack of these important properties. Further insight into this aspect will be given within the next section and will be illustrated by a various number of numerical examples in Section 3.4.4.

3.4.2 Nitsche's Method and the Role of the Trace Inequality

Enforcing Dirichlet boundary conditions on embedded surfaces using cut finite elements has become an active research field over the last years. As most Lagrange-multiplier methods are not guaranteed to fulfill an inf-sup condition on unfitted meshes and stabilized Lagrange multipliers often lose the possibility of element-wise condensation of the additional multiplier degrees of freedom, Nitsche's method became very popular for such problem settings. Often this methodology is also favored by its simplicity from an implementation point of view.

Regarding stability of Nitsche's method for boundary-value as well as interface problems on unfitted meshes, several publications are available in literature. Hansbo and Hansbo [138] utilized Nitsche's method for Poisson interface problems with discontinuous coefficients discretized on unfitted meshes. To ensure inf-sup stability, weighted averages of interfacial normal fluxes are used. Their definition is based on information about the location of the interface within the element. Mathematically spoken, this cut-cell weighting has to be chosen to fulfill a certain trace inequality as will be elaborated in more detail later in this section. A Nitsche-type domain decomposition technique based on composite grids, where a classical finite element mesh overlaps with another non-interface-fitted mesh, was developed by Hansbo *et al.* [139]. When an uncut mesh overlaps an unfitted mesh, stability can be easily ensured similar to the original Nitsche method by defining interface fluxes at the boundary of the uncut mesh. Different strategies for enforcing interfacial constraints and evaluating jump conditions within the extended finite element method were investigated by Ji and Dolbow [158] with focus on inf-sup stability issues. An overview about the high versatility of Nitsche's method for differently approximated interface problems in computational mechanics can be found in a review article by Hansbo [140].

Stability issues occurring in the weak constraint enforcement of Dirichlet boundary conditions in the extended and cut finite element method has been analyzed by Moës *et al.* [189] for Lagrange-multiplier methods. Fernández-Méndez and Huerta [109] used Nitsche's method to impose Dirichlet boundary conditions in the context of meshfree approximations, and Embar *et al.* [99] utilized it for second- and fourth-order boundary-value problems with spline-based approximations. Nitsche's method for boundary and embedded interface problems using cut-cell information were analyzed by Dolbow and Harari [87], Harari and Dolbow [144] and Hautefeuille *et al.* [146]. An adaption of flux weighting strategies for elliptic interface problems, which allows to account also for high contrast in the material parameters, has been made by Barrau *et al.* [14] and Annavarapu *et al.* [2]. A detailed review article on Nitsche's method for the numerical treatment of Dirichlet boundary conditions as well as the coupling between elliptic sub-problems including contrast in their characteristic material parameters was published by Burman and Zunino [62]. Most of the aforementioned variants of Nitsche's method do not account for the often reported conditioning issue for the linear matrix system. Such problems arise for particular intersection scenarios when classical PDE approximations are applied, which have been originally developed for boundary-fitted meshes, and certain stabilization measures in the boundary or interface zone are not added. Furthermore, most of these methods also lack optimal uniform control of important interface quantities as investigated by Schott and Wall [230] in the context of incompressible single-phase flow and fluid-structure interaction. To overcome such issues, Burman [50] developed a novel stabilization technique which is called *ghost penalty*. An extensive literature overview of this technique will be given in Section 3.4.3.

In the following, the role of so-called *trace estimates* on cut elements is revised before its significant impact on inf-sup stability estimates for Nitsche's method will be pointed out. Afterwards, the so-called *ghost-penalty* stabilization technique will be introduced and its improvements regarding system conditioning, stability and optimality of convergence rates will be discussed. Its enhanced stability behavior will be theoretically investigated and numerically validated by means of several simulation studies for incompressible flows.

3.4.2.1 The Decisive Role of the Trace Inequality

As already shown for the coercivity estimate of Nitsche's method on boundary-fitted meshes in Section 3.3.2.4, there is a strong dependency of stability statements on trace inequalities for functions $v_h \in \mathcal{V}_h$. Furthermore, such numerical tools are also required throughout the numerical analysis of CIP-stabilizations as introduced in Section 3.1.3.2. Therefore, a closer insight into trace inequalities as introduced in (3.47) for element boundaries and in (3.48) for arbitrarily intersected elements, needs to be given in the following.

To simplify the subsequent elaborations, the role of the trace inequalities is explained exemplarily for simplicial elements of order $k = 1$. For linear triangular and tetrahedral elements $T \in \mathcal{T}_h$, the gradients $\nabla v_h|_T = \boldsymbol{k}_T = \mathbf{const}$ reduce to element-wise constant vectors. The following relation between trace normal derivatives and bulk gradients can be easily shown

$$\begin{aligned}\|\nabla v_h \cdot \boldsymbol{n}\|^2_{\Gamma_h \cap T} &\leqslant \int_{\Gamma_h \cap T} |\nabla v_h|^2 \cdot |\boldsymbol{n}|^2 \,\mathrm{d}s = |\Gamma_h \cap T| \cdot |\boldsymbol{k}_T|^2 = \frac{|\Gamma_h \cap T|}{|\Omega_h \cap T|} \cdot |\boldsymbol{k}_T|^2 \int_{\Omega_h \cap T} 1 \,\mathrm{d}x \\ &= \frac{|\Gamma_h \cap T|}{|\Omega_h \cap T|} \int_{\Omega_h \cap T} |\nabla v_h|^2 \,\mathrm{d}x = \frac{|\Gamma_h \cap T|}{|\Omega_h \cap T|} \|\nabla v_h\|^2_{\Omega_h \cap T}.\end{aligned} \tag{3.126}$$

In this case the trace inequality relating element-wise physical boundary and domain emerges to

$$\|\nabla v_h \cdot \boldsymbol{n}\|_{\Gamma_h \cap T} \leqslant f_T \|\nabla v_h\|_{\Omega_h \cap T}, \qquad \text{where} \qquad f_T = \left(\frac{|\Gamma_h \cap T|}{|\Omega_h \cap T|}\right)^{1/2} \tag{3.127}$$

is a piecewise constant, dimensional function which depends on the intersection of T.

The Fitted Mesh Case. For boundary-fitted shape regular meshes, which guarantee boundedness of $f_T^2 \leqslant C_T^2 h_T^{-1}$, the trace inequality stated in (3.47) can be recovered as

$$\|\nabla v_h \cdot \boldsymbol{n}\|_{0,\Gamma_h \cap T} \leqslant \|\nabla v_h \cdot \boldsymbol{n}\|_{0,\partial T} \leqslant C_T h_T^{-1/2} \|\nabla v_h\|_{0,T} \tag{3.128}$$

with a non-dimensional constant C_T which depends only on type, shape regularity and polynomial order of elements $T \in \mathcal{T}_h$ and $\mathcal{V}_h$; proofs for $k > 1$ have been provided, e.g., by Burman and Ern [54].

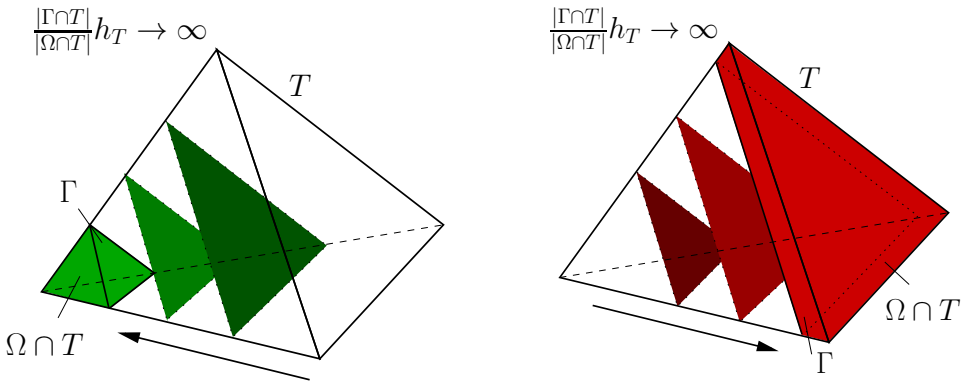

Figure 3.5: Trace inequalities for pathological element intersections of unfitted meshes: The "dotted cut" case (a) and the "sliver cut" situation (b) exhibit critical scalings $f_T^2 h_T = |\Gamma \cap T|/|\Omega \cap T| h_T \to \infty$ in contrast to the fitted mesh case, where $f_T^2 h_T = |\Gamma \cap T|/|\Omega \cap T| h_T \leqslant C_T^2$ is bounded by a certain constant. This is due to the vanishing physical volume and may lead to stability issues in the boundary region.

The Unfitted Mesh Case. Assuming that the boundary Γ does not intersect an element T multiple times, i.e. basic assumptions specified in Section 3.2.1 hold, then $|\Gamma_h \cap T| \lesssim |\partial T|$. In this case, similar to the fitted mesh case the following generalized trace inequality for intersecting boundaries holds

$$\|\nabla v_h \cdot \boldsymbol{n}\|_{0,\Gamma_h \cap T} \lesssim \|\nabla v_h \cdot \boldsymbol{n}\|_{0,\partial T} \leqslant C_T h_T^{-1/2} \|\nabla v_h\|_{0,T} \quad \text{(weakened trace inequality)}. \tag{3.129}$$

Note that ∇v_h on the right-hand side is measured in the entire element T. It has to be pointed out that the inequality does not keep valid with a scaling $C_T h_T^{-1/2}$ if the control on the entire element T gets reduced to the physical element volume $\Omega_h \cap T$. This often would be desirable, as variational formulations without further particular measures in the interface region can only guarantee control on the physical part of the element. Such an inequality, however, remains valid only with a non-dimensional scaling f_T, which depends on the interface location

$$\|\nabla v_h \cdot \boldsymbol{n}\|_{0,\Gamma_h \cap T} \leqslant f_T \|\nabla v_h\|_{0,\Omega_h \cap T}. \tag{3.130}$$

Considering the two pathological intersection scenarios introduced in Section 3.4.1, i.e. "dotted cuts" and "sliver cuts", the scaling f_T exhibits the following behavior:

While the "dotted cut" case is particularly critical for the conditioning, as physical boundary and physical volume are vanishing at the same time, both cases show severe issues due to deteriorating scalings $f_T^2 h_T$. Let d denote the distance of the cut boundary segment to the next interior mesh node, the ratio of element boundary to associated physical volume behaves as $\omega(d^{-1})$, i.e.

$$f_T^2 h_T = \frac{|\Gamma_h \cap T|}{|\Omega_h \cap T|} h_T \gtrsim h_T/d \to \infty \quad \text{for } d \to 0, \tag{3.131}$$

and as a result this may lead to unbounded scalings. Inf-sup stability and optimality of *a priori* error estimates are thus highly endangered, as will be discussed in the next section. A visualization for the dotted and sliver cut scenarios are given in Figure 3.5a and Figure 3.5b, respectively.

Note that all preceding elaborations were based on linear simplicial elements. In general, all statements remain valid even for higher polynomial orders as well as non-simplicial element types, however, with modified constants that take into account these additional properties. For an accurate prediction of the scalings f_T, in particular for curvilinear elements and boundaries, it is recommended to utilize element-wise estimation procedures, as suggested, e.g., by Embar *et al.* [99] and Hautefeuille *et al.* [146]. The fundamental idea therein was first proposed by Griebel and Schweitzer [132]. For each element $T \in \mathcal{T}_\Gamma$, the scaling f_T^2 can be estimated by the maximum eigenvalue $\rho_T^{\max}$ of a generalized eigenvalue problem $\boldsymbol{A}_T \tilde{V}_T = \rho_T^{\max} \boldsymbol{B}_T \tilde{V}_T$, where $\boldsymbol{A}_T, \boldsymbol{B}_T$ are the element matrices

$$\boldsymbol{A}_T = \langle \nabla v_h \cdot \boldsymbol{n}, \nabla v_h \cdot \boldsymbol{n} \rangle_{0,\Gamma_h \cap T} \qquad \text{and} \qquad \boldsymbol{B}_T = (\nabla v_h, \nabla v_h)_{0,X} \tag{3.132}$$

resulting from the trace and bulk L^2-norms belonging to the desired trace inequality

$$\|\nabla v_h \cdot \boldsymbol{n}\|_{0,\Gamma_h \cap T}^2 \leqslant f_T^2 \|\nabla v_h\|_{0,X}^2. \tag{3.133}$$

Therein, $X \subseteq T$ denotes the element part of interest. The corresponding eigenvector is denoted with $\tilde{V}_T$. Alternatively, instead of solving eigenvalue problems, the scaling f_T for the weakened trace estimate (3.129) can be approximated as

$$f_T^2 = C_T^2 h_T^{-1} \rho_{\text{safety}} \tag{3.134}$$

with constants C_T as provided by Burman and Ern [54] or pre-estimated from fitted-mesh eigenvalue problems to account for element type and polynomial degree. Herein, ρ_{safety} is a safety margin to account for possibly inclined element intersections. An overview of estimated constants C_T^2 is given in Table 3.1.

Table 3.1: Estimates for non-dimensional trace inequality constants C_T^2 provided by Burman and Ern [54] and estimated via approximative eigenvalue problems for different element types and polynomial orders k ($\mathbb{P}$ simplices, $\mathbb{Q}$ quadrilaterals and $\mathbb{W}$ wedge-shaped elements).

C_T^2	$\mathbb{P}^k_{d=2}$	$\mathbb{Q}^k_{d=2}$	$\mathbb{P}^k_{d=3}$	$\mathbb{Q}^k_{d=3}$	$\mathbb{W}^k_{d=3}$
$k=1$	1	1.4	1	1.6	1.6
$k=2$	3	4.2	8/3	4.3	4.3

3.4.2.2 Nitsche's Method using Cut-Cell Information

Subsequently, the impact of the trace inequality on the weak imposition of boundary conditions with Nitsche's method will be theoretically analyzed. Results will be corroborated by numerical simulations later in Section 3.4.4.

From coercivity proofs in Section 3.3.2.4, strong dependencies of the stability estimates on the trace inequality could be deduced already for boundary-fitted meshes. Utilizing an equivalent energy norm defined with respect to the physical domain Ω and its boundary Γ,

$$|||v_h||| \overset{\text{def}}{=} (|v_h|_{1,\Omega}^2 + \|v_h\|_{1/2,h,\Gamma}^2 + \|\nabla v_h \cdot \boldsymbol{n}\|_{-1/2,h,\Gamma}^2)^{1/2}, \tag{3.135}$$

an equivalent argumentation to (3.121) yields a stability estimate for unfitted meshes

$$\mathscr{B}_h(v_h, v_h) \geqslant \min\{1 - 2f_T^2 h_T/\epsilon, \gamma' - \epsilon, 1/\epsilon\} |||v_h|||^2. \tag{3.136}$$

Note that for the discrete formulation (3.113), bulk control $|v_h|_{1,\Omega}$ is guaranteed only within the physical domain Ω and a coercivity proof is based on a trace estimate as stated in (3.130). Then, however, the incorporated scaling function depends on h and, thus, on the cut configuration. For instance, when desiring a uniform control within the bulk, it requires that $\epsilon = 4f_T^2 h_T$ and therefore the stabilization parameter has to be chosen depending on the interface location within the element, i.e. $\gamma' > 4f_T^2 h_T$. Note that the included h_T-scaling cancels out with h^{-1} in the definition of the Nitsche penalty term such that this term is finally scaled with *cut-cell information* as

$$\langle \alpha(u_h - g), v_h \rangle_\Gamma \qquad \text{with} \qquad \alpha = \gamma f_T^2, \tag{3.137}$$

as suggested in various works by, e.g., Dolbow and Harari [87], Harari and Dolbow [144], Hautefeuille *et al.* [146].

Note that both critical scenarios, "dotted cuts" and "sliver cuts", show scalings f_T^2 which are not bounded from above by a certain constant for fixed h_T, see (3.131). This requires unbounded penalty scalings α and can deteriorate the stability estimate and as a further consequence even convergence rates, as stated in relation (3.85). Furthermore, this again can cause ill-conditioning of the system matrix and induce local over-penalization of the boundary condition.

These issues can be drastically reduced for the non-symmetric method, as shown in (3.122). As no lower bound for γ depending on f_T needs to be exceeded for that variant, but $\gamma > 0$ is sufficient, a uniformly chosen $\gamma = \text{const} > 0$ guarantees inf-sup stability with respect to the norm $|v_h|_{1,\Omega}^2 + \|v_h\|_{1/2,h,\Gamma}^2$ with stability constant $c_s = \min\{1, \gamma\} > 0$ independent of h and the interface location.

Nevertheless, all these variants still lack control on the interfaces fluxes. Following (3.121) and (3.123), additional flux-control $\|\nabla v_h \cdot \boldsymbol{n}\|_{-1/2,h,\Gamma}^2$ in the energy-norm can be recovered by utilizing the trace inequality. Note that most discrete formulations control the gradients $|v_h|_{1,\Omega}$ just within Ω_h, however, not sufficiently within Ω_h^*. Furthermore, the stability constant, which emanates from the additional flux control, becomes $1/(f_T^2 h_T)$ and depends on the interface location. Thus, critical cuts may lack control over interface fluxes as $1/(f_T^2 h_T) \to 0$, resulting in stability constants which tend to zero. As a consequence, following relation (3.85), this deteriorates the constant arising from the *a priori* error estimate. Indeed, this dependency of the interface flux errors on the interface location can be clearly observed in numerical simulations. Moreover, all these cut-cell-based variants of Nitsche's method do not guarantee control over $|v_h|_{1,\Omega_h^*}$ on the entire computational mesh Ω_h^*, but only on Ω_h, which results again in a conditioning issue for the global system matrix as described in Section 3.4.1.

3.4.2.3 Analogies to the Mixed/Hybrid Stress-based Formulation

From the discussions of the last sections about the role of the trace inequality, it is obvious that the residual-stabilized Lagrange-multiplier method by Stenberg and Barbosa and Hughes [12, 13, 241] exhibit equivalent issues with regard to inf-sup stability and their sensitivity of *a priori* error estimates on the interface location as cut-cell-based Nitsche methods reviewed in the previous section. Similar stability issues for the mixed/hybrid stress-based formulation

by Gerstenberger [123], see Section 3.3.2.3, were observed by Schott and Wall [230] for weak Dirichlet boundary value problems and by Kruse [167] and Shahmiri [235] for interface flow problems. These can be theoretically explained as follows:

Following the analysis in Baiges *et al.* [10] and Stenberg [241], formulation (3.101) can be rewritten in matrix form with vectors of nodal values $\boldsymbol{U}$ and $\boldsymbol{\Sigma}$ as

$$\begin{pmatrix} (1 \mp \frac{1}{n})\boldsymbol{K}_{uu} & \pm\frac{1}{n}\boldsymbol{K}_{u\sigma} - \boldsymbol{G}_{u\sigma} \\ \frac{1}{n}\boldsymbol{K}_{\sigma u} - \boldsymbol{G}_{\sigma u} & -\frac{1}{n}\boldsymbol{K}_{\sigma\sigma} \end{pmatrix} \cdot \begin{pmatrix} \boldsymbol{U} \\ \boldsymbol{\Sigma} \end{pmatrix} = \begin{pmatrix} \boldsymbol{f} \\ -\boldsymbol{g} \end{pmatrix} \tag{3.138}$$

with different matrices $\boldsymbol{K}_{uu} \Leftrightarrow (\nabla u_h, \nabla v_h)$, $\boldsymbol{G}_{u\sigma} \Leftrightarrow \langle \boldsymbol{\sigma}_h \cdot \boldsymbol{n}, v_h \rangle$, $\boldsymbol{G}_{\sigma u} \Leftrightarrow \langle u_h, \boldsymbol{\tau}_h \cdot \boldsymbol{n} \rangle$, $\boldsymbol{K}_{\sigma u} \Leftrightarrow \sum_{T \in \mathcal{T}_h} (\nabla u_h, \boldsymbol{\tau}_h)_{\Omega \cap T}$, $\boldsymbol{K}_{u\sigma} \Leftrightarrow \sum_{T \in \mathcal{T}_h} (\boldsymbol{\sigma}_h, \nabla v_h)_{\Omega \cap T}$ and $\boldsymbol{K}_{\sigma\sigma} \Leftrightarrow \sum_{T \in \mathcal{T}_h} (\boldsymbol{\sigma}_h, \boldsymbol{\tau}_h)_{\Omega \cap T}$. The right-hand-side vectors are given as $\boldsymbol{f} \Leftrightarrow (f, v_h)$ and $\boldsymbol{g} \Leftrightarrow \langle g, \boldsymbol{\tau}_h \cdot \boldsymbol{n} \rangle$. Choosing the function space Σ_h being element-wise discontinuous allows to condense the multiplier unknowns from the system with

$$\boldsymbol{\Sigma}(\boldsymbol{U}) = \boldsymbol{K}_{\sigma\sigma}^{-1} \left[(\boldsymbol{K}_{\sigma u} - n\boldsymbol{G}_{\sigma u})\boldsymbol{U} + n\boldsymbol{g} \right] \tag{3.139}$$

provided that $\boldsymbol{K}_{\sigma\sigma}$ is invertible. Then, the solution can be expressed purely in unknowns $\boldsymbol{U}$

$$\begin{aligned} \left[(1 \mp \frac{1}{n})\boldsymbol{K}_{uu} - \boldsymbol{G}_{u\sigma}\boldsymbol{K}_{\sigma\sigma}^{-1}\boldsymbol{K}_{\sigma u} \mp \boldsymbol{K}_{u\sigma}\boldsymbol{K}_{\sigma\sigma}^{-1}\boldsymbol{G}_{\sigma u} + n\boldsymbol{G}_{u\sigma}\boldsymbol{K}_{\sigma\sigma}^{-1}\boldsymbol{G}_{\sigma u} \pm \frac{1}{n}\boldsymbol{K}_{u\sigma}\boldsymbol{K}_{\sigma\sigma}^{-1}\boldsymbol{K}_{\sigma u} \right] \boldsymbol{U} \\ = \boldsymbol{f} + [(\mp\boldsymbol{K}_{u\sigma} + n\boldsymbol{G}_{u\sigma})\boldsymbol{K}_{\sigma\sigma}^{-1}\boldsymbol{g}]. \end{aligned} \tag{3.140}$$

Assuming that the Lagrange-multiplier space is rich enough to represent gradients ∇v_h exactly, i.e. there exists $\boldsymbol{\tau}_h \in \Sigma_h$ such that $\boldsymbol{\tau}_h = \nabla v_h$, the following equivalences from [10] hold:

$$\boldsymbol{G}_{u\sigma}\boldsymbol{K}_{\sigma\sigma}^{-1}\boldsymbol{K}_{\sigma u} \quad \Leftrightarrow \quad \langle \nabla u_h \cdot \boldsymbol{n}, v_h \rangle, \tag{3.141}$$

$$\boldsymbol{K}_{u\sigma}\boldsymbol{K}_{\sigma\sigma}^{-1}\boldsymbol{G}_{\sigma u} \quad \Leftrightarrow \quad \langle u_h, \nabla v_h \cdot \boldsymbol{n} \rangle, \tag{3.142}$$

$$\boldsymbol{K}_{u\sigma}\boldsymbol{K}_{\sigma\sigma}^{-1}\boldsymbol{K}_{\sigma u} \quad \Leftrightarrow \quad (\nabla u_h, \nabla v_h) \Leftrightarrow \boldsymbol{K}_{uu}. \tag{3.143}$$

The proofs are based on the exactness properties of the element-wise L^2-projections $\boldsymbol{K}_{\sigma u}, \boldsymbol{K}_{u\sigma}$ between the additional stress field $\boldsymbol{\tau}_h$ and ∇v_h on elements $T \cap \Omega_h$. Note that this property can numerically get lost for pathological intersections $|T \cap \Omega_h| \to 0$, which render in ill-conditioned unstable cut-cell-wise L^2-projections with projection mass matrices $\boldsymbol{K}_{\sigma\sigma}$. Note that the last term (3.143) cancels out with the $\mp 1/n$ contribution of the elliptic term in (3.140). The first term (3.141) is equivalent to the standard consistency term of Nitsche's method. The second term (3.142) is related to the term that makes a Nitsche formulation adjoint (in-)consistent. Hereby, the signs $\mp$ in (3.138) reflect the symmetric and non-symmetric variants of Nitsche's method.

Special consideration is required for the symmetric positive term $n\boldsymbol{G}_{u\sigma}\boldsymbol{K}_{\sigma\sigma}^{-1}\boldsymbol{G}_{\sigma u}$. Under the assumption of constant normals $\boldsymbol{n}$ within each element and equal order interpolations for $\mathcal{V}_h$ and Σ_h, the element matrices $\boldsymbol{G}_{\sigma u}, \boldsymbol{G}_{u\sigma}$ are boundary-cell-wise L^2-projections of v_h onto the space of normal stresses $\boldsymbol{\tau}_h \cdot \boldsymbol{n} = v_h$ on $\Gamma_h \cap T$ and vice versa. The element matrix $\boldsymbol{K}_{\sigma\sigma}^{-1}$ is an interposed volume-cell based L^2-projection in $\Omega_h \cap T$. For linear triangular or tetrahedral elements T, this allows to directly relate this term to the cut-cell-based Nitsche penalty term proposed in Section 3.4.2.2 as

$$n \underbrace{\boldsymbol{G}_{u\sigma}}_{|\Gamma_h \cap T|} \underbrace{\boldsymbol{K}_{\sigma\sigma}^{-1}}_{|\Omega_h \cap T|^{-1}} \underbrace{\boldsymbol{G}_{\sigma u}}_{|\Gamma_h \cap T|} \quad \Leftrightarrow \quad \gamma \underbrace{\frac{|\Gamma_h \cap T|}{|\Omega_h \cap T|}}_{f_T^2} \langle u_h, v_h \rangle_{\Gamma_h \cap T} \tag{3.144}$$

with n, γ dimensionless parameters which are both independent of the element shape, type or polynomial order and independent of the interface position. For both methods, these terms, which are of comparable magnitude, introduce the required control on the boundary $\|u_h\|_{1/2,h,\Gamma}$ to ensure inf-sup stability, respectively. However, as already discussed in the previous section for Nitsche's method, the final stability constant c_s and therewith the control over the enforcement of the boundary condition and finally the control over the boundary fluxes depend on the interface location; even though the fact that $c_s > 0$, together with continuity, guarantees at least existence of a unique discrete solution. Both methods allow to switch between a symmetric and a non-symmetric variant with analogous stability properties. The mixed/hybrid stress-based formulation, however, incorporates this penalty-like term by construction, also for the non-symmetric formulation. In particular for "sliver cuts" its presence renders in an additional source for unbounded condition numbers as $|\Gamma_h \cap T|^2/|\Omega_h \cap T| \to \infty$, although this term is not required to ensure inf-sup stability.

While the mixed-hybrid method shows many advantages in particular for higher-order approximations for boundary-fitted meshes due to its incorporated stability features given in terms of the stable element-wise L^2-projections, for unfitted meshes it exhibits an even worse behavior than cut-cell-based Nitsche methods. This manifests in several aspects: first, the interfacial error measures exhibit dependencies on the interface position and, second, in addition to the already bad system conditioning further issues arise from the unbounded penalty-like term; and third, the incorporated cut-cell and boundary-cell based L^2-projections, given in terms of $\boldsymbol{K}_{\sigma u}, \boldsymbol{K}_{u\sigma}$ and $\boldsymbol{K}_{\sigma\sigma}$, may become ill-posed and unstable. This behavior will be further elucidated with numerical studies in Section 3.4.4.

Fortunately, the predominant issues of cut-cell-based Nitsche methods can be avoided by utilizing certain interface zone stabilization techniques, as will be elaborated in the next section. Unfortunately, such a technique cannot be applied to the mixed/hybrid stress-based formulation in a straightforward manner to overcome all the mentioned issues. For unfitted meshes, this fact makes Nitsche's method superior to the mixed/hybrid stress-based formulation, as will be shown subsequently.

3.4.3 Ghost Penalty - Controlling Polynomials in the Interface Region

To overcome the previously discussed main issues of CutFEMs all at once, that is the ill-conditioning of the global system matrix due to bad intersections of the computational grid and the dependency of stability and *a priori* error estimates on the interface position, Burman [50] introduced a stabilization technique which is called "Ghost penalty – La pénalisation fantôme".

This technique consists of adding weakly consistent stabilization operators in the boundary zone to control the solution outside the physical domain, i.e. in $\Omega_h^* \backslash \Omega_h$. For elements intersected by the boundary, this is done by computing a natural smooth extension of the solution which is sufficiently controlled in the interior of the physical domain Ω_h. Ideas for developing this methodology can be found, for instance, in the CIP-stabilization technique, see Section 3.1.3.2, or in the usage of CIP-related jump-penalty terms to stabilize interface Lagrange multipliers. For the first time, Becker *et al.* [20] utilized CIP stabilizations for unfitted meshes to stabilize the pressure field for incompressible elasticity interface problems. Key idea therein was to stabilize the pressure solution of each subdomain by integrating the whole intersected face in the intersected region. In another context, similar interior jump penalty terms were proposed

by Burman and Hansbo [43] to stabilize Lagrange multipliers for the finite-element solution of elliptic interface problems. This stabilization technique has been extended to fictitious domain Lagrange-multiplier methods for weakly imposing boundary conditions on unfitted background meshes. Among others, the aforementioned stabilized methods build the basis for the theoretical framework on the *ghost penalty* (GP) technique, see Burman [50]. In the original publication, it was shown that stabilization of the discrete polynomials in the interface zone guarantees inf-sup stability with respect to the entire computational mesh $\mathcal{T}_h$ and, thus, allows to derive optimal bounds for the conditioning of the global system matrix as discussed in Section 3.4.1.

Over the recent years, this innovative approach became fundamental for a various number of continuous and discontinuous Galerkin CUTFEMs. In the early years after establishing this technique, Burman and Hansbo proposed an extensive numerical analysis and several studies on a ghost penalty extended Nitsche method for the weak imposition of boundary condition on fictitious domains in [45], and further for Stokes' problem in [60]. Massing *et al.* [181] proposed a fictitious domain method for Stokes' problem which is closely related to the latter one, however, with different pressure ghost-penalty forms extended to three spatial dimensions. The first application of the ghost penalties to a Nitsche-type method for solving high-Reynolds number flows on cut meshes governed by the incompressible Navier-Stokes equations was proposed by Schott and Wall [230]. It was shown how such interface-zone stabilizations can be naturally combined with classical CIP fluid stabilization terms in the interior of the domain for solving transient convective-dominant flows. Different CIP stabilization operators, as introduced in Section 3.1.3.2, together with ghost penalty jump terms for velocity and pressure in the vicinity of the boundary, which were adapted to guarantee optimality and stability in the different flow regimes, were utilized. Several numerical investigations and studies underlined robustness and accuracy of that stabilized formulation. Recently, a numerical analysis for this Nitsche-type CUTFEM was proposed by Massing *et al.* [183]. In this article, inf-sup stability and optimal *a priori* error estimates are proven for Oseen's problem at low and high Reynolds numbers. This numerical analysis will be reviewed in Section 3.5.

The combination of CIP and GP stabilizations for incompressible Navier-Stokes equations introduced in [183, 230] were further extended to different multiphysics problems. Schott and Rasthofer *et al.* [231] proposed a stabilized Nitsche-type extended variational multiscale method for incompressible two-phase flow. Adaption to domain decomposition for incompressible flows with overlapping meshes were made by Schott and Shahmiri *et al.* [232], a technique which was enhanced to fluid-structure interaction problems with overlapping fluid domains by Shahmiri [235]. Unfitted Nitsche-type fluid-structure interactions utilizing similar stabilization techniques were recently considered by Burman and Fernández [58].

Further developments on different discretization approaches and application fields based on the ghost penalty stabilization technique are available in literature: Ghost penalties for high order DG methods were utilized by Johansson and Larson [160]. Burman *et al.* [64] proposed a fictitious domain method for the three-field Stokes problem and unfitted Stokes interface problems were analyzed, e.g., by Hansbo *et al.* [141]. Moreover, a lot more ghost penalty based approximation techniques have been recently developed for coupled bulk-surface problems by different groups named already before. This class of problem settings, however, is beyond the scope of this thesis.

3.4.3.1 The Fundamental Idea of Ghost-Penalty Operators

The objective of ghost penalty stabilization is to control discrete polynomials in the vicinity of the boundary. Sufficient control on degrees of freedom which are associated with ghost nodes located in the unphysical domain $\Omega_h^* \backslash \Omega_h$ needs to be added. For this purpose, physical information from the interior of the domain is utilized and transferred to the interface zone. Provided that a sufficient number of uncut elements are located next to small and tiny element parts, which result from the intersection of elements and are the reason for critical conditioning and stability, a smooth natural extension for discrete polynomials $v_h \in \mathcal{V}_h$ in the boundary zone can be guaranteed. In practice, two different types of ghost-penalty terms are utilized to provide such an extension: inter-element face-jump penalties or patch-wise L^2-projection-based ghost penalties.

Inter-Element Face-Jump Ghost Penalties. In particular for low order finite elements, jump penalties acting on inter-element faces similar to the CIP stabilization technique introduced in Section 3.1.3.2 are useful, as suggested, e.g., by Burman and Hansbo [45]. A face-jump ghost-penalty operator, which allows to extend L^2-norm control, is defined as

$$g(u_h, v_h) = \sum_{F \in \mathcal{F}_\Gamma} \sum_{0 \leqslant j \leqslant k} h_F^{2j+1} \langle [\![\partial_{\boldsymbol{n}}^j u_h]\!], [\![\partial_{\boldsymbol{n}}^j v_h]\!] \rangle_F. \tag{3.145}$$

Such jump-penalty terms act on all discontinuous normal derivatives $\partial_{\boldsymbol{n}}^j v_h$ of order $0 \leqslant j \leqslant k$ for piecewise polynomials $v_h \in \mathcal{V}_h$ of order at most k. In a sum over all derivative orders, each addend tries to minimize corresponding inter-element derivative jumps in a facewise L^2-least-squares sense, i.e. roughly spoken $\| [\![\partial_{\boldsymbol{n}}^j v_h]\!] \|_{0,F}^2 \stackrel{!}{=} \min$. The different orders are thereby weighted with appropriate h-scalings to guarantee weak consistency and full L^2-norm control of the operator g. The aspect of weak consistency of the different GP stabilizations will be analyzed in more detail in Section 3.5.6 (see Lemma 3.17) in the context of the Oseen problem.

The penalty mechanism of such face-jump terms is visualized in Figure 3.6 for continuous and discontinuous finite element approximations. In the one-dimensional case, such terms reduce to point evaluations at nodes next to the interface. The zero-order derivative term, i.e. $j = 0$, simplifies to a jump penalty on the polynomial v_h itself and remains active only for discontinuous Galerkin approximations. In contrast, continuous Galerkin approximations guarantee continuity by construction. The first-order derivative jump, i.e. $j = 1$, penalizes kinks between the two linear polynomials of adjacent elements, whereas for a second-order approximation ($k = 2$), even changes in the curvature of the two polynomials need to be controlled additionally. Summarizing all derivative orders yields a smooth extension of the solution $v_h|_{\Omega_h \backslash \Omega_\Gamma}$ from uncut elements to the entire computational mesh Ω_h^*. By stabilizing all faces $F \in \mathcal{F}_\Gamma$, elements which are intersected by Γ are connected to the physical domain, which is sufficiently controlled by uncut finite elements.

It has to be emphasized that in three spatial dimensions, for faces which are intersected by the interface, jump terms have to be evaluated on the whole faces $F \in \mathcal{F}_\Gamma$ and not only on their physical segments. This ensures that discrete derivatives are integrated on a sufficient large part of the boundary of cut elements. This improves the system conditioning and ensures discrete stability with respect to the entire enlarged computational mesh. A visualization of this is shown in Figure 3.1. For details on the analysis, the reader is referred, e.g., to the publications [50, 181].

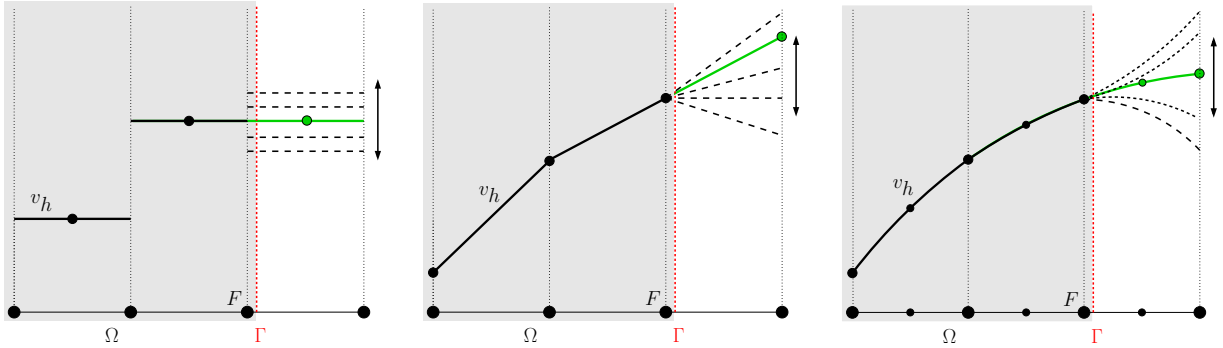

Figure 3.6: Mechanism of the face jump ghost penalty stabilization: (Left) Discontinuous Galerkin approximations, e.g., $\mathcal{V}_h = \mathscr{X}_0^{\mathrm{dc}}$, require control on inter-element jumps of the discontinuous polynomials, i.e. $\|[\![v_h]\!]\|_{0,F}^2 = \min$. (Middle) For continuous Galerkin approximations with $k \geqslant 1$ kinks between two neighboring linear polynomials are penalized, i.e. $\|[\![\partial_{\boldsymbol{n}} v_h]\!]\|_{0,F}^2 = \min$. (Right) For higher order approximations, as, e.g., $k = 2$, in addition to control on first-order normal derivatives also all second- and higher-order normal derivative jumps need to be controlled for stability and well-conditioning. Note, to preserve consistency, all jump terms of different orders have to be weighted with appropriate h-scalings.

Patch-wise L^2-Projection Ghost Penalties. As for higher-order polynomials the implementation of higher-order normal derivatives required for the jump-penalty terms can become quite cumbersome, it is suggested to utilize patch-wise L^2-projection-based ghost penalty stabilization terms, see, e.g., in [50, 60]. Instead of controlling polynomials outside the physical domain via face jump terms, the fluctuation between discrete functions v_h on elements T and L^2-projections onto element patches $\pi_P v_h$ can be penalized. For instance, such element patches can be associated with faces $F \in \mathscr{F}_\Gamma$ and consist of their two neighboring elements T_F^+ and T_F^- which share the face F, i.e. $P_F = T_F^+ \cup T_F^-$. A projection-based ghost penalty operator for extending L^2-norm control can then be defined as

$$\tilde{g}(u_h, v_h) = \sum_{F \in \mathscr{F}_\Gamma} (u_h - \pi_{P_F} u_h, v_h)_{P_F}, \tag{3.146}$$

which due to the Galerkin orthogonality of the patch-wise L^2-projection is equivalent to

$$\tilde{g}(u_h, v_h) = \sum_{F \in \mathscr{F}_\Gamma} (u_h - \pi_{P_F} u_h, v_h - \pi_{P_F} v_h)_{P_F}. \tag{3.147}$$

This clearly shows the symmetry of this operator similar to the face-jump variant. Here, $(\cdot,\cdot)_{P_F}$ denotes the volumetric L^2-inner product on patches P_F associated with faces F. Similar to the face jump penalties, cut elements have to be connected to uncut elements via a bounded number of such patches, which then allows information transfer from the sufficiently controlled physical domain to the boundary zone.

3.4.3.2 Properties from a Mathematical Point of View

The key mathematical properties implied by both GP techniques are norm equivalences for discrete functions, as proven by Burman and Hansbo [45] and Massing *et al.* [181]:

Lemma 3.4 *Let Ω, Ω_h^* and $\mathcal{F}_\Gamma$ be defined as in Section 2.1.4.1 and Section 2.2.2. Then for scalar functions $q_h \in \mathcal{V}_h$ as well as for vector-valued equivalents $\boldsymbol{v}_h \in [\mathcal{V}_h]^d$ the following estimates hold*

$$\|q_h\|^2_{\Omega_h^*} \lesssim \big(\|q_h\|^2_\Omega + \sum_{F\in\mathcal{F}_\Gamma}\sum_{1\leqslant j\leqslant k} h^{2j+1}\langle[\![\partial_{\boldsymbol{n}}^j q_h]\!],[\![\partial_{\boldsymbol{n}}^j q_h]\!]\rangle_F\big) \lesssim \|q_h\|^2_{\Omega_h^*}, \tag{3.148}$$

$$\|\boldsymbol{v}_h\|^2_{\Omega_h^*} \lesssim \big(\|\boldsymbol{v}_h\|^2_\Omega + \sum_{F\in\mathcal{F}_\Gamma}\sum_{1\leqslant j\leqslant k} h^{2j+1}\langle[\![\partial_{\boldsymbol{n}}^j \boldsymbol{v}_h]\!],[\![\partial_{\boldsymbol{n}}^j \boldsymbol{v}_h]\!]\rangle_F\big) \lesssim \|\boldsymbol{v}_h\|^2_{\Omega_h^*}, \tag{3.149}$$

$$\|\nabla\boldsymbol{v}_h\|^2_{\Omega_h^*} \lesssim \big(\|\nabla\boldsymbol{v}_h\|^2_\Omega + \sum_{F\in\mathcal{F}_\Gamma}\sum_{1\leqslant j\leqslant k} h^{2j-1}\langle[\![\partial_{\boldsymbol{n}}^j \boldsymbol{v}_h]\!],[\![\partial_{\boldsymbol{n}}^j \boldsymbol{v}_h]\!]\rangle_F\big) \lesssim \|\nabla\boldsymbol{v}_h\|^2_{\Omega_h^*}, \tag{3.150}$$

where the hidden constants in the relation ($\lesssim$) depend only on the shape-regularity and the polynomial order, but not on the mesh or the location of Γ_h within $\mathcal{T}_h$.

Fundamental assumption for this norm equivalence is assumption (G3) from Section 3.2.1, which roughly spoken states that the number of faces to be crossed in order to "walk" from an uncut element to a cut element requires being upper bounded and, in particular, being independent of h. As a result of the previous Lemma, adding appropriate ghost-penalty terms to an existing discrete formulation defined on Ω_h, allows to extend different norm controls onto the enlarged domain Ω_h^*, as shown here for the L^2-norm and H^1-semi-norm for scalar and vector-valued polynomials.

3.4.3.3 Implementation and Practical Aspects

Whereas both types of ghost-penalty operators ensure the same desirable features, from a practical point of view the different operators show certain advantages and drawbacks. Stabilization control of all orders of normal derivatives for the face-based variant requires high implementation effort in particular for higher order elements as well as additional evaluate and assembly routines for face-jump terms. Especially weighting of the different derivative levels with high-order h^{2j+1}-scalings can become critical when anisotropic meshes are used, like, for instance, in combination with ALE-based moving mesh techniques. Then a precise definition of the characteristic mesh size parameter h becomes crucial. In contrast, these issues are highly improved for projection-based ghost penalties. The entire information about higher order elements, their shape as well as polynomial degree are contained in the patch-wise L^2-projections. In particular the sensitivity on h is highly reduced for that operator. Nevertheless, both techniques require additional data structures providing information about elements and their neighbors. While face-jump penalties require topological mesh information about faces and adjacent elements, projection-based methods require the construction of function spaces on element patches or at least the evaluation of polynomials of neighboring elements. In this sense, compared to classical continuous Galerkin finite element approximations, both techniques require additional measures for parallel computing. Furthermore, both operators g and $\tilde{g}$ entail expanded couplings

between polynomials of neighboring elements, which, on the one hand, is the desired key effect of these stabilization techniques in terms of controlling polynomials via neighbors. On the other hand, this results in an enlarged pattern of non-zero entries in the global system matrix. In contrast to standard continuous finite element methods, changes in existing code frameworks with regard to parallel computing and evaluation as well as assembly strategies for additional ghost penalty terms is indispensable. For the sake of completeness, it has to be emphasized that the computational costs for solvers can increase and the changed pattern can influence the efficiency of preconditioners similar to CIP fluid stabilizations. Nevertheless, the gain in stability and the improved conditioning of the system matrix exceeds all mentioned drawbacks by a multiple.

Despite the large number of advantages of the projection-based method over the face-jump penalties, throughout this work only face-jump ghost penalty terms are analyzed further and considered for all numerical simulations. This is due to implementational reasons and due to their close relation to face-oriented CIP stabilizations, which allows to simplify numerical analyses. For low-order approximations on regular meshes, as exclusively used in this work, no larger differences between these two different ghost penalty stabilization techniques are expected.

3.4.3.4 Nitsche's Method Supported by Ghost Penalties

As discussed in Section 3.4.2.2, the classical Nitsche method on unfitted meshes without any additional measures exhibit different issues regarding inf-sup stability, ill-conditioning and sub-optimality of *a priori* error estimates; even though cut-cell information is incorporated in the respective Nitsche penalty term.

In the following, the effect of ghost-penalty stabilizations and its interrelation with Nitsche's method is reviewed. This serves as basis for a CUTFEM for Oseen's problem proposed later in Section 3.5. More theoretical details can be found in the original publication Burman [50].

Definition 3.11 (Nitsche's method stabilized with ghost penalties)
Let be $\mathcal{V}_h \subset \mathcal{V}$, then the discrete stabilized form of Nitsche's method using ghost penalty stabilization, see [50], reads as follows: find $u_h \in \mathcal{V}_h$ such that

$$\mathcal{B}_h^{\mathrm{NIT}}(u_h, v_h) + \mathcal{G}_h^{\mathrm{GP}}(u_h, v_h) = \mathcal{L}_h^{\mathrm{NIT}}(v_h) \quad \forall\, v_h \in \mathcal{V}_h, \tag{3.151}$$

where

$$\mathcal{B}_h^{\mathrm{NIT}}(u_h, v_h) \overset{def}{=} (\nabla u_h, \nabla v_h)_\Omega - \langle \nabla u_h \cdot \boldsymbol{n}, v_h\rangle_\Gamma \mp \langle u_h, \nabla v_h \cdot \boldsymbol{n}\rangle_\Gamma + \langle (\gamma/h) u_h, v_h\rangle_\Gamma, \tag{3.152}$$

$$\mathcal{G}_h^{\mathrm{GP}}(u_h, v_h) \overset{def}{=} \gamma_g \sum\nolimits_{F\in\mathcal{F}_\Gamma} \sum\nolimits_{1\leqslant j\leqslant k} h^{2j-1} \langle [\![\partial_{\boldsymbol{n}}^j u_h]\!], [\![\partial_{\boldsymbol{n}}^j v_h]\!]\rangle_F, \tag{3.153}$$

$$\mathcal{L}_h^{\mathrm{NIT}}(v_h) \overset{def}{=} (f, v_h)_\Omega \mp \langle g, \nabla v_h \cdot \boldsymbol{n}\rangle_\Gamma + \langle (\gamma/h) g, v_h\rangle_\Gamma. \tag{3.154}$$

Compared to the classical Nitsche method, see Definition 3.10, the role of the additional ghost penalty stabilization term $\mathcal{G}_h^{\mathrm{GP}}$ is to extend control on the H^1-semi-norm, which is given in terms of the elliptic bulk term, to the enlarged domain Ω_h^* by exploiting norm equivalence (3.150).

As already discussed in Section 3.4.2.1, for intersected elements a weakened trace inequality

$$\|\nabla v_h \cdot \boldsymbol{n}\|_{0,\Gamma_h\cap T} \leqslant C_T h_T^{-1/2} \|\nabla v_h\|_{0,T}, \tag{3.155}$$

see (3.48) and (3.129), holds with respect to the entire element T. Therein, C_T only depends on the element shape and its polynomial degree, however, not on the intersection of the element. Applying this suboptimal inequality to estimate standard and adjoint consistency boundary terms, leads to a momentary uncontrolled lack of coercivity within the unphysical domain $\Omega_h^* \backslash \Omega_h$

$$\begin{aligned} 2\langle v_h, \nabla v_h \cdot \boldsymbol{n} \rangle &\leqslant 1/\epsilon \|\nabla v_h \cdot \boldsymbol{n}\|^2_{-1/2,h,\Gamma} + \epsilon \|v_h\|^2_{1/2,h,\Gamma} \\ &\leqslant C_T^2/\epsilon |v_h|^2_{1,\Omega_h^*} + \epsilon \|v_h\|^2_{1/2,h,\Gamma} \\ &\leqslant C_{\mathscr{g}} C_T^2/\epsilon (|v_h|^2_{1,\Omega} + \mathscr{g}_h^{\mathrm{GP}}(v_h, v_h)) + \epsilon \|v_h\|^2_{1/2,h,\Gamma}, \end{aligned} \tag{3.156}$$

with $C_{\mathscr{g}}$ denoting the hidden constant in the norm equivalence (3.150), which depends on γ_g. This is due to the fact that the elliptic bulk term allows to compensate ∇v_h just within the physical domain Ω_h. Now, thanks to the additional ghost-penalty term and the H^1-semi-norm equivalence, this negative norm control can be balanced and inf-sup stability can be recovered on the entire computational mesh with an energy norm defined as

$$|||v_h|||_*^2 \overset{\text{def}}{=} |||v_h|||^2 + \mathscr{g}_h^{\mathrm{GP}}(v_h, v_h) = |v_h|^2_{1,\Omega} + \|v_h\|^2_{1/2,h,\Gamma} + \mathscr{g}_h^{\mathrm{GP}}(v_h, v_h) \tag{3.157}$$

such that

$$|v_h|^2_{1,\Omega_h^*} + \|v_h\|^2_{1/2,h,\Gamma} \lesssim |||v_h|||_*^2 \lesssim |v_h|^2_{1,\Omega_h^*} + \|v_h\|^2_{1/2,h,\Gamma}. \tag{3.158}$$

Stability of Nitsche's Method with respect to $|||v_h|||_*$. Utilizing estimate (3.156), coercivity for the symmetric Nitsche method can be proven as

$$\begin{aligned} \mathscr{B}_h^{\mathrm{NIT}}(v_h, v_h) + \mathscr{g}_h^{\mathrm{GP}}(v_h, v_h) &= |v_h|^2_{1,\Omega} + \mathscr{g}_h^{\mathrm{GP}}(v_h, v_h) - 2\langle v_h, \nabla v_h \cdot \boldsymbol{n} \rangle_\Gamma + \gamma \|v_h\|^2_{1/2,h,\Gamma} \\ &\geqslant (1 - C_{\mathscr{g}} C_T^2/\epsilon)(|v_h|^2_{1,\Omega} + \mathscr{g}_h^{\mathrm{GP}}(v_h, v_h)) + (\gamma - \epsilon)\|v_h\|^2_{1/2,h,\Gamma} \\ &\geqslant \min\{1 - C_{\mathscr{g}} C_T^2/\epsilon, \gamma - \epsilon\} |||v_h|||_*^2 \\ &\geqslant c_s |||v_h|||_*^2 \end{aligned} \tag{3.159}$$

and stability is guaranteed for $\epsilon = C_{\mathscr{g}} C_T^2/2$ and $\gamma > \epsilon$. Note that for the symmetric Nitsche method, again, the Nitsche penalty parameter γ has to be sufficiently large, however, now depending on the weakened trace inequality. Provided that the mesh assumptions from Section 3.2.1 are fulfilled, this constant is upper bounded and does not deteriorate in contrast to cut-cell-based variants.

It should be mentioned that the hidden constant $C_{\mathscr{g}}$ of the norm equivalence (3.150) enters the coercivity estimate and thus introduces a dependency on γ_g . In practice, it is suggested to choose $\gamma_g < 1$ to not worsen the accuracy near the boundary due to strong smoothing effects of the jump penalties. As a consequence, the Nitsche penalty parameter has to be large enough depending on the size of γ_g to still ensure coercivity.

Such dependencies vanish for the non-symmetric Nitsche method and any positive $\gamma_g, \gamma > 0$ are sufficient to guarantee stability with respect to $|||v_h|||_*$. For the non-symmetric variant the coercivity estimate simplifies due to out-canceling boundary terms

$$\begin{aligned} \mathscr{B}_h^{\mathrm{NIT}}(v_h, v_h) + \mathscr{g}_h^{\mathrm{GP}}(v_h, v_h) &= |v_h|^2_{1,\Omega} + \mathscr{g}_h^{\mathrm{GP}}(v_h, v_h) + \gamma \|v_h\|^2_{1/2,h,\Gamma} \\ &\geqslant \min\{1, \gamma\} |||v_h|||_*^2 \\ &\geqslant c_s |||v_h|||_*^2. \end{aligned} \tag{3.160}$$

The conditioning issue for $\gamma_g \to 0$, however, still remains due to the deterioration of the norm.

Similar to the elaborations in Section 3.3.2.4, for both variants additional control on the interface flux can be recovered by applying a trace inequality. As now stability is ensured on the enlarged domain Ω_h^*, the weakened estimate (3.155) guarantees uniform control on the interface fluxes in terms of C_T. In fact, this constant depends on the element shape and the polynomial degree, however, does not dependent on the interface location. The modified coercivity estimate then emerges to

$$\mathscr{B}_h^{\mathrm{NIT}}(v_h, v_h) + \mathscr{G}_h^{\mathrm{GP}}(v_h, v_h) \geqslant \tilde{c}_s(|||v_h|||_*^2 + \|\nabla v_h \cdot \boldsymbol{n}\|_{-1/2,h,\Gamma}^2) \tag{3.161}$$

with $\tilde{c}_s$ independent of the interface position and h.

For the sake of completeness, it has to be mentioned that even the non-symmetric penalty-free method is proven to be stable on unfitted meshes, as shown by Boiveau and Burman [27] and Boiveau [26]. However, the proof in how to gain the required control over $\|v_h\|_{1/2,h,\Gamma}$ then substantially differs.

3.4.4 Numerical Studies for Incompressible Flow

All theoretically analyzed aspects concerning different techniques for the weak imposition of Dirichlet boundary conditions on unfitted grids, which have been discussed within the last sections, will be corroborated now by several numerical studies. Although most effects were numerically analyzed for the linear elliptic Poisson problem, all discussed stability issues equivalently occur for solutions to the incompressible Navier-Stokes equations. Since main focus of the present work is directed towards developing CUTFEMs for incompressible flows, all investigations presented subsequently are performed for the incompressible Navier-Stokes equations. To mimic major stability issues from the Poisson problem, low-Reynolds-number flows are considered such that the elliptic viscous term in (3.4) is dominating. Further effects that are characteristic for convective-dominated flows will be studied afterwards as well.

First, in Section 3.4.4.1, issues arising from pathological element intersections, which may render in stability and conditioning issues at nodes located outside the physical domain, are shown. In Section 3.4.4.2 different methods for the weak constraint enforcement are compared. The claimed close relation between the stabilized mixed/hybrid stress-based formulation by Gerstenberger [123] and the cut-cell-weighted Nitsche method discussed in Section 3.4.2.3 will be affirmed. Furthermore, different variants of Nitsche's method and their effects on accuracy and robustness are numerically investigated to support the theoretical statements provided throughout Section 3.4.2.2. Their different behavior is compared by means of a spatial error convergence study. Moreover, the influence of different fluid stabilizations provided in Section 3.1.3, together with the influence of additional stabilizing measures in the interface region, will be pointed out. The great improvement of stability and system conditioning for face-jump ghost penalty stabilizations in the interface zone is demonstrated. Finally, in Section 3.4.4.3, additional studies are presented regarding the sensitivity of Nitsche's method on involved stabilization parameters, that is the Nitsche penalty parameter as well as the parameter of a viscous ghost-penalty stabilization.

The following different discrete formulations are examined in this section:

- The original mixed/hybrid Cauchy-stress-based formulation by Gerstenberger [123] used for the weak imposition of boundary conditions. In the interior fluid domains the standard Galerkin formulation is stabilized by a PSPG residual-based variational multiscale term, as introduced in Section 3.1.3.1. Note that no CIP or GP stabilizations are applied here. This formulation is abbreviated with MHS throughout the studies.

- A classical symmetric Nitsche method (NIT) with penalty term $\langle(\alpha_\nu\rho)\boldsymbol{u}_h, \boldsymbol{v}_h\rangle_\Gamma$ supported by a PSPG fluid stabilization. The scaling α_ν is chosen as defined for boundary-fitted meshes, i.e. $\alpha_\nu = \gamma\nu/h$, see Section 3.3.2.4.

- A symmetric Nitsche-type method using penalty term scalings based on element-wise cut-cell information, i.e. $\alpha_\nu = \gamma\nu|\Gamma_T|/|\Omega_T|$ with $\Gamma_T = \Gamma \cap T$ and $\Omega_T = \Omega \cap T$, to appropriately account for trace estimates on the physical domain, see Section 3.4.2.2.

- Additionally, combinations with different types of pressure stabilizations are investigated: a residual-based PSPG stabilization form Section 3.1.3.1 and a face-oriented stabilized pressure CIP method (p-CIP) from Section 3.1.3.2. Note, for the latter one, intersected faces in the interface zone are stabilized entirely.

- A symmetric Nitsche-type method supported by a viscous ghost penalty stabilization (GP) for the velocity field

$$\mathcal{G}_h^{\mathrm{GP}}(\boldsymbol{u}_h, \boldsymbol{v}_h) = \gamma_\nu \sum_{F\in\mathscr{F}_\Gamma} \sum_{1\leqslant j\leqslant k} \nu\rho h^{2j-1} \langle [\![\partial_{\boldsymbol{n}}^j \boldsymbol{u}_h]\!], [\![\partial_{\boldsymbol{n}}^j \boldsymbol{v}_h]\!] \rangle_F, \tag{3.162}$$

  as proposed in Section 3.4.3.4. For this variant, the Nitsche penalty term scaling is chosen as $\alpha_\nu = \gamma\nu/h$ based on the weakened trace inequality (3.155).

- A fully stabilized CutFEM including further stabilizations for low- and high-Reynolds-number flows proposed by Schott and Wall [230]. CIP fluid stabilizations for low- and high-Reynolds-number flows from Section 3.1.3.2 are used and the Nitsche-penalty scaling is extended to account for mass conservation and inflow instabilities for high Reynolds numbers

$$\langle(\alpha_u\rho)\boldsymbol{u}_h, \boldsymbol{v}_h\rangle_\Gamma \quad \text{with} \quad \alpha_u = \max\{\gamma\nu/h, |\boldsymbol{u}_h \cdot \boldsymbol{n}|, 1\}. \tag{3.163}$$

  A closely related method will be analyzed for Oseen's problem in Section 3.5 and finally reviewed in Section 3.6 for transient incompressible Navier-Stokes equations.

The subsequent numerical studies are based on work published in Schott and Wall [230]. If not indicated otherwise, for Nitsche's method, the stabilization parameters are chosen as $\gamma = 35.0$ for the penalty terms and $\gamma_\nu = 0.05$ for the viscous ghost penalty stabilization equivalent to scalings in the CIP method. Stabilization parameters for CIP and RBVM terms are taken unchanged from Section 3.1.3. For all subsequent simulations the density is set to $\rho = 1.0$.

3.4.4.1 Stabilizing the Ghost Domain - The Role of Interface-Zone Penalties

As an example, the fluid flow around different obstacles located within a fluid domain is considered. The setup of this flow problem has been already described in Section 2.2.4 and visualized in Figure 2.16. The intention of this example is to demonstrate general stability issues of many CUTFEMs, as discussed in Section 3.4.1. The beneficial effect of different interface zone face-jump penalty terms, these are the continuous interior penalties as well as the ghost penalties (see Section 3.1.3.2 and Section 3.4.3), will be shown.

Ghost-DOFs for Moderate and Critical Cut Situations. Keeping in mind the overall objective of coupled multiphysics flow problems with moving interfaces, the location of the interface is changing within finite elements. Due to interface motion the influence region of ghost-DOFs on the overall solution can get reduced or enlarged. In the latter case, it seems obvious that the quality of ghost values may influence robustness of time-dependent simulations.

A close-up view of the interface zone around a cylindrical obstacle in Figure 3.7 demonstrates mentioned stability issues for velocity and pressure when using cut finite element approximations in the interface zone. To show the effect of the different interface zone stabilizations on ghost values, results for differently stabilized Nitsche-type fluid formulations are presented: A first variant is sufficiently stabilized by a viscous ghost-penalty stabilization for the velocity field as well as by velocity and pressure CIP stabilizations. All related terms are evaluated along whole cut faces. The second variant uses a residual-based SUPG stabilization for velocity in the interior of the domain but no velocity face jump stabilization. A jump penalty term for the pressure is still active. The third variant consists of a purely RBVM formulation without any additional velocity and pressure face-jump stabilizations in the interface zone.

For all considered methods, the velocity solution within the physical domain looks quite similar. Compared to the fully stabilized method, see Figure 3.7a (left), the variant without face jump terms for $\boldsymbol{u}_h$, however, looses control over velocity ghost-DOFs. This is obvious from the exaggerated magnitude and the uncontrolled directions of the velocity vectors associated with nodes located in the ghost domain shown in Figure 3.7a (middle). A similar, still more distinctive effect can be observed for the purely residual-based stabilized method in Figure 3.7a (right).

As long as a face-oriented pressure stabilization is utilized for cut faces and in that way stabilizes like a ghost-penalty operator, a smoothly extended pressure solution in the interface zone is obtained. Sufficiently controlled pressure DOFs outside the physical domain in Figure 3.7b demonstrates the inf-sup stability of the stabilized velocity-pressure product space. However, once the pressure face-jump terms are omitted and only the residual-based pressure stabilization (PSPG) term remains, pressure ghost values get uncontrolled due to the violated inf-sup stability. This further negatively affects even the velocity solution in the fictitious domain. Uncontrolled ghost values for the pressure and their negative influence even on the physical solution close to the interface can be seen in close-up views of the pressure field.

It has to be mentioned that for interface locations, like those shown in Figure 3.7, the physical supports of shape functions associated with critical ghost nodes are not too pathological. For such element intersections, blocking strategies, as suggested by, e.g., Reusken [218] or Sauerland and Fries [225], seem to be unpractical for realistic problem settings. Otherwise, the solution would suffer from too large errors caused by strongly reduced approximation spaces. This clearly shows the advantage of combinations of CIP/GP stabilizations and indicates their importance for time-dependent moving boundary problems.

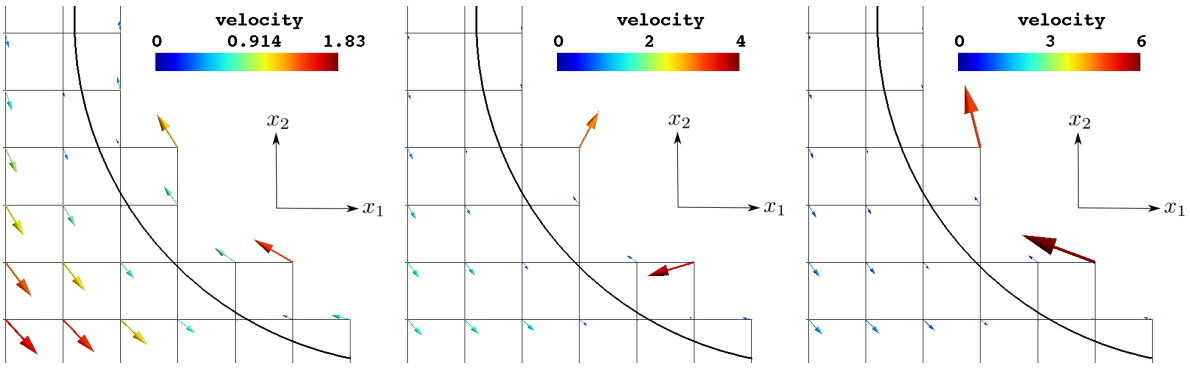

(a) Velocity solution $\boldsymbol{u}_h$ around a cylinder.

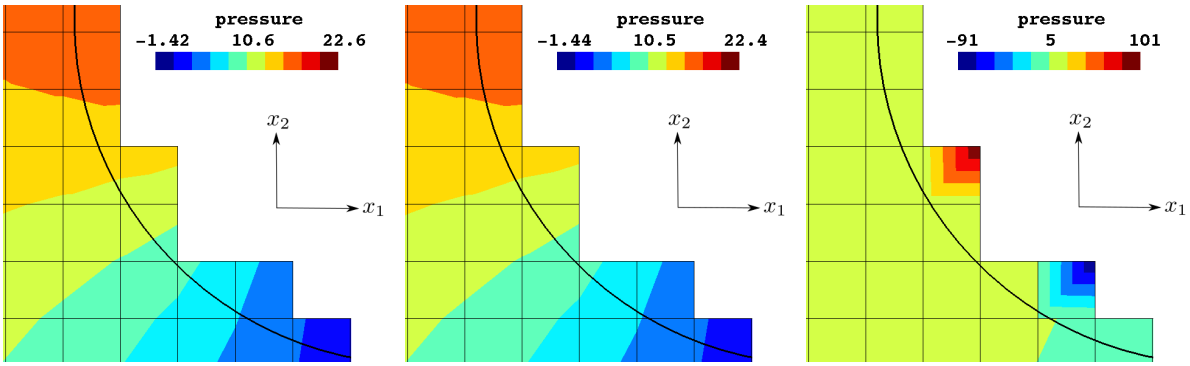

(b) Pressure solution p_h around a cylinder.

Figure 3.7: Close-up view of the flow around a cylinder with $x_1 \in [0.05; 0.225]$, $x_2 \in [0.05; 0.225]$: (Left) A Nitsche-type method with velocity and pressure face-jump-penalty stabilizations. (Middle) A variant with SUPG stabilization within the domain, but without face-jump penalties for the velocity $\boldsymbol{u}_h$. A face-oriented pressure stabilization term (p-CIP) still controls the pressure solution in the interface zone. (Right) Insufficiently controlled solution of a pure residual-based stabilized formulation (SUPG/PSPG) without ghost penalties for $\boldsymbol{u}_h$ and p_h. Note the different scales.

Face-Jump Penalties for Expanded Cut Finite Element Function Spaces Considering solutions to the incompressible Navier-Stokes equations approximated in complex domains utilizing the expanded cut finite element function space introduced in Section 2.2.4, evaluation and assembly of face-jump-penalty terms in the interface zone requires special consideration.

A close-up view around the left upper tip of the thin structural obstacle of the previous example has been visualized in Figure 2.17. As already elaborated in Section 2.2.4, to represent independent solutions on different sides of thin structures accurately, multiple DOFs per node are required. The structural surface subdivides the support of the nodal shape function near the interface into independent non-connected volume-cells. Following Algorithm 2.1, the number of volume-cell connections around nodes then determines the number of nodal DOFs, as depicted in Figure 2.17a. Within the support of a node's shape function, volume-cells V_i, V_j are connected to physically meaningful contiguous regions if and only if there is a common (possibly cut) facet $f \subseteq F \in \mathcal{F}_i$ in between, such that $f = V_i \cap V_j$. The number of such physical facets f per face F determines how often face-jump-penalty terms have to be evaluated along the entire parent face $F \in \mathcal{F}_\Gamma$.

In Figure 2.17b, all uncut internal faces $F \in \mathcal{F}_i \backslash \mathcal{F}_\Gamma$ as well as faces $f \in \mathcal{F}_\Gamma$ in the interface zone are exemplarily shown for the previous example. Away from the interface only classical face-oriented CIP fluid stabilizations, as defined in Section 3.1.3.2, have to be evaluated. Such faces are marked with green color in Figure 2.17b. For faces near the interface, i.e. $F \in \mathcal{F}_\Gamma$ (colored red), in addition to the CIP fluid stabilizations also ghost-penalty terms (GP) become active. Numbers shown in Figure 2.17b indicate how many times faces in the interface zone have to be evaluated. Each evaluation thereby corresponds to a physical face segment $f \subset F$ of intersected faces and thus stabilizes fluid regions on different sides of the structure. More precisely, the different evaluations stabilize disjunct volume-cell connections.

The resulting pressure distribution around the thin structural obstacle is shown in Figure 2.17c. Therein, the smoothness of the pressure contour lines around the structural tip needs to be pointed out which is due to the sufficient stability control given by face-jump-penalty terms.

3.4.4.2 Weak Dirichlet Constraint Enforcement - A Comparison of Methods

In subsequent numerical convergence studies, different variants for weak imposition of Dirichlet constraints are compared to confirm theoretical results on inf-sup stability and error convergence of the different techniques listed at the beginning of Section 3.4.4.

2D Taylor Problem. The convergence of errors is investigated for the frequently used two-dimensional Taylor problem, see, e.g., in [73, 162, 213]. Periodic time-dependent analytical velocity and pressure fields $(\boldsymbol{u}, p)$ are given as

$$u_1(x_1, x_2, t) = -\cos(a\pi x_1)\sin(a\pi x_2) \cdot g_u(t), \tag{3.164}$$

$$u_2(x_1, x_2, t) = \sin(a\pi x_1)\cos(a\pi x_2) \cdot g_u(t), \tag{3.165}$$

$$p(x_1, x_2, t) = -0.25(\cos(2a\pi x_1) + \cos(2a\pi x_2)) \cdot g_p(t), \tag{3.166}$$

such that $\nabla \cdot \boldsymbol{u} = 0$. It is chosen $a = 2$. The time-scaling factors $g_p(t)$ and $g_u(t)$ will be specified below for the different studies. Numerical solutions are computed within a circular fluid domain

$$\Omega^{\mathrm{f}} = \left\{ \boldsymbol{x} = (x_1, x_2) \in \mathbb{R}^2 \;\middle|\; |\boldsymbol{x} - (0.5, 0.5)| < 0.45 \right\} \tag{3.167}$$

approximated with unfitted background fluid meshes $\widehat{\mathcal{T}}_h$ defined on $[0, 1]^2$, which are rotated by $45°$ about the x_3-axis, as shown in Figure 3.8. All background meshes consist of regular quadrilateral $\mathbb{Q}^1$-elements. The mesh size parameters are $h = 1/n_x = 1/n_y$ with $n_x = n_y$ the varying number of elements in each direction, as specified below. The boundary Γ_h is approximated explicitly by the inner trace mesh of the ring-shaped domain

$$\Omega^{\mathrm{s}} = \left\{ \boldsymbol{x} = (x_1, x_2) \in \mathbb{R}^2 \;\middle|\; 0.45 < |\boldsymbol{x} - (0.5, 0.5)| < 0.9 \right\}, \tag{3.168}$$

where the circular interface line Γ consists of $6n_x$ regular intervals.

Dirichlet boundary conditions given by the analytical solution are imposed on the entire boundary of the fluid domain, i.e. $\Gamma = \Gamma_{\mathrm{D}}$. To remove the uncontrolled constant pressure mode, the pressure is fixed at the middle node $(0.5, 0.5)$ using the value from (3.166). The right-hand side $\boldsymbol{f}$ in the Navier-Stokes equations is adapted such that (3.164)–(3.166) are solution of the stationary or transient incompressible Navier-Stokes equations, respectively.

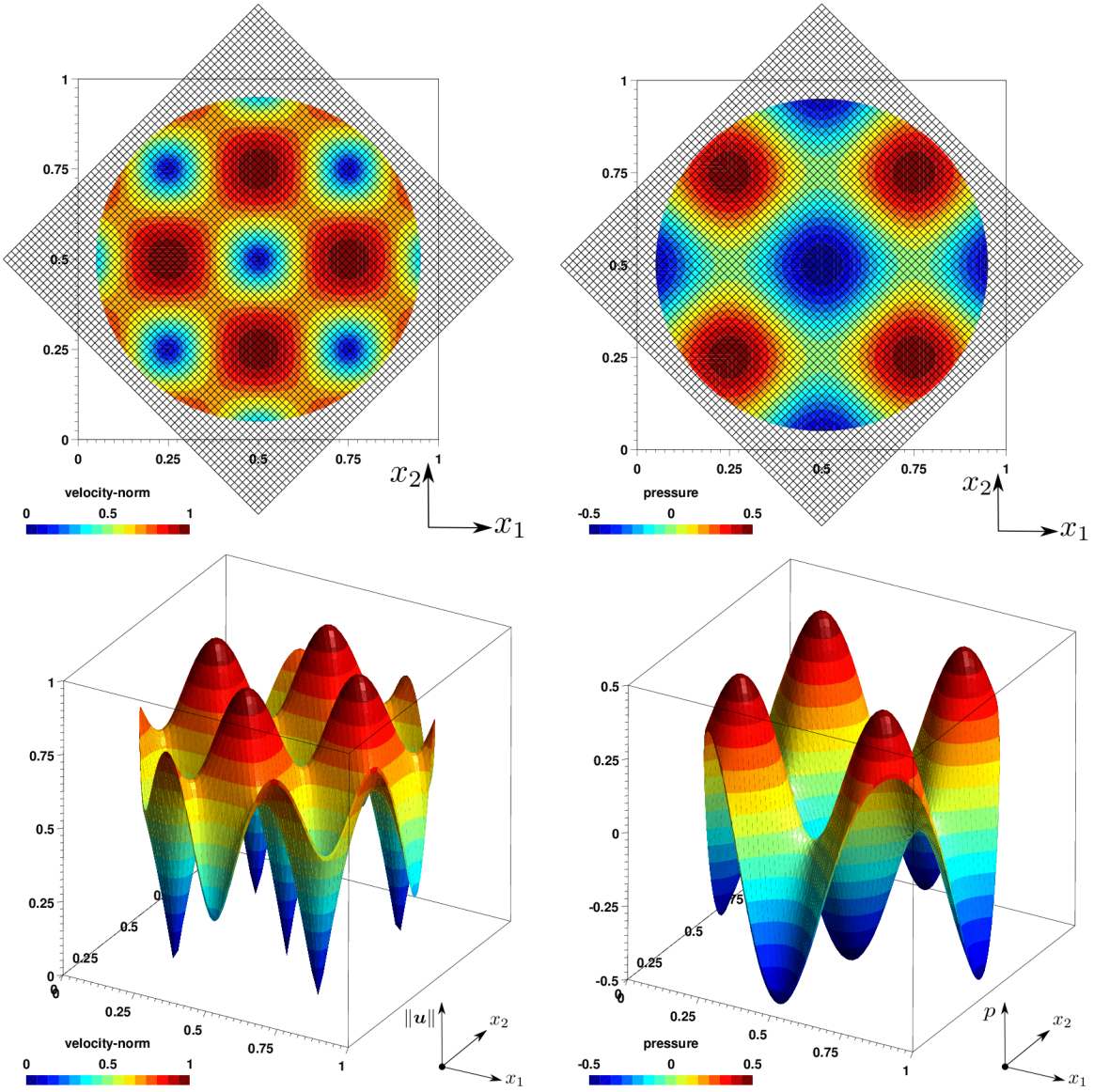

Figure 3.8: Stationary Taylor problem with $\nu = 10^{-1}$: solution $\|\boldsymbol{u}_h\|$ and p_h with 64×64 $\mathbb{Q}^1$-elements.

As the analytical solution (3.164)–(3.166) is sufficiently regular, in analogy to the linear Stokes and Oseen problems, see Burman and Hansbo [60] and Massing *et al.* [183], the following optimal convergence rates for viscous-dominant flows approximated with linearly-interpolated continuous finite elements can be expected for an optimally convergent numerical scheme:

$$\|\boldsymbol{u} - \boldsymbol{u}_h\|_\Omega = \mathcal{O}(h^2), \tag{3.169}$$
$$\|\nabla(\boldsymbol{u} - \boldsymbol{u}_h)\|_\Omega = \mathcal{O}(h), \tag{3.170}$$
$$\|p - p_h\|_\Omega = \mathcal{O}(h), \tag{3.171}$$
$$\|\nu^{1/2}(\boldsymbol{u} - \boldsymbol{u}_h)\|_{1/2,h,\Gamma} = \mathcal{O}(h), \tag{3.172}$$
$$\|\nu^{1/2}\nabla(\boldsymbol{u} - \boldsymbol{u}_h)\cdot\boldsymbol{n}\|_{-1/2,h,\Gamma} = \mathcal{O}(h), \tag{3.173}$$
$$\|\nu^{-1/2}(p - p_h)\|_{-1/2,h,\Gamma} = \mathcal{O}(h). \tag{3.174}$$

In addition to the standard bulk norms for velocity and pressure, also mesh-dependent interface norms as considered in the context of Nitsche's method in Section 3.4.2.2 are analyzed. The $H^{1/2}$-interface norm defined in (3.172) accounts for the imposition of the boundary condition. For advanced coupling algorithms, such as fluid-structure interaction, boundary fluxes on Γ are of special interest, since these are quite sensitive to perturbations and to the interface location, as already discussed in Section 3.4.2.2. For fluids, flux errors can be split into viscous and pressure parts as defined in (3.173) and (3.174).

For more detailed information on the expected convergence rates in the different flow regimes, the reader is referred to the numerical analysis part in Section 3.5, in particular to the definition of appropriate weighted graph based energy-type norms in (3.250), to the *a priori* error estimate from Theorem 3.19 and interpretations of that in Remark 3.23 and Remark 3.24.

Viscous-Dominated Flow - Convergence Study. For a higher viscosity, which here is given as $\nu = 10^{-1}\, m^2/s$ resulting in $\mathrm{Re} = 9$ based on domain diameter and maximum velocity, the flow is assumed to be steady and the time derivative $\dot{\boldsymbol{u}}$ in the Navier-Stokes equations can be omitted. The scaling factors included in (3.164)–(3.166) are set $g_u(t) = g_p(t) = 1.0$. As no convective-dominant effects are expected, additional stability measures which account for related instabilities in the interior of the domain or near the boundary can be neglected. The pressure solution and the Euclidean norm of the velocity solution obtained for a fully stabilized Nitsche-type method based on CIP and GP stabilizations are visualized for a 64×64 mesh $\widehat{\mathcal{T}}_h$ in Figure 3.8. For the velocity and pressure field, smoothness along the circular boundary Γ has to be highlighted. This is a result of the jump penalty stabilizations acting on cut faces as explained in Section 3.4.3.

For the spatial convergence study, an equal number of elements in each coordinate direction is used, i.e. $n = n_x = n_y \in \{10, 16, 24, 48, 64, 100, 160, 240\}$. Convergence results for all bulk and interface errors are shown in Figure 3.9. As can be seen, the velocity errors measured in the L^2-norm and H^1-semi-norm (Figure 3.9a, Figure 3.9b) are comparable for all different stabilization techniques and variants of imposing boundary conditions and exhibit optimal rates as expected in (3.169) and (3.170). In contrast, the pressure solution (Figure 3.9c) and the interface fluxes (Figure 3.9e, Figure 3.9f) react much more sensitive to instabilities arising from insufficient pressure or interface control of some methods. As can be seen from the pressure error, the Cauchy-stress-based Lagrange-multiplier approach exhibits a clear lack of inf-sup stability, whereas all variants of Nitsche's method lead to similar pressure errors independent of the definition of α_ν. The stability issue of Nitsche's method related to the trace inequality, as explained in Section 3.4.2, is clearly visible for a uniform element-length-based definition of $\alpha_\nu \propto \nu/h$ (blue curve in Figure 3.9e). Depending on the interface-location, the viscous flux-errors vary over a very large range as the trace estimate is not appropriately accounted for, which results in interface instabilities in particular for the so-called "sliver cut" cases. A significantly improved error behavior for viscous and pressure fluxes (Figure 3.9e and Figure 3.9f) can be observed for the stress-based Lagrange-multiplier approach and the Nitsche variant using cut-cell information $\alpha_\nu \propto \nu|\Gamma_T|/|\Omega_T|$. The close relationship between these methods has been already indicated in Section 3.4.2.3. The reduced errors of those methods compared to the uniform Nitsche scaling are due to the ensured coercivity of the elliptic part of the PDE, see (3.136), even though the energy norms or the stability constants incorporate dependencies on the interface location. This

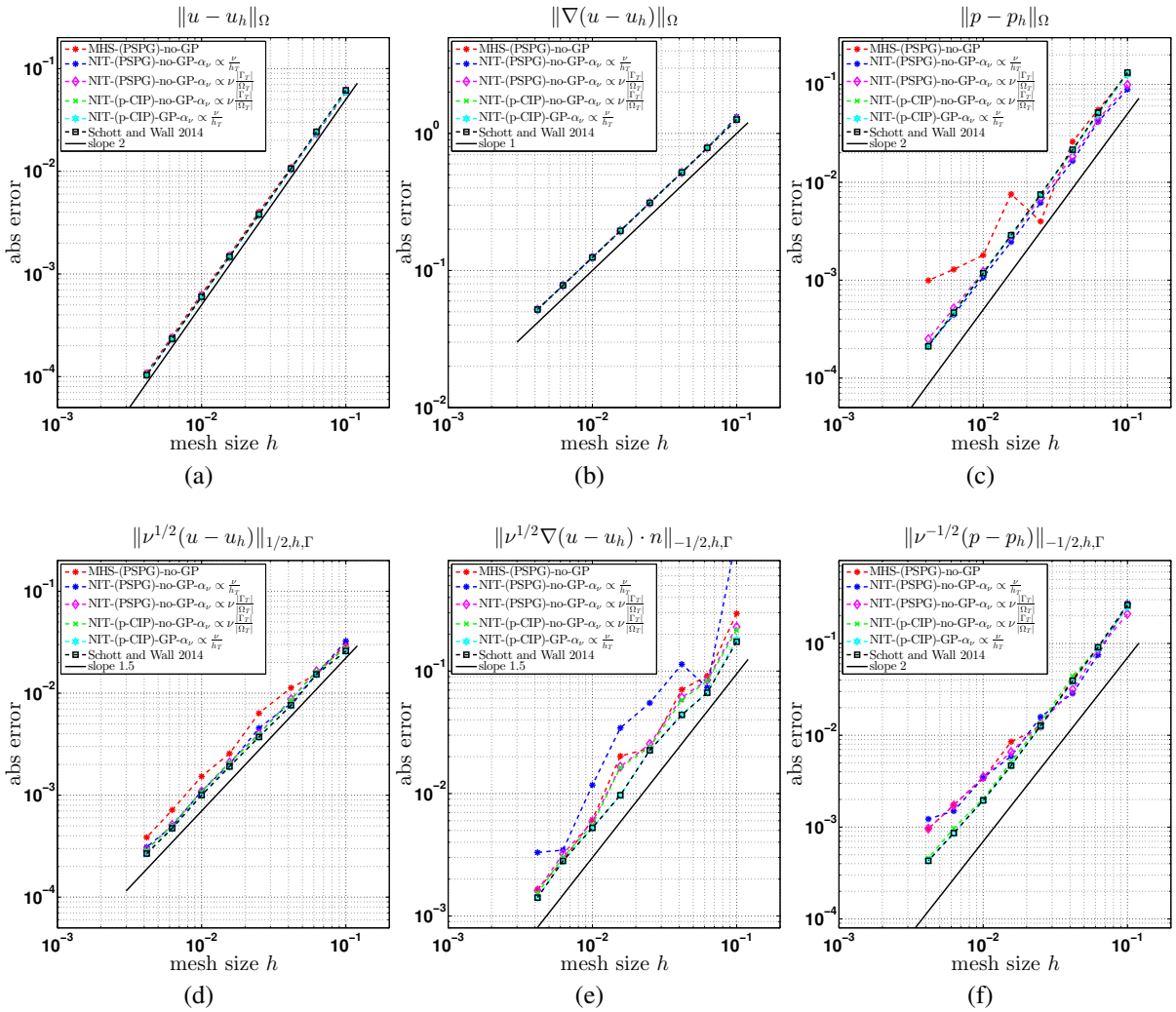

Figure 3.9: Stationary Taylor problem with $\nu = 10^{-1}$: spatial error convergence versus element length h, different norms (a)–(f). A mixed/hybrid stress-based Lagrange-multiplier approach (MHS) with PSPG pressure stabilization without ghost penalty (red). Nitsche's method (NIT) with PSPG pressure stabilization, without ghost penalty (GP) stabilization, however, with different Nitsche-penalty scalings: $\alpha_\nu \propto \nu/h$ (blue), $\alpha_\nu \propto \nu|\Gamma_T|/|\Omega_T|$ (magenta). Two variants of Nitsche's method with p-CIP pressure stabilization: without ghost penalty using a Nitsche penalty scaling $\alpha_\nu \propto \nu|\Gamma_T|/|\Omega_T|$ (green), with ghost penalty using a Nitsche penalty scaling $\alpha_\nu \propto \nu/h$ (turquoise). Stabilized method by Schott and Wall [230] (black).

manifests itself in a rather uneven error convergence for the viscous fluxes. The enforcement of the boundary conditions (Figure 3.9d) is similar for all shown variants of Nitsche's method. A clear improvement regarding the pressure fluxes can be obtained using a face-oriented pressure stabilization (p-CIP) instead of a residual-based pressure stabilization (PSPG) only. Finally, to obtain optimal error convergence independent of the interface location also for the viscous fluxes (Figure 3.9e), an additional ghost penalty stabilization for the velocity (GP) (3.162) is required. As elaborated in Section 3.4.3.4, combining this interface control with the uniform Nitsche penalty scaling, which ensures equally distributed control on the boundary condition without

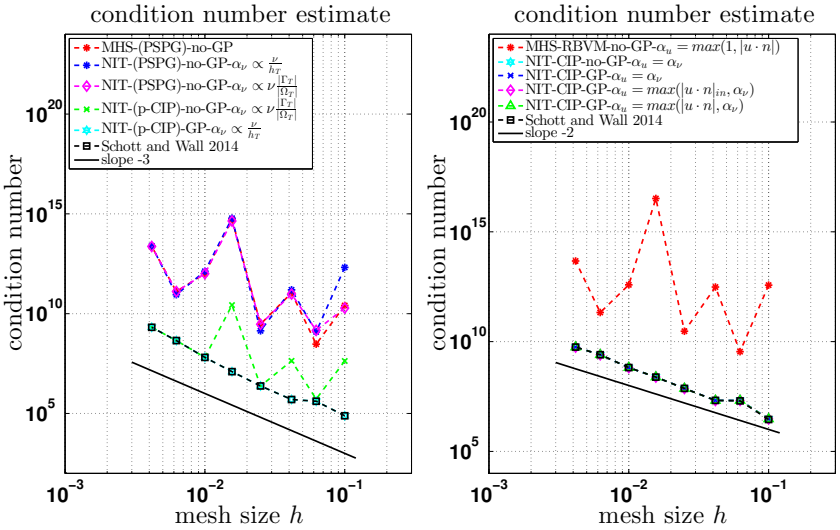

Figure 3.10: Taylor problem: condition numbers for viscous dominated flow (left) and for convective-dominated flow (right).

losing inf-sup stability, guarantees uniform optimal convergence for all considered interface error measures. Moreover, it has to be mentioned that the additional interface stabilizations (3.163) according to the convective limit and related additional CIP fluid stabilizations do not deteriorate convergence rates in the viscous regime. It has to be mentioned that the rate for the velocity interface norms (Figure 3.9d, Figure 3.9e) is half an order better than the expected rate in (3.170) and (3.171). This effect has been addressed in the work by Horger *et al.* [153]. With respect to all investigated measures, the method proposed by Schott and Wall [230] leads to optimal convergence rates independent of the interface location and to smaller error levels compared to other considered methods. Furthermore, a clear improvement of the system conditioning due to all incorporated face-jump-penalty terms next to the boundary, the GP and the CIP stabilizations for pressure and velocity, can be seen in Figure 3.10. Note that the observed suboptimal rate $\kappa = \mathcal{O}(h^{-3})$ for the conditioning in the low-Reynolds-number case instead of the optimal rate $\kappa = \mathcal{O}(h^{-2})$ is most likely due to the setup of this simulation as a pseudo-two-dimensional example approximated with one layer of three-dimensional finite elements and strong Dirichlet values for the third spatial dimension. Obviously, these negatively affect the final system conditioning. The latter formulation will be analyzed in detail in Sections 3.5 and 3.6.

Convective-Dominated Flow - Convergence Study. In addition to the study on inf-sup stability and convergence behavior of different methods for viscous-dominated flows, the following investigation serves as a preliminary study on interface instabilities which might arise in locally convective-dominated boundary regions. For the subsequent study the viscosity is $\nu = 10^{-4}\, m^2/s$ and the transient incompressible Navier-Stokes equations are solved for $t \in [0, T]$ with $T = 0.1\, s$ and $\Delta t = 0.01\, s$. The time-dependent scaling factors are now chosen as

$$g_u(t) = \exp(-2a^2\pi^2\nu t) \quad \text{and} \quad g_p(t) = \exp(-4a^2\pi^2\nu t) \tag{3.175}$$

and indicate an exponential decay of the initial flow field. In the following, the stabilized Nitsche-type method by Schott and Wall [230] is applied, which includes all CIP fluid stabiliza-

tions for velocity and pressure proposed in Section 3.1.3.2. In the interface zone, these terms act like ghost penalties when jump penalties are evaluated on the entire cut faces. In this study, the influence of different contributions to the Nitsche penalty term in (3.163) is investigated. For the temporal discretization, a backward Euler scheme is applied. Errors are evaluated at final time T and plotted against the element length h for different methods and variants in Figure 3.11. The first curve shows the error behavior for the Cauchy-stress-based Lagrange-multiplier approach (MHS) from [123] supported by an additional Nitsche-like penalty term with convective scalings from (3.163). For Nitsche's method (NIT) different definitions for α_u are compared: the second and third curves show results without and with the viscous ghost penalty (GP) operator (3.162), however, both variants without any additional convective or penalty contributions from (3.163). Curve four shows the variant with additional convective stabilizations active only at inflow parts $|\boldsymbol{u}_h \cdot \boldsymbol{n}|_{\text{in}}$ where $\boldsymbol{u}_h \cdot \boldsymbol{n} < 0$. The fifth curve activates the convective stabilization term also at outflow parts and the last curve shows results of a stabilized formulation based on the full parameter definition (3.163) from [230] which sufficiently accounts for mass conservation even for convective-dominant flows.

Within the domain, for almost all variants optimal error convergence can be observed in Figures 3.11a–3.11c, except for the mixed/hybrid Cauchy-stress-based method that lacks pressure stability. Similar to the viscous case, for the interface errors again convergence rates are obtained better than expected, see (3.172)–(3.174). The influence of the different convective stabilization variants is clearly visible from the boundary condition errors (Figure 3.11d) and the flux errors (Figure 3.11e). Missing convective interface stabilizations compared to (3.163) lead to increased interfacial errors, especially for coarse meshes, as those exhibit higher local element Reynolds numbers. Balancing these convective interface instabilities by appropriate scalings for the Nitsche penalty term, a clear improvement of the stability and accuracy can be observed. Best results are obtained when adding additional control on the mass conservation, here specified by the safety factor of 1.0 from (3.163), which corresponds to $\|\boldsymbol{\beta}\|$ in the scaling (3.467), see Section 3.6. This ensures uniform penalty on the boundary condition for convective-dominated flows. For a closer understanding of the different scalings, the reader is referred to the numerical analysis of a CutFEM for the Oseen problem in Section 3.5.

It needs to be mentioned that for convective-dominated flows the ghost penalty control of the velocity field is overtaken by the face-oriented CIP stabilizations (3.29) and (3.30). These additionally ensure streamline and incompressibility control. Replacing CIP fluid stabilizations by a purely residual-based RBVM approach (PSPG/SUPG/LSIC) results in no or poor convergence of the Newton-scheme. This behavior indicates an unstable configuration as no control over ghost values can be retained. Note that in this case the viscous ghost penalty term (3.162) is not sufficient anymore owing to the too small scaling $\nu \ll |\boldsymbol{u}_h| h$. However, combinations of the RBVM stabilization in the domain Ω supported by CIP/GP stabilizations, which need to be activated in the boundary zone only, can render formulations stable, as will be investigated later in Section 3.6.1.2.

A comparison of estimated condition numbers for the different investigated methods is shown in Figure 3.10. The improvement for CIP/GP stabilized methods is clearly visible. This is caused by the aforementioned fact that face-jump-penalty terms are integrated along the entire intersected faces, see also elaborations in Section 3.4.3. Note that for similar reason as for the viscous case, again a suboptimal rate $\kappa = \mathcal{O}(h^{-2})$ compared to the expected rate of $\kappa = \mathcal{O}(h^{-1})$ was obtained for the conditioning. The gain of one power of h compared to the viscous case, however, could be confirmed.

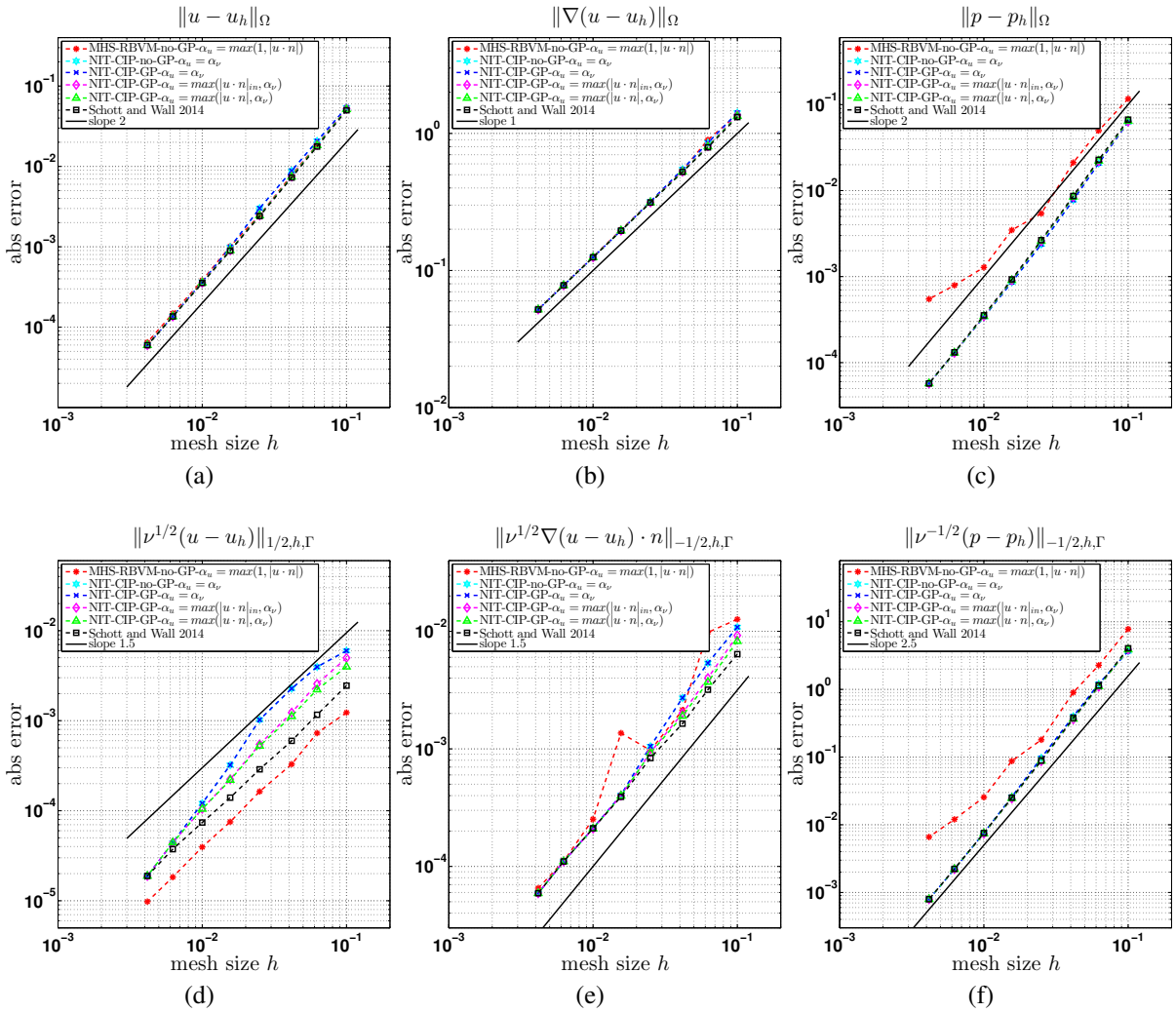

Figure 3.11: Instationary Taylor problem with $\nu = 10^{-4}$ at time $T = 0.1\,s$ with $\Delta t = 0.01\,s$: spatial error convergence versus element length h, different norms (a)–(f). A residual-based stabilized (RBVM) mixed/hybrid stress-based Lagrange-multiplier approach (MHS) with additional convective stabilization (red), Nitsche's method (NIT) with face-oriented stabilization (CIP) (without ghost penalty (GP) and only viscous part of α_u (turquoise), additional ghost penalty (blue), additional convective inflow interface stabilization on Γ_{in} (magenta), convective interface stabilization on whole Γ (green), Schott and Wall [230] (black)).

3.4.4.3 Nitsche's Method - Studies on the Penalty Parameters

The following studies aim at investigating the sensitivity of Nitsche-type methods with regard to inf-sup stability and accuracy depending on the Nitsche penalty parameter γ in (3.163) and the viscous ghost-penalty parameter γ_ν in (3.162).

Inf-Sup Stability of a Symmetric Nitsche Method Depending on the Penalty Parameter γ. The influence of the Nitsche parameter γ is tested for viscous flows such that $\gamma\nu/h$ plays the dominating part in the definition of α_u in (3.163). The convective contributions therein can be neglected, i.e. $\alpha_u = \gamma\nu/h$. For this purpose norms (3.169)–(3.174) are calculated for a wide

range of $\gamma \in \{5, 7, 10, 20, 35, 50, 100, 500, 1000, 10000\}$. All simulations are run with a fixed ghost-penalty parameter $\gamma_\nu = 0.01$. Results are shown in Figure 3.12 for three different meshes with $n \in \{16, 64, 240\}$.

Bulk errors for velocity and pressure are almost constant over a wide range of γ (Figure 3.12a-Figure 3.12c). Slightly increasing L^2-errors for the pressure can be observed for parameters $\gamma > 100$. Values of $\gamma < 10$ indicate the expected instability of a symmetric Nitsche method. This can be seen for all considered (semi-)norms and is more distinctive for interface errors. For all analyzed meshes, decreasing interface errors can be observed for increasing γ up to $\gamma \approx 20$. Between $\gamma = 20$ and $\gamma = 50$ a clear minimum of the viscous flux errors (Figure 3.12e) as well as a plateau for the boundary condition error (Figure 3.12d) can be identified. The latter one could be further reduced using a stronger penalty effect of $\gamma > 100$ which, however, results in large viscous flux errors. Moreover, the pressure-flux errors monotonously increase, the larger γ is chosen (Figure 3.12f). Qualitatively comparable error behavior for all considered mesh sizes indicates the appropriate scaling $\alpha_\nu \propto 1/h_K$ as obtained from the analysis. If not indicated otherwise, for all simulations throughout the rest of this work the Nitsche parameter is chosen equal to $\gamma = 35.0$. Choosing the stabilization parameter γ in this range ensures inf-sup stability as well as accurate results within the bulk and in the vicinity of the boundary.

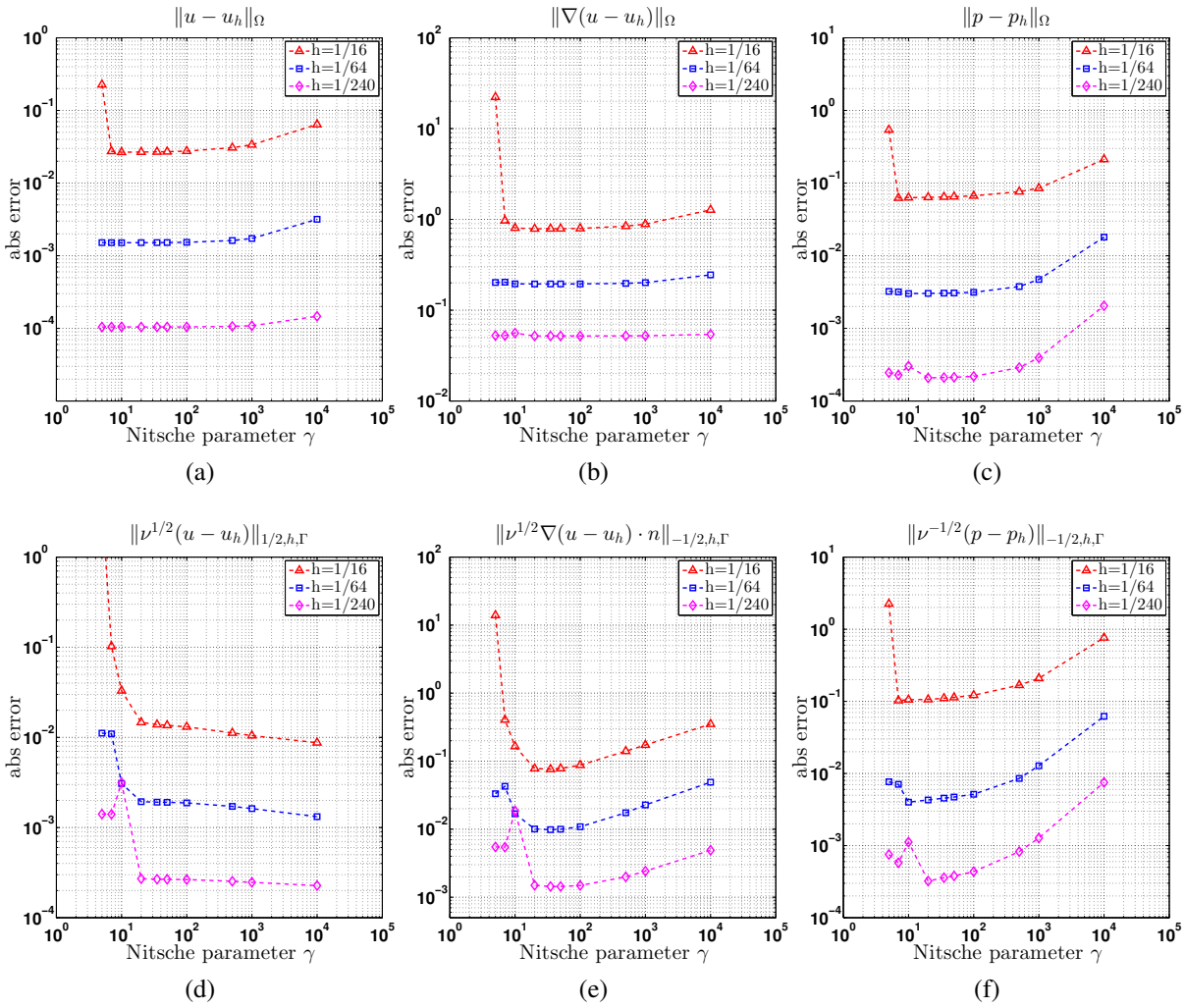

Figure 3.12: Stationary Taylor problem with $\nu = 10^{-1}$ and fixed $\gamma_\nu = 0.01$: error behavior for varying Nitsche parameter γ.

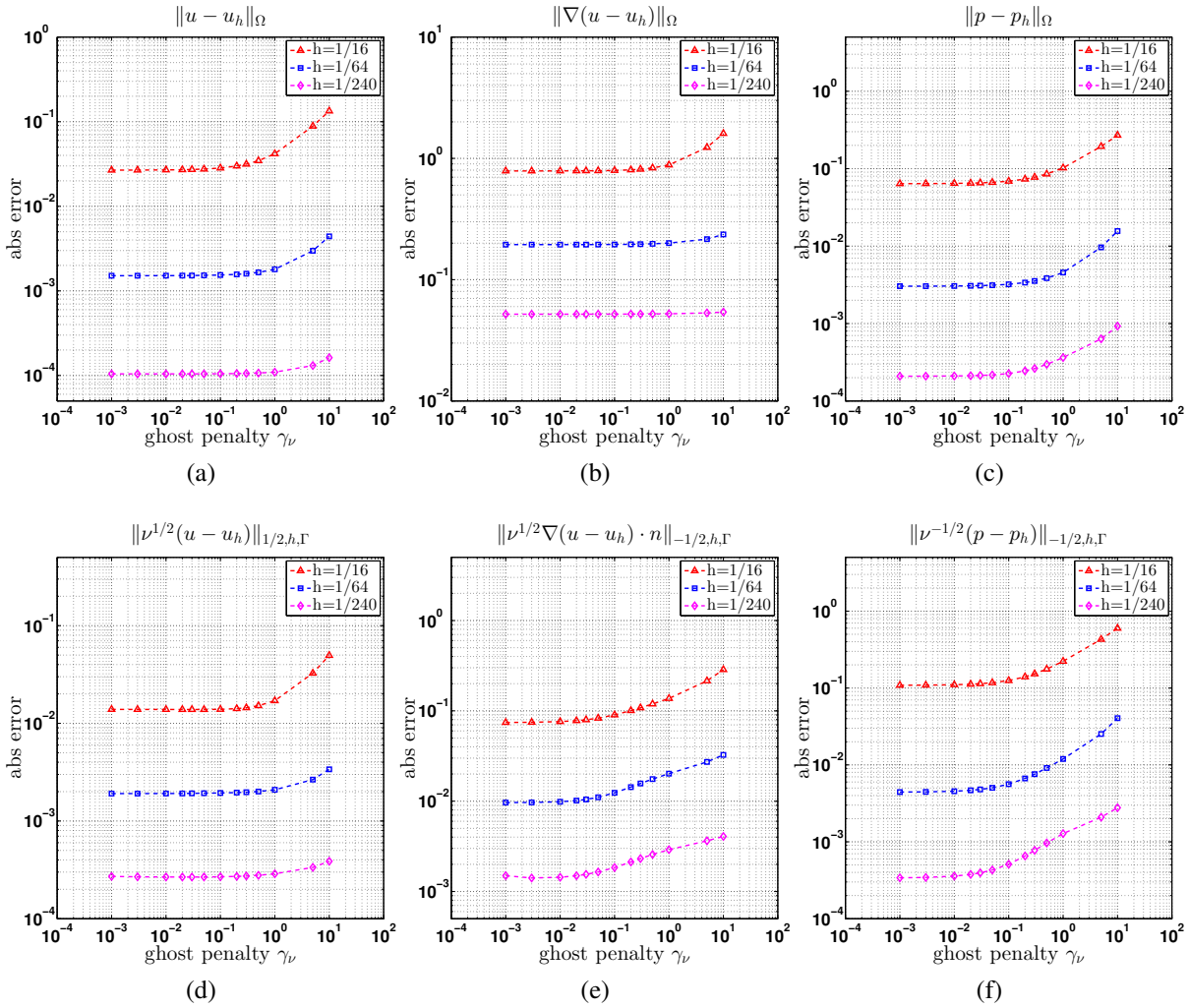

Figure 3.13: Stationary Taylor problem with $\nu = 10^{-1}$ and fixed $\gamma = 35.0$: error behavior for varying ghost-penalty parameter γ_ν.

Influence of the Ghost Penalty Stabilization Parameter γ_ν. A similar study for the ghost penalty parameter γ_ν from (3.162) is presented next. To ensure stability, the Nitsche penalty parameter is set unchanged equal to $\gamma = 35.0$. Again, studies are presented for three different grid sizes $h = 1/n$ with $n \in \{16, 64, 240\}$ using a varying ghost-penalty parameter within a reasonable range of $\gamma_\nu \in [0.001, 10]$. Results are shown in Figure 3.13.

For all considered values of γ_ν results are stable. While the domain errors for the velocity (Figure 3.13a, Figure 3.13b) as well as the boundary condition enforcement (Figure 3.13d) remain almost unaffected for $\gamma_\nu < 0.5$, the pressure L^2-norm error (Figure 3.13c) increases already for $\gamma_\nu > 0.1$. As expected, most sensitive measures regarding the interface position but also regarding artificial penalty effects are the boundary fluxes. A negative influence of the ghost-penalty stabilization on the viscous fluxes (Figure 3.13e) and the pressure fluxes (Figure 3.13f) can be observed already for $\gamma_\nu > 0.05$. From this study it is recommended to choose the ghost-penalty parameter γ_ν within a moderate range of $[0.01, 0.05]$, which coincides with recommended values for CIP fluid stabilizations, see Section 3.1.3.2.

3.5 A Cut Finite Element Method for Oseen's Problem - A Numerical Analysis

In this section, a stabilized Nitsche-type CUTFEM for a linear model problem of the non-linear incompressible Navier-Stokes equations, the so-called Oseen problem, is proposed. It serves as linear auxiliary problem for the theoretical analysis and numerical convergence studies proposed within the next sections. Therein, the technique of CIP fluid stabilizations introduced in Section 3.1.3.2 is recalled and adapted to unfitted meshes. The need for additional ghost-penalty stabilizations in the vicinity of the boundary zone for flows with low and high Reynolds numbers is discussed. After introducing fundamentals on the Oseen equations in Section 3.5.1, the stabilized CUTFEM will be proposed in Section 3.5.2 and major differences to the classical CIP method by Burman *et al.* [48] for fitted meshes will be pointed out. Sections 3.5.5 and 3.5.6 are devoted to the stability and *a priori* error analysis of the proposed method. Therein, main focus is directed to stability and optimality in all flow regimes. Finally, in Section 3.5.7 theoretical results of the provided analysis are confirmed by two- and three-dimensional test cases. Extensions of this CUTFEM to the transient incompressible Navier-Stokes equations with stationary and moving boundaries are proposed in Section 3.6 afterwards. Elaborations and the numerical analysis provided next are based on work by Massing *et al.* [183].

3.5.1 Oseen's Equations - A Linear Model Problem

In the following, a linear auxiliary problem is introduced which serves as a model problem for the non-linear incompressible Navier-Stokes equations, the *generalized Oseen problem*. It is well known that finite-element-based approximation techniques to the solution of the weak form of the Navier-Stokes equations (3.9) suffer from different instabilities which are introduced by spatial discretization schemes. Thereby, the numerical analysis of discrete formulations simplifies when linearized problems are considered, while most of the numerical issues remain. A standard numerical treatment of such transient non-linear problems consists in semi-discretizing the problem formulation in time via time-stepping methods and approximating the non-linearity within each time step by a sequence of fix-point Picard iterations or Newton-like iterative schemes until convergence between iterations is reached. Such auxiliary problems are often of Oseen type which in their strong form are governed by the following system of equations:

$$\sigma \boldsymbol{u} + (\boldsymbol{\beta} \cdot \nabla)\boldsymbol{u} - \nabla \cdot (2\nu \boldsymbol{\epsilon}(\boldsymbol{u})) + \nabla p = \boldsymbol{f} \qquad \text{in } \Omega, \tag{3.176}$$

$$\nabla \cdot \boldsymbol{u} = 0 \qquad \text{in } \Omega, \tag{3.177}$$

$$\boldsymbol{u} = \boldsymbol{g}_{\mathrm{D}} \qquad \text{on } \Gamma, \tag{3.178}$$

$$\textstyle\int_{\Omega} p = 0. \tag{3.179}$$

The Oseen equations are defined in an open and bounded domain $\Omega \subset \mathbb{R}^d$, $d = 2, 3$ with Lipschitz boundary $\Gamma = \partial\Omega$. For simplicity with regard to the numerical analysis, a pure Dirichlet problem setting, i.e. $\Gamma_{\mathrm{N}} = \emptyset$ and $\Gamma \equiv \Gamma_{\mathrm{D}}$, with boundary data $\boldsymbol{g}_{\mathrm{D}} \in [H^{1/2}(\Gamma)]^d$ is considered. Additionally, the pressure is constrained to exhibit a zero mean average. Stabilized discrete formulations can be easily extended to boundary value problems with $\Gamma_{\mathrm{N}} \neq \emptyset$ by applying

standard techniques, as will be shown in Section 3.6. To shorten the notation, compared to the Navier-Stokes system the constant density ρ is omitted. The Oseen-type momentum equation is comprised of a (pseudo-)reactive part with reaction coefficient $\sigma > 0$ that usually arises from temporal discretization of the time derivative $\partial_t \boldsymbol{u}$ with a finite difference based scheme, an elliptic term $\nabla \cdot (2\nu\boldsymbol{\epsilon}(\boldsymbol{u}))$ with kinematic viscosity $\nu = \mu/\rho > 0$ and a volumetric force term $\boldsymbol{f} \in [L^2(\Omega)]^d$. The non-linear convective term in the Navier-Stokes equations is linearized to an advective term $(\boldsymbol{\beta} \cdot \nabla)\boldsymbol{u}$ with advective velocity field $\boldsymbol{\beta} \in \mathbb{R}^d$, which is assumed to be independent of the flow $\boldsymbol{u}$ and solenoidal, i.e. $\nabla \cdot \boldsymbol{\beta} = 0$. Even the steady-state Navier-Stokes equations can be approximated with the Oseen problem by setting $\sigma \equiv 0$, provided that viscous flow effects dominate over advective transport, i.e. $\|\boldsymbol{\beta}\|_{0,\infty,\Omega} L < \nu$.

The weak formulation of the Oseen problem (3.176)–(3.179) is related to (3.9) and reads: find the velocity and the pressure field $(\boldsymbol{u}, p) \in \mathcal{V}_{g_\mathrm{D}} \times \mathcal{Q} = [H^1_{g_\mathrm{D}}(\Omega)]^d \times L^2_0(\Omega)$ such that

$$a(\boldsymbol{u}, \boldsymbol{v}) + b(p, \boldsymbol{v}) - b(q, \boldsymbol{u}) = l(\boldsymbol{v}) \quad \forall\, (\boldsymbol{v}, q) \in \mathcal{V}_{\boldsymbol{0}} \times \mathcal{Q}, \tag{3.180}$$

where

$$a(\boldsymbol{u}, \boldsymbol{v}) \overset{\text{def}}{=} (\sigma \boldsymbol{u}, \boldsymbol{v})_\Omega + ((\boldsymbol{\beta} \cdot \nabla)\boldsymbol{u}, \boldsymbol{v})_\Omega + (2\nu\boldsymbol{\epsilon}(\boldsymbol{u}), \boldsymbol{\epsilon}(\boldsymbol{v}))_\Omega, \tag{3.181}$$

$$b(p, \boldsymbol{v}) \overset{\text{def}}{=} -(p, \nabla \cdot \boldsymbol{v})_\Omega, \tag{3.182}$$

$$l(\boldsymbol{v}) \overset{\text{def}}{=} (\boldsymbol{f}, \boldsymbol{v})_\Omega. \tag{3.183}$$

Similar to the non-linear incompressible Navier-Stokes equations, a standard Galerkin finite element approximation for velocity and pressure to the Oseen problem (3.180) suffers from different sources of instabilities:

- it leads to unphysical oscillations in the numerical solution and sub-optimal error estimates in the case of locally convection-dominant flow, i.e. $\mathrm{Re}_T \gg 1$ for $T \in \mathcal{T}_h$,
- due to the saddle-point structure and the use of equal-order interpolation spaces in the definition of $\mathcal{V}_h \subset \mathcal{V}$ and $\mathcal{Q}_h \subset \mathcal{Q}$, the resulting discretization violates the discrete inf-sup condition and thus is not stable in the sense of Babuška–Brezzi [36], and
- to impose Dirichlet boundary conditions weakly, consistent stabilization terms at the boundary Γ, which guarantee stability and optimal error estimates in the low- as well as in the high-Reynolds-number regime, are required.

Compared to the full Navier-Stokes system, the complexity of the numerical analysis is reduced for Oseen's system of equations: first, due to the linearity with respect to the velocity field $\boldsymbol{u}$ and, second, due to the higher regularity assumption on $\boldsymbol{\beta}$ which is not guaranteed for the discrete convective velocity $\boldsymbol{u}_h \in \mathcal{V}_h$. Furthermore, the assumption $\nabla \cdot \boldsymbol{\beta} = 0$ almost everywhere (a.e.) in Ω is not satisfied in general for the discrete velocity, i.e. $\nabla \cdot \boldsymbol{u}_h \neq 0$. The well-posedness and solvability of the continuous problem (3.180) is well-known (see, for instance, the textbooks by Girault and Raviart [127] and Roos *et al.* [222]).

3.5.2 A Nitsche-type CIP/GP Cut Finite Element Method

The presentation of the discrete stabilized formulation with cut finite element meshes relies on generalized notation on CutFEMs introduced in Sections 2.1.4.1 and 2.2.2 and utilizes stabilization operators introduced in the context of CIP and GP stabilizations in Sections 3.1.3.2 and 3.4.3. Moreover, throughout the subsequent numerical analysis, computational meshes are assumed to fulfill geometric assumption (G1)–(G3) as provided in Section 3.2.1. Discrete continuous cut finite element function spaces

$$\mathscr{X}_h \overset{\text{def}}{=} \left\{ v_h \in C^0(\Omega_h^*) : v_h|_T \in \mathbb{P}^k(T) \,\forall\, T \in \mathscr{T}_h \right\} \tag{3.184}$$

defined therein as well as their vector-valued equivalents are basis for the discrete approximation spaces of velocity and pressure, which are assumed to be interpolated with equal order, i.e.

$$\mathscr{V}_h \overset{\text{def}}{=} [\mathscr{X}_h^k]^d, \qquad \mathscr{Q}_h \overset{\text{def}}{=} \mathscr{X}_h^k, \qquad \mathscr{W}_h \overset{\text{def}}{=} \mathscr{V}_h \times \mathscr{Q}_h. \tag{3.185}$$

For these function spaces, approximation properties introduced in Section 3.2.2 hold.

Starting from the continuous weak formulation (3.180)–(3.183), a possible discrete cut finite element formulation of the Oseen problem including Nitsche-type weak enforcement of Dirichlet-type boundary conditions, CIP-type fluid stabilizations in the interior of the domain and boundary-zone GP stabilizations reads as follows:

Definition 3.12 (Nitsche-type CIP/GP-CutFEM for Oseen's problem)
Find velocity and pressure $U_h = (\boldsymbol{u}_h, p_h) \in \mathscr{V}_h \times \mathscr{Q}_h$ *such that for all* $V_h = (\boldsymbol{v}_h, q_h) \in \mathscr{V}_h \times \mathscr{Q}_h$

$$\mathscr{A}_h^{\text{CIP/GP}}(U_h, V_h) = \mathscr{L}_h^{\text{CIP/GP}}(V_h), \tag{3.186}$$

where

$$\mathscr{A}_h^{\text{CIP/GP}}(U_h, V_h) \overset{def}{=} (\mathscr{B}_h + \mathscr{S}_h^{\text{CIP}} + \mathscr{G}_h^{\text{GP}})((\boldsymbol{u}_h, p_h), (\boldsymbol{v}_h, q_h)), \tag{3.187}$$

$$\mathscr{L}_h^{\text{CIP/GP}}(V_h) \overset{def}{=} \mathscr{L}_h(\boldsymbol{v}_h, q_h) \tag{3.188}$$

with

$$\mathscr{B}_h((\boldsymbol{u}_h, p_h), (\boldsymbol{v}_h, q_h)) = a_h(\boldsymbol{u}_h, \boldsymbol{v}_h) + b_h(p_h, \boldsymbol{v}_h) - b_h(q_h, \boldsymbol{u}_h), \tag{3.189}$$

$$\mathscr{S}_h^{\text{CIP}}((\boldsymbol{u}_h, p_h), (\boldsymbol{v}_h, q_h)) = (s_\beta + s_u + s_p)((\boldsymbol{u}_h, p_h), (\boldsymbol{v}_h, q_h)), \tag{3.190}$$

$$\mathscr{G}_h^{\text{GP}}((\boldsymbol{u}_h, p_h), (\boldsymbol{v}_h, q_h)) = (g_\beta + g_u + g_p + g_\nu + g_\sigma)((\boldsymbol{u}_h, p_h), (\boldsymbol{v}_h, q_h)), \tag{3.191}$$

$$\begin{aligned} \mathscr{L}_h(\boldsymbol{v}_h, q_h) = {} & (\boldsymbol{f}, \boldsymbol{v}_h) - \langle (\boldsymbol{\beta} \cdot \boldsymbol{n}) \boldsymbol{g}_{\text{D}}, \boldsymbol{v}_h \rangle_{\Gamma_{\text{in}}} \\ & \mp \langle \boldsymbol{g}_{\text{D}}, 2\nu \boldsymbol{\epsilon}(\boldsymbol{v}_h) \boldsymbol{n} \rangle_\Gamma + \langle \gamma(\nu/h) \boldsymbol{g}_{\text{D}}, \boldsymbol{v}_h \rangle_\Gamma \\ & - \langle \boldsymbol{g}_{\text{D}} \cdot \boldsymbol{n}, q_h \rangle_\Gamma + \langle \gamma(\phi/h) \boldsymbol{g}_{\text{D}} \cdot \boldsymbol{n}, \boldsymbol{v}_h \cdot \boldsymbol{n} \rangle_\Gamma. \end{aligned} \tag{3.192}$$

The Dirichlet-type boundary condition (3.178) is imposed weakly using a Nitsche-type method, which results in additional boundary terms to the standard Galerkin formulation

$$\begin{aligned} a_h(\boldsymbol{u}_h, \boldsymbol{v}_h) = {} & (\sigma \boldsymbol{u}_h, \boldsymbol{v}_h)_\Omega + ((\boldsymbol{\beta} \cdot \nabla) \boldsymbol{u}_h, \boldsymbol{v}_h)_\Omega - \langle (\boldsymbol{\beta} \cdot \boldsymbol{n}) \boldsymbol{u}_h, \boldsymbol{v}_h \rangle_{\Gamma_{\text{in}}} \\ & + (\boldsymbol{\epsilon}(\boldsymbol{u}_h), 2\nu \boldsymbol{\epsilon}(\boldsymbol{v}_h))_\Omega - \langle 2\nu \boldsymbol{\epsilon}(\boldsymbol{u}_h) \boldsymbol{n}, \boldsymbol{v}_h \rangle_\Gamma \mp \langle \boldsymbol{u}_h, 2\nu \boldsymbol{\epsilon}(\boldsymbol{v}_h) \boldsymbol{n} \rangle_\Gamma \\ & + \langle \gamma(\nu/h) \boldsymbol{u}_h, \boldsymbol{v}_h \rangle_\Gamma + \langle \gamma(\phi/h) \boldsymbol{u}_h \cdot \boldsymbol{n}, \boldsymbol{v}_h \cdot \boldsymbol{n} \rangle_\Gamma, \end{aligned} \tag{3.193}$$

$$b_h(p_h, \boldsymbol{v}_h) = -(p_h, \nabla \cdot \boldsymbol{v}_h)_\Omega + \langle p_h, \boldsymbol{v}_h \cdot \boldsymbol{n} \rangle_\Gamma, \tag{3.194}$$

with $\Gamma_{\text{in}} = \{\boldsymbol{x} \in \Gamma : (\boldsymbol{\beta} \cdot \boldsymbol{n})(\boldsymbol{x}) < 0\}$. CIP *stabilization terms are as defined in Section 3.1.3.2*

$$s_\beta(\boldsymbol{u}_h, \boldsymbol{v}_h) = \gamma_\beta \sum_{F \in \mathcal{F}_i} \phi_{\beta,F} h \langle [\![(\boldsymbol{\beta}_h \cdot \nabla)\boldsymbol{u}_h]\!], [\![(\boldsymbol{\beta}_h \cdot \nabla)\boldsymbol{v}_h]\!] \rangle_F, \tag{3.195}$$

$$s_u(\boldsymbol{u}_h, \boldsymbol{v}_h) = \gamma_u \sum_{F \in \mathcal{F}_i} \phi_{u,F} h \langle [\![\nabla \cdot \boldsymbol{u}_h]\!], [\![\nabla \cdot \boldsymbol{v}_h]\!] \rangle_F, \tag{3.196}$$

$$s_p(p_h, q_h) = \gamma_p \sum_{F \in \mathcal{F}_i} \phi_{p,F} h \langle [\![\nabla p_h]\!], [\![\nabla q_h]\!] \rangle_F. \tag{3.197}$$

As a last ingredient to formulate a CIP*-based* CutFEM *for the Oseen problem on unfitted meshes, different ghost penalties (*GP*) for velocity and pressure are required*

$$g_\beta(\boldsymbol{u}_h, \boldsymbol{v}_h) = \gamma_\beta \sum_{F \in \mathcal{F}_\Gamma} \sum_{0 \leqslant j \leqslant k-1} \phi_{\beta,F} h^{2j+1} \langle [\![(\boldsymbol{\beta}_h \cdot \nabla)\partial_{\boldsymbol{n}}^j \boldsymbol{u}_h]\!], [\![(\boldsymbol{\beta}_h \cdot \nabla)\partial_{\boldsymbol{n}}^j \boldsymbol{v}_h]\!] \rangle_F, \tag{3.198}$$

$$g_u(\boldsymbol{u}_h, \boldsymbol{v}_h) = \gamma_u \sum_{F \in \mathcal{F}_\Gamma} \sum_{0 \leqslant j \leqslant k-1} \phi_{u,F} h^{2j+1} \langle [\![\nabla \cdot \partial_{\boldsymbol{n}}^j \boldsymbol{u}_h]\!], [\![\nabla \cdot \partial_{\boldsymbol{n}}^j \boldsymbol{v}_h]\!] \rangle_F, \tag{3.199}$$

$$g_p(p_h, q_h) = \gamma_p \sum_{F \in \mathcal{F}_\Gamma} \sum_{1 \leqslant j \leqslant k} \phi_{p,F} h^{2j-1} \langle [\![\partial_{\boldsymbol{n}}^j p_h]\!], [\![\partial_{\boldsymbol{n}}^j q_h]\!] \rangle_F, \tag{3.200}$$

$$g_\nu(\boldsymbol{u}_h, \boldsymbol{v}_h) = \gamma_\nu \sum_{F \in \mathcal{F}_\Gamma} \sum_{1 \leqslant j \leqslant k} \nu h^{2j-1} \langle [\![\partial_{\boldsymbol{n}}^j \boldsymbol{u}_h]\!], [\![\partial_{\boldsymbol{n}}^j \boldsymbol{v}_h]\!] \rangle_F, \tag{3.201}$$

$$g_\sigma(\boldsymbol{u}_h, \boldsymbol{v}_h) = \gamma_\sigma \sum_{F \in \mathcal{F}_\Gamma} \sum_{1 \leqslant j \leqslant k} \sigma h^{2j+1} \langle [\![\partial_{\boldsymbol{n}}^j \boldsymbol{u}_h]\!], [\![\partial_{\boldsymbol{n}}^j \boldsymbol{v}_h]\!] \rangle_F. \tag{3.202}$$

Included piecewise constant scaling functions $\phi, \phi_\beta, \phi_u, \phi_p$ *are recalled from Section 3.1.3.2 as*

$$\phi_T = \nu + c_u(\|\boldsymbol{\beta}^*\|_{0,\infty,T} h_T) + c_\sigma(\sigma h_T^2), \quad \phi_{\beta,T} = \phi_{p,T} = h_T^2 \phi_T^{-1}, \quad \phi_{u,T} = \phi_T, \tag{3.203}$$

where for the respective face averages it is written $\phi_{\beta,F}$, $\phi_{u,F}$, *and* $\phi_{p,F}$.

For the choice of CIP *stabilization parameters it is referred to Section 3.1.3.2. Equivalent parameters are used for related ghost-penalty terms (3.198)–(3.200). As studied in Section 3.4.4.3, it is chosen* $\gamma = 35.0$ *for the Nitsche-penalty terms and* $\gamma_\nu = \gamma_\beta = \gamma_p$ *for the viscous ghost-penalty term (3.201). The (pseudo-)reactive ghost-penalty term (3.202), however, is scaled with a considerably smaller value of* $\gamma_\sigma = 0.05\gamma_\nu$. *Assumptions on the functions* $\boldsymbol{\beta}^*$ *and* $\boldsymbol{\beta}_h$ *in the boundary zone are specified below in Section 3.5.3. Note that to shorten the presentation, the scalings* c_u, c_σ *in the definition of* ϕ *(3.203) are set to* 1.0 *throughout the numerical analysis.*

Remark 3.9 *Note that the classical* CIP *method by Burman* et al. *[48] was introduced on fitted meshes and that only the gradient and no higher-order derivatives are penalized. That is, for fitted meshes, all ghost-penalty terms comprised in operator* $\mathcal{G}_h^{\text{GP}}$ *can be neglected. The control on higher-order derivatives is only required to overcome stability and ill-conditioning issues in the vicinity of the boundary on unfitted meshes, as elaborated in Section 3.4.*

Remark 3.10 *Note that for low-order linear approximations, i.e.* $\mathbb{P}^1$, *the* GP *stabilizations (3.198)–(3.200) reduce to the* CIP *stabilizations (3.195)–(3.197). In this case, fitted and unfitted formulations only differ in the additional terms* g_ν, g_σ. *It has to be mentioned that these are of the same type and only differ in their parameters and* h*-scalings. The different ghost-penalty terms in (3.198)–(3.202) are presented separately just to point out their respective meaning throughout the analysis. For implementations, however, several terms are of the same type and only exhibit different effective scaling functions. On this topic, see also alternative formulations for* s_β *and* s_u *discussed in Section 3.1.3.2.*

Remark 3.11 *The different orders of derivatives appearing in the ghost-penalty operators introduced in* (3.198)–(3.202) *can be scaled differently. In this work, second-order derivatives occurring in terms* (3.198)–(3.202) *are scaled with* $\gamma^{\text{2nd}} = 0.05\gamma^{\text{1st}}$ *for all relevant numerical simulations.*

Remark 3.12 *Compared to Nitsche's method for the Poisson problem, as introduced in Section 3.4.3.4, locally high-Reynolds-number flows require to weaken the fulfillment of the wall-tangential parts of the Dirichlet constraint* (3.178)*, but still to preserve mass conservation in the convective limit, i.e.* $\boldsymbol{u} \cdot \boldsymbol{n} = \boldsymbol{g}_{\text{D}} \cdot \boldsymbol{n}$ *for* $\nu \ll \|\boldsymbol{\beta}\|_{0,\infty,T} h_T$*. Note that this adjustment between the different mesh-related flow regimes is provided by the scaling* ϕ *in the mass conserving Nitsche penalty term and by the different adjoint boundary terms in* (3.193)–(3.194)*.*

Remark 3.13 *Note that the different signs* ($\mp$) *in* (3.192) *and* (3.193) *allow to choose between a symmetric adjoint-consistent and a non-symmetric adjoint-inconsistent viscous elliptic part in this Nitsche-type formulation. Following elaborations from Section 3.3.2.4, the subsequent stability analysis is valid for both variants, provided that* $\gamma > 0$ *is chosen sufficiently large. An analysis of a penalty-free adjoint-inconsistent formulation is not presented in this work. For further details on this topic, see elaborations and reference given in Section 3.3.2.4.*

3.5.3 Assumptions and Preliminaries

To reduce technicality throughout the analysis, the meshes $\widehat{\mathcal{T}}_h$ are assumed to be shape-regular and quasi-uniform, consisting of linear triangular or tetrahedral elements for $d = 2, 3$. That is, all elements $T, T' \in \mathcal{T}_h$ are of regular shape and have comparable mesh sizes $h_{T'} \lesssim h_T \lesssim h_{T'} \sim h$.

Similar to Burman *et al.* [48], in addition to the condition on $\boldsymbol{\beta}$ being divergence-free a.e. in Ω with respect to the Lebesgue measure on $\mathbb{R}^d$, it is required that $\boldsymbol{\beta} \in [W^{1,\infty}(\Omega)]^d$. Utilizing the extension operator E defined in (3.56) (see Section 3.2.2.2), there exists a $\boldsymbol{\beta}^* \overset{\text{def}}{=} E\boldsymbol{\beta}$ extended from Ω to a fixed Lipschitz-domain Ω^* satisfying $\Omega^* \supset \Omega_h^* \; \forall\, h$ with

$$\|\boldsymbol{\beta}^*\|_{1,\infty,\Omega_h^*} \lesssim \|\boldsymbol{\beta}^*\|_{1,\infty,\Omega^*} \lesssim \|\boldsymbol{\beta}\|_{1,\infty,\Omega}. \tag{3.204}$$

Note that since $\boldsymbol{\beta}^* \in [W^{1,\infty}(\Omega^*)]^d \subseteq [C^{0,1}(\Omega^*)]^d$ it holds that $\boldsymbol{\beta}^*$ is (Lipschitz-)continuous by assumption and therefore $\boldsymbol{\beta}^* \cdot \boldsymbol{n}_F$ single-valued on faces $F \in \mathcal{F}_i$. To simplify the notation, it is simply written $\boldsymbol{\beta}$, which implies to use the extension $\boldsymbol{\beta}^*$ whenever necessary.

Throughout the analysis, it is made use of a piecewise constant discrete vector field $\boldsymbol{\beta}_h^0$, which is assumed to approximate $\boldsymbol{\beta}$ such that

$$\|\boldsymbol{\beta} - \boldsymbol{\beta}_h^0\|_{0,\infty,T} \lesssim h|\boldsymbol{\beta}|_{1,\infty,T} \quad \text{and} \quad \|\boldsymbol{\beta}_h^0\|_{0,\infty,T} \lesssim \|\boldsymbol{\beta}\|_{0,\infty,T} \quad \forall\, T \in \mathcal{T}_h. \tag{3.205}$$

The simple choice of taking the value of $\boldsymbol{\beta}$ at some point in T guarantees both, the approximation and boundedness property (3.205) and the possibility to define $\boldsymbol{\beta}_h^0$ on cut elements $T \in \mathcal{T}_\Gamma$ even without explicit knowledge of the extension $\boldsymbol{\beta}^*$.

Remark 3.14 *It needs to be commented on the construction of* $\boldsymbol{\beta}_h$ *appearing in the definition of the stabilization forms* (3.195)–(3.202) *in the unfitted mesh case. The discrete vector field* $\boldsymbol{\beta}_h$ *is assumed to be a continuous approximation of* $\boldsymbol{\beta}$ *for which hold approximation properties as in* (3.205)*. From a practical point of view,* $\boldsymbol{\beta}$ *will be either given as analytical expression allowing*

to construct $\boldsymbol{\beta}_h$ by interpolation, or as the finite element approximation of $\boldsymbol{u}$ from a previous time or iteration step, as the case when solving the incompressible Navier-Stokes equations. From a theoretical point of view, owing to the existence of an extension $\boldsymbol{\beta}^* \in [W^{1,\infty}(\Omega^*)]^d$, a $\boldsymbol{\beta}_h$ satisfying (3.205) can be constructed by proper interpolation.

Remark 3.15 *Following the discussion of Braack* et al. *[31] and Burman [38], and (3.43) in Section 3.1.3.2, it is possible to replace the convection and incompressibility related stabilization forms ((3.195), (3.198) and (3.196), (3.199)) by a single stabilization and ghost penalty operator of the form*

$$\overline{s}_\beta(\boldsymbol{u}_h, \boldsymbol{v}_h) \overset{def}{=} \sum_{F \in \mathcal{F}_i} \overline{\phi}^{1,1}_{\beta,F} h \langle [\![\partial_{\boldsymbol{n}} \boldsymbol{u}_h]\!], [\![\partial_{\boldsymbol{n}} \boldsymbol{v}_h]\!] \rangle_F, \tag{3.206}$$

$$\overline{g}_\beta(\boldsymbol{u}_h, \boldsymbol{v}_h) \overset{def}{=} \sum_{F \in \mathcal{F}_\Gamma} \sum_{1 \leqslant j \leqslant k} \overline{\phi}^{j,k}_{\beta,F} h^{2j-1} \langle [\![\partial^j_{\boldsymbol{n}} \boldsymbol{u}_h]\!], [\![\partial^j_{\boldsymbol{n}} \boldsymbol{v}_h]\!] \rangle_F, \tag{3.207}$$

with

$$\overline{\phi}^{j,k}_{\beta,F} \overset{def}{=} \begin{cases} \gamma_\beta \phi_{\beta,F} \|\boldsymbol{\beta}\|^2_{0,\infty,F} + \gamma_u \phi_{u,F} & \text{for } j < k, \\ \gamma_\beta \phi_{\beta,F} \|\boldsymbol{\beta} \cdot \boldsymbol{n}\|^2_{0,\infty,F} + \gamma_u \phi_{u,F} & \text{for } j = k. \end{cases} \tag{3.208}$$

We refer to Lemma 3.9 for the details. Note that employing $\|\boldsymbol{\beta}\|_{0,\infty,F}$ in $\overline{\phi}^{j,k}_{\beta,F}$ introduces some additional (order preserving) cross-wind diffusion. The use of $\overline{s}_\beta$ and $\overline{g}_\beta$ greatly simplifies the implementation of the purposed method as each employed stabilization is then the sum of properly scaled face contributions of the form $\langle [\![\partial^j_{\boldsymbol{n}} \boldsymbol{u}_h]\!], [\![\partial^j_{\boldsymbol{n}} \boldsymbol{v}_h]\!] \rangle_F$.

As assumed in [48], it is additionally required that the flow field $\boldsymbol{\beta}$ is sufficiently resolved by the mesh in the sense that for some constant $c_\beta > 1$ and $\forall\, T \in \mathcal{T}_h$

$$c_\beta^{-1} \|\boldsymbol{\beta}\|_{0,\infty,T'} \leqslant \|\boldsymbol{\beta}\|_{0,\infty,T} \leqslant c_\beta \|\boldsymbol{\beta}\|_{0,\infty,T'} \quad \forall\, T' \in \omega(T). \tag{3.209}$$

Here, $\omega(T)$ denotes a local patch of elements neighboring T. Assumption (3.209) can be ensured if, e.g., an inverse-estimate-like property

$$|\boldsymbol{\beta}|_{1,\infty,\omega(T)} \leqslant d_\beta h^{-1} \|\boldsymbol{\beta}\|_{0,\infty,\omega(T)} \quad \forall\, T \in \mathcal{T}_h \tag{3.210}$$

is satisfied for some patch constant $c_\omega \overset{\text{def}}{=} h / \operatorname{diam}(\omega(T)) > d_\beta$. Then

$$\|\boldsymbol{\beta}\|_{0,\infty,\omega(T)} \leqslant \|\boldsymbol{\beta}\|_{0,\infty,T'} + \operatorname{diam}(\omega(T)) |\boldsymbol{\beta}|_{1,\infty,\omega(T)} \leqslant \|\boldsymbol{\beta}\|_{0,\infty,T'} + c_\omega^{-1} d_\beta \|\boldsymbol{\beta}\|_{0,\infty,\omega(T)} \tag{3.211}$$

and, consequently, assumption (3.209) holds with $c_\beta^{-1} \overset{\text{def}}{=} 1 - c_\omega^{-1} d_\beta$, since for any $T, T' \in \omega(T)$

$$(1 - c_\omega^{-1} d_\beta) \|\boldsymbol{\beta}\|_{0,\infty,T} \leqslant (1 - c_\omega^{-1} d_\beta) \|\boldsymbol{\beta}\|_{0,\infty,\omega(T)} \leqslant \|\boldsymbol{\beta}\|_{0,\infty,T'}. \tag{3.212}$$

Due to assumption (3.209), the piecewise constant stabilization parameters are comparable in the sense that for $\phi \in \{\phi_u, \phi_\beta, \phi_p\}$

$$(c_\beta c_{\mathcal{T}_h})^{-1} \phi_{T'} \leqslant \phi_T \leqslant (c_\beta c_{\mathcal{T}_h}) \phi_{T'} \quad \forall\, T' \in \omega(T), \tag{3.213}$$

where $c_{\mathcal{T}_h}$ characterizes the quasi-uniformness of $\mathcal{T}_h$. With this in mind, throughout this work, it is therefore simply written

$$\phi_T \sim \phi_{T'} \quad \forall\, T' \in \omega(T), \qquad \phi_F \sim \phi_{T'} \quad \forall\, T' \in \omega(F). \tag{3.214}$$

In the forthcoming stability and *a priori* error analysis it will be made heavy use of certain continuous, piecewise linear versions of the stabilization parameters defined by

$$\widetilde{\phi} \overset{\text{def}}{=} \mathcal{O}_h^1(\phi), \quad \phi \in \{\phi_\beta, \phi_u, \phi_p\}, \tag{3.215}$$

where $\mathcal{O}_h^1 : \mathscr{X}_h^{\mathrm{dc},0} \to \mathscr{X}_h^1$ denotes the Oswald interpolation onto linear functions, see elaborations in Section 3.2.2.2 for details. Then by the definition of the Oswald interpolant and the local comparability of the stabilization parameters (3.214) it holds

$$\widetilde{\phi}_T \sim \phi_T, \quad \phi \in \{\phi_\beta, \phi_u, \phi_p\}. \tag{3.216}$$

The following lemma states quasi-local stability of the Oswald interpolation (3.64) from Section 3.2.2.2 in certain weighted norms.

Lemma 3.5 *Let $v_h \in \mathscr{X}_h^{\mathrm{dc}}$ and let ϕ be a piecewise constant function defined on $\mathscr{T}_h$, which satisfies the local comparability property* (3.214)*. Then*

$$\|\phi^{\frac{1}{2}}\mathcal{O}_h(v_h)\|_T \lesssim \|\phi^{\frac{1}{2}} v_h\|_{\omega(T)} \quad \forall T \in \mathscr{T}_h, \tag{3.217}$$

where $\omega(T)$ denotes a sufficiently large patch of elements surrounding element T.

Proof. The proof is a simple consequence of the Lemma 3.1 from Section 3.2.2.2 and the inverse inequality (3.47):

$$\begin{aligned} \|\phi^{\frac{1}{2}}\mathcal{O}_h(v_h)\|_T^2 &\leqslant \|\phi^{\frac{1}{2}} v_h\|_T^2 + \|\phi^{\frac{1}{2}}(\mathcal{O}_h(v_h) - v_h)\|_T^2 \lesssim \|\phi^{\frac{1}{2}} v_h\|_T^2 + h\|\phi_T^{\frac{1}{2}}[\![v_h]\!]\|_{\mathscr{F}_i(T)}^2 && (3.218)\\ &\lesssim \|\phi^{\frac{1}{2}} v_h\|_T^2 + \|\phi^{\frac{1}{2}} v_h\|_{\omega(T)}^2. && (3.219) \end{aligned}$$

□

3.5.4 Norms and Ghost Penalties

Norms for Boundary-Fitted Meshes. Following the works by Burman *et al.* [48] and Braack *et al.* [31], natural norms required for stability and *a priori* estimates are associated with the discrete variational formulation. For boundary-fitted meshes, this is given by $\mathscr{A}_h^{\mathrm{CIP}} = \mathscr{L}_h^{\mathrm{CIP}}$, with $\mathscr{A}_h^{\mathrm{CIP}} \overset{\text{def}}{=} \mathscr{B}_h + \mathscr{S}_h^{\mathrm{CIP}}$ and $\mathscr{L}_h^{\mathrm{CIP}} \overset{\text{def}}{=} \mathscr{L}_h$ from (3.189), (3.190) and (3.192).

For the velocity $\boldsymbol{u}_h \in \mathscr{V}_h$ and the pressure $p_h \in \mathscr{Q}_h$, suitable norms and semi-norms are induced by terms of the discrete variational formulation and are defined by

$$\begin{aligned} |||\boldsymbol{u}_h|||^2 &\overset{\text{def}}{=} \|\sigma^{\frac{1}{2}}\boldsymbol{u}_h\|_\Omega^2 + \|\nu^{\frac{1}{2}}\nabla\boldsymbol{u}_h\|_\Omega^2 + \|(\gamma(\nu/h))^{\frac{1}{2}}\boldsymbol{u}_h\|_\Gamma^2 + s_u(\boldsymbol{u}_h, \boldsymbol{u}_h)\\ &\quad + \||\boldsymbol{\beta}\cdot\boldsymbol{n}|^{\frac{1}{2}}\boldsymbol{u}_h\|_\Gamma^2 + \|(\gamma(\phi/h))^{\frac{1}{2}}\boldsymbol{u}_h\cdot\boldsymbol{n}\|_\Gamma^2 + s_\beta(\boldsymbol{u}_h, \boldsymbol{u}_h), && (3.220)\\ |||p_h|||^2 &\overset{\text{def}}{=} \Phi_p\|p_h\|_\Omega^2 + |p_h|_\Omega^2, && (3.221) \end{aligned}$$

with the pressure semi-norm

$$|p_h|_\Omega^2 \overset{\text{def}}{=} s_p(p_h, p_h), \tag{3.222}$$

where the pressure L^2-norm scaling in (3.221) is defined as

$$\Phi_p^{-1} \overset{\text{def}}{=} \nu + \|\boldsymbol{\beta}\|_{0,\infty,\Omega} C_P + \sigma C_P^2 + \left(\frac{\|\boldsymbol{\beta}\|_{0,\infty,\Omega} C_P}{\sqrt{\nu + \sigma C_P^2}} \right)^2 . \tag{3.223}$$

The norm for the product space $\mathcal{W}_h = \mathcal{V}_h \times Q_h$ from (3.185) is given as

$$|||V_h|||^2 \overset{\text{def}}{=} |||\boldsymbol{u}_h|||^2 + |||p_h|||^2 \qquad \forall\, V_h \overset{\text{def}}{=} (\boldsymbol{u}_h, p_h) \in \mathcal{V}_h \times Q_h. \tag{3.224}$$

The involved semi-norms reflect the reactive and viscous bulk terms, the CIP stabilizations and the different symmetric Nitsche-type boundary terms of the stabilized formulation. Note that the so-called Poincaré constant C_P (see (3.51)) appearing the definition of Φ_p scales as the diameter of the domain. Using similar norms, inf-sup stability and energy-type error estimates for fitted meshes were proven by Burman *et al.* [48].

Extension of Control to Non-Boundary-Fitted Meshes. As elaborated in Section 3.4, the main challenge in developing Nitsche-type cut finite element methods is to establish stability and *a priori* error estimates which are independent of the positioning of the unfitted boundary within the background mesh. The key idea now is to add certain (weakly) consistent ghost-penalty stabilization terms in the vicinity of the boundary which allow to extend suitable norms for finite element functions from the physical domain Ω to the entire fictitious domain Ω_h^*, which is given by the active (background) mesh $\mathcal{T}_h$. Their fundamental idea and mathematical properties have been introduced in Section 3.4.3.

Recalling Lemma 3.4 from Section 3.4.3 on norm equivalences for scalar and vector-valued discrete functions, the following Corollary on estimates for scaled semi-norms included in (3.220) and (3.221) can be stated:

Corollary 3.6 *Let Ω, Ω_h^* and $\mathcal{F}_\Gamma$ be defined as in Section 2.1.4.1 and Section 2.2.2. Then for $\boldsymbol{u}_h \in \mathcal{V}_h$ the following scaled estimates hold*

$$\|\nu^{\frac{1}{2}} \nabla \boldsymbol{u}_h\|_{\Omega_h^*}^2 \lesssim \big(\|\nu^{\frac{1}{2}} \nabla \boldsymbol{u}_h\|_\Omega^2 + \underbrace{\sum_{F \in \mathcal{F}_\Gamma} \sum_{1 \leqslant j \leqslant k} \nu h^{2j-1} \langle [\![\partial_{\boldsymbol{n}}^j \boldsymbol{u}_h]\!], [\![\partial_{\boldsymbol{n}}^j \boldsymbol{u}_h]\!] \rangle_F}_{\sim g_\nu(\boldsymbol{u}_h, \boldsymbol{u}_h)} \big) \lesssim \|\nu^{\frac{1}{2}} \nabla \boldsymbol{u}_h\|_{\Omega_h^*}^2 \tag{3.225}$$

$$\|\sigma^{\frac{1}{2}} \boldsymbol{u}_h\|_{\Omega_h^*}^2 \lesssim \big(\|\sigma^{\frac{1}{2}} \boldsymbol{u}_h\|_\Omega^2 + \underbrace{\sum_{F \in \mathcal{F}_\Gamma} \sum_{1 \leqslant j \leqslant k} \sigma h^{2j+1} \langle [\![\partial_{\boldsymbol{n}}^j \boldsymbol{u}_h]\!], [\![\partial_{\boldsymbol{n}}^j \boldsymbol{u}_h]\!] \rangle_F}_{\sim g_\sigma(\boldsymbol{u}_h, \boldsymbol{u}_h)} \big) \lesssim \|\sigma^{\frac{1}{2}} \boldsymbol{u}_h\|_{\Omega_h^*}^2, \tag{3.226}$$

where the ghost-penalty operators g_ν and g_σ are as defined in (3.201) and (3.202). Note that the hidden constants depend only on the shape-regularity and the polynomial order, but not on the mesh or the positioning of the boundary within the mesh.

Remark 3.16 *The previous Corollary 3.6 shows that the ghost-penalties g_ν and g_σ extend control over the viscous H^1-semi-norm and over the reactive L^2-norm contained in the velocity norm (3.220) from Ω to Ω_h^*, which is fundamental to ensure stability and to improve system conditioning, see also discussion in Section 3.4.3.*

One major difference to the numerical analysis proposed by Burman *et al.* [48] consists in the extended inf-sup stability derived in this work. In [48] inf-sup stability was proven with respect to a weaker semi-norm and orthogonality and approximation properties of the L^2-projection were exploited to establish *a priori* error estimates. An extension of this projection operator to cut finite element approximations has been considered, e.g., in the work by Burman *et al.* [64]. As its use for higher-order approximations, i.e. $k > 1$, causes difficulties in controlling boundary-zone inconsistency terms, in the subsequent stability analysis, further control over weakly scaled semi-norms

$$\|\phi_u^{\frac{1}{2}} \nabla \cdot \boldsymbol{u}_h\|_\Omega, \quad \|\phi_\beta^{\frac{1}{2}}((\boldsymbol{\beta} \cdot \nabla)\boldsymbol{u}_h + \nabla p_h)\|_\Omega, \quad \|p_h\|_\Omega \tag{3.227}$$

is gained with the help of the CIP stabilization operators s_β, s_u, s_p. To ensure stability and optimality for cut finite element approximations in the different flow regimes, these semi-norms need to be extended to the enlarged domain Ω_h^* with the help of related ghost-penalty operators g_β, g_u, g_p. For this purpose, useful estimates according to the aforementioned norms are derived in the following.

Corollary 3.7 *Let Ω, Ω_h^* and $\mathcal{F}_\Gamma$ be defined as in Section 2.1.4.1 and Section 2.2.2. Then for $p_h \in \mathcal{Q}_h$ and $\boldsymbol{u}_h \in \mathcal{V}_h$ with Φ_p from (3.223), the following estimates hold*

$$\Phi_p \|p_h\|_{\Omega_h^*}^2 \lesssim \Phi_p \|p_h\|_\Omega^2 + \underbrace{\sum_{F \in \mathcal{F}_\Gamma} \sum_{1 \leqslant j \leqslant k} \phi_{p,F} h^{2j-1} \langle [\![\partial_{\boldsymbol{n}}^j p_h]\!], [\![\partial_{\boldsymbol{n}}^j p_h]\!] \rangle_F}_{\sim g_p(p_h, p_h)}, \tag{3.228}$$

$$\|\phi_u^{\frac{1}{2}} \nabla \cdot \boldsymbol{u}_h\|_{\Omega_h^*}^2 \lesssim \|\phi_u^{\frac{1}{2}} \nabla \cdot \boldsymbol{u}_h\|_\Omega^2 + \underbrace{\sum_{F \in \mathcal{F}_\Gamma} \sum_{0 \leqslant j \leqslant k-1} \phi_{u,F} h^{2j+1} \langle [\![\nabla \cdot \partial_{\boldsymbol{n}}^j \boldsymbol{u}_h]\!], [\![\nabla \cdot \partial_{\boldsymbol{n}}^j \boldsymbol{u}_h]\!] \rangle_F}_{\sim g_u(\boldsymbol{u}_h, \boldsymbol{u}_h)} \tag{3.229}$$

with piecewise constant stabilization functions ϕ_p, ϕ_u (3.203) and their face averages $\phi_{p,F}, \phi_{u,F}$.

Proof. The estimate for the scaled pressure L^2-norm follows from applying Lemma 3.4 to $\Phi_p^{\frac{1}{2}} p_h$ and the fact that $\Phi_p h^2 \lesssim \phi_{p,T} \sim \phi_{p,F}$, see definitions (3.223) and (3.203), together with $h \lesssim C_P$.

The estimate for the weakly scaled incompressibility results from a localized variant of the ghost-penalty lemma 3.4, the comparability assumption $\phi_{u,T} \sim \phi_{u,T'} \sim \phi_{u,F}$ (3.214) on patches of elements $T' \in \omega(T)$ surrounding intersected elements $T \in \mathcal{T}_\Gamma$. Note that the size of the boundary-zone patches $\omega(T)$ required to walk from a cut element to an uncut element is bounded independent of h owing to the mesh assumption G3, see Section 3.2.1.

□

More subtle is the role of the mixed norm incorporating the advective term and the pressure gradient. Estimates using the ghost-penalty operators g_β and g_p can be deduced as follows.

Lemma 3.8 *Let the scaling functions ϕ_β, ϕ_p be defined as in (3.203), i.e. $\phi_{\beta,T} = \phi_{p,T} = h^2/\phi_T$ being piecewise constant on $\mathcal{T}_h$. For a continuous approximation $\boldsymbol{\beta}_h$ and a piecewise constant*

approximation $\boldsymbol{\beta}_h^0 \in [\mathscr{X}_h^{\mathrm{dc},0}]^d$ *to* $\boldsymbol{\beta}$ *on* $\mathscr{T}_h$*, which both guarantee the approximation properties specified in* (3.205)*, the following estimates for the streamline diffusion norm hold*

$$\|\phi_\beta^{\frac{1}{2}}((\boldsymbol{\beta}_h - \boldsymbol{\beta})\cdot\nabla)\boldsymbol{u}_h\|_{\Omega_h^*}^2 \lesssim \omega_h\big(\|\nu^{\frac{1}{2}}\nabla\boldsymbol{u}_h\|_{\Omega_h^*}^2 + \|\sigma^{\frac{1}{2}}\boldsymbol{u}_h\|_{\Omega_h^*}^2\big), \tag{3.230}$$

$$\|\phi_\beta^{\frac{1}{2}}((\boldsymbol{\beta}_h^0 - \boldsymbol{\beta})\cdot\nabla)\boldsymbol{u}_h\|_{\Omega_h^*}^2 \lesssim \omega_h\big(\|\nu^{\frac{1}{2}}\nabla\boldsymbol{u}_h\|_{\Omega_h^*}^2 + \|\sigma^{\frac{1}{2}}\boldsymbol{u}_h\|_{\Omega_h^*}^2\big). \tag{3.231}$$

The mixed advective-pressure-gradient semi-norm can be estimated as

$$\begin{aligned}\|\phi_\beta^{\frac{1}{2}}((\boldsymbol{\beta}_h^0\cdot\nabla)\boldsymbol{u}_h + \nabla p_h)\|_{\Omega_h^*}^2 \lesssim \|\phi_\beta^{\frac{1}{2}}((\boldsymbol{\beta}\cdot\nabla)\boldsymbol{u}_h + \nabla p_h)\|_\Omega^2 + g_\beta(\boldsymbol{u}_h,\boldsymbol{u}_h) + g_p(p_h,p_h)\\ + \omega_h\big(\|\nu^{\frac{1}{2}}\nabla\boldsymbol{u}_h\|_{\Omega_h^*}^2 + \|\sigma^{\frac{1}{2}}\boldsymbol{u}_h\|_{\Omega_h^*}^2\big),\end{aligned} \tag{3.232}$$

with the non-dimensional scaling function

$$\omega_h \overset{def}{=} h^2|\boldsymbol{\beta}|_{1,\infty,\Omega_h^*}(\nu + \sigma h^2)^{-1}. \tag{3.233}$$

Proof.
Estimates (3.230) **and** (3.231)**:** Both estimates can be derived analogously under the same optimality assumptions on $\boldsymbol{\beta}_h$ and $\boldsymbol{\beta}_h^0$. From a simple application of the Cauchy-Schwarz inequality, it can be obtained

$$\|\phi_\beta^{\frac{1}{2}}((\boldsymbol{\beta}_h^0 - \boldsymbol{\beta})\cdot\nabla)\boldsymbol{u}_h\|_{\Omega_h^*}^2 \lesssim \sum\nolimits_{T\in\mathscr{T}_h}\phi_\beta\|\boldsymbol{\beta}_h^0 - \boldsymbol{\beta}\|_{0,\infty,T}^2\|\nabla\boldsymbol{u}_h\|_T^2. \tag{3.234}$$

Now using the interpolation property of $\boldsymbol{\beta}_h^0$ (3.205) and the simple fact that $\phi_\beta\|\boldsymbol{\beta}\|_{0,\infty,T} \lesssim h$ (see definition (3.203)), it can be further estimated that

$$\phi_\beta\|\boldsymbol{\beta}_h^0 - \boldsymbol{\beta}\|_{0,\infty,T}^2 \lesssim \phi_\beta\|\boldsymbol{\beta}\|_{0,\infty,T}h|\boldsymbol{\beta}|_{1,\infty,T} \lesssim h^2|\boldsymbol{\beta}|_{1,\infty,T} \tag{3.235}$$

while a simple application of the inverse inequality (3.46) shows that

$$\|\nabla\boldsymbol{u}_h\|_T = \frac{\nu+\sigma h^2}{\nu+\sigma h^2}\|\nabla\boldsymbol{u}_h\|_T^2 \lesssim \frac{1}{\nu+\sigma h^2}(\|\nu^{\frac{1}{2}}\nabla\boldsymbol{u}_h\|_T^2 + \|\sigma^{\frac{1}{2}}\boldsymbol{u}_h\|_T^2). \tag{3.236}$$

This gives the desired estimate by taking the maximum over all elements and by defining ω_h as in (3.233). The estimate for $\boldsymbol{\beta}_h$ can be derived analogously.

Estimate (3.232)**:** Note that the function $\boldsymbol{v}_h \overset{\text{def}}{=} \phi_\beta((\boldsymbol{\beta}_h^0\cdot\nabla)\boldsymbol{u}_h + \nabla p_h)$ is a piecewise polynomial function of order $k-1$ owing to the fact that ϕ_β and $\boldsymbol{\beta}_h^0$ are piecewise constant. Applying the norm equivalence from Lemma 3.4 to $\boldsymbol{v}_h$ and using that $\phi_\beta \sim \phi_p$, as assumed in (3.203), and the local comparability of ϕ (3.214) consequently yields

$$\begin{aligned}&\|\phi_\beta^{\frac{1}{2}}((\boldsymbol{\beta}_h^0\cdot\nabla)\boldsymbol{u}_h + \nabla p_h)\|_{\Omega_h^*}^2\\ &\lesssim \|\phi_\beta^{\frac{1}{2}}((\boldsymbol{\beta}_h^0\cdot\nabla)\boldsymbol{u}_h + \nabla p_h)\|_\Omega^2 + \sum\nolimits_{j=0}^{k-1}\phi_\beta h^{2j+1}\|[\![\partial_{\boldsymbol{n}}^j((\boldsymbol{\beta}_h^0\cdot\nabla)\boldsymbol{u}_h + \nabla p_h)]\!]\|_{\mathscr{F}_\Gamma}^2 &(3.237)\\ &\lesssim \|\phi_{\beta,F}^{\frac{1}{2}}((\boldsymbol{\beta}_h^0\cdot\nabla)\boldsymbol{u}_h + \nabla p_h)\|_\Omega^2 + \sum\nolimits_{j=0}^{k-1}\phi_{\beta,F}h^{2j+1}\|[\![\partial_{\boldsymbol{n}}^j\nabla p_h]\!]\|_{\mathscr{F}_\Gamma}^2\\ &\quad + \sum\nolimits_{j=0}^{k-1}\phi_{\beta,F}h^{2j+1}\|[\![(\boldsymbol{\beta}_h^0\cdot\nabla)\partial_{\boldsymbol{n}}^j\boldsymbol{u}_h]\!]\|_{\mathscr{F}_\Gamma}^2 &(3.238)\end{aligned}$$

$$\lesssim \|\phi_\beta^{\frac{1}{2}}((\boldsymbol{\beta}_h^0\cdot\nabla)\boldsymbol{u}_h+\nabla p_h)\|_\Omega^2+\sum_{j=0}^{k-1}\phi_{\beta,F}h^{2j+1}\|[\![\partial_{\boldsymbol{n}}^j\nabla p_h]\!]\|_{\mathscr{F}_\Gamma}^2$$
$$+\sum_{j=0}^{k-1}\phi_{\beta,F}h^{2j+1}\|[\![((\boldsymbol{\beta}_h^0-\boldsymbol{\beta}_h)\cdot\nabla)\partial_{\boldsymbol{n}}^j\boldsymbol{u}_h]\!]\|_{\mathscr{F}_\Gamma}^2$$
$$+\sum_{j=0}^{k-1}\phi_{\beta,F}h^{2j+1}\|[\![(\boldsymbol{\beta}_h\cdot\nabla)\partial_{\boldsymbol{n}}^j\boldsymbol{u}_h]\!]\|_{\mathscr{F}_\Gamma}^2 \tag{3.239}$$
$$\lesssim \|\phi_\beta^{\frac{1}{2}}((\boldsymbol{\beta}_h^0\cdot\nabla)\boldsymbol{u}_h+\nabla p_h)\|_\Omega^2+g_\beta(\boldsymbol{u}_h,\boldsymbol{u}_h)+g_p(p_h,p_h)$$
$$+\omega_h\big(\|\nu^{\frac{1}{2}}\nabla\boldsymbol{u}_h\|_{\Omega_h^*}^2+\|\sigma^{\frac{1}{2}}\boldsymbol{u}_h\|_{\Omega_h^*}^2\big). \tag{3.240}$$

Here, in the last step, the gradient $\nabla p_h=(\partial_{\boldsymbol{n}}p_h)\boldsymbol{n}_F+\boldsymbol{P}_F\nabla p_h$ has been decomposed into its normal and tangential gradient part using the tangential projection $\boldsymbol{P}_F\overset{\text{def}}{=}\boldsymbol{I}-\boldsymbol{n}_F\otimes\boldsymbol{n}_F$ and the inverse estimate $\|[\![\boldsymbol{P}_F\nabla\partial_{\boldsymbol{n}}^j p_h]\!]\|_F^2=\|\boldsymbol{P}_F\nabla[\![\partial_{\boldsymbol{n}}^j p_h]\!]\|_F^2\lesssim h^{-2}\|[\![\partial_{\boldsymbol{n}}^j p_h]\!]\|_F^2$ has been employed on the tangential part to obtain

$$h^{2j+1}\|[\![\partial_{\boldsymbol{n}}^j\nabla p_h]\!]\|_F^2\lesssim h^{2j+1}\|[\![\partial_{\boldsymbol{n}}^{j+1}p_h]\!]\|_F^2+h^{2j-1}\|[\![\partial_{\boldsymbol{n}}^j p_h]\!]\|_F^2. \tag{3.241}$$

Choosing the stabilization parameters $\gamma_\beta,\gamma_p>0$ sufficiently large allows to control the facet terms in the vicinity of Γ by the two higher-order ghost penalty terms g_β,g_p. For the facet term which includes the difference $\boldsymbol{\beta}_h^0-\boldsymbol{\beta}_h$, a trace inequality can be applied, followed by a triangle inequality and the estimates (3.230) and (3.231), which completes the proof of (3.232).

□

Finally, following up on Remark 3.15, a short proof is presented showing how the convective and divergence related ghost penalties (3.198) and (3.199) can be simplified and replaced by the simple ghost-penalty form $\overline{g}_\beta$ (3.207).

Lemma 3.9 *Let $\boldsymbol{u}_h\in\mathscr{V}_h$ and define $\overline{\phi}_{\beta,F}^{j,k}$ as in (3.208). Then*

$$g_\beta(\boldsymbol{u}_h,\boldsymbol{u}_h)+g_u(\boldsymbol{u}_h,\boldsymbol{u}_h)\lesssim\sum_{F\in\mathscr{F}_\Gamma}\sum_{1\leqslant j\leqslant k}\overline{\phi}_{\beta,F}^{j,k}h^{2j-1}\langle[\![\partial_{\boldsymbol{n}}^j\boldsymbol{u}_h]\!],[\![\partial_{\boldsymbol{n}}^j\boldsymbol{u}_h]\!]\rangle_F, \tag{3.242}$$

Similar estimates hold for s_β and s_u.

Proof. Similar to the derivation of (3.241), the first estimate in (3.242) follows from decomposing the higher-order stream-line derivative into a face-normal and face-tangential part. While the latter part vanishes for $j=0$ in (3.198), for the higher order contributions $1\leqslant j<k-1$ a face-based inverse estimate can be applied:

$$\phi_{\beta,F}h^{2j+1}\|[\![\boldsymbol{\beta}\cdot\nabla\partial_{\boldsymbol{n}}^j\boldsymbol{u}_h]\!]\|_F^2 \tag{3.243}$$
$$\lesssim\phi_{\beta,F}h^{2j+1}\left(\|\boldsymbol{\beta}\cdot\boldsymbol{n}\|_{0,\infty,F}^2\|[\![\partial_{\boldsymbol{n}}^{j+1}\boldsymbol{u}_h]\!]\|_F^2+\|\boldsymbol{P}_F\boldsymbol{\beta}\|_{0,\infty,F}^2\|[\![\boldsymbol{P}_F\nabla\partial_{\boldsymbol{n}}^j\boldsymbol{u}_h]\!]\|_F^2\right) \tag{3.244}$$
$$\lesssim\phi_{\beta,F}h^{2j+1}\left(\|\boldsymbol{\beta}\cdot\boldsymbol{n}\|_{0,\infty,F}^2\|[\![\partial_{\boldsymbol{n}}^{j+1}\boldsymbol{u}_h]\!]\|_F^2+\|\boldsymbol{\beta}\|_{0,\infty,F}^2h^{-2}\|[\![\partial_{\boldsymbol{n}}^j\boldsymbol{u}_h]\!]\|_F^2\right). \tag{3.245}$$

Note that the last estimate introduces order-preserving crosswind diffusion also for the summands $j<k$ of (3.242), see definition of $\overline{\phi}_{\beta,F}^{j,k}$ in (3.208). The second estimate in (3.242) follows after similar calculations directly from definition (3.32) of ϕ_u.

□

Norms related to the CIP/GP Cut Finite Element Method. The final extended versions of semi-norms and energy-norms provided in (3.220)–(3.224) according to the Nitsche-type cut finite element formulation (3.189) for velocity $\boldsymbol{u}_h \in \mathcal{V}_h$ and pressure $p_h \in \mathcal{Q}_h$ are defined by

$$|||\boldsymbol{u}_h|||_*^2 \overset{\text{def}}{=} |||\boldsymbol{u}_h|||^2 + g_\sigma(\boldsymbol{u}_h, \boldsymbol{u}_h) + g_\nu(\boldsymbol{u}_h, \boldsymbol{u}_h) + g_\beta(\boldsymbol{u}_h, \boldsymbol{u}_h) + g_u(\boldsymbol{u}_h, \boldsymbol{u}_h), \tag{3.246}$$

$$|||p_h|||_*^2 \overset{\text{def}}{=} \Phi_p \|p_h\|_\Omega^2 + |p_h|_*^2 = |||p_h|||^2 + g_p(p_h, p_h) \tag{3.247}$$

with an extended pressure semi-norm with respect to Ω_h^*

$$|p_h|_*^2 \overset{\text{def}}{=} s_p(p_h, p_h) + g_p(p_h, p_h), \tag{3.248}$$

a semi-norm for the product space $\mathcal{W}_h$

$$|U_h|_*^2 \overset{\text{def}}{=} |(\boldsymbol{u}_h, p_h)|_*^2 = |||\boldsymbol{u}_h|||_*^2 + |p_h|_*^2, \quad \forall\, U_h = (\boldsymbol{u}_h, p_h) \in \mathcal{V}_h \times \mathcal{Q}_h \tag{3.249}$$

and, finally, a full energy-type norm

$$|||U_h|||_*^2 \overset{\text{def}}{=} |U_h|_*^2 + \|\phi_u^{\frac{1}{2}} \nabla \cdot \boldsymbol{u}_h\|_\Omega^2 + \frac{1}{1+\omega_h} \|\phi_\beta^{\frac{1}{2}}((\boldsymbol{\beta} \cdot \nabla)\boldsymbol{u}_h + \nabla p_h)\|_\Omega^2 + \Phi_p \|p_h\|_\Omega^2 \tag{3.250}$$

with ω_h defined as in (3.233).

3.5.5 Stability Properties

In this section, the numerical analysis of the proposed cut finite element method (3.186) is started by proving that the bi-linear form $\mathcal{A}_h^{\text{CIP/GP}} \overset{\text{def}}{=} \mathcal{B}_h + \mathcal{S}_h^{\text{CIP}} + \mathcal{G}_h^{\text{GP}}$ satisfies an inf-sup condition with respect to a suitable norm $|||U_h|||_*$ (3.250), with the inf-sup constant being independent of how the boundary cuts the underlying background mesh. The proof of the inf-sup stability is split into three major steps. First, the coercivity from Lemma 3.10 in a semi-norm (3.249) is used

$$|U_h|_*^2 = |(\boldsymbol{u}_h, p_h)|_*^2 = |||\boldsymbol{u}_h|||_*^2 + |p_h|_*^2 \qquad \text{with} \qquad |p_h|_*^2 = s_p(p_h, p_h) + g_p(p_h, p_h). \tag{3.251}$$

In a second step, control over additional norm terms

$$\|\phi_u^{\frac{1}{2}} \nabla \cdot \boldsymbol{u}_h\|_\Omega, \quad \|\phi_\beta^{\frac{1}{2}}((\boldsymbol{\beta} \cdot \nabla)\boldsymbol{u}_h + \nabla p_h)\|_\Omega, \quad \|p_h\|_\Omega \tag{3.252}$$

is gained in Lemma 3.11, 3.12 and 3.14. Finally, the previous two parts are combined to obtain the desired inf-sup stability with respect to the full energy norm $|||U_h|||_*$ in Theorem 3.15.

Coercivity Estimate of $\mathcal{A}_h^{\text{CIP/GP}}$ with respect to Semi-Norm $|U_h|_*$. The stability estimate is started by proving coercivity of the stabilized formulation on $\mathcal{W}_h$ with respect to $|U_h|_*$, as stated by the following lemma.

Lemma 3.10 *For $U_h = (\boldsymbol{u}_h, p_h) \in \mathcal{W}_h$ the cut finite element formulation is coercive with respect to $|U_h|_*$, i.e. it holds*

$$|U_h|_*^2 \lesssim \mathscr{B}_h(U_h, U_h) + \mathscr{S}_h^{\mathrm{CIP}}(U_h, U_h) + \mathscr{G}_h^{\mathrm{GP}}(U_h, U_h) \tag{3.253}$$

whenever the stability parameters $\gamma, \gamma_\nu, \gamma_\sigma, \gamma_\beta, \gamma_u, \gamma_p > 0$ are chosen large enough.

Proof. Starting from the definition of $\mathscr{B}_h$ in (3.189), diagonal testing $V_h = U_h$ yields

$$\begin{aligned}\mathscr{B}_h(U_h, U_h) &= a_h(\boldsymbol{u}_h, \boldsymbol{u}_h) &(3.254)\\ &= \|\sigma^{\frac{1}{2}}\boldsymbol{u}_h\|_\Omega^2 + ((\boldsymbol{\beta}\cdot\nabla)\boldsymbol{u}_h, \boldsymbol{u}_h) - \langle(\boldsymbol{\beta}\cdot\boldsymbol{n})\boldsymbol{u}_h, \boldsymbol{u}_h\rangle_{\Gamma_{\mathrm{in}}} + \|(\gamma(\phi/h))^{\frac{1}{2}}\boldsymbol{u}_h\cdot\boldsymbol{n}\|_\Gamma^2\\ &\quad + \|(2\nu)^{\frac{1}{2}}\boldsymbol{\epsilon}(\boldsymbol{u}_h)\|_\Omega^2 - 4\langle\nu\boldsymbol{\epsilon}(\boldsymbol{u}_h)\boldsymbol{n}, \boldsymbol{u}_h\rangle_\Gamma + \|(\gamma(\nu/h))^{\frac{1}{2}}\boldsymbol{u}_h\|_\Gamma^2. &(3.255)\end{aligned}$$

Integration by parts for the advective term together with continuity of $\boldsymbol{\beta}$ (see assumptions in Section 3.5.2) yields

$$((\boldsymbol{\beta}\cdot\nabla)\boldsymbol{u}_h, \boldsymbol{u}_h) = \frac{1}{2}\langle(\boldsymbol{\beta}\cdot\boldsymbol{n})\boldsymbol{u}_h, \boldsymbol{u}_h\rangle_\Gamma - \frac{1}{2}((\nabla\cdot\boldsymbol{\beta})\boldsymbol{u}_h, \boldsymbol{u}_h). \tag{3.256}$$

Using the assumption $\nabla\cdot\boldsymbol{\beta} = 0$, the advective terms can be rewritten as

$$\begin{aligned}((\boldsymbol{\beta}\cdot\nabla)\boldsymbol{u}_h, \boldsymbol{u}_h) - \langle(\boldsymbol{\beta}\cdot\boldsymbol{n})\boldsymbol{u}_h, \boldsymbol{u}_h\rangle_{\Gamma_{\mathrm{in}}} &= \frac{1}{2}\langle(\boldsymbol{\beta}\cdot\boldsymbol{n})\boldsymbol{u}_h, \boldsymbol{u}_h\rangle_\Gamma - \langle(\boldsymbol{\beta}\cdot\boldsymbol{n})\boldsymbol{u}_h, \boldsymbol{u}_h\rangle_{\Gamma_{\mathrm{in}}} &(3.257)\\ &= \frac{1}{2}\||\boldsymbol{\beta}\cdot\boldsymbol{n}|^{\frac{1}{2}}\boldsymbol{u}_h\|_\Gamma^2. &(3.258)\end{aligned}$$

Applying a δ-scaled Cauchy-Schwarz inequality and a trace inequality (3.48) yields

$$\begin{aligned}\langle\nu\boldsymbol{\epsilon}(\boldsymbol{u}_h)\boldsymbol{n}, \boldsymbol{u}_h\rangle_\Gamma &\lesssim \delta\|(\nu h)^{\frac{1}{2}}\boldsymbol{\epsilon}(\boldsymbol{u}_h)\boldsymbol{n}\|_\Gamma^2 + \delta^{-1}\|(\gamma(\nu/h))^{\frac{1}{2}}\boldsymbol{u}_h\|_\Gamma^2 &(3.259)\\ &\lesssim \delta\|\nu^{\frac{1}{2}}\nabla\boldsymbol{u}_h\|_{\Omega_h^*}^2 + \delta^{-1}\|(\gamma(\nu/h))^{\frac{1}{2}}\boldsymbol{u}_h\|_\Gamma^2 &(3.260)\\ &\lesssim \delta\big(\|\nu^{\frac{1}{2}}\nabla\boldsymbol{u}_h\|_\Omega^2 + g_\nu(\boldsymbol{u}_h, \boldsymbol{u}_h)\big) + \delta^{-1}\|(\gamma(\nu/h))^{\frac{1}{2}}\boldsymbol{u}_h\|_\Gamma^2, &(3.261)\end{aligned}$$

where in the last estimate the norm equivalence from Corollary 3.6 is used. Now observe that thanks to the Nitsche boundary penalty with $0 < h \lesssim 1$ and Korn's inequality (3.55), the viscous bulk term can be estimated by

$$\|\nu^{\frac{1}{2}}\boldsymbol{\epsilon}(\boldsymbol{u}_h)\|_\Omega^2 + \frac{1}{2}\|(\gamma(\nu/h))^{\frac{1}{2}}\boldsymbol{u}_h\|_\Gamma^2 \gtrsim \|\nu^{\frac{1}{2}}\boldsymbol{\epsilon}(\boldsymbol{u}_h)\|_\Omega^2 + \|\nu^{\frac{1}{2}}\boldsymbol{u}_h\|_\Gamma^2 \gtrsim \|\nu^{\frac{1}{2}}\nabla\boldsymbol{u}_h\|_\Omega^2, \tag{3.262}$$

which combined with the previous inequality (3.261) shows that

$$\begin{aligned}&\|(2\nu)^{\frac{1}{2}}\boldsymbol{\epsilon}(\boldsymbol{u}_h)\|_\Omega^2 + g_\nu(\boldsymbol{u}_h, \boldsymbol{u}_h) - 4\langle\nu\boldsymbol{\epsilon}(\boldsymbol{u}_h)\boldsymbol{n}, \boldsymbol{u}_h\rangle_\Gamma + \|(\gamma(\nu/h))^{1/2}\boldsymbol{u}_h\|_\Gamma^2\\ &\qquad\gtrsim \|\nu^{\frac{1}{2}}\nabla\boldsymbol{u}_h\|_\Omega^2 + \frac{1}{2}\|(\gamma(\nu/h))^{1/2}\boldsymbol{u}_h\|_\Gamma^2 + g_\nu(\boldsymbol{u}_h, \boldsymbol{u}_h) &(3.263)\end{aligned}$$

for $\delta > 0$ sufficiently small and the Nitsche penalty parameter $\gamma > 0$ large enough. The claim follows by combining estimates (3.255), (3.256), (3.263) and incorporating the stabilization terms $\mathscr{S}_h^{\mathrm{CIP}}$, $\mathscr{G}_h^{\mathrm{GP}}$.

□

Remark 3.17 *For a more detailed discussion on the viscous parts of Nitsche's method occurring in the coercivity estimate and for more precise estimates and elaborations on the relation of the Nitsche boundary terms to the viscous ghost-penalty stabilization g_ν in the context of the important role of trace estimates, the reader is referred to Section 3.4. Statements made therein can be transferred from the simplified elliptic Poisson model problem to the viscous-dominated Oseen problem by analogy.*

Remark 3.18 *The need for convective inflow stabilization at the boundary Γ_{in}, that is whenever the advective velocity $\boldsymbol{\beta}$ is directed into the fluid domain, i.e. $(\boldsymbol{\beta}\cdot\boldsymbol{n}) < 0$, can be clearly seen from estimate (3.256). Without a consistently added balancing term, the negative semi-norm contribution $\langle(\boldsymbol{\beta}\cdot\boldsymbol{n})\boldsymbol{u}_h,\boldsymbol{u}_h\rangle^2_{\Gamma_{\text{in}}} = -\||\boldsymbol{\beta}\cdot\boldsymbol{n}|^{\frac{1}{2}}\boldsymbol{u}_h\|^2_{\Gamma_{\text{in}}} < 0$ would deteriorate the coercivity estimate for convective dominated flows and cause boundary instabilities if $|\boldsymbol{\beta}\cdot\boldsymbol{n}|h \gg \nu$. These instabilities are reduced or even vanish for viscous flows, i.e. whenever $\nu \gg \|\boldsymbol{\beta}\|_{0,\infty,T}h$. Then, the viscous Nitsche penalty term is indeed sufficient to control the boundary condition on whole Γ, as can be seen from the proof.*

Remark 3.19 *Fundamental in the coercivity proof is the assumption that $\nabla\cdot\boldsymbol{\beta} = 0$ almost everywhere in Ω. For the incompressible Navier-Stokes equations, from which the Oseen equations are deduced as an auxiliary problem, this is not guaranteed point-wise in practice. However, either the L^2-norm control given by the reactive part, which often results from temporal discretization of the time derivative, is large enough such that $\sigma - \frac{1}{2}\nabla\cdot\boldsymbol{\beta} \geqslant c > 0$, or an additional balancing term can be consistently added. Further details on this aspect, which is important when considering the incompressible Navier-Stokes equations, will be provided in Section 3.6.1.*

Control over Incompressibility. The next lemma shows how an additional control over the weakly scaled incompressibility

$$\|\phi_u^{1/2}\nabla\cdot\boldsymbol{u}_h\|^2_\Omega \tag{3.264}$$

can be recovered with the help of the CIP and GP terms s_u and g_u defined in (3.196) and (3.199). Note its close relation to the control given by the well-known LSIC stabilized formulation in the context of the RBVM stabilization technique (cf. (3.26) in Section 3.1.3.1).

Lemma 3.11 *There is a constant $c_1 > 0$ such that for $\boldsymbol{u}_h \in \mathcal{V}_h$ there exists a $q_h \in \mathcal{Q}_h$ satisfying*

$$-b_h(q_h,\boldsymbol{u}_h) \gtrsim \|\phi_u^{\frac{1}{2}}\nabla\cdot\boldsymbol{u}_h\|^2_\Omega - c_1\Big(s_u(\boldsymbol{u}_h,\boldsymbol{u}_h) + g_u(\boldsymbol{u}_h,\boldsymbol{u}_h) + \|(\phi/h)^{\frac{1}{2}}\boldsymbol{u}_h\cdot\boldsymbol{n}\|^2_\Gamma\Big) \tag{3.265}$$

and the stability estimate in the pressure norm

$$\Phi_p\|q_h\|^2_\Omega + |q_h|^2_* \lesssim \|\phi_u^{\frac{1}{2}}\nabla\cdot\boldsymbol{u}_h\|^2_{\Omega_h^*} \lesssim \|\phi_u^{\frac{1}{2}}\nabla\cdot\boldsymbol{u}_h\|^2_\Omega + g_u(\boldsymbol{u}_h,\boldsymbol{u}_h) \tag{3.266}$$

whenever the stability parameters $\gamma,\gamma_\nu,\gamma_\sigma,\gamma_\beta,\gamma_u,\gamma_p$ are chosen large enough.

Proof. Define $q_h \overset{\text{def}}{=} \mathcal{O}_h(\widetilde{\phi}_u \nabla \cdot \boldsymbol{u}_h)$ with $\widetilde{\phi}_u \overset{\text{def}}{=} \mathcal{O}_h^1(\phi_u)$ being a smoothed, piecewise linear version of ϕ_u as defined in (3.215), for which local comparability in the sense of $\widetilde{\phi}_u|_T \sim \phi_u|_T$ (3.216) holds. Then

$$
\begin{aligned}
-b_h(q_h, \boldsymbol{u}_h) &= \|\widetilde{\phi}_u^{\frac{1}{2}} \nabla \cdot \boldsymbol{u}_h\|_\Omega^2 \\
&\quad + (\mathcal{O}_h(\widetilde{\phi}_u \nabla \cdot \boldsymbol{u}_h) - \widetilde{\phi}_u \nabla \cdot \boldsymbol{u}_h, \nabla \cdot \boldsymbol{u}_h)_\Omega - \langle \mathcal{O}_h(\widetilde{\phi}_u \nabla \cdot \boldsymbol{u}_h), \boldsymbol{u}_h \cdot \boldsymbol{n} \rangle_\Gamma && (3.267) \\
&= \|\widetilde{\phi}_u^{\frac{1}{2}} \nabla \cdot \boldsymbol{u}_h\|_\Omega^2 + I + II. && (3.268)
\end{aligned}
$$

By using $\phi_{u,T}^{-1} \widetilde{\phi}_{u,T}^2 \lesssim \phi_{u,F}$, now the first term can be treated as follows

$$
\begin{aligned}
I &= (\phi_u^{-\frac{1}{2}} (\mathcal{O}_h(\widetilde{\phi}_u \nabla \cdot \boldsymbol{u}_h) - \widetilde{\phi}_u \nabla \cdot \boldsymbol{u}_h), \phi_u^{\frac{1}{2}} \nabla \cdot \boldsymbol{u}_h)_\Omega && (3.269) \\
&\gtrsim -\delta \|\phi_u^{\frac{1}{2}} \nabla \cdot \boldsymbol{u}_h\|_\Omega^2 - \delta^{-1} \|\phi_u^{-\frac{1}{2}} (\mathcal{O}_h(\widetilde{\phi}_u \nabla \cdot \boldsymbol{u}_h) - \widetilde{\phi}_u \nabla \cdot \boldsymbol{u}_h)\|_\Omega^2 && (3.270) \\
&\gtrsim -\delta \|\phi_u^{\frac{1}{2}} \nabla \cdot \boldsymbol{u}_h\|_\Omega^2 - \delta^{-1} \sum\nolimits_{F \in \mathcal{F}_i} \phi_{u,F} h \|[\![\nabla \cdot \boldsymbol{u}_h]\!]\|_F^2 && (3.271) \\
&\gtrsim -\delta \|\phi_u^{\frac{1}{2}} \nabla \cdot \boldsymbol{u}_h\|_\Omega^2 - \delta^{-1} s_u(\boldsymbol{u}_h, \boldsymbol{u}_h). && (3.272)
\end{aligned}
$$

The second one can be dealt with using the mass conserving Nitsche boundary terms and $\phi_u \sim \phi$

$$
\begin{aligned}
II &= -\langle h^{\frac{1}{2}} \phi_u^{-\frac{1}{2}} \mathcal{O}_h(\widetilde{\phi}_u \nabla \cdot \boldsymbol{u}_h), h^{-\frac{1}{2}} \phi_u^{\frac{1}{2}} \boldsymbol{u}_h \cdot \boldsymbol{n} \rangle_\Gamma && (3.273) \\
&\gtrsim -\delta \|h^{\frac{1}{2}} \phi_u^{-\frac{1}{2}} \mathcal{O}_h(\widetilde{\phi}_u \nabla \cdot \boldsymbol{u}_h)\|_\Gamma^2 - \delta^{-1} \|h^{-\frac{1}{2}} \phi_u^{\frac{1}{2}} \boldsymbol{u}_h \cdot \boldsymbol{n}\|_\Gamma^2 && (3.274) \\
&\gtrsim -\delta \|\phi_u^{-\frac{1}{2}} \mathcal{O}_h(\widetilde{\phi}_u \nabla \cdot \boldsymbol{u}_h)\|_{\Omega_h^*}^2 - \delta^{-1} \|(\phi/h)^{\frac{1}{2}} \boldsymbol{u}_h \cdot \boldsymbol{n}\|_\Gamma^2 && (3.275) \\
&\gtrsim -\delta \|\phi_u^{\frac{1}{2}} \nabla \cdot \boldsymbol{u}_h\|_{\Omega_h^*}^2 - \delta^{-1} \|(\phi/h)^{\frac{1}{2}} \boldsymbol{u}_h \cdot \boldsymbol{n}\|_\Gamma^2 && (3.276) \\
&\gtrsim -\delta (\|\phi_u^{\frac{1}{2}} \nabla \cdot \boldsymbol{u}_h\|_\Omega^2 + g_u(\boldsymbol{u}_h, \boldsymbol{u}_h)) - \delta^{-1} \|(\phi/h)^{\frac{1}{2}} \boldsymbol{u}_h \cdot \boldsymbol{n}\|_\Gamma^2, && (3.277)
\end{aligned}
$$

where after applying a δ-scaled Young's inequality and the trace inequality (3.48), the quasi-local stability property of the Oswald interpolation (3.217) and the local averaging property $\phi_u^{-\frac{1}{2}} \widetilde{\phi}_u \lesssim \phi_u^{\frac{1}{2}}$ (3.216) was used. Recalling the norm equivalence (3.229) from Corollary 3.7

$$
\|\phi_u^{\frac{1}{2}} \nabla \cdot \boldsymbol{u}_h\|_{\Omega_h^*}^2 \lesssim \|\phi_u^{\frac{1}{2}} \nabla \cdot \boldsymbol{u}_h\|_\Omega^2 + g_u(\boldsymbol{u}_h, \boldsymbol{u}_h), \tag{3.278}
$$

which was applied in the last step, results in

$$
\begin{aligned}
-b_h(q_h, \boldsymbol{u}_h) &\gtrsim (1 - 2\delta) \|\phi_u^{\frac{1}{2}} \nabla \cdot \boldsymbol{u}_h\|_\Omega^2 \\
&\quad - (\delta + \delta^{-1}) \Big(s_u(\boldsymbol{u}_h, \boldsymbol{u}_h) + g_u(\boldsymbol{u}_h, \boldsymbol{u}_h) + \|(\phi/h)^{\frac{1}{2}} \boldsymbol{u}_h \cdot \boldsymbol{n}\|_\Gamma^2 \Big) && (3.279) \\
&\gtrsim \|\phi_u^{\frac{1}{2}} \nabla \cdot \boldsymbol{u}_h\|_\Omega^2 - c_1 \Big(s_u(\boldsymbol{u}_h, \boldsymbol{u}_h) + g_u(\boldsymbol{u}_h, \boldsymbol{u}_h) + \|(\phi/h)^{\frac{1}{2}} \boldsymbol{u}_h \cdot \boldsymbol{n}\|_\Gamma^2 \Big) && (3.280)
\end{aligned}
$$

and completes the estimate (3.265) by choosing $\delta > 0$ sufficiently small for some constant $c_1 > 0$. Finally, the stability bound can be easily proven by observing that

$$\Phi_p\|q_h\|_\Omega^2 + |q_h|_*^2 \lesssim \Phi_p\|\mathcal{O}_h(\widetilde{\phi}_u\nabla\cdot\boldsymbol{u}_h)\|_\Omega^2 + \sum_{F\in\mathcal{F}_i}\sum_{j=0}^{k-1}\phi_{p,F}h^{2j+1}\|[\![\partial_{\boldsymbol{n}}^j\mathcal{O}_h(\widetilde{\phi}_u\nabla\cdot\boldsymbol{u}_h)]\!]\|_F^2 \tag{3.281}$$

$$\lesssim \Phi_p\|\widetilde{\phi}_u\nabla\cdot\boldsymbol{u}_h\|_{\mathcal{T}_h}^2 + \sum_{T\in\mathcal{T}_h}\phi_{p,T}\|\mathcal{O}_h(\widetilde{\phi}_u\nabla\cdot\boldsymbol{u}_h)\|_T^2 \tag{3.282}$$

$$\lesssim \sum_{T\in\mathcal{T}_h}\|\phi_u^{\frac{1}{2}}\nabla\cdot\boldsymbol{u}_h\|_T^2 \lesssim \|\phi_u^{\frac{1}{2}}\nabla\cdot\boldsymbol{u}_h\|_\Omega^2 + g_u(\boldsymbol{u}_h,\boldsymbol{u}_h), \tag{3.283}$$

where the trace inequality (3.47), the quasi-local stability of the Oswald interpolant (3.217) and the averaging property $\phi_p\widetilde{\phi}_u^2 \lesssim \phi_u$ (3.216) and $\Phi_p\widetilde{\phi}_u^2 \lesssim \phi_u$ were used. The last step results from applying the norm equivalence from Lemma 3.229.

□

Control over Mixed Advective-Pressure-Gradient Norm. In a next step, the subsequent lemma shows how additional control over a semi-norm of the form

$$\|\phi_\beta^{\frac{1}{2}}((\boldsymbol{\beta}\cdot\nabla)\boldsymbol{u}_h + \nabla p_h)\|_\Omega^2 \tag{3.284}$$

can be recovered, which is closely related to the well-known mixed norm control given by a SUPG/PSPG stabilized formulation in the context of the RBVM stabilization technique (cf. (3.26) in Section 3.1.3.1).

Lemma 3.12 *There is a constant $c_2 > 0$ such that for a given function $U_h = (\boldsymbol{u}_h, p_h) \in \mathcal{W}_h$ there exists a $\boldsymbol{v}_h \in \mathcal{V}_h$ satisfying*

$$((\boldsymbol{\beta}\cdot\nabla)\boldsymbol{u}_h + \nabla p_h, \boldsymbol{v}_h)_\Omega \gtrsim \|\phi_\beta^{\frac{1}{2}}((\boldsymbol{\beta}\cdot\nabla)\boldsymbol{u}_h + \nabla p_h)\|_\Omega^2 - c_2(1+\omega_h)|U_h|_*^2 \tag{3.285}$$

whenever the stability parameters $\gamma, \gamma_\nu, \gamma_\sigma, \gamma_\beta, \gamma_u, \gamma_p$ are chosen large enough. Note that the first part on the right-hand side exhibits the desired norm control. Moreover, the test function $\boldsymbol{v}_h$, the streamline-diffusion and the incompressibility terms satisfy the stability estimate

$$|||\boldsymbol{v}_h|||_*^2 + \|\phi_\beta^{\frac{1}{2}}(\boldsymbol{\beta}\cdot\nabla)\boldsymbol{v}_h\|_\Omega^2 + \|\phi_u^{\frac{1}{2}}\nabla\cdot\boldsymbol{v}_h\|_\Omega^2 \lesssim \|\phi_\beta^{\frac{1}{2}}((\boldsymbol{\beta}\cdot\nabla)\boldsymbol{u}_h + \nabla p_h)\|_\Omega^2 + (1+\omega_h)|U_h|_*^2. \tag{3.286}$$

Proof. To gain control of the $\|\phi_\beta^{\frac{1}{2}}((\boldsymbol{\beta}\cdot\nabla)\boldsymbol{u}_h + \nabla p_h)\|_\Omega^2$ term, a suitable test function $\boldsymbol{v}_h \in \mathcal{V}_h$ is constructed. First, an element-wise constant, vector-valued function $\boldsymbol{\beta}_h^0$ is introduced which satisfies the approximation property and stability bound from (3.205). The simplest choice is to take the value of $\boldsymbol{\beta}$ at some point of T for each $T \in \mathcal{T}_h$. Set $\boldsymbol{w}_h \overset{\text{def}}{=} (\boldsymbol{\beta}_h^0\cdot\nabla)\boldsymbol{u}_h + \nabla p_h$ and note that $\boldsymbol{w}_h$ is a piecewise polynomial function of order $k-1$, however, is discontinuous between elements. For the piecewise constant stabilization parameter function ϕ_β from (3.203), introduce the smoothed, continuous, piecewise linear stabilization parameter $\widetilde{\phi}_\beta \overset{\text{def}}{=} \mathcal{O}_h^1(\phi_\beta)$ as

defined in (3.215) such that $\widetilde{\phi}_\beta \boldsymbol{w}_h$ is a polynomial of order k. Finally, define the test function $\boldsymbol{v}_h \overset{\text{def}}{=} \mathcal{O}_h(\widetilde{\phi}_\beta \boldsymbol{w}_h) \in \mathcal{V}_h$, where $\mathcal{O}_h : \mathscr{X}_h^{\mathrm{dc},k} \to \mathscr{X}_h^k$ denotes the Oswald interpolation onto polynomials of order k as defined in (3.64) (see Section 3.2.2.2).

Testing with $\boldsymbol{v}_h$ and consistently adding and subtracting

$$\pm (((\boldsymbol{\beta}\cdot\nabla)\boldsymbol{u}_h + \nabla p_h), \widetilde{\phi}_\beta(\boldsymbol{\beta}_h^0\cdot\nabla)\boldsymbol{u}_h)_\Omega, \tag{3.287}$$

$$\pm (((\boldsymbol{\beta}\cdot\nabla)\boldsymbol{u}_h + \nabla p_h), \widetilde{\phi}_\beta(\boldsymbol{\beta}\cdot\nabla)\boldsymbol{u}_h)_\Omega, \tag{3.288}$$

$$\pm (((\boldsymbol{\beta}\cdot\nabla)\boldsymbol{u}_h + \nabla p_h), \widetilde{\phi}_\beta\nabla p_h)_\Omega, \tag{3.289}$$

it can now be observed that

$$\begin{aligned}((\boldsymbol{\beta}\cdot\nabla)\boldsymbol{u}_h + \nabla p_h, \boldsymbol{v}_h) &= \|\widetilde{\phi}_\beta^{\frac{1}{2}}((\boldsymbol{\beta}\cdot\nabla)\boldsymbol{u}_h + \nabla p_h)\|_\Omega^2 \\ &\quad + ((\boldsymbol{\beta}\cdot\nabla)\boldsymbol{u}_h + \nabla p_h, \mathcal{O}_h(\widetilde{\phi}_\beta\boldsymbol{w}_h) - \widetilde{\phi}_\beta\boldsymbol{w}_h)_\Omega \\ &\quad + ((\boldsymbol{\beta}\cdot\nabla)\boldsymbol{u}_h + \nabla p_h, \widetilde{\phi}_\beta(\boldsymbol{\beta}_h^0 - \boldsymbol{\beta})\cdot\nabla\boldsymbol{u}_h)_\Omega \qquad (3.290)\\ &= \|\widetilde{\phi}_\beta^{\frac{1}{2}}((\boldsymbol{\beta}\cdot\nabla)\boldsymbol{u}_h + \nabla p_h)\|_\Omega^2 + I + II \qquad (3.291)\\ &\gtrsim \|\phi_\beta^{\frac{1}{2}}((\boldsymbol{\beta}\cdot\nabla)\boldsymbol{u}_h + \nabla p_h)\|_\Omega^2 - |I| - |II|, \qquad (3.292)\end{aligned}$$

where in the last step the local equivalence (3.216) was used. It remains to estimate the two terms I, II and, finally, to prove the stability bound for $|||\boldsymbol{v}_h|||_*$.

Estimate of I. From successively applying a δ-Cauchy-Schwarz inequality, Lemma 3.1 to estimate the fluctuation $\mathcal{O}_h(\widetilde{\phi}_\beta\boldsymbol{w}_h) - \widetilde{\phi}_\beta\boldsymbol{w}_h$, the local comparability $\widetilde{\phi}_{\beta,T} \sim \phi_{\beta,T}$ and a Cauchy-Schwarz inequality, it can be deduced that

$$\begin{aligned}|I| &= |(\phi_\beta^{\frac{1}{2}}((\boldsymbol{\beta}\cdot\nabla)\boldsymbol{u}_h + \nabla p_h), \phi_\beta^{-\frac{1}{2}}(\mathcal{O}_h(\widetilde{\phi}_\beta\boldsymbol{w}_h) - \widetilde{\phi}_\beta\boldsymbol{w}_h))_\Omega| \qquad (3.293)\\ &\lesssim \delta\|\phi_\beta^{\frac{1}{2}}((\boldsymbol{\beta}\cdot\nabla)\boldsymbol{u}_h + \nabla p_h)\|_\Omega^2 + \delta^{-1}\sum_{T\in\mathcal{T}_h}\|\phi_{\beta,T}^{-\frac{1}{2}}(\mathcal{O}_h(\widetilde{\phi}_\beta\boldsymbol{w}_h) - \widetilde{\phi}_\beta\boldsymbol{w}_h)\|_{T\cap\Omega}^2 \qquad (3.294)\\ &\lesssim \delta\|\phi_\beta^{\frac{1}{2}}((\boldsymbol{\beta}\cdot\nabla)\boldsymbol{u}_h + \nabla p_h)\|_\Omega^2 + \delta^{-1}\sum_{T\in\mathcal{T}_h}\phi_{\beta,T}^{-1}h\|[\![\widetilde{\phi}_\beta\boldsymbol{w}_h]\!]\|_{\mathscr{F}_h(T)}^2 \qquad (3.295)\\ &\lesssim \delta\|\phi_\beta^{\frac{1}{2}}((\boldsymbol{\beta}\cdot\nabla)\boldsymbol{u}_h + \nabla p_h)\|_\Omega^2 + \delta^{-1}\sum_{T\in\mathcal{T}_h}\phi_{\beta,T}^{-1}\widetilde{\phi}_{\beta,F}^2 h\|[\![\boldsymbol{w}_h]\!]\|_{\mathscr{F}_h(T)}^2 \qquad (3.296)\\ &\lesssim \delta\|\phi_\beta^{\frac{1}{2}}((\boldsymbol{\beta}\cdot\nabla)\boldsymbol{u}_h + \nabla p_h)\|_\Omega^2 + \delta^{-1}\sum_{T\in\mathcal{T}_h}\phi_{\beta,F}h\|[\![(\boldsymbol{\beta}_h\cdot\nabla)\boldsymbol{u}_h + \nabla p_h]\!]\|_{\mathscr{F}_h(T)}^2 \\ &\quad + \delta^{-1}\sum_{T\in\mathcal{T}_h}\phi_{\beta,F}h\|[\![((\boldsymbol{\beta}_h^0 - \boldsymbol{\beta}_h)\cdot\nabla)\boldsymbol{u}_h]\!]\|_{\mathscr{F}_h(T)}^2 \qquad (3.297)\\ &\lesssim \delta\|\phi_\beta^{\frac{1}{2}}((\boldsymbol{\beta}\cdot\nabla)\boldsymbol{u}_h + \nabla p_h)\|_\Omega^2 + \delta^{-1}(s_\beta(\boldsymbol{u}_h,\boldsymbol{u}_h) + s_p(p_h,p_h) + \omega_h|||\boldsymbol{u}_h|||_*^2). \qquad (3.298)\end{aligned}$$

In the last step, a combination of the inverse estimate (3.47), a triangle inequality for

$$\|((\boldsymbol{\beta}_h^0 - \boldsymbol{\beta}_h)\cdot\nabla)\boldsymbol{u}_h\|_T \leqslant \|((\boldsymbol{\beta}_h^0 - \boldsymbol{\beta})\cdot\nabla)\boldsymbol{u}_h\|_T + \|((\boldsymbol{\beta} - \boldsymbol{\beta}_h)\cdot\nabla)\boldsymbol{u}_h\|_T \tag{3.299}$$

and estimates (3.230) and (3.231) were used to obtain

$$\sum_{T\in\mathcal{T}_h} \phi_{\beta,F} h \|[\![((\boldsymbol{\beta}_h^0 - \boldsymbol{\beta}_h)\cdot\nabla)\boldsymbol{u}_h]\!]\|^2_{\mathcal{F}_h(T)} \lesssim \omega_h |||\boldsymbol{u}_h|||_*^2. \tag{3.300}$$

Splitting the facet terms

$$\|[\![(\boldsymbol{\beta}_h\cdot\nabla)\boldsymbol{u}_h + \nabla p_h]\!]\|_F^2 \lesssim \|[\![(\boldsymbol{\beta}_h\cdot\nabla)\boldsymbol{u}_h]\!]\|_F^2 + \|[\![\nabla p_h]\!]\|_F^2 \tag{3.301}$$

for all facets $F \in \mathcal{F}_h(T)$ and using $\phi_\beta \sim \phi_p$ (3.203), these can be bounded by the CIP stabilization operators s_β and s_p defined in (3.195) and (3.197). Note that estimating the fluctuation in (3.294) on $T \cap \Omega$ requires to integrate facets $F \in \mathcal{F}_h(T)$ in the boundary region entirely. Owing to this fact, the CIP stabilization operators g_β, g_p need to be evaluated along the whole facet whenever it is intersected by Γ.

Estimate of II. By a simple application of a δ-Cauchy-Schwarz inequality and estimate (3.231)

$$|II| \lesssim \delta \|\phi_\beta^{\frac{1}{2}}((\boldsymbol{\beta}\cdot\nabla)\boldsymbol{u}_h + \nabla p_h)\|_\Omega^2 + \delta^{-1}\|\phi_\beta^{\frac{1}{2}}((\boldsymbol{\beta}_h^0 - \boldsymbol{\beta})\cdot\nabla)\boldsymbol{u}_h\|_\Omega^2 \tag{3.302}$$

$$\lesssim \delta \|\phi_\beta^{\frac{1}{2}}((\boldsymbol{\beta}\cdot\nabla)\boldsymbol{u}_h + \nabla p_h)\|_\Omega^2 + \delta^{-1}\omega_h\big(\|\nu^{\frac{1}{2}}\nabla\boldsymbol{u}_h\|_{\Omega_h^*}^2 + \|\sigma^{\frac{1}{2}}\boldsymbol{u}_h\|_{\Omega_h^*}^2\big) \tag{3.303}$$

$$\lesssim \delta \|\phi_\beta^{\frac{1}{2}}((\boldsymbol{\beta}\cdot\nabla)\boldsymbol{u}_h + \nabla p_h)\|_\Omega^2 + \delta^{-1}\omega_h |||\boldsymbol{u}_h|||_*^2. \tag{3.304}$$

Estimate of (3.285). Now choose $\delta > 0$ small enough and combine the estimates for I and II to conclude that

$$((\boldsymbol{\beta}\cdot\nabla)\boldsymbol{u}_h + \nabla p_h, \boldsymbol{v}_h)$$

$$\gtrsim \|\phi_\beta^{\frac{1}{2}}((\boldsymbol{\beta}\cdot\nabla)\boldsymbol{u}_h + \nabla p_h)\|_\Omega^2 - |I| - |II| \tag{3.305}$$

$$\gtrsim \|\phi_\beta^{\frac{1}{2}}((\boldsymbol{\beta}\cdot\nabla)\boldsymbol{u}_h + \nabla p_h)\|_\Omega^2 - c_1(s_\beta(\boldsymbol{u}_h,\boldsymbol{u}_h) + s_p(p_h,p_h)) - \omega_h |||\boldsymbol{u}_h|||_*^2 \tag{3.306}$$

$$\gtrsim \|\phi_\beta^{\frac{1}{2}}((\boldsymbol{\beta}\cdot\nabla)\boldsymbol{u}_h + \nabla p_h)\|_\Omega^2 - c_2(1+\omega_h)|U_h|_*^2 \tag{3.307}$$

for some constant $c_2 > 0$, where for the last step the definition of the semi-norm $|U_h|_*$ from (3.249) was used.

Estimate of $|||\boldsymbol{v}_h|||_*$. Throughout the next steps, it will be made heavy use of the fact that

$$(\nu h^{-2} + \|\boldsymbol{\beta}\|_{0,\infty,T} h^{-1} + \sigma)\phi_\beta \sim \phi_u h^{-2}\phi_\beta \sim \phi h^{-2}\phi_\beta \lesssim 1 \tag{3.308}$$

by the very definition of $\phi_\beta, \phi_u, \phi_p$ and ϕ from (3.203).

Due to the pseudo-local L^2-stability property of the Oswald interpolant (3.217) and the local comparability $\widetilde{\phi}_\beta \sim \phi_\beta$ (3.216), for $\boldsymbol{v}_h$ it holds

$$\|\bar{\phi}\mathcal{O}_h(\boldsymbol{v}_h)\|_{\Omega_h^*} \lesssim \|\bar{\phi}\boldsymbol{v}_h\|_{\Omega_h^*} = \|\bar{\phi}\widetilde{\phi}_\beta((\boldsymbol{\beta}_h^0\cdot\nabla)\boldsymbol{u}_h + \nabla p_h)\|_{\Omega_h^*} \tag{3.309}$$

$$\lesssim \|\bar{\phi}\phi_\beta((\boldsymbol{\beta}_h^0\cdot\nabla)\boldsymbol{u}_h + \nabla p_h)\|_{\Omega_h^*}. \tag{3.310}$$

Starting with the viscous and reaction terms from the norm definition (3.246), it holds

$$\nu\|\nabla\boldsymbol{v}_h\|_{\Omega_h^*}^2 + \sigma\|\boldsymbol{v}_h\|_{\Omega_h^*}^2 \lesssim (\nu h^{-2} + \sigma)\|\widetilde{\phi}_\beta((\boldsymbol{\beta}_h^0\cdot\nabla)\boldsymbol{u}_h + \nabla p_h)\|_{\Omega_h^*}^2 \tag{3.311}$$

$$\lesssim \underbrace{(\nu h^{-2} + \sigma)\phi_\beta}_{\lesssim 1 \text{ see (3.308)}} \|\phi_\beta^{\frac{1}{2}}((\boldsymbol{\beta}_h^0\cdot\nabla)\boldsymbol{u}_h + \nabla p_h)\|_{\Omega_h^*}^2, \tag{3.312}$$

where for the reaction term an inverse inequality (3.46) has been applied, followed by (3.310). Turning to the boundary terms appearing in $|||\cdot|||_*$, the convective boundary part is bounded by

$$|||\boldsymbol{\beta}\cdot\boldsymbol{n}|^{\frac{1}{2}}\boldsymbol{v}_h\|_\Gamma^2 \lesssim \sum_{T\in\mathcal{T}_\Gamma} \|\boldsymbol{\beta}\|_{0,\infty,T}\|\mathcal{O}_h(\boldsymbol{v}_h)\|_{T\cap\Gamma}^2 \tag{3.313}$$

$$\lesssim \sum_{T\in\mathcal{T}_\Gamma} \|\boldsymbol{\beta}\|_{0,\infty,T}\|\mathcal{O}_h(\widetilde{\phi}_\beta((\boldsymbol{\beta}_h^0\cdot\nabla)\boldsymbol{u}_h+\nabla p_h))\|_{T\cap\Gamma}^2 \tag{3.314}$$

$$\lesssim \sum_{T\in\mathcal{T}_\Gamma} \underbrace{\|\boldsymbol{\beta}\|_{0,\infty,T}h^{-1}\phi_\beta}_{\lesssim 1 \text{ see (3.308)}}\|\phi_\beta^{\frac{1}{2}}((\boldsymbol{\beta}_h^0\cdot\nabla)\boldsymbol{u}_h+\nabla p_h)\|_T^2, \tag{3.315}$$

where the trace inequality (3.48) was used to pass from $T\cap\Gamma$ to T. The remaining boundary terms can be similarly bounded:

$$\|(\nu/h)^{\frac{1}{2}}\boldsymbol{v}_h\|_\Gamma^2+\|(\phi/h)^{\frac{1}{2}}\boldsymbol{v}_h\cdot\boldsymbol{n}\|_\Gamma^2 \lesssim \sum_{T\in\mathcal{T}_\Gamma} \underbrace{(\nu+\phi)h^{-2}\phi_\beta}_{\lesssim 1 \text{ see (3.308)}}\|\phi_\beta^{\frac{1}{2}}((\boldsymbol{\beta}_h^0\cdot\nabla)\boldsymbol{u}_h+\nabla p_h)\|_T^2. \tag{3.316}$$

Next, the velocity related norm terms contributed from the stabilization operators $\mathcal{S}_h^{\mathrm{CIP}}$ and $\mathcal{G}_h^{\mathrm{GP}}$ need to be estimated. A bound for $s_\beta(\boldsymbol{v}_h,\boldsymbol{v}_h)$ and $s_u(\boldsymbol{v}_h,\boldsymbol{v}_h)$ can be derived by first employing the trace and inverse inequalities (3.47) and (3.46) and then recalling the definition of $\boldsymbol{v}_h$ and estimate (3.308):

$$s_\beta(\boldsymbol{v}_h,\boldsymbol{v}_h) \lesssim \sum_{F\in\mathcal{F}_i}\phi_{\beta,F}h\|[\![(\boldsymbol{\beta}_h\cdot\nabla)\boldsymbol{v}_h]\!]\|_F^2 \lesssim \sum_{T\in\mathcal{T}_h}\|\boldsymbol{\beta}\|_{0,\infty,T}^2h^{-2}\phi_{\beta,T}\|\boldsymbol{v}_h\|_T^2 \tag{3.317}$$

$$\lesssim \sum_{T\in\mathcal{T}_h}\underbrace{\|\boldsymbol{\beta}\|_{0,\infty,T}^2h^{-2}\phi_{\beta,T}^2}_{\lesssim 1 \text{ see (3.308)}}\|\phi_\beta^{\frac{1}{2}}((\boldsymbol{\beta}_h^0\cdot\nabla)\boldsymbol{u}_h+\nabla p_h)\|_T^2, \tag{3.318}$$

$$s_u(\boldsymbol{v}_h,\boldsymbol{v}_h) \lesssim \sum_{F\in\mathcal{F}_i}\phi_{u,F}h\|[\![\nabla\cdot\boldsymbol{v}_h]\!]\|_F^2 \lesssim \sum_{T\in\mathcal{T}_h}\phi_{u,T}h^{-2}\|\boldsymbol{v}_h\|_T^2 \tag{3.319}$$

$$\lesssim \sum_{T\in\mathcal{T}_h}\underbrace{\phi_{u,T}h^{-2}\phi_{\beta,T}}_{\lesssim 1 \text{ see (3.308)}}\|\phi_\beta^{\frac{1}{2}}((\boldsymbol{\beta}_h^0\cdot\nabla)\boldsymbol{u}_h+\nabla p_h)\|_T^2. \tag{3.320}$$

The corresponding ghost-penalty terms can be estimated in the exact same manner, yielding

$$g_\beta(\boldsymbol{v}_h,\boldsymbol{v}_h)+g_u(\boldsymbol{v}_h,\boldsymbol{v}_h) \lesssim \|\phi_\beta^{\frac{1}{2}}((\boldsymbol{\beta}_h^0\cdot\nabla)\boldsymbol{u}_h+\nabla p_h)\|_{\Omega_h^*}^2, \tag{3.321}$$

where it was applied a trace inequality (3.47). Finally, another application of the inverse estimate (3.47) in combination with the already established bound (3.312) for the viscous and reaction norm terms gives

$$g_\nu(\boldsymbol{v}_h,\boldsymbol{v}_h)+g_\sigma(\boldsymbol{v}_h,\boldsymbol{v}_h) \lesssim \|\nu^{\frac{1}{2}}\nabla\boldsymbol{v}_h\|_{\Omega_h^*}^2+\|\sigma^{\frac{1}{2}}\boldsymbol{v}_h\|_{\Omega_h^*}^2 \lesssim \|\phi_\beta^{\frac{1}{2}}((\boldsymbol{\beta}_h^0\cdot\nabla)\boldsymbol{u}_h+\nabla p_h)\|_{\Omega_h^*}^2. \tag{3.322}$$

Estimate of $\|\phi_\beta^{\frac{1}{2}}(\boldsymbol{\beta}\cdot\nabla)\boldsymbol{v}_h\|_\Omega$. Similarly, the streamline-diffusion term in (3.286) can be bounded

$$\|\phi_\beta^{\frac{1}{2}}(\boldsymbol{\beta}\cdot\nabla)\boldsymbol{v}_h\|_\Omega^2 \lesssim \sum_{T\in\mathcal{T}_h}\|\boldsymbol{\beta}\|_{0,\infty,T}^2h^{-2}\phi_{\beta,T}\|\boldsymbol{v}_h\|_T^2 \tag{3.323}$$

$$\lesssim \sum_{T\in\mathcal{T}_h}\underbrace{\|\boldsymbol{\beta}\|_{0,\infty,T}^2h^{-2}\phi_{\beta,T}^2}_{\lesssim 1 \text{ see (3.308)}}\|\phi_\beta^{\frac{1}{2}}((\boldsymbol{\beta}_h^0\cdot\nabla)\boldsymbol{u}_h+\nabla p_h)\|_T^2. \tag{3.324}$$

Estimate of $\|\phi_u^{\frac{1}{2}}\nabla\cdot\boldsymbol{v}_h\|_\Omega$. The incompressibility term can be estimated similarly

$$\begin{aligned}\|\phi_u^{\frac{1}{2}}\nabla\cdot\boldsymbol{v}_h\|_\Omega^2 &= \|\phi_u^{\frac{1}{2}}\nabla\cdot\mathcal{O}_h(\widetilde{\phi}_\beta((\boldsymbol{\beta}_h^0\cdot\nabla)\boldsymbol{u}_h+\nabla p_h))\|_\Omega^2 &(3.325)\\ &\lesssim \|\phi_\beta^{-\frac{1}{2}}\widetilde{\phi}_\beta((\boldsymbol{\beta}_h^0\cdot\nabla)\boldsymbol{u}_h+\nabla p_h)\|_{\Omega_h^*}^2 &(3.326)\\ &\lesssim \|\phi_\beta^{\frac{1}{2}}((\boldsymbol{\beta}_h^0\cdot\nabla)\boldsymbol{u}_h+\nabla p_h)\|_{\Omega_h^*}^2, &(3.327)\end{aligned}$$

where an inverse inequality, the stability of the Oswald interpolant and $\phi_u\sim h^2\phi_\beta^{-1}$ was used.
Estimate of (3.286). After collecting all terms and employing estimate (3.232), the desired stability bound is obtained:

$$\begin{aligned}&|||\boldsymbol{v}_h|||_*^2+\|\phi_\beta^{\frac{1}{2}}(\boldsymbol{\beta}\cdot\nabla)\boldsymbol{v}_h\|_\Omega^2+\|\phi_u^{\frac{1}{2}}\nabla\cdot\boldsymbol{v}_h\|_\Omega^2\\ &\quad\lesssim \|\phi_\beta^{\frac{1}{2}}((\boldsymbol{\beta}_h^0\cdot\nabla)\boldsymbol{u}_h+\nabla p_h)\|_{\Omega_h^*}^2 &(3.328)\\ &\quad\lesssim \|\phi_\beta^{\frac{1}{2}}((\boldsymbol{\beta}\cdot\nabla)\boldsymbol{u}_h+\nabla p_h)\|_\Omega^2\\ &\qquad+g_\beta(\boldsymbol{u}_h,\boldsymbol{u}_h)+g_p(p_h,p_h)+\omega_h\big(\|\nu^{\frac{1}{2}}\nabla\boldsymbol{u}_h\|_{\Omega_h^*}^2+\|\sigma^{\frac{1}{2}}\boldsymbol{u}_h\|_{\Omega_h^*}^2\big) &(3.329)\\ &\quad\lesssim \|\phi_\beta^{\frac{1}{2}}((\boldsymbol{\beta}\cdot\nabla)\boldsymbol{u}_h+\nabla p_h)\|_\Omega^2+(1+\omega_h)|U_h|_*^2. &(3.330)\end{aligned}$$

□

The following lemma provides useful estimates of the velocity energy norm $|||\boldsymbol{v}_h|||_*$ and the advective term $(\boldsymbol{u}_h,(\boldsymbol{\beta}\cdot\nabla)\boldsymbol{v}_h)_\Omega$ and motivates the definition of the pressure L^2-norm scaling Φ_p from (3.223).

Lemma 3.13 *Let $\boldsymbol{u}_h,\boldsymbol{v}_h\in\mathcal{V}_h$, then the following estimates hold*

$$\begin{aligned}&|||\boldsymbol{v}_h|||_*+(1+\omega_h)^{-\frac{1}{2}}\|\phi_\beta^{\frac{1}{2}}(\boldsymbol{\beta}\cdot\nabla)\boldsymbol{v}_h\|_\Omega+\|\phi_u^{\frac{1}{2}}\nabla\cdot\boldsymbol{v}_h\|_\Omega\\ &\qquad\lesssim\big(\nu+\|\boldsymbol{\beta}\|_{0,\infty,\Omega}h+\sigma C_P^2\big)^{\frac{1}{2}}\big(\|\nabla\boldsymbol{v}_h\|_{\Omega_h^*}+\|h^{-\frac{1}{2}}\boldsymbol{v}_h\|_\Gamma\big) &(3.331)\\ &\qquad\lesssim\Phi_p^{-\frac{1}{2}}\big(\|\nabla\boldsymbol{v}_h\|_{\Omega_h^*}+\|h^{-\frac{1}{2}}\boldsymbol{v}_h\|_\Gamma\big), &(3.332)\\ |(\boldsymbol{u}_h,\boldsymbol{\beta}\cdot\nabla\boldsymbol{v}_h)_\Omega|&\lesssim|||\boldsymbol{u}_h|||_*\frac{\|\boldsymbol{\beta}\|_{0,\infty,\Omega}C_P}{\sqrt{\nu+\sigma C_P^2}}\|\nabla\boldsymbol{v}_h\|_\Omega\lesssim|||\boldsymbol{u}_h|||_*\Phi_p^{-\frac{1}{2}}\|\nabla\boldsymbol{v}_h\|_\Omega. &(3.333)\end{aligned}$$

Proof. It is started with estimate (3.332). The reactive term in the norm definition (3.246) can be bounded using the Poincaré inequality (3.53) showing that

$$\|\nu^{\frac{1}{2}}\nabla\boldsymbol{v}_h\|_\Omega^2+\|\sigma^{\frac{1}{2}}\boldsymbol{v}_h\|_\Omega^2\lesssim(\nu+\sigma C_P^2)(\|\nabla\boldsymbol{v}_h\|_\Omega^2+\|h^{-\frac{1}{2}}\boldsymbol{v}_h\|_\Gamma^2). \tag{3.334}$$

The remaining bulk terms can be estimated as

$$\begin{aligned}&(1+\omega_h)^{-1}\|\phi_\beta^{\frac{1}{2}}(\boldsymbol{\beta}\cdot\nabla)\boldsymbol{v}_h\|_\Omega^2+\|\phi_u^{\frac{1}{2}}\nabla\cdot\boldsymbol{v}_h\|_\Omega^2\\ &\qquad\lesssim\|\boldsymbol{\beta}\|_{0,\infty,\Omega}h\|\nabla\boldsymbol{v}_h\|_{\Omega_h^*}^2+(\nu+\|\boldsymbol{\beta}\|_{0,\infty,\Omega}h+\sigma h^2)\|\nabla\boldsymbol{v}_h\|_{\Omega_h^*}^2. &(3.335)\end{aligned}$$

The corresponding ghost-penalties g_σ and g_ν can be simply estimated by applying the inverse inequality (3.47) to obtain $h^{2j+1}\|[\![\partial_{\boldsymbol{n}}^j \boldsymbol{v}_h]\!]\|_F^2 \lesssim h^2\|\nabla \boldsymbol{v}_h\|^2_{T_F^+\cup T_F^-}$ and thus

$$g_\nu(\boldsymbol{v}_h,\boldsymbol{v}_h)+g_\sigma(\boldsymbol{v}_h,\boldsymbol{v}_h)\lesssim(\nu+\sigma h^2)\|\nabla\boldsymbol{v}_h\|^2_{\Omega_h^*}\lesssim(\nu+\sigma C_P^2)\|\nabla\boldsymbol{v}_h\|^2_{\Omega_h^*}. \tag{3.336}$$

The contribution from the remaining GP and CIP stabilization terms can be treated similarly,

$$(s_u+g_u)(\boldsymbol{v}_h,\boldsymbol{v}_h)\lesssim\|\phi_u^{\frac12}\nabla\boldsymbol{v}_h\|^2_{\Omega_h^*}\lesssim(\nu+\|\boldsymbol{\beta}\|_{0,\infty,\Omega}h+\sigma h^2)\|\nabla\boldsymbol{v}_h\|^2_{\Omega_h^*}, \tag{3.337}$$

$$(s_\beta+g_{\boldsymbol{\beta}})(\boldsymbol{v}_h,\boldsymbol{v}_h)\lesssim\sum_{T\in\mathcal{T}_h}\|\boldsymbol{\beta}_h\|^2_{0,\infty,T}\phi_{\beta,T}\|\nabla\boldsymbol{v}_h\|^2_T\lesssim\|\boldsymbol{\beta}\|_{0,\infty,\Omega}h\|\nabla\boldsymbol{v}_h\|^2_{\Omega_h^*}. \tag{3.338}$$

Finally, the boundary contributions are clearly bounded by

$$\|(\nu/h)^{\frac12}\boldsymbol{v}_h\|^2_\Gamma+\|(\phi/h)^{\frac12}\boldsymbol{v}_h\|^2_\Gamma+\||\boldsymbol{\beta}\cdot\boldsymbol{n}|^{\frac12}\boldsymbol{v}_h\|^2_\Gamma\lesssim(\nu+\|\boldsymbol{\beta}\|_{0,\infty,\Omega}h+\sigma h^2)\|h^{-\frac12}\boldsymbol{v}_h\|^2_\Gamma, \tag{3.339}$$

which concludes the proof of estimate (3.332) by the very definition of Φ_p (3.223).

Turning to estimate (3.333), it can be observed first that the L^2-norm $\|\boldsymbol{u}_h\|_\Omega$ can be bounded by $|||\boldsymbol{u}|||_*$ in two different ways. First, by $\|\boldsymbol{u}_h\|_\Omega\lesssim\sigma^{-\frac12}|||\boldsymbol{u}_h|||_*$, and second, after another application of the Poincaré inequality (3.53), via

$$\|\boldsymbol{u}_h\|_\Omega\lesssim C_P(\|\nabla\boldsymbol{u}_h\|_\Omega+\|h^{-\frac12}\boldsymbol{u}_h\|_\Gamma)\lesssim\nu^{-\frac12}C_P|||\boldsymbol{u}_h|||_*. \tag{3.340}$$

Taking the minimum of these two bounds, depending whether the reactive or viscous regime is dominating, the proof can be concluded by observing that

$$|(\boldsymbol{u}_h,(\boldsymbol{\beta}\cdot\nabla)\boldsymbol{v}_h)_\Omega|\lesssim|||\boldsymbol{u}_h|||_*\min\{\sigma^{-\frac12},\nu^{-\frac12}C_P\}\|\boldsymbol{\beta}\|_{0,\infty,\Omega}\|\nabla\boldsymbol{v}_h\|_\Omega \tag{3.341}$$

$$\lesssim|||\boldsymbol{u}_h|||_*\frac{\|\boldsymbol{\beta}\|_{0,\infty,\Omega}C_P}{\sqrt{\nu+\sigma C_P^2}}\|\nabla\boldsymbol{v}_h\|_\Omega, \tag{3.342}$$

where the last scaling defines an additional contribution in the definition of Φ_p (3.223).

□

Control over Pressure L^2-Norm. The next lemma shows how control over the pressure L^2-norm can be gained from the symmetric CIP stabilization operator s_p.

Lemma 3.14 *There is a constant $c_3>0$ such that for $p_h\in\mathcal{Q}_h$ there exists a $\boldsymbol{v}_h\in\mathcal{V}_h$ satisfying*

$$b_h(p_h,\boldsymbol{v}_h)\gtrsim\Phi_p\|p_h\|^2_\Omega-c_3s_p(p_h,p_h) \tag{3.343}$$

and the stability estimate

$$\begin{aligned}&|||\boldsymbol{v}_h|||_*+(1+\omega_h)^{-\frac12}\|\phi_\beta^{\frac12}(\boldsymbol{\beta}\cdot\nabla)\boldsymbol{v}_h\|_\Omega+\|\phi_u^{\frac12}\nabla\cdot\boldsymbol{v}_h\|_\Omega\\&\quad\lesssim\Phi_p^{-\frac12}(\|\nabla\boldsymbol{v}_h\|_{\Omega_h^*}+\|h^{-\frac12}\boldsymbol{v}_h\|_\Gamma)\lesssim\Phi_p^{\frac12}\|p_h\|_\Omega+g_p(p_h,p_h)^{\frac12}\end{aligned} \tag{3.344}$$

whenever the stability parameters $\gamma,\gamma_\nu,\gamma_\sigma,\gamma_\beta,\gamma_u,\gamma_p$ are chosen large enough.

Proof. For given $p_h \in \mathcal{Q}_h$, the test function $\boldsymbol{v}_h$ is constructed in two steps following Verfürth's technique.

Step 1. Due to the surjectivity of the divergence operator $\nabla\cdot : [H_0^1(\Omega)]^d \to L^2(\Omega)$ there exists a function $\boldsymbol{v}_p \in [H_0^1(\Omega)]^d$ such that $\nabla\cdot\boldsymbol{v}_p = -\Phi_p p_h$ and $\|\boldsymbol{v}_p\|_{1,\Omega} \sim \|\nabla\boldsymbol{v}_p\|_\Omega \lesssim \Phi_p\|p_h\|_\Omega$. To obtain a discrete test function, set $\boldsymbol{v}_h^1 \overset{\text{def}}{=} \boldsymbol{\pi}_h^*\boldsymbol{v}_p \in \mathcal{V}_h$ based on the Clément interpolant (see Section 3.2.2.2). Recall that $\boldsymbol{v}_p|_\Gamma = \boldsymbol{0}$, since $\boldsymbol{v}_p \in H_0^1(\Omega)$, to get

$$
\begin{aligned}
b_h(p_h,\boldsymbol{v}_h^1) &= b_h(p_h,\boldsymbol{v}_p) + b_h(p_h,\boldsymbol{\pi}_h^*\boldsymbol{v}_p - \boldsymbol{v}_p) && (3.345)\\
&= -(p_h,\nabla\cdot\boldsymbol{v}_p)_\Omega + (\nabla p_h,(\boldsymbol{\pi}_h^*\boldsymbol{v}_p - \boldsymbol{v}_p))_\Omega && (3.346)\\
&= \Phi_p\|p_h\|_\Omega^2 + \big(\Phi_p^{\frac12}h\nabla p_h, \Phi_p^{-\frac12}h^{-1}(\boldsymbol{\pi}_h^*\boldsymbol{v}_p - \boldsymbol{v}_p)\big)_\Omega, && (3.347)
\end{aligned}
$$

where the second term in (3.345) was integrated by parts using the fact that $p_h \in C^0(\Omega)$. Now a combination of a δ-scaled Cauchy-Schwarz inequality, the interpolation estimate (3.61), and finally, the stability bound $\|\nabla\boldsymbol{v}_p\|_\Omega \lesssim \Phi_p\|p_h\|_\Omega$ yields

$$
\begin{aligned}
b_h(p_h,\boldsymbol{v}_h^1) &\gtrsim \Phi_p\|p_h\|_\Omega^2 - \delta^{-1}\|\Phi_p^{\frac12}h\nabla p_h\|_\Omega^2 - \delta\Phi_p^{-1}\|\boldsymbol{v}_p\|_{1,\Omega}^2 && (3.348)\\
&\gtrsim (1-\delta)\Phi_p\|p_h\|_\Omega^2 - \delta^{-1}\|\Phi_p^{\frac12}h\nabla p_h\|_\Omega^2. && (3.349)
\end{aligned}
$$

Step 2. Next, it is shown how to compensate for the $\|\Phi_p^{\frac12}h\nabla p_h\|_\Omega^2$ term appearing in (3.349) using the stabilization form s_p. To construct a suitable test function, set $\boldsymbol{v}_h^2 \overset{\text{def}}{=} \Phi_p h^2\mathcal{C}_h(\nabla p_h) \in \mathcal{V}_h$, where $\mathcal{C}_h$ denotes the Oswald interpolation (3.64) (see Section 3.2.2.2). Then inserting $\boldsymbol{v}_h^2$ into b_h shows after an integration by parts that

$$
\begin{aligned}
b_h(p_h,\boldsymbol{v}_h^2) &= -(p_h,\nabla\cdot\boldsymbol{v}_h^2)_\Omega + \langle p_h,\boldsymbol{v}_h^2\cdot\boldsymbol{n}\rangle_\Gamma && (3.350)\\
&= (\nabla p_h,\Phi_p h^2\mathcal{C}_h(\nabla p_h))_\Omega && (3.351)\\
&= \|\Phi_p^{\frac12}h\nabla p_h\|_\Omega^2 + \big(\Phi_p^{\frac12}h\nabla p_h,\Phi_p^{\frac12}h(\mathcal{C}_h(\nabla p_h)-\nabla p_h)\big)_\Omega && (3.352)\\
&\gtrsim (1-\delta)\|\Phi_p^{\frac12}h\nabla p_h\|_\Omega^2 - \delta^{-1}s_p(p_h,p_h), && (3.353)
\end{aligned}
$$

where it was combined a δ-scaled Young's inequality and the Oswald interpolant Lemma 3.1 to gain control over the fluctuation in terms of the pressure CIP operator

$$
\|\Phi_p^{\frac12}h(\mathcal{C}_h(\nabla p_h)-\nabla p_h)\|_\Omega^2 \lesssim \sum_{F\in\mathcal{F}_i}\underbrace{\Phi_p h^2}_{\lesssim\phi_{p,F}}h\|[\![\nabla p_h]\!]\|_F^2 \lesssim s_p(p_h,p_h). \tag{3.354}
$$

Finally, using the same $\delta \sim 0.5$ in (3.349) and (3.353), it is set $\boldsymbol{v}_h \overset{\text{def}}{=} \boldsymbol{v}_h^1 + 2\delta^{-1}\boldsymbol{v}_h^2$ yielding

$$
b_h(p_h,\boldsymbol{v}_h) \gtrsim \Phi_p\|p_h\|_\Omega^2 - c_3 s_p(p_h,p_h) \tag{3.355}
$$

for some constant $c_3 > 0$.

Estimate (3.344)**.** Utilizing the stability bound (3.332) for $\boldsymbol{v}_h$ it is sufficient to prove

$$
\begin{aligned}
\|\nabla\boldsymbol{v}_h^1\|_{\Omega_h^*} + \|h^{-\frac12}\boldsymbol{v}_h^1\|_\Gamma &= \|\nabla\boldsymbol{\pi}_h^*\boldsymbol{v}_p\|_{\Omega_h^*} + \|h^{-\frac12}(\boldsymbol{\pi}_h^*\boldsymbol{v}_p - \boldsymbol{v}_p)\|_\Gamma && (3.356)\\
&\lesssim \|\nabla\boldsymbol{\pi}_h^*\boldsymbol{v}_p\|_{\Omega_h^*} + \|h^{-1}(\boldsymbol{\pi}_h^*\boldsymbol{v}_p - \boldsymbol{v}_p)\|_{\Omega_h^*} && (3.357)\\
&\lesssim \|\nabla\boldsymbol{v}_p\|_\Omega \lesssim \Phi_p\|p_h\|_\Omega, && (3.358)
\end{aligned}
$$

where it was used the fact that $\boldsymbol{v}_p|_\Gamma = 0$, followed by a trace inequality and the interpolation and stability properties of the Clément interpolant (3.61) and (3.63). After applying inverse inequalities (3.46) and (3.48), the pseudo-local stability property of the Oswald interpolant (3.217) and an inverse estimate, it equivalently holds

$$\|\nabla \boldsymbol{v}_h^2\|_{\Omega_h^*} + \|h^{-\frac{1}{2}}\boldsymbol{v}_h^2\|_\Gamma \lesssim \|h^{-1}\boldsymbol{v}_h^2\|_{\Omega_h^*} \lesssim \|h^{-1}\mathcal{O}_h(h^2\Phi_p\nabla p_h)\|_{\Omega_h^*} \tag{3.359}$$

$$\lesssim \|h\Phi_p\nabla p_h\|_{\Omega_h^*} \lesssim \|\Phi_p p_h\|_{\Omega_h^*} \tag{3.360}$$

$$\lesssim \Phi_p\|p_h\|_\Omega + \Phi_p^{\frac{1}{2}} g_p(p_h,p_h)^{\frac{1}{2}}, \tag{3.361}$$

where in the last step, the ghost-penalty norm equivalence for the pressure from Corollary 3.7 was applied. Consequently, combing the stability bounds (3.358) and (3.361) with stability bound (3.332) from Lemma 3.13 gives

$$\begin{aligned}&|||\boldsymbol{v}_h|||_* + (1+\omega_h)^{-\frac{1}{2}}\|\phi_\beta^{\frac{1}{2}}(\boldsymbol{\beta}\cdot\nabla)\boldsymbol{v}_h\|_\Omega + \|\phi_u^{\frac{1}{2}}\nabla\cdot\boldsymbol{v}_h\|_\Omega \\ &\quad\lesssim \Phi_p^{-\frac{1}{2}}(\|\nabla\boldsymbol{v}_h\|_{\Omega_h^*} + \|h^{-\frac{1}{2}}\boldsymbol{v}\|_\Gamma) \lesssim \Phi_p^{\frac{1}{2}}\|p_h\|_\Omega + g_p(p_h,p_h)^{\frac{1}{2}}.\end{aligned} \tag{3.362}$$

□

Global Inf-Sup Stability of $\mathcal{A}_h^{\mathrm{CIP/GP}}$ with respect to $|||U_h|||_*$. As a consequence of the previous lemmas it can be now proven that the bilinear form $\mathcal{A}_h^{\mathrm{CIP/GP}}$ defined in (3.186) satisfies an inf-sup condition with respect to the energy-type norm (3.250)

$$|||U_h|||_*^2 = |U_h|_*^2 + \|\phi_u^{\frac{1}{2}}\nabla\cdot\boldsymbol{u}_h\|_\Omega^2 + \frac{1}{1+\omega_h}\|\phi_\beta^{\frac{1}{2}}(\boldsymbol{\beta}\cdot\nabla\boldsymbol{u}_h + \nabla p_h)\|_\Omega^2 + \Phi_p\|p_h\|_\Omega^2, \tag{3.363}$$

which is constructed from the semi-norm $|U_h|_*^2$ (3.249) and additional norm parts $\|\phi_u^{1/2}\nabla\cdot\boldsymbol{u}_h\|_\Omega^2$, $\|\phi_\beta^{1/2}(\boldsymbol{\beta}\cdot\nabla\boldsymbol{u}_h + \nabla p_h)\|_\Omega^2$ and $\Phi_p\|p_h\|_\Omega^2$ as treated in Lemma 3.11, 3.12 and 3.14. This finally guarantees existence and uniqueness of a discrete velocity and pressure solution of the cut finite element formulation (3.186). The global inf-sup stability estimate reads as follows:

Theorem 3.15 (Global Inf-Sup Stability) *Let $U_h = (\boldsymbol{u}_h, p_h) \in \mathcal{W}_h$ be a pair of discrete velocity and pressure functions. Then, under the assumptions of Lemma 3.10, 3.11, 3.12 and 3.14 on the stabilization parameters, the cut finite element formulation is inf-sup stable*

$$|||U_h|||_* \lesssim \sup_{V_h\in\mathcal{W}_h\setminus\{0\}} \frac{\mathcal{B}_h(U_h,V_h) + \mathcal{J}_h^{\mathrm{CIP}}(U_h,V_h) + \mathcal{G}_h^{\mathrm{GP}}(U_h,V_h)}{|||V_h|||_*}, \tag{3.364}$$

where the hidden stability constant is independent of the mesh size h and the position of the boundary relative to the background mesh.

Proof. For given $U_h \in \mathcal{W}_h$ a suitable test function $V_h \in \mathcal{W}_h$ is constructed on basis of statements provided in Lemma 3.10, 3.11, 3.12 and 3.14. Fundamental idea thereby is to combine the

semi-norm control given by the Nitsche terms and the viscous and reactive ghost penalties (see Lemma 3.10) with additional control gained by the convective and pressure stabilizations $s_\beta, g_\beta, s_p, g_p$ (see Lemma 3.12) and by the divergence stabilizations s_u, g_u (see Lemma 3.11). Moreover, control over the pressure L^2-norm is obtained by utilizing the pressure stabilizations s_p, g_p (see Lemma 3.14).

Step 1. In a first step, control of the weakly scaled divergence $\nabla \cdot \boldsymbol{u}_h$ is gained by testing with the function $V_h^1 \overset{\text{def}}{=} (0, q_h^1)$ with q_h^1 chosen as in Lemma 3.11. Then

$$
\begin{aligned}
&(\mathscr{B}_h + \mathscr{S}_h^{\mathrm{CIP}} + \mathscr{G}_h^{\mathrm{GP}})(U_h, V_h^1) \\
&\quad = -b_h(q_h^1, \boldsymbol{u}_h) + s_p(p_h, q_h^1) + g_p(p_h, q_h^1) && (3.365)\\
&\quad \gtrsim \|\phi_u^{\frac{1}{2}} \nabla \cdot \boldsymbol{u}_h\|_\Omega^2 - c_1\big(s_u(\boldsymbol{u}_h, \boldsymbol{u}_h) + g_u(\boldsymbol{u}_h, \boldsymbol{u}_h) + \|(\phi/h)^{\frac{1}{2}} \boldsymbol{u}_h \cdot \boldsymbol{n}\|_\Gamma^2\big) \\
&\qquad - \delta^{-1}\big(s_p(p_h, p_h) + g_p(p_h, p_h)\big) - \delta\big(s_p(q_h^1, q_h^1) + g_p(q_h^1, q_h^1)\big) && (3.366)\\
&\quad \gtrsim (1-\delta)\|\phi_u^{\frac{1}{2}} \nabla \cdot \boldsymbol{u}_h\|_\Omega^2 - (c_1 + \delta + \delta^{-1})|U_h|_*^2 && (3.367)\\
&\quad \gtrsim \|\phi_u^{\frac{1}{2}} \nabla \cdot \boldsymbol{u}_h\|_\Omega^2 - C_1(\delta)|U_h|_*^2, && (3.368)
\end{aligned}
$$

where in (3.366) the stability estimate (3.266) was used for $|q_h^1|_*^2 = s_p(q_h^1, q_h^1) + g_p(q_h^1, q_h^1)$ (see definition (3.248)).

Step 2. Next, for the same U_h it is set $V_h^2 \overset{\text{def}}{=} (\boldsymbol{v}_h^2, 0)$ with $\boldsymbol{v}_h^2$ taken from Lemma 3.12 and $q_h^2 = 0$. Inserting V_h^2 into $\mathscr{B}_h$ and integrating the remaining b_h by parts leads to

$$
\begin{aligned}
&\mathscr{B}_h(U_h, V_h^2) \\
&\quad = a_h(\boldsymbol{u}_h, \boldsymbol{v}_h^2) + b_h(p_h, \boldsymbol{v}_h^2) && (3.369)\\
&\quad \gtrsim -|||\boldsymbol{u}_h|||_* |||\boldsymbol{v}_h^2|||_* + ((\boldsymbol{\beta} \cdot \nabla)\boldsymbol{u}_h + \nabla p_h, \boldsymbol{v}_h^2)_\Omega && (3.370)\\
&\quad \gtrsim -\delta^{-1}|||\boldsymbol{u}_h|||_*^2 - \delta|||\boldsymbol{v}_h^2|||_*^2 + \|\phi_\beta^{\frac{1}{2}}((\boldsymbol{\beta} \cdot \nabla)\boldsymbol{u}_h + \nabla p_h)\|_\Omega^2 - c_2(1+\omega_h)|U_h|_*^2 && (3.371)\\
&\quad \gtrsim (1-\delta)\|\phi_\beta^{\frac{1}{2}}((\boldsymbol{\beta} \cdot \nabla)\boldsymbol{u}_h + \nabla p_h)\|_\Omega^2 - (c_2(1+\omega_h) + \delta^{-1} + \delta(1+\omega_h))|U_h|_*^2. && (3.372)
\end{aligned}
$$

To obtain (3.370), the boundedness of a_h with respect to $|||\cdot|||_*$ is used, which is obtained by simply applying Cauchy-Schwarz inequalities to all terms except for the non-symmetric advective bulk term. The latter one is comprised with the pressure gradient resulting from integration by parts for b_h. Utilizing estimate (3.285) and applying a δ-scaled Young's inequality yields (3.371). After employing the stability bound (3.286) and the estimate $|||\boldsymbol{u}_h|||_* \lesssim |U_h|_*$ (see definition (3.249)) and resorting of the resulting terms, the estimate (3.372) is obtained. Performing the same steps to the remaining stabilization terms $\mathscr{S}_h^{\mathrm{CIP}} + \mathscr{G}_h^{\mathrm{GP}}$ shows that

$$
\begin{aligned}
&(\mathscr{S}_h^{\mathrm{CIP}} + \mathscr{G}_h^{\mathrm{GP}})(U_h, V_h^2) \\
&\quad \gtrsim -\delta^{-1}|||\boldsymbol{u}_h|||_*^2 - \delta|||\boldsymbol{v}_h^2|||_*^2 && (3.373)\\
&\quad \gtrsim -\delta\|\phi_\beta^{\frac{1}{2}}((\boldsymbol{\beta} \cdot \nabla)\boldsymbol{u}_h + \nabla p_h)\|_\Omega^2 - (\delta^{-1} + \delta(1+\omega_h))|U_h|_*^2, && (3.374)
\end{aligned}
$$

where for (3.374) the stability estimate (3.286) for $\boldsymbol{v}_h^2$ was used. Thus after combining (3.372) and (3.374) and choosing $\delta \sim 0.25$ sufficiently small, it holds

$$
(\mathscr{B}_h + \mathscr{S}_h^{\mathrm{CIP}} + \mathscr{G}_h^{\mathrm{GP}})(U_h, V_h^2) \gtrsim \|\phi_\beta^{\frac{1}{2}}((\boldsymbol{\beta} \cdot \nabla)\boldsymbol{u}_h + \nabla p_h)\|_\Omega^2 - C_2(\delta)(1+\omega_h)|U_h|_*^2, \quad (3.375)
$$

owing to the fact that $(1+c_2)(1+\omega_h) + 2\delta^{-1} + 2\delta(1+\omega_h) \lesssim (1+\omega_h)$.

Step 3. The pressure L^2-norm term can be constructed by testing with $V_h^3 = (\boldsymbol{v}_h^3, 0)$ where $\boldsymbol{v}_h^3$ is now chosen as in Lemma 3.14. Then, by making use of the estimates (3.332), (3.333) and (3.344) and after integrating the advective term by parts

$$\begin{aligned}
\mathscr{B}_h(U_h, V_h^3) &= a_h(\boldsymbol{u}_h, \boldsymbol{v}_h^3) + b_h(p_h, \boldsymbol{v}_h^3) && (3.376)\\
&\gtrsim -|||\boldsymbol{u}_h|||_*|||\boldsymbol{v}_h^3|||_* - (\boldsymbol{u}_h, \boldsymbol{\beta}\cdot\nabla\boldsymbol{v}_h^3)_\Omega + \Phi_p\|p_h\|_\Omega^2 - c_3 s_p(p_h,p_h) && (3.377)\\
&\gtrsim -\delta^{-1}|||\boldsymbol{u}_h|||_*^2 - \delta\Phi_p^{-1}(\|\nabla\boldsymbol{v}_h^3\|_{\Omega_h^*}^2 + \|h^{-\frac{1}{2}}\boldsymbol{v}_h^3\|_\Gamma^2)\\
&\quad - \delta^{-1}|||\boldsymbol{u}_h|||_*^2 - \delta\Phi_p^{-1}\|\nabla\boldsymbol{v}_h^3\|_\Omega^2 + \Phi_p\|p_h\|_\Omega^2 - c_3 s_p(p_h,p_h) && (3.378)\\
&\gtrsim (1-2\delta)\Phi_p\|p_h\|_\Omega^2 - 2\delta^{-1}|||\boldsymbol{u}_h|||_*^2 - c_3 s_p(p_h,p_h) - 2\delta g_p(p_h,p_h) && (3.379)\\
&\gtrsim (1-2\delta)\Phi_p\|p_h\|_\Omega^2 - (c_3 + 2\delta + 2\delta^{-1})|U_h|_*^2. && (3.380)
\end{aligned}$$

Analogously to **Step 2**, by using (3.344) the stabilization terms can be estimated as

$$\begin{aligned}
(\mathscr{S}_h^{\mathrm{CIP}} + \mathscr{G}_h^{\mathrm{GP}})(U_h, V_h^3) &\gtrsim -|||\boldsymbol{u}_h|||_*|||\boldsymbol{v}_h^3|||_* && (3.381)\\
&\gtrsim -\delta\Phi_p\|p_h\|_\Omega^2 - \delta g_p(p_h,p_h) - \delta^{-1}|||\boldsymbol{u}_h|||_*^2 && (3.382)\\
&\gtrsim -\delta\Phi_p\|p_h\|_\Omega^2 - (\delta+\delta^{-1})|U_h|_*^2 && (3.383)
\end{aligned}$$

such that after combining (3.380) and (3.383)

$$(\mathscr{B}_h + \mathscr{S}_h^{\mathrm{CIP}} + \mathscr{G}_h^{\mathrm{GP}})(U_h, V_h^3) \gtrsim \Phi_p\|p_h\|_\Omega^2 - C_3(\delta)|U_h|_*^2. \tag{3.384}$$

Step 4. To gain control over the last missing $|U_h|_*^2$ term in the definition of (3.250), set $V_h^4 \overset{\mathrm{def}}{=} U_h$. The coercivity estimate from Lemma 3.10 shows that

$$\mathscr{B}_h(U_h, V_h^4) + \mathscr{S}_h^{\mathrm{CIP}}(U_h, V_h^4) + \mathscr{G}_h^{\mathrm{GP}}(U_h, V_h^4) \gtrsim |U_h|_*^2. \tag{3.385}$$

Step 5. Finally it is chosen δ sufficiently small. For given U_h, the final test function is defined as

$$V_h^5 \overset{\mathrm{def}}{=} \eta(V_h^1 + (1+\omega_h)^{-1}V_h^2 + V_h^3) + V_h^4. \tag{3.386}$$

Choosing $\eta > 0$ sufficiently small for some $2\eta \sim (C_1(\delta) + C_2(\delta) + C_3(\delta))^{-1}$ allows to gain control over all desired norm parts in $|||U_h|||_*$ and at the same time to absorb the defective $|U_h|_*$-contribution, which results from testing with V_h^1, V_h^2, V_h^3, by the $|U_h|_*$-control obtained from testing with V_h^4. Consequently,

$$\begin{aligned}
&(\mathscr{B}_h + \mathscr{S}_h^{\mathrm{CIP}} + \mathscr{G}_h^{\mathrm{GP}})(U_h, V_h^5)\\
&\quad\gtrsim (1 - \eta(C_1(\delta) + C_2(\delta) + C_3(\delta)))|U_h|_*^2\\
&\qquad + \eta\left(\|\phi_u^{\frac{1}{2}}\nabla\cdot\boldsymbol{u}_h\|_\Omega^2 + \frac{1}{1+\omega_h}\|\phi_\beta^{\frac{1}{2}}((\boldsymbol{\beta}\cdot\nabla)\boldsymbol{u}_h + \nabla p_h)\|_\Omega^2 + \Phi_p\|p_h\|_\Omega^2\right) && (3.387)\\
&\quad\gtrsim |||U_h|||_*^2. && (3.388)
\end{aligned}$$

For inf-sup stability, it still remains to proof that $|||V_h^5|||_* \lesssim |||U_h|||_*$, where

$$|||V_h^5|||_* \leqslant |||U_h|||_* + \eta|||V_h^1|||_* + \frac{\eta}{1+\omega_h}|||V_h^2|||_* + \eta|||V_h^3|||_*. \tag{3.389}$$

Thanks to the stability estimate (3.286) and norm definitions (3.249) and (3.250) it holds

$$|||V_h^2|||_*^2 = |V_h^2|_*^2 + \frac{1}{1+\omega_h}\|\phi_\beta^{\frac{1}{2}}((\boldsymbol{\beta}\cdot\nabla)\boldsymbol{v}_h^2 + 0)\|_\Omega^2 + \|\phi_u^{\frac{1}{2}}\nabla\cdot\boldsymbol{v}_h^2\|_\Omega^2 \tag{3.390}$$

$$= |||\boldsymbol{v}_h^2|||_*^2 + g_p(0,0) + s_p(0,0) + \frac{1}{1+\omega_h}\|\phi_\beta^{\frac{1}{2}}(\boldsymbol{\beta}\cdot\nabla)\boldsymbol{v}_h^2\|_\Omega^2 + \|\phi_u^{\frac{1}{2}}\nabla\cdot\boldsymbol{v}_h^2\|_\Omega^2 \tag{3.391}$$

$$\lesssim (1+\frac{1}{1+\omega_h})(\|\phi_\beta^{\frac{1}{2}}((\boldsymbol{\beta}\cdot\nabla)\boldsymbol{u}_h^2 + \nabla p_h)\|_\Omega^2 + (1+\omega_h)|U_h|_*^2) \tag{3.392}$$

$$\lesssim (1+\frac{1}{1+\omega_h})(1+\omega_h)|||U_h|||_*^2 \tag{3.393}$$

$$\lesssim (1+\omega_h)|||U_h|||_*^2. \tag{3.394}$$

Similarly, the stability bound (3.266) for q_h^1 implies that $|||V_h^1|||_*^2 = \Phi_p\|q_h^1\|_\Omega^2 + |q_h^1|_*^2 \lesssim |||U_h|||_*^2$ and from (3.344) it is obtained that

$$|||V_h^3|||_*^2 = |||\boldsymbol{v}_h^3|||_*^2 + (1+\omega_h)^{-1}\|\phi_\beta^{\frac{1}{2}}(\boldsymbol{\beta}\cdot\nabla)\boldsymbol{v}_h^3\|_\Omega^2 + \|\phi_u^{\frac{1}{2}}\nabla\cdot\boldsymbol{v}_h^3\|_\Omega^2 \tag{3.395}$$

$$\lesssim \Phi_p^{-1}(\|\nabla\boldsymbol{v}_h^3\|_{\Omega_h^*}^2 + \|\boldsymbol{v}_h^3 h^{-\frac{1}{2}}\|_\Gamma^2) \lesssim |||U_h|||_*^2. \tag{3.396}$$

As a result it holds

$$|||V_h^5|||_* \lesssim (1+\eta+\eta(1+\omega_h)^{-\frac{1}{2}}+\eta)|||U_h|||_* \lesssim |||U_h|||_*. \tag{3.397}$$

This concludes the proof of inf-sup stability with

$$(\mathscr{B}_h + \mathscr{S}_h^{\mathrm{CIP}} + \mathscr{G}_h^{\mathrm{GP}})(U_h, V_h^5) \gtrsim |||U_h|||_*|||V_h^5|||_*, \tag{3.398}$$

followed by a division by $|||V_h^5|||_*$ and choosing the supremum over $V_h \in \mathscr{W}_h\backslash\{0\}$.

□

Remark 3.20 *As a major consequence of the previous inf-sup stability theorem, existence and uniqueness of a discrete solution $U_h = (\boldsymbol{u}_h, p_h) \in \mathscr{W}_h$ of the stabilized Nitsche-type cut finite element method is guaranteed.*

Remark 3.21 *Note that in the previous theorem inf-sup stability is proven with respect to an energy-norm $|||U_h|||_*$, which is based on the underlying (active) background mesh $\mathscr{T}_h$. Thereby, the different ghost-penalty operators $g_\nu, g_\sigma, g_\beta, g_u, g_p$ ensure sufficient control over discrete polynomials defined on the entire (active) computational mesh and so significantly improve the system conditioning of the resulting linear matrix system - for all different flow regimes and independent of how the boundary intersects the mesh. For further details on the improvement of the system conditioning owing to the use of ghost-penalties, the reader is referred to Sections 3.4.1 and 3.4.3 with regard to detailed elaborations and to works by Burman and Hansbo [45] and Massing* et al. *[180] for numerical analyses.*

3.5.6 A Priori Error Estimates

Equipped with the inf-sup condition (3.364), the main *a priori* error estimates can be proven as stated in Theorem 3.19 at the end of this section. It is proceeded in four steps. First, a weak Galerkin orthogonality property for $\mathscr{B}_h$ is provided. Second, a further lemma is concerned with potential consistency errors introduced by the CIP and GP stabilization forms $\mathscr{S}_h^{\mathrm{CIP}}$ and $\mathscr{G}_h^{\mathrm{GP}}$ and, third, interpolation error estimates are derived. Finally, the previous steps are combined and an *a priori* estimate is proven for the velocity and pressure error.

Galerkin Orthogonality. The first lemma shows that the discrete formulation (3.186) satisfies a weakened form of the Galerkin orthogonality.

Lemma 3.16 *Suppose that the solution $U \overset{def}{=} (\boldsymbol{u}, p)$ of the variational formulation (3.180) is in $[H^2(\Omega)]^d \times H^1(\Omega)$ and let $U_h \overset{def}{=} (\boldsymbol{u}_h, p_h) \in \mathscr{V}_h \times \mathscr{Q}_h$ be the finite element solution to the discrete weak formulation (3.186). Then*

$$\mathscr{B}_h(U - U_h, V_h) = \mathscr{S}_h^{\mathrm{CIP}}(U_h, V_h) + \mathscr{G}_h^{\mathrm{GP}}(U_h, V_h). \tag{3.399}$$

Proof. The proof follows immediately from the fact that the continuous solution U satisfies $\mathscr{B}_h(U, V_h) = \mathscr{L}_h(V_h)$ due to the definition of the weak problem (3.180) and the strong consistency of all boundary terms related to the Nitsche method.

□

Consistency Error Estimates. The next lemma ensures that the remainder term arising in the weakened Galerkin orthogonality (3.399) does not deteriorate the convergences rate of the proposed scheme and thus is weakly consistent.

Lemma 3.17 *Assume that the solution U provides the regularity $(\boldsymbol{u}, p) \in [H^r(\Omega)]^d \times H^s(\Omega)$ and let $r_u \overset{def}{=} \min\{r, k+1\}$ and $s_p \overset{def}{=} \min\{s, k+1\}$, where k is the polynomial degree of the approximation spaces for the velocity and pressure. Then*

$$\begin{aligned}\mathscr{S}_h^{\mathrm{CIP}}(\Pi_h^* U, \Pi_h^* U) + \mathscr{G}_h^{\mathrm{GP}}(\Pi_h^* U, \Pi_h^* U) \lesssim (\nu + \|\boldsymbol{\beta}\|_{0,\infty,\Omega} h + \sigma h^2) h^{2r_u - 2} \|\boldsymbol{u}\|_{r_u,\Omega}^2 \\ + \max_{T \in \mathscr{T}_h} \left\{ \frac{1}{\nu + \|\boldsymbol{\beta}\|_{0,\infty,T} h + \sigma h^2} \right\} h^{2s_p} \|p\|_{s_p,\Omega}^2,\end{aligned} \tag{3.400}$$

where $\Pi_h^* U \in \mathscr{W}_h$ denotes the Clément interpolant of the velocity and pressure solution U.

Proof. Recall the definition of the GP operators

$$\begin{aligned}\mathscr{G}_h^{\mathrm{GP}}(\Pi_h^* U, \Pi_h^* U) = g_\sigma(\boldsymbol{\pi}_h^* \boldsymbol{u}, \boldsymbol{\pi}_h^* \boldsymbol{u}) + g_\nu(\boldsymbol{\pi}_h^* \boldsymbol{u}, \boldsymbol{\pi}_h^* \boldsymbol{u}) + g_\beta(\boldsymbol{\pi}_h^* \boldsymbol{u}, \boldsymbol{\pi}_h^* \boldsymbol{u}) + g_u(\boldsymbol{\pi}_h^* \boldsymbol{u}, \boldsymbol{\pi}_h^* \boldsymbol{u}) \\ + g_p(\pi_h^* p, \pi_h^* p),\end{aligned} \tag{3.401}$$

it is enough to derive the desired estimate for g_β and g_p. All other terms can be bounded similarly.

Owing to the fact that $p \in H^{s_p}(\Omega)$, its traces $\partial_{\boldsymbol{n}}^j p|_F$ at interior faces $F \in \mathscr{F}_i$ are uniquely defined for $0 \leqslant j \leqslant s_p - 1$ and therefore, $[\![\partial_{\boldsymbol{n}}^j p]\!] = 0$. Consequently

$$g_p(\pi_h^* p, \pi_h^* p) \lesssim \sum_{F \in \mathscr{F}_\Gamma} \sum_{j=1}^{k} \phi_{p,F} h^{2j-1} \langle [\![\partial_{\boldsymbol{n}}^j \pi_h^* p]\!], [\![\partial_{\boldsymbol{n}}^j \pi_h^* p]\!] \rangle_F \tag{3.402}$$

$$= \sum_{F \in \mathscr{F}_\Gamma} \left(\sum_{j=1}^{s_p-1} \phi_{p,F} h^{2j-1} \langle [\![\partial_{\boldsymbol{n}}^j (\pi_h^* p - p)]\!], [\![\partial_{\boldsymbol{n}}^j (\pi_h^* p - p)]\!] \rangle_F \right. \tag{3.403}$$

$$\left. + \sum_{j=s_p}^{k} \phi_{p,F} h^{2j-1} \langle [\![\partial_{\boldsymbol{n}}^j \pi_h^* p]\!], [\![\partial_{\boldsymbol{n}}^j \pi_h^* p]\!] \rangle_F \right) = I_p + II_p, \tag{3.404}$$

where I_p and II_p represents the consistent and inconsistent part of the ghost-penalty term g_p, respectively. Now, using trace and inverse inequalities (3.49) and (3.46), the interpolation estimate for π_h^* (3.61) and the definition of ϕ_p (3.203)

$$I_p \lesssim \sum_{F \in \mathscr{F}_\Gamma} \sum_{j=1}^{s_p-1} \phi_{p,F} h^{2j-1} \|D^j (\pi_h^* p - p)\|_F^2 \tag{3.405}$$

$$\lesssim \sum_{T \in \mathscr{T}_\Gamma} \sum_{j=1}^{s_p-1} \phi_{p,T} h^{2j-1} \left(h^{-1} \|D^j (\pi_h^* p - p)\|_T^2 + h \|D^{j+1} (\pi_h^* p - p)\|_T^2 \right) \tag{3.406}$$

$$\lesssim \sum_{T \in \mathscr{T}_\Gamma} (\phi_{p,T} h^{2j-1} h^{-1} h^{2s_p - 2j}) \|p^*\|_{s_p,\omega(T)}^2 \tag{3.407}$$

$$\lesssim \max_{T \in \mathscr{T}_h} \left\{ \frac{1}{\nu + \|\boldsymbol{\beta}\|_{0,\infty,T} h + \sigma h^2} \right\} h^{2s_p} \|p^*\|_{s_p,\Omega}^2. \tag{3.408}$$

To estimate II_p, the trace and inverse inequalities (3.47) and (3.46) are simply combined with the stability (3.63) of the interpolator π_h^*

$$II_p \lesssim \sum_{F \in \mathscr{F}_\Gamma} \sum_{j=s_p}^{k} \phi_{p,F} h^{2j-1} ([\![\partial_{\boldsymbol{n}}^j \pi_h^* p]\!], [\![\partial_{\boldsymbol{n}}^j \pi_h^* p]\!])_F \tag{3.409}$$

$$\lesssim \sum_{T \in \mathscr{T}_\Gamma} \sum_{j=s_p}^{k} \phi_{p,T} h^{2j-2} \|D^j \pi_h^* p\|_T^2 \tag{3.410}$$

$$\lesssim \sum_{T \in \mathscr{T}_\Gamma} \phi_{p,T} h^{2s_p-2} \|D^{s_p} \pi_h^* p\|_T^2 \lesssim \max_{T \in \mathscr{T}_h} \left\{ \frac{1}{\nu + \|\boldsymbol{\beta}\|_{0,\infty,T} h + \sigma h^2} \right\} h^{2s_p} \|p^*\|_{s_p,\Omega}^2. \tag{3.411}$$

Together with the stability of the extension operator (3.57), this yields the desired estimate. The corresponding estimates for g_ν, g_σ and g_u can be derived analogously, resulting in

$$g_\nu(\boldsymbol{\pi}_h^* \boldsymbol{u}, \boldsymbol{\pi}_h^* \boldsymbol{u}) \lesssim \nu h^{2r_u - 2} \|\boldsymbol{u}\|_{r_u,\Omega}^2, \tag{3.412}$$

$$g_\sigma(\boldsymbol{\pi}_h^* \boldsymbol{u}, \boldsymbol{\pi}_h^* \boldsymbol{u}) \lesssim (\sigma h^2) h^{2r_u - 2} \|\boldsymbol{u}\|_{r_u,\Omega}^2, \tag{3.413}$$

$$g_u(\boldsymbol{\pi}_h^* \boldsymbol{u}, \boldsymbol{\pi}_h^* \boldsymbol{u}) \lesssim \phi_u h^{2r_u - 2} \|\boldsymbol{u}\|_{r_u,\Omega}^2 \tag{3.414}$$

$$\lesssim (\nu + \|\boldsymbol{\beta}\|_{0,\infty,\Omega} h + \sigma h^2) h^{2r_u - 2} \|\boldsymbol{u}\|_{r_u,\Omega}^2. \tag{3.415}$$

Special attention has to be directed to g_β. Since $\boldsymbol{u} \in [H^r(\Omega)]^d$, its traces $\partial_{\boldsymbol{n}}^j \boldsymbol{u}|_F$ are uniquely defined for $0 \leqslant j \leqslant r_u - 1$ and therefore $[\![(\boldsymbol{\beta}_h \cdot \nabla)\partial_{\boldsymbol{n}}^j \boldsymbol{u}]\!] = \boldsymbol{0}$ for $0 \leqslant j \leqslant r_{\boldsymbol{u}} - 2$. Consequently

$$g_{\boldsymbol{\beta}}(\boldsymbol{\pi}_h^* \boldsymbol{u}, \boldsymbol{\pi}_h^* \boldsymbol{u}) \lesssim \sum_{F \in \mathscr{F}_\Gamma} \left(\sum_{j=0}^{r_u-2} h^{2j-1} \|\phi_{\beta,F}^{\frac{1}{2}} [\![(\boldsymbol{\beta}_h \cdot \nabla)\partial_{\boldsymbol{n}}^j (\boldsymbol{\pi}_h^* \boldsymbol{u} - \boldsymbol{u})]\!]\|_F^2 + \sum_{j=r_u-1}^{k-1} h^{2j-1} \|\phi_{\beta,F}^{\frac{1}{2}} [\![(\boldsymbol{\beta}_h \cdot \nabla)\partial_{\boldsymbol{n}}^j \boldsymbol{\pi}_h^* \boldsymbol{u}]\!]\|_F^2 \right) = I_\beta + II_\beta. \tag{3.416}$$

The interpolation estimate (3.62) together with the fact that by definition of the stabilization parameter $\phi_{\beta,T} \lesssim \|\boldsymbol{\beta}\|_{0,\infty,T} h$ implies now that the first term can be bounded by

$$I_\beta \lesssim \sum_{T \in \mathscr{T}_h} \sum_{j=0}^{r_u-2} h^{2j-1} \phi_{\beta,T} \|\boldsymbol{\beta}_h\|_{0,\infty,T}^2 \|\nabla \partial_{\boldsymbol{n}}^j (\boldsymbol{\pi}_h^* \boldsymbol{u} - \boldsymbol{u})\|_{\partial T}^2 \tag{3.417}$$

$$\lesssim \sum_{T \in \mathscr{T}_h} \|\boldsymbol{\beta}\|_{0,\infty,T} h^{2r_u-1} \|\boldsymbol{u}^*\|_{r_u,\omega(T)}^2 \lesssim \|\boldsymbol{\beta}\|_{0,\infty,\Omega} h^{2r_u-1} \|\boldsymbol{u}\|_{r_u,\Omega}^2. \tag{3.418}$$

Turning to the second term II_β, a simple application of the inverse estimate (3.47) shows that

$$II_\beta \lesssim \sum_{T \in \mathscr{T}_h} \phi_{\beta,T} \|\boldsymbol{\beta}\|_{0,\infty,T}^2 h^{2r_u-2} \|D^{r_u} \boldsymbol{\pi}_h^* \boldsymbol{u}\|_T^2 \lesssim \|\boldsymbol{\beta}\|_{0,\infty,\Omega} h^{2r_u-1} \|\boldsymbol{u}\|_{r_u,\Omega}^2 \tag{3.419}$$

after observing that $\boldsymbol{\pi}_h^*$ is stable thanks to (3.63).

The estimate for $\mathscr{G}_h^{\mathrm{GP}}$ being replaced by $\mathscr{S}_h^{\mathrm{CIP}}$ now follows simply by applying the same estimates to all interior facets $F \in \mathscr{F}_i$.

□

Interpolation Error Estimates. The next lemma ensures that the interpolation error between continuous solution and its Clément interpolation converges with optimal rates.

Lemma 3.18 *Assume that $\boldsymbol{u} \in [H^r(\Omega)]^d$ and $p \in H^s(\Omega)$ and let $r_u \overset{def}{=} \min\{r, k+1\} \geqslant 2$ and $s_p \overset{def}{=} \min\{s, k+1\} \geqslant 1$ where k is the polynomial degree of the approximation spaces. Let $|||\boldsymbol{u}|||$ be the natural energy norm as defined in (3.220) and $\boldsymbol{\pi}_h^* \boldsymbol{u} \in \mathscr{V}_h$ and $\pi_h^* p \in \mathscr{Q}_h$ the extended Clément interpolant of $\boldsymbol{u}$ and p, then*

$$|||\boldsymbol{u}^* - \boldsymbol{\pi}_h^* \boldsymbol{u}||| \lesssim (\nu + \|\boldsymbol{\beta}\|_{0,\infty,\Omega} h + \sigma h^2)^{\frac{1}{2}} h^{r_u-1} \|\boldsymbol{u}\|_{r_u,\Omega}, \tag{3.420}$$

$$\|p^* - \pi_h^* p\|_\Omega \lesssim h^{s_p} \|p\|_{s_p,\Omega}. \tag{3.421}$$

Proof. The proof is only sketched. First, recall the definition of ϕ_u (3.203) and use the trace inequality (3.50) together with the interpolation estimate (3.61) to show that the boundary terms can be estimated in terms of the element contributions:

$$\|(\nu + \phi)^{\frac{1}{2}} h^{-\frac{1}{2}} (\boldsymbol{u}^* - \boldsymbol{\pi}_h^* \boldsymbol{u})\|_\Gamma^2 \lesssim (\nu + \|\boldsymbol{\beta}\|_{0,\infty,\Omega} h + \sigma h^2) \big(h^{-2} \|\boldsymbol{u}^* - \boldsymbol{\pi}_h^* \boldsymbol{u}\|_{\Omega_h^*}^2 + \|\nabla(\boldsymbol{u}^* - \boldsymbol{\pi}_h^* \boldsymbol{u})\|_{\Omega_h^*}^2 \big) \tag{3.422}$$

$$\lesssim (\nu + \|\boldsymbol{\beta}\|_{0,\infty,\Omega} h + \sigma h^2) h^{2(r_u-1)} \|\boldsymbol{u}\|_{r_u,\Omega}^2, \tag{3.423}$$

$$\begin{aligned}\|\|\boldsymbol{\beta}\cdot\boldsymbol{n}\|^{\frac{1}{2}}(\boldsymbol{u}^*-\boldsymbol{\pi}_h^*\boldsymbol{u})\|_\Gamma^2 &\lesssim \|\boldsymbol{\beta}\|_{0,\infty,\Omega}(h^{-1}\|\boldsymbol{u}^*-\boldsymbol{\pi}_h^*\boldsymbol{u}\|_{\Omega_h^*}^2+h\|\nabla(\boldsymbol{u}^*-\boldsymbol{\pi}_h^*\boldsymbol{u})\|_{\Omega_h^*}^2) &(3.424)\\ &\lesssim (\|\boldsymbol{\beta}\|_{0,\infty,\Omega}h)h^{2r_u-2}\|\boldsymbol{u}\|_{r_u,\Omega}^2. &(3.425)\end{aligned}$$

The viscous and reactive parts can be estimated analogously as

$$\|\nu^{\frac{1}{2}}\nabla(\boldsymbol{u}^*-\boldsymbol{\pi}_h^*\boldsymbol{u})\|_\Omega^2+\|\sigma^{\frac{1}{2}}(\boldsymbol{u}^*-\boldsymbol{\pi}_h^*\boldsymbol{u})\|_\Omega^2\lesssim(\nu+\sigma h^2)h^{2r_u-2}\|\boldsymbol{u}\|_{r_u,\Omega}^2. \tag{3.426}$$

The remaining s_β and s_u terms can be estimated exactly in the same way as in the consistent part in the error estimate for g_β and g_u, see (3.417)–(3.418). The estimate for the pressure follows directly from (3.61).

□

Energy-type A Priori Error Estimates. The subsequent theorem states the main *a priori* error estimate for the velocity in a natural energy norm and for the pressure in an L^2-norm.

Theorem 3.19 *Assume that $U \overset{def}{=} (\boldsymbol{u},p)\in[H^r(\Omega)]^d\times H^s(\Omega)$ is the weak solution of the Oseen problem (3.180) and let $U_h\overset{def}{=}(\boldsymbol{u}_h,p_h)\in\mathcal{V}_h\times\mathcal{Q}_h$ be the discrete solution of the Nitsche-type cut finite element formulation (3.186). Then*

$$\begin{aligned}|\|\boldsymbol{u}^*-\boldsymbol{u}_h\|| &\lesssim (1+\omega_h)^{\frac{1}{2}}\left(\nu+\|\boldsymbol{\beta}\|_{0,\infty,\Omega}h+\sigma h^2\right)^{\frac{1}{2}}h^{r_u-1}\|\boldsymbol{u}\|_{r_u,\Omega}\\ &\quad+\max_{T\in\mathcal{T}_h}\left\{\frac{1}{\nu+\|\boldsymbol{\beta}\|_{0,\infty,T}h+\sigma h^2}\right\}^{\frac{1}{2}}h^{s_p}\|p\|_{s_p,\Omega}, &(3.427)\\ \|p^*-p_h\|_\Omega &\lesssim \Phi_p^{-\frac{1}{2}}(1+\omega_h)^{\frac{1}{2}}\left(\nu+\|\boldsymbol{\beta}\|_{0,\infty,\Omega}h+\sigma h^2\right)^{\frac{1}{2}}h^{r_u-1}\|\boldsymbol{u}\|_{r_u,\Omega}\\ &\quad+\left(1+\Phi_p^{-\frac{1}{2}}\max_{T\in\mathcal{T}_h}\left\{\frac{1}{\nu+\|\boldsymbol{\beta}\|_{0,\infty,T}h+\sigma h^2}\right\}^{\frac{1}{2}}\right)h^{s_p}\|p\|_{s_p,\Omega}, &(3.428)\end{aligned}$$

where $r_u\overset{def}{=}\min\{r,k+1\}$ and $s_p\overset{def}{=}\min\{s,k+1\}$. The constant Φ_p and the bounded scaling function ω_h are defined as in (3.223) and (3.233). Note that the hidden constants are independent of h and particularly independent of how the boundary intersects the mesh $\mathcal{T}_h$.

Proof. The two estimates are obtained by splitting the error into projection and discrete errors

$$\begin{aligned}|\|\boldsymbol{u}^*-\boldsymbol{u}_h\|| &\lesssim \|\boldsymbol{u}^*-\boldsymbol{\pi}_h^*\boldsymbol{u}\|_\Omega+\|\boldsymbol{\pi}_h^*\boldsymbol{u}-\boldsymbol{u}_h\|_\Omega\lesssim\|\boldsymbol{u}^*-\boldsymbol{\pi}_h^*\boldsymbol{u}\|_\Omega+|\|\Pi_h^*U-U_h\||_*, &(3.429)\\ \|p^*-p_h\|_\Omega &\lesssim \|p^*-\pi_h^*p\|_\Omega+\|\pi_h^*p-p_h\|_\Omega\lesssim\|p^*-\pi_h^*p\|_\Omega+\Phi_p^{-\frac{1}{2}}|\|\Pi_h^*U-U_h\||_*. &(3.430)\end{aligned}$$

Thanks to the interpolation estimates (3.427) and (3.428), it is enough to estimate the discrete error $|\|\Pi_h^*U-U_h\||_*$. The inf-sup condition (3.364) from Theorem 3.15 ensures that there exists a V_h with $|\|V_h\||_*=1$ such that together with the weak Galerkin orthogonality (3.399) from Lemma 3.16

$$\begin{aligned}|\|\Pi_h^*U-U_h\||_* &\lesssim \mathscr{B}_h(\Pi_h^*U-U_h,V_h)+\mathscr{S}_h^{\mathrm{CIP}}(\Pi_h^*U-U_h,V_h)+\mathscr{G}_h^{\mathrm{GP}}(\Pi_h^*U-U_h,V_h)\\ &=\mathscr{B}_h(\Pi_h^*U-U,V_h)+\mathscr{S}_h^{\mathrm{CIP}}(\Pi_h^*U,V_h)+\mathscr{G}_h^{\mathrm{GP}}(\Pi_h^*U,V_h). &(3.431)\end{aligned}$$

After applying a Cauchy-Schwarz inequality in combination with Lemma 3.17, the last two terms in (3.431) can be bounded by

$$\begin{aligned}
&\mathscr{S}_h^{\mathrm{CIP}}(\Pi_h^* U, V_h) + \mathscr{G}_h^{\mathrm{GP}}(\Pi_h^* U, V_h) \\
&\quad\lesssim \Bigg((\nu + \|\boldsymbol{\beta}\|_{0,\infty,\Omega} h + \sigma h^2)^{\frac{1}{2}} h^{r_u - 1} \|\boldsymbol{u}\|_{r_u,\Omega} \\
&\qquad + \max_{T \in \mathcal{T}_h} \left\{ \frac{1}{\nu + \|\boldsymbol{\beta}\|_{0,\infty,T} h + \sigma h^2} \right\}^{\frac{1}{2}} h^{s_p} \|p\|_{s_p,\Omega} \Bigg) \cdot \underbrace{|||V_h|||_*}_{=1},
\end{aligned} \tag{3.432}$$

and thus it remains to estimate $\mathscr{B}_h(\Pi_h^* U - U, V_h)$. Recalling definition (3.189), it holds that

$$\begin{aligned}
&\mathscr{B}_h(\Pi_h^* U - U, V_h) \\
&\quad = a_h(\boldsymbol{\pi}_h^* \boldsymbol{u} - \boldsymbol{u}, \boldsymbol{v}_h) + b_h(\pi_h^* p - p, \boldsymbol{v}_h) - b_h(q_h, \boldsymbol{\pi}_h^* \boldsymbol{u} - \boldsymbol{u}) && (3.433) \\
&\quad \lesssim |||\boldsymbol{\pi}_h^* \boldsymbol{u} - \boldsymbol{u}|||||\boldsymbol{v}_h||| - (\boldsymbol{\pi}_h^* \boldsymbol{u} - \boldsymbol{u}, (\boldsymbol{\beta} \cdot \nabla)\boldsymbol{v}_h + \nabla q_h) + b_h(\pi_h^* p - p, \boldsymbol{v}_h) && (3.434) \\
&\quad = I + II + III && (3.435)
\end{aligned}$$

after integrating $b_h(q_h, \boldsymbol{\pi}_h^* \boldsymbol{u} - \boldsymbol{u})$ and the convective part in a_h by parts and applying a Cauchy-Schwarz inequality to the remaining terms in a_h.

Term I. A simple application of the interpolation estimate (3.427) together with the inequality $|||\boldsymbol{v}_h||| \lesssim |||V_h|||_*$ gives the desired estimate

$$I \lesssim (\nu + \|\boldsymbol{\beta}\|_{0,\infty,\Omega} h + \sigma h^2)^{\frac{1}{2}} h^{r_u - 1} \|\boldsymbol{u}\|_{r_u,\Omega} \cdot \underbrace{|||V_h|||_*}_{=1}. \tag{3.436}$$

Term II. Applying a Cauchy-Schwarz inequality, followed by the interpolation estimate (3.59) together with the definition of ϕ_β (3.203), yields

$$\begin{aligned}
II &\lesssim (1 + \omega_h)^{\frac{1}{2}} \|\phi_\beta^{-\frac{1}{2}} (\boldsymbol{\pi}_h^* \boldsymbol{u}_h - \boldsymbol{u})\|_\Omega \cdot (1 + \omega_h)^{-\frac{1}{2}} \|\phi_\beta^{\frac{1}{2}} ((\boldsymbol{\beta} \cdot \nabla)\boldsymbol{v}_h + \nabla q_h)\|_\Omega && (3.437) \\
&\lesssim (1 + \omega_h)^{\frac{1}{2}} (\nu + \|\boldsymbol{\beta}\|_{0,\infty,\Omega} h + \sigma h^2)^{\frac{1}{2}} h^{r_u - 1} \|\boldsymbol{u}\|_{r_u,\Omega} \cdot \underbrace{|||V_h|||_*}_{=1}. && (3.438)
\end{aligned}$$

Term III. Similarly, by applying a Cauchy-Schwarz inequality, a trace inequality (3.50) and the interpolation estimate (3.59) together with the definition of ϕ_u, it is obtained that

$$\begin{aligned}
III &= -(\pi_h^* p - p, \nabla \cdot \boldsymbol{v}_h)_\Omega + \langle \pi_h^* p - p, \boldsymbol{v}_h \cdot \boldsymbol{n} \rangle_\Gamma && (3.439) \\
&\lesssim \left(\|\phi_u^{-\frac{1}{2}} (\pi_h^* p - p)\|_\Omega + \|h^{\frac{1}{2}} \phi_u^{-\frac{1}{2}} (\pi_h^* p - p)\|_\Gamma \right) \left(\|\phi_u^{\frac{1}{2}} \nabla \cdot \boldsymbol{v}_h\|_\Omega + \|(\phi_u / h)^{\frac{1}{2}} \boldsymbol{v}_h \cdot \boldsymbol{n}\|_\Gamma \right) && (3.440) \\
&\lesssim \|\phi_u^{-\frac{1}{2}} (\pi_h^* p - p)\|_{\Omega_h^*} |||V_h|||_* \lesssim \left(\sum_{T \in \mathcal{T}_h} \frac{h^{2 s_p} \|p^*\|_{s_p,\omega(T)}^2}{\nu + \|\boldsymbol{\beta}\|_{0,\infty,T} h + \sigma h^2} \right)^{\frac{1}{2}} \cdot |||V_h|||_* && (3.441) \\
&\lesssim \max_{T \in \mathcal{T}_h} \left\{ \frac{1}{\nu + \|\boldsymbol{\beta}\|_{0,\infty,T} h + \sigma h^2} \right\}^{\frac{1}{2}} h^{s_p} \|p^*\|_{s_p,\Omega} \cdot \underbrace{|||V_h|||_*}_{=1}, && (3.442)
\end{aligned}$$

which shows the need for the mass conserving Nitsche penalty term and introduces the dependency of the energy-norm estimate on the pressure solution.

Combining (3.429), (3.430), (3.431), (3.432) with the estimates for I, II and III and the interpolation error estimates (3.420) and (3.421) from Lemma 3.18 concludes the final *a priori* error estimates (3.427) and (3.428).

□

Remark 3.22 *It has to be noted that the derived* a priori *error estimate shows similar error convergence behavior, as proven by Burman* et al. *[48] for boundary-fitted meshes. Depending on the dominant part in the Oseen equations, the velocity part of the energy norm error scales as expected with ν for viscous flows, with $\|\boldsymbol{\beta}\|_{0,\infty,\Omega}h$ for advective dominant flows and with σh^2 if reaction dominates in the partial differential equation. The dependency on the pressure error thereby behaves the exact inverse. The scaling ω_h (3.233) appearing in the estimate reflects the approximation of the advective velocity $\boldsymbol{\beta}$ by a discrete counterpart $\boldsymbol{\beta}_h$ as indicated by the incorporated norm $|\boldsymbol{\beta}|_{1,\infty,\Omega_h^*}$ in relation to the viscous and reactive parts.*

Remark 3.23 *For high Reynolds-number flows, i.e. $\nu \leqslant \|\boldsymbol{\beta}\|_{0,\infty,\Omega}h$, from the* a priori *error estimate the velocity is expected to converge with suboptimal rate $\|\boldsymbol{u}^* - \boldsymbol{u}_h\|_\Omega = \mathcal{O}\left(h^{k+\frac{1}{2}}\right)$ in the L^2-norm, as usual for convective-dominant problems, if for the pressure holds $p \in H^{k+1}(\Omega)$.*

Remark 3.24 *Note that the energy-norm estimate would yield just $\|\boldsymbol{u}^* - \boldsymbol{u}_h\|_\Omega = \mathcal{O}\left(h^k\right)$ for the low-Reynolds-number case, i.e. $\nu \geqslant \|\boldsymbol{\beta}\|_{0,\infty,\Omega}h$. However, similar as shown in the work by Burman* et al. *[48], for the low-Reynolds-number case, an optimal error convergence with respect to the velocity L^2-norm $\|\boldsymbol{u}^* - \boldsymbol{u}_h\|_\Omega = \mathcal{O}\left(h^{k+1}\right)$ can be derived for the adjoint-consistency Nitsche formulation. A proof of this uses the standard Aubin–Nitsche duality technique and the deduced energy-norm estimate. A detailed presentation, however, goes beyond the scope of this thesis.*

3.5.7 Numerical Convergence Studies

To validate the proposed stabilized unfitted finite element method different numerical examples are investigated. Theoretical results for the Oseen equations obtained from the *a priori* error analysis stated in Theorem 3.19 will be confirmed by several basic test examples, the Taylor problem in two dimensions and the Beltrami-flow problem in three dimensions. Thereby, convergence properties are examined for the low- and the high-Reynolds-number regime.

3.5.7.1 Two-Dimensional Taylor Problem

To confirm the optimal order *a priori* error estimate proposed in Theorem 3.19, error convergence for the two-dimensional Taylor problem is studied. The periodic steady velocity and pressure fields $(\boldsymbol{u}, p)$ have been already introduced in Section 3.4.4.2, see (3.164)–(3.166) with $g_u(t) = g_p(t) = 1.0$. A numerical approximation is computed on a circular fluid domain

$$\Omega^{\mathrm{f}} = \{\boldsymbol{x} = (x_1, x_2) \in \mathbb{R}^2 \mid \phi(\boldsymbol{x}) = \sqrt{(x_1 - 0.5)^2 + (x_2 - 0.5)^2} - 0.45 < 0\}, \tag{3.443}$$

where the boundary Γ is represented implicitly by the zero-level set of the function ϕ. The field

is defined within a background square $[0,1]^2$ and approximated on a background mesh $\widehat{\mathcal{T}}_h$ consisting of linear right-angled triangular elements $\mathbb{P}^1(T)$. The right-hand side $\boldsymbol{f}$ is adapted such that (3.164)–(3.166) are solution to the Oseen problem (3.176)–(3.178) which then emerges to $\boldsymbol{f} = \boldsymbol{u}/\Delta t + \boldsymbol{u}\cdot\nabla\boldsymbol{u} - \nabla\cdot(2\nu\boldsymbol{\epsilon}(\boldsymbol{u})) + \nabla p$. The boundary condition $\boldsymbol{g}_\mathrm{D}$ is given by the analytical solution (3.164)–(3.166) and is imposed using the unfitted Nitsche-type technique introduced in Section 3.5.2. The constant pressure mode is filtered out in the iterative solver, such that $\int_\Omega p_h - p\,\mathrm{d}x = 0$. The resulting Oseen system can be interpreted as a single time step of a backward Euler time-discretization scheme applied to the linearized Navier-Stokes equations, where $\sigma = 1/\Delta t$ is the inverse of the time-step length. The advective velocity is given by the exact solution $\boldsymbol{\beta} = \boldsymbol{u}$ with $\boldsymbol{\beta}_h = I_h\boldsymbol{u}$ its nodal interpolation.

All background meshes $\widehat{\mathcal{T}}_h$ consist of equal-sized triangles with mesh sizes $h = 1/n$ and $n \in [10; 240]$, where h denotes the short length of the triangles, respectively. It has to be noted that the set of active elements $\mathcal{T}_h$ used for approximating $\boldsymbol{u}_h$ and p_h varies with mesh refinement since all background meshes are non-boundary-fitted. In the following, linear equal-order approximations $\mathbb{P}^1$ for velocity and pressure in $\mathcal{V}_h^1 \times \mathcal{Q}_h^1$ are investigated.

Related to the triple norm $|||\cdot|||$ defined in (3.220)–(3.224), different L^2- and H^1-semi-norms are computed to measure velocity and pressure approximation errors $(\boldsymbol{u}_h - \boldsymbol{u})$ and $(p_h - p)$ in the bulk Ω and on the boundary Γ, respectively. To examine convergence rates for different Reynolds-number regimes, all errors are computed for two different viscosities of $\nu = 0.1$ and $\nu = 0.0001$. Furthermore, to investigate the effect of possibly dominating σ-scalings in the fluid stabilizations and the mass-conservation boundary terms, but also to demonstrate the importance of the (pseudo-)reactive ghost-penalty term g_σ, the studies are carried out for varying σ.

Viscous-Dominated Flow. In the viscous case with $\nu = 0.1$, for all considered meshes element Reynolds numbers are small, i.e. $\mathrm{Re}_T = \|\boldsymbol{\beta}\|_{0,\infty,T} h/\nu \leqslant 1$ since $\|\boldsymbol{\beta}\|_{0,\infty,\Omega} \leqslant 1$. While all viscous scalings appearing in the boundary terms related to Nitsche's method as well as in the pressure-stabilization terms, i.e. $\phi, \phi_\beta, \phi_u, \phi_p$ (3.203), are highly important to guarantee inf-sup stability, all advective contributions to incorporated scalings are not required for this setting. Furthermore, the CIP terms s_β, s_u as well as related ghost-penalty terms g_β, g_u are not essential to guarantee stability in this case. Note that the applied scalings (3.32) only contribute a little and so do not deteriorate convergence rates or increase the error levels. In Figure 3.14 computed errors for the stabilized CutFEM from (3.186) are presented. As desired, optimal convergence is obtained for all considered velocity norms, while for the pressure a super-convergent rate of order $3/2$ can be observed in the asymptotic range; this is due to the high regularity of the solution as has been already frequently reported in literature before, see, e.g., in Burman *et al.* [48]. Moreover, the L^2-optimality $\mathcal{O}(h^2)$ of the velocity in the low-Reynolds-number regime could be confirmed, see Remark 3.24.

To further investigate the effect of large scalings $\sigma \gg 1$, which corresponds to the choice of small time steps when σ results from temporal discretization, the error behavior is shown for different $\sigma \in \{1, 100, 10000\}$. While the velocity errors are robust when σ becomes large, the pressure L^2 error shows deteriorating convergence behavior. This is most likely due to the effect that, even though the right hand side is adapted being solution to the strong form of the Oseen problem, the right hand side contains a discrete initial velocity field which is not discrete divergence-free, particularly due to the presence of the symmetric pressure stabilization

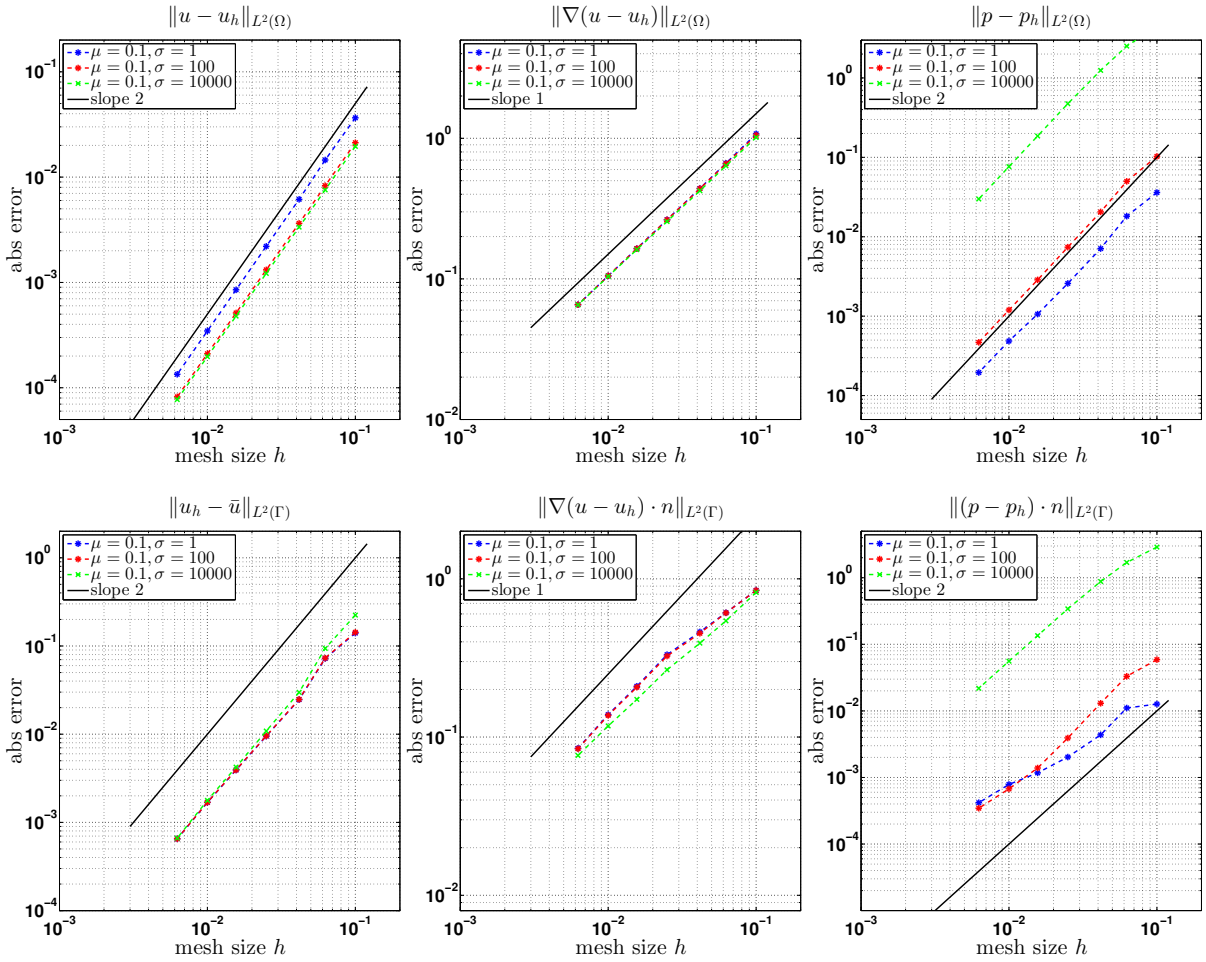

Figure 3.14: Low-Reynolds-number 2D Taylor problem with $\nu = 0.1$: Convergence rates in L^2-norms for velocity, velocity gradient and pressure in the domain (top row) and on the boundary (bottom row).

terms. The effect of a polluted incompressibility rendering in an unstable problem for the pressure has been analyzed by Burman and Fernández [55] for the transient Stokes problem. The numerical results presented in the latter work are quite similar to the behavior observed in Figure 3.14–Figure 3.15. Note that for practical flow problems, for which the transient incompressible Navier-Stokes equations are solved and the simulation usually starts from a quiescent flow, i.e. $\boldsymbol{u} = \mathbf{0}$, it is expected that this effect does not occur.

Convection-Dominant Flow. The same studies are carried out for convection-dominant flow with $\nu = 0.0001$. For this setting the resulting Oseen system exhibits highly varying element Reynolds numbers Re_T due to the locally dominating advective term $(\boldsymbol{\beta}\cdot\nabla)\boldsymbol{u}$. In contrast to the study before, now, the full stabilization parameter scalings $\phi, \phi_\beta, \phi_u, \phi_p$ (3.203), including advective and reactive contributions, are required in all CIP and related GP stabilizations as well as in the mass-conserving Nitsche penalty term to ensure inf-sup stability and optimality of the error convergence. In Figure 3.15 errors are reported for an equivalent family of triangulations as for the viscous study. Again, velocity approximations exhibit optimality in the domain and on the boundary. Even the velocity shows second-order accuracy in the L^2-norm

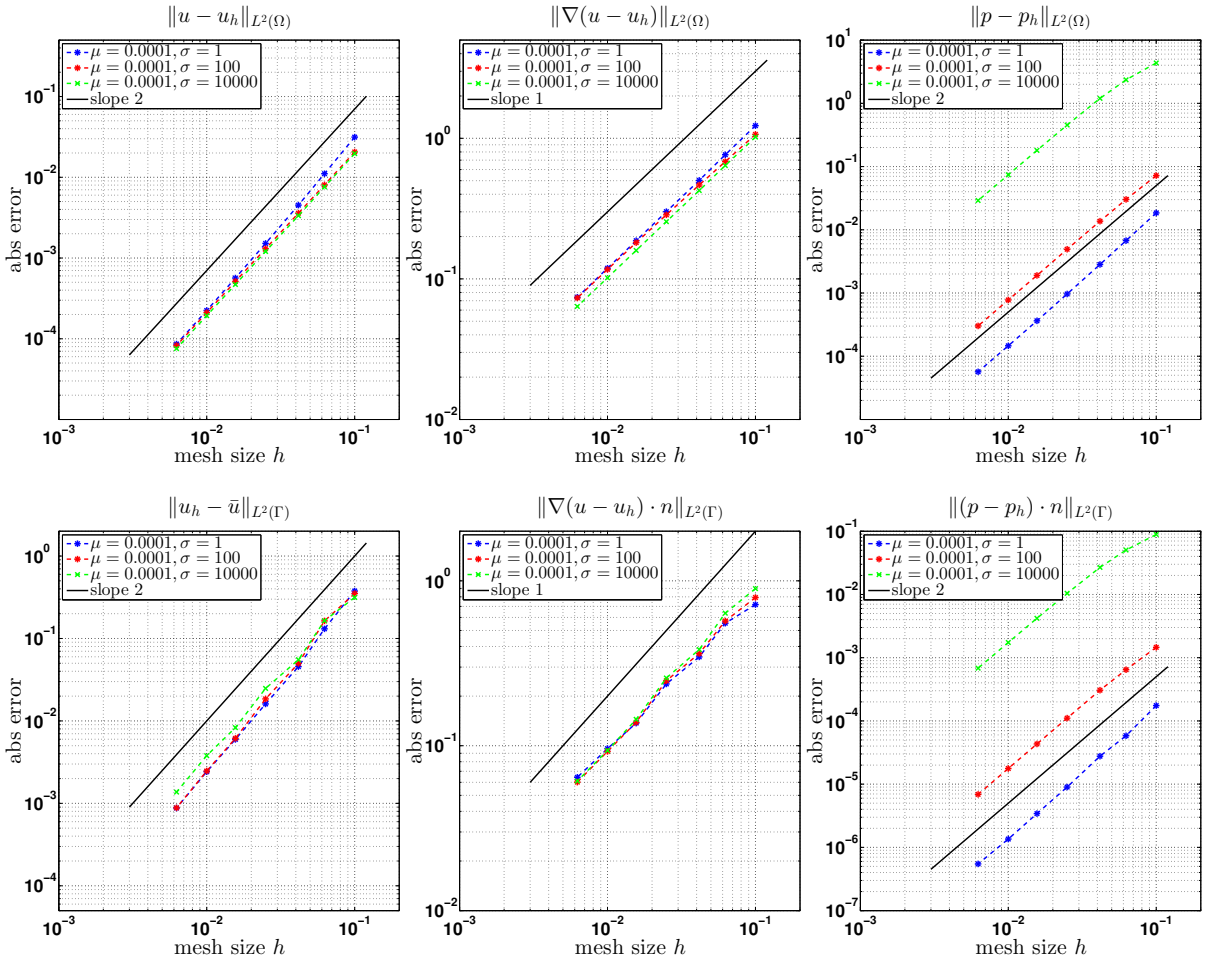

Figure 3.15: High-Reynolds-number 2D Taylor problem with $\nu = 0.0001$: Convergence rates in L^2-norms for velocity, velocity gradient and pressure in the domain (top row) and on the boundary (bottom row).

(compare Remark 3.23), which is due to the smoothness of the continuous solution. Also, for the pressure, second-order convergence is observed, which confirms the potential gain of half an order compared to the viscous flow regime, similar to observations made by Burman *et al.* [48]; see also the *a priori* estimate (3.428). Results for second-order interpolated elements have been presented in [183] and show analogous behavior.

3.5.7.2 Three-Dimensional Beltrami Flow

To support the theoretical results also in three spatial dimensions, the well-studied Beltrami-flow is considered, see, e.g., descriptions in [48, 103]. The steady Beltrami flow is given as

$$u_1(\boldsymbol{x}) = be^{a(x_1-x_3)+b(x_2-x_3)} - ae^{a(x_3-x_2)+b(x_1-x_2)}, \tag{3.444}$$

$$u_2(\boldsymbol{x}) = be^{a(x_2-x_1)+b(x_3-x_1)} - ae^{a(x_1-x_3)+b(x_2-x_3)}, \tag{3.445}$$

$$u_3(\boldsymbol{x}) = be^{a(x_3-x_2)+b(x_1-x_2)} - ae^{a(x_2-x_1)+b(x_3-x_1)}, \tag{3.446}$$

$$p(\boldsymbol{x}) = (a^2 + b^2 + ab)[e^{a(x_1-x_2)+b(x_1-x_3)} + e^{a(x_2-x_3)+b(x_2-x_1)} + e^{a(x_3-x_1)+b(x_3-x_2)}] \tag{3.447}$$

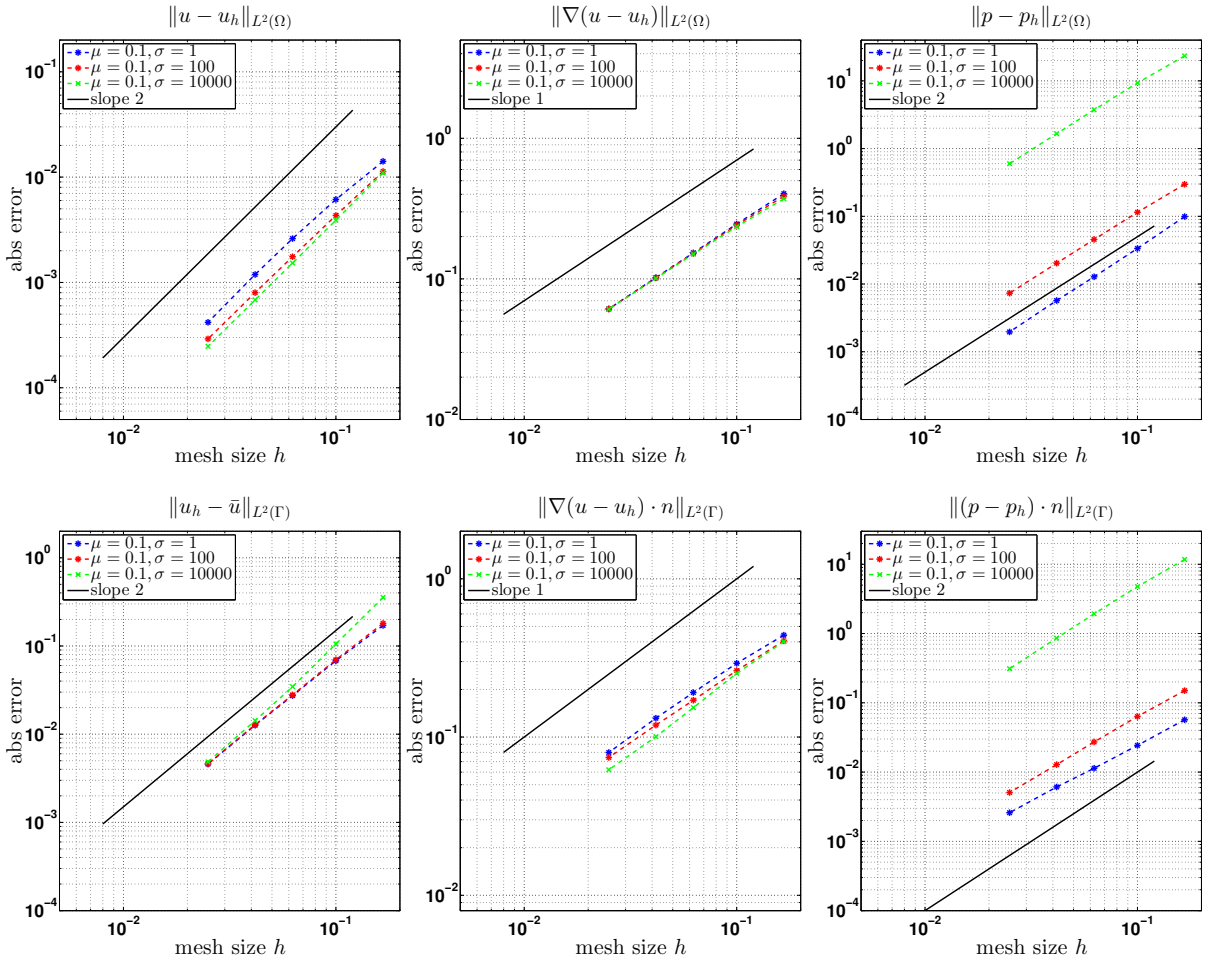

Figure 3.16: Low-Reynolds-number 3D Beltrami flow with $\nu = 0.1$: Convergence rates in L^2-norms for velocity, velocity gradient and pressure in the domain (top row) and on the boundary (bottom row).

with $\boldsymbol{x} = (x_1, x_2, x_3)$ and $a = b = \pi/4$. The velocity field $\boldsymbol{u}$ is solenoidal by construction. The right-hand side $\boldsymbol{f}$ and the boundary data $\boldsymbol{g}_\mathrm{D}$ are adapted to the Oseen problem accordingly.

Numerical solutions are computed on a spherical fluid domain with radius $r = 0.45$, where its center is located at $(1.0, 0.5, 0.5)$. The domain is given implicitly as

$$\Omega^\mathrm{f} = \{\boldsymbol{x} \in \mathbb{R}^3 \mid \phi(\boldsymbol{x}) = \sqrt{(x_1 - 1.0)^2 + (x_2 - 0.5)^2 + (x_3 - 0.5)^2} - 0.45 < 0\}. \tag{3.448}$$

The level-set field ϕ and all solution fields are approximated on respective active parts of a family of background meshes $\widehat{\mathcal{T}}_h$ covering a background cube $[0.5, 1.5] \times [0, 1]^2$. Thereby, all meshes are constructed of n^3 cubes, where each cube is subdivided into six tetrahedra $\mathbb{P}^1(T)$. Here, n denotes the number of cubes in each coordinate direction and $h = 1/n$ is the short length of each tetrahedra T. Similar to the two-dimensional Taylor problem, a low- and a high-Reynolds-number setting is considered, characterized by two different viscosities $\nu = 0.1$ and $\nu = 0.0001$. Computed velocity and pressure approximation errors $(\boldsymbol{u}_h - \boldsymbol{u})$ and $(p_h - p)$ are shown in Figure 3.16 for the low-Reynolds-number case and in Figure 3.17 for the high-Reynolds-number case. The same optimal rates for velocity errors as well as super-convergence for the pressure can be observed similar to the two-dimensional example.

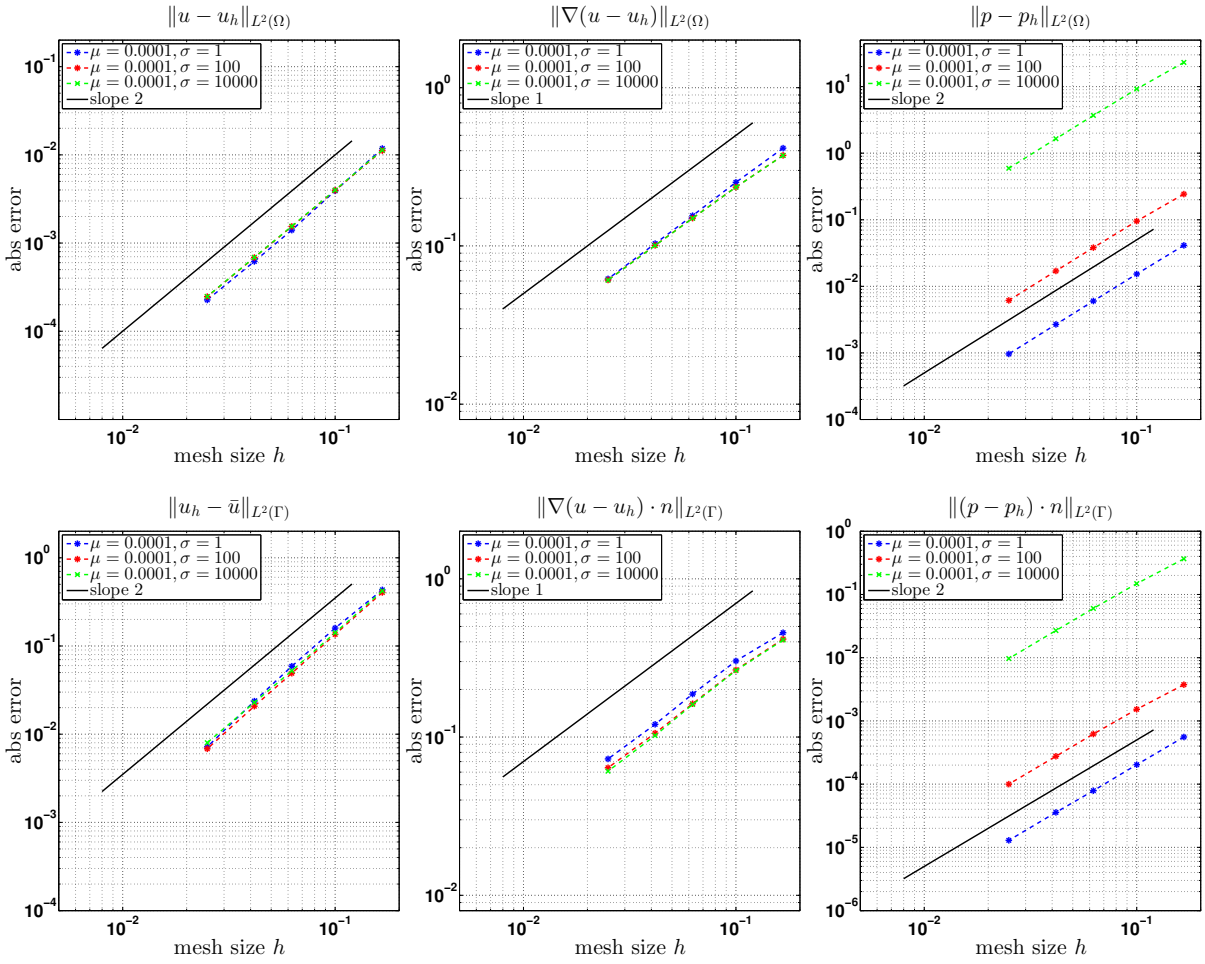

Figure 3.17: High-Reynolds-number 3D Beltrami flow with $\nu = 0.0001$: Convergence rates in L^2-norms for velocity, velocity gradient and pressure in the domain (top row) and on the boundary (bottom row).

To underline the stability of the velocity and pressure solutions for the high-Reynolds-number setting, in Figure 3.18, velocity streamlines and the pressure solution along cross-sections computed on a coarse non-boundary-fitted mesh are visualized. It is clearly visible that the solutions do not exhibit any oscillatory behavior, neither in the interior of the domain nor near the boundary which is due the different proposed CIP and GP stabilizations. That fact underlines the stability of the proposed formulation even though the solution exhibits highly varying element Reynolds numbers within the computational domain.

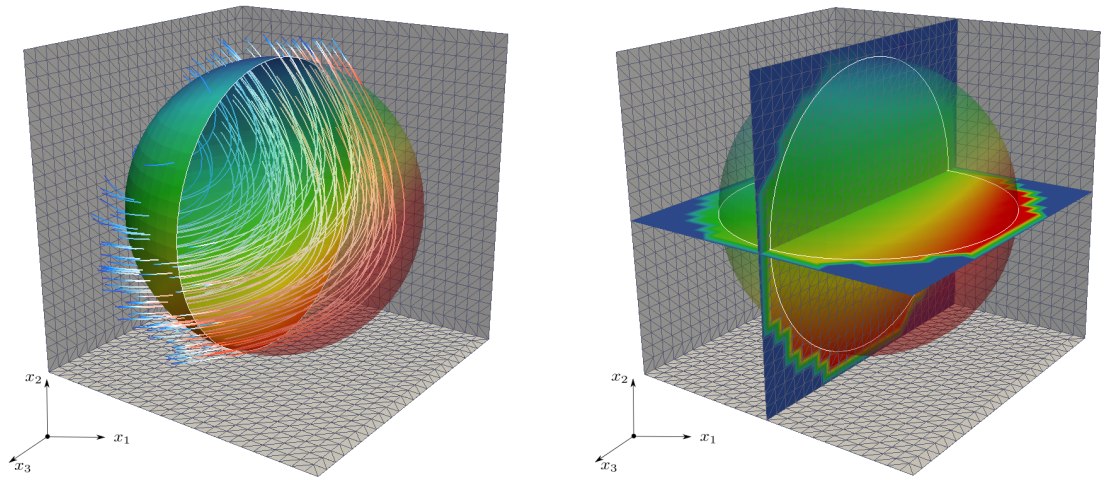

Figure 3.18: High-Reynolds-number 3D Beltrami flow: Computed velocity and pressure solutions on unfitted mesh with $h = 1/24$. Stable solutions in the interior of the domain and in the boundary zone due to sufficient control ensured by different CIP and GP stabilization terms. (Left) Streamlines colored by velocity magnitude and half-sphere ($x_1 < 1.0$) colored by pressure distribution. (Right) Pressure solution at cross-sections defined by $x_1 = 1.0$ and $x_2 = 0.5$.

3.6 Stabilized Cut Finite Element Methods for Transient Incompressible Navier-Stokes Equations

The present section is devoted to cut finite element methods for the transient incompressible Navier-Stokes equations. Stable and accurate formulations for low- and high-Reynolds-number flows will be proposed and numerically investigated. One major aspect being addressed subsequently is extending solution algorithms from stationary to moving boundary value problems. Such techniques are essential for coupled multiphysics flow problems as will be considered throughout Chapters 4 and 5.

The Oseen CUTFEM analyzed in the previous section serves as basis for stabilized discrete formulations to the non-linear incompressible Navier-Stokes equations. Two differently stabilized formulations will be applied for different flow problems considered later in this thesis: Both approaches are based on the Nitsche-type weak imposition of boundary conditions on unfitted meshes and utilize face-jump ghost-penalty (GP) stabilizations in the interface zone, as introduced for the Oseen problem in the last section. The two methods differ in the stabilization technique used in the interior of the respective fluid phase: either residual-based variational multiscale (RBVM) terms are applied, see Section 3.1.3.1, or the continuous interior penalty stabilization technique (CIP) is applied. The latter one has been introduced in Section 3.1.3.2 for boundary-fitted meshes and extended to cut finite element approximations in Section 3.5. These two discrete formulations are based on the following works. For the CIP/GP face-jump-penalty stabilized formulation, the reader is referred to the publications by Schott and Wall [230] and Massing *et al.* [183]. The combined RBVM/GP technique has been suggested in works by Schott and Rasthofer *et al.* [231] and Schott and Shahmiri *et al.* [232].

In this thesis, these two stabilized formulations are referred to as

- a *Nitsche-type face-jump-penalty stabilized cut finite element method*, denoted as CIP/GP-CUTFEM, and
- a *Nitsche-type residual-based variational multiscale cut finite element method*, denoted as RBVM/GP-CUTFEM.

Temporal and spatial discretizations for both variants will be proposed in Section 3.6.1. Stability and accuracy of the formulations are examined with different two- and three-dimensional flow simulations in complex-shaped domains with stationary boundaries. Finally, issues arising for domains with moving boundaries discretized on non-boundary-fitted fixed grids will be elaborated in Section 3.6.3. Possible solution strategies are provided and discussed. To indicate the applicability of those methods to multiphysics problems, simulations for incompressible single-phase flows at low and higher Reynolds numbers with boundaries which undergo large motions will demonstrate the capability of CUTFEMs for incompressible fluid flows.

3.6.1 Stabilized Discrete Formulations

In the following, temporal and spatial semi-discrete formulations of the aforementioned unfitted CUTFEM for the transient incompressible Navier-Stokes equations will be proposed. Within this section, boundaries are assumed to be stationary. Computational meshes are fixed in time and the variational formulation $\mathscr{A}(U,V) = \mathscr{L}(U,V)$ of the incompressible Navier-Stokes equations from Section 3.1.2 is described in an Eulerian formalism, i.e. $\hat{\boldsymbol{u}} = \boldsymbol{0}$ and $\frac{\partial \boldsymbol{u}_{\boldsymbol{X}}}{\partial t} \circ \boldsymbol{\Phi}^{-1}(\cdot, T) = \frac{\partial \boldsymbol{u}(t)}{\partial t}$. To simplify the notation on function spaces, Dirichlet-type boundary conditions on Γ_{D} are exclusively enforced weakly. Combinations with strongly incorporated conditions at boundary parts which fit to the mesh is straightforward and functions spaces would change accordingly, see Section 3.1.2.

3.6.1.1 A Nitsche-type CIP/GP Cut Finite Element Method

The spatial semi-discrete Nitsche-type cut finite element formulation for the incompressible Navier-Stokes equations (3.9) with stabilizing continuous interior penalty (CIP) terms in the interior of the domain and ghost penalty (GP) terms in the boundary zone reads as follows:

Definition 3.13 (Semi-discrete formulation of the Nitsche-type CIP/GP-CUTFEM)
For all $t \in (T_0, T)$, find fluid velocity and pressure $U_h(t) = (\boldsymbol{u}_h(t), p_h(t)) \in \mathcal{V}_h \times \mathcal{Q}_h$ such that for all $V_h = (\boldsymbol{v}_h, q_h) \in \mathcal{V}_h \times \mathcal{Q}_h$

$$\mathscr{A}_h^{\mathrm{CIP/GP}}(U_h, V_h) = \mathscr{L}_h^{\mathrm{CIP/GP}}(U_h, V_h), \tag{3.449}$$

where

$$\mathscr{A}_h^{\mathrm{CIP/GP}}(U_h, V_h) \overset{def}{=} (\rho \frac{\partial \boldsymbol{u}_h(t)}{\partial t}, \boldsymbol{v}_h)_\Omega + (\mathscr{B}_h + \mathscr{S}_h^{\mathrm{CIP}} + \mathscr{G}_h^{\mathrm{GP}})(\boldsymbol{u}_h; (\boldsymbol{u}_h, p_h), (\boldsymbol{v}_h, q_h)), \tag{3.450}$$

$$\mathscr{L}_h^{\mathrm{CIP/GP}}(U_h, V_h) \overset{def}{=} \mathscr{L}_h(\boldsymbol{u}_h; (\boldsymbol{v}_h, q_h)) \tag{3.451}$$

with

$$\begin{aligned}
\mathscr{B}_h(\boldsymbol{u}_h;(\boldsymbol{u}_h,p_h),(\boldsymbol{v}_h,q_h)) &= (c_h+a_h)(\boldsymbol{u}_h;\boldsymbol{u}_h,\boldsymbol{v}_h)+b_h(p_h,\boldsymbol{v}_h)-b_h(q_h,\boldsymbol{u}_h), && (3.452)\\
\mathscr{S}_h^{\mathrm{CIP}}(\boldsymbol{u}_h;(\boldsymbol{u}_h,p_h),(\boldsymbol{v}_h,q_h)) &= (s_\beta+s_u+s_p)(\boldsymbol{u}_h;(\boldsymbol{u}_h,p_h),(\boldsymbol{v}_h,q_h)), && (3.453)\\
\mathscr{G}_h^{\mathrm{GP}}(\boldsymbol{u}_h;(\boldsymbol{u}_h,p_h),(\boldsymbol{v}_h,q_h)) &= (g_\beta+g_u+g_p+g_\nu+g_\sigma)(\boldsymbol{u}_h;(\boldsymbol{u}_h,p_h),(\boldsymbol{v}_h,q_h)), && (3.454)\\
\mathscr{L}_h(\boldsymbol{u}_h;(\boldsymbol{v}_h,q_h)) &= (\rho\boldsymbol{f},\boldsymbol{v}_h)_\Omega+\langle\boldsymbol{h}_{\mathrm{N}},\boldsymbol{v}_h\rangle_{\Gamma_{\mathrm{N}}}-\langle\rho(\boldsymbol{u}_h\cdot\boldsymbol{n})\boldsymbol{g}_{\mathrm{D}},\boldsymbol{v}_h\rangle_{\Gamma_{\mathrm{in}}}\\
&\quad\mp\langle\boldsymbol{g}_{\mathrm{D}},2\mu\boldsymbol{\epsilon}(\boldsymbol{v}_h)\boldsymbol{n}\rangle_{\Gamma_{\mathrm{D}}}+\langle\gamma(\mu/h)\boldsymbol{g}_{\mathrm{D}},\boldsymbol{v}_h\rangle_{\Gamma_{\mathrm{D}}} && (3.455)\\
&\quad-\langle\boldsymbol{g}_{\mathrm{D}}\cdot\boldsymbol{n},q_h\rangle_{\Gamma_{\mathrm{D}}}+\langle\gamma(\phi\rho/h)\boldsymbol{g}_{\mathrm{D}}\cdot\boldsymbol{n},\boldsymbol{v}_h\cdot\boldsymbol{n}\rangle_{\Gamma_{\mathrm{D}}}.
\end{aligned}$$

Terms according to the standard Galerkin formulation and to Nitsche's method are given as

$$\begin{aligned}
c_h(\boldsymbol{u}_h;\boldsymbol{u}_h,\boldsymbol{v}_h) &= (\rho(\boldsymbol{u}_h\cdot\nabla)\boldsymbol{u}_h,\boldsymbol{v}_h)_\Omega-\langle\rho(\boldsymbol{u}_h\cdot\boldsymbol{n})\boldsymbol{u}_h,\boldsymbol{v}_h\rangle_{\Gamma_{\mathrm{in}}}+\tfrac{1}{2}(\rho(\nabla\cdot\boldsymbol{u}_h)\boldsymbol{u}_h,\boldsymbol{v}_h), && (3.456)\\
a_h(\boldsymbol{u}_h;\boldsymbol{u}_h,\boldsymbol{v}_h) &= (\boldsymbol{\epsilon}(\boldsymbol{u}_h),2\mu\boldsymbol{\epsilon}(\boldsymbol{v}_h))_\Omega-\langle 2\mu\boldsymbol{\epsilon}(\boldsymbol{u}_h)\boldsymbol{n},\boldsymbol{v}_h\rangle_{\Gamma_{\mathrm{D}}}\mp\langle\boldsymbol{u}_h,2\mu\boldsymbol{\epsilon}(\boldsymbol{v}_h)\boldsymbol{n}\rangle_{\Gamma_{\mathrm{D}}}\\
&\quad+\langle\gamma(\mu/h)\boldsymbol{u}_h,\boldsymbol{v}_h\rangle_{\Gamma_{\mathrm{D}}}+\langle\gamma(\phi\rho/h)\boldsymbol{u}_h\cdot\boldsymbol{n},\boldsymbol{v}_h\cdot\boldsymbol{n}\rangle_{\Gamma_{\mathrm{D}}}, && (3.457)\\
b_h(p_h,\boldsymbol{v}_h) &= -(p_h,\nabla\cdot\boldsymbol{v}_h)_\Omega+\langle p_h,\boldsymbol{v}_h\cdot\boldsymbol{n}\rangle_{\Gamma_{\mathrm{D}}}, && (3.458)
\end{aligned}$$

and continuous interior penalty stabilization terms are defined with $u_{\boldsymbol{n},\infty,F}\overset{def}{=}\|\boldsymbol{u}_h\cdot\boldsymbol{n}\|_{0,\infty,F}$ *as*

$$\begin{aligned}
s_\beta(\boldsymbol{u}_h;\boldsymbol{u}_h,\boldsymbol{v}_h) &= \gamma_\beta\sum\nolimits_{F\in\mathscr{F}_i}\phi_{\beta,F}\rho u_{\boldsymbol{n},\infty,F}^2h_F\langle[\![\nabla\boldsymbol{u}_h]\!],[\![\nabla\boldsymbol{v}_h]\!]\rangle_F, && (3.459)\\
s_u(\boldsymbol{u}_h;\boldsymbol{u}_h,\boldsymbol{v}_h) &= \gamma_u\sum\nolimits_{F\in\mathscr{F}_i}\phi_{u,F}\rho h_F\langle[\![\nabla\cdot\boldsymbol{u}_h]\!],[\![\nabla\cdot\boldsymbol{v}_h]\!]\rangle_F, && (3.460)\\
s_p(\boldsymbol{u}_h;p_h,q_h) &= \gamma_p\sum\nolimits_{F\in\mathscr{F}_i}\phi_{p,F}\rho^{-1}h_F\langle[\![\nabla p_h]\!],[\![\nabla q_h]\!]\rangle_F, && (3.461)
\end{aligned}$$

Defining $u_{\infty,F}\overset{def}{=}\|\boldsymbol{u}_h\|_{0,\infty,F}$*, interface zone face-jump ghost-penalty terms are given by*

$$\begin{aligned}
g_\beta(\boldsymbol{u}_h;\boldsymbol{u}_h,\boldsymbol{v}_h) &= \gamma_\beta\sum\nolimits_{F\in\mathscr{F}_\Gamma}\sum\nolimits_{1\leqslant j\leqslant k}\phi_{\beta,F}\rho u_{\infty,F}^2h_F^{2j-1}\langle[\![\partial_{\boldsymbol{n}}^j\boldsymbol{u}_h]\!],[\![\partial_{\boldsymbol{n}}^j\boldsymbol{v}_h]\!]\rangle_F, && (3.462)\\
g_u(\boldsymbol{u}_h;\boldsymbol{u}_h,\boldsymbol{v}_h) &= \gamma_u\sum\nolimits_{F\in\mathscr{F}_\Gamma}\sum\nolimits_{0\leqslant j\leqslant k-1}\phi_{u,F}\rho h_F^{2j+1}\langle[\![\nabla\cdot\partial_{\boldsymbol{n}}^j\boldsymbol{u}_h]\!],[\![\nabla\cdot\partial_{\boldsymbol{n}}^j\boldsymbol{v}_h]\!]\rangle_F, && (3.463)\\
g_p(\boldsymbol{u}_h;p_h,q_h) &= \gamma_p\sum\nolimits_{F\in\mathscr{F}_\Gamma}\sum\nolimits_{1\leqslant j\leqslant k}\phi_{p,F}\rho^{-1}h_F^{2j-1}\langle[\![\partial_{\boldsymbol{n}}^jp_h]\!],[\![\partial_{\boldsymbol{n}}^jq_h]\!]\rangle_F, && (3.464)\\
g_\nu(\boldsymbol{u}_h,\boldsymbol{v}_h) &= \gamma_\nu\sum\nolimits_{F\in\mathscr{F}_\Gamma}\sum\nolimits_{1\leqslant j\leqslant k}\nu\rho h_F^{2j-1}\langle[\![\partial_{\boldsymbol{n}}^j\boldsymbol{u}_h]\!],[\![\partial_{\boldsymbol{n}}^j\boldsymbol{v}_h]\!]\rangle_F, && (3.465)\\
g_\sigma(\boldsymbol{u}_h,\boldsymbol{v}_h) &= \gamma_\sigma\sum\nolimits_{F\in\mathscr{F}_\Gamma}\sum\nolimits_{1\leqslant j\leqslant k}\sigma\rho h_F^{2j+1}\langle[\![\partial_{\boldsymbol{n}}^j\boldsymbol{u}_h]\!],[\![\partial_{\boldsymbol{n}}^j\boldsymbol{v}_h]\!]\rangle_F. && (3.466)
\end{aligned}$$

Moreover, $\boldsymbol{u}_h$ *has to fulfill the initial condition* $\boldsymbol{u}_h(T_0)=\boldsymbol{u}_0$ *in* Ω*. Note, to shorten the presentation of the stabilized formulation, the time variable in* $U_h(t)=(\boldsymbol{u}_h(t),p_h(t))$ *has been omitted. The scaling* σ *denotes a (pseudo-)reaction which results from temporal discretization of the spatial semi-discrete form* (3.449) *as will be introduced later in Section 3.6.1.3, see* (3.476) *and* (3.479)*. Stabilization parameters for* CIP *terms and* CIP*-related* GP *terms are taken from the Oseen problem, see Section 3.5.2. The scaling functions related to the Nitsche's method, the* CIP *terms as well as all* GP *terms are recalled from Section 3.1.3.2 and Section 3.5.2*

$$\phi_T=\nu+c_u(\|\boldsymbol{u}_h\|_{0,\infty,T}h_T)+c_\sigma(\sigma h_T^2),\qquad \phi_{\beta,T}=\phi_{p,T}=h_T^2\phi_T^{-1},\qquad \phi_{u,T}=\phi_T. \quad (3.467)$$

Remark 3.25 *The* CIP/GP-CutFEM *formulation proposed in Definition 3.13 is an extension of the stabilized formulation for Oseen's problem analyzed and numerically investigated in Section 3.5. Here, the advective velocity $\boldsymbol{\beta}$ therein is replaced by the discrete convective velocity $\boldsymbol{u}_h \in \mathcal{V}_h$ which introduces a non-linearity into all stabilization operators. For* ALE*-based formulations, $\boldsymbol{\beta}$ is the relative convective velocity $\boldsymbol{u}_h - \hat{\boldsymbol{u}}_h$. Furthermore, the formulation is scaled with the density ρ as required for coupled problem settings and includes Neumann boundary conditions on Γ_{N}, see (3.455). Note that the definition of the advective ghost-penalty operator (3.462) is based on elaborations provided in Remark 3.15.*

Remark 3.26 *Due to the weak enforcement of the incompressibility constraint, in general, it does not hold $\nabla \cdot \boldsymbol{u}_h = 0$ a.e. in Ω. Recalling Remark 3.19 and the coercivity proof of Lemma 3.10 in Section 3.5.5, the need for the last term added in (3.456) arises from (3.256). In practice, however, it often holds $\sigma - \frac{1}{2}\nabla \cdot \boldsymbol{u}_h \geqslant c > 0$ provided the time-step length $\Delta t \sim 1/\sigma$ is chosen sufficiently small (see (3.476) and (3.479) for definitions). Then, this additional term can be neglected as done for all simulations considered in this work.*

Remark 3.27 *Note that similar to the elaborations for the Oseen problem in Section 3.5, see Remark 3.15, also the incompressibility ghost-penalty term (3.463) can be replaced by a pure velocity based jump-penalty term similar to (3.462).*

For further detailed elaborations on the meaning of the Nitsche-based boundary terms and the different CIP and GP stabilizations, the reader is referred to Section 3.5.

3.6.1.2 A Nitsche-type RBVM/GP Cut Finite Element Method

Definition 3.14 (Semi-discrete formulation of the Nitsche-type RBVM/GP-CutFEM) *For all $t \in (T_0, T]$, find fluid velocity and pressure $U_h(t) = (\boldsymbol{u}_h(t), p_h(t)) \in \mathcal{V}_h \times \mathcal{Q}_h$ such that for all $V_h = (\boldsymbol{v}_h, q_h) \in \mathcal{V}_h \times \mathcal{Q}_h$*

$$\mathcal{A}_h^{\mathrm{RBVM/GP}}(U_h, V_h) = \mathcal{L}_h^{\mathrm{RBVM/GP}}(U_h, V_h), \tag{3.468}$$

where

$$\begin{aligned}
\mathcal{A}_h^{\mathrm{RBVM/GP}}(U_h, V_h) &\overset{def}{=} (\rho\frac{\partial \boldsymbol{u}_h(t)}{\partial t}, \boldsymbol{v}_h) + (\mathcal{B}_h + \mathcal{G}_h^{\mathrm{GP}})(\boldsymbol{u}_h; (\boldsymbol{u}_h, p_h), (\boldsymbol{v}_h, q_h)) \\
&\quad + \sum\nolimits_{T \in \mathcal{T}_h} \Big(\rho\frac{\partial \boldsymbol{u}_h(t)}{\partial t} + \boldsymbol{r}_{\mathrm{M}}(\boldsymbol{u}_h, p_h), \tau_{\mathrm{M}}(\rho(\boldsymbol{u}_h \cdot \nabla)\boldsymbol{v}_h + \nabla q_h)\Big)_{T\cap\Omega} \\
&\quad + \sum\nolimits_{T \in \mathcal{T}_h} \Big(r_{\mathrm{C}}(\boldsymbol{u}_h), \tau_{\mathrm{C}}\nabla \cdot \boldsymbol{v}_h\Big)_{T\cap\Omega},
\end{aligned} \tag{3.469}$$

$$\begin{aligned}
\mathcal{L}_h^{\mathrm{RBVM/GP}}(U_h, V_h) &\overset{def}{=} \mathcal{L}_h(\boldsymbol{v}_h, q_h) \\
&\quad + \sum\nolimits_{T \in \mathcal{T}_h} \Big(\rho\boldsymbol{f}, \tau_{\mathrm{M}}(\rho(\boldsymbol{u}_h \cdot \nabla)\boldsymbol{v}_h + \nabla q_h)\Big)_{T\cap\Omega}
\end{aligned} \tag{3.470}$$

with

$$\boldsymbol{r}_{\mathrm{M}}(\boldsymbol{u}_h, p_h) = \rho(\boldsymbol{u}_h \cdot \nabla)\boldsymbol{u}_h + \nabla p_h - 2\mu\nabla \cdot \boldsymbol{\epsilon}(\boldsymbol{u}_h) \qquad \text{and} \qquad r_{\mathrm{C}}(\boldsymbol{u}_h) = \nabla \cdot \boldsymbol{u}_h. \tag{3.471}$$

The operators $\mathcal{B}_h$ and $\mathcal{G}_h^{\mathrm{GP}}$ are defined in (3.452) and (3.454). The stabilization scaling functions $\tau_{\mathrm{M}}, \tau_{\mathrm{C}}$ are introduced in (3.21)–(3.22).

3.6.1.3 Time-Stepping for Fluids

The stabilized semi-discrete CUTFEM formulations proposed in Section 3.6.1.1–3.6.1.2 can be written in an abstract form as first order ordinary differential equations (ODE) as follows: for any time $t \in (T_0, T]$ find fluid velocity and pressure fields $\boldsymbol{u}_h(t) \in \mathcal{V}_h$ and $p_h(t) \in \mathcal{Q}_h$ such that for all $(\boldsymbol{v}_h, q_h) \in \mathcal{V}_h \times \mathcal{Q}_h$

$$(\rho \frac{\partial \boldsymbol{u}_h(t)}{\partial t}, \Upsilon(\boldsymbol{v}_h, q_h)) + F(t, (\boldsymbol{u}_h(t), p_h(t)), (\boldsymbol{v}_h, q_h)) = 0, \tag{3.472}$$

where Υ is linear with respect to $(\boldsymbol{v}_h, q_h)$. For the CIP/GP-CUTFEM this function is given by $\Upsilon(\boldsymbol{v}_h, q_h) = \boldsymbol{v}_h$ and by $\Upsilon(\boldsymbol{v}_h, q_h) = \boldsymbol{v}_h + \tau_{\mathrm{M}}(\rho(\boldsymbol{u}_h \cdot \nabla)\boldsymbol{v}_h + \nabla q_h)$ for the RBVM/GP-CUTFEM formulation. The respective functions F, which incorporate standard Galerkin terms, stabilization operators and external loads, i.e. $\mathcal{B}_h, \mathcal{G}_h, \mathcal{S}_h, -\mathcal{L}_h$, can be defined accordingly and do not include further time derivatives of $\boldsymbol{u}_h$. Then, a multitude of one- and multi-step time discretization schemes are applicable to such spatial semi-discrete finite dimensional systems of ODEs. In this thesis, two well-established techniques are utilized for fluids: a *one-step-θ method* (OST) and a two-step *backward differentiation formula* (BDF2).

For time stepping, let the time domain $(T_0, T]$ be partitioned into N equal-sized time-step intervals $J^n = (t^{n-1}, t^n]$ of size Δt. The discrete time levels are defined as $t^n = T_0 + n\Delta t$ and $t^N = T$. Discrete velocity and pressure fields are then approximated by temporal approximations $\boldsymbol{u}_h^n \approx \boldsymbol{u}_h(t^n)$ and $p_h^n \approx p_h(t^n)$.

The subsequent elaborations are based on work published by Dettmer and Perić [84] and Förster [110]. In the latter work, both schemes are written in the form

$$(\rho \boldsymbol{u}_h^n, \Upsilon(\boldsymbol{v}_h, q_h)) + \sigma^{-1} F^n((\boldsymbol{u}_h^n, p_h^n), (\boldsymbol{v}_h, q_h)) - H^{n-1}(\boldsymbol{v}_h, q_h) = 0, \tag{3.473}$$

where σ represents a time-dependent scalar which is characteristic for the temporal discretization. The function H contains history data from one or several old time steps.

The One-Step-θ Family (OST). For an ODE of type $\dot{y}(t) = f(t, y(t))$, the one-step-θ scheme with $\theta \in [0, 1]$ is classically given as

$$y^n = y^{n-1} + \theta \Delta t f(t^n, y^n) + (1-\theta)\Delta t f(t^{n-1}, y^{n-1}). \tag{3.474}$$

For fluid problems of type (3.472) this scheme can be equivalently rewritten in terms of unknowns $\boldsymbol{u}_h^n, p_h^n$ and an additional unknown acceleration approximation $\boldsymbol{a}_h^n \approx \frac{\partial \boldsymbol{u}_h(t)}{\partial t}$ as: find approximations $\boldsymbol{u}_h^n, p_h^n, \boldsymbol{a}_h^n$ such that

$$(\rho \boldsymbol{u}_h^n, \Upsilon(\boldsymbol{v}_h, q_h)) + \sigma_\theta^{-1} F^n((\boldsymbol{u}_h^n, p_h^n), (\boldsymbol{v}_h, q_h)) - H_\theta^{n-1}(\boldsymbol{v}_h) = 0 \tag{3.475}$$

with

$$\sigma_\theta = (\theta \Delta t)^{-1} \quad \text{and} \quad H_\theta^{n-1}(\boldsymbol{v}_h) = (\rho \boldsymbol{u}_h^{n-1}, \Upsilon(\boldsymbol{v}_h, q_h)) + (1-\theta)\Delta t(\rho \boldsymbol{a}_h^{n-1}, \boldsymbol{v}_h). \tag{3.476}$$

For given $\boldsymbol{u}_h^n$, the acceleration vector can be updated by utilizing a OST-scheme (3.474) for $\frac{\partial \boldsymbol{u}_h(t)}{\partial t} = \boldsymbol{a}_h(t)$

$$\boldsymbol{a}_h^n = \frac{\boldsymbol{u}_h^n - \boldsymbol{u}_h^{n-1}}{\Delta t} - \frac{1-\theta}{\theta} \boldsymbol{a}_h^{n-1}. \tag{3.477}$$

Note that using this technique, the stabilized formulations to the incompressible Navier-Stokes equations hidden in F^n have to be evaluated only for the current time step t^n. The one-step-θ family is unconditionally A-stable for $\theta \in [1/2, 1]$ and guarantees first-order accuracy for all $\theta \neq 1/2$. The scheme is second-order accurate if and only if $\theta = 1/2$. The latter variant is called *Crank-Nicolson method*.

The Two-Step Backward Differentiation Formula (BDF2). The well-known BDF2 time-stepping scheme utilizes a second-order backward differentiation formula at t^n to approximate the time derivative and therefore requires history data from two previous time levels t^{n-1}, t^{n-2}:

$$(\rho \boldsymbol{u}_h^n, \Upsilon(\boldsymbol{v}_h, q_h)) + \sigma_{\mathrm{BDF2}}^{-1} F^n((\boldsymbol{u}_h^n, p_h^n), (\boldsymbol{v}_h, q_h)) - H_{\mathrm{BDF2}}^{n-1}(\boldsymbol{v}_h) = 0 \tag{3.478}$$

with

$$\sigma_{\mathrm{BDF2}} = (\frac{2}{3}\Delta t)^{-1} \quad \text{and} \quad H_{\mathrm{BDF2}}^{n-1}(\boldsymbol{v}_h) = -\frac{4}{3}(\rho \boldsymbol{u}_h^{n-1}, \Upsilon(\boldsymbol{v}_h, q_h)) + \frac{1}{3}(\rho \boldsymbol{u}_h^{n-2}, \Upsilon(\boldsymbol{v}_h, q_h)). \tag{3.479}$$

The BDF2 scheme is of second-order accuracy and provides unconditional A-stability.

Remarks on Temporal Discretization. Such fully discretized finite element methods for the incompressible Navier-Stokes equations render in non-linear systems of equations for the solution approximations $\boldsymbol{u}_h^n, p_h^n$ of each time step. Non-linearities given in terms of the convective velocity in the standard Galerkin formulation and corresponding stabilization terms can then be approximated with a series of Picard or Newton-like iterations. Thereby, velocities occurring in different stabilization parameters are evaluated at the last iteration step.

Temporal discretizations of such stabilized formulations have been written down more detailed in, e.g., Schott [229]. For an analysis of different time integration algorithms for the finite element solutions of incompressible Navier-Stokes equations based on residual-stabilized formulations, the interested reader is referred to the work by Dettmer and Perić [84]. Further analysis of stabilized schemes for transient problems have been provided by Burman [51] for the SUPG stabilization and by Burman and Fernández [57] for the PSPG stabilization. Numerical analyses of time-discrete CIP-stabilized methods can be found in, e.g., Burman and Fernández [56], Burman and Fernández [55] or Burman *et al.* [67].

Note that using the temporal discretization techniques provided above, all involved stabilization operators as well as Nitsche terms used for imposing the boundary conditions, which are hidden in F^n, have to be evaluated at the current time level t^n. For the one-step-θ scheme, history data from previous time steps are then incorporated in the acceleration variable $\boldsymbol{a}_h^n$.

3.6.2 Numerical Tests for Incompressible Flow in Non-Moving Domains

The Nitsche-type cut finite element methods introduced in Section 3.6.1 are validated for stationary and transient flows in domains with non-moving boundaries. While numerical convergence tests in Section 3.5.7 already confirmed optimality and stability of the stabilized Oseen scheme, the following test cases demonstrate applicability of the formulations to transient flows governed by the incompressible Navier-Stokes equations. A comparison of the CIP/GP scheme with other computational approaches is provided for a well-established stationary two-dimensional laminar

cylinder benchmark example. A transient higher-Reynolds-number flow around a cylinder will demonstrate accuracy and robustness of interfacial forces. The flow through a three-dimensional helical pipe illustrates the high potential of fixed-grid cut finite element schemes for flows in complex domains. Furthermore, capabilities in view of simplified mesh generation are indicated for a potential industrial problem setting for which the mesh does not fit to the domain boundary and for which generating a three-dimensional conforming high quality computational grid might become time-consuming and challenging. Most of the presented results are based on work published by Schott and Wall [230] and Massing *et al.* [183].

3.6.2.1 Two-Dimensional Incompressible Flow around a Cylinder

The Laminar Cylinder Benchmark 2D-1 by Schäfer and Turek. To investigate accuracy properties of the proposed CIP/GP scheme, results are presented for the well-known stationary two-dimensional cylinder benchmark test case 2D-1 by Schäfer and Turek [227]. For a comparison, equal-order interpolated velocity-pressure approximation spaces based on quadrilateral $\mathbb{Q}^k$-elements with $k = 1, 2$ are utilized.

The geometric setup for this example is taken unchanged from the original publication. The fluid domain consists of a box $\Omega^{\mathrm{f}} = (0, 2.2) \times (0, 0.41) \backslash \Omega^{\mathrm{s}}$ with an embedded cylinder Ω^{s} of radius $r = 0.05$ which is located at $(0.2, 0.2)$. The cylinder surface defines the boundary Γ at which $\boldsymbol{g}_{\mathrm{D}} = \mathbf{0}$ is enforced using Nitsche's method. The fluid is assumed Newtonian with kinematic viscosity $\nu = 0.000125$. The simulation is calculated as a quasi two-dimensional problem with one layer of elements in the x_3-direction. At the upper and lower side walls, 'no-slip' boundary conditions are enforced strongly via the discrete function space. A parabolic inflow with a maximum velocity of $u_1^{\max} = 0.3$ and a zero-traction boundary condition at the outflow are prescribed.

For the cut finite element approximation different mesh resolutions are compared. Initially, a coarse underlying background mesh $\widehat{\mathcal{T}}_h$ with mesh size $h \approx 0.0239$ serves as starting point. Regular mesh refinements are performed within a rectangular block $[0, 0.7] \times [0, 0.41]$ containing the cylinder. For the coarsest discretization of the refined block, the cylinder height is approximated with 14 elements in each coordinate direction such that $h \approx 7.3 \cdot 10^{-3}$. For all finer meshes, the refined block is consecutively divided in half in each direction. It has to be mentioned that no adaptive refinements of the mesh towards the cylinder are performed in order to retain the fixed-grid character of the cut finite element approximation.

Resulting lift and drag coefficients $(c_{\mathrm{lift}}, c_{\mathrm{drag}})$ as well as pressure differences Δp between the front end and the back end of the obstacle are presented in Table 3.2. Note that all simulations are performed based on a three-dimensional implementation utilizing one element layer in the third dimension. For linearly-interpolated 8-node $\mathbb{Q}^1$-elements, two refinements are necessary to predict the pressure drop. For one further refinement step also the lift value is within given reference bounds and the drag value almost matches the given range. In contrast, utilizing quadratically-interpolated 20-node $\mathbb{Q}^2$-elements, the drag value matches already for the coarsest mesh. After one refinement even the pressure drop fits. For the second refinement, finally, all measures are within the given reference bounds. The more accurate approximation space based on *hex20* elements clearly improves the quality of viscous forces and is able to approximate the boundary condition more accurately compared to *hex8* elements. It needs to be mentioned that higher-order cut finite element methods additionally would require measures to compensate

the low-order geometric approximation along possibly curved boundaries within intersected elements. However, this need is not accounted for in this study and convergence rates are expected to be suboptimal. Developing such measures to reduce geometrical approximation errors and to retain optimal convergence rates is still subject of intense research. Possible techniques to improve this were introduced, e.g., by Burman *et al.* [65] and Lehrenfeld [175]. Despite sub-optimality of the rates, in this example convergence towards the right lift/drag values and pressure drop could be confirmed for linear as well as quadratic interpolations.

Fluid element type	h around cylinder	c_{drag}	c_{lift}	Δp
hex8	$7.3E-003$	5.49227	0.03903	0.11545
	$3.7E-003$	5.52247	0.00509	0.11628
	$1.8E-003$	5.55581	0.00915	0.11729
	$9.2E-004$	5.56727	0.01044	0.11736
hex20	$7.3E-003$	5.58219	0.01280	0.11766
	$3.7E-003$	5.58019	0.01145	0.11738
	$1.8E-003$	5.57914	0.01060	0.11731
Ref. lower bound [227]	–	5.5700	0.0104	0.1172
Ref. upper bound [227]	–	5.5900	0.0110	0.1176

Table 3.2: Laminar cylinder benchmark 2D-1 at $\mathrm{Re} = 20$: computed lift and drag coefficients and pressure difference between front and back end of the cylinder compared to reference values from [227]. Results for linearly- and quadratically-interpolated equal-order approximations based on *hex8* and *hex20* cut finite elements are shown.

A Two-Dimensional Flow around a Cylinder at $\mathrm{Re} = 800$. To investigate robustness of the proposed stabilized scheme for convective-dominant flows, a higher-Reynolds-number flow around a cylinder, as proposed by Shahmiri *et al.* [236], serves as test example.

The geometric setup is identical to the cylinder benchmark by Schäfer and Turek as described in the previous example. Now, the flow is time-dependent and driven by an inflow velocity which is directed along the x_1-axis and is parabolic with respect to x_2. The prescribed dynamic inflow is starting from a zero velocity at $T_0 = 0$ and reaches its maximum $u_1^{\max} = 1.5$ at $T_1 = 1$ such that

$$u_1(x_1 = 0, x_2, t) = u_1^{\max} \frac{4x_2(H - x_2)}{H^2} \cdot \begin{cases} 0.5(1 - \cos(\pi \frac{t}{T_1})) & t = [0, T_1], \\ 1 & t = (T_1, T], \end{cases} \tag{3.480}$$

$$u_2(x_1 = 0, x_2, t) = 0, \tag{3.481}$$

with $H = 0.41$ denoting the channel height. The final time is $T = 8$. Following the definition in [227], the Reynolds number based on the cylinder diameter and the mean velocity $u_1^{\text{mean}} = 2/3 u_1^{\max}$ emerges to $\mathrm{Re} = 800$. For the temporal discretization, a second-order BDF2 time-stepping scheme is applied with a time-step length of $\Delta t = 0.01$. At the circular boundary a zero-velocity $\boldsymbol{g}_{\text{D}} = \mathbf{0}$ is imposed weakly using the proposed Nitsche technique supported by CIP/GP stabilizations. The pressure solution in the vicinity of the cylinder is

shown in Figure 3.19. Indicated by the smoothness of the pressure contour lines, no perturbation of the pressure field in the vicinity of the interface could be observed. In view of envisioned fluid-structure-interaction applications, the temporal robustness of boundary forces is investigated, which are visualized in Figure 3.20. Forces resulting from fluid normal stresses $\boldsymbol{\sigma}(\boldsymbol{u}_h^{\mathrm{f}}, p_h^{\mathrm{f}}) = -p_h^{\mathrm{f}}\boldsymbol{I} + 2\mu\boldsymbol{\epsilon}(\boldsymbol{u}_h^{\mathrm{f}})$ are projected onto the structural trace mesh. Nodal forces acting on structural interface nodes l are defined as

$$\boldsymbol{f}_l^{\mathrm{s}} = \int_\Gamma N_l^{\mathrm{s}} \boldsymbol{\sigma}(\boldsymbol{u}_h^{\mathrm{f}}, p_h^{\mathrm{f}}) \cdot \boldsymbol{n}^{\mathrm{f}} \, \mathrm{d}s, \tag{3.482}$$

where N_l^{s} denotes finite element basis function at node l of the structural trace mesh. Figure 3.20a illustrates the force vectors at time $t = 0.85$ during the initial phase when the inflow velocity gets raised. The maximum inflow velocity is reached at time $T_1 = 1.0$. The corresponding state is shown in Figure 3.20b. Further discrete time levels $t = 3.25$ and $t = 3.40$ are picked out to visualize the periodically recurring pattern of tensile and compressive forces when the vortex shedding is fully developed, see Figure 3.20c and Figure 3.20d. Over the entire simulation time, interface forces are smoothly distributed along the structural surface. This underlines accuracy and stability of the pressure solution as well as of the velocity gradients in the vicinity of the cylinder. Figure 3.21 illustrates the Euclidean norm of the velocity and the evolution of the vortex shedding in the backflow of the structure at different times t.

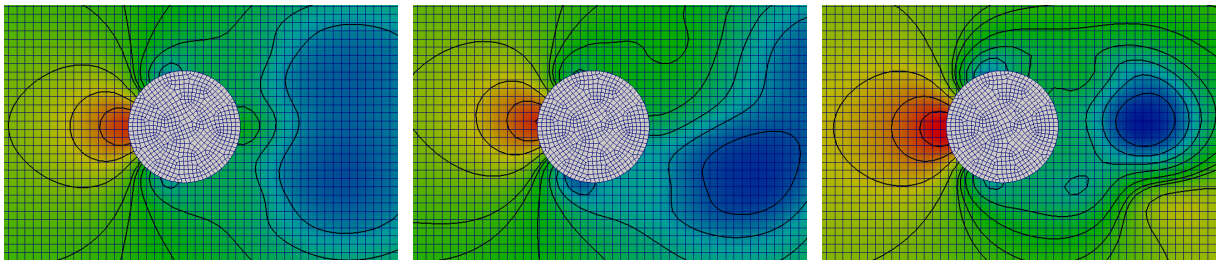

(a) $t = 1.35$ (b) $t = 2.25$ (c) $t = 3.15$

Figure 3.19: Two-dimensional flow around a cylinder at $RE = 800$: close-up views of the pressure field with contour lines at different times t.

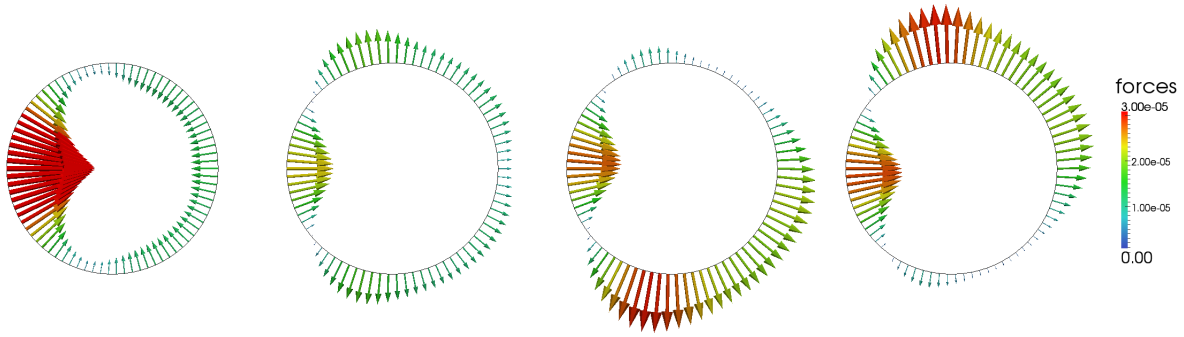

(a) $t = 0.85$ (b) $t = 1.00$ (c) $t = 3.25$ (d) $t = 3.40$

Figure 3.20: Two-dimensional flow around a cylinder at $RE = 800$: interface forces acting on the structural surface at different times t.

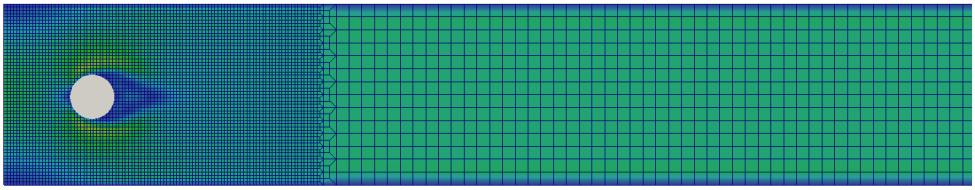

(a) $t = 0.7$

(b) $t = 1.35$

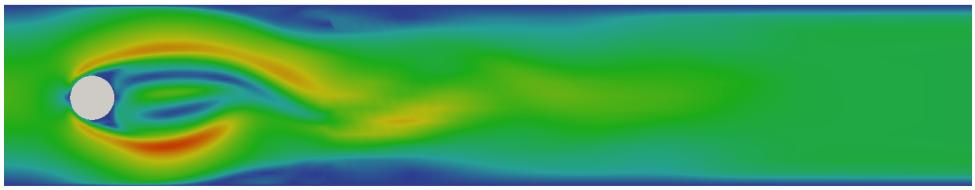

(c) $t = 1.95$

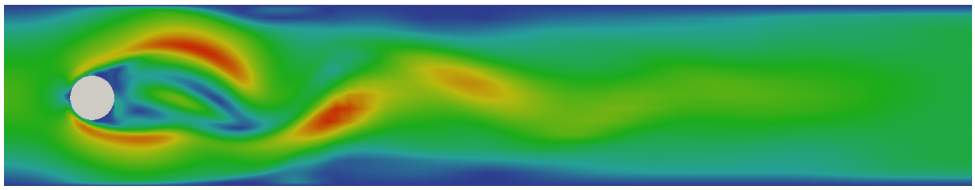

(d) $t = 2.25$

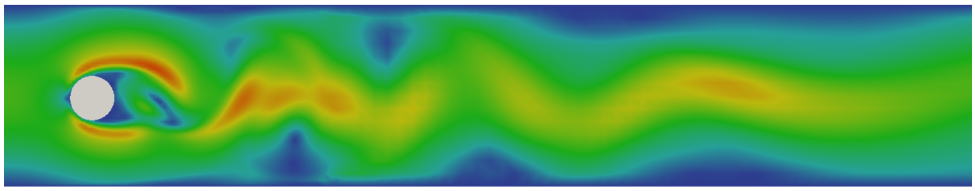

(e) $t = 2.85$

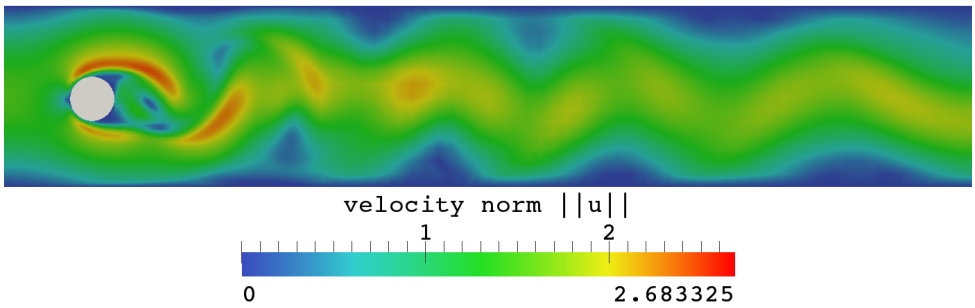

(f) $t = 3.15$

Figure 3.21: Two-dimensional flow around a cylinder at $RE = 800$: velocity norm $\|\boldsymbol{u}\|$ and vortex shedding in the backflow of the cylinder at different times t.

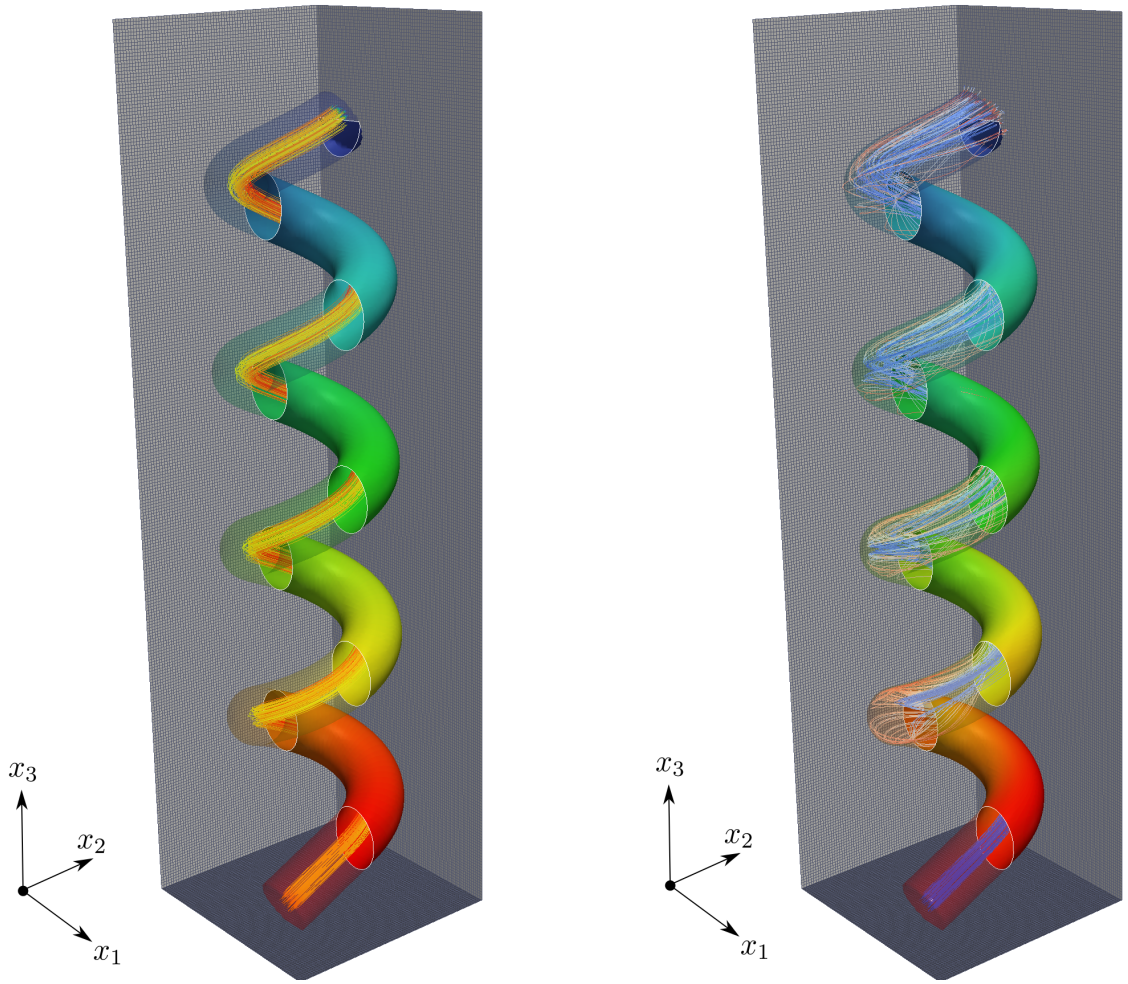

Figure 3.22: Helical Pipe Flow at $\mathrm{Re} = 100$: (a) Flow during the ramp phase at $t = 0.5$. (b) Laminar flow including twisted streamlines at $t = 3.0$ when flow reaches steady state. Streamlines start at inflow boundary located within a radius of 0.04 around pipe centerline and are colored by velocity magnitude at $t = 0.5$ and by vorticity at $t = 3.0$. Pressure distribution is visualized along the pipe surface.

3.6.2.2 Laminar Helical Pipe Flow

To demonstrate the high capabilities of the proposed cut finite element formulation in view of simplified mesh generation, the stabilized Nitsche-type CIP/GP-CUTFEM is applied to incompressible transient flow through a helical pipe. The relevance of curved pipe flows ranges from basic industrial applications like chemical reactors, heat exchangers and pipelines to medical applications considering physiological flows in the human body. Helical pipe flows have been extensively studied in literature, see, e.g., the works by Germano [122], Wang [263] or Zabielski and Mestel [274].

The geometric setup of the pipe considered in this work is depicted in Figure 3.22 and described as follows: The cross-section of the pipe is defined by a circle with radius $r = 0.1$. This is expanded along a helical curve which is parametrized as $\boldsymbol{x}_{\text{curv}}(s) = (R\cos(2\pi s), R\sin(2\pi s), \alpha s)$.

This three-dimensional curve turns around the x_3-axis at a constant distance of $R = 0.2$ and a constant thread pitch of $\alpha = 0.6$. The spiral twists four times, i.e. $s \in [-2, 2]$. A detailed description of the level-set representation of such a finite helical pipe is given in Appendix A, see formula (A.21). It is visualized in Figure A.1. Additionally, a finite cylinder as defined in (A.8) is put on the lower end of the spiral. Its radius is equal to the cross-section radius r and has a length of $h = 0.35$. Its orientation is aligned to the tangential vector $\boldsymbol{t}(s) = \partial \boldsymbol{x}_{\text{curv}}(s)/\partial s$ of the helix evaluated at $s = -2$. The final composed fluid domain is shown in Figure 3.22.

The front end of the expanding cylinder defines the inflow boundary Γ_{in} where a velocity $\boldsymbol{g}_{\text{D}} = u_{\text{in}}\boldsymbol{n}$ is imposed. Here, $\boldsymbol{n} \overset{\text{def}}{=} \boldsymbol{t}(s = -2)$ denotes the unit vector which is normal to the circular cross section. Along the cylindrical and helical pipe surfaces, no-slip boundary conditions $\boldsymbol{g}_{\text{D}} = \boldsymbol{0}$ are weakly enforced. At the back end of the helical pipe a zero-traction Neumann boundary condition $\boldsymbol{h}_{\text{N}} = \boldsymbol{0}$ is prescribed. All boundary conditions are enforced weakly utilizing the Nitsche-type CIP/GP method proposed in Section 3.6.1.1.

The implicitly defined geometry as well as the flow solution are approximated on a cut background mesh $\widehat{\mathcal{T}}_h$ covering a background cuboid $[-0.4, 0.4] \times [-0.4, 0.4] \times [-1.5, 1.5]$ consisting of $76 \times 76 \times 285$ tri-linearly-interpolated hexahedral $\mathbb{Q}^1$-elements. In total, the number of active velocity and pressure degrees of freedom is 859612.

In the following, a laminar pipe flow at $\text{Re} = 100$ is considered, where the characteristic Reynolds number is defined as $\text{Re} = u_{\text{eff}} r/\nu$ with an effective cross-section averaged velocity u_{eff}, the pipe radius r and the viscosity of the fluid ν. At the inflow a constant velocity of $u_{\text{in}} = u_{\text{eff}} = 3.8$ is imposed which drives the mass flow. Thereby, the velocity is chosen according to a wall Reynolds number of $\text{Re}_\tau = 180$ for pipe flows, see, e.g., Carlos *et al.* [68] for further explanations. For this setup the viscosity is $\nu = 1.9 \cdot 10^{-3}$. The pipe flow is investigated for a total simulation time of $T = 3$, which is the approximated time needed for three runs through the entire pipe along its centerline. For the temporal discretization a one-step-θ scheme with $\theta = 0.5$ is applied and the time-step length is set to $\Delta t = 0.001$, which ensures a maximum CFL-number of $\text{CFL} < 0.5$. The inflow velocity is initially increased within $t \in (0, T_1]$ by a ramp function $1/2(1 - \cos(\pi t/T_1))$ with $T_1 = 0.1$.

The solution to the pipe flow is visualized at $t = 0.5$ during the ramp phase and when the flow is fully developed and has reached steady state, as expected for this laminar setting in Figure 3.22. During the ramp phase, when the flow enters the helical pipe, streamlines follow the helical main curve through the pipe. Within the first turn, the distance of the line of highest velocities to the x_3-axis decreases from initially R, however, remains almost unchanged for all following turns. A snapshot of the ramp phase including streamlines and pressure distribution along the pipe surface is shown in Figure 3.22a. Contour lines of the velocity magnitude at a cross-section clip plane $x_2 = 0.0$ is shown in Figure 3.23a for the pipe range of $s \in [0, 1.5]$. Pressure isocontours along the pipe surface are visualized in Figure 3.23b. The accurate enforcement of the no-slip boundary condition along the pipe surface as well as stability of velocity and pressure solutions are clearly visible.

When the flow has been fully developed, the flow pattern clearly changes and streamlines get twisted. However, the flow reaches steady state after some time which is captured in a snapshot in Figure 3.22b at $t = 3.0$. Therein, streamlines are colored by vorticity and the pressure distribution is depicted along the helical surface. It is inherently linked to the weak enforcement technique that the strength of fulfilling the boundary condition in wall-tangential direction

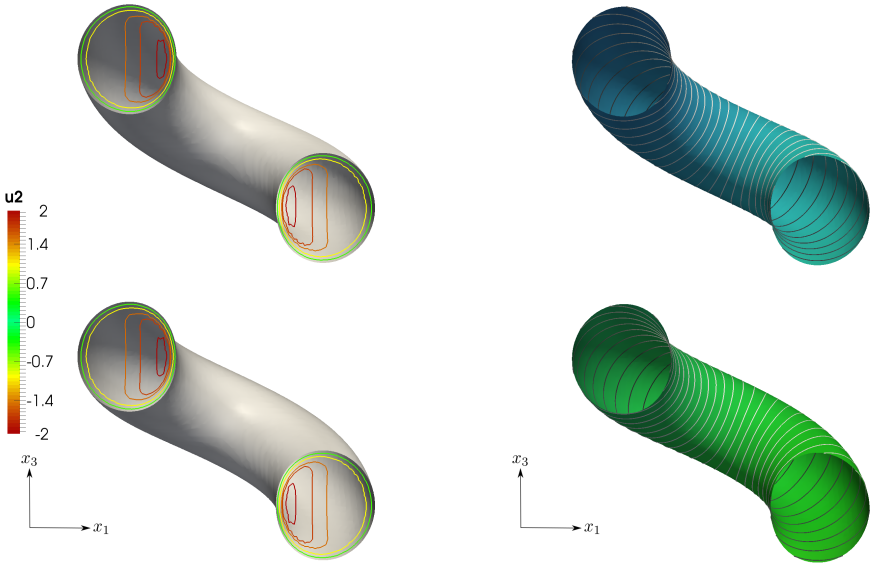

(a) (b)

Figure 3.23: Helical Pipe Flow at $\mathrm{Re} = 100$ at $t = 0.5$: (a) Isocontours of velocity magnitude at a cross section defined by a clip plane $x_2 = 0.0$ for a helix range of $s \in [0, 1.5]$ indicate higher velocities with decreasing distance to the x_3-axis due to higher mass flow rate. The zero boundary condition at the helix surface is accurately enforced and the velocity solution is stable in the interior of the fluid domain as well as near the boundary. (b) Pressure contour lines at the helix surface underline the stability of the pressure solution near the boundary.

gets weakened, the higher the local element Reynolds number becomes in the vicinity of the boundary. Though, the non-penetration condition in wall-normal direction of the pipe, which ensures mass conservation, is still sufficiently enforced. Moreover, the solution exhibits non-oscillatory stable velocity and pressure due to stabilizing effects of the different applied CIP/GP stabilization operators in the interior of the fluid domain as well as near the boundary zone. At steady state, contour lines are visualized in Figure 3.24a for the velocity and in Figure 3.24b for the pressure.

3.6.2.3 Flow in a Complex-Shaped Domain Composed of Level-Set Fields

In order to demonstrate the high capabilities of the proposed fluid solver, a complex three-dimensional flow setting is considered. Its full benefits are reaped when cut finite element fluid formulations are combined with simple boundary representation techniques.

In this example, the flow through a complex-shaped fluid domain is simulated. Its boundary is implicitly defined by the zero-level of the function defined in (A.36), see Appendix A.3. Visualizations of the domain Ω^{f} and of its construction steps are given in Figure A.2. It consists of a hollow cylindrical inflow region from which the flow is entering a channel composed of cylinders, a sphere and several limiting boundary planes. Furthermore, a spiral-shaped obstacle is embedded into the channel. For the approximation of the level-set field and of the fluid fields a regularly meshed background grid $\widehat{\mathcal{T}}_h$ covering a cuboid $[-0.7, 0.1] \times [-0.5, 0.5] \times [-1.5, 1.5]$

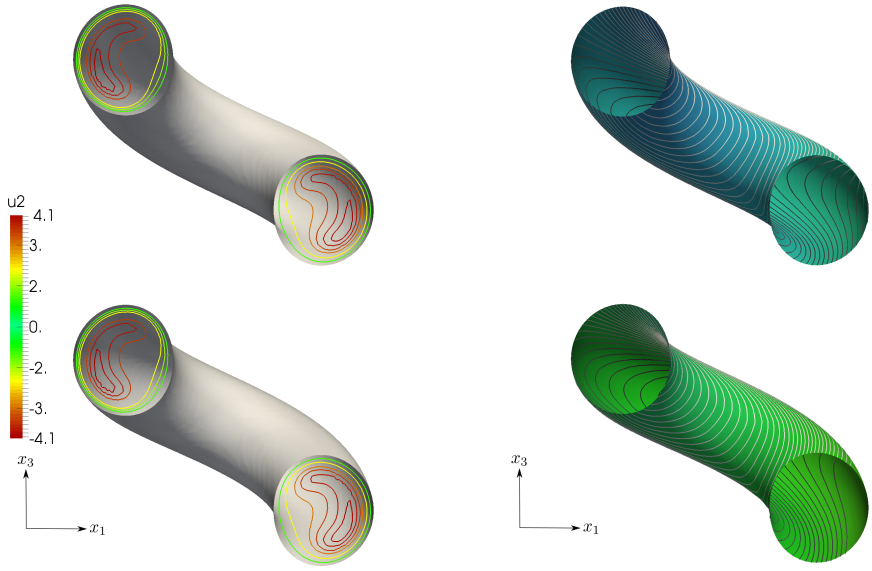

(a) (b)

Figure 3.24: Helical Pipe Flow at $\mathrm{Re} = 100$ at $t = 3.0$ when the flow has reached steady state: (a) Isocontours of velocity magnitude at a cross section defined by a clip plane $x_2 = 0.0$ for a helix range of $s \in [0, 1.5]$ indicate stable velocity solution in the interior of the fluid domain as well as near the boundary. (b) Pressure contour lines at the helix surface demonstrate a stable pressure solution in the vicinity of the boundary.

is utilized. The mesh consists of tri-linearly-interpolated hexahedral $\mathbb{Q}^1$-elements with a mesh size of $h = 0.02$ in each coordinate direction.

All boundary conditions are enforced weakly using the Nitsche-type technique combined with the RBVM/GP stabilization technique as described in Section 3.6.1.2. At the circular inflow boundary, which is located at $x_3 = -1.49$, a rotationally symmetric parabolic velocity field $\boldsymbol{g}_{\mathrm{D}}(\boldsymbol{x}) = (0, 0, u_3)(\boldsymbol{x})$ is imposed. It is directed along the positive x_3-coordinate with a maximal velocity of $u_3^{\max} = 1$ reached at the center point $\boldsymbol{x}^{\max} = (-0.2, 0, -1.49)$. The parabolic profile is given as

$$u_3(x_1, x_2, x_3 = -1.49) = u_3^{\max}(1 - ((x_1 - x_1^{\max})^2 + (x_2 - x_2^{\max})^2)/r^2), \tag{3.483}$$

where $r = 0.14$ denotes the inner radius of the cylindrical inflow region. At the outflow, which is limited by the halfspace $\phi_{\text{HSpace,out}}$ at $x_3 = 1.5$, a zero-traction Neumann boundary condition $\boldsymbol{h}_{\mathrm{N}} = \boldsymbol{0}$ is prescribed. For all remaining boundaries and along the surface of the spiral-shaped obstacle, which are all defined by the zero-isocontour of ϕ_{Fluid} in (A.36), 'no-slip' Dirichlet boundary conditions $\boldsymbol{g}_{\mathrm{D}} = \boldsymbol{0}$ are weakly imposed. The inflow is initially ramped utilizing the function $1/2(1 - \cos(\pi t/T_1))$ within $t \in (0, T_1]$ with $T_1 = 1$. The overall simulation time is set to $T = 18$ and is temporally resolved with a time-step length of $\Delta t = 0.01$ using an OST scheme without numerical damping, i.e. $\theta = 0.5$. The flow is highly convective-dominated based on a viscosity of $\nu = 10^{-4}$. The resulting complex flow pattern, which develops when entering the bulk and hitting the spiral, is visualized in Figure 3.25 with the help of streamlines. These start at the inflow and wind around the spiral object through the fluid domain. Boundary conditions along the entire surface are accurately enforced. Stability at boundaries, inflow

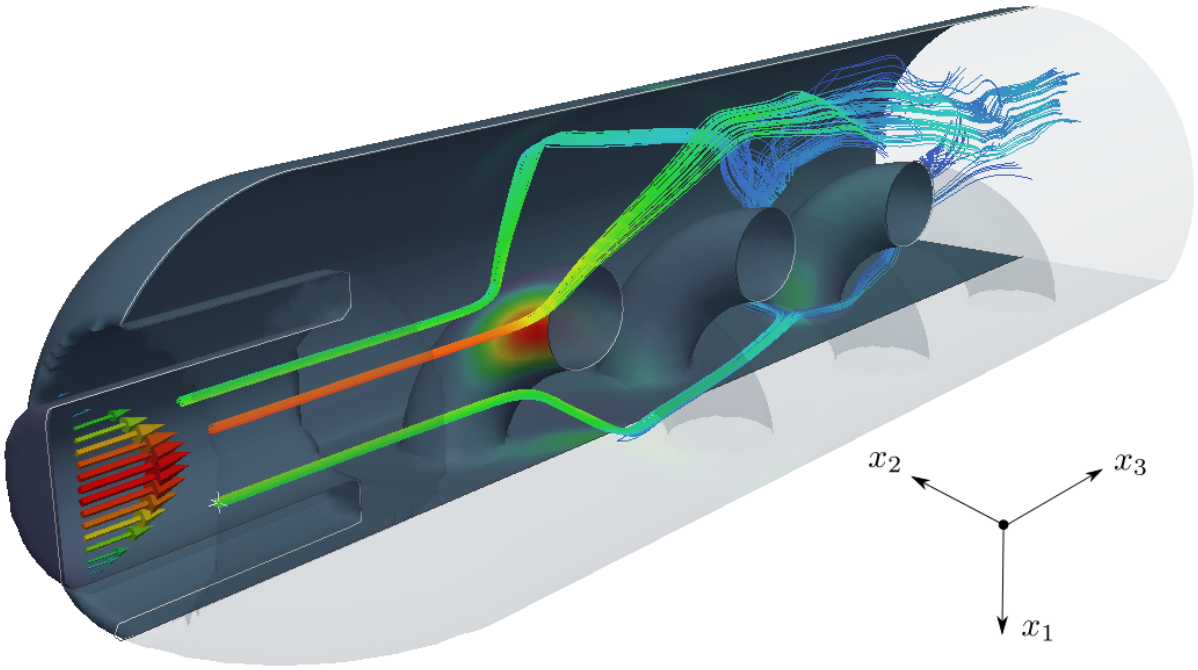

Figure 3.25: Flow through a complex-shaped fluid domain:bThe boundary of this fluid domain is defined implicitly utilizing Boolean set operations for various level-set fields as defined in (A.36), see in Appendix A.3. Level-set field and fluid solutions are approximated with an unfitted mesh consisting of $\mathbb{Q}^1$-elements. The highly convective-dominated flow is computed with the RBVM/GP-CUTFEM based on an OST($\theta = 0.5$) time stepping scheme. Streamlines are colored by the velocity magnitude and the domain boundary is colored by the pressure distribution at time $T = 18$.

regions as well as in the interior domain is underlined by means of the applied temporal discretization scheme which does not introduce any numerical damping over the entire simulation time. As demonstrated, combining the proposed CUTFEM formulation with simple techniques to describe domain boundaries allows to easily setup and simulate challenging incompressible flows without any effort with regard to computational grid generation. The next task is to extend this methodology to flows in moving domains.

3.6.3 Extension to Flow in Moving Domains

Cut finite element methods show their high capabilities in particular for incompressible flows where the domain boundaries or interfaces evolve in time. Unfitted approximation techniques for one- or multiphase problems like free-surface flows, two-phase flows, fluid domain decomposition settings or fluid-structure interaction are prominent and well-established fields of application. While for boundary-fitted meshes ALE-based formulations are the method of choice when dealing with moving domains, unfitted mesh techniques mainly aim at utilizing pure Eulerian reference frames for the description of the fluid phases. Particularly the advantage of fixed-grid techniques to avoid mesh distortion and thus the change of the spatial approximation space at each time step cause severe issues for the temporal discretization based on classical time-stepping schemes. Due to the change of the spatial approximation, for such schemes,

which are usually based on finite difference approximations of the time derivative as introduced in Section 3.6.1.3, it is reasonable to first discretize in time and then in space, a technique which is called a *Rothe method*, see Rothe [223]. When solving for a discrete approximation to the new time step, all terms are then evaluated at the corresponding new time level. As discussed by Zunino [279], the so-called *method of lines*, i.e. to first discretize in space and afterwards in time, is not applicable anymore. Furthermore, related numerical analyses only allow to proof convergence rates for spatial L^2-errors measured at the final time which may become sub-optimal with $\mathcal{O}\left(h^2(\Delta t)^{-1}\right)$ compared to an optimal rate $\mathcal{O}\left(h^2 + \Delta t\right)$ which would at least be expected for linearly interpolated approximations in space and first-order approximations in time. Although no numerical analysis for such schemes has been provided for a long time, such discretizations gained rapidly increasing attention even for many practical applications. As an example, a rigorous analysis for the backward Euler scheme in combination with any spatial interpolation order $k \geqslant 1$ was provided by Zunino [279]. Spatial and temporal errors are proven being decoupled and optimal as $\mathcal{O}\left(h^{k+1} + \Delta t\right)$. Approximating all integrals at one time level, however, theoretically restricts time-stepping scheme to first order temporal accuracy. For second-order ODE time-stepping schemes, Fries and Zilian [117] observed reduced convergence rates in the unfitted case. While higher-order spatial discretizations improve related spatial estimates as expected, provided that numerical integration on cut elements ensures the required order of accuracy, extensions to higher-order temporal accuracy becomes more delicate.

Different techniques have been developed for related problem settings in moving domains. However, most of them were presented without numerical analysis. Among simple and sub-optimal projection techniques as introduced, e.g., by Gerstenberger [123], a semi-Lagrangean technique has been introduced by Henke *et al.* [148] and applied to an extended finite element method for premixed combustion problems by Henke [147]. A fixed-mesh ALE approach, in which virtual ALE techniques within single time steps are combined with data transfer operators to project discrete solutions between finite element meshes, has been proposed by Codina *et al.* [76]. The projections utilized therein take the strong form of the respective governing equations into consideration. Recently, a space-time Galerkin technique based on linearly-interpolated continuous approximations for the temporal dimension, which ensures second-order accuracy even in time, has been developed by Frei and Richter [113]. Characteristic Galerkin techniques for CutFEMs on time dependent surfaces have been considered by Hansbo *et al.* [142]. Space-time approximations for coupled bulk-surface problems on time-dependent domains utilizing discontinuous linear approximations for the discrete time slabs have been introduced by Hansbo *et al.* [143]. Recently, a Nitsche-based discontinuous Galerkin space-time method has been proposed by Lehrenfeld [174]. Even though optimal rates of convergence are guaranteed for the latter method provided that the numerical integration is accurate enough, space-time techniques are often difficult to implement in existing finite element code frameworks. For domains with three spatial dimensions, a linear approximation of the interface motion in time then requires cutting four-dimensional space-time slabs. The resulting four-dimensional polytopes finally form the physical space-time domain. It has to be mentioned that already for level-set-based interface descriptions the intersection of elements in four dimensions is a challenging task as demonstrated in [174]. Moreover, adaption to composite mesh techniques, where the interface is given explicitly by a moving trace mesh, renders in an unlimited number of intersection scenarios and robust implementations seem difficult to realize. Furthermore, for space-time approaches the size of the final discrete system is approximately doubled compared to time-

stepping schemes. Also developing optimal preconditioners for such linear systems is still subject of current research. Even though space-time CUTFEMs provide attractive features for flow problems, their incorporation into most if not all existing FEM-based multiphysics code environments is not straightforward and further demands other physical fields of coupled problems to be also formulated in a space-time framework.

It has to be mentioned that developing CUTFEMs which ensure higher-order temporal accuracy is not in the focus of the present work. For reasons of simplicity and practicality with regard to coupling of fluids with other physical fields, the one-step-θ time-stepping scheme based on the Rothe discretization technique is exclusively considered in this work. A possibly reduced temporal accuracy of first order even for the Crank-Nicolson scheme, i.e. $\theta = 1/2$, is thereby to be accepted.

3.6.3.1 Discrete Nitsche-type Cut Finite Element Method in Moving Domains

In this section, the motion of the boundary $\Gamma(t)$ of a fluid domain $\Omega(t)$ is assumed being predefined for all times $t \in (T_0, T]$. Coupled problem settings in which the location of $\Gamma(t)$ depends on the flow solution itself will be addressed in Chapters 4 and 5. Boundary conditions are assumed to be defined accordingly for each time level as $\boldsymbol{u}(t) = \boldsymbol{g}_{\mathrm{D}}(t)$ on $\Gamma_{\mathrm{D}}(t)$ and $\boldsymbol{\sigma}(\boldsymbol{u}(t), p(t)) \cdot \boldsymbol{n}(t) = \boldsymbol{h}_{\mathrm{N}}(t)$ on $\Gamma_{\mathrm{N}}(t)$.

Let the time domain $(T_0, T]$ be partitioned into N equal-sized time intervals $J^n = (t^{n-1}, t^n]$ of size Δt with discrete time levels $t^n = T_0 + n\Delta t$ and $t^N = T$. Within each interval J^n, let $\mathcal{V}_h^n \subset \mathcal{V}(t^n)$ and $\mathcal{Q}_h^n \subset \mathcal{Q}(t^n)$ be the respective discrete cut finite element subspace with discrete velocity and pressure approximations $\boldsymbol{u}_h^n \approx \boldsymbol{u}(t^n)$ and $p_h^n \approx p(t^n)$. The physical domain approximation is assumed fixed within each time slab $Q^n \overset{\text{def}}{=} \Omega_h(t^n) \times J^n$ associated with J^n. Note that all function spaces $\mathcal{V}_h^n, \mathcal{Q}_h^n$ of different time intervals J^n are constructed on the same mesh $\widehat{\mathcal{T}}_h$. The active parts $\mathcal{T}_h^n$, however, usually change and the number of DOFs is varying. Furthermore, due to changing mesh intersections all boundary-/interface-dependent cut-related entities become time-dependent; i.e., for instance, interface zone elements $\mathcal{T}_\Gamma^n$, face sets $\mathcal{F}_i^n, \mathcal{F}_\Gamma^n$ and related facets f or volume-cells V, see also in Section 2.2.2.

In the following, a fully discretized Nitsche-type CIP/GP-CUTFEM, as introduced in Section 3.6.1.1, is presented for moving domains. The temporal discretization follows (3.475) and is based on a one-step-θ scheme. Analogously, a fully-discrete Nitsche-type RBVM/GP-CUTFEM from Section 3.6.1.2 could be derived which, however, is not presented explicitly here.

Definition 3.15 (The OST-discretized Nitsche-type CIP/GP-CUTFEM)
Find a sequence of discrete velocity and pressure functions $U_h^n = (\boldsymbol{u}_h^n, p_h^n) \in \mathcal{V}_h^n \times \mathcal{Q}_h^n$ associated with time intervals J^n such that for all $V_h = (\boldsymbol{v}_h, q_h) \in \mathcal{V}_h^n \times \mathcal{Q}_h^n$

$$\begin{aligned}(\rho \boldsymbol{u}_h^n, \boldsymbol{v}_h)_{\Omega_h^n} + \theta\Delta t(\mathcal{B}_h + \mathcal{S}_h^{\mathrm{CIP}} + \mathcal{G}_h^{\mathrm{GP}} - \mathcal{L}_h)((\boldsymbol{u}_h^n, p_h^n), (\boldsymbol{v}_h, q_h)) \\ - (\rho \tilde{\boldsymbol{u}}_h^{n-1}, \boldsymbol{v}_h)_{\Omega_h^n} - (1-\theta)\Delta t(\rho \tilde{\boldsymbol{a}}_h^{n-1}, \boldsymbol{v}_h)_{\Omega_h^n} = 0\end{aligned} \tag{3.484}$$

with acceleration approximation

$$\boldsymbol{a}_h^n = \frac{\boldsymbol{u}_h^n - \tilde{\boldsymbol{u}}_h^{n-1}}{\Delta t} - \frac{1-\theta}{\theta}\tilde{\boldsymbol{a}}_h^{n-1} \in \mathcal{V}_h^n. \tag{3.485}$$

Note that all bulk, interface and face integrals appearing in the operators $\mathcal{B}_h, \mathcal{S}_h^{\mathrm{CIP}}, \mathcal{G}_h^{\mathrm{GP}}$ and $\mathcal{L}_h$, see (3.452)–(3.455), are evaluated with respect to the current time level t^n, i.e. in the domain Ω_h^n, on the boundary Γ_h^n, and on faces $F \in \mathcal{F}_i^n, \mathcal{F}_\Gamma^n$ for CIP *and* GP *terms, respectively. The superscript $(\cdot)^n$ indicates that all involved quantities belong to the current time level t^n and are discretized with respect to the discrete function spaces $\mathcal{V}_h^n, \mathcal{Q}_h^n$, respectively.*

Remark 3.28 *Temporal time-stepping schemes from $t^{n-1} \to t^n$ which are based on Rothe's technique, consist of approximating solutions of discrete time levels t^{n-1} and t^n on different function spaces, i.e. $U^{n-1} \in \mathcal{W}^{n-1}$ and $U^n \in \mathcal{W}^n$. In contrast to space-time methods, here, for moving domains the time-dependent change of cut finite element approximation spaces is not tracked continuously over time, i.e. discrete finite dimensional spaces do not match in general, i.e. $\mathcal{W}_h^{n-1} \neq \mathcal{W}_h^n$, since corresponding domains are not equal, i.e. $\Omega_h^{n-1} \neq \Omega_h^n$. Obviously, this fact becomes an issue when evaluating inner products in Ω_h^n that incorporate quantities from previous time levels $\boldsymbol{u}_h^{n-1}, \boldsymbol{a}_h^{n-1} \notin \mathcal{V}_h^n$ which do not fit the current approximation space. To compensate this mismatch between the approximation space $\mathcal{V}_h^n$ of the current time level and the solution fields from the previous time level, projected approximations $\tilde{\boldsymbol{u}}_h^{n-1}, \tilde{\boldsymbol{a}}_h^{n-1} \in \mathcal{V}_h^n$ adapting $\boldsymbol{u}_h^{n-1}, \boldsymbol{a}_h^{n-1}$ to the current domain Ω_h^n are necessary. Possible projection operators $P^n : \mathcal{V}_h^{n-1} \to \mathcal{V}_h^n$ between function spaces applicable to velocity and acceleration approximation as $\tilde{\boldsymbol{u}}_h^{n-1} \overset{def}{=} P^n \boldsymbol{u}_h^{n-1}$ and $\tilde{\boldsymbol{a}}_h^{n-1} \overset{def}{=} P^n \boldsymbol{a}_h^{n-1}$ will be introduced subsequently.*

3.6.3.2 Solution Projection between Function Spaces

The fundamental idea of constructing transfer operators between two different cut finite element function spaces is first introduced for scalar functions in a simplified one-dimensional single-phase problem and afterwards generalized to the multidimensional case as well as vector-valued approximations. The final objective is to project an approximate solution $\boldsymbol{u}_h^{n-1} \in \mathcal{V}_h^{n-1}$ computed at time level t^{n-1} onto the function space $\mathcal{V}_h^n$ which is associated with the current time interval J^n, however, with possibly changed interface position.

Projecting Solutions from $\mathcal{X}_h^{n-1}$ onto $\mathcal{X}_h^n$ - the One-Dimensional Case. Possible characteristic scenarios are visualized for a simplified one-dimensional problem setting in Figure 3.26 and can be distinguished as follows:

Interface motion within a cut element: In Figures 3.26a and 3.26b, interface motions $\Gamma_h^{n-1} \to \Gamma_h^n$ within a cut finite element are considered. For these cases the respective influence regions of basis functions N_s associated with nodes of the intersected element vary since the physically meaningful parts of their supports change, i.e. $\mathrm{supp}\,(N_s) \cap \Omega_h^{n-1} \neq \mathrm{supp}\,(N_s) \cap \Omega_h^n$. However, both function spaces of the two time levels rely on the same discrete function basis. In such situations, discrete finite dimensional vectors can be copied component-wise, i.e. $\tilde{\boldsymbol{u}}_h^{n-1} = \boldsymbol{u}_h^{n-1}$, and the projection operator becomes the identity mapping, i.e. $\boldsymbol{P}^n = \boldsymbol{I}$. The procedure for these cases is similar to that suggested by Alauzet *et al.* [1].
Interface motion across nodes with reduced influence region of basis functions: A further standard scenario is visualized in Figure 3.26c. Even though here the interface crosses a node, with regard to temporal discretization this case is closely related to that shown in Figure 3.26a. The influence of basis function N_2 associated with a node located within the physical domain Ω_h^{n-1} gets continuously reduced when $\Gamma_h(t)$ is moving within J^n. While node s_2 changes

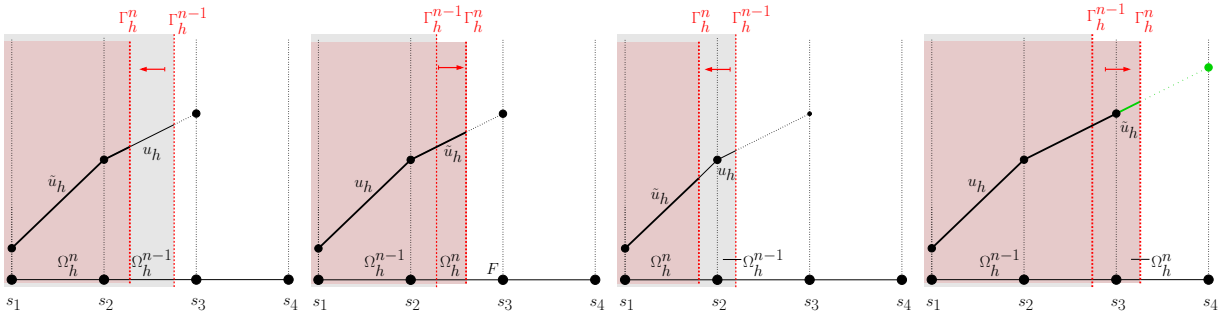

Figure 3.26: Standard scenarios for the TRANSFER/COPY-PHASE: (a) and (b) Interface motion within an intersected finite element with identical function spaces at t^{n-1} and t^n, DOFs can be transcribed from $\mathcal{X}_h^{n-1}$ to $\mathcal{X}_h^n$, i.e. $\tilde{\boldsymbol{u}}_h^{n-1} = \boldsymbol{u}_h^{n-1}$. (c) Reduced influence region of basis function N_2 associated with node s_2, which changes its location from inside the physical domain Ω_h^{n-1} to outside of the physical domain Ω_h^n such that $\tilde{u}_h^{n-1} = \boldsymbol{P}^n u_h^{n-1}$ with $(\tilde{u}_1^{n-1}, \tilde{u}_2^{n-1}) = (u_1^{n-1}, u_2^{n-1})$. (d) Interface motion across node and newly activated DOF at node s_4. Until time $t^* \in (t^{n-1}, t^n)$ when $\Gamma(t)$ crosses s_3, a natural extension via transcribing DOFs is given by $(\tilde{u}_1^{n-1}, \tilde{u}_2^{n-1}, \tilde{u}_3^{n-1}) = (u_1^{n-1}, u_2^{n-1}, u_3^{n-1})$. For $t \in (t^*, t^n)$, basis function N_4 requires reconstructing $\tilde{u}_4$ via an extension technique $\tilde{u}_4^{n-1} = \boldsymbol{E}^*(\tilde{u}_2^{n-1}, \tilde{u}_3^{n-1})$, for instance, defined by a face-jump penalty extension operator (3.486). The final projection from $\mathcal{X}_h^{n-1}$ to $\mathcal{X}_h^n$ results in $\tilde{u}_h^{n-1} = \boldsymbol{P}^n u_h^{n-1}$ with $(\tilde{u}_1^{n-1}, \tilde{u}_2^{n-1}, \tilde{u}_3^{n-1}, \tilde{u}_4^{n-1}) = (u_1^{n-1}, u_2^{n-1}, u_3^{n-1}, \boldsymbol{E}^*(\tilde{u}_2^{n-1}, \tilde{u}_3^{n-1}))$.

its location from inside the physical domain Ω_h^{n-1} to outside of the physical domain Ω_h^n, the shape function N_3, which was located within the ghost domain $\Omega_h^{n-1,*} \backslash \Omega_h^{n-1}$ already at t^n, completely lost its influence region, i.e. $\text{supp}\,(N_3) \cap \Omega_h^n = \emptyset$. Its associated nodal value is not utilized for the function space projection which is defined as $\tilde{u}_h^{n-1} = \boldsymbol{P}^n u_h^{n-1}$ with $(\tilde{u}_1^{n-1}, \tilde{u}_2^{n-1}) = (u_1^{n-1}, u_2^{n-1})$.

Interface motion with newly activated degrees of freedom: A contrary and much more challenging situation is indicated in Figure 3.26d. Here, the physical domain increases and one node, which is located outside the physical domains at t^{n-1} and t^n, however, did not carry a DOF at the previous time step t^{n-1}, gets activated and contributes to the approximation space at the current time level t^n. As no natural extension in terms of already existing degrees of freedom is available, an expansion of u_h^{n-1} to Ω_h^n needs to be computed similar to the configuration depicted in Figure 3.26b. When virtually moving the interface continuously from Γ_h^{n-1} to Γ_h^n, a natural extension is defined by copying DOFs as long as the boundary has not crossed node s_3 yet, i.e. $(\tilde{u}_1^{n-1}, \tilde{u}_2^{n-1}, \tilde{u}_3^{n-1}) = (u_1^{n-1}, u_2^{n-1}, u_3^{n-1})$. When continuing with interface tracking from an intermediate time t^*, which is defined as the time level when the boundary crosses node s_3, the existent approximation would become sub-optimal if the newly activated DOF associated with node s_4 would be neglected. An extension beyond node s_3 can be obtained, for instance, by defining $\tilde{u}_4^{n-1}$ such that the kink between the two piecewise polynomials gets minimized, as demonstrated in Figure 3.26d. Based on the key idea to control DOFs associated with ghost-nodes in pathological element intersection cases via ghost-penalty (GP) operators, a similar technique can be utilized to compute a natural extension even for purposes of time stepping. Such a technique applicable to arbitrary spatial dimensions will be proposed and elaborated within the next paragraph. Once the newly created ghost-DOF associated with N_4 has been computed, the final projection can defined as

$\tilde{u}_h^{n-1} = \boldsymbol{P}^n u_h^{n-1}$ with $(\tilde{u}_1^{n-1}, \tilde{u}_2^{n-1}, \tilde{u}_3^{n-1}, \tilde{u}_4^{n-1}) = (u_1^{n-1}, u_2^{n-1}, u_3^{n-1}, \boldsymbol{E}^*(\tilde{u}_2^{n-1}, \tilde{u}_3^{n-1}))$. Therein, $\tilde{u}_4^{n-1} = \boldsymbol{E}^*(\tilde{u}_2^{n-1}, \tilde{u}_3^{n-1})$ denotes the computed value based on an aforementioned extension technique, which usually depends on the DOFs of all neighboring uncut elements. Note that such a procedure requires Δt being chosen sufficiently small such that interface motions per time step become less than the length of one element, i.e. $\|u_\Gamma\|\Delta t \leqslant h$, where u_Γ denotes the interface normal velocity. This restriction is related to the so-called *Courant–Friedrichs–Lewy condition* which is a common stability condition for discretization schemes in fluid mechanics.

Algorithmic Procedure for Function Space Projections from $\mathscr{X}_h^{n-1}$ onto $\mathscr{X}_h^n$. The fundamental idea of projecting solutions between two distinct function spaces associated with two consecutive time levels t^n and t^{n-1} is subsequently generalized to the multidimensional case, i.e. $d = 2, 3$, based on the expanded cut finite element approximation space introduced in Section 2.2.4. For each DOF $\tilde{u}_k^{n-1}$, i.e. $1 \leqslant k \leqslant \mathrm{numdof}\,(s)$, of active nodes $s \in \mathcal{N}$ at the current time level t^n an appropriate value has to be constructed on basis of the solution $u_h^{n-1} \in \mathscr{X}_h^{n-1}$. The final procedure suggested for this task is summarized in Algorithm 3.1 and is split into two phases:

- a first TRANSFER/COPY-PHASE and
- a second EXTENSION-PHASE.

The TRANSFER/COPY-PHASE comprises standard transfer techniques applicable to nodes and their associated DOFs as visualized in Figures 3.26a–3.26c for the one-dimensional setting. These configurations aim at *directly copying* DOFs from the previous configuration to the current configuration. The previously introduced transcription techniques for selected DOFs can be adapted to expanded function spaces $\mathscr{X}_h$, which have been defined in Section 2.2.4, as follows: being applicable to a DOF $\tilde{u}_k^{n-1}$ of the current function space $\mathscr{X}_h^n$, which belongs to a grid node s, requires to identify another DOF u_i^{n-1} associated with the space $\mathscr{X}_h^{n-1}$ at the same node location. Thereby, reasonable DOF-pairs $(\tilde{u}_k^{n-1}, u_i^{n-1})$ have to exhibit a related meaning for the solution approximation in their respective physical domains. Identifying such DOF-pairs relies on information about DOF-associated volume-cell connections $C \in \mathscr{C}_s$ located within the support of its shape function N_s, see also elaborations in Section 2.2.4. As indicated in Figures 3.26a–3.26c, different pairs between standard and ghost-DOFs of current and previous time levels might be reasonable. Common scenarios where the TRANSFER/COPY-PHASE yields reasonable DOF-pairs are visualized in Figure 3.27. Note that identification of DOF-pairs should be possible for all DOFs at the current time level t^n whose node is located within the physical domain Ω_h^n. If $\mathrm{supp}\,(N_s)$ for a given DOF is intersected at the current time level, it was also intersected at the previous time level. Otherwise, the CFL-like condition on the interface motion has been violated.

After performing the TRANSFER/COPY-PHASE there may remain some ghost-DOFs which have been newly activated compared to the previous intersection configuration. Such DOFs belong to the scenario Figure 3.26d, i.e. to $\mathscr{X}_h^n \backslash \mathscr{X}_h^{n-1}$, and are visualized exemplarily in Figure 3.27 for $d = 2$. For multidimensional problem settings, missing ghost-DOFs can be computed in a second step, called the EXTENSION-PHASE. Fixing values which have been already determined during the TRANSFER/COPY-PHASE by setting Dirichlet constraints to $\mathscr{X}_h^n$, whose resulting trial and test function spaces are then denoted as $\bar{\mathscr{X}}_h^n$ and $\bar{\mathscr{X}}_{h,0}^n$, a linear global extension system can

Algorithm 3.1 Function space projection from $\mathscr{X}_h^{n-1}$ to $\mathscr{X}_h^n$ for CUTFEMs with moving domains

1: INPUT: function spaces $\mathscr{X}_h^{n-1}$ and $\mathscr{X}_h^n$ including cut-related entities, discrete scalar field $u_h \in \mathscr{X}_h^{n-1}$ to be projected onto $\mathscr{X}_h^n$.
2: TRANSFER/COPY-PHASE (identify related node-wise DOF pairs $(\tilde{u}, u)$ associated with the function spaces $\mathscr{X}_h^n, \mathscr{X}_h^{n-1}$ which are reasonable to transcribe/copy their DOFs $u \mapsto \tilde{u}$)
3: **for** each active node $s \in \mathcal{N}$ with $\text{numdof}\,(s) \stackrel{\text{def}}{=} |\mathscr{C}_s| \geqslant 1$ at current time level t^n **do**
4: **for** each DOF $\tilde{u}_k$ $(1 \leqslant k \leqslant \text{numdof}\,(s))$ with associated volume-cell connection $C_k \in \mathscr{C}_s$ **do**
5: Identify DOF $u_i \in (u_1, ..., u_s)$ from $u_h \in \mathscr{X}_h^{n-1}$ with $s = |\mathscr{C}_s(t^{n-1})|$ the number of DOFs for node s at the previous time level t^{n-1}.
6: **if** (identification successful) **then**
7: Set DOF pair $(\tilde{u}_k, u_i)$ and copy value $u_i \mapsto \tilde{u}_k$.
8: **else if** (identification **not** successful for ghost-DOF $\tilde{u}_k$) **then**
9: Mark DOF $\tilde{u}_k$ for EXTENSION-PHASE.
10: **else**
11: Throw exception ("the CFL-like condition is not satisfied!").
12: **end if**
13: **end for**
14: **end for**
15: EXTENSION-PHASE (extend solution into the interface zone)
16: Build constraint function space $\bar{\mathscr{X}}_h^n$ with Dirichlet values for all DOFs successfully identified in the TRANSFER/COPY-PHASE.
17: Solve linear global extension system: Find $\tilde{u}_h \in \bar{\mathscr{X}}_h^n$ such that $\mathscr{E}_h^n(\tilde{u}_h, \tilde{v}_h) = 0 \,\forall\, \tilde{v}_h \in \bar{\mathscr{X}}_{h,0}^n$.
18: OUTPUT: final projection $\boldsymbol{P}^n : \mathscr{X}_h^{n-1} \to \mathscr{X}_h^n$ with solution $\tilde{u}_h^{n-1} = \boldsymbol{P}^n u_h^{n-1}$.

be set up as follows: find $\tilde{u}_h \in \bar{\mathscr{X}}_h^n$ such that

$$\mathscr{E}_h^n(\tilde{u}_h, \tilde{v}_h) = \sum_{F \in \mathscr{F}_\Gamma^n} \sum_{0 \leqslant j \leqslant k} h_F^{2j+1} \langle [\![\partial_{\boldsymbol{n}}^j \tilde{u}_h]\!], [\![\partial_{\boldsymbol{n}}^j \tilde{v}_h]\!] \rangle_F = 0 \qquad \forall\, \tilde{v}_h \in \bar{\mathscr{X}}_{h,0}^n, \tag{3.486}$$

which is a face-jump ghost-penalty operator, as defined in (3.145). Note that even though the linear system to be solved is defined globally, in average the number of non-zero entries per matrix row is much less compared to those which result from the non-linear discrete systems to be solved in each time step for the incompressible Navier-Stokes equations. This is due to the fact that for practical situations only a few ghost-DOFs have to be determined via this extension technique. At least all standard DOFs associated with nodes located in the interior of the domain Ω_h^n have been determined previously in the TRANSFER/COPY-PHASE and are treated as Dirichlet values in the extension system. These DOFs can be either completely removed from the global linear system or can be simply deactivated by setting trivial diagonal 1-entries in the corresponding matrix rows and adapting the right-hand side accordingly.

Combining the TRANSFER/COPY-PHASE with a consecutive EXTENSION-PHASE allows to define the final projection $\boldsymbol{P}^n : \mathscr{X}_h^{n-1} \to \mathscr{X}_h^n$ with $\tilde{u}_h^{n-1} = \boldsymbol{P}^n u_h^{n-1}$. Adaption to vector-valued function spaces, i.e. sets of DOFs as required for velocities and accelerations, is straightforward. Note that this extension technique retains the optimal order of the spatial approximation. Due

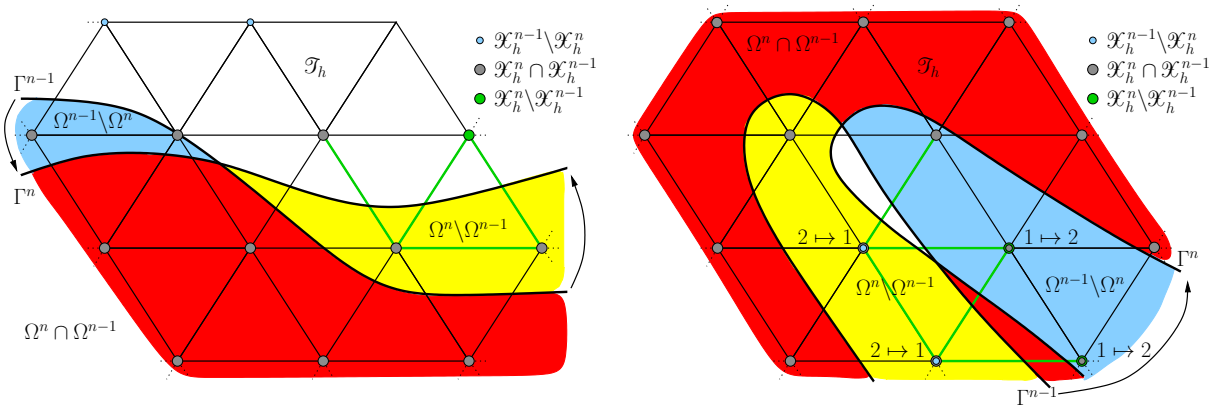

Figure 3.27: Two-dimensional scenarios for projection of functions between discrete function spaces of different time levels with interfaces moving from Γ^{n-1} to Γ^n: (Left) Maximal one DOF per node at current and previous time step contained in approximation space. For almost all DOFs in $\mathcal{X}_h^n$, pairs with DOFs of the previous time level can be identified and transcribed between $\mathcal{X}_h^{n-1}$ and $\mathcal{X}_h^n$ (gray markers), some DOFs get deactivated (blue markers) and one ghost-DOF gets newly activated whose value $\tilde{u}$ will be determined in the EXTENSION-PHASE (green marker). (Right) Moving domain example with more than one DOF per node within the ghost domain. DOFs in $\mathcal{X}_h^n$ for which physically meaningful values can be copied from $\mathcal{X}_h^{n-1}$ are marked in gray color. Note that a few nodes located in $\Omega^{n-1} \setminus \Omega^n$ carry newly activated ghost-DOFs for which no corresponding values from the previous time level are available. For these DOFs, values will be reconstructed with an extension technique (green marker). Some DOFs of double-valued nodes located in $\Omega^n \setminus \Omega^{n-1}$ become inactive at the new time level (blue marker). Faces evaluated for face-jump-penalty extension operators (3.486) are colored in green.

to the optimal convergence properties of the ghost-penalty terms, see Section 3.4.3, the order of convergence of the approximation error is not reduced. Furthermore, splitting this procedure into two phases guarantees that the change of the solution in the interior of the domain is kept at a minimum. Note that if the interface does not move, i.e. $u_\Gamma = 0$, the spaces $\mathcal{X}_h^{n-1}$ and $\mathcal{X}_h^n$ are identical and the proposed projection operator simplifies to an identity mapping $\boldsymbol{P}^n = \boldsymbol{I}$.

For the sake of completeness, it has to be mentioned that a technique related to the EXTENSION-PHASE as introduced above has been applied by Burman and Fernández [58] for an overlapping mesh technique for fluid-structure interaction. In their work, however, the function spaces for velocity and pressure are not adapted individually for each time step, but the solution is computed on a discrete space according to the entire mesh $\widehat{\mathcal{T}}_h$. All DOFs which are associated with nodes outside the physcial domain are controlled by ghost-penalty stabilizations that are evaluated along all interior faces $F \in \mathcal{F}_i$ of the mesh, even when large regions of the mesh are not covered by the physical domain. This avoids the necessity for projection steps as introduced in this thesis, however, may also drastically reduce the accuracy of solutions within the fluid domains. Already for non-moving interfaces, different regions of the physical domain are artificially coupled via ghost-penalty terms when evaluating them within the entire ghost domain. Moreover, handling of multiple DOFs per node as required for complex topologies, see discussion in Section 2.2.4, is not supported there. From the perspective of accuracy, the projection procedure established in this thesis exhibits fundamental advantages. Furthermore, the proposed technique is not restricted to single-phase flow problems. Extensions to coupled multiphysics or multiphase-flow problems is straightforward, since the technique can be applied to each fluid phase individually. Applications will be proposed later in Chapters 4 and 5.

3.6.3.3 Solution Algorithm for Flow in Time-Dependent Moving Domains

Combining the fully discrete CutFEM formulations, as proposed for the CIP/GP stabilization technique with a one-step-θ scheme in Section 3.6.3.1, with the projection procedures between non-matching function spaces from Section 3.6.3.2, a non-linear solution algorithm for approximating flows in time-dependent moving domains can be formulated. The algorithm is summarized in Algorithm 3.2 and consists of the following solution steps:

Algorithm 3.2 Non-linear solution algorithm for flows in time-dependent moving domains

1: INPUT: initial condition $\boldsymbol{u}_0$ in domain $\Omega_h(T_0)$, set $\boldsymbol{a}_0 = \boldsymbol{0}$ or choose $\theta = 1.0$ for $n = 1$.
2: **for** time steps $1 \leqslant n \leqslant N$ **do**
3: Update time level $t^n = T_0 + n\Delta t$.
4: Update interface position to Γ_h^n according to current time level t^n.
5: Intersect the mesh $\widehat{\mathcal{T}}_h$ and update the active computational mesh $\mathcal{T}_h^n$ as well as face and element sets $\mathcal{F}_\Gamma^n, \mathcal{T}_\Gamma^n$.
6: Perform Algorithm 2.1, allocate DOFs and define continuous function space $\mathcal{V}_h^n \times \mathcal{Q}_h^n$.
7: Perform Algorithm 3.1 to project solution vectors $\boldsymbol{u}_h^{n-1}, \boldsymbol{a}_h^{n-1} \in \mathcal{V}_h^{n-1}$ of previous time level t^{n-1} to current function space: $\tilde{\boldsymbol{u}}_h^{n-1} = \boldsymbol{P}^n \boldsymbol{u}_h^{n-1} \in \mathcal{V}_h^n$, $\tilde{\boldsymbol{a}}_h^{n-1} = \boldsymbol{P}^n \boldsymbol{a}_h^{n-1} \in \mathcal{V}_h^n$.
8: Evaluate boundary conditions $\boldsymbol{g}_\mathrm{D}(t^n)$, $\boldsymbol{h}_\mathrm{N}(t^n)$.
9: Solve non-linear discrete system (3.484) iteratively until convergence of iterations $\{(\boldsymbol{u}_h^n, p_h^n)_i\}_{i \geqslant 1}$ is reached. As an initial guess, $(\boldsymbol{u}_h^n, p_h^n)_0 = (\tilde{\boldsymbol{u}}_h^{n-1}, \tilde{p}_h^{n-1})$ is used.
10: Update the acceleration approximation $\boldsymbol{a}_h^n(\boldsymbol{u}_h^n, \tilde{\boldsymbol{u}}_h^{n-1}, \tilde{\boldsymbol{a}}_h^{n-1})$ related to the one-step-θ scheme via (3.485).
11: **end for**
12: OUTPUT: velocity and pressure solution approximations $\{(\boldsymbol{u}_h^n, p_h^n)\}_{1 \leqslant n \leqslant N}$ for discrete time levels $\{t^n\}_{1 \leqslant n \leqslant N}$ belonging to time-varying physical and fictitious domains $\Omega_h^n, \Omega_h^{n,*}$.

Within the overall cycle over time steps, first, the interface position is adapted to the current time level t^n and the underlying mesh gets intersected which defines the current computational mesh $\mathcal{T}_h$, i.e. the active part of the underlying grid $\widehat{\mathcal{T}}_h$. The new intersection configuration further defines all cut-related entities required for evaluating the stabilized formulation, like $\mathcal{F}_\Gamma^n, \mathcal{T}_\Gamma^n$, volume-cells and interface-segments. After defining function spaces $\mathcal{V}_h \times \mathcal{Q}_h$ for velocity and pressure belonging to the intersection at time level t^n via utilizing Algorithm 2.1, solutions of the previous time level have to be projected onto $\mathcal{V}_h^n$ via the TRANSFER/COPY-PHASE and the EXTENSION-PHASE as described in Algorithm 3.1. For the one-step-θ scheme, this is the velocity field $\tilde{\boldsymbol{u}}_h^{n-1}$ and $\tilde{\boldsymbol{a}}_h^{n-1}$, if $\theta \neq 1$. Afterwards, the actual non-linear fluid system (3.484) needs to be iteratively solved utilizing a Newton-like or a Picard-iteration scheme until convergence for iterations $(\boldsymbol{u}_h, p_h)_i$ is reached. For the one-step-θ scheme, this solution step is followed by an update of the acceleration approximation $\boldsymbol{a}_h^n$ via (3.485). The computed approximation $(\boldsymbol{u}_h^n, p_h^n, \boldsymbol{a}_h^n)$ then serves as history for the next time step.

Note that the procedure described in Algorithm 3.2 can be easily adapted to other temporal discretization schemes as well as the Nitsche-type RBVM/GP-CutFEM. The BDF2 scheme, for instance, additionally requires the solution $\boldsymbol{u}_h^{n-2} \in \mathcal{V}_h^{n-2}$ being projected onto the current function space $\mathcal{V}_h^n$. To avoid the need for identifying volume-cell connections between $\mathcal{V}_h^{n-2}$ and

$\mathcal{V}_h^n$, one can simply project the solution $\boldsymbol{u}_h^{n-2} \in \mathcal{V}_h^{n-2}$ twice. In a first step it is transcribed from $\mathcal{V}_h^{n-2}$ to $\mathcal{V}_h^{n-1}$ and in a second step from $\mathcal{V}_h^{n-1}$ to $\mathcal{V}_h^n$, i.e. $\tilde{\tilde{\boldsymbol{u}}}_h^{n-2} \overset{\text{def}}{=} \boldsymbol{P}^n(\boldsymbol{P}^{n-1}\boldsymbol{u}_h^{n-2})$. Compared to the one-step-θ scheme, which requires to project $\boldsymbol{u}_h^{n-1}, \boldsymbol{a}_h^{n-1} \in \mathcal{V}_h^{n-1}$ onto $\mathcal{V}_h^n$ in each time step, for the BDF2 time stepping scheme $\boldsymbol{u}_h^{n-1}, \tilde{\boldsymbol{u}}_h^{n-2} \in \mathcal{V}_h^{n-1}$ have to be adapted to $\mathcal{V}_h^n$. The computational costs for projecting vectors remain the same for both schemes.

3.6.4 Numerical Tests for Incompressible Flow in Moving Domains

Different temporal discretization schemes in combination with the solution technique for flows in time-dependent moving domains, as summarized in Algorithms 3.1 and 3.2, are validated for the different Nitsche-type CUTFEM formulations proposed in Sections 3.6.1.1 and 3.6.1.2. To demonstrate the accuracy and the robustness of the proposed function space projection technique introduced in Section 3.6.3.2, a test example with analytical solution is considered. For this purpose, the already well-studied Taylor problem is solved on a time-dependent domain which undergoes large variations. In order to illustrate the performance and the capabilities of the stabilized discrete fluid formulations in largely changing fluid domains for viscous- as well as convective-dominated flows, two simulations inspired by fluid-structure interactions are investigated: A beam-like structure is embedded into a viscous surrounding incompressible flow and subjected to a time-dependent rigid body rotation. To investigate the quality of the fluid solution near the boundary zone, a higher-Reynolds-number flow around a translationally moved rigid cylinder serves as test example.

3.6.4.1 Taylor Problem in a Moving Domain

As a first test case, the two-dimensional Taylor problem (3.164)–(3.166) with $g_u(t) = g_p(t) = 1.0$ and $\nu = 0.0001$, introduced in Section 3.4.4.2, is considered. While the solution is steady, the fluid domain is temporally moving and boundary conditions are imposed at the fluid boundary using the proposed Nitsche technique. The time-dependent fluid domain is of ellipsoidal shape for all times $t \in (0, 1]$ with time-varying main axes $a_1(t), a_2(t)$ which are pre-defined as

$$a_1(t) = r(0.75 + 0.25\cos(4\pi t)) \quad \text{and} \quad a_2(t) = r(0.75 + 0.25\cos(2\pi t)) \tag{3.487}$$

such that initial and final configuration coincide and are of circular shape with radius $r = 0.45$. For the domain approximation an implicit level-set representation $\phi(\boldsymbol{x} - \boldsymbol{c}; a_1(t), a_2(t))$ is utilized as stated in (A.6) with center point $\boldsymbol{c} = (0.5, 0.5)$. The level-set field and the solution fields are approximated with a coarse unfitted background mesh $\widehat{\mathcal{T}}_h$ which covers the square domain $[0, 1]^2$ and consists of linear right-angled triangular elements $\mathbb{P}^1$ with $h = 1/56$ denoting their short lengths. The spatial discretization is based on the Nitsche-type CIP/GP-CUTFEM as formulated in Section 3.6.1.1. For the temporal discretization, the time-step length is chosen as $\Delta t = 0.005$. This test case is performed for three different time-stepping schemes: the OST-scheme with $\theta = 1.0$ and $\theta = 0.5$ as well as the BDF2 scheme. The computed solutions are almost indistinguishable and the results for the OST variant with $\theta = 0.5$ are visualized at different intermediate time levels in Figure 3.28. It is obvious that the large variations in the computational domain and the projections of discrete solutions between function spaces do not deteriorate accuracy and robustness. Initial and final solution are almost identical. For the sake of completeness, the L^2-velocity error for the visualized solution at the final time $T = 1$ is $\|\boldsymbol{u} - \boldsymbol{u}_h\|_\Omega = 8.611 \cdot 10^{-4}$ and comparable to a setting with a non-moving domain.

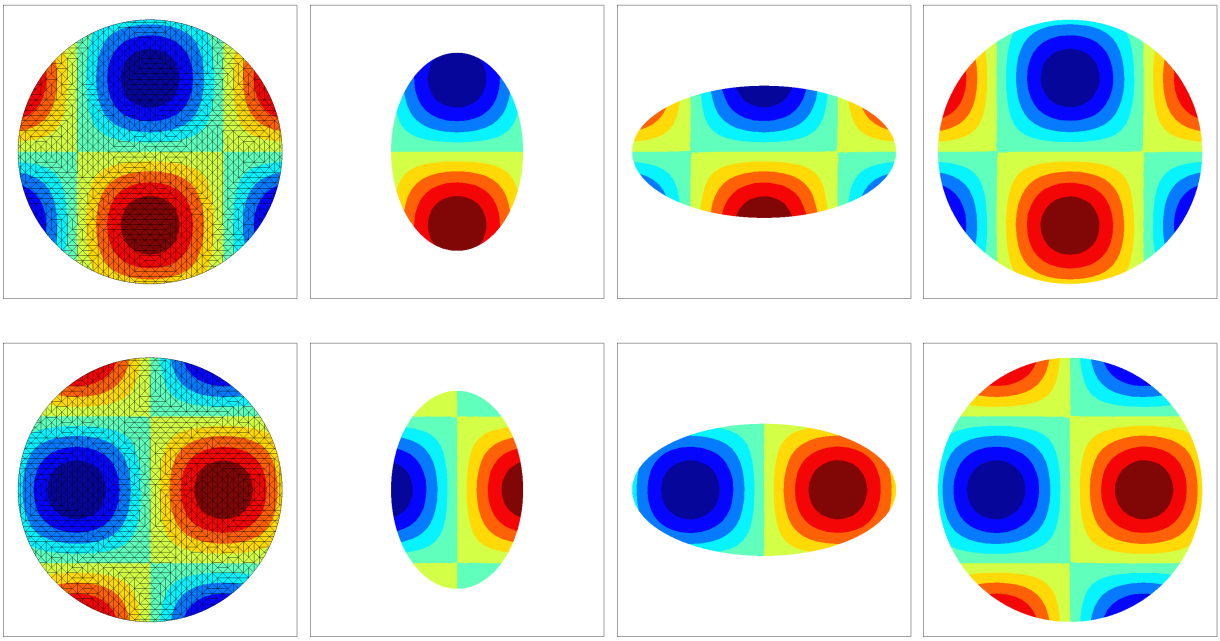

Figure 3.28: Taylor problem in a time-dependent moving domain: computed velocity components u_1 (top row) and u_2 (bottom row) at different intermediate time levels $T_0 = 0, T_1 = 0.25, T_2 = 0.5$ and $T = 1.0$ (from left to right) based on the CIP/GP-CUTFEM, an OST scheme with $\theta = 0.5$ and an unfitted background mesh with $h = 1/56$.

3.6.4.2 Flow over a Rotating Beam

In order to illustrate the performance of the stabilized discrete formulation with largely changing fluid domains, the viscous flow over a rotating rigid beam-like structure is shown. The overall mesh $\widehat{\mathcal{T}}_h$ consists of 200×200 bi-linearly-interpolated quadrilateral $\mathbb{Q}^1$-elements and covers a domain $(-0.5, 0.5)^2$ into which a beam $\Omega^{\mathrm{s}}(t)$ of height $H = 0.475$ and thickness $B = 0.075$ is embedded. Its tips are rounded in a semicircle of radius $B/2$ and it is vertically oriented at $T_0 = 0$. Its center point is located at $\boldsymbol{x}_{\mathrm{c}} = (0, 0)$. The body is subjected to a prescribed rotational motion around $\boldsymbol{x}_{\mathrm{c}}$ given by a rotation matrix

$$\boldsymbol{R}(t) = \begin{pmatrix} \cos(\vartheta(t)) & -\sin(\vartheta(t)) \\ \sin(\vartheta(t)) & \cos(\vartheta(t)) \end{pmatrix}, \tag{3.488}$$

where the rotation angle $\vartheta(t)$ is defined time-dependent based on a maximum angular velocity of $\omega = 2\pi/T$ and $T = 16.0$ as

$$\vartheta(t) = \begin{cases} 0 & \forall\, t \in (0, T_1] \quad \text{(no rotation)}, \\ \omega\left[\dfrac{1}{2}(t - T_1) - \dfrac{1}{2}\sin\left(\pi\dfrac{t - T_1}{T_2 - T_1}\right)\dfrac{T_2 - T_1}{\pi}\right] & \forall\, t \in (T_1, T_2] \quad \text{(acceleration phase)}, \\ \vartheta(T_2) + \omega(t - T_2) & \forall\, t \in (T_2, T_3] \quad \text{(anti clockwise rotation)}, \\ \vartheta(T_3) + \omega\sin\left(\pi\dfrac{t - T_3}{T_4 - T_3}\right)\dfrac{T_4 - T_3}{\pi} & \forall\, t \in (T_3, T_4] \quad \text{(reverse phase)}, \\ \vartheta(T_4) - \omega(t - T_4) & \forall\, t \in (T_4, T_5] \quad \text{(clockwise rotation)}. \end{cases} \tag{3.489}$$

The first interval $(0, T_1]$ with $T_1 = 1.0$ is a ramp phase to let the flow develop around the fixed obstacle. During $(T_1, T_2]$ with $T_2 = T_1 + 1.0$, the beam starts increasing its velocity until a maximum angular velocity ω is reached at T_2. Afterwards, the beam rotates counter clockwise with constant ω in $(T_2, T_3]$ with $T_3 = T_2 + 12.0$. Next, the rotation turns its direction. Within $(T_3, T_4]$ the rotation decreases and the angular velocity turns its sign until a negative angular velocity of $-\omega$ is reached at $T_4 = T_3 + 2.0$. Finally, the beam rotates clockwise one full cycle of 2π until $T_5 = 32.0$. Note that $\vartheta(t)$ is defined such that $\dot{\vartheta}(t), \ddot{\vartheta}(t)$ are continuous within $[0, T_5]$.

The time-dependent fluid domain is then defined as $\Omega^{\mathrm{f}}(t) \overset{\text{def}}{=} (\cup_{T \in \widehat{\mathcal{T}}_h} T) \backslash \Omega^{\mathrm{s}}(t)$. At the moving boundary $\Gamma(t)$, the structural velocity is imposed as Dirichlet boundary condition for the fluid utilizing the Nitsche-type technique. The boundary condition is given as $\boldsymbol{g}_{\mathrm{D}} = \boldsymbol{u}_h(t) = \dot{\boldsymbol{x}}_h^{\mathrm{s}}(t)$. This setup can be seen as a one-sided fluid-structure interaction with prescribed rigid body rotational motion. Similar to fluid-structure interaction algorithms, as will be considered later in Chapter 5, the structural velocity $\boldsymbol{u}_h^{\mathrm{s}}(t)$ is approximated based on the current structural coordinates $\boldsymbol{x}_h^{\mathrm{s}}(t)$ utilizing a one-step-θ scheme for the ODE $\dot{\boldsymbol{x}}_h^{\mathrm{s}}(t) = \boldsymbol{u}_h^{\mathrm{s}}(t)$ resulting in

$$\boldsymbol{u}_h^{\mathrm{s},n} = \frac{\boldsymbol{x}_h^{\mathrm{s}}(t^n) - \boldsymbol{x}_h^{\mathrm{s}}(t^{n-1})}{\theta \Delta t} - \frac{1-\theta}{\theta} \boldsymbol{u}_h^{\mathrm{s},n-1}. \tag{3.490}$$

For the rotational motion, the coordinates of the structural body are defined as

$$\boldsymbol{x}_h^{\mathrm{s}}(t) = \boldsymbol{R}(t)(\boldsymbol{x}_h^{\mathrm{s}}(T_0) - \boldsymbol{x}_{\mathrm{c}}) + \boldsymbol{x}_{\mathrm{c}}. \tag{3.491}$$

Further boundary conditions at the outer fluid boundary need to be imposed: a Dirichlet inflow boundary condition is strongly set at $x_1 = -0.5$ defined by a parabolic profile for the u_1-component as $u_1 = 4(0.5 + x_2)(0.5 - x_2)$ and by $u_2 = 0$. The velocity is increased during the initial ramp phase $(0, T_1]$ utilizing the function $1/2(1 - cos(\pi t / T_1))$. At the top and bottom walls $(x_2 = \pm 0.5)$ no-slip is enforced, i.e. $\boldsymbol{u} = \boldsymbol{0}$, and a zero-traction Neumann outflow condition is imposed at $x_1 = 0.5$. For temporal discretization a one-step-θ scheme is applied with $\theta = 1.0$ and a time-step length of $\Delta t = 0.03$. The kinematic viscosity is set to $\nu = 0.1$. The resulting viscous flow around the rotating beam-like structure computed with the Nitsche-type RBVM/GP-CutFEM introduced in Section 3.6.1.2 and approximated by the solution procedure proposed in Algorithms 3.1 and 3.2 is shown in Figure 3.29. This example clearly demonstrates the general applicability of this established CutFEM to industrially relevant problem settings where, for instance, structural components are subjected to large rotations in surrounding fluids and underlines the obvious superiority over classical ALE-based moving fitted-mesh FEM approaches.

3.6.4.3 Flow over a Moving Cylinder

A translationally moved rigid cylinder in a rectangular fluid domain serves as test case to demonstrate the robustness of the proposed cut finite element method for highly dynamic higher-Reynolds-number flows. The setup of this example is inspired by a setting proposed by Codina *et al.* [76]. A cylindrical rigid body Ω^{s} with diameter $d = 0.2$ and initial center position $(0.3, 0.23)$ at $t = T_0$ is embedded into an unfitted regular mesh $\widehat{\mathcal{T}}_h$ consisting of 450×90 linearly-interpolated quadrilateral $\mathbb{Q}^1$ finite elements which defines a domain $(0, 2.2) \times (0, 0.44)$. Note that compared to the setup considered in [76], the initial location of the cylinder is chosen slightly more non-symmetric with respect to the background domain. This makes the test

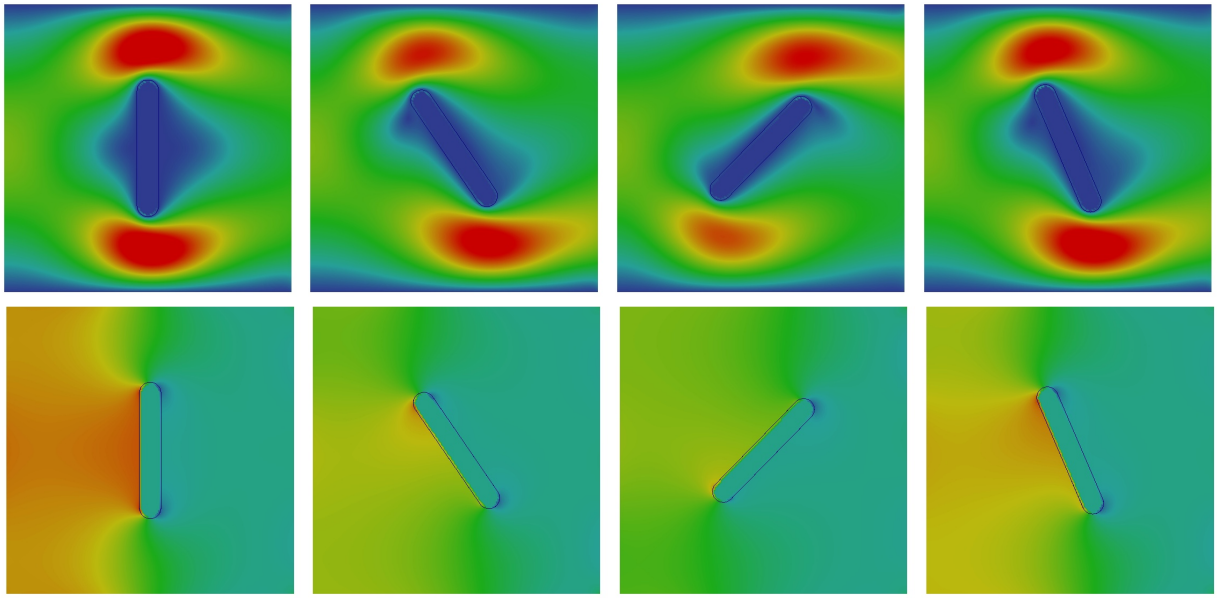

Figure 3.29: Flow over a rotating two-dimensional rigid beam-like structure: velocity norm $\|\boldsymbol{u}_h\|$ (top) and pressure p_h (bottom) at different time levels $t = 0.9$, $t = 3.0$, $t = 7.5$ and $t = 10.5$ (from left to right) (velocity color scale $[0, 1.56]$, pressure color scale $[-3.9, 10.7]$).

case much more demanding due to stronger vortex shedding which arises when starting to move the body. The structure is pulled in x_1-direction with a prescribed displacement field $d_1(t) = 1.1 + 0.8 \sin\left(\frac{2}{3}\pi(t - 0.75)\right)$ such that it will be returned to its starting position after a simulation time of $T = 3$. The flow is initially at rest and no-slip wall boundary conditions $\boldsymbol{u} = \boldsymbol{0}$ are set strongly at top, bottom and left side of the fluid domain. At $x_1 = 2.2$ the square fluid domain is opened and a zero-traction boundary condition is imposed, i.e. $\boldsymbol{h}_{\mathrm{N}} = \boldsymbol{0}$. At the circular interface $\Gamma(t)$, the structural velocity is computed utilizing the same approximation technique as proposed for the previous example in (3.490). For the spatial and temporal discretization, the Nitsche-type RBVM/GP-CutFEM introduced in Section 3.6.1.2 has been applied in combination with the moving domain Algorithms 3.1 and 3.2. The temporal discretization is based on a one-step-θ scheme with $\theta = 1.0$ and $\Delta t = 0.001$.

Compared to the previous rotating beam example, due to a lower viscosity of $\nu = 0.001$, a strongly non-symmetric flow pattern develops in the backflow of the cylinder when moving it in positive x_1-direction. The Reynolds number emerges to a maximum of approximately $\mathrm{Re} \approx 300$ where its definition is based on the diameter d and the maximum cylinder velocity. The resulting highly dynamic velocity and pressure solutions are visualized in Figure 3.30. While moving the structure in opposite direction during $t \in (1.5, 3)$, highly dynamic time-dependent forces act on the structural surface. Visualizations of interfacial forces $\boldsymbol{f}_l^{\mathrm{s}}$ computed at nodes l of the structural trace mesh utilizing formula (3.482) underline the complexity of the flow and the robustness of the stabilized CutFEM in the vicinity of the moving interface zone. Additionally, in Figure 3.31, forces $\boldsymbol{f} = (f_1, f_2)$ acting at the left-most and top-most points of the circular interface are plotted over time for two different time-step sizes $\Delta t = 0.001$ and $\Delta t = 0.002$. Particularly in view of fluid-structure-interaction problem settings, the quality of this interfacial measure is an important indicator for the robustness and the high capability of the proposed fluid solver as well as of the algorithmic procedure for convective-dominated flow in time-dependent moving domains. Such problem configurations will be considered further in Chapter 5.

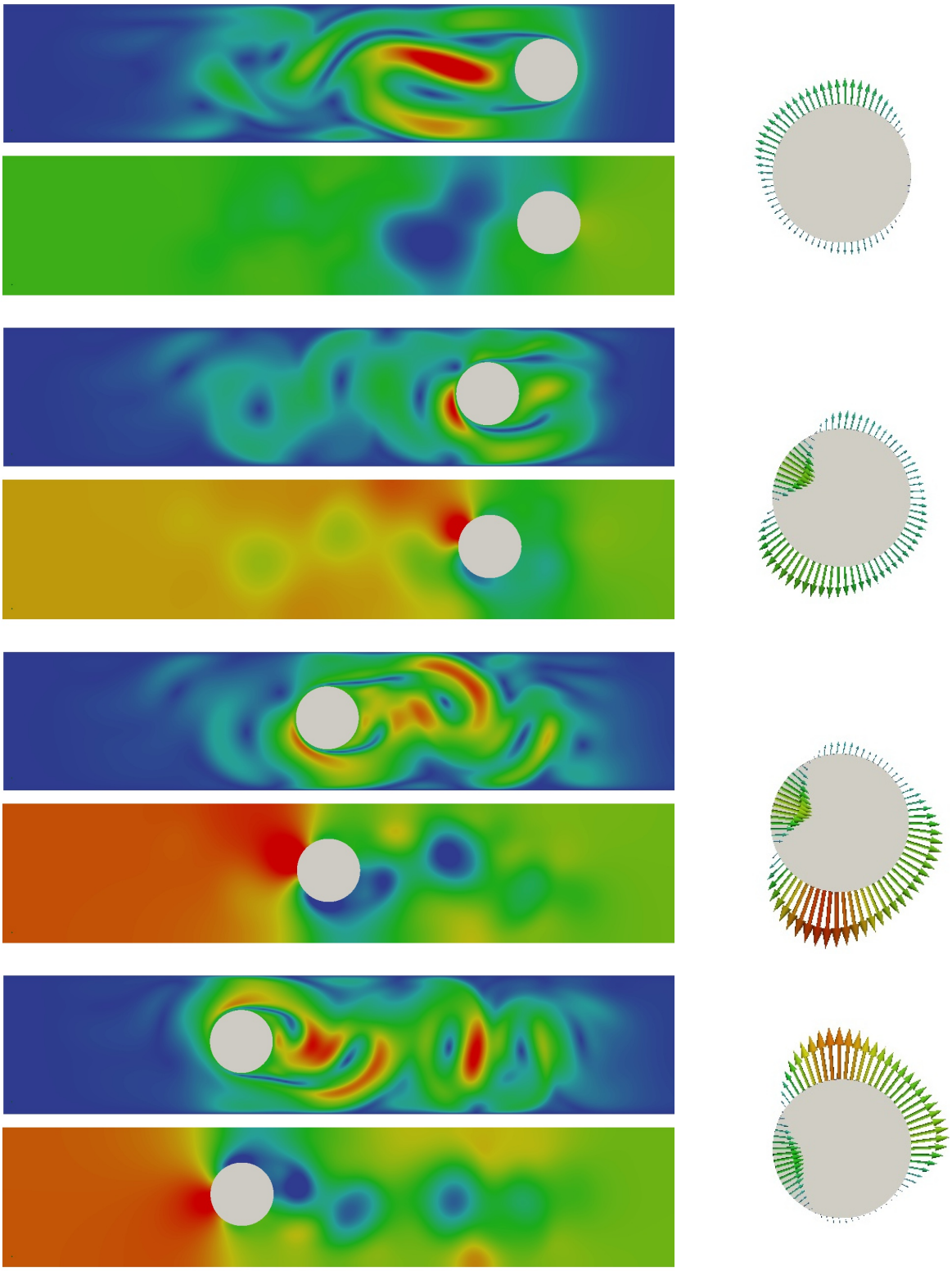

Figure 3.30: Flow over a two-dimensional moving cylinder with a maximum $RE \approx 300$: (Left) velocity norm $\|\boldsymbol{u}_h\|$ and pressure p_h at times $t = 1.18$, $t = 1.97$, $t = 2.29$ and $t = 2.46$ (from top to bottom) (velocity color scale $[0, 3]$, pressure color scale $[-5.6, 3.5]$). (Right) forces acting on moving interface Γ (color scale $[0, 0.000443]$) at aforementioned times t (from top to bottom).

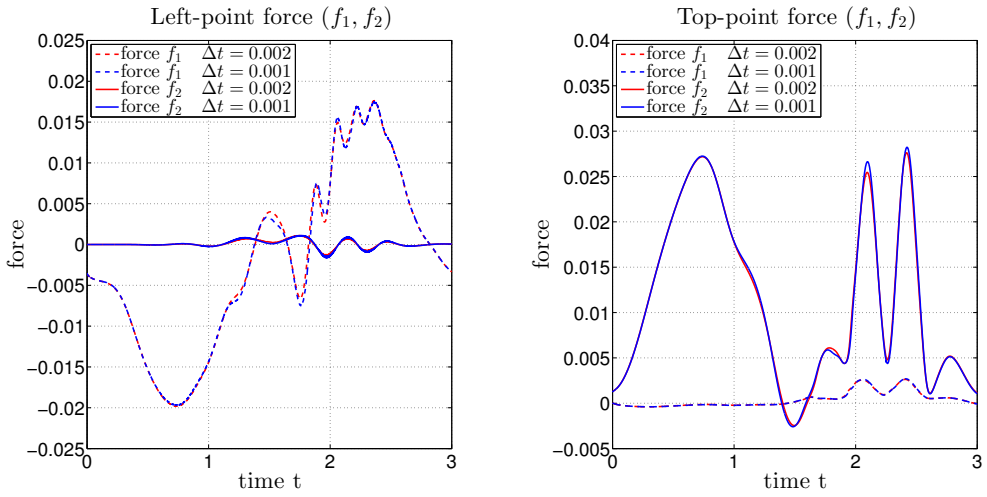

Figure 3.31: Flow over a two-dimensional moving cylinder with a maximum $RE \approx 300$: nodal forces $\boldsymbol{f}_l = (f_1, f_2)_l$ acting at selected points of the cylindrical surface $\Gamma(t)$ over time $t \in (0, 3)$ computed with two different time-step sizes $\Delta t = 0.001$ and $\Delta t = 0.002$. (Left) force for the most-left structural point. (Right) force for the most-top structural point.

Chapter 4

Unfitted Domain Decomposition Methods for Incompressible Single- and Two-Phase Flows

This chapter aims at developing numerical cut finite element approaches for incompressible flow problems in which fluid phases interact. The key idea is to combine the generalized framework of domain decomposition based on non-interface-fitted computational meshes, as introduced in Section 2.1.4, with stabilized cut finite element methods for the respective subregions, as developed throughout Chapter 3.

Allowing for different unfitted approximation spaces in distinct regions of the entire computational domain, together with sharp approximations of the subdomains and their discrete solutions with cut finite element techniques, makes such approaches attractive for a wide range of coupled flow problems. Their applicability ranges from mesh-tying techniques for single-phase flows to the interaction of several fluid phases with different material properties. For single-phase flows, the domain can be split into separate subregions such that unfitted techniques play to their strengths in utilizing appropriate approximation spaces in particular regions of interest. As an example, boundary layers around structural bodies can be efficiently captured with this approach. Since mass transport across the interfaces is supported due to the same material properties in the subdomains, interfaces can then be considered either stationary or arbitrarily moving. Immiscible two-phase flows, in contrast, are usually subjected to large interfacial motions and the interface remains the separating manifold between the two different physical fluid phases. The use of unfitted techniques allows for largely changing topologies and their stability and optimality properties are guaranteed independent of the interface locations for low- and high-Reynolds-number flows. These aspects render such approaches highly promising.

In this chapter, the focus is turned to physics at separating phase boundaries in Section 4.1 and the numerical treatment of modeled coupling constraints within the framework of Nitsche-type methods utilized for their weak constraint enforcement in Section 4.2. A stabilized formulation for coupling solution fields which belong to different subdomains and discrete approximation spaces will be proposed. Moreover, numerical issues concerning interface stability are examined from a mathematical point of view and possible solution techniques are developed and discussed. Later on, the performance of the computational approach will be demonstrated for an overlapping mesh domain decomposition method applied to fluid mesh-tying problem settings in Section 4.3. The high capabilities of unfitted mesh methods for incompressible two-phase

flows will finally be shown as an outlook in Section 4.4. The subsequent elaborations are mainly based on work available in Schott and Wall [230], Massing *et al.* [183], Schott and Rasthofer *et al.* [231] and Schott and Shahmiri *et al.* [232].

4.1 Domain Decomposition Problem Setup for Coupled Flows

This section provides fundamentals on physical models applicable to mesh-tying approaches for single-phase flows as well as immiscible multiphase flows. Such problem settings are formulated in terms of an abstract coupled interface initial boundary value problem. A presentation of such flow setups based on decomposing domains will be given in strong and variational forms.

4.1.1 Multiple Fluid Phases - Domains and Interfaces

Computational Domains. The notation and terminology on single fluid phases, associated subdomains and interfaces for coupled flows used throughout the subsequent sections are based on the abstract multidomain problem setting introduced in Section 2.1.1. The overall computational domain is given by $\Omega \overset{\text{def}}{=} \cup_{1 \leqslant i \leqslant N_{\text{dom}}} \Omega^i$ with possibly moving interfaces $\Gamma^{ij} \overset{\text{def}}{=} \overline{\Omega^i} \cap \overline{\Omega^j}$ $(i < j)$ which separate fluid phases with possibly different material parameters μ^i, ρ^i or split single phases into artificial partitions for mesh-tying purposes; an overview about possible strategies was given in Section 2.1.4.3. Respective Dirichlet and Neumann boundary parts of the fluid subdomains are denoted with $\Gamma^i_{\text{D}}, \Gamma^i_{\text{N}}$ and satisfy $\partial\Omega^i = (\Gamma^i_{\text{D}} \cup \Gamma^i_{\text{N}}) \bigcup_{j \neq i} \Gamma^{ij}$. Note that all geometric entities are possibly time-dependent. For sake of clarity, if unmistakable, occasionally the temporal index t as well as the superscript $(\cdot)^{\text{f}}$ denoting fluid quantities are omitted. Weighted average and jump operators $\{\cdot\}, \langle\cdot\rangle$ and $[\![\cdot]\!]$ are as defined in (2.1)–(2.3). The normal vector at Γ^{ij} follows the convention from Section 2.1.1 being outward pointing from Ω^i to Ω^j, where $i < j$.

Interfacial Constraints between Fluid Phases. At fluid-fluid interfaces, which is an umbrella term for interfaces between two fluid phases, i.e. liquids or gases, different physical models can be deduced to account for different physical phenomena which may emanate from highly varying length scales. Hereby, modeling approaches range from molecular to microscopic up to macroscopic view points. Commonly used modeling approaches deduce kinematic and dynamic relations from basic conservation principles for mass, linear and angular momentum on a macroscopic level as shown below.

Observing conservation of mass and momentum on a time-dependent control volume including a part of the interface Γ^{ij}, which moves in its own normal direction $\boldsymbol{n}^{ij}$ with an interfacial speed u^{ij}_Γ, allows to state conservation laws for those $\forall\, \boldsymbol{x} \in \Gamma^{ij}(t)$ as

$$\rho^i(\boldsymbol{u}^i \cdot \boldsymbol{n}^{ij} - u^{ij}_\Gamma) = -M = \rho^j(\boldsymbol{u}^j \cdot \boldsymbol{n}^{ij} - u^{ij}_\Gamma), \tag{4.1}$$

$$\rho^i \boldsymbol{u}^i(\boldsymbol{u}^i \cdot \boldsymbol{n}^{ij} - u^{ij}_\Gamma) - \boldsymbol{\sigma}(\boldsymbol{u}^i, p^i) \cdot \boldsymbol{n}^{ij} = \rho^j \boldsymbol{u}^j(\boldsymbol{u}^j \cdot \boldsymbol{n}^{ij} - u^{ij}_\Gamma) - \boldsymbol{\sigma}(\boldsymbol{u}^j, p^j) \cdot \boldsymbol{n}^{ij} \tag{4.2}$$

with the mass flow rate M for Ω^i across the interface Γ^{ij}. Mass conservation (4.1) can be reformulated by means of a jump condition for fluid velocities in interface normal direction to

$$[\![\boldsymbol{u}]\!] \cdot \boldsymbol{n}^{ij} = (\boldsymbol{u}^i - \boldsymbol{u}^j) \cdot \boldsymbol{n}^{ij} = u^{ij}_\Gamma - M/\rho^i - (u^{ij}_\Gamma - M/\rho^j) = -M[\![\rho^{-1}]\!] \quad \forall\, \boldsymbol{x} \in \Gamma^{ij}(t). \tag{4.3}$$

Furthermore, for viscous fluids, i.e. $\mu^i, \mu^j > 0$, interface tangential velocities are modeled being continuous

$$[\![\boldsymbol{u}]\!] \cdot \boldsymbol{t}_r^{ij} = 0 \qquad \forall\, \boldsymbol{x} \in \Gamma^{ij}(t) \tag{4.4}$$

in all interface-tangential directions $(r = 1, ..., (d-1))$. Combining momentum balance (4.2) with mass conservation (4.3) and (4.4) results in jump conditions for normal and tangential parts of interface tractions

$$\boldsymbol{n}^{ij} \cdot [\![\boldsymbol{\sigma}(\boldsymbol{u}, p)]\!] \cdot \boldsymbol{n}^{ij} = -M[\![\boldsymbol{u}]\!] \cdot \boldsymbol{n}^{ij} = M^2[\![\rho^{-1}]\!] \qquad \forall\, \boldsymbol{x} \in \Gamma^{ij}(t), \tag{4.5}$$

$$\boldsymbol{t}_r^{ij} \cdot [\![\boldsymbol{\sigma}(\boldsymbol{u}, p)]\!] \cdot \boldsymbol{n}^{ij} = -M[\![\boldsymbol{u}]\!] \cdot \boldsymbol{t}_r^{ij} = 0 \qquad \forall\, \boldsymbol{x} \in \Gamma^{ij}(t). \tag{4.6}$$

Combining the resulting interfacial constraints, from a macroscopic point of view, kinematic and dynamical constraints between fluid phase i and fluid phase j can then be modeled as

$$[\![\boldsymbol{u}]\!] = -M[\![\rho^{-1}]\!]\boldsymbol{n}^{ij} \qquad \forall\, \boldsymbol{x} \in \Gamma^{ij}(t), \tag{4.7}$$

$$[\![\boldsymbol{\sigma}(\boldsymbol{u}, p)]\!] \cdot \boldsymbol{n}^{ij} = M^2[\![\rho^{-1}]\!]\boldsymbol{n}^{ij} \qquad \forall\, \boldsymbol{x} \in \Gamma^{ij}(t). \tag{4.8}$$

Depending on the material combination at the common fluid-fluid interface and on the mass flow rate M across the interface, for different problem settings like fluid mesh-tying or incompressible two-phase flow, commonly used interfacial constraints are reviewed subsequently.

Fluid mesh tying: Considering same fluid properties on both sides of the interface, i.e. $\rho^i = \rho^j$ and $\mu^i = \mu^j > 0$, which holds when one single fluid phase is artificially split for discrete approximation purposes, the interfacial constraints previously deduced from conservation of mass and linear momentum simplify due to $[\![\rho^{-1}]\!] = 0$ to

$$[\![\boldsymbol{u}]\!] = \boldsymbol{0} \qquad \forall\, \boldsymbol{x} \in \Gamma^{ij}(t), \tag{4.9}$$

$$[\![\boldsymbol{\sigma}(\boldsymbol{u}, p)]\!] \cdot \boldsymbol{n}^{ij} = \boldsymbol{0} \qquad \forall\, \boldsymbol{x} \in \Gamma^{ij}(t). \tag{4.10}$$

These conditions keep valid independent of the motion of the interface. If the interface follows the fluid particles in their motion, no mass flow across the interface is present, i.e. $M = 0$. If $M \neq 0$, fluid particles are convected across the interface which is allowed due to the same physical fluid properties in both subdomains.

Two-phase flow including surface tension: Different immiscible fluid or gas phases are characterized by discontinuous material properties $\mu^i \neq \mu^j$ and $\rho^i \neq \rho^j$ such that $[\![\rho^{-1}]\!] \neq 0$. For incompressible two-phase flow the phase boundaries $\Gamma^{ij}(t)$ are advected with the fluid particles such that no mass flow across the interface occurs, i.e. $M = 0$ and $[\![\boldsymbol{u}]\!] = \boldsymbol{0}$. Additionally, due to the fact that fluid properties change discontinuously, molecular forces of attraction between molecules of the same type, so-called *cohesion forces*, are stronger than attraction between molecules of different type, so-called *adhesion forces*. From a microscopic point of view these forces imply surface tension; more detailed elaborations can be found, e.g., in the work by Brackbill *et al.* [32]. Surface-tension effects depend on the curvature $\kappa = -\nabla \cdot \boldsymbol{n}^{ij}$ of the phase surface and the combination of material properties expressed in terms of a surface-tension coefficient ι_{st}, which is assumed to be constant along the manifold throughout this thesis. The

interfacial constraints for incompressible two-phase flows including surface tension are then modeled as

$$[\![\boldsymbol{u}]\!] = \boldsymbol{0} \qquad \forall\, \boldsymbol{x} \in \Gamma^{ij}(t), \tag{4.11}$$

$$[\![\boldsymbol{\sigma}(\boldsymbol{u}, p)]\!] \cdot \boldsymbol{n}^{ij} = \iota_{\mathrm{st}} \kappa \boldsymbol{n}^{ij} \qquad \forall\, \boldsymbol{x} \in \Gamma^{ij}(t). \tag{4.12}$$

Modeling of premixed combustion: One example for two-phase flow including mass flow in interface normal direction across the interface, i.e. $M \neq 0$, can be found in the modeling of premixed combustion. For such applications, the mass change from the unburned (i) to the burned (j) fluid phase emanates from the chemical combustion processes in the vicinity of the interface. The combustion zone can be thereby assumed infinitesimal thin. The mass flow itself can be expressed as $M = -\rho^i s_{\mathrm{L}}$ in terms of a so-called laminar flame speed s_{L}. This denotes the relative speed of the propagating flame front with respect to the velocity in the unburned fluid phase in negative normal direction, i.e. $s_{\mathrm{L}} = -(u_\Gamma - \boldsymbol{u}^i \cdot \boldsymbol{n}^{ij})$. The interfacial constraints (4.7)–(4.8) can be formulated based on the laminar flame speed and the material densities as

$$[\![\boldsymbol{u}]\!] = \rho^i s_{\mathrm{L}} [\![\rho^{-1}]\!] \boldsymbol{n}^{ij} \qquad \forall\, \boldsymbol{x} \in \Gamma^{ij}(t), \tag{4.13}$$

$$[\![\boldsymbol{\sigma}(\boldsymbol{u}, p)]\!] \cdot \boldsymbol{n}^{ij} = (\rho^i s_{\mathrm{L}})^2 [\![\rho^{-1}]\!] \boldsymbol{n}^{ij} \qquad \forall\, \boldsymbol{x} \in \Gamma^{ij}(t). \tag{4.14}$$

More details on this modeling approach for premixed combustion can be found, e.g., in the works by van der Bos and Gravemeier [255] or Henke [147].

Generalized abstract form of interfacial constraints: All of the above introduced kinematic and dynamical constraints can be embedded into an abstract form as

$$[\![\boldsymbol{u}]\!] = \boldsymbol{g}_\Gamma^{ij} \qquad \forall\, \boldsymbol{x} \in \Gamma^{ij}(t), \tag{4.15}$$

$$[\![\boldsymbol{\sigma}(\boldsymbol{u}, p)]\!] \cdot \boldsymbol{n}^{ij} = \boldsymbol{h}_\Gamma^{ij} \qquad \forall\, \boldsymbol{x} \in \Gamma^{ij}(t) \tag{4.16}$$

with functions $\boldsymbol{g}_\Gamma^{ij}$ and $\boldsymbol{h}_\Gamma^{ij}$ which are characteristic for the different fluid-fluid interface types and modeling approaches.

4.1.2 Coupled Interface Initial Boundary Value Problem

The coupled system consisting of several incompressible fluids can be composed of initial boundary value problems, see Section 3.1.1, for each fluid phase in Ω^i, which are governed by the incompressible Navier-Stokes equations with possibly different material properties and complemented with outer Dirichlet and Neumann boundary conditions at respective boundaries $\Gamma^i_{\mathrm{D}}, \Gamma^i_{\mathrm{N}}$. Furthermore, initial conditions $\boldsymbol{u}^i_0$ for the velocities $\boldsymbol{u}^i$ at $t = T_0$ are assumed. Additionally, at Γ^{ij} the different fluid phases are coupled together via previously derived conditions (4.15)–(4.16) and prescribed conditional functions $\boldsymbol{g}_\Gamma^{ij}, \boldsymbol{h}_\Gamma^{ij}$.

The strong formulation of the non-linear coupled initial boundary value problem reads: for any time $t \in (T_0, T]$, find fluid velocity and pressure $\boldsymbol{u}(t) : \Omega(t) \mapsto \mathbb{R}^d$, $p(t) : \Omega(t) \mapsto \mathbb{R}$ with restrictions $\boldsymbol{u}^i(t) = \boldsymbol{u}(t)\big|_{\Omega^i(t)}$ and $p^i(t) = p(t)\big|_{\Omega^i(t)}$ such that

$$\rho^i \frac{\partial \boldsymbol{u}^i}{\partial t} + \rho^i(\boldsymbol{u}^i \cdot \nabla)\boldsymbol{u}^i + \nabla p^i - 2\mu^i \nabla \cdot \boldsymbol{\epsilon}(\boldsymbol{u}^i) = \rho^i \boldsymbol{f}^i \qquad \forall\, \boldsymbol{x} \in \Omega^i(t), \tag{4.17}$$

$$\nabla \cdot \boldsymbol{u}^i = 0 \qquad \forall\, \boldsymbol{x} \in \Omega^i(t), \tag{4.18}$$

$$\boldsymbol{u}^i = \boldsymbol{g}^i_{\mathrm{D}} \qquad \forall\, \boldsymbol{x} \in \Gamma^i_{\mathrm{D}}(t), \tag{4.19}$$

$$\boldsymbol{\sigma}(\boldsymbol{u}^i, p^i) \cdot \boldsymbol{n}^i = \boldsymbol{h}^i_{\mathrm{N}} \qquad \forall\, \boldsymbol{x} \in \Gamma^i_{\mathrm{N}}(t), \tag{4.20}$$

$$[\![\boldsymbol{u}]\!] = \boldsymbol{u}^i - \boldsymbol{u}^j = \boldsymbol{g}^{ij}_{\Gamma} \qquad \forall\, \boldsymbol{x} \in \Gamma^{ij}(t), \tag{4.21}$$

$$[\![\boldsymbol{\sigma}(\boldsymbol{u}, p)]\!] \cdot \boldsymbol{n}^{ij} = (\boldsymbol{\sigma}(\boldsymbol{u}^i, p^i) - \boldsymbol{\sigma}(\boldsymbol{u}^j, p^j)) \cdot \boldsymbol{n}^{ij} = \boldsymbol{h}^{ij}_{\Gamma} \qquad \forall\, \boldsymbol{x} \in \Gamma^{ij}(t), \tag{4.22}$$

$$\boldsymbol{u}^i(T_0) = \boldsymbol{u}^i_0 \qquad \forall\, \boldsymbol{x} \in \Omega^i(T_0). \tag{4.23}$$

For the sake of simplicity, note that all fluid phases governed by the incompressible Navier-Stokes equations are here formulated in an Eulerian frame of reference. Analogously, applying an ALE formalism with adapted time derivative and a relative convective term as introduced in (3.4) would be straightforward.

4.1.3 Coupled Variational Formulation

The variational formulation for the coupled system of incompressible fluid phases comprises the variational formulations of each fluid subdomain as proposed in Section 3.1.2. The functional spaces for admissible velocity and pressure fields are given by the broken Sobolev spaces $\mathcal{V}_{\boldsymbol{g}_{\mathrm{D}}} = H^1_{\Gamma_{\mathrm{D}},\boldsymbol{g}_{\mathrm{D}}}(\Omega(t)) \subseteq H^1(\Omega(t))$ and $\mathcal{Q} = L^2(\Omega(t))$ if $\Gamma_{\mathrm{N}} \neq \emptyset$ with $\Omega(t) = \cup_{1 \leqslant i \leqslant N_{\mathrm{dom}}} \Omega^i(t)$. The respective test function spaces are denoted with $\mathcal{V}_{\boldsymbol{0}}$ and $\mathcal{Q}$.

The coupled non-linear variational formulation then reads as follows: for all $t \in (T_0, T]$, find fluid velocity and pressure $U(t) = (\boldsymbol{u}(t), p(t)) \in \mathcal{V}_{\boldsymbol{g}_{\mathrm{D}}} \times \mathcal{Q}$ with $U^i(t) = (\boldsymbol{u}^i(t), p^i(t)) = U(t)\big|_{\Omega^i(t)}$ such that for all $V(t) \in \mathcal{V}_{\boldsymbol{0}} \times \mathcal{Q}$

$$\widetilde{\mathcal{A}}(U, V) = \widetilde{\mathcal{L}}(V) \tag{4.24}$$

with $[\![\boldsymbol{u}]\!]\big|_{\Gamma^{ij}(t)}$, where

$$\widetilde{\mathcal{A}}(U, V) \overset{\text{def}}{=} \sum\nolimits_{1 \leqslant i \leqslant N_{\mathrm{dom}}} \mathcal{A}^i(U, V), \tag{4.25}$$

$$\widetilde{\mathcal{L}}(V) \overset{\text{def}}{=} \sum\nolimits_{1 \leqslant i \leqslant N_{\mathrm{dom}}} \left(\mathcal{L}^i(V) + \sum\nolimits_{j > i} \langle \boldsymbol{h}^{ij}_{\Gamma}, \langle \boldsymbol{v} \rangle \rangle_{\Gamma^{ij}(t)} \right) \tag{4.26}$$

and

$$\mathcal{A}^i(U, V) \overset{\text{def}}{=} (\rho^i \frac{\partial \boldsymbol{u}^i}{\partial t}, \boldsymbol{v}^i)_{\Omega^i(t)} + c^i(\boldsymbol{u}^i; \boldsymbol{u}^i, \boldsymbol{v}^i) + a^i(\boldsymbol{u}^i, \boldsymbol{v}^i) + b^i(p^i, \boldsymbol{v}^i) - b^i(q^i, \boldsymbol{u}^i), \tag{4.27}$$

$$\mathcal{L}^i(V) \overset{\text{def}}{=} l^i(\boldsymbol{v}^i) \tag{4.28}$$

denote the standard variational formulations of single-phase flows with operators c^i, a^i, b^i and l^i as defined in (3.12)–(3.15). The superscript $(\cdot)^i$ indicates incorporated integrals and material

parameters being evaluated in respective subdomains $\Omega^i(t)$ and on boundaries $\Gamma^i_{\mathrm{N}}(t)$. Note that for this variational formulation, the flux coupling constraints $[\![\boldsymbol{\sigma}(\boldsymbol{u},p)]\!]\cdot\boldsymbol{n}^{ij}=\boldsymbol{h}^{ij}_{\Gamma}$ and the Neumann boundary conditions $\boldsymbol{h}^i_{\mathrm{N}}$ are already included in the right-hand-side term $\widetilde{\mathscr{L}}(V)$. This can be seen as follows:

Starting as for deriving variational formulations (3.9) for each subdomain Ω^i, after multiplying the strong formulation with test functions $\boldsymbol{v}^i$ and integrating all viscous and pressure bulk terms by parts, the following boundary terms arise on $\partial\Omega^i(t)$ which can be rewritten as

$$\begin{aligned}
&\sum_{1\leqslant i\leqslant N_{\mathrm{dom}}}\left(-\langle\boldsymbol{\sigma}(\boldsymbol{u}^i,p^i)\cdot\boldsymbol{n}^i,\boldsymbol{v}^i\rangle_{\partial\Omega^i}\right) \qquad (4.29)\\
&=\sum_{1\leqslant i\leqslant N_{\mathrm{dom}}}\left(-\langle\boldsymbol{h}^i_{\mathrm{N}},\boldsymbol{v}^i\rangle_{\Gamma^i_{\mathrm{N}}}-\sum\nolimits_{j>i}\int_{\Gamma^{ij}}(\boldsymbol{\sigma}(\boldsymbol{u}^i,p^i)\cdot\boldsymbol{n}^i)\cdot\boldsymbol{v}^i+(\boldsymbol{\sigma}(\boldsymbol{u}^j,p^j)\cdot\boldsymbol{n}^j)\cdot\boldsymbol{v}^j\,\mathrm{d}\Gamma\right)\\
&=\sum_{1\leqslant i\leqslant N_{\mathrm{dom}}}\left(-\langle\boldsymbol{h}^i_{\mathrm{N}},\boldsymbol{v}^i\rangle_{\Gamma^i_{\mathrm{N}}}-\sum\nolimits_{j>i}\int_{\Gamma^{ij}}[\![(\boldsymbol{\sigma}(\boldsymbol{u},p)\cdot\boldsymbol{n}^{ij})\cdot\boldsymbol{v}]\!]\,\mathrm{d}\Gamma\right)\\
&=\sum_{1\leqslant i\leqslant N_{\mathrm{dom}}}\left(-\langle\boldsymbol{h}^i_{\mathrm{N}},\boldsymbol{v}^i\rangle_{\Gamma^i_{\mathrm{N}}}-\sum\nolimits_{j>i}\int_{\Gamma^{ij}}([\![\boldsymbol{\sigma}(\boldsymbol{u},p)]\!]\cdot\boldsymbol{n}^{ij})\cdot\langle\boldsymbol{v}\rangle+(\{\boldsymbol{\sigma}(\boldsymbol{u},p)\}\cdot\boldsymbol{n}^{ij})\cdot[\![\boldsymbol{v}]\!]\,\mathrm{d}\Gamma\right).
\end{aligned}$$

For splitting the jump term in line three, relation (2.4) has been utilized. The second term in the last line allows to incorporate the flux coupling condition $[\![\boldsymbol{\sigma}(\boldsymbol{u},p)]\!]\cdot\boldsymbol{n}^{ij}=\boldsymbol{h}^{ij}_{\Gamma}$. Note that the last term vanishes due to $[\![\boldsymbol{v}]\!]|_{\Gamma^{ij}}=\boldsymbol{0}$, provided the coupling $[\![\boldsymbol{u}]\!]=\boldsymbol{g}^{ij}_{\Gamma}$ is incorporated in the continuous function space $\mathscr{V}_{\boldsymbol{g}_{\mathrm{D}}}$. This is no longer valid for composed discrete approximation spaces, as will be discussed in the context of Nitsche-type techniques in the next section. Therein, the importance of the choice of average weights w^i, w^j incorporated in the definition of $\{\cdot\}, \langle\cdot\rangle$ will be elucidated. Finally, shifting all remaining terms to the right-hand side results in definition (4.26) of $\widetilde{\mathscr{L}}(V)$ and operators therein.

4.2 A Stabilized Cut Finite Element Method for Coupled Incompressible Flows

This section is devoted to cut finite element methods for coupled transient incompressible Navier-Stokes flows with stationary or moving subdomains and interfaces. Stabilized semi-discrete fluid formulations will be proposed for the general multidomain problem setting introduced in Section 4.1.2 including possibly different material parameters and characteristic interfacial constraints. The major objective of discretization methods to be developed is to support independent finite dimensional approximation spaces for the different fluid subdomains and associated solution fields. All computational meshes are thereby allowed to be chosen independently, either fitted or unfitted to the phase boundaries and to outer boundaries as visualized in Figure 2.9. After introducing stabilized formulations for this generalized problem setting, remarks on stability properties for certain mesh and material combinations will be made. The proposed formulation will be tested for overlapping fluid mesh-tying approaches including combinations of fitted and unfitted meshes in Section 4.3 and for incompressible two-phase flows based on unfitted meshes in Section 4.4. Simplifications with regard to stabilization techniques for these applications as well as related peculiarities will be addressed later in the respective sections.

4.2.1 Nitsche-type Cut Finite Element Methods for Domain Decomposition

Let $\mathcal{V}_h^i$ and $\mathcal{Q}_h^i$ be the discrete approximation spaces for velocity and pressure associated with the different fluid phases in possibly time-dependent subdomains Ω_h^i. Moreover, let $\mathcal{W}_h^i \overset{\text{def}}{=} \mathcal{V}_h^i \times \mathcal{Q}_h^i$ denote their product spaces. In general, the associated meshes are assumed to be non-fitted to domain boundaries $\Gamma_{\text{D}}^i, \Gamma_{\text{N}}^i$ and, in particular, non-node-matching at interfaces Γ_h^{ij}. The overall discrete approximation space defined in the entire domain Ω_h can be composed of subdomain product spaces as $\mathcal{W}_h \overset{\text{def}}{=} \oplus_{i=1}^{N_{\text{dom}}} \mathcal{W}_h^i = \oplus_{i=1}^{N_{\text{dom}}} (\mathcal{V}_h^i \times \mathcal{Q}_h^i)$ such that $V_h = (\boldsymbol{v}_h, q_h) \in \mathcal{W}_h$ is a pair of velocity and pressure solutions defined on Ω_h for which holds

$$V_h|_{\Omega^i} = V_h^i = (\boldsymbol{v}_h^i, q_h^i) \in \mathcal{V}_h^i \times \mathcal{Q}_h^i, \quad 1 \leqslant i \leqslant N_{\text{dom}}. \tag{4.30}$$

Note that the overall function space may in that way incorporate different element types, polynomial orders of approximation and different mesh sizes on their respective sub-grids $\mathcal{T}_h^i$. Due to this construction, functions $V_h \in \mathcal{W}_h$ are in general discontinuous at interfaces Γ^{ij}. This requires interfacial constraints being enforced weakly with, for instance, Nitsche-type techniques. To unify the notation in this section, also all boundary conditions on $\partial\Omega$ are assumed to be imposed weakly. If parts of the meshes $\mathcal{T}_h^i$ match the domain boundary, Dirichlet boundary conditions can be also straightforwardly incorporated into the respective trial and test function spaces.

A Nitsche-type Domain Decomposition CutFEM for Coupled Flows. In the following, a spatial semi-discrete formulation for a system of fluid phases (4.17)–(4.23) governed by the incompressible Navier-Stokes equations will be proposed. All outer boundary conditions and interfacial constraints between different fluid phases are enforced with Nitsche-type techniques. To stabilize the flow in the interior of the respective subdomains and on their potentially unfitted sub-grids, either CIP/GP or RBVM/GP stabilization approaches can be utilized; detailed elaborations on stabilizing the single phases on unfitted grids have been provided throughout Chapter 3.

Definition 4.1 (Semi-discrete Nitsche-type CutFEM for coupled flows)
Let $\mathcal{W}_h \overset{\text{def}}{=} \oplus_{i=1}^{N_{dom}} \mathcal{W}_h^i$, then a Nitsche-type stabilized formulation for coupling incompressible flows reads as follows: for all $t \in (T_0, T]$, find fluid velocity and pressure $U_h(t) = (\boldsymbol{u}_h(t), p_h(t)) \in \mathcal{W}_h$ such that for all $V_h = (\boldsymbol{v}_h, q_h) \in \mathcal{W}_h$

$$\widetilde{\mathcal{A}}_h(U_h, V_h) = \widetilde{\mathcal{L}}_h(U_h, V_h), \tag{4.31}$$

where

$$\widetilde{\mathcal{A}}_h(U_h, V_h) \overset{\text{def}}{=} \sum_{1 \leqslant i \leqslant N_{dom}} \left(\mathcal{A}_h^{i,\text{X}_i}(U_h, V_h) + \sum_{j>i} \mathcal{C}_h^{ij}(\boldsymbol{u}_h; (\boldsymbol{u}_h, p_h), (\boldsymbol{v}_h, q_h)) \right), \tag{4.32}$$

$$\widetilde{\mathcal{L}}_h(U_h, V_h) \overset{\text{def}}{=} \sum_{1 \leqslant i \leqslant N_{dom}} \left(\mathcal{L}_h^{i,\text{X}_i}(U_h, V_h) + \sum_{j>i} \mathcal{L}_h^{ij}(\boldsymbol{u}_h; (\boldsymbol{v}_h, q_h)) \right). \tag{4.33}$$

The coupled formulation includes stabilized single-phase formulations $\mathcal{A}_h^{i,\text{X}_i} - \mathcal{L}_h^{i,\text{X}_i}$ for each fluid phase, where X_i indicates the respective stabilized method, i.e. a CIP/GP *or a* RBVM/GP

*technique; see Section 3.6.1.1 and Section 3.6.1.2 for the corresponding formulations. Therein, the operators $\mathcal{A}_h^i$ and $\mathcal{L}_h^i$ comprise the standard Galerkin formulation, fluid stabilization in the interior of the subdomain (*RBVM *or* CIP*), ghost-penalty operators (*GP*) in the respective boundary/interface zones of $\partial\Omega^i$ and Nitsche-type boundary terms for the weak imposition of Dirichlet boundary conditions on Γ_{D}^i, respectively. Note that the superscript $(\cdot)^i$ indicates that included quantities like domains, interfaces, integrals, element- and face-sets as well as material parameters ρ^i, μ^i and functions $(\boldsymbol{v}_h^i, q_h^i) \in \mathcal{W}_h^i$ belong to the respective fluid phase.*

To impose the required coupling constraints (4.21)–(4.22) at interfaces Γ^{ij}, further Nitsche-type interfacial coupling terms $\mathcal{C}_h^{ij} - \mathcal{L}_h^{ij}$ need to be consistently added:

$$\begin{aligned}
\mathcal{C}_h^{ij}(\boldsymbol{u}_h;(\boldsymbol{u}_h,p_h),(\boldsymbol{v}_h,q_h)) = &-\langle\{2\mu\boldsymbol{\epsilon}(\boldsymbol{u}_h)\}\,\boldsymbol{n}^{ij},[\![\boldsymbol{v}_h]\!]\rangle_{\Gamma^{ij}} + \langle\{p_h\}\,,[\![\boldsymbol{v}_h]\!]\cdot\boldsymbol{n}^{ij}\rangle_{\Gamma^{ij}} && (4.34)\\
&\mp\langle[\![\boldsymbol{u}_h]\!],\{2\mu\boldsymbol{\epsilon}(\boldsymbol{v}_h)\}\,\boldsymbol{n}^{ij}\rangle_{\Gamma^{ij}} - \langle[\![\boldsymbol{u}_h]\!]\cdot\boldsymbol{n}^{ij},\{q_h\}\rangle_{\Gamma^{ij}} && (4.35)\\
&+\langle\gamma(\{\varphi\}\,/2)[\![\boldsymbol{u}_h]\!],[\![\boldsymbol{v}_h]\!]\rangle_{\Gamma^{ij}} && (4.36)\\
&+\langle\gamma(\{\rho\phi/h\}\,/2)[\![\boldsymbol{u}_h]\!]\cdot\boldsymbol{n}^{ij},[\![\boldsymbol{v}_h]\!]\cdot\boldsymbol{n}^{ij}\rangle_{\Gamma^{ij}} && (4.37)\\
&+\langle(\{\rho\boldsymbol{u}_h\}_{\mathrm{m}}\cdot\boldsymbol{n}^{ij})[\![\boldsymbol{u}_h]\!],\{\boldsymbol{v}_h\}_{\mathrm{m}}\rangle_{\Gamma^{ij}} && (4.38)\\
&+\langle\gamma_{\mathrm{upw}}|(\{\rho\boldsymbol{u}_h\}_{\mathrm{m}}\cdot\boldsymbol{n}^{ij})|[\![\boldsymbol{u}_h]\!],[\![\boldsymbol{v}_h]\!]\rangle_{\Gamma^{ij}}, && (4.39)
\end{aligned}$$

$$\begin{aligned}
\mathcal{L}_h^{ij}(\boldsymbol{u}_h;(\boldsymbol{v}_h,q_h)) = &\langle\boldsymbol{h}_\Gamma^{ij},\langle\boldsymbol{v}_h\rangle\rangle_{\Gamma^{ij}} && (4.40)\\
&\mp\langle\boldsymbol{g}_\Gamma^{ij},\{2\mu\boldsymbol{\epsilon}(\boldsymbol{v}_h)\}\,\boldsymbol{n}^{ij}\rangle_{\Gamma^{ij}} - \langle\boldsymbol{g}_\Gamma^{ij}\cdot\boldsymbol{n}^{ij},\{q_h\}\rangle_{\Gamma^{ij}} && (4.41)\\
&+\langle\gamma(\{\varphi\}\,/2)\boldsymbol{g}_\Gamma^{ij},[\![\boldsymbol{v}_h]\!]\rangle_{\Gamma^{ij}} && (4.42)\\
&+\langle\gamma(\{\rho\phi/h\}\,/2)\boldsymbol{g}_\Gamma^{ij}\cdot\boldsymbol{n}^{ij},[\![\boldsymbol{v}_h]\!]\cdot\boldsymbol{n}^{ij}\rangle_{\Gamma^{ij}} && (4.43)\\
&+\langle(\{\rho\boldsymbol{u}_h\}_{\mathrm{m}}\cdot\boldsymbol{n}^{ij})\boldsymbol{g}_\Gamma^{ij},\{\boldsymbol{v}_h\}_{\mathrm{m}}\rangle_{\Gamma^{ij}} && (4.44)\\
&+\langle\gamma_{\mathrm{upw}}|(\{\rho\boldsymbol{u}_h\}_{\mathrm{m}}\cdot\boldsymbol{n}^{ij})|\boldsymbol{g}_\Gamma^{ij},[\![\boldsymbol{v}_h]\!]\rangle_{\Gamma^{ij}}. && (4.45)
\end{aligned}$$

The terms (4.34) and (4.40) are so-called standard consistency terms as they result form integration by parts performed on the adjacent subdomains Ω^i, Ω^j, as derived in (4.29). Note that due to a possible discontinuity between $\boldsymbol{v}_h^i \in \mathcal{V}_h^i$ and $\boldsymbol{v}_h^j \in \mathcal{V}_h^j$, all interface terms derived there do not vanish in the discrete case. Neumann boundary terms remaining at Γ_{N}^i are included in $\mathcal{L}_h^{i,X_i}$, see (3.455). The terms (4.35) and (4.41) comprise consistently added viscous and pressure terms. Thereby, the sign choice $(\mp)$ allows to switch between a symmetric adjoint-consistent $(-)$ and a non-symmetric adjoint-inconsistent $(+)$ viscous elliptic part of the formulation. The different variants result in changes of inf-sup stability properties and restrictions on the choice of γ, as already discussed in Section 3.3.2.4 and Section 3.4.3.4 in the context of single-phase flow problems. In contrast, the sign of the pressure term is fixed to guarantee inf-sup stability. In (4.36)–(4.37) and (4.42)–(4.43), Nitsche-like penalty terms guarantee inf-sup stability with regard to the interfacial constraints for low- and high-Reynolds-number flows. The scaling ϕ occurring in the latter term is the stabilization scaling from (3.467) to account for the different flow regimes. To cope with instabilities arising from the convective terms, to control mass transport across interfaces and to deal with issues due to the discontinuity of the convective velocity $\boldsymbol{u}_h$, additional control on the interfacial constraint is ensured by the terms (4.38)–(4.39) and (4.44)–(4.45). These are so-called upwinding terms *which are well known from*

discontinuous Galerkin methods. The equal structure of terms (4.36) and (4.39) has to be noted. Due to their different role concerning stability, however, these terms are presented separately.

Note, the weights occurring in the weighted average operators $\{\cdot\}, \langle\cdot\rangle$ are defined as

$$w^i \overset{def}{=} \varphi^j/(\varphi^i+\varphi^j) \quad \textit{and} \quad w^j \overset{def}{=} \varphi^i/(\varphi^i+\varphi^j), \tag{4.46}$$

where $\varphi^i \overset{def}{=} \mu^i (f^i)^2$ and f^i is the scaling obtained from a weakened trace inequality (3.129), for which in the simplest case holds $(f^i)^2 \approx 1/h^i$. More detailed elaborations will be provided later in Section 4.2.2. Furthermore, $\{\cdot\}_{\mathrm{m}}$ denotes the mean average with $w^i_{\mathrm{m}} = w^j_{\mathrm{m}} = 1/2$.

Moreover, the solution U_h needs to fulfill the initial condition $\boldsymbol{u}_h(T_0) = \boldsymbol{u}_0$ in Ω. Note that this requires being conform to the coupling constraints $\boldsymbol{g}^{ij}_{\Gamma}$ at Γ^{ij} and boundary conditions $\boldsymbol{g}^i_{\mathrm{D}}$ on Γ^i_{D} at $t = T_0$. To shorten the presentation of the coupled formulation, the time variable is occasionally omitted in $U_h(t) = (\boldsymbol{u}_h(t), p_h(t))$. For further details on the stabilized single-phase formulations for each fluid phase, the reader is referred to Sections 3.6.1.1 and 3.6.1.2

The semi-discrete formulation (4.31) can be straightforwardly discretized in time using techniques proposed in Section 3.6.1.3. Resulting non-linear systems of equations for each discrete time step can be approximated using Newton-Raphson-like iterations. Further possible issues due to changing function spaces during iterative procedures will be discussed in the context of unfitted CUTFEMs for fluid-structure interaction in Chapter 5. Possible solution techniques are suggested in Section 5.3 and supported by numerical simulations in Sections 5.3 and 5.4. Within this chapter, interfaces are assumed either non-moving, as sometimes the case for mesh-tying applications, or fixed during the Newton-Raphson-like non-linear iterative solution procedure, as common for multiphase flows.

4.2.2 Enforcing Interfacial Constraints - The Role of Weighted Averages

As already discussed in detail in the context of weak imposition of boundary conditions in Sections 3.4–3.6, for non-boundary-fitted meshes, Nitsche-type approaches provide powerful techniques. These come along with desired inf-sup stability and optimal *a priori* error estimates which hold independent of the location of the interface within an underlying unfitted mesh. These optimality properties need to be preserved when imposing interfacial constraints between non-matching cut approximation spaces. The key idea of subsequently provided techniques is to exploit the stability control gained over the respective active computational meshes $\mathcal{T}^i_h$. For each fluid phase which is equipped with an unfitted approximation space, subdomain-related ghost-penalty operators known from single-phase flows can be utilized, respectively.

One can proceed similar to the stability estimate for single-phase problems as proposed in Section 3.5.5. Starting as in the proof of coercivity in Lemma 3.10, the viscous standard and adjoint consistency terms occurring in (4.34) and (4.35) can be estimated as follows

$$\begin{aligned}
&2\langle\{2\mu\boldsymbol{\epsilon}(\boldsymbol{u}_h)\}\,\boldsymbol{n}^{ij}, [\![\boldsymbol{u}_h]\!]\rangle_{\Gamma^{ij}} \\
&\quad\leqslant \epsilon^{-1}\|\,\{\mu\boldsymbol{\epsilon}(\boldsymbol{u}_h)\}\,\boldsymbol{n}^{ij}\|^2_{\Gamma^{ij}} + 4\epsilon\|[\![\boldsymbol{u}_h]\!]\|^2_{\Gamma^{ij}} \\
&\quad\leqslant \epsilon^{-1}\left((w^i)^2\|\mu^i\boldsymbol{\epsilon}(\boldsymbol{u}^i_h)\boldsymbol{n}^{ij}\|^2_{\Gamma^{ij}} + (w^j)^2\|\mu^j\boldsymbol{\epsilon}(\boldsymbol{u}^j_h)\boldsymbol{n}^{ij}\|^2_{\Gamma^{ij}}\right) + 4\epsilon\|[\![\boldsymbol{u}_h]\!]\|^2_{\Gamma^{ij}} \\
&\quad\leqslant \epsilon^{-1}\left((w^i)^2(\mu^i(f^i)^2)\|(\mu^i)^{1/2}\nabla\boldsymbol{u}^i_h\|^2_{\Omega^{i*}_h} + (w^j)^2(\mu^j(f^j)^2)\|(\mu^j)^{1/2}\nabla\boldsymbol{u}^j_h\|^2_{\Omega^{j*}_h}\right) + 4\epsilon\|[\![\boldsymbol{u}_h]\!]\|^2_{\Gamma^{ij}} \\
&\quad\leqslant \epsilon^{-1}\left((w^i)^2\varphi^i\|(\mu^i)^{1/2}\nabla\boldsymbol{u}^i_h\|^2_{\Omega^{i*}_h} + (w^j)^2\varphi^j\|(\mu^j)^{1/2}\nabla\boldsymbol{u}^j_h\|^2_{\Omega^{j*}_h}\right) + 4\epsilon\|[\![\boldsymbol{u}_h]\!]\|^2_{\Gamma^{ij}}
\end{aligned} \tag{4.47}$$

by applying an ϵ-scaled Young's inequality, a triangle inequality and the weakened trace inequalities (3.129) to estimate normal derivatives by the bulk gradients on the respective entire computational meshes Ω_h^{i*}. Hereby, f^i denote the piecewise constant scaling functions $f = C_T h_T^{-1/2}$ from (3.129) for the respective phase i. Note that φ^i is a scaling which needs to guarantee

$$\mu^i (f^i)^2 \leqslant \varphi^i \qquad \text{and} \qquad \mu^j (f^j)^2 \leqslant \varphi^j \tag{4.48}$$

and will be specified below. Appropriate choices of the weights $w^i = 1 - w^j$ allow to define sufficiently small bounded ϵ-scalings such that the stabilizing Nitsche-penalty term scales as small as possible. To allow absorbing the viscous subdomain semi-norms from (4.47) by respective energy-norms $|||(\rho^i)^{\frac{1}{2}} \boldsymbol{u}_h^i|||_*^2$ from (3.246), it is required that

$$\epsilon^{-1} (w^i)^2 \varphi^i \leqslant c \qquad \text{and} \qquad \epsilon^{-1} (w^j)^2 \varphi^j \leqslant c \tag{4.49}$$

with c sufficiently small. It has to be remarked that applying the weakened trace estimate was possible as viscous ghost-penalty operators for each subdomain ensure control $\|(\mu^i)^{1/2} \nabla \boldsymbol{u}_h^i\|_{\Omega_h^{i*}}$ on the respective entire active computational mesh Ω_h^{i*}.

A common choice for w^i, w^j are the *φ-harmonic weights*

$$w^i \overset{\text{def}}{=} \frac{\varphi^j}{\varphi^i + \varphi^j} \qquad \text{and} \qquad w^j \overset{\text{def}}{=} \frac{\varphi^i}{\varphi^i + \varphi^j}. \tag{4.50}$$

These fulfill $w^i + w^j = 1$ and guarantee boundedness of $(w^i)^2 \varphi^i$ in terms of the average $\{\varphi\}$

$$(w^i)^2 \varphi^i = \frac{(\varphi^j)^2}{(\varphi^i + \varphi^j)^2} \varphi^i = \frac{\varphi^i \varphi^j}{\varphi^i + \varphi^j} \cdot \frac{\varphi^j}{\varphi^i + \varphi^j} \leqslant \frac{\varphi^i \varphi^j}{\varphi^i + \varphi^j} = \frac{\{\varphi\}}{2}. \tag{4.51}$$

It equivalently holds $(w^j)^2 \varphi^j \leqslant \{\varphi\}/2$. Defining $\epsilon = \{\varphi\}/(2c)$ yields the required property

$$\epsilon^{-1} (w^i)^2 \varphi^i \leqslant c \qquad \text{and} \qquad \epsilon^{-1} (w^j)^2 \varphi^j \leqslant c \tag{4.52}$$

such that the coercivity estimate (4.47) can be finalized

$$\begin{aligned} 2\langle \{2\mu \boldsymbol{\epsilon}(\boldsymbol{u}_h)\} \boldsymbol{n}^{ij}, [\![\boldsymbol{u}_h]\!] \rangle_{\Gamma^{ij}} \leqslant c \left(\|(\mu^i)^{1/2} \nabla \boldsymbol{u}_h^i\|_{\Omega_h^{i*}}^2 + \|(\mu^j)^{1/2} \nabla \boldsymbol{u}_h^j\|_{\Omega_h^{j*}}^2 \right) \\ + \gamma(\{\varphi\}/2) \|[\![\boldsymbol{u}_h]\!]\|_{\Gamma^{ij}}^2. \end{aligned} \tag{4.53}$$

Combining the techniques provided in the proof of Lemma 3.10 and adding the consistent penalty term introduced in (4.36) and (4.42) to the coupled formulation guarantees coercivity of the viscous part of the discrete formulation (4.31) with respect to the following energy norm

$$|||\boldsymbol{u}_h|||_*^2 = \sum_{1 \leqslant i \leqslant N_{\text{dom}}} \left(|||(\rho^i)^{\frac{1}{2}} \boldsymbol{u}_h^i|||_*^2 + \sum_{j>i} \|(\gamma \{\varphi\}/2)^{1/2} [\![\boldsymbol{u}_h]\!]\|_{\Gamma^{ij}}^2 \right), \tag{4.54}$$

provided that the stabilization parameter $\gamma > 4/c$ is chosen sufficiently large. Therein, $|||\boldsymbol{u}_h^i|||_*^2$ is as defined in (3.246) for single-phase flows. Note that the resulting penalty scaling based on φ-harmonic weights ensures to be limited by the minimum of both values

$$\frac{\{\varphi\}}{2} = \frac{\varphi^i \varphi^j}{\varphi^i + \varphi^j} \leqslant \min\{\varphi^i, \varphi^j\}. \tag{4.55}$$

The property to ensure small penalty scalings is desired in particular for problem settings with high contrast in the functions φ, as will be elaborated subsequently.

It remains the question of how to define φ^i, φ^j for the different coupled flow problems addressed in Section 4.1.1. The most natural way to define those functions is to claim equality in (4.48). Such a definition takes possibly highly different material properties μ^i, μ^j into consideration. And, moreover, it accounts for different mesh properties like types, shapes, polynomial orders or aspect ratios of elements of adjacent fluid phases, characteristics which are hidden in the scaling functions f^i resulting from the trace inequalities (3.129), respectively. For different specific problem settings this definition simplifies and can be interpreted as follows:

Fluid Mesh Tying. For mesh-tying applications with equal material properties $\mu^i = \mu^j$, the introduced scalings $\varphi^i = \mu(f^i)^2$ only differ in the mesh properties. Considering the coupling of two meshes, where $h^j \ll h^i$ with almost regular elements satisfying $C_T^j \lesssim C_T^i \lesssim C_T^j$, it holds $f^j \gg f^i$ and thus $\varphi^j \gg \varphi^i$. Then, it holds $w^i \to 1, w^j \to 0$ for the weights. That is, the flux average weighting is shifted to the coarser one of the two meshes $\mathcal{T}_h^i, \mathcal{T}_h^j$.

A similar shift occurs when meshes with highly different aspect ratios are coupled. This is often the case when a boundary layer mesh $\mathcal{T}_h^j$ with strong refinement in wall-normal directions, i.e. $C_T^j \gg 1$, is embedded into a mostly regular unfitted background mesh $\mathcal{T}_h^i$. Then, again, $f^j \gg f^i$ and a flux weighting is suggested on that mesh which exhibits the lower aspect ratios to avoid ill-conditioning or too strong penalty effects on the coupling constraints due to large penalty scalings $\gamma\{\varphi\}$. Such a behavior has been discussed in detail in the work by Schott and Shahmiri *et al.* [232]. Simulation results for fluid mesh-tying applications based on the latter work will be proposed in Section 4.3.

Multiphase Flows. Characteristic for two-phase flow is the high contrast in material parameters, i.e. $0 < \mu^i \ll \mu^j$, which often results in steep gradients of the physical velocity solution in that fluid phase which is equipped with the lower viscosity. To numerically resolve such effects would demand a very fine mesh resolution in $\mathcal{T}_h^i$. Otherwise, in such cases, the key idea of weak constraint enforcement is to relax the strength of imposing the interfacial constraint to the benefit of improved accuracy in the vicinity of Γ^{ij}. Such techniques often highly improve robustness and eliminate oscillations which otherwise would artificially develop as a result of an insufficient resolution of the present physical effects.

Since cut finite element approximations of multiphase flows like, for instance, incompressible two-phase flows or premixed combustion applications, are usually based on identical meshes $\widehat{\mathcal{T}}_h^i \equiv \widehat{\mathcal{T}}_h^j$ such that $f^i \equiv f^j \overset{\text{def}}{=} f^{ij}$ holds for the weakened trace estimate scalings, the proposed φ-harmonic weighting simplifies to a purely viscosity-based μ-harmonic weighting

$$w^i = \frac{\mu^j}{\mu^i + \mu^j}, \quad w^j = \frac{\mu^i}{\mu^i + \mu^j} \qquad \text{and} \qquad \frac{\{\varphi\}}{2} = \frac{\mu^i \mu^j}{\mu^i + \mu^j}(f^{ij})^2, \tag{4.56}$$

as suggested, e.g., by Schott and Rasthofer *et al.* [231] for a Nitsche-type extended variational multiscale method for incompressible two-phase flow.

Remark 4.1 *Based on the assumption that* $\boldsymbol{u}_h^i \approx \boldsymbol{u}_h^j$ *and* $h^i = h^j$*, this* μ*-weighting can be interpreted as a weighting strategy based on local element Reynolds numbers* $\mathrm{Re}_T^i, \mathrm{Re}_T^j$*. These are an appropriate measure for resolving physical convective effects by the mesh on both sides of the interface. Then, the higher* $\mathrm{Re}_T^j \gg \mathrm{Re}_T^i$*, the more the flux weights tend to* $w^i \to 1$ *and* $w^j \to 0$ *such that the Nitsche penalty term scales with* $\{\varphi\} \lesssim \|\boldsymbol{u}_h\| / \max\{\mathrm{Re}_T^i, \mathrm{Re}_T^j\}$.

Remark 4.2 *It has to be further noted that the proposed* φ*-weighting is conform with the imposition of Dirichlet constraints for single-phase flows. That is when* $\varphi^i = \mathrm{const}$ *and* $\varphi^j \to \infty$*, which limits in coupling with an infinite viscous/stiff phase* j *or with a numerically fully resolved phase with mesh size parameter* $h^j \to 0$.

Neglecting for a moment the convective term, total inf-sup stability of the formulation (4.31) can be proven following the concept shown for single-phase flows in Section 3.5.5. By analogy to Lemma 3.10, to finalize the coercivity estimate with respect to a composed semi-norm

$$|U_h|_*^2 \overset{\text{def}}{=} \sum_{1 \leqslant i \leqslant N_{\text{dom}}} \left(|U_h^i|_*^2 + \sum_{j>i} \left(\|(\gamma \{\varphi\} / 2)^{\frac{1}{2}} [\![\boldsymbol{u}_h]\!]\|_{\Gamma^{ij}}^2 + \|(\gamma \{\rho\phi / h\})^{\frac{1}{2}} [\![\boldsymbol{u}_h]\!] \cdot \boldsymbol{n}^{ij}\|_{\Gamma^{ij}}^2 \right) \right) \tag{4.57}$$

where $|U_h^i|_*^2 = |||(\rho^i)^{\frac{1}{2}} \boldsymbol{u}_h^i|||_*^2 + |p_h^i|_*^2$ is based on (3.249), a pressure adjoint consistency term is consistently added in (4.35) and (4.41). This cancels out with the standard consistency pressure term (4.34) when testing diagonally for the coercivity proof, i.e. $V_h = U_h$. Similar to Lemma 3.11, control over the divergence semi-norm for each subdomain $\|(\rho^i \phi_u^i)^{\frac{1}{2}} \nabla \cdot \boldsymbol{u}_h^i\|_{\Omega^i}^2$ is gained from testing with $V_h = (V_h^i, V_h^j)$ with $V_h^i = (0, q_h^i)$. Following the proof of this lemma, in (3.273) now an additional interface term arises, which can be estimated analogously as

$$\begin{aligned} II &= -\langle \{\rho\phi/h\}^{-\frac{1}{2}} \{\mathcal{C}_h(\rho \widetilde{\phi}_u \nabla \cdot \boldsymbol{u}_h)\}, \{\rho\phi/h\}^{\frac{1}{2}} [\![\boldsymbol{u}_h]\!] \cdot \boldsymbol{n}^{ij} \rangle_{\Gamma^{ij}} && (4.58) \\ &\gtrsim -\delta(\|(\rho^i \phi_u^i)^{\frac{1}{2}} \nabla \cdot \boldsymbol{u}_h^i\|_{\mathcal{T}_h^i}^2 + \|(\rho^j \phi_u^j)^{\frac{1}{2}} \nabla \cdot \boldsymbol{u}_h^j\|_{\mathcal{T}_h^j}^2) - \delta^{-1} \| \{\rho\phi/h\}^{\frac{1}{2}} [\![\boldsymbol{u}_h]\!] \cdot \boldsymbol{n}^{ij}\|_{\Gamma^{ij}}^2 && (4.59) \end{aligned}$$

by using the fact that $\omega^i \{\rho\phi/h\}^{-\frac{1}{2}} (h^i)^{-\frac{1}{2}} \widetilde{\phi}_u^i \lesssim (\rho^i \phi^i)^{-\frac{1}{2}} \widetilde{\phi}_u^i \lesssim (\rho^i \phi_u^i)^{\frac{1}{2}}$. This ensures the desired divergence control and the remaining interface term can be compensated by the Nitsche interface penalty terms (4.37) and (4.43) when finalizing the inf-sup stability proof similar to that of Theorem 3.15, as proposed in Section 3.5.5. Note, the scalings $(\rho\phi/h)^i = \mu^i/h^i + c_u \rho^i |\boldsymbol{u}_h^i| + c_\sigma \rho^i \sigma h^i$ from (3.467) belong to the different subdomains and occur φ-weighted in the interface semi-norm $\| \{\rho\phi/h\}^{\frac{1}{2}} [\![\boldsymbol{u}_h]\!] \cdot \boldsymbol{n}^{ij}\|_{\Gamma^{ij}}$.

Further attention has to be devoted to the optimality of the formulation with respect to the pressure solution. Similar to single-phase flows, as provided in the *a priori* estimate in (3.439) in the proof of Theorem 3.19, the need for the additional mass conservation interface terms (4.37) and (4.43) can be boiled down to an estimate of the form

$$\begin{aligned} &\langle \{\rho\phi_u/h\}^{-\frac{1}{2}} \{\pi_h^* p - p\}, \{\rho\phi_u/h\}^{\frac{1}{2}} [\![\boldsymbol{v}_h]\!] \cdot \boldsymbol{n}^{ij} \rangle_{\Gamma^{ij}} && (4.60) \\ &\quad \lesssim (\|(\rho^i \phi_u^i)^{-\frac{1}{2}} (\pi_h^* p - p)^i\|_{\mathcal{T}_h^i} + \|(\rho^j \phi_u^j)^{-\frac{1}{2}} (\pi_h^* p - p)^j\|_{\mathcal{T}_h^j}) \cdot \| \{\rho\phi/h\}^{\frac{1}{2}} [\![\boldsymbol{v}_h]\!] \cdot \boldsymbol{n}^{ij}\|_{\Gamma^{ij}}, \end{aligned}$$

where again the aforementioned relation for the weighted coefficients was used and yields the desired *a priori* error estimate thanks to the Nitsche interface terms.

A full inf-sup stability proof and an *a priori* error analysis for the coupled problem goes beyond the scope of this thesis. For such purposes, however, different techniques proposed in literature could be combined straightforwardly: see Massing *et al.* [183] and Sections 3.5.5 and 3.5.6 concerning the Oseen single-field problem, the work by Hansbo *et al.* [141] on Stokes' interface problems and the publication by Massing *et al.* [180] for overlapping domain decomposition for Stokes' problem.

For the sake of completeness, similar to single-phase problems, also a non-symmetric adjoint-inconsistent viscous formulation can be utilized as defined for the $(+)$-signs in (4.35) and (4.41). This variant has been investigated in more detail for viscous-dominated domain decomposition problems in Schott and Shahmiri *et al.* [232]. For details on a penalty-free version, the reader is referred to works by Boiveau [26] and Boiveau and Burman [27].

To conclude, it has to be recalled that the proposed weighting strategy is founded on utilizing ghost-penalty stabilizations $\mathcal{G}_h^{\mathrm{GP},i}$ for each fluid phase. In particular the viscous ghost-penalty stabilizations g_ν^i (3.465) allow to estimate the viscous boundary terms despite the use of weakened trace inequalities. In contrast, other techniques which take into account cut-cell information for their weighting strategies, i.e. scalings f^i as proposed in (3.130) and suggested for interface problems, e.g., by Annavarapu *et al.* [2], Barrau *et al.* [14] or Hansbo *et al.* [141], still suffer from the well-known issues to render in ill-conditioned system matrices, interface-position dependent flux errors and strong penalty effects on the coupling constraints. These issues have been elucidated in detail in Section 3.4.2.

4.2.3 Controlling Convective Effects at Interfaces

Coupled flow problems require special measures with regard to mass conservation and convective mass transport across interfaces Γ^{ij}. Interface instabilities which emanate from the non-linear convective terms need to be balanced. The stabilization terms provided in (4.38)–(4.39) and (4.44)–(4.45) account for these and can be derived as follows:

Recalling the continuity of the advective velocity $\boldsymbol{\beta}_h^i \in \mathcal{V}_h^i$ within each subdomain Ω^i, it can be proceeded as in the coercivity proof of Lemma 3.10. Testing diagonally for the convective terms, which are notated with tri-linear forms $c^i(\boldsymbol{\beta}_h^i; \boldsymbol{u}_h^i, \boldsymbol{v}_h^i)$ (3.12) and included in the operator $\widetilde{A}^i$ (4.27), together with integration by parts yields

$$\sum_{1\leqslant i\leqslant N_{\mathrm{dom}}} c^i(\boldsymbol{\beta}_h^i; \boldsymbol{u}_h^i, \boldsymbol{u}_h^i) = \sum_{1\leqslant i\leqslant N_{\mathrm{dom}}} \left\{ -\frac{1}{2}(\rho^i(\nabla\cdot\boldsymbol{\beta}_h^i)\boldsymbol{u}_h^i, \boldsymbol{u}_h^i)_{\Omega^i} + \frac{1}{2}\langle \rho^i(\boldsymbol{\beta}_h^i\cdot\boldsymbol{n}^i)\boldsymbol{u}_h^i, \boldsymbol{u}_h^i\rangle_{\partial\Omega^i\cap\partial\Omega} \right\} + \sum_{1\leqslant i\leqslant N_{\mathrm{dom}}} \sum_{j>i} \frac{1}{2}\int_{\Gamma^{ij}} [\![\rho(\boldsymbol{\beta}_h\cdot\boldsymbol{n}^{ij})\boldsymbol{u}_h\boldsymbol{u}_h]\!]\,\mathrm{d}\Gamma. \tag{4.61}$$

Note, the first two terms on the right-hand side are already known from single-phase flows and are stabilized by consistently added bulk and boundary terms included in c_h^i, see (3.456). It has to be recalled that in practice only the boundary terms at inflow regions are required being controlled. The difficulty of $\boldsymbol{u}_h$ being divergence-free just in a weak sense can be compensated by discretizing the time-derivative with a sufficiently small time-step size Δt satisfying $\sigma - \frac{1}{2}\nabla\cdot\boldsymbol{u}_h \geqslant c > 0$, where $\sigma = \sigma(\Delta t)$ from (3.476) or (3.479). For coupled problems, the interface terms summed up in the second line can be estimated utilizing an extension of (2.4)

$$[\![ab^2]\!] = \{a\}_{\mathrm{m}}[\![b^2]\!] + [\![a]\!]\{b^2\}_{\mathrm{m}} = 2\{a\}_{\mathrm{m}}[\![b]\!]\{b\}_{\mathrm{m}} + [\![a]\!]\{b^2\}_{\mathrm{m}}, \tag{4.62}$$

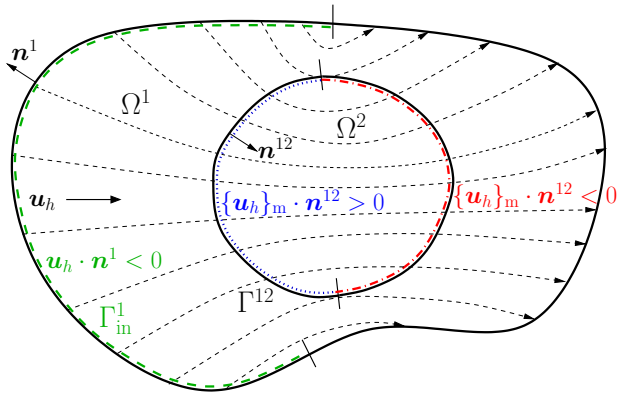

Figure 4.1: Convective upwinding flux scheme for fluid mesh tying at interface: Upwinding with respect to the subdomain Ω^i the flow is directed into. In case of $\rho\{\boldsymbol{u}_h\}_{\mathrm{m}} \cdot \boldsymbol{n}^{12} > 0$, upwinding with respect to Ω^2, and in case of $\rho\{\boldsymbol{u}_h\}_{\mathrm{m}} \cdot \boldsymbol{n}^{12} < 0$, upwinding with respect to Ω^1 is chosen. Inflow into subdomain Ω^1 at Γ^1_{in} is controlled by c^1_h, see (3.456).

which allows to rewrite each interface term as

$$\begin{aligned}
&\frac{1}{2}\int_{\Gamma^{ij}} [\![\rho(\boldsymbol{\beta}_h \cdot \boldsymbol{n}^{ij})\boldsymbol{u}_h\boldsymbol{u}_h]\!]\,\mathrm{d}\Gamma \\
&\qquad = \langle(\{\rho\boldsymbol{\beta}_h\}_{\mathrm{m}} \cdot \boldsymbol{n}^{ij})[\![\boldsymbol{u}_h]\!], \{\boldsymbol{u}_h\}_{\mathrm{m}}\rangle_{\Gamma^{ij}} + \frac{1}{2}\langle([\![\rho\boldsymbol{\beta}_h]\!] \cdot \boldsymbol{n}^{ij}), \{\boldsymbol{u}_h\boldsymbol{u}_h\}_{\mathrm{m}}\rangle_{\Gamma^{ij}} = I + II, \qquad (4.63)
\end{aligned}$$

as shown, e.g., in the textbook by Di Pietro and Ern [85]. In the latter work the subsequent adaption of the discrete formulation is called *Temam's modification*; for further details see also the references therein. The interface term I on the right-hand side can be easily balanced by consistently adding

$$I_a = -\langle(\{\rho\boldsymbol{\beta}_h\}_{\mathrm{m}} \cdot \boldsymbol{n}^{ij})[\![\boldsymbol{u}_h]\!], \{\boldsymbol{v}_h\}_{\mathrm{m}}\rangle_{\Gamma^{ij}} + \langle(\{\rho\boldsymbol{\beta}_h\}_{\mathrm{m}} \cdot \boldsymbol{n}^{ij})\boldsymbol{g}^{ij}_\Gamma, \{\boldsymbol{v}_h\}_{\mathrm{m}}\rangle_{\Gamma^{ij}}, \qquad (4.64)$$

$$I_b = +\gamma_{\mathrm{upw}}\langle|(\{\rho\boldsymbol{\beta}_h\}_{\mathrm{m}} \cdot \boldsymbol{n}^{ij})|[\![\boldsymbol{u}_h]\!], [\![\boldsymbol{v}_h]\!]\rangle_{\Gamma^{ij}} - \gamma_{\mathrm{upw}}\langle|(\{\rho\boldsymbol{\beta}_h\}_{\mathrm{m}} \cdot \boldsymbol{n}^{ij})|\boldsymbol{g}^{ij}_\Gamma, [\![\boldsymbol{v}_h]\!]\rangle_{\Gamma^{ij}}, \qquad (4.65)$$

where (4.64) is indeed sufficient to circumvent the difficulty arising from I. Furthermore, adding (4.65) with $\gamma_{\mathrm{upw}} \geqslant 0$ renders these two lines in a so-called *upwinding flux scheme*. This can be easily shown for the common choice $\gamma_{\mathrm{upw}} = \frac{1}{2}$ in $I_a + I_b$ for which then holds

$$\begin{aligned}
I_a + I_b &= -(\{\rho\boldsymbol{\beta}_h\}_{\mathrm{m}} \cdot \boldsymbol{n}^{ij})([\![\boldsymbol{u}_h]\!] - \boldsymbol{g}^{ij}_\Gamma)\,\{\boldsymbol{v}_h\}_{\mathrm{m}} + \frac{1}{2}|(\{\rho\boldsymbol{\beta}_h\}_{\mathrm{m}} \cdot \boldsymbol{n}^{ij})|([\![\boldsymbol{u}_h]\!] - \boldsymbol{g}^{ij}_\Gamma)[\![\boldsymbol{v}_h]\!] \\
&= \begin{cases} (\{\rho\boldsymbol{\beta}_h\}_{\mathrm{m}} \cdot \boldsymbol{n}^{ij})\boldsymbol{v}^j_h(\boldsymbol{u}^j_h - \boldsymbol{u}^i_h + \boldsymbol{g}^{ij}_\Gamma) & \text{if } (\{\rho\boldsymbol{\beta}_h\}_{\mathrm{m}} \cdot \boldsymbol{n}^{ij}) > 0, \\ |\{\rho\boldsymbol{\beta}_h\}_{\mathrm{m}} \cdot \boldsymbol{n}^{ij}|\boldsymbol{v}^i_h(\boldsymbol{u}^i_h - \boldsymbol{u}^j_h - \boldsymbol{g}^{ij}_\Gamma) & \text{if } (\{\rho\boldsymbol{\beta}_h\}_{\mathrm{m}} \cdot \boldsymbol{n}^{ij}) \leqslant 0. \end{cases} \qquad (4.66)
\end{aligned}$$

Such a scheme controls inflow into the respective subdomain depending on the flow direction as discussed, e.g., in Schott and Shahmiri *et al.* [232]. A visualization of the upwinding scheme with mass transport across Γ^{ij} for a fluid mesh-tying setting is given in Figure 4.1. In terms of establishing inf-sup stability and *a priori* estimates, the upwinding part I_b introduces semi-norm control in addition to the already defined energy-type semi-norm from (4.57), i.e.

$$|U_h|^2_* + \sum_{1 \leqslant i \leqslant N_{\mathrm{dom}}} \left(\sum_{j>i} \|(\gamma_{\mathrm{upw}}|\{\rho\boldsymbol{\beta}_h\}_{\mathrm{m}} \cdot \boldsymbol{n}^{ij}|)^{1/2}[\![\boldsymbol{u}_h]\!]\|^2_{\Gamma^{ij}} \right). \qquad (4.67)$$

The part I_a directly cancels out with I when testing diagonally for the coercivity proof. For further explanations, the reader is also referred to, e.g., [10, 61, 91].

Balancing the remaining term II in (4.63) is more delicate. For mesh-tying applications with $\rho^i = \rho^j \stackrel{\text{def}}{=} \rho^{ij}$, a counteracting term can be easily constructed in a consistent way as

$$-\frac{1}{2}\langle(\rho^{ij}[\![\boldsymbol{u}_h]\!]\cdot\boldsymbol{n}^{ij}),\{\boldsymbol{u}_h\boldsymbol{v}_h\}_{\mathrm{m}}\rangle_{\Gamma^{ij}}+\frac{1}{2}\langle(\rho^{ij}\boldsymbol{g}_\Gamma^{ij}\cdot\boldsymbol{n}^{ij}),\{\boldsymbol{u}_h\boldsymbol{v}_h\}_{\mathrm{m}}\rangle_{\Gamma^{ij}}, \tag{4.68}$$

which cancels out with II when proving coercivity; the close relation to issues occurring in discontinuous Galerkin approximations as discussed, e.g., in [85] has to be noted. However, constructing consistent terms for the cases $\rho^i \neq \rho^j$ requires information about the interface transport velocity u_Γ^{ij} to ensure mass conservation in terms of $[\![\rho\boldsymbol{u}_h]\!]\cdot\boldsymbol{n}^{ij} - [\![\rho]\!]u_\Gamma^{ij}$ as claimed in (4.1). Then, a potential balancing term could be constructed as

$$-\frac{1}{2}\langle([\![\rho\boldsymbol{u}_h]\!]\cdot\boldsymbol{n}^{ij}),\{\boldsymbol{u}_h\boldsymbol{v}_h\}_{\mathrm{m}}\rangle_{\Gamma^{ij}}+\frac{1}{2}\langle([\![\rho]\!]u_\Gamma^{ij}),\{\boldsymbol{u}_h\boldsymbol{v}_h\}_{\mathrm{m}}\rangle_{\Gamma^{ij}}. \tag{4.69}$$

Since u_Γ is most commonly given implicitly and depends non-linearly on the convective flow velocity $\boldsymbol{u}_h$, such a term would introduce further non-linearities and dependencies between the transport solver for interfaces and the flow solver. Moreover, numerical simulations proposed later in this thesis, but also extensive tests in related published works by Schott and Shahmiri *et al.* [232] and by Schott and Rasthofer *et al.* [231], demonstrate robustness even without such a term. Therefore, this term is neglected throughout this thesis even though the resulting formulation is not proven to be fully controlled in terms of a strong mathematical numerical analysis.

4.3 Fluid Mesh Tying - An Overlapping Mesh Domain Decomposition Approach

This section aims at demonstrating the high capabilities of the proposed stabilized Nitsche-type method from Section 4.2 for domain decomposition applied to single-phase flows. For the approach investigated subsequently, a fluid domain Ω is decomposed and approximated with overlapping meshes as introduced in Section 2.1.4.3 and visualized in Figure 2.10b. A fluid patch $\mathcal{T}_h^2 \equiv \widehat{\mathcal{T}}_h^2$ with $\Omega_h^2 \equiv \Omega_h^{2*}$ is embedded into a potentially unfitted background fluid mesh $\mathcal{T}_h^1 \subseteq \widehat{\mathcal{T}}_h^1$ with $\Omega_h^1 \subseteq \Omega_h^{1*}$ such that $\Gamma_h^{12} \stackrel{\text{def}}{=} \partial\Omega_h^2$. Furthermore, it holds $\rho^1 = \rho^2 = 1.0$ and $\mu^1 = \mu^2$.

Different domain decomposition ideas have been widely considered in literature and are based on different coupling strategies. Former developed embedding mesh techniques like Chimera methods, as proposed, e.g., by Wang and Parthasarathy [265], Gamnitzer and Wall [120] or Steger *et al.* [239], make use of the overlapping zone of the two meshes to get a converged solution. While iterating between both fluid domains, the solutions are often coupled weakly by a Dirichlet/Neumann strategy as proposed, e.g., in Houzeaux and Codina [154]. This, however, introduces an additional step in the solution procedure and increases computational costs. Besides, to achieve a converged solution, the overlapping domain has to be large enough which, thus, results in a mesh dependency for such techniques as discussed, e.g., by Wall *et al.* [260]. In contrast, using cut finite element approximations on the background mesh enables the coupling

of the subdomain solutions to take place just at the interface and allows to solve the coupled system at once. Such embedding mesh approaches do not incorporate mesh dependencies and allow for a joint solution of the entire fluid field without the need for iterating between the two subdomains.

Different coupling techniques for composed approximation spaces have been developed, however, many of them were originally designed for interface-fitted meshes or just for flow-related problems. Domain decomposition for incompressible Navier-Stokes equations with non-overlapping meshes in the framework of discontinuous Galerkin methods has been considered by Girault *et al.* [126]. Mesh tying for advection-diffusion-reaction problems utilizing Nitsche's method has been analyzed and investigated by Burman and Zunino [61]. A mesh-tying method for incompressible flows based on a dual mortar approach for interface-fitted meshes has been recently published by Ehrl *et al.* [98]. The basic idea of using composite grids together with cut finite element approximations dates back to the works by Hansbo *et al.* [139] and Becker *et al.* [19]. Their idea was picked up and extended to incompressible viscous flow problems by Shahmiri *et al.* [236]. A similar overlapping mesh formulation for Stokes' problem including also a numerical analysis has been developed by Massing *et al.* [180]. The great advantages of such unfitted techniques are clearly pointed out considering computational grid generation in complex domains. They allow for locally increased resolutions in embedded fluid patches independent from size and structure of the background mesh. Their highly promising extensibility to FSI applications has been demonstrated by Shahmiri [235] and Massing *et al.* [182].

Recently, Schott and Shahmiri *et al.* [232] investigated robustness and accuracy of the Nitsche-type CUTFEM introduced in Section 4.2 with regard to different flux weighting strategies and provided extensive numerical studies. Therein, the authors confirmed stability and optimal convergence for the RBVM/GP stabilization technique. For details on these studies, which are closely related to those shown for single-phase flows in Sections 3.4.4.2 and 3.4.4.3, the interested reader is referred to the latter publication. Further numerical simulations for fluid domain decomposition applications will be proposed subsequently and are based on the work published in [232].

The introduced Nitsche-type RBVM/GP approach is tested for two challenging numerical examples: To analyze the quality of the fluid-fluid coupling for laminar flows, results of two- and three-dimensional benchmark computations of stationary as well as transient flows around cylinders are compared to reference values known from literature. Furthermore, to validate the stabilized fluid formulation in the high-Reynolds-number regime, a complex three-dimensional fully turbulent recirculating flow in a lid-driven cavity at $\mathrm{Re} = 10000$ is studied. The high potential of this methodology in combination with fluid-structure interaction approaches will be demonstrated later in Chapter 5.

If not indicated otherwise, all considered meshes consist of tri-linearly-interpolated $\mathbb{Q}^1$ elements. An adjoint-consistent Nitsche coupling is applied with $\gamma = 35.0$ in combination with an upwinding scheme, i.e. $\gamma_{\mathrm{upw}} = 1/2$. As very low aspect ratios and almost equal-sized elements in the background grid $\mathcal{T}_h^1$ and the embedded fluid patch $\mathcal{T}_h^2$ are used, the flux weighting can be arbitrarily chosen and is set to $w^2 = 1 - w^1 = 1$ in the following.

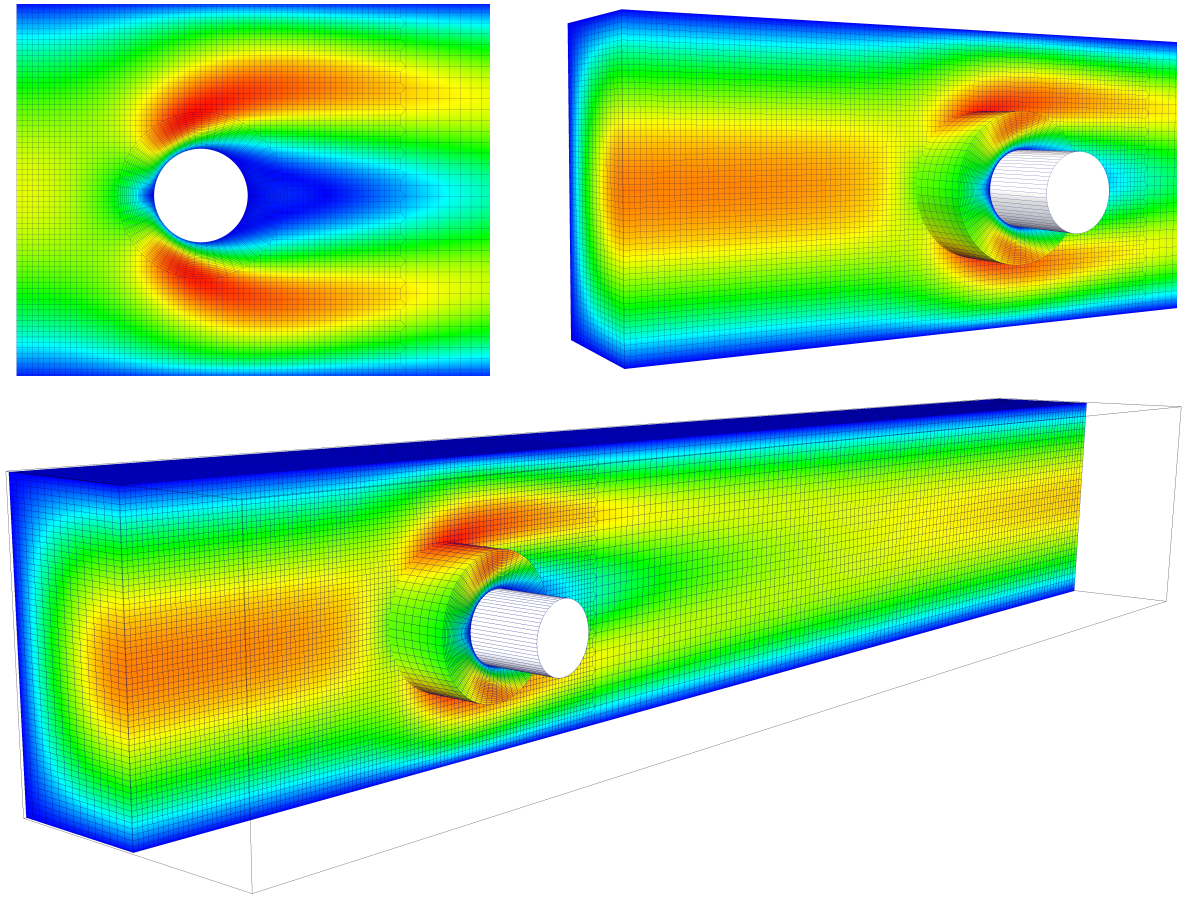

Figure 4.2: Problem configurations for cylinder benchmarks: CUTFEM-based overlapping mesh fluid domain decomposition technique consisting of an embedded boundary layer mesh $\mathcal{T}_h^2$ around the cylinder and a background mesh $\mathcal{T}_h^1$. Close-up view of the different meshes around the cylinder for configuration 2D-x (x=1,2,3) and velocity magnitude for case 2D-1 (top left) as well as for configuration 3D-1Z (top right). Full geometric setup and velocity magnitude for case 3D-1Z (bottom).

4.3.1 Benchmark Computations of Laminar Flows around Cylinders

To verify the proposed fluid domain decomposition formulation for laminar flows, stationary as well as transient 2D and 3D benchmark computations simulating the incompressible flow around cylinders at $\mathrm{Re} = 20$–100 are investigated. The configurations 2D-1, 2D-2, 2D-3 and 3D-1Z, as originally introduced by Schäfer and Turek [227], are considered in the following.

The problem configurations are taken unchanged from the original publication: For the 2D benchmarks, a circular cylinder Ω^{s} with diameter $d = 0.1$ is located at $(0.2, 0.2)$ inside a channel with dimensions $(0, 2.2) \times (0, 0.41)$. For the 3D-1Z case, the flow in a channel with dimensions $(0, 2.5) \times (0, 0.41) \times (0, 0.41)$ is computed where a cylinder with circular cross-section of diameter $d = 0.1$ and a length of 0.41 is centered at $(0.5, 0.2, 0.205)$. Similar to [236], a boundary layer mesh $\mathcal{T}_h^2$ around the cylinder is embedded into a regular background mesh $\mathcal{T}_h^1$, as visualized in Figure 4.2 for the different configurations.

For all simulations, the viscosity is given as $\nu = 10^{-3}$ and traction-free Neumann conditions at the outflow and no-slip conditions at the side walls are applied. At the inflow, a parabolic velocity field in x_1-direction is prescribed with a maximum velocity $u_1^{\max}$. For the test case

2D-1, a maximum velocity $u_1^{\max} = 0.3$ is given which results in $\mathrm{Re} = 20$, where $\mathrm{Re} = u_1^{\mathrm{mean}} d/\nu$ is based on the cylinder diameter d and the mean velocity $u_1^{\mathrm{mean}} = 2/3 u_1^{\max}$. For the transient configuration 2D-2, the parabolic velocity profile is increased by a ramp function $1/2(1 - \cos(\pi t))$ within $0 \leqslant t \leqslant 1$ until $u_1^{\max} = 1.5$ is reached, which then yields $\mathrm{Re} = 100$. For the case 2D-3 with a maximum velocity of $u_1^{\max} = 1.5$, the parabolic inflow is varied by a sinusoidal function $\sin(\pi t/8)$ in a time-interval $0 \leqslant t \leqslant 8$ resulting in a varying Reynolds number $0 \leqslant \mathrm{Re} \leqslant 100$. For the stationary 3D configuration, the maximum velocity is set to $u_1^{\max} = 0.45$ which leads to a Reynolds number of $\mathrm{Re} = 20$. For both time-dependent 2D setups, a Crank-Nicolson scheme, i.e. $\theta = 0.5$, has been applied with a time-step length of $\Delta t = 0.002$.

In Table 4.1, computed (maximum) lift and drag values $(c_{\mathrm{lift}}, c_{\mathrm{drag}})$ as well as the pressure difference Δp between front and back end of the cylinder are compared to reference values from [227]. Moreover, the effective number of degrees of freedom $N_{\boldsymbol{u},p}^{\mathrm{DOF}}$ for the 2D and 3D cases are reported. For the time-dependent 2D configurations, lift and drag coefficients are plotted over time in Figure 4.3. For all configurations, a perfect agreement with the given reference bounds could be achieved. The high quality of the results already for this low number of required degrees of freedom underlines the high potential of the proposed technique, which enables to use a fine-resolved embedded mesh in the region of interest around the cylinders embedded into a coarser background fluid mesh. On the one hand, this allows to reduce the total number of degrees of freedom, but also simplifies mesh generation as the respective embedded meshes for a given structural mesh can be generated quite easily. On the other hand, this technique becomes still more powerful when moving structures are considered as issues of mesh distortion do not occur anymore.

In addition, to visualize the robust coupling between the two meshes, velocity magnitude and pressure solution around the cylinder are depicted for the time-dependent benchmark simulation 2D-2 in Figure 4.4 at $t = 6.0$. The quality of the interface coupling between embedded and unfitted background mesh is independent of the interface location. This is mainly thanks to the stable Nitsche-type coupling (4.34)–(4.45) and the accompanying interface zone fluid and ghost-penalty stabilization terms (3.453) and (3.454).

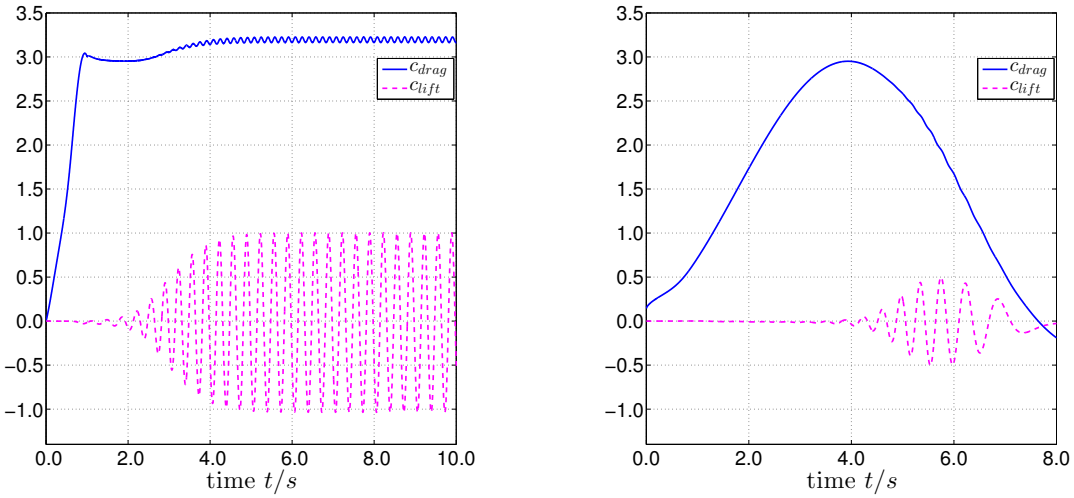

Figure 4.3: Cylinder benchmark 2D-2 (left) and 2D-3 (right): Computed lift and drag coefficients $c_{\mathrm{lift}}(t)$ and $c_{\mathrm{drag}}(t)$ over time t.

Table 4.1: Laminar cylinder benchmarks: Computed lift and drag values and pressure difference between front and back end of cylinders compared to reference values from [227]. $N_{\boldsymbol{u},p}^{\text{DOF}}$ denotes the total number of nodal velocity and pressure degrees of freedom used for the simulations.

Configuration	approach	$N_{\boldsymbol{u},p}^{\text{DOF}}$	c_{drag}	c_{lift}	Δp
2D-1	Ref. lower bound [227]	-	5.5700	0.0104	0.1172
	Ref. upper bound [227]	-	5.5900	0.0110	0.1176
	Nitsche-RBVM/GP method	$\simeq 47351$	**5.5836**	**0.0108**	**0.1175**
2D-2	Ref. lower bound [227]	-	3.2200	0.9900	2.4600
	Ref. upper bound [227]	-	3.2400	1.0100	2.5000
	Nitsche-RBVM/GP method	$\simeq 47351$	**3.2271**	**1.0020**	**2.4856**
2D-3	Ref. lower bound [227]	-	2.9300	0.4700	-0.1150
	Ref. upper bound [227]	-	2.9700	0.4900	-0.1050
	Nitsche-RBVM/GP method	$\simeq 47351$	**2.9513**	**0.4974**	$\mathbf{-0.1061}$
3D-1Z	Ref. lower bound [227]	-	6.0500	0.0080	0.1650
	Ref. upper bound [227]	-	6.2500	0.0100	0.1750
	Nitsche-RBVM/GP method	102148	**6.1717**	**0.0096**	**0.1712**

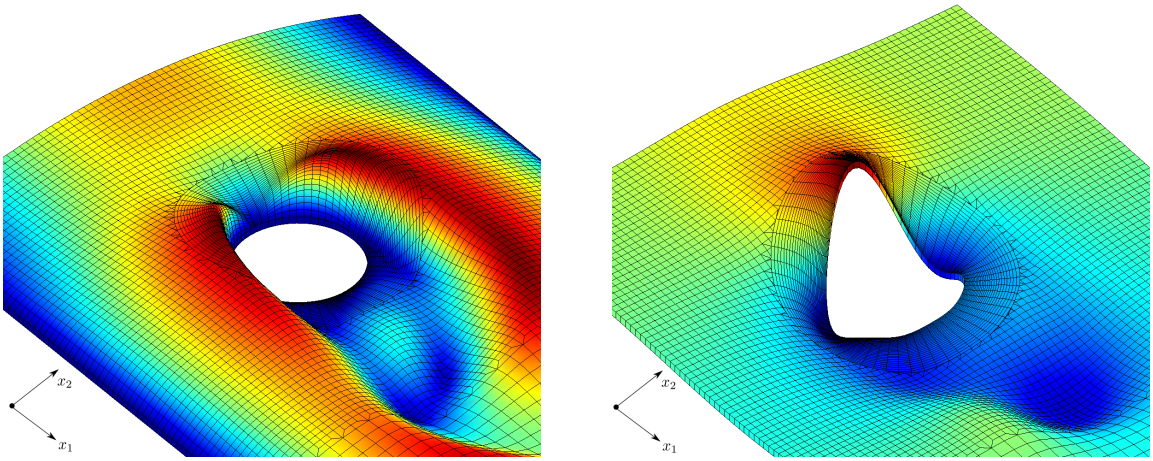

Figure 4.4: Cylinder benchmark 2D-2: Close up view around the cylinder showing velocity magnitude (left) and the pressure field (right) at $t = 6.0$. The smooth continuity of the velocity and pressure solution at the interface Γ demonstrates an accurate and stable coupling independent of the interface position.

4.3.2 Turbulent Recirculating Flow in a Lid-Driven Cavity

The second example consists of a complex turbulent three-dimensional flow in a lid-driven cavity, which has been established as a numerical test example: see, e.g., the works by Zang *et al.* [275], Bouffanais *et al.* [30] or Gravemeier *et al.* [130]. Results of numerical simulations can be compared with experimental data provided, e.g., by Prasad and Koseff [210] and with data available from direct numerical simulations (DNS) by, e.g., Leriche and Gavrilakis [176].

In this example, a cubic cavity $\Omega = (-L/2, L/2)^3$ with edge length $L = 1$ is considered. Following [130] and references therein, the Reynolds number is defined as $\text{Re} = (U_0 L)/\nu$ based on the lid velocity U_0. Choosing $U_0 = 1.0$ and the viscosity as $\nu = 10^{-4}$, the Reynolds number

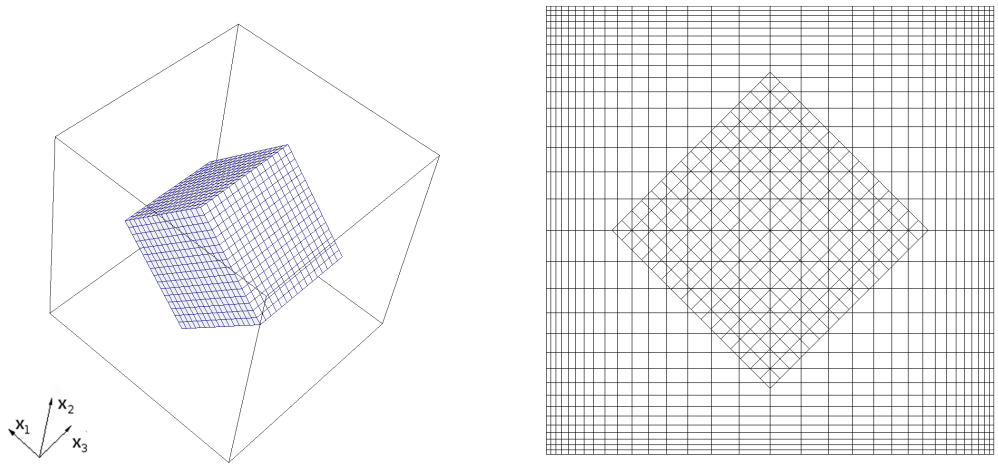

Figure 4.5: Lid-driven cavity flow at $\mathrm{Re} = 10000$: Cubic cavity discretized with 32 elements in each direction for the background mesh $\mathcal{T}_h^1$ and a cubic, centrally located, regular embedded mesh $\mathcal{T}_h^2$ with 16 elements along each edge. Position of the embedded mesh in 3D (left) and visualization of mesh size and grading towards walls and lid in the background fluid mesh (right).

is given as $\mathrm{Re} = 10000$ and the flow becomes fully turbulent and exhibits a complex three-dimensional vortex distribution in the entire domain; see, e.g., the work by Shankar and Deshpande [237] for elaboration.

As suggested in [130], the background mesh $\mathcal{T}_h^1$ is discretized with 32 elements in each direction including a refinement towards the walls and the lid, resulting in a minimum element length of $h^{\min} = 0.01$. To adapt this setup to a fluid domain decomposition configuration, a cubic fluid patch $\mathcal{T}_h^2$ with an edge length of $l = 0.5$ is embedded into the cavity. The final configuration is obtained by rotating the initially concentric embedded mesh by $45°$ around the x_3-axis, see Figure 4.5. Statistics are evaluated along the x_1- and x_2-coordinate axes. Each evaluation path therefore crosses the embedded domain. Except for the driven lid, no-slip boundary conditions are assumed on all cavity walls. Starting from a quiescent flow, the lid-velocity is increased within the first 100 steps using a time-step length of $\Delta t = 0.1$ and a ramp function $U_{\mathrm{lid}}(t) = 1/2(1 - \cos(\pi t/10))U_0$. It is expected that the flow becomes fully developed within the first 3000 time-steps. Afterwards, statistics are collected in the time period during steps 3001–10000, which is a sampling period that is highly recommended to obtain reliable statistical data. For the temporal discretization, a Crank-Nicolson scheme with $\theta = 0.5$ has been applied.

As statistical measures, mean stream-wise velocities $\langle u_1 \rangle$, $\langle u_2 \rangle$, stream-wise root-mean-square velocities $\mathrm{rms}\, u_1, \mathrm{rms}\, u_2$ and the Reynolds-stress component $\langle u_1', u_2' \rangle$ along the centerlines of the mid-plane $x_3 = 0$ are analyzed. The results are compared with experimental data from [210], referred to as "EXP", and with DNS-data from [176], denoted by "DNS" in the following. As indicated in [130], it may be difficult to adequately capture the turbulent statistics, as even DNS exhibits significant differences to experimental data. It has to be emphasized that it is not the objective of the present work to discuss the need for turbulence models or to address the differences between experiments and DNS, but rather to demonstrate the robustness and accuracy of the proposed interface coupling technique for high-Reynolds-number flows. To further examine these effects, the proposed domain-decomposition approach, denoted as "CUT-FEM-DD" in the following, is compared to a classical RBVM stabilized fitted-mesh FEM, as

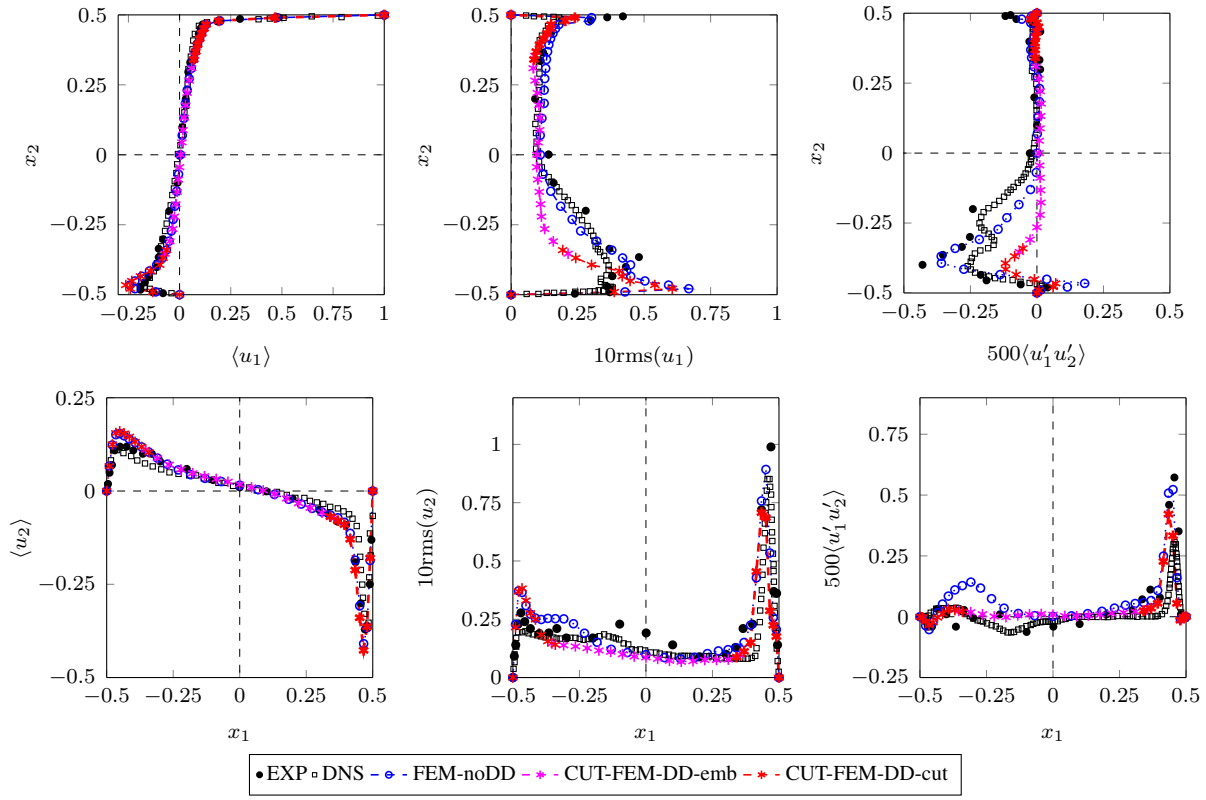

Figure 4.6: Lid-driven cavity flow at $\mathrm{Re} = 10000$: Statistical measures from left to right and from top to bottom: mean stream-wise velocity $\langle u_1 \rangle$, stream-wise root-mean-square velocity $10\,\mathrm{rms}\,u_1$ and Reynolds-stress component $500\langle u_1', u_2' \rangle$ along x_2-axis as well as lid-normal velocity $\langle u_2 \rangle$, lid-normal root-mean-square velocity $10\,\mathrm{rms}\,u_2$ and Reynolds-stress component $500\langle u_1', u_2' \rangle$ along x_1-axis.

introduced in Section 3.1.3.1. The latter method is denoted as "FEM-noDD". Numerical results as well as experimental and DNS data for all statistical measures are depicted in Figure 4.6.

For both numerical approaches, the "FEM-noDD" and the "CUT-FEM-DD", almost indistinguishable results are obtained for the mean velocities $\langle u_1 \rangle$, $\langle u_2 \rangle$ which provide a good prediction of the DNS and experimental data. Concerning root-mean-square velocities and Reynolds-stress components, the proposed domain decomposition approach matches experimental and DNS data in large parts very well. Moreover, for the domain decomposition approach, no artificial discontinuities between embedded mesh ("CUT-FEM-DD-emb") and cut background mesh ("CUT-FEM-DD-cut") could be noticed in the graphs.

This example of a turbulent recirculating flow puts great demands on the robustness and the accuracy of the interface coupling. No destabilizing effects of the Nitsche-type coupling could be observed during the overall, long simulation time and mass conservation could be fully guaranteed, even though mass and vortices are continuously transported across the fluid-fluid interface. Moreover, it has to be pointed out that the chosen OST temporal discretization scheme with $\theta = 0.5$ does not introduce numerical damping, which underlines the long-time robustness of the proposed unfitted fluid mesh-tying domain decomposition formulation. Additionally, a contour plot of the velocity magnitude illustrates the velocity coupling of the proposed method across the interface in Figure 4.7. For more details on this example and with regards to the interpretation of turbulence statistics, the reader is referred to works by, e.g., Zang *et al.* [275], Bouffanais *et al.* [30] and Gravemeier *et al.* [130].

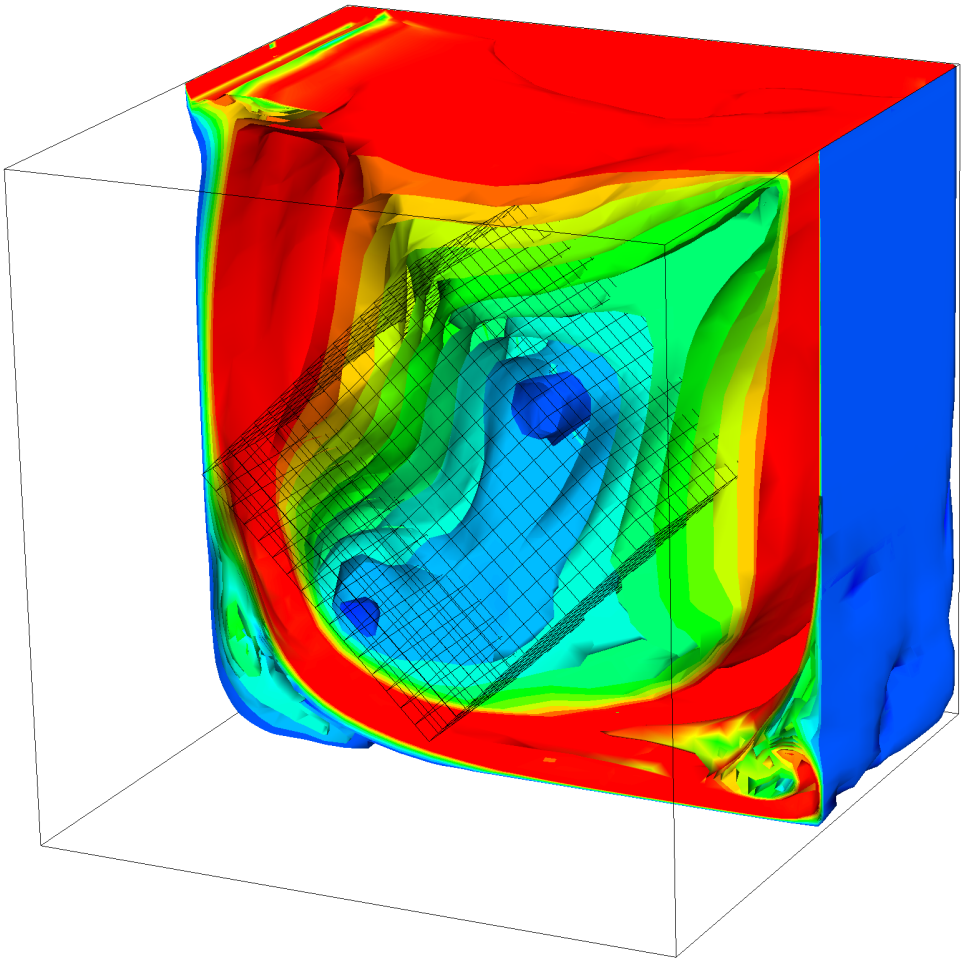

Figure 4.7: Lid-driven cavity flow at $\mathrm{Re} = 10000$: Isosurface plot of velocity magnitude at $t = 440.0$.

4.4 Outlook towards Incompressible Two-Phase Flow - An Unfitted Mesh Method

The objective of this section is to give an outlook towards two-phase-flow applications for which the stabilized Nitsche-type formulation proposed in Section 4.2 can be utilized and shows severe advantages over other computational approaches. Expansion to several fluid phases would be straightforward, the subsequent presentation, however, is simplified to two fluid phases for which $\rho^1 \neq \rho^2$ and $\mu^1 \neq \mu^2$ holds in general. Characteristic for two-phase flow is the dependency of the interface motion on the surrounding fluid flow. This can cause large and complex interface deformations as well as topological changes. To allow the interface to arbitrarily move and thereby to sharply capture the phase limit, the separate fluid phases are approximated using the unfitted technique introduced in Section 2.1.4.3, as visualized in Figure 2.10c. The geometric approximation of the two immiscible fluid subdomains and their associated flow fields rely on identical coinciding non-interface-fitted background meshes $\widehat{\mathcal{T}}_h^1 \equiv \widehat{\mathcal{T}}_h^2$. The active mesh parts $\mathcal{T}_h^1 \neq \mathcal{T}_h^2$, however, as well as their associated fictitious domains $\Omega_h^{1*} \supseteq \Omega_h^1$ differ. The set of elements intersected by the interface is $\Omega_h^{2*} \supseteq \Omega_h^2$, where $\mathcal{T}_h^1 \cap \mathcal{T}_h^2 = \mathcal{T}_\Gamma^1 = \mathcal{T}_\Gamma^2$.

Different computational approaches applicable to highly convective transient incompressible two-phase flow including high contrast in material properties have been developed. Classical FEM-based techniques make use of smoothed material properties and the interface is artificially thickened over a few element layers in the vicinity of the interface. This enables to numerically approximate smooth transitions of material characteristics as well as solution fields based on the underlying discrete finite element approximation space; see, e.g., works by Nagrath *et al.* [194], Groß *et al.* [136] and Marchandise and Remacle [178]. Surface-tension forces can be incorporated via a local volume force modeled by the continuum surface force approach established by Brackbill *et al.* [32]. Similar approaches in finite difference or finite volume frameworks have been proposed, e.g., by Sussman *et al.* [248]. An extensive survey of numerical methods for two-phase incompressible flows can be found in the textbook by Groß and Reusken [133].

Over the recent years, different XFEM/CUTFEM-based approaches to multiphase flows have been proposed. Originally established by Chessa *et al.* [72], Groß and Reusken [134] introduced a pressure enriched function space to sharply capture pressure discontinuities arising from surface-tension effects. Rasthofer *et al.* [214] developed an extended residual-based variational multiscale method utilizing a kink-enrichment strategy for the velocity field and different enrichment strategies for the pressure. Related works have been published by Sauerland and Fries [225]. Furthermore, enriched approaches towards premixed combustion applications have been considered; as first by van der Bos and Gravemeier [255]. In the context of this application field, Nitsche-type coupling techniques utilizing cut-cell-based flux averaging strategies for mainly laminar two-phase flow settings have been developed by Schott [229] and further enhanced to turbulent premixed combustion problem settings by Henke [147]. Further related works can be found in the literature overview provided in Section 2.2.1.

As discussed in the previous sections, the Nitsche-type RBVM/GP method analyzed in Section 4.2 in combination with the expanded cut finite element approximation space is expected to exhibit higher accuracy compared to the aforementioned FEMs but also improved stability over other CUTFEMs due to the GP stabilization technique and the use of expanded approximation spaces. To investigate the proposed Nitsche-type coupling, it is exemplarily applied to two different challenging examples incorporating fluid phases which exhibit highly different material properties: For classical incompressible two-phase flows, the well-established Rayleigh-Taylor instability is analyzed for different Atwood numbers including the effect of surface tension. Results for exponential growth rates obtained from numerical simulations can be compared to analytically deduced solutions. To emphasize the possibility of enforcing non-zero jump constraints even for the velocity field, an outlook towards premixed combustion applications is given by means of a laminar flame-vortex-interaction example. The subsequent elaborations on two-phase flows are based on work published by Schott and Rasthofer *et al.* [231] and with regard to premixed combustion the reader is referred to Schott [229] and Henke [147].

All subsequently presented simulations are computed with the stabilized Nitsche-type CUTFEM from Section 4.2 utilizing RBVM/GP stabilizations for both fluid phases on the respective time-dependent active mesh parts $\mathcal{T}_h^1, \mathcal{T}_h^2$. Their spatial approximations are based on non-interface-fitted computational grids consisting of linearly-interpolated $\mathbb{Q}^1$-elements. Interfacial constraints are weakly imposed using the adjoint-consistent Nitsche-type method. Upwinding schemes at the fluid interface are not applied for these examples. As identical meshes are utilized

in both fluid subdomains, the proposed flux weighting strategy reduces to a harmonic weighting which is purely based on the viscosities as elaborated in (4.56). The interface transport is computed by solving a scalar transport PDE for the level-set field ϕ, whose zero-isocontour represents the interface front as introduced in (2.50). Therein, the advective transport velocity $\boldsymbol{u}$ is given by the continuous flow solution for classical incompressible two-phase flows and by the absolute flame speed $\boldsymbol{u} = \boldsymbol{u}^i - s_L \cdot \boldsymbol{n}^{ij}$ for the considered premixed combustion application; for details see also elaborations in Section 4.1.1. The purely advective transport PDE is stabilized with an SUPG term and is constructed analogously to fluids as elaborated in Section 3.1.3.1. For the temporal discretizations, the OST scheme is applied with $\theta = 0.5$ for the transport solver and with $\theta = 1.0$ for the CUTFEM flow solver. Fluid flow and interface transport are alternately solved. For evaluating surface tension, the interface curvature κ is calculated based on formula (2.53). For further details, the reader is referred to works by Schott and Rasthofer *et al.* [231], Schott [229] and Henke [147].

4.4.1 A Rayleigh-Taylor Instability including Surface Tension

As a first example, the well-studied Rayleigh-Taylor-instability problem is considered to validate the proposed CUTFEM for classical two-phase flows. The evolution of a hydrodynamic instability of an interface separating two immiscible fluids, which are subjected to a gravitational force, is investigated. The goal is to quantify the accuracy of the computational approach in terms of growth rates obtained from the numerical simulations compared to analytical solutions. Moreover, the stabilizing effect of surface tension can be studied. This test case has been already established for such purposes in literature; see, e.g., works by Nourgaliev *et al.* [198], Popinet and Zaleski [208], Puckett *et al.* [212] and Pochet *et al.* [207].

The geometric and computational setup is described as follows: Within a rectangular domain $\Omega = (-L/2, L/2) \times (-H/2, H/2)$ with $L = 1.0$ and $H = 4.0$, two fluids are separated by a horizontal interface which is initially located at $x_2 = -h/2$ where h denotes the characteristic element length of the computational background mesh $\widehat{\mathcal{T}}_h$. The heavier of both fluids with a density ρ^+ is placed on top of the lighter fluid with density ρ^- (i.e. $\rho^- < \rho^+$). The flow is subjected to gravitational acceleration $g = 10.0$ which is initially perpendicular to the interface such that $\boldsymbol{f} = (0, -g)^{\mathrm{T}}$ in both fluid phases. Assuming a slight imperfection of the interface in terms of a single-mode perturbation $a_0 \cos(kx_1)$, where a_0 denotes its initial amplitude reached at $x_1 = 0$ and $k = 2\pi/L$ its wave number such that $\phi_0(x_1, x_2) = x_2 - a_0 \cos(kx_1) + h/2$, the gravitational force causes evolution of this disturbance in time. Depending on the material properties, the interface evolves differently and eventually becomes unstable over time. In contrast, if surface tension is present, this instability gets stabilized and its growth is damped. This instability can be characterized by two non-dimensional numbers, the Reynolds number and the Atwood number, which are defined as

$$\mathrm{Re} \overset{\text{def}}{=} \frac{\rho^+ \sqrt{Hg} L}{\mu^+} \quad \text{and} \quad \mathrm{At} \overset{\text{def}}{=} \frac{\rho^+ - \rho^-}{\rho^+ + \rho^-}.$$

For all simulations, the unfitted discretization consists of 64×256 $\mathbb{Q}^1$-elements. Periodic boundary conditions are applied at the side walls to mimic the periodicity of analytical reference solutions and no-slip boundary conditions are set at top and bottom walls. The velocity field is

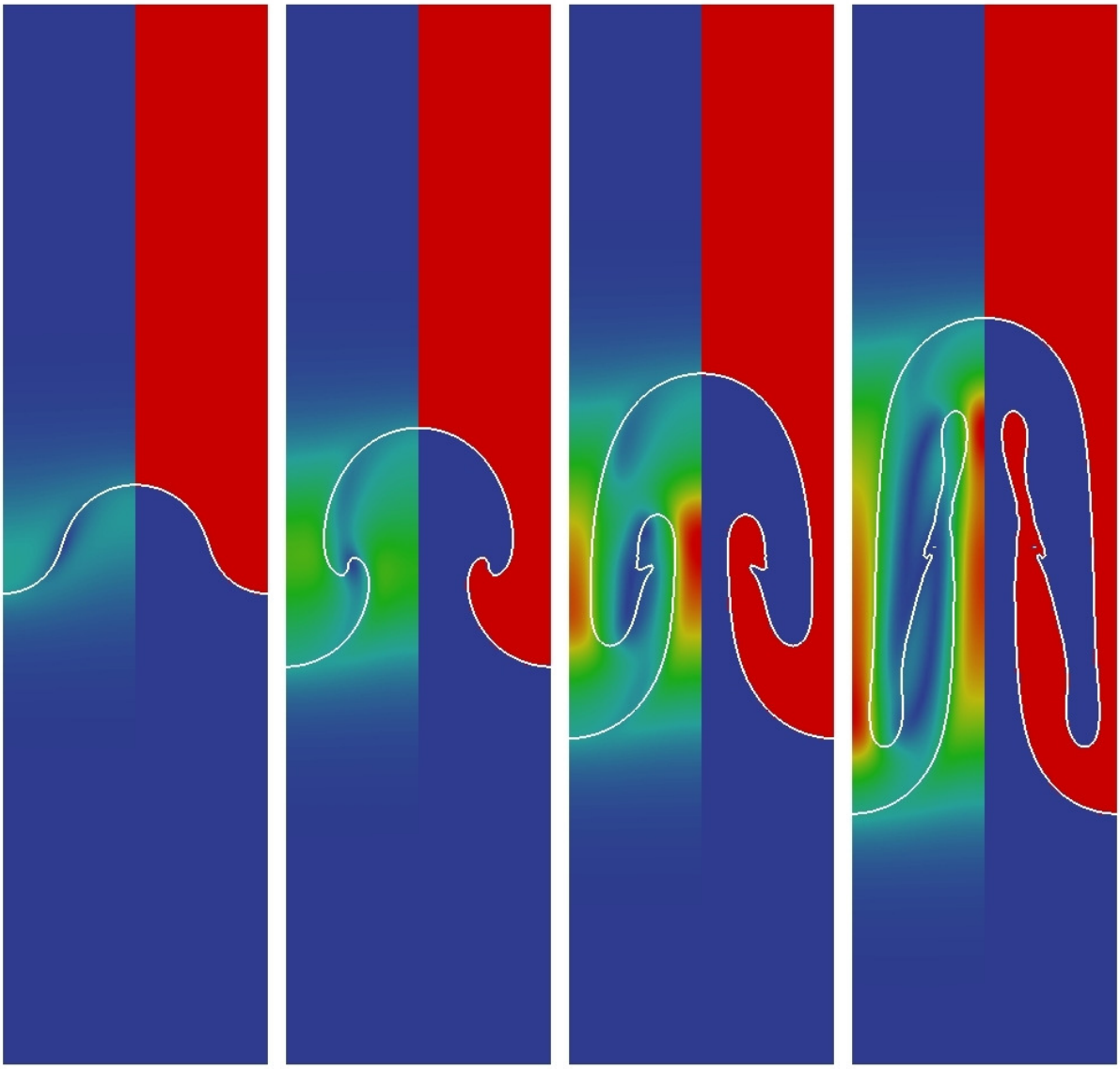

Figure 4.8: Rayleigh-Taylor instability with initial amplitude $a_0 = 0.005$, $\mathrm{Re} = 1000$ and $\mathrm{At} = 0.2$ at times $t = 1.5, 2.0, 2.5$ and 3.0 (from left to right): instantaneous velocity magnitude distribution are visualized on left half (red color indicates high velocity and blue color low velocity) and subdomains are indicated on right half of the figures, where Ω^+ is colored in red and Ω^- in blue.

initially at rest and for the temporal discretization a time-step length of $\Delta t = 0.005$ is used. For all considered settings, kinematic viscosities are assumed being equal, i.e. $\nu = \nu^+ = \nu^-$, and defined as $\nu^+ = \mu^+/\rho^+$ and $\nu^- = \mu^-/\rho^-$. In Figure 4.8, the evolution of an interface instability for a low density ratio is exemplarily depicted at various times t. For the visualized setting, the densities are chosen as $\rho^+ = 1.5$ and $\rho^- = 1.0$ and the kinematic viscosity is $\nu = 0.006349$ resulting in dynamic viscosities $\mu^+ = 0.009535$ and $\mu^- = 0.006349$ for the two fluids. The two dimensionless numbers yield to $\mathrm{Re} = 1000$ and $\mathrm{At} = 0.2$. The initial amplitude for this setting was set equal to $a_0 = 0.005$.

Following the elaborations by Chandrasekhar [70], in the initial stage the growth of the interface disturbance is in accordance with linear stability theory. An initial perturbation a_0 is expected to grow exponentially in time, i.e.

$$a(t, x_1 = 0) = a_0 \exp(\alpha t) \tag{4.70}$$

with a growth rate α. An analytical relation between the growth of the initial perturbation a_0 and characteristic properties has been deduced in [70]. Defining a non-dimensional wave number as $k^* = (\nu^2/g)^{\frac{1}{3}} k$ and a non-dimensional growth rate as $\alpha^* = (\nu/g^2)^{\frac{1}{3}} \alpha$, the following relation holds

$$\alpha^* = [(y(k^*))^2 - 1] \cdot (k^*)^2, \tag{4.71}$$

where $y(k^*)$ is the solution of the fourth-order polynomial

$$y^4 + y^3(4\delta^*) + y^2(2 - 12\delta^*) - y(4 - 12\delta^*) + (1 - 4\delta^*) - (k^*)^{-3}\,\mathrm{At} + (k^*)^{-1}\iota^* = 0. \tag{4.72}$$

Therein, the surface-tension coefficient ι is non-dimensioned as $\iota^* = \iota/[(\rho^+ + \rho^-)(g\nu^4)^{1/3}]$ and the parameter δ^* is defined as $\delta^* = \delta^+\delta^-$, where $\delta^+ = \rho^+/(\rho^- + \rho^+)$ and $\delta^- = \rho^-/(\rho^- + \rho^+)$. For given k^* and densities, equation (4.72) can be numerically solved for its root $y(k^*)$ using Newton's method.

The growth of an initial disturbance is examined for two different ratios of densities: for a lower density ratio $\rho^+/\rho^- = 1.5$ with $\rho^- = 1.0$ resulting in $\mathrm{At} = 0.2$ and for a higher density ratio of $\rho^+/\rho^- = 1000$ with $\rho^+ = 1.0$ and $\rho^- = 0.001$ resulting in $\mathrm{At} = 0.998$. Initial amplitudes are chosen as $a_0 = 0.005$ for the lower density ratio and as $a_0 = 0.0001$ for the higher one.

For all simulations, k^* is adapted by varying the kinematic viscosity $\nu = \nu^+ = \nu^-$. To determine α corresponding to the numerical simulations, a linear least-squares fit is utilized within the time interval which exhibits the exponential growth. The analytical relation between k^* and α^* for the low-density-ratio case $\rho^+/\rho^- = 1.5$ is displayed in Figure 4.9a, and the computed growth rates are indicated by markers. Figure 4.9b illustrates the linear fit of the simulation data. Results for the high-density-ratio case $\rho^+/\rho^- = 1000$ are shown in Figure 4.10a and Figure 4.10b, respectively. An excellent agreement between analytical solution and numerical results over a wide range of wave numbers can be observed for both density ratios. This underlines the high accuracy of the proposed CutFEM solver.

In Figure 4.11, the effect of surface tension on growth rates of such instabilities is demonstrated. For this study, the dimensionless wave number is fixed to $k^* = 1.0$ and densities are taken from the low density ratio, set to $\rho^+ = 1.5$ and $\rho^- = 1.0$. Increasing the surface-tension coefficient ι damps the evolution of the instability until the unstable behavior converts into a stable one. At a certain critical surface-tension coefficient, the initial perturbation of the interface remains constant over time with $\alpha^* = 0$. This value is perfectly matched by the computational approach and results for varying surface tension are in excellent agreement with the analytically predicted damping behavior which highlights the accuracy provided by this computational approach. This example clearly demonstrates the high capabilities of the proposed CutFEM fluid solver for classical incompressible two-phase flow including surface tension.

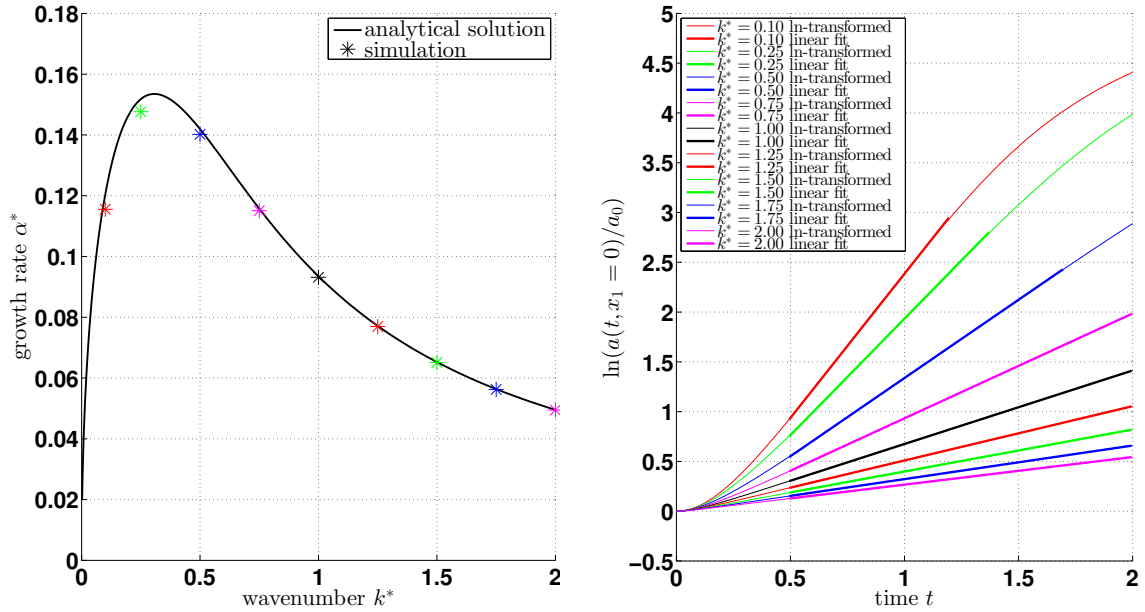

(a) (b)

Figure 4.9: Rayleigh-Taylor instability with a low density ratio $\rho^+/\rho^- = 1.5$ (At $= 0.2$, $a_0 = 0.005$): (a) comparison of non-dimensional growth rates α^* obtained from simulations with analytical solution for different non-dimensional wave numbers k^*, (b) linear fit of transformed amplitudes $\ln(a(t, x_1 = 0)/a_0)$ at interface front over time.

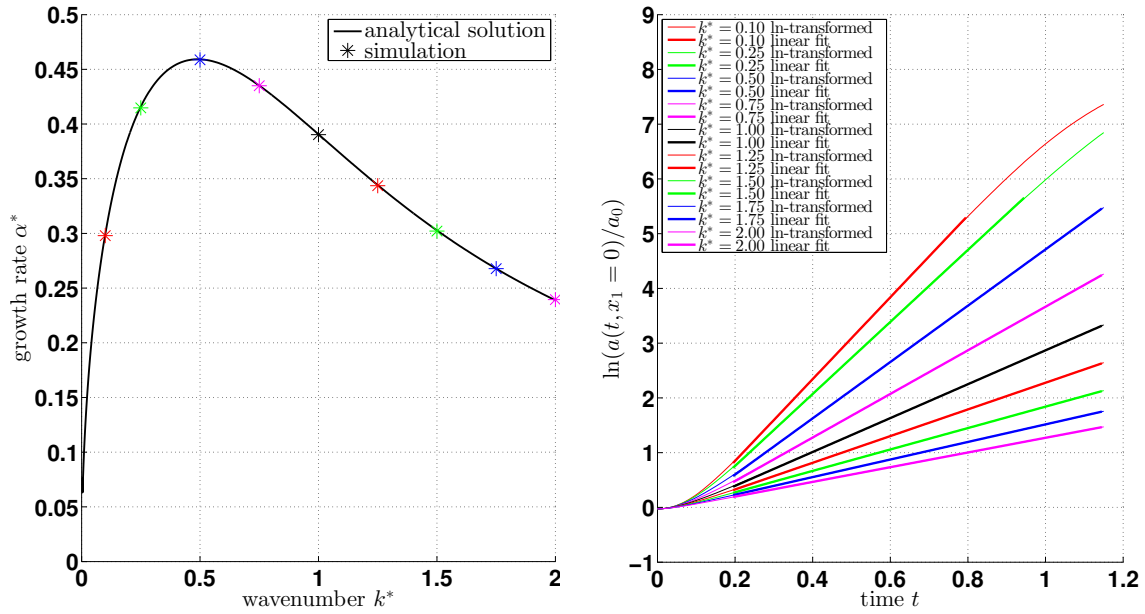

(a) (b)

Figure 4.10: Rayleigh-Taylor instability with a high density ratio $\rho^+/\rho^- = 1000$ (At $= 0.998$, $a_0 = 0.0001$): (a) comparison of non-dimensional growth rates α^* obtained from simulations with analytical solution for different non-dimensional wave numbers k^*, (b) linear fit of transformed amplitudes $\ln(a(t, x_1 = 0)/a_0)$ at interface front over time.

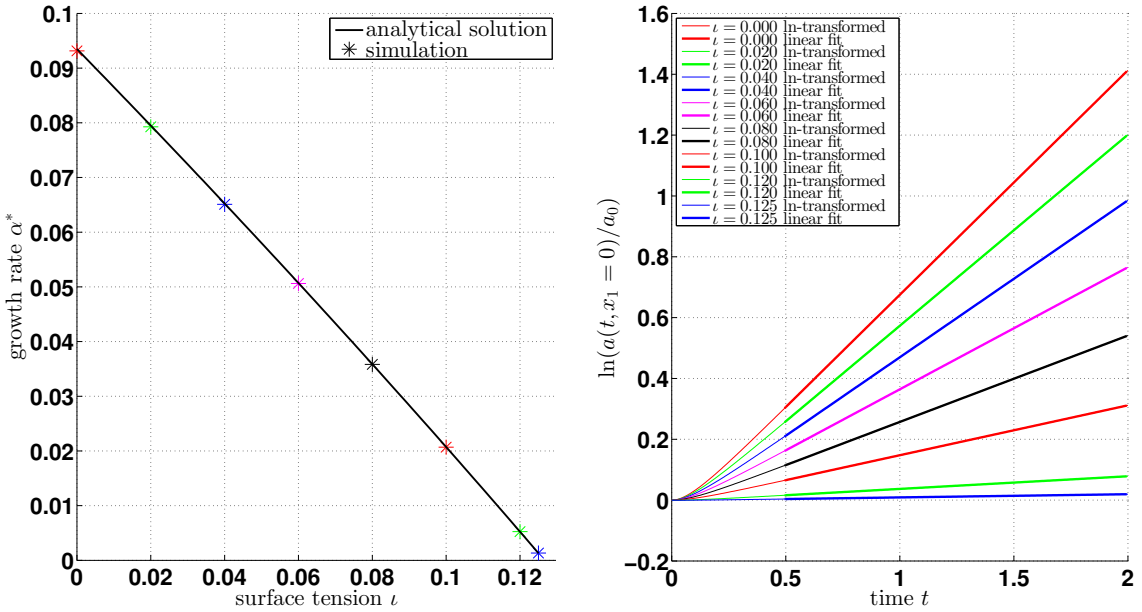

(a) (b)

Figure 4.11: Rayleigh-Taylor instability with a low density ratio $\rho^+/\rho^- = 1.5$ ($k^* = 1.0$, At $= 0.2$, $a_0 = 0.005$): (a) damping of non-dimensional growth rate α^* for increasing dimensional surface tension ι compared to analytical relation, (b) linear fit of transformed amplitudes $\ln(a(t, x_1 = 0)/a_0)$ at interface front over time.

4.4.2 Premixed Combustion - A Flame-Vortex Interaction

To finally highlight the versatility of the two-phase CUTFEM solver developed throughout this chapter, as a last example for incompressible two-phase flows a premixed combustion model problem is investigated. Fundamentals of a potential and rather elementary modeling approach to the underlying physics based on the conservation laws for mass and momentum have been introduced in Section 4.1.1. At this stage it should be pointed out that details of premixed combustion modeling and its underlying physics cannot be comprehensively presented within the scope of this thesis. For further details, the reader is referred to extensive derivations by, e.g., Williams [270]. The subsequent considerations rather shall give an outlook to possible application fields for the cut finite element methodology and demonstrate the contribution and further developments of this work in view of more robust and accurate unfitted computational approaches required for such demanding applications.

A detailed survey on different computational methods as well as modeling approaches towards premixed combustion is given in the thesis by Henke [147]. Moreover, in the latter work, an extended finite element method has been developed and algorithmically coupled with a G-equation approach for the transport of the flame front. The fundamental techniques introduced and observations made therein are the basis for further developments made throughout this thesis, as will be discussed subsequently. As concluding remarks, two fundamental issues of XFEM-based approaches existing so far have been formulated by Henke [147]: a limited representability of the fluid fields in zones of high interface curvature and the numerical issue of providing a stable cut finite element approximation in the vicinity of the interface. Both of these aspects are

highly improved by the present CUTFEM solver. The first issue is accounted for by the usage of an expanded cut finite element approximation space introduced in Section 2.2.5, and the second one by developing the stabilized Nitsche-type RBVM/GP formulation for moving domains as proposed in Section 4.2 and analyzed for single-phase flows throughout Chapter 3.

The well-studied flame-vortex interaction serves as test example in which a pair of counter-rotating vortices interacts with a premixed flame front. Such types of interactions have been investigated in various settings. While experiments have been presented in works by, e.g., Roberts and Driscoll [221] and Mueller *et al.* [192], computational approaches based on different frameworks have been developed, for which this vortex interaction has been studied; see, exemplarily, Hartmann *et al.* [145] for a cut-cell flow solver in a finite volume framework, Gravemeier and Wall [129] for a finite-element-based progress-variable approach and Henke [147] for an extended finite element method.

The setup of this example follows the description by Henke [147]. An initially horizontal flame front with flame speed $s_\mathrm{L} = 1.0$ is embedded into a box-shaped overall domain of size $\Omega_h = (0, 100) \times (0, 200)$. It is defined implicitly by the isocontour of $\phi(\boldsymbol{x}, t_0) = x_2 - 100$. The subdomain $\Omega_h^1 \subset \Omega_h$ is defined by points carrying negative level-set values and contains the unburned fluid phase, whereas $\Omega_h^2 = \Omega_h \backslash \Omega_h^1$ denotes the burned gas correspondingly. At $x_2 = 0$, an inlet of unburned fluid into the domain is given by $\boldsymbol{u} = (0, s_\mathrm{L})$. As the flame speed equals the inflow speed, the interface is in a steady state initially. Furthermore, no-slip boundary conditions are prescribed at the side-walls $x_1 = 0$ and $x_1 = 100$ as well as a zero-traction Neumann outflow condition at $x_2 = 200$. Due to the combustion process, the fluid gets accelerated in normal direction to the flame front. For given fluid properties $\rho^1 = 1.16$, $\rho^2 = 0.157$ and $\mu^1 = 0.812$, $\mu^2 = 2.88$ taken from [147], utilizing relation (4.13) the initial unperturbed flow velocity for the unburned phase is constant, i.e. $\boldsymbol{u}^\mathrm{pc}|_{\Omega_h^2} = (0, s_\mathrm{L} - \rho^1 s_\mathrm{L} [\![\rho^{-1}]\!])$. The resulting piecewise constant flow field $\boldsymbol{u}^\mathrm{pc}$ is superposed by two counter-rotating vortices, which interact with the flame. Their centers are located at $\boldsymbol{x}_\mathrm{l} = (37.5, 75)$ and $\boldsymbol{x}_\mathrm{r} = (62.5, 75)$ with stream functions

$$\Psi_\mathrm{l,r}(\boldsymbol{x}) \overset{\text{def}}{=} C_\mathrm{l,r} \exp\left(-\frac{\|\boldsymbol{x} - \boldsymbol{x}_\mathrm{l,r}\|^2}{2R^2}\right) \tag{4.73}$$

with center peak values $C_\mathrm{l} = 70, C_\mathrm{r} = -70$ and a radius $R = 4$. The resulting vortex induced velocity components are given as $u_1^\mathrm{vort} = \frac{\partial(\Psi_\mathrm{l}+\Psi_\mathrm{r})}{\partial y}$ and $u_2^\mathrm{vort} = -\frac{\partial(\Psi_\mathrm{l}+\Psi_\mathrm{r})}{\partial x}$ such that the final initial flow field in Ω_h can be prescribed as $\boldsymbol{u}_0 = \boldsymbol{u}^\mathrm{pc} + \boldsymbol{u}^\mathrm{vort}$, which exhibits the desired jump arising from the combustion model. The initial flow setting and its evolution over time is depicted in Figure 4.12. The visualized results have been computed on a relatively coarse regular mesh $\widehat{\mathcal{T}}_h$ consisting of 65×129 $\mathbb{Q}^1$-elements; see [147] for studies on the effect of different mesh sizes on capturing topological characteristics of this flame-vortex interaction. The approximation is based on the stabilized RBVM/GP technique and an OST scheme with $\theta = 1.0$ and $\Delta t = 0.15$ for an overall simulation time of $T = 30$. Reinitialization of the level-set field has been performed every time step. For its need and impact on the interface shape, the reader is referred to [147].

Initially, due to the inlet of fresh gas at the bottom boundary, the vortices are convected upwards to the horizontal flame front. When their area of influence reaches the flame front, the higher flow velocity between the two vortices first cause the formation of a tongue-shaped interface. For the given strength of vortices, it is expected to elongate and form a mushroom-shaped pocket, which afterwards secludes. In this computation, the pinch-off time for this drop-like structure is given as $t \approx 23.1$ and takes place slightly earlier than reported by Henke [147].

Similar to [147], this pocket moves upwards and is fully burned after $t \approx 24.6$. The earlier detachment is due to a more accurate flow representation for high-curvature interfaces enabled by the expanded approximation space at times when flame fronts are approaching, as visualized in Figure 2.19. The flow solution of the burned fluid phase in the vicinity of the thin-neck-shaped unburned fluid subdomain can be accurately captured due to independent sets of DOFs for both sides of the burned subdomain. Details of this advantageous novel enriching strategy for CutFEMs have been presented in Section 2.2.5. As a second substantial improvement compared to the approach established in [147], the stability of the proposed CutFEM flow solver is highlighted. Independent of the position of the flame front with respect to the underlying unfitted computational grid, stable velocity and pressure solutions are obtained for both fluid phases, in particular, also in the vicinity of the interface and despite the presence of topological changes. This is due to the introduced ghost-penalty stabilization technique and the adapted Nitsche-type coupling for two-phase flows.

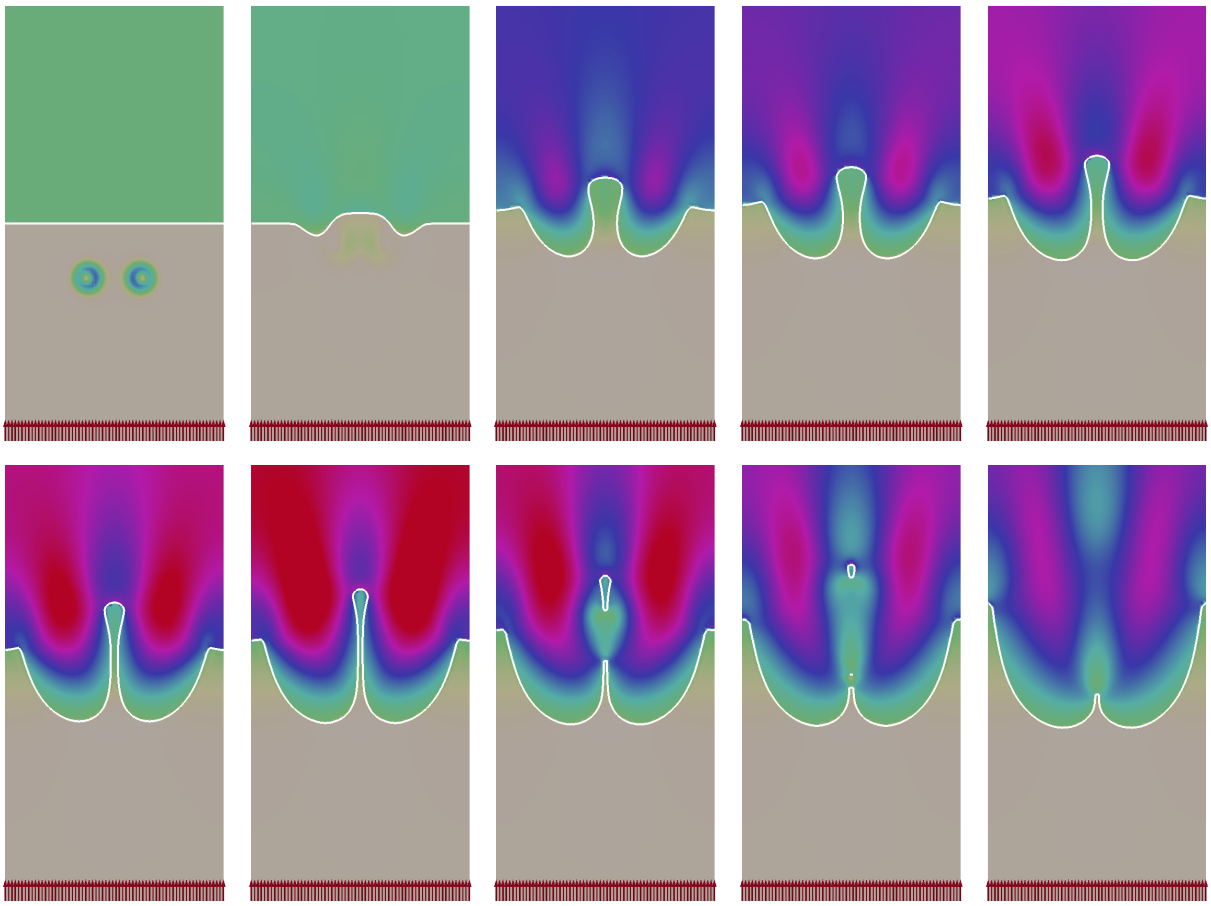

Figure 4.12: Flame-vortex interaction: time evolution of the flame front at different times $T_0 = 0.0$, $T_1 = 15.0$, $T_2 = 19.5$, $T_3 = 20.25$, $T_4 = 21.0$, $T_5 = 21.75$, $T_6 = 22.5$, $T_7 = 23.25$, $T_8 = 24.0$, $T_9 = 24.75$ (from left to right and from top to bottom). Inlet of fresh gas at bottom side drives the evolution and convects the vortices. The flame front is indicated by a white line at which the flow solution exhibits a jump in velocity and pressure. Subdomains belonging to unburned and burned fluid phases are colored by velocity magnitude (gray/red colors indicate low/high velocity scaled within $[0, 20]$).

Chapter 5

Stabilized Approaches to Fluid-Structure Interaction using Cut Finite Elements

This chapter aims at extending cut finite element approaches and coupling techniques, which have been developed throughout Chapter 3 for single-phase flows and adapted to domain decomposition and multiphase flows in Chapter 4, to one of the most frequent and important multiphysics phenomena – fluid-structure interaction (FSI). Internal flows which interact with deformable structural boundaries or surround movable and compressible structures occur in various different fields of industrial, biological and medical engineering. Depending on flow characteristics and material properties of fluids and solids, different and often highly dynamical effects may appear which are in general too complex to get analytically predicted. In particular in biomedical settings, even experiments are limited in their applicability and measuring physical quantities of interest is often difficult to realize. In such cases numerical simulations provide a powerful tool to support such purposes. Among many others, due to these reasons the benefit of computational approaches for capturing such challenging physical phenomena is undisputed.

Over the recent years, their range of applicability has been expanded to various biomedical settings [169], for instance, considering the blood flow in arteries and veins, simulating opening and closing processes of heart valves, up to predicting rupture risks of abdominal aortic aneurysm in the human body [177]. Examples in industrial environments are flows induced by largely moving or rotating components, like ship or helicopter propellers. But also the other way around, studying the impact of fluid flow on structural motions as, for instance, on rotor blades of wind turbines [16] or aircraft wings is of high interest. The usability of computational FSI approaches includes also biological and chemical scientific fields. As an example, recent developments have been made to support investigations on different formations of biofilm architectures living in complex flow environments. There, computational approaches are applied to reliably predict their growth within a surrounding fluid as well as their interaction with that [77, 249]. Further potential application fields are summarized in the introduction Chapter 1.

An Overview of Computational Approaches for Fluid-Structure Interaction. Most popular and widely used computational FSI approaches are based on ALE techniques and use interface-fitted grids for the fluid and solid subdomains as described in Section 2.1.4.2 and visualized in Figures 2.7 and 2.8. This well-established technique dates back to early works

by Hirt *et al.* [150], Donéa *et al.* [89], Belytschko and Kennedy [22], Belytschko *et al.* [23], Hughes *et al.* [155] and Donéa *et al.* [90]. Therein, a Lagrangean formalism for the structure is combined with an arbitrary Eulerian description of the flow field whose computational grid follows the fluid-solid interface in its motion. The major advantage of this technique is that the computational meshes are not changed over time and utilizing refined meshes in the vicinity of the interface allows to accurately capture flow characteristics. This methodology has been further developed over the recent decades with regard to different aspects. Stabilized finite element methods for FSI have been established by Wall [258] and Förster [110]. Efficiency of different solution strategies has been investigated by Küttler [168] and the effect of single-field predictors on monolithically solved fluid-structure-interaction systems has been studied by Mayr *et al.* [185]. An overview of general challenges and directions in computational fluid-structure interaction has been given by Bazilevs *et al.* [17].

As elaborated in Section 2.1.4.2, interface-fitted moving mesh approaches lack accuracy and robustness or even may totally fail due to mesh distortion in case of too large structural motions or deformations. Such issues have been addressed in several publications, see, e.g., the article by Le Tallec and Mouro [171] and the publication by Wall *et al.* [259] for an introduction to this topic. Different attempts to relax the strong constraints on interface motion in FSI have been made. Klöppel *et al.* [164] integrated dual mortar interface coupling methods into ALE-based FSI frameworks to cope with non-conforming meshes at the fluid-structure interface and so to enable large rotational motions. Non-matching discretizations in the framework of isogeometric FSI have been considered by Bazilevs *et al.* [16] and successfully applied to simulate the FSI of wind turbines. Recently, Farhat and Lakshminarayan [104] proposed an ALE formulation of embedded boundary methods for tracking boundary layers in turbulent FSI problems. The key idea of this approach is that non-interface-fitted embedded meshes are rigidly translated and/or rotated to track the rigid component of the dynamic body motion.

A class of FSI approaches which enables to overcome the difficulty of mesh distortion inherent to moving mesh techniques are the so-called *fixed-grid methods*. While structural dynamics are still described in a Lagrangean formalism, the fluid flow is approximated on a fixed non-interface-fitted non-moving computational grid. This allows the structure to arbitrarily move within the fluid mesh. The solid mesh, which overlaps with the fluid grid, decomposes the latter one into an active physical fluid subdomain and an inactive subdomain covered by the structural domain. This part of the fluid mesh is often referred to as fictitious domain. Fixed-grid schemes differ in the numerical treatment of this overlap region, i.e. in the enforcement of the coupling constraints at the FSI interface as well as in the solution technique applied to the overall fluid-solid system.

Early fixed-grid schemes, for which lots of modifications and variations have been proposed over many decades, belong to the class of *Immersed Boundary* (IB) methods. This methodology can be traced back to methods by Peskin [201] and Peskin [202], which were used to simulate flow patterns around heart valves. An introduction to the IB method can be found in the work by Peskin [203]. Therein, structural variables are formulated in a Lagrangean frame of reference and fluid variables are observed from an Eulerian view point. These are linked by equivalent volumetric force terms within the fluid domain. Such incorporated interaction equations involve smoothed approximations to the Dirac-delta function. Further, appropriate transfer operators for data between the two meshes are required. Adaption based on higher-order reproducing kernel approximations to the incorporated delta function has been proposed by Zhang *et al.* [276], called

the Immersed Finite Element Method, and developments on an Extended Immersed Boundary Method have been provided by Wang and Liu [264]. An extensive survey on IB methods and other Cartesian grid methods can be found in an overview article by Mittal and Iaccarino [187].

For most of the IB approaches, the coupling of fluid and solid phases takes place at the fictitious fluid domain which does not exhibit physical meaning. Smeared approximations and often induced artificial incompressibility to the structural field are sources of inaccuracy and are desired to be avoided, as discussed by Wall *et al.* [260]. In the latter publication, different domain decomposition ideas for fluid-structure interaction based on fixed fluid grids have been introduced. As reviewed in Section 2.1.4.3, utilizing unfitted cut finite element approximations for the fluid field, overlapped by a structural mesh which fits to the fluid-solid interface, allows for sharp approximations of the flow field. Different XFEM-based interface-coupling strategies have been developed over the recent years and applied to FSI problems. Gerstenberger and Wall [124] investigated the use of Lagrange multipliers with unfitted overlapping discretizations for FSI. A combination of fixed-grid and ALE techniques applied to FSI has been proposed by Baiges and Codina [9], a technique which is called *fixed-mesh ALE approach*. Gerstenberger [123] established a stress-based Lagrange-multiplier method for the weak constraint enforcement of coupling conditions. The latter methodology has been expanded to XFEM-based fluid-structure-contact-interaction problem settings by Mayer *et al.* [184], which enables simulating contact of submersed bodies. Extensions of related methods towards fluid-structure-fracture interaction have been developed by Sudhakar [244]. Fully Eulerian formulations have been introduced by Wick [268] and Richter [219]. Court *et al.* [80] developed a stabilized Lagrange-multiplier-based fictitious domain approach applicable to XFEM-based Stokes flow approximations. This has been extended to FSI by Court and Fournié [79] in which the flow is governed by the incompressible Navier-Stokes equations. Recently, a Nitsche-based CUTFEM for FSI has been analyzed by Burman and Fernández [58] for Stokes flow interacting with linear elastic structures. A comparison of various coupling strategies of an incompressible fluid with immersed thin-walled structures has been recently provided by Alauzet *et al.* [1]. Moreover, different formulations applicable to fixed-grid methods based on utilizing an additional embedded fluid patch, which fits to the fluid-structure interface but overlaps with a fixed background fluid grid in an unfitted fashion, as visualized in Figure 2.11c, have been developed in the thesis by Shahmiri [235] and considered further in an article by Massing *et al.* [181].

Computational FSI approaches require strategies for coupling the fluid and the structural subproblems. Two different classes of coupling techniques can be distinguished: staggered or partitioned schemes and full-implicitly or monolithically solved schemes. For latter methods, fluid and structural equations including coupling constraints are set up as one global non-linear system which is solved for discrete fluid and structural approximations at once. The advantage of this methodology is the incorporated robustness and temporal stability for time-stepping schemes, even though their solution entails high computational costs. Newton or pseudo-Newton methods for approximating the solution of resulting global systems have been considered, e.g., in works by Fernández and Moubachir [107], Küttler and Wall [170] or Mayr *et al.* [185]. Monolithic algebraic multigrid techniques have been developed by Gee *et al.* [121] and preconditioning techniques for the efficient solution of such coupled systems have been introduced by Verdugo and Wall [256]. To reduce computational complexity and to allow for flexibility in coupling different code environments for the single fluid and structural subproblems, partitioned schemes are often attractive and widely used. However, in contrast to full-implicitly coupled

methods, time advancing schemes which only explicitly couple the two subproblems, without iterating until convergence between the two fields has been achieved, exhibit stability issues. Strong added-mass effects have been observed and studied in the works by, e.g., Causin *et al.* [69] and Förster *et al.* [111]. Fixed-point iteration schemes incorporating dynamic relaxation for convergence acceleration have been investigated by Küttler and Wall [170] and partitioned procedures utilizing Robin transmission conditions and algebraic splitting schemes have been developed by Badia *et al.* [7] and Badia *et al.* [8]. To cope with instabilities arising from time advancing schemes, stabilized explicit coupling schemes have been introduced by Burman and Fernández [39] and further developed by Burman and Fernández [40, 59], Fernández *et al.* [106] and Fernández *et al.* [108]. A comprehensive comparison of full-implicit, semi-implicit and explicit coupling strategies for fitted mesh FSI approaches has been presented by Fernández [105]. Extensions to unfitted mesh methods have been recently made by Alauzet *et al.* [1]. For the sake of completeness, besides classical time-stepping schemes, also space-time FEM-based computational FSI approaches have been developed; see, e.g., the works by Tezduyar *et al.* [253], Legay *et al.* [172], Zilian and Legay [278] and Legay *et al.* [173].

This chapter is outlined as follows: In Section 5.1, a classical finite element formulation for non-linear structural elastodynamics is reviewed. An initial boundary value problem is formulated in its strong and variational form and a FEM-based spatial approximation combined with a temporal generalized-α time-stepping scheme is provided. Afterwards, in Section 5.2 fundamentals of modeling physics at fluid-structure interfaces are presented and an initial boundary value problem for the coupled FSI system is formulated. Section 5.3 is devoted to the development of a stabilized CutFEM-based FSI solver. In analogy to the coupling between distinct fluid phases, a semi-discrete stabilized Nitsche-type method for the coupling of a single incompressible fluid with a compressible elastic structural body is introduced. Peculiarities with regard to stability will be pointed out. Afterwards, the final full-implicitly coupled finite-dimensional system of non-linear residuals is formulated and iterative solution techniques are suggested. Therein, focus is turned to the issue of potential changes of the fluid approximation space. The performance of the proposed unfitted FSI solver is demonstrated by challenging test examples. In Section 5.4, the unfitted FSI coupling scheme is enhanced by combining it with the unfitted fluid domain decomposition technique provided in Sections 4.2 and 4.3 and a powerful unfitted Nitsche-type fluid-fluid-structure coupling is set up. Concluding, its high versatility for a variety of FSI applications is demonstrated by means of a challenging FSI problem.

5.1 A Finite Element Method for Structures

In the following, fundamentals on structural dynamics and kinematics are recalled. An initial boundary value problem is formulated and a classical FEM approximation utilizing boundary-fitted structural meshes is reviewed. Details on structural time-stepping are discussed.

5.1.1 Governing Equations for Solid Mechanics

Throughout this thesis, the structural field is assumed to be governed by the non-linear elastodynamics equations. Fundamentals of solid mechanics are briefly reviewed in the following. More detailed explanations can be found in textbooks by, for example, Wriggers [272] or Zienkiewicz and Taylor [277].

Kinematic Relations. Under the assumption of moderate structural deformations it is common to observe structural dynamics from a Lagrangean view point. The observer then follows a material particle $\boldsymbol{X}$ in its motion from reference configuration $\Omega_0^{\mathrm{s}} = \Omega^{\mathrm{s}}(T_0)$ to current configuration $\Omega^{\mathrm{s}}(t)$ which mathematically can be expressed in terms of the mapping $\boldsymbol{\varphi}$, as introduced in (2.5). Then, kinematics can be formulated by means of the unknown displacement field $\boldsymbol{d}$ between current and initial particle position and its first- and second-order time derivatives, the velocity and acceleration fields $\boldsymbol{u}$, $\boldsymbol{a}$, as

$$\boldsymbol{d}(\boldsymbol{X},t) \stackrel{\text{def}}{=} \boldsymbol{x}_{\boldsymbol{X}}(\boldsymbol{X},t) - \boldsymbol{X} \qquad \forall\, \boldsymbol{X} \in \Omega^{\mathrm{s}}(T_0), \tag{5.1}$$

$$\boldsymbol{u}(\boldsymbol{X},t) \stackrel{\text{def}}{=} \frac{\mathrm{d}\boldsymbol{d}(\boldsymbol{X},t)}{\mathrm{d}t} = \dot{\boldsymbol{d}}(\boldsymbol{X},t) \qquad \forall\, \boldsymbol{X} \in \Omega^{\mathrm{s}}(T_0), \tag{5.2}$$

$$\boldsymbol{a}(\boldsymbol{X},t) \stackrel{\text{def}}{=} \frac{\mathrm{d}^2\boldsymbol{d}(\boldsymbol{X},t)}{\mathrm{d}t^2} = \ddot{\boldsymbol{d}}(\boldsymbol{X},t) \qquad \forall\, \boldsymbol{X} \in \Omega^{\mathrm{s}}(T_0) \tag{5.3}$$

with $\boldsymbol{d}, \boldsymbol{u}$ and $\boldsymbol{a}$ given in material description at any time t. In continuum mechanics, the gradient tensor of the spatial part of the invertible mapping $\boldsymbol{\varphi}$, i.e. $\boldsymbol{x}_{\boldsymbol{X}}$ from (2.5), is often called *deformation gradient tensor*

$$\boldsymbol{F}(\boldsymbol{X},t) = \frac{\partial \boldsymbol{x}_{\boldsymbol{X}}(\boldsymbol{X},t)}{\partial \boldsymbol{X}} = (\boldsymbol{I} + \frac{\partial \boldsymbol{d}}{\partial \boldsymbol{X}})(\boldsymbol{X},t) \tag{5.4}$$

and depends on $\boldsymbol{d}$. Its determinant is notated with $J_{\boldsymbol{X}\mapsto\boldsymbol{x}} \stackrel{\text{def}}{=} \det(\boldsymbol{F}(\boldsymbol{X},t))$. Performing polar decomposition into a volume-preserving orthonormal rigid body rotation $\boldsymbol{R}$ and a symmetric positive definite stretch part $\boldsymbol{U}$ such that

$$\boldsymbol{F} = \boldsymbol{R} \cdot \boldsymbol{U}, \tag{5.5}$$

the symmetric *right Cauchy-Green tensor* can be defined as

$$\boldsymbol{C} \stackrel{\text{def}}{=} \boldsymbol{F}^T \cdot \boldsymbol{F} = \boldsymbol{U}^T \cdot \boldsymbol{R}^T \cdot \boldsymbol{R} \cdot \boldsymbol{U} = \boldsymbol{U}^T \cdot \boldsymbol{U} = \boldsymbol{U}^2, \tag{5.6}$$

which clearly exhibits an invariance under rigid body rotations. For solids subjected to large deformations but moderate stretching or compressing, the *Green-Lagrange strain tensor*

$$\boldsymbol{E} \stackrel{\text{def}}{=} \frac{1}{2}(\boldsymbol{F}^T \cdot \boldsymbol{F} - \boldsymbol{I}) = \frac{1}{2}(\boldsymbol{C} - \boldsymbol{I}) \tag{5.7}$$

serves as suitable strain measure defined in material configuration. This measure further ensures zero strain in the initial configuration.

Constitutive Laws. Introducing constitutive laws starts from Cauchy's first equation of motion, which results from balance of linear and angular momentum and was deduced for material configuration in (2.36) and (2.37). Transforming between current and reference configuration, the following relation between the physical symmetric Cauchy stress tensor $\boldsymbol{\sigma}_{\boldsymbol{x}}$, which is associated to the *a priori* unknown current configuration, as obtained from Cauchy's fundamental lemma in (2.33), and the non-symmetric two-point first Piola–Kirchhoff stress tensor $\boldsymbol{P}$ emerges as

$$\boldsymbol{P} \stackrel{\text{def}}{=} \boldsymbol{\sigma}_{\boldsymbol{X}} = J_{\boldsymbol{X}\mapsto\boldsymbol{x}} \boldsymbol{\sigma}_{\boldsymbol{x}} \cdot \boldsymbol{F}^{-T}. \tag{5.8}$$

Equivalently, a symmetric stress tensor in reference configuration can be constructed as

$$\boldsymbol{S} \overset{\text{def}}{=} \boldsymbol{F}^{-1} \cdot \boldsymbol{P} = J_{\boldsymbol{X}\mapsto\boldsymbol{x}} \boldsymbol{F}^{-1} \cdot \boldsymbol{\sigma}_{\boldsymbol{x}} \cdot \boldsymbol{F}^{-T}, \tag{5.9}$$

which is called *second Piola–Kirchhoff stress tensor*.

Depending on the material model, different relations between strain and stress measures can be employed. An extensive overview about different constitutive laws can be found in, e.g., the textbook by Holzapfel [152]. For the sake of simplicity only homogeneous structural bodies that exhibit hyper-elastic material behavior are considered throughout this thesis. Assuming the existence of a so-called strain-energy function $\tilde{\Psi}(\boldsymbol{C}) = \Psi(\boldsymbol{E})$ the second Piola–Kirchhoff stress tensor is defined as

$$\boldsymbol{S} = 2\frac{\partial \tilde{\Psi}}{\partial \boldsymbol{C}} = \frac{\partial \Psi}{\partial \boldsymbol{E}}, \tag{5.10}$$

where the dependency solely on the Cauchy-Green tensor implies objectivity and thus independence of rigid body rotations $\boldsymbol{R}$.

Exemplarily, strain energy functions for two material models used in this work are presented next. The *St.-Venant–Kirchhoff* (SVK) material behavior is modeled with a strain energy function which is quadratic in the strain variable and thus relates Green-Lagrange strains $\boldsymbol{E}$ and second Piola–Kirchhoff stresses $\boldsymbol{S}$ linearly as

$$\Psi_{\text{SVK}}(\boldsymbol{E}) \overset{\text{def}}{=} \frac{\lambda^{\text{s}}}{2}(\text{tr}\,(\boldsymbol{E}))^2 + \mu^{\text{s}} \boldsymbol{E} : \boldsymbol{E} \tag{5.11}$$

with λ^{s} and μ^{s} the Lamé parameters, which can be expressed in terms of Young's modulus $E^{\text{s}} > 0$ and Poisson's ratio $\nu^{\text{s}} \in (-1, 0.5)$ as

$$\lambda^{\text{s}} = \frac{E^{\text{s}}\nu^{\text{s}}}{(1+\nu^{\text{s}})(1-2\nu^{\text{s}})} \quad \text{and} \quad \mu^{\text{s}} = \frac{E^{\text{s}}}{2(1+\nu^{\text{s}})}. \tag{5.12}$$

In contrast to the St.-Venant–Kirchhoff model, which exhibits non-linearity only in a geometric sense, the strain energy function for *Neo-Hookean* (NH) materials introduces a non-linear relationship between strains and stresses as

$$\tilde{\Psi}_{\text{NH}}(\boldsymbol{C}) \overset{\text{def}}{=} \frac{\mu^{\text{s}}}{2}(\text{tr}\,(\boldsymbol{C}) - 3) - \mu^{\text{s}} \ln(J_{\boldsymbol{X}\mapsto\boldsymbol{x}}) + \frac{\lambda^{\text{s}}}{2}(\ln(J_{\boldsymbol{X}\mapsto\boldsymbol{x}}))^2 \tag{5.13}$$

with $J_{\boldsymbol{X}\mapsto\boldsymbol{x}} = \det(\boldsymbol{F}) = (\det(\boldsymbol{C}))^{1/2}$.

Initial Boundary Value Problem. Combining kinematic description in a Lagrangean configuration with balance equations for mass, linear and angular momentum, i.e. (2.26), (2.36) and (2.37), in this work structural dynamics are assumed to be governed by the non-linear elastodynamics PDEs

$$\rho^{\text{s}} \frac{\mathrm{d}^2 \boldsymbol{d}}{\mathrm{d}t^2} - \nabla \cdot (\boldsymbol{F} \cdot \boldsymbol{S})(\boldsymbol{d}) = \rho^{\text{s}} \boldsymbol{f}^{\text{s}} \qquad \forall\,(\boldsymbol{X}, t) \in \Omega_0^{\text{s}} \times (T_0, T] \tag{5.14}$$

with the unknown time-dependent displacement field $\boldsymbol{d}(t)$ defined in reference configuration Ω_0^{s}. Therein, ρ^{s} denotes the structural material density $\rho^{\text{s}} \overset{\text{def}}{=} \rho_{\boldsymbol{X}}^{0,\text{s}} = \rho_{\boldsymbol{X}}^{\text{s}} J_{\boldsymbol{X}\mapsto\boldsymbol{x}}$, which is defined in

the initial referential configuration $\boldsymbol{X}$ and is constant over time due to mass conservation, see also the derivation in (2.27). Further, $\nabla \cdot (\cdot) = \nabla_{\boldsymbol{X}} \cdot (\cdot)$ is the divergence operator with respect to material referential coordinates. Appropriate Dirichlet and Neumann boundary conditions on disjunct parts of the possibly moving solid boundary $\partial\Omega^{\mathrm{s}}(t) = \Gamma^{\mathrm{s}}_{\mathrm{D}}(t) \dot{\cup} \Gamma^{\mathrm{s}}_{\mathrm{N}}(t)$ and its equivalents in referential configuration $\partial\Omega^{\mathrm{s}}_0 = \Gamma^{\mathrm{s}}_{\mathrm{D},0} \dot{\cup} \Gamma^{\mathrm{s}}_{\mathrm{N},0}$ read

$$\boldsymbol{d} = \boldsymbol{g}^{\mathrm{s}}_{\mathrm{D}} \qquad \forall (\boldsymbol{X}, t) \in \Gamma^{\mathrm{s}}_{\mathrm{D},0} \times (T_0, T], \tag{5.15}$$

$$(\boldsymbol{F} \cdot \boldsymbol{S}) \cdot \boldsymbol{N} = \boldsymbol{h}^{\mathrm{s}}_{\mathrm{N}} \qquad \forall (\boldsymbol{X}, t) \in \Gamma^{\mathrm{s}}_{\mathrm{N},0} \times (T_0, T], \tag{5.16}$$

where $\boldsymbol{N}$ denotes the outward pointing unit normal on the boundary in reference configuration and $\boldsymbol{g}^{\mathrm{s}}_{\mathrm{D}}$ and $\boldsymbol{h}^{\mathrm{s}}_{\mathrm{N}}$ are prescribed displacements and surface tractions on the respective boundaries. The second order initial boundary value problem (IBVP) is complemented with given initial values for displacements and velocities

$$\boldsymbol{d}(\boldsymbol{X}, T_0) = \boldsymbol{d}_0(\boldsymbol{X}) \qquad \forall\, \boldsymbol{X} \in \Omega^{\mathrm{s}}_0, \tag{5.17}$$

$$\frac{\mathrm{d}\boldsymbol{d}}{\mathrm{d}t}(\boldsymbol{X}, T_0) = \dot{\boldsymbol{d}}_0(\boldsymbol{X}) \qquad \forall\, \boldsymbol{X} \in \Omega^{\mathrm{s}}_0. \tag{5.18}$$

Equations (5.14)–(5.18) can be referred to as *strong form* of non-linear solid mechanics.

5.1.2 Variational Structure Problem

For deriving the weak formulation of the structural initial boundary value problem, appropriate function space have to be introduced. For the solid weak formulation, the space of admissible displacements $\mathscr{D}_{\boldsymbol{g}_{\mathrm{D}}} \overset{\text{def}}{=} [H^1_{\Gamma_{\mathrm{D}},\boldsymbol{g}_{\mathrm{D}}}(\Omega^{\mathrm{s}}_0)]^d \subset [H^1(\Omega^{\mathrm{s}}_0)]^d$ satisfies the Dirichlet boundary condition (5.15), whereas the space of admissible test functions $\mathscr{D}_{\boldsymbol{0}}$ exhibits zero trace on Γ_{D}. Furthermore, $\mathscr{Z} \subseteq [H^1(\Omega^{\mathrm{s}}_0)]^d$ denotes the admissible space for structural velocities.

The weak formulation of the non-linear structural problem (5.14)-(5.18) then reads as follow: for any time $t \in (T_0, T]$, find solid displacements $\boldsymbol{d}(t) \in \mathscr{D}_{\boldsymbol{g}_{\mathrm{D}}}$ and velocities $\dot{\boldsymbol{d}}(t) \in \mathscr{Z}$ such that for all $(\boldsymbol{w}, \boldsymbol{z}) \in \mathscr{D}_{\boldsymbol{0}} \times \mathscr{Z}$

$$(\rho^{\mathrm{s}}(\frac{\mathrm{d}\boldsymbol{d}}{\mathrm{d}t} - \dot{\boldsymbol{d}}), \boldsymbol{z}) + (\rho^{\mathrm{s}} \frac{\mathrm{d}\dot{\boldsymbol{d}}}{\mathrm{d}t}, \boldsymbol{w}) + ((\boldsymbol{F} \cdot \boldsymbol{S})(\boldsymbol{d}), \nabla \boldsymbol{w}) = (\rho^{\mathrm{s}} \boldsymbol{f}^{\mathrm{s}}, \boldsymbol{w}) + \langle \boldsymbol{h}^{\mathrm{s}}_{\mathrm{N}}, \boldsymbol{w} \rangle_{\Gamma^{\mathrm{s}}_{\mathrm{N},0}}, \tag{5.19}$$

where $(\cdot, \cdot)$, $\langle \cdot, \cdot \rangle_{\Gamma^{\mathrm{s}}_{\mathrm{N},0}}$ denote the inner products associated with L^2 in the domain Ω^{s}_0 and on the boundary part $\Gamma^{\mathrm{s}}_{\mathrm{N},0}$. Introducing the following operators

$$a^{\mathrm{s}}(\boldsymbol{d}, \boldsymbol{w}) \overset{\text{def}}{=} ((\boldsymbol{F} \cdot \boldsymbol{S})(\boldsymbol{d}), \nabla \boldsymbol{w})_{\Omega^{\mathrm{s}}_0}, \tag{5.20}$$

$$l^{\mathrm{s}}(\boldsymbol{w}) \overset{\text{def}}{=} (\rho^{\mathrm{s}} \boldsymbol{f}^{\mathrm{s}}, \boldsymbol{w}) + \langle \boldsymbol{h}^{\mathrm{s}}_{\mathrm{N}}, \boldsymbol{w} \rangle_{\Gamma^{\mathrm{s}}_{\mathrm{N},0}}, \tag{5.21}$$

where the elastic form a^{s} is linear in the variable $\boldsymbol{w}$, however, in general non-linear in the displacement field $\boldsymbol{d}$. The weak formulation (5.19) can be rewritten in operator form as

$$(\rho^{\mathrm{s}}(\frac{\mathrm{d}\boldsymbol{d}}{\mathrm{d}t} - \dot{\boldsymbol{d}}), \boldsymbol{z}) + (\rho^{\mathrm{s}} \frac{\mathrm{d}\dot{\boldsymbol{d}}}{\mathrm{d}t}, \boldsymbol{w}) + a^{\mathrm{s}}(\boldsymbol{d}, \boldsymbol{w}) = l^{\mathrm{s}}(\boldsymbol{w}). \tag{5.22}$$

5.1.3 Spatial Finite Element Discretization

The space semi-discretization of the structural weak formulation (5.19) follows the concepts provided in Section 2.1.3.1 for PDEs formulated with respect to Lagrangean descriptions on boundary-fitted meshes and uses the notation and terminology introduced in Section 2.1.4.1.

For the finite-dimensional spatial discretization of the solid domain Ω_0^{s}, let $\{\mathcal{T}_h^{\mathrm{s}}\}_h$ be a family of boundary-fitted quasi-uniform meshes with mesh size parameter $h > 0$. Each mesh $\mathcal{T}_h^{\mathrm{s}}$ consists of a family of isoparametric possibly curvilinear finite elements $T \in \mathcal{T}_h^{\mathrm{s}}$ with existing bijective mappings $S_T(t) : \hat{T} \mapsto T$ with respect to the element parameter space and approximates the structural domain in referential configuration $\Omega_0^{\mathrm{s}} \approx \Omega_{0,h}^{\mathrm{s}} = \cup_{T \in \mathcal{T}_h^{\mathrm{s}}} T$. For the approximation of solid displacements and velocities $\boldsymbol{d}, \dot{\boldsymbol{d}}$, standard continuous isoparametric finite element spaces

$$\mathscr{X}_{0,h} = \left\{ x_h \in C^0(\overline{\Omega_{0,h}^{\mathrm{s}}}) : x_h|_T = v_{\hat{T}} \circ S_T^{-1}(t) \text{ with } v_{\hat{T}} \in \mathbb{V}^k(\hat{T}) \, \forall \, T \in \mathcal{T}_h^{\mathrm{s}} \right\} \tag{5.23}$$

were introduced in (2.43). The discrete displacement and velocity approximation and test function spaces are defined as $\mathscr{D}_{h,\boldsymbol{g}_{\mathrm{D}}} \overset{\text{def}}{=} [\mathscr{X}_{0,h}]^d \cap \mathscr{D}_{\boldsymbol{g}_{\mathrm{D}}}$, $\mathscr{L}_h \overset{\text{def}}{=} [\mathscr{X}_{0,h}]^d \cap \mathscr{L}$ and $\mathscr{D}_{h,\boldsymbol{0}} \overset{\text{def}}{=} [\mathscr{X}_{0,h}]^d \cap \mathscr{D}_{\boldsymbol{0}}$ taking into account the respective trace values.

The space semi-discrete approximation to problem (5.22) reads: for any $t \in (T_0, T]$, find solid displacements $\boldsymbol{d}_h(t) \in \mathscr{D}_{h,\boldsymbol{g}_{\mathrm{D}}}$ and velocities $\dot{\boldsymbol{d}}_h(t) \in \mathscr{L}_h$ such that for all $(\boldsymbol{w}_h, \boldsymbol{z}_h) \in \mathscr{D}_{h,\boldsymbol{0}} \times \mathscr{L}_h$

$$(\rho^{\mathrm{s}}(\frac{\mathrm{d}\boldsymbol{d}_h}{\mathrm{d}t} - \dot{\boldsymbol{d}}_h), \boldsymbol{z}_h)_{\Omega_{0,h}^{\mathrm{s}}} + (\rho^{\mathrm{s}} \frac{\mathrm{d}\dot{\boldsymbol{d}}_h}{\mathrm{d}t}, \boldsymbol{w}_h)_{\Omega_{0,h}^{\mathrm{s}}} + a_h^{\mathrm{s}}(\boldsymbol{d}_h, \boldsymbol{w}_h) = l_h^{\mathrm{s}}(\boldsymbol{w}_h), \tag{5.24}$$

with $a_h^{\mathrm{s}} = a^{\mathrm{s}}$ and $l_h^{\mathrm{s}} = l^{\mathrm{s}}$ as defined in (5.20) and (5.21). All domain and boundary integrals associated with inner products are defined on the discrete counterparts $\Omega_{0,h}^{\mathrm{s}}, \Gamma_{N,0,h}^{\mathrm{s}}$, respectively. After performing transformations to simplicial reference elements $\hat{T}$, Gaussian quadrature rules can be applied.

Assembly of local element-wise contributions of the discrete weak formulation on elements T into global finite-dimensional vector-valued displacement and velocity fields $\boldsymbol{D}(t) \in \mathbb{R}^{\mathrm{ndof}}$ and $\boldsymbol{V}(t) \in \mathbb{R}^{\mathrm{ndof}}$ allows to rewrite the discrete weak formulation of structural dynamics (5.24) in terms of $2 \cdot \mathrm{ndof}$ non-linear ordinary differential equations (ODEs) of first order

$$\boldsymbol{M}\dot{\boldsymbol{U}} + \boldsymbol{C}\dot{\boldsymbol{D}} + \boldsymbol{F}_{\mathrm{int}}(\boldsymbol{D}) - \boldsymbol{F}_{\mathrm{ext}} = \boldsymbol{0}, \tag{5.25}$$

$$\dot{\boldsymbol{D}} - \boldsymbol{U} = \boldsymbol{0}, \tag{5.26}$$

where $\boldsymbol{M}$ is the global mass matrix, $\boldsymbol{F}_{\mathrm{int}}$ the vector of non-linear internal forces resulting from a_h^{s} and $\boldsymbol{F}_{\mathrm{ext}}$ external forces resulting from l_h^{s}. Furthermore, $\boldsymbol{C}$ is an additional global damping matrix which introduces the widely used Rayleigh model for viscous damping. Hereby, $\boldsymbol{C} \overset{\text{def}}{=} c_M \boldsymbol{M} + c_K \boldsymbol{K}_0$ can be defined as a linear combination of mass matrix $\boldsymbol{M}$ and an initial tangent stiffness matrix $\boldsymbol{K}_0$, which denotes the partial derivative of the internal forces vector $\boldsymbol{F}_{\mathrm{int}}$ with respect to the displacements $\boldsymbol{D}$ in reference configuration at $\boldsymbol{D} = \boldsymbol{0}$. It has to be noted that due to the regularity of the mass matrix $\boldsymbol{M}$ the system of differential equations $\boldsymbol{M}(\dot{\boldsymbol{D}} - \boldsymbol{U}) = \boldsymbol{0}$, which results from (5.24), can be resolved to $\dot{\boldsymbol{D}} - \boldsymbol{U} = \boldsymbol{0}$ in (5.26).

5.1.4 Structural Time Stepping

After introducing a spatial discretization, the resulting system of ordinary differential equations can be discretized in time applying the *method of lines*. For time stepping, the time interval $(T_0, T]$ is partitioned into $N \in \mathbb{N}$ equal-sized time-step intervals $J^n = (t^{n-1}, t^n]$ of size Δt with discrete time steps $t^n = T_0 + n\Delta t$ and $t^N = T$. There exists a multitude of one- and multi-step time discretization schemes applicable to systems of *stiff* initial value problems. However, throughout this thesis only one-step algorithms are considered for structural dynamics which require only solution history from the last discrete time step t^{n-1} for approximating displacements and velocities $\boldsymbol{D}^n \approx \boldsymbol{D}(t^n)$ and $\boldsymbol{V}^n \approx \boldsymbol{V}(t^n)$.

The Generalized-α Family for Temporal Discretization. In the following, the so-called family of *Generalized-α* (G-α) time-stepping schemes is considered, as established by Chung and Hulbert [74]. This class of time-integration schemes is commonly used in structural mechanics as it endows several desired properties. Among classical requirements as unconditional A-stability or second-order accuracy, numerical schemes are often desired to entail numerical dissipation in the high-frequency range to damp insufficiently resolved spurious high-frequency modes introduced for instance by insufficient temporal or spatial discretization of the physical problem. To keep damping of low-frequency modes at a minimum at the same time is of greatest importance. Regarding numerical dissipation, the G-α method achieves a optimum between these two requirements. This matter of fact makes the family of G-α algorithms very robust compared to for instance the classical Crank-Nicolson scheme which does not introduce numerical damping at all. Concerning a detailed numerical analysis and studies of the G-α scheme, the interested reader is referred to Erlicher *et al.* [100].

The G-α method is classified as one-step, three-stage time integration scheme, where the latter designation refers to the three solution vectors $\boldsymbol{D}^n, \boldsymbol{V}^n, \boldsymbol{A}^n$ which occur during construction. Assuming given initial data for $\boldsymbol{d}_h(T_0)$ and $\dot{\boldsymbol{d}}_h(T_0)$, i.e. for $\boldsymbol{D}^0, \boldsymbol{V}^0$, from the initial boundary value problem, an initial acceleration can be computed satisfying the elastodynamics equations at T_0

$$\boldsymbol{A}^0 \overset{\text{def}}{=} -\boldsymbol{M}^{-1}(\boldsymbol{C}\boldsymbol{V}^0 + \boldsymbol{F}_{\text{int}}(\boldsymbol{D}^0) - \boldsymbol{F}_{\text{ext}}(T_0)). \tag{5.27}$$

Approximations $\boldsymbol{D}^n, \boldsymbol{V}^n, \boldsymbol{A}^n$ associated with a new time step t^n are then constructed as follows

$$\boldsymbol{D}^n(\boldsymbol{A}^n) = \boldsymbol{D}^{n-1} + \Delta t \boldsymbol{V}^{n-1} + (\Delta t)^2 \left((1/2 - \beta)\boldsymbol{A}^{n-1} + \beta \boldsymbol{A}^n\right), \tag{5.28}$$

$$\boldsymbol{V}^n(\boldsymbol{A}^n) = \boldsymbol{V}^{n-1} + \Delta t \left((1-\gamma)\boldsymbol{A}^{n-1} + \gamma \boldsymbol{A}^n\right) \tag{5.29}$$

and

$$\boldsymbol{M}\boldsymbol{A}^{n-\alpha_m} + \boldsymbol{C}\boldsymbol{V}^{n-\alpha_f} + \boldsymbol{F}_{\text{int}}^{n-\alpha_f}(\boldsymbol{D}^n) - \boldsymbol{F}_{\text{ext}}(t^{n-\alpha_f}) = \boldsymbol{0} \tag{5.30}$$

with $\gamma \in (0, 1]$ and $\beta \in (0, 1/2]$. The generalized mid-point quantities are defined by means of linear interpolations with generalized trapezoidal rules

$$\boldsymbol{D}^{n-\alpha_f}(\boldsymbol{D}^n) = (1-\alpha_f)\boldsymbol{D}^n + \alpha_f \boldsymbol{D}^{n-1}, \tag{5.31}$$

$$\boldsymbol{V}^{n-\alpha_f}(\boldsymbol{V}^n) = (1-\alpha_f)\boldsymbol{V}^n + \alpha_f \boldsymbol{V}^{n-1}, \tag{5.32}$$

$$\boldsymbol{A}^{n-\alpha_m}(\boldsymbol{A}^n) = (1-\alpha_m)\boldsymbol{A}^n + \alpha_m \boldsymbol{A}^{n-1}, \tag{5.33}$$

and the generalized mid-point time

$$t^{n-\alpha_f} = (1-\alpha_f)t^n + \alpha_f t^{n-1}, \tag{5.34}$$

characterized with two parameters $\alpha_f, \alpha_m \in [0,1)$. The internal and external forces can be approximated either by a generalized mid-point rule (GMR) or by a generalized trapezoidal rule (GTR) as

$$\boldsymbol{F}^{n-\alpha_f}(\boldsymbol{D}^n) = \boldsymbol{F}((1-\alpha_f)\boldsymbol{D}^n + \alpha_f \boldsymbol{D}^{n-1}) \quad \text{(GMR)}, \tag{5.35}$$

$$\boldsymbol{F}^{n-\alpha_f}(\boldsymbol{D}^n) = (1-\alpha_f)\boldsymbol{F}(\boldsymbol{D}^n) + \alpha_f \boldsymbol{F}(\boldsymbol{D}^{n-1}) \quad \text{(GTR)}. \tag{5.36}$$

The latter option is exclusively used throughout this thesis.

Using the linear relations between quantities associated with time step t^n in (5.28), (5.29) and (5.31)–(5.33), the three-stage system for non-linear elastodynamics can be conflated resulting in a non-linear formulation depending solely on the unknown approximation $\boldsymbol{D}^n$.

$$\begin{aligned}
\boldsymbol{0} = \boldsymbol{R}(\boldsymbol{D}^n) \overset{\text{def}}{=} \boldsymbol{M}&\left[\frac{1-\alpha_m}{\beta\Delta t^2}(\boldsymbol{D}^n - \boldsymbol{D}^{n-1}) - \frac{1-\alpha_m}{\beta\Delta t}\boldsymbol{V}^{n-1} - \frac{1-\alpha_m-2\beta}{2\beta}\boldsymbol{A}^{n-1}\right] \\
&+ \boldsymbol{C}\left[\frac{(1-\alpha_f)\gamma}{\beta\Delta t}(\boldsymbol{D}^n - \boldsymbol{D}^{n-1}) - \frac{(1-\alpha_f)\gamma-\beta}{\beta}\boldsymbol{V}^{n-1}\right. \\
&\qquad \left. - \frac{(\gamma-2\beta)(1-\alpha_f)\Delta t}{2\beta}\boldsymbol{A}^{n-1}\right] \\
&+ (1-\alpha_f)(\boldsymbol{F}^n_{\text{int}}(\boldsymbol{D}^n) - \boldsymbol{F}^n_{\text{ext}}) + \alpha_f(\boldsymbol{F}^{n-1}_{\text{int}}(\boldsymbol{D}^{n-1}) - \boldsymbol{F}^{n-1}_{\text{ext}}) \\
= \left(\boldsymbol{M}\frac{1-\alpha_m}{\beta\Delta t^2} + \boldsymbol{C}\frac{(1-\alpha_f)\gamma}{\beta\Delta t}\right)&\boldsymbol{D}^n + (1-\alpha_f)(\boldsymbol{F}^n_{\text{int}}(\boldsymbol{D}^n) - \boldsymbol{F}^n_{\text{ext}}) \\
&- \boldsymbol{H}^{n-1}(\boldsymbol{D}^{n-1}, \boldsymbol{V}^{n-1}, \boldsymbol{A}^{n-1}).
\end{aligned} \tag{5.37}$$

For the last equation, all terms which belong to the old time-level are comprised in $\boldsymbol{H}^{n-1}$. Once $\boldsymbol{D}^n$ is computed, approximations to $\boldsymbol{V}^n$ and $\boldsymbol{A}^n$ can be recovered, viz.

$$\boldsymbol{A}^n(\boldsymbol{D}^n) = [\boldsymbol{D}^n - (\boldsymbol{D}^{n-1} + \Delta t\boldsymbol{V}^{n-1} + (1/2-\beta)(\Delta t)^2\boldsymbol{A}^{n-1})] \cdot (\beta(\Delta t)^2)^{-1}, \tag{5.38}$$

$$\boldsymbol{V}^n(\boldsymbol{A}^n) = \boldsymbol{V}^{n-1} + (1-\gamma)\Delta t\boldsymbol{A}^{n-1} + \gamma\Delta t\boldsymbol{A}^n. \tag{5.39}$$

Afterwards it can be proceeded with the next time step.

To guarantee second-order accuracy for the displacement approximation, the G-α scheme is required to be consistent in the accelerations which requires

$$\gamma = \frac{1}{2} - \alpha_m + \alpha_f. \tag{5.40}$$

Furthermore, maximizing high-frequency dissipation of the schemes results in a condition for β

$$\beta = \frac{1}{4}(1-\alpha_m+\alpha_f)^2. \tag{5.41}$$

The two remaining free parameters α_f, α_m have to be chosen such that unconditional stability is guaranteed. This holds provided that

$$\alpha_m \leqslant \alpha_f \leqslant \frac{1}{2}. \tag{5.42}$$

The high-frequency dissipation can be regularized in terms of the spectral radius ρ_∞ which can be interpreted as user-defined value. Following Chung and Hulbert [74], the spectral radius can be obtained as

$$\rho_\infty = \left| \frac{\alpha_f - \alpha_m - 1}{\alpha_f - \alpha_m + 1} \right| \in [0, 1]. \tag{5.43}$$

For a given desired high-frequency damping, the low-frequency damping is minimized whenever $\alpha_f = (\alpha_m + 1)/3$ such that an optimal setting of parameters $(\alpha_m, \alpha_f, \beta, \gamma)$ can be formulated in terms of a single user-defined spectral radius as

$$\alpha_m = \frac{2\rho_\infty - 1}{\rho_\infty + 1} \qquad \text{and} \qquad \alpha_f = \frac{\rho_\infty}{\rho_\infty + 1} \tag{5.44}$$

together with (5.40) and (5.41). It has to be noted that a spectral radius of $\rho_\infty = 1$ does not introduce any numerical high-frequency damping, whereas for $\rho_\infty = 0$ the algorithm is in the so-called case of *asymptotic annihilation*. The resulting G-α schemes are unconditionally A-stable, guarantee second-order accuracy in the displacements and thereby provide an optimal combination of high-frequency and low-frequency numerical dissipation. For further details, the reader is referred to the original publication by Chung and Hulbert [74] and an extensive analysis provided by Erlicher *et al.* [100]. In these publications, also the relation between G-α schemes and other implicit time stepping schemes is comprehensively discussed. Widely used sets of G-α parameters are provided in Table 5.1.

Table 5.1: Optimal parameter settings for the G-α scheme without ($\rho_\infty = 1.0$), with medium ($\rho_\infty = 0.8$) and with strong ($\rho_\infty = 0.5$) numerical dissipation in the high-frequency range.

ρ_∞	α_m	α_f	γ	β
1.0	1/2	1/2	1/2	1/4
0.8	1/3	4/9	11/18	25/81
0.5	0	1/3	10/12	4/9

For the sake of completeness, different other implicit time-stepping schemes can be considered as special cases of the G-α family. The classical Newmark method can be obtained for $\alpha_m = \alpha_f = 0$, which shifts the evaluation of terms of the ODE to the end of the time interval, i.e. to t^n. The well-known *one-step-θ* scheme can be interpreted as a special representative of the G-α family with $\alpha_m = \alpha_f = 1 - \gamma$ and $\gamma = \theta$. Condition (5.40) reflects the property that the one-step-θ scheme exhibits second-order accuracy if and only if $\theta = 1/2$ together with the A-stability property provided $\theta \in [0.5, 1]$. The popular *Crank-Nicolson method* with $\theta = 1/2$ so guarantees second-order accuracy and unconditional A-stability, however, does not provide any numerical damping. This is due to the fact that $\rho_\infty = 1$ in contrast to the previously introduced more general G-α scheme.

Linearization and Non-linear Solution Techniques. Due to the non-linearity of the internal force vector $\boldsymbol{F}_{\text{int}}(\boldsymbol{D})$ in the displacement field, the computation of new displacements $\boldsymbol{D}^n$ requires non-linear iterative solution techniques. In this work, the discrete vector $\boldsymbol{D}^n$, which is defined as solution of the effective structural equation (5.37), the well-established Newton-Raphson algorithm is applied. For a given start approximation $\boldsymbol{D}^n_{i=1}$, the solution $\boldsymbol{D}^n$ is approximated iteratively for $i \geqslant 1$ by solving linearized systems for increments $\Delta\boldsymbol{D}^n_i$

$$\left.\frac{\partial \boldsymbol{R}(\boldsymbol{D})}{\partial \boldsymbol{D}}\right|_{\boldsymbol{D}=\boldsymbol{D}^n_i} \cdot \Delta\boldsymbol{D}^n_i = -\boldsymbol{R}(\boldsymbol{D}^n_i) \tag{5.45}$$

followed by updates with these incremental solutions

$$\boldsymbol{D}^n_{i+1} = \boldsymbol{D}^n_i + \Delta\boldsymbol{D}^n_i \tag{5.46}$$

until convergence up to a certain tolerance is reached in iteration k such that $\boldsymbol{D}^n_k \longrightarrow \boldsymbol{D}^n$.

5.2 The Coupled Fluid-Structure-Interaction Problem

In this section, fundamentals of coupled systems between incompressible fluids and elastic deformable structures are introduced. First, physical modeling at the fluid-solid phase boundary is addressed and coupling constraints are formulated. Afterwards, governing equations for the respective bulk phases are complemented with these interfacial constraints and boundary as well as initial conditions. All together, an initial boundary value problem for coupled fluid-structure interaction problems is composed. Finally, a variational formulation of that will be presented.

5.2.1 Domains and the Fluid-Solid Interface

The notation and terminology on domains and interfaces used in the subsequent sections for the coupled FSI problem is based on the abstract setting introduced in Section 2.1.1.

Computational Domains. For the sake of clarity, in the following, the interaction between only one fluid phase $\Omega^{\text{f}} = \Omega^1 \subset \mathbb{R}^d$ and one structural body $\Omega^{\text{s}} = \Omega^2 \subset \mathbb{R}^d$ are considered. Note that the extension to multiple fluid and solid phases is straightforward, see Section 4.1.1. Following Section 2.1.1, the overall computational domain is given by $\Omega = \Omega^{\text{f}}(t) \cup \Omega^{\text{s}}(t)$ with moving fluid-solid interface $\Gamma^{\text{fs}}(t) \stackrel{\text{def}}{=} \overline{\Omega^{\text{f}}(t)} \cap \overline{\Omega^{\text{s}}(t)}$ and respective outer Dirichlet and Neumann boundary parts of the fluid and solid subdomains $\Gamma^{\text{f}}_{\text{D}}, \Gamma^{\text{s}}_{\text{D}}, \Gamma^{\text{f}}_{\text{N}}, \Gamma^{\text{s}}_{\text{N}}$ such that $\partial\Omega^{\text{f}} = \Gamma^{\text{f}}_{\text{D}} \cup \Gamma^{\text{f}}_{\text{N}} \cup \Gamma^{\text{fs}}$ and $\partial\Omega^{\text{s}} = \Gamma^{\text{s}}_{\text{D}} \cup \Gamma^{\text{s}}_{\text{N}} \cup \Gamma^{\text{fs}}$. The normal vector at Γ^{fs} follows the convention $\boldsymbol{n}^{\text{fs}} = \boldsymbol{n}^{\text{f}} = -\boldsymbol{n}^{\text{s}}$. For scalar or vector-valued quantities f which are continuous within Ω^{f} and Ω^{s}, however, exhibit a discontinuity across Γ^{fs}, the usual average and jump operators $\{f\}$, $\langle f \rangle$ and $[\![f]\!]$ are defined as in (2.1)–(2.3).

Interfacial Constraints. Commonly used modeling approaches to fluid-solid interaction are based on macroscopic considerations and state conservation of mass and momentum. Similar to deducing coupling constraints between several fluid phases, these conservation laws claim

$$\rho_{\boldsymbol{x}}^{\mathrm{f}}(\boldsymbol{u}^{\mathrm{f}} \cdot \boldsymbol{n}^{\mathrm{fs}} - u_{\Gamma}) = -M = \rho_{\boldsymbol{x}}^{\mathrm{s}}(\boldsymbol{u}^{\mathrm{s}} \cdot \boldsymbol{n}^{\mathrm{fs}} - u_{\Gamma}), \tag{5.47}$$

$$\rho_{\boldsymbol{x}}^{\mathrm{f}}\boldsymbol{u}^{\mathrm{f}}(\boldsymbol{u}^{\mathrm{f}} \cdot \boldsymbol{n}^{\mathrm{fs}} - u_{\Gamma}) - \boldsymbol{\sigma}_{\boldsymbol{x}}(\boldsymbol{u}^{\mathrm{f}}, p^{\mathrm{f}}) \cdot \boldsymbol{n}^{\mathrm{fs}} = \rho_{\boldsymbol{x}}^{\mathrm{s}}\boldsymbol{u}^{\mathrm{s}}(\boldsymbol{u}^{\mathrm{s}} \cdot \boldsymbol{n}^{\mathrm{fs}} - u_{\Gamma}) - \boldsymbol{\sigma}_{\boldsymbol{x}}(\boldsymbol{d}^{\mathrm{s}} \circ \boldsymbol{\varphi}_t^{-1}) \cdot \boldsymbol{n}^{\mathrm{fs}}, \tag{5.48}$$

where $\boldsymbol{u}^{\mathrm{s}} = \frac{\mathrm{d}\boldsymbol{d}^{\mathrm{s}}}{\mathrm{d}t} \circ \boldsymbol{\varphi}_t^{-1}$ denotes the structural velocity and $\boldsymbol{\sigma}_{\boldsymbol{x}} = \boldsymbol{\sigma}_{\boldsymbol{x}}(\boldsymbol{u}^{\mathrm{f}}, p^{\mathrm{f}})$ the Cauchy stresses defined on fluid side and $\boldsymbol{\sigma}_{\boldsymbol{x}} = \boldsymbol{\sigma}_{\boldsymbol{x}}(\boldsymbol{d}^{\mathrm{s}} \circ \boldsymbol{\varphi}_t^{-1})$ the stresses on the structural side of the interface. Following the elaborations in Section 4.1.1, it is naturally assumed that no phase change at the interface occurs and the interface is driven by fluid and solid particles such that $M = 0$. For viscous fluids with $\mu > 0$, the kinematic and dynamic interface constraints being enforced then emerge as

$$[\![\boldsymbol{u}]\!] = \boldsymbol{u}^{\mathrm{f}} - \frac{\mathrm{d}\boldsymbol{d}^{\mathrm{s}}}{\mathrm{d}t} \circ \boldsymbol{\varphi}_t^{-1} = \boldsymbol{g}_{\Gamma}^{\mathrm{fs}} \qquad \forall\, \boldsymbol{x} \in \Gamma^{\mathrm{fs}}(t), \tag{5.49}$$

$$[\![\boldsymbol{\sigma}]\!] \cdot \boldsymbol{n}^{\mathrm{fs}} = (\boldsymbol{\sigma}_{\boldsymbol{x}}(\boldsymbol{u}^{\mathrm{f}}, p^{\mathrm{f}}) - \boldsymbol{\sigma}_{\boldsymbol{x}}(\boldsymbol{d}^{\mathrm{s}} \circ \boldsymbol{\varphi}_t^{-1})) \cdot \boldsymbol{n}^{\mathrm{fs}} = \boldsymbol{h}_{\Gamma}^{\mathrm{fs}} \qquad \forall\, \boldsymbol{x} \in \Gamma^{\mathrm{fs}}(t) \tag{5.50}$$

with functions $\boldsymbol{g}_{\Gamma}^{\mathrm{fs}} = \boldsymbol{0}$ and $\boldsymbol{h}_{\Gamma}^{\mathrm{fs}} = \boldsymbol{0}$. Note that in the limit case of $\mu \to 0$, the constraint (5.49) on the tangential component needs to be relaxed and only mass conservation in interface normal direction is allowed to be ensured, i.e. $[\![\boldsymbol{u}]\!] \cdot \boldsymbol{n}^{\mathrm{fs}} = 0$. This aspect will be naturally accounted for by a Nitsche-type weak enforcement, as will be discussed in Section 5.3. More complex physical models that take roughness of the structural surface into consideration usually render in generalized Robin-type coupling constraints. As such conditions require special numerical treatment to guarantee stability and optimality in a discrete fashion, as proposed, e.g., in the work by Juntunen and Stenberg [161], such models are not treated within the scope of this work.

5.2.2 Coupled Initial Boundary Value Problem

The coupled system between an incompressible fluid and a compressible structure can be composed of two initial boundary value problems, a first one for the fluid phase in Ω^{f}, see Section 3.1.1, and a second one for the structural phase in Ω^{s}, see Section 5.1.1, complemented with outer Dirichlet and Neumann boundary conditions at their boundaries, respectively. Both phases are glued together by the interfacial coupling constraints (5.49) and (5.50).

The mixed Eulerian-Lagrangean strong formulation of the non-linear coupled fluid-solid initial boundary value problem is given as follows: for time $t \in (T_0, T]$, find fluid velocity and pressure $\boldsymbol{u}(t) : \Omega^{\mathrm{f}}(t) \mapsto \mathbb{R}^d$, $p(t) : \Omega^{\mathrm{f}}(t) \mapsto \mathbb{R}$ and solid displacement and velocity $\boldsymbol{d}(t) : \Omega_0^{\mathrm{s}} \mapsto \mathbb{R}^d$, $\dot{\boldsymbol{d}}(t) : \Omega_0^{\mathrm{s}} \mapsto \mathbb{R}^d$ which satisfy

$$\rho^{\mathrm{f}}\frac{\partial \boldsymbol{u}}{\partial t} + \rho^{\mathrm{f}}(\boldsymbol{u} \cdot \nabla)\boldsymbol{u} + \nabla p - 2\mu\nabla \cdot \boldsymbol{\epsilon}(\boldsymbol{u}) = \rho^{\mathrm{f}}\boldsymbol{f}^{\mathrm{f}} \qquad \forall\, \boldsymbol{x} \in \Omega^{\mathrm{f}}(t), \tag{5.51}$$

$$\nabla \cdot \boldsymbol{u} = 0 \qquad \forall\, \boldsymbol{x} \in \Omega^{\mathrm{f}}(t), \tag{5.52}$$

$$\boldsymbol{u} = \boldsymbol{g}_{\mathrm{D}}^{\mathrm{f}} \qquad \forall\, \boldsymbol{x} \in \Gamma_{\mathrm{D}}^{\mathrm{f}}(t), \tag{5.53}$$

$$\boldsymbol{\sigma}(\boldsymbol{u}, p) \cdot \boldsymbol{n} = \boldsymbol{h}_{\mathrm{N}}^{\mathrm{f}} \qquad \forall\, \boldsymbol{x} \in \Gamma_{\mathrm{N}}^{\mathrm{f}}(t), \tag{5.54}$$

and

$$\rho^{\mathrm{s}}\frac{\mathrm{d}\dot{\boldsymbol{d}}}{\mathrm{d}t} - \nabla\cdot(\boldsymbol{F}\cdot\boldsymbol{S})(\boldsymbol{d}) = \rho^{\mathrm{s}}\boldsymbol{f}^{\mathrm{s}} \qquad \forall\,\boldsymbol{X}\in\Omega_0^{\mathrm{s}}, \tag{5.55}$$

$$\rho^{\mathrm{s}}(\frac{\mathrm{d}\boldsymbol{d}}{\mathrm{d}t} - \dot{\boldsymbol{d}}) = \boldsymbol{0} \qquad \forall\,\boldsymbol{X}\in\Omega_0^{\mathrm{s}}, \tag{5.56}$$

$$\boldsymbol{d} = \boldsymbol{g}_{\mathrm{D}}^{\mathrm{s}} \qquad \forall\,\boldsymbol{X}\in\Gamma_{\mathrm{D},0}^{\mathrm{s}}, \tag{5.57}$$

$$(\boldsymbol{F}\cdot\boldsymbol{S})\cdot\boldsymbol{N} = \boldsymbol{h}_{\mathrm{N}}^{\mathrm{s}} \qquad \forall\,\boldsymbol{X}\in\Gamma_{\mathrm{N},0}^{\mathrm{s}}, \tag{5.58}$$

with coupling and initial conditions

$$[\![\boldsymbol{u}]\!] = \boldsymbol{u} - (\dot{\boldsymbol{d}}\circ\boldsymbol{\varphi}_t^{-1}) = \boldsymbol{0} \qquad \forall\,\boldsymbol{x}\in\Gamma^{\mathrm{fs}}(t), \tag{5.59}$$

$$[\![\boldsymbol{\sigma}]\!]\cdot\boldsymbol{n}^{\mathrm{f}} = (\boldsymbol{\sigma}_{\boldsymbol{x}}(\boldsymbol{u},p) - \boldsymbol{\sigma}_{\boldsymbol{x}}(\boldsymbol{d}\circ\boldsymbol{\varphi}_t^{-1}))\cdot\boldsymbol{n}^{\mathrm{f}} = \boldsymbol{0} \qquad \forall\,\boldsymbol{x}\in\Gamma^{\mathrm{fs}}(t), \tag{5.60}$$

$$\boldsymbol{u}(T_0) = \boldsymbol{u}_0 \qquad \forall\,\boldsymbol{x}\in\Omega^{\mathrm{f}}(T_0), \tag{5.61}$$

$$\boldsymbol{d}(T_0) = \boldsymbol{d}_0 \qquad \forall\,\boldsymbol{X}\in\Omega^{\mathrm{s}}(T_0), \tag{5.62}$$

$$\dot{\boldsymbol{d}}(T_0) = \dot{\boldsymbol{d}}_0 \qquad \forall\,\boldsymbol{X}\in\Omega^{\mathrm{s}}(T_0). \tag{5.63}$$

The mixture between Eulerian and Lagrangean formulation is clearly visible from the mapping $\boldsymbol{\varphi}_t = (\boldsymbol{I} + \boldsymbol{d}(t), 1)$ for solid quantities between reference and current configuration. Note further the different meaning of gradient and divergence operators for fluids and solids in spatial and material coordinates $\boldsymbol{x}, \boldsymbol{X}$, respectively, as well as $\rho^{\mathrm{s}} = \rho_{\boldsymbol{X}}^{\mathrm{s}}$ as in (5.14).

5.2.3 Coupled Variational Formulation

The variational formulation of the coupled fluid-structure-interaction problem comprises variational formulations for fluid and solid phases proposed in Section 3.1.2 and Section 5.1.2. The functional spaces for fluid and solid are given as for the single phase problems to $\mathcal{V}_{\boldsymbol{g}_{\mathrm{D}}}, \mathcal{Q}$ for fluid velocity and pressure and $\mathcal{D}_{\boldsymbol{g}_{\mathrm{D}}}, \mathcal{Z}$ for solid displacement and velocity. The respective test function spaces are given by $\mathcal{V}_{\boldsymbol{0}}, \mathcal{Q}$ for the fluid and by $\mathcal{D}_{\boldsymbol{0}}, \mathcal{Z}$ for the solid. The coupled non-linear variational formulation then reads as follows: for all $t\in(T_0,T]$, find fluid velocity and pressure as well as solid displacement and velocity $(\boldsymbol{u}(t), p(t), \boldsymbol{d}(t), \dot{\boldsymbol{d}}(t)) \in (\mathcal{V}_{\boldsymbol{g}_{\mathrm{D}}}\times\mathcal{Q})\oplus(\mathcal{D}_{\boldsymbol{g}_{\mathrm{D}}}\times\mathcal{Z})$ such that

$$\begin{aligned}
&(\rho^{\mathrm{f}}\frac{\partial\boldsymbol{u}}{\partial t}, \boldsymbol{v})_{\Omega^{\mathrm{f}}(t)} + c^{\mathrm{f}}(\boldsymbol{u};\boldsymbol{u},\boldsymbol{v}) + a^{\mathrm{f}}(\boldsymbol{u},\boldsymbol{v}) + b^{\mathrm{f}}(p,\boldsymbol{v}) - b^{\mathrm{f}}(q,\boldsymbol{u}) \\
&\qquad + (\rho^{\mathrm{s}}(\frac{\mathrm{d}\boldsymbol{d}}{\mathrm{d}t} - \dot{\boldsymbol{d}}), \boldsymbol{z})_{\Omega_0^{\mathrm{s}}} + (\rho^{\mathrm{s}}\frac{\mathrm{d}\dot{\boldsymbol{d}}}{\mathrm{d}t}, \boldsymbol{w})_{\Omega_0^{\mathrm{s}}} + a^{\mathrm{s}}(\boldsymbol{d},\boldsymbol{w}) = l^{\mathrm{f}}(\boldsymbol{v}) + l^{\mathrm{s}}(\boldsymbol{w}), \\
&[\![\boldsymbol{u}]\!]\big|_{\Gamma^{\mathrm{fs}}(t)} = \boldsymbol{0} \quad \text{with} \quad \boldsymbol{u}^{\mathrm{f}} = \boldsymbol{u} \quad \text{and} \quad \boldsymbol{u}^{\mathrm{s}} = \dot{\boldsymbol{d}}\circ\boldsymbol{\varphi}_t^{-1},
\end{aligned} \tag{5.64}$$

for all $(\boldsymbol{v}, q, \boldsymbol{w}, \boldsymbol{z}) \in (\mathcal{V}_{\boldsymbol{0}}\times\mathcal{Q})\oplus(\mathcal{D}_{\boldsymbol{0}}\times\mathcal{Z})$, with fluid operators $c^{\mathrm{f}}, a^{\mathrm{f}}, b^{\mathrm{f}}, l^{\mathrm{f}}$ as defined in equations (3.12)–(3.15) and structural operators $a^{\mathrm{s}}, l^{\mathrm{s}}$ as defined in (5.20) and (5.21). Note that by proceeding analogously to (4.29) for fluid-fluid interfaces, after integration by parts on the two bulk phases, the traction coupling constraint $\boldsymbol{h}_{\Gamma}^{\mathrm{fs}} = \boldsymbol{0}$ is incorporated into the variational formulation. Enforcement of coupling constraints on discrete subspaces which do not inherently guarantee continuity as claimed in (5.49) and (5.50) across Γ^{fs} will be discussed in the next section.

5.3 An Unfitted Full-Implicit Nitsche-type Approach for Fluid-Structure Interaction

The objective in this section is to establish an unfitted FSI solver which allows to relax strong limitations of most computational FSI approaches and builds the basis for future developments on more advanced fluid-solid-interaction applications. Approximating the structure in a Lagrangean setting with an interface-fitted moving mesh which overlaps with a non-interface-fitted cut Eulerian background fluid mesh, as depicted in Figures 2.11a, allows for arbitrary motions of compressible structural bodies in surrounding flow environments. Additionally, it enables to accurately capture the flow solution without smearing the solution fields in contrast to many other fixed-grid schemes as the case, for instance, for many IB methods. It has to be mentioned that this approach has been developed in view of more advanced coupled problem settings like fluid-structure-contact interaction, as considered in works by Gerstenberger [123] and Mayer *et al.* [184], or fluid-structure-fracture interaction addressed in the work by Sudhakar [244]. Major differences to incorporated FSI solvers of the aforementioned approaches consist in the improved stability behavior of the fluid field combined with a more accurate cut finite element approximation space as well as a full-implicit coupling strategy for a more robust and efficient behavior of iterative solution procedures. Iterative approximation techniques which are able to cope with the issue of potential changes of the discrete fluid function space are suggested in this section. The subsequently introduced unfitted FSI solver represents a significant further development compared to closely related FSI approaches recently published by Burman and Fernández [58] and Alauzet *et al.* [1]. Compared to [58], non-linearities are incorporated into the fluid field as the flows are governed by the non-linear transient incompressible Navier-Stokes equations. Compared to Alauzet *et al.* [1], further complexity is introduced by the usage of structural materials which exhibit non-linear material behavior. Unlike in the latter work, in which thin-walled bodies are considered exclusively, in the present work, numerical tests are carried out not only for two-dimensional but also for challenging highly dynamic three-dimensional flows interacting with full-dimensional structural bodies. Particularly the adaption of this solver to fully three-dimensional FSI problem settings highly increases complexity of code implementations with regard to computational geometry on the one hand, as well as with regard to different aspects of efficient parallel computing on the other hand. Further differences exist in the use of different time-stepping schemes for fluids and solids as well as the treatment of varying fluid approximation spaces. Moreover, this FSI solver is investigated for flows in the low- as well as the higher-Reynolds-number regime where embedded structures undergo large deformations.

5.3.1 Semi-Discrete Nitsche-type Cut Finite Element Method

In the following, a semi-discrete coupled formulation for fluid-structure interaction problem settings as introduced in (5.64) will be proposed. Thereby, different non-conforming approximation spaces between the structural body and the fluid phase are enabled. Structural governing equations are formulated in Lagrangean description and related approximation spaces for displacement and velocity $\mathcal{W}^{\mathrm{s}}_{h,\boldsymbol{g}_{\mathrm{D}}} \overset{\mathrm{def}}{=} \mathcal{D}_{h,\boldsymbol{g}_{\mathrm{D}}} \times \mathcal{Z}_h$ as well as test spaces $\mathcal{W}^{\mathrm{s}}_{h,\boldsymbol{0}} \overset{\mathrm{def}}{=} \mathcal{D}_{h,\boldsymbol{0}} \times \mathcal{Z}_h$ are based on interface-fitted triangulations $\mathcal{T}^{\mathrm{s}}_h$, as described in Section 5.1.3. For solids, Dirichlet boundary

conditions are imposed strongly via the function space. In contrast, the fluid subdomain may be either approximated with interface-fitted meshes utilizing ALE techniques for discretizing the time derivative, or with computational meshes that do not necessarily fit to the fluid-solid interface Γ^{fs}, i.e. $\mathcal{T}_h^{\mathrm{f}} \subset \widehat{\mathcal{T}}_h^{\mathrm{f}}$ with $\Omega_h^{\mathrm{f}} \subsetneq \Omega_h^{\mathrm{f}*}$. Associated function spaces are denoted as $\mathcal{W}_h^{\mathrm{f}} \overset{\mathrm{def}}{=} \mathcal{V}_h \times \mathcal{Q}_h$ with boundary conditions assumed enforced weakly. An overview about possible discretization techniques for fluid-structure-interaction problem settings, to which the subsequently proposed coupling strategy is applicable, or can be easily extended to, was given in Section 2.1.4.3, see (2.65)–(2.68). Furthermore, incorporating fluid domain decomposition techniques as provided in Chapter 4 is also possible. Visualizations of potential settings are given in Figure 2.11.

A spatial semi-discrete formulation for the coupled fluid-structure system (5.64) can be composed of a classical finite approximation for the solid from Section 5.1.3, a stabilized flow formulation on possibly unfitted meshes with moving boundaries from Section 3.6.3 and additional Nitsche-type coupling terms for the fluid-structure interface. Coupling constraints at the fluid-structure interface can be imposed in analogy to the coupling of different fluid phases as provided in Section 4.2.1.

Definition 5.1 (Semi-discrete Nitsche-type formulation for fluid-structure interaction) *Let $\mathcal{W}_{h,\boldsymbol{g}_{\mathrm{D}}} \overset{def}{=} \mathcal{W}_h^{\mathrm{f}} \oplus \mathcal{W}_{h,\boldsymbol{g}_{\mathrm{D}}}^{\mathrm{s}}$ be the admissible space for discrete solutions, then a Nitsche-type stabilized formulation for the fluid-structure problem setting reads as follows: for all $t \in (T_0, T]$, find fluid velocity and pressure $U_h(t) = (\boldsymbol{u}_h(t), p_h(t)) \in \mathcal{W}_h^{\mathrm{f}}$ as well as solid displacement and velocity $D_h(t) = (\boldsymbol{d}_h(t), \dot{\boldsymbol{d}}_h(t)) \in \mathcal{W}_{h,\boldsymbol{g}_{\mathrm{D}}}^{\mathrm{s}}$ such that $\forall\, (V_h, W_h) = (\boldsymbol{v}_h, q_h, \boldsymbol{w}_h, \boldsymbol{z}_h) \in \mathcal{W}_h^{\mathrm{f}} \oplus \mathcal{W}_{h,\boldsymbol{0}}^{\mathrm{s}}$*

$$\mathcal{A}_h^{\mathrm{f,X}}(U_h, V_h) + \mathcal{A}_h^{\mathrm{s}}(D_h, W_h) + \mathcal{C}_h^{\mathrm{fs}}((U_h, D_h), (V_h, W_h)) = \mathcal{L}_h^{\mathrm{f,X}}(U_h, V_h) + \mathcal{L}_h^{\mathrm{s}}(W_h), \quad (5.65)$$

where the coupled formulation includes the stabilized single-phase fluid formulation $\mathcal{A}_h^{\mathrm{f,X}} - \mathcal{L}_h^{\mathrm{f,X}}$ where X *indicates the type of fluid stabilization, i.e. a* CIP/GP *or a* RBVM/GP *technique, as introduced in Sections 3.6.1.1 and 3.6.1.2, respectively. The incorporated form $\mathcal{A}_h^{\mathrm{s}} - \mathcal{L}_h^{\mathrm{s}}$ denotes the structural discrete formulation proposed in (5.24) evaluated in the structural subdomain.*

Nitsche-type fluid-solid coupling terms at Γ^{fs} are comprised in the operator $\mathcal{C}_h^{\mathrm{fs}}$. The formulation is similar to couplings between fluid phases, see (4.34)–(4.39), and emerges to

$$\begin{aligned}
\mathcal{C}_h^{\mathrm{fs}}((U_h, D_h), (V_h, W_h)) = &-\langle 2\mu\boldsymbol{\epsilon}(\boldsymbol{u}_h)\boldsymbol{n}^{\mathrm{fs}}, [\![\boldsymbol{v}_h]\!]\rangle_{\Gamma^{\mathrm{fs}}} + \langle p_h, [\![\boldsymbol{v}_h]\!]\cdot\boldsymbol{n}^{\mathrm{fs}}\rangle_{\Gamma^{\mathrm{fs}}} && (5.66)\\
&\mp \langle [\![\boldsymbol{u}_h]\!], 2\mu\boldsymbol{\epsilon}(\boldsymbol{v}_h)\boldsymbol{n}^{\mathrm{fs}}\rangle_{\Gamma^{\mathrm{fs}}} - \langle [\![\boldsymbol{u}_h]\!]\cdot\boldsymbol{n}^{\mathrm{fs}}, q_h\rangle_{\Gamma^{\mathrm{fs}}} && (5.67)\\
&+ \langle \gamma(\mu/h)[\![\boldsymbol{u}_h]\!], [\![\boldsymbol{v}_h]\!]\rangle_{\Gamma^{\mathrm{fs}}} && (5.68)\\
&+ \langle \gamma(\rho^{\mathrm{f}}\phi/h)[\![\boldsymbol{u}_h]\!]\cdot\boldsymbol{n}^{\mathrm{fs}}, [\![\boldsymbol{v}_h]\!]\cdot\boldsymbol{n}^{\mathrm{fs}}\rangle_{\Gamma^{\mathrm{fs}}} && (5.69)
\end{aligned}$$

with $[\![\boldsymbol{u}_h]\!] = \boldsymbol{u}_h^{\mathrm{f}} - \boldsymbol{u}_h^{\mathrm{s}} = \boldsymbol{u}_h - \dot{\boldsymbol{d}}_h \circ \boldsymbol{\varphi}_t^{-1}$ and $[\![\boldsymbol{v}_h]\!] = \boldsymbol{v}_h^{\mathrm{f}} - \boldsymbol{v}_h^{\mathrm{s}} = \boldsymbol{v}_h - \boldsymbol{z}_h$. It has to be noted that due to the constraints $\boldsymbol{g}_\Gamma^{\mathrm{fs}} = \boldsymbol{0}$ and $\boldsymbol{h}_\Gamma^{\mathrm{fs}} = \boldsymbol{0}$, all right-hand-side terms provided in (4.40)–(4.45) vanish, i.e. $\mathcal{L}_h^{\mathrm{fs}} \equiv 0$. In contrast to the proposed Nitsche coupling between two fluids, at fluid-solid interfaces the average weights are chosen as $w^{\mathrm{f}} = 1 - w^{\mathrm{s}} = 1$, which renders in a fluid-sided flux weighting strategy. This choice simplifies ensuring stability for couplings with nonlinear elastic structural materials. Since throughout this thesis fluids are assumed being less viscous/stiff than solids, these weights conform to the optimality of harmonic weighting when high contrast in material properties are present, as discussed in Section 4.2.2. Due to this choice, material parameters occuring in stabilization scalings of (5.68) and (5.69) belong to the fluid

phase only. Furthermore, the stabilization scaling function ϕ is defined in (3.467). Note that utilizing fluid elements with high aspect ratios or higher polynomial orders, the characteristic element length scaling $1/h = 1/h^{\mathrm{f}}$ should be replaced by a more precise piecewise constant scaling $(f^{\mathrm{f}})^2$ which emanates from the weakened trace inequality for fluid elements, as suggested in (3.134). It has to be recalled that inf-sup stability for unfitted fluid meshes, proven in terms of coercivity, is founded on using ghost-penalty stabilizations as contained in the operators $\mathscr{A}_h^{\mathrm{f,X}}(U_h, V_h)$, see Sections 3.6.1.1 and 3.6.1.2. The Nitsche penalty parameter γ is chosen as suggested in Section 3.4.4.3. Again, the different signs in (5.67) allow to switch between an adjoint-consistent $(-)$ and an adjoint-inconsistent formulation $(+)$, see Section 3.3.2.4 for further elaborations.

The question for convective interface stabilizations as proposed in (4.38) and (4.39) requires further discussion. Note that due to the Lagrangean formalism utilized for the structural dynamics, no convective term occurs for the solid phase and the treatment of possible convective instabilities would reduce to the fluid side similar to single-phase flows. However, adding inflow control on the fluid side analogously to the boundary term in (3.456), that is, consistently imposing $\boldsymbol{u}^{\mathrm{f}} - \boldsymbol{u}^{\mathrm{s}} = \boldsymbol{0}$, may possibly render in a destabilizing effect for the solid. This can be seen from the term $-\langle \rho^f (\boldsymbol{u}_h \cdot \boldsymbol{n}^{\mathrm{fs}})(-\boldsymbol{v}^{\mathrm{s}}), \boldsymbol{v}^{\mathrm{f}} \rangle$, which then remains mathematically unbalanced in proving coercivity; a situation which might become critical when the solid displaces fluid. Note further that such issues do not arise when interface-fitted fluid and solid meshes are used and the fluid is consistently formulated in an ALE *description. Then, no relative convective velocities occur at Γ^{fs}, since $\boldsymbol{u}_h = \hat{\boldsymbol{u}}_h$.*

5.3.2 Time Stepping for Nitsche-Coupled Fluid-Structure Systems

This section aims at formulating a fully discrete finite-dimensional system of non-linear equations for the Nitsche-coupled system (5.65) consisting of one fluid and one structural phase, which is to be solved for each discrete time level.

For time stepping, let the time domain $(T_0, T]$ be partitioned into N equal-sized time step intervals $J^n = (t^{n-1}, t^n]$ of size Δt with discrete time levels $t^n = T_0 + n\Delta t$ and $t^N = T$. For the temporal discretization of the coupled system, different single-field time-stepping schemes can be utilized. Subsequently, a discrete coupled formulation is exemplarily provided for the combination of a G-α method for the structural elastodynamics equations $\mathscr{A}_h^{\mathrm{s}} - \mathscr{L}_h^{\mathrm{s}}$ and a one-step-θ scheme for the stabilized fluid formulation $\mathscr{A}_h^{\mathrm{f,X}} - \mathscr{L}_h^{\mathrm{f,X}}$. Neglecting the Nitsche couplings $\mathscr{C}_h^{\mathrm{fs}}$ in (5.65) for a moment, the temporally discretized non-linear decoupled systems for fluids and solids, $\boldsymbol{R}^{\mathrm{f}}(\boldsymbol{U}^n, \boldsymbol{P}^n)$ and $\boldsymbol{R}^{\mathrm{s}}(\boldsymbol{D}^n)$, can be recalled as

$$\begin{aligned}\boldsymbol{R}^{\mathrm{f}}(\boldsymbol{U}^n, \boldsymbol{P}^n) &= \boldsymbol{M}^{\mathrm{f},n}(\boldsymbol{U}^n, \boldsymbol{P}^n) + \sigma^{-1}\boldsymbol{F}^{\mathrm{f},n}(\boldsymbol{U}^n, \boldsymbol{P}^n) \\ &\quad - \boldsymbol{H}^{\mathrm{f},n-1}(\tilde{\boldsymbol{U}}^{n-1}, \tilde{\boldsymbol{A}}^{n-1}), \qquad (5.70)\\ \boldsymbol{R}^{\mathrm{s}}(\boldsymbol{D}^n) &= \left(\boldsymbol{M}^{\mathrm{s}} \frac{1-\alpha_m}{\beta \Delta t^2} + \boldsymbol{C}^{\mathrm{s}} \frac{(1-\alpha_f)\gamma}{\beta \Delta t} \right) \boldsymbol{D}^n + (1-\alpha_f)(\boldsymbol{F}_{\mathrm{int}}^{\mathrm{s},n}(\boldsymbol{D}^n) - \boldsymbol{F}_{\mathrm{ext}}^{\mathrm{s},n}) \\ &\quad - \boldsymbol{H}^{\mathrm{s},n-1}(\boldsymbol{D}^{n-1}, \boldsymbol{V}^{n-1}, \boldsymbol{A}^{n-1}). \qquad (5.71)\end{aligned}$$

The fluid residual is recalled from (3.473) where the matrix $\boldsymbol{M}^{\mathrm{f},n}$ results from the time derivative term $(\rho^{\mathrm{f}} \boldsymbol{u}_h^n, \Upsilon(\boldsymbol{v}_h, q_h))$ with Υ depending on the type of fluid stabilization, as elaborated in Section 3.6.1.3. Furthermore, $\boldsymbol{F}^{\mathrm{f},n}$ denotes all operators to be evaluated at time level t^n, i.e. all

standard Galerkin terms, stabilization operators as well as Nitsche terms according to the weak imposition of boundary conditions. Terms belonging to the previous time levels are comprised in $\boldsymbol{H}^{\mathrm{f},n-1}$. The structural residual is defined as in (5.37) based on a generalized trapezoidal rule (GTR) approximation for internal and external forces, see (5.36), and $\boldsymbol{H}^{\mathrm{s},n-1}$ comprises all terms evaluated at the previous time level t^{n-1}. Note that the system of first-order structural ODEs could be expressed solely in the unknown displacement vector $\boldsymbol{D}^n$.

Expressing structural interface velocities $\boldsymbol{u}_h^{\mathrm{s}} = \dot{\boldsymbol{d}}_h \circ \boldsymbol{\varphi}_t^{-1}$, which are defined in spatial coordinates, in terms of structural displacements $\boldsymbol{D}$, which are defined with respect to the reference system, an independent temporal discretization at the fluid-solid interface can be introduced. Applying a one-step-θ scheme to this ODE yields

$$\boldsymbol{U}_\Gamma^{\mathrm{s},n}(\boldsymbol{D}_\Gamma^n) = \frac{\boldsymbol{D}_\Gamma^n - \boldsymbol{D}_\Gamma^{n-1}}{\theta_\Gamma \Delta t} - \frac{1-\theta_\Gamma}{\theta_\Gamma}\boldsymbol{U}_\Gamma^{\mathrm{s},n-1}, \tag{5.72}$$

where $\boldsymbol{U}_\Gamma^{\mathrm{s},n}$ is a vector-valued approximation on the structural interface velocities at time level t^n, i.e. $\boldsymbol{u}_h^{\mathrm{s}} \circ \boldsymbol{\varphi}_{t^n} = \dot{\boldsymbol{d}}_h(t^n)$. Denoting internal forces, which have to be in equilibrium at the fluid-solid interface Γ^{fs}, with $\boldsymbol{F}_{\Gamma^{\mathrm{fs}}}^{\mathrm{s},n}$ and $\boldsymbol{F}_{\Gamma^{\mathrm{fs}}}^{\mathrm{f},n}$ for the solid and fluid phase, respectively, residuals can be formulated as

$$\boldsymbol{R}^{\mathrm{f}}(\boldsymbol{U}^n, \boldsymbol{P}^n) - \sigma^{-1}\boldsymbol{F}_{\Gamma^{\mathrm{fs}}}^{\mathrm{f},n}, \tag{5.73}$$

$$\boldsymbol{R}^{\mathrm{s}}(\boldsymbol{D}^n) - ((1-\alpha_f)\boldsymbol{F}_{\Gamma^{\mathrm{fs}}}^{\mathrm{s},n} + \alpha_f \boldsymbol{F}_{\Gamma^{\mathrm{fs}}}^{\mathrm{s},n-1}) \tag{5.74}$$

with σ the characteristic temporal factors as defined in (3.476) and (3.479). The interfacial forces are replaced by numerical forces in the discrete setting. These are given by the strongly consistent Nitsche-coupling terms (5.66)–(5.69), for which holds $\boldsymbol{F}_{\Gamma^{\mathrm{fs}}}^{\mathrm{f},n} = -\boldsymbol{C}^{\mathrm{fs}}((\boldsymbol{U}^n, \boldsymbol{P}^n), \boldsymbol{D}^n)$ and $\boldsymbol{F}_{\Gamma^{\mathrm{fs}}}^{\mathrm{s},n} = -\boldsymbol{C}^{\mathrm{sf}}((\boldsymbol{U}^n, \boldsymbol{P}^n), \boldsymbol{D}^n)$, where

$$\begin{aligned}
\boldsymbol{C}^{\mathrm{fs}}((\boldsymbol{U}^n, \boldsymbol{P}^n), \boldsymbol{D}^n) \quad \Leftrightarrow \quad & - \langle 2\mu\boldsymbol{\epsilon}(\boldsymbol{u}_h)\boldsymbol{n}^{\mathrm{fs}}, \boldsymbol{v}_h\rangle_{\Gamma^{\mathrm{fs}}} \\
& + \langle p_h, \boldsymbol{v}_h \cdot \boldsymbol{n}^{\mathrm{fs}}\rangle_{\Gamma^{\mathrm{fs}}} \\
& \mp \langle [\![\boldsymbol{u}_h]\!], 2\mu\boldsymbol{\epsilon}(\boldsymbol{v}_h)\boldsymbol{n}^{\mathrm{fs}}\rangle_{\Gamma^{\mathrm{fs}}} \\
& - \langle [\![\boldsymbol{u}_h]\!] \cdot \boldsymbol{n}^{\mathrm{fs}}, q_h\rangle_{\Gamma^{\mathrm{fs}}} \\
& + \langle \gamma(\mu/h)[\![\boldsymbol{u}_h]\!], \boldsymbol{v}_h\rangle_{\Gamma^{\mathrm{fs}}} \\
& + \langle \gamma(\rho^{\mathrm{f}}\sigma h + \rho^{\mathrm{f}}|\boldsymbol{u}_h^{\mathrm{f}}| + \mu/h)[\![\boldsymbol{u}_h]\!] \cdot \boldsymbol{n}^{\mathrm{fs}}, \boldsymbol{v}_h \cdot \boldsymbol{n}^{\mathrm{fs}}\rangle_{\Gamma^{\mathrm{fs}}},
\end{aligned} \tag{5.75}$$

$$\begin{aligned}
\boldsymbol{C}^{\mathrm{sf}}((\boldsymbol{U}^n, \boldsymbol{P}^n), \boldsymbol{D}^n) \quad \Leftrightarrow \quad & - \langle 2\mu\boldsymbol{\epsilon}(\boldsymbol{u}_h)\boldsymbol{n}^{\mathrm{fs}}, (-\boldsymbol{z}_h)\rangle_{\Gamma^{\mathrm{fs}}} \\
& + \langle p_h, (-\boldsymbol{z}_h) \cdot \boldsymbol{n}^{\mathrm{fs}}\rangle_{\Gamma^{\mathrm{fs}}} \\
& + \langle \gamma(\mu/h)[\![\boldsymbol{u}_h]\!], (-\boldsymbol{z}_h)\rangle_{\Gamma^{\mathrm{fs}}} \\
& + \langle \gamma(\rho^{\mathrm{f}}\sigma h + \rho^{\mathrm{f}}|\boldsymbol{u}_h^{\mathrm{f}}| + \mu/h)[\![\boldsymbol{u}_h]\!] \cdot \boldsymbol{n}^{\mathrm{fs}}, (-\boldsymbol{z}_h) \cdot \boldsymbol{n}^{\mathrm{fs}}\rangle_{\Gamma^{\mathrm{fs}}}.
\end{aligned} \tag{5.76}$$

These can be identified by splitting contributions into fluid and structural residuals, i.e. with respect to $\boldsymbol{v}_h$ and $\boldsymbol{z}_h$. Furthermore, the structural interface force from the previous time level t^{n-1} occurring in (5.73) can be recovered from the respective structural coupling matrix

$$\boldsymbol{F}_{\Gamma^{\mathrm{fs}}(t^{n-1})}^{\mathrm{s},n-1} = -\boldsymbol{C}^{\mathrm{sf},n-1}((\boldsymbol{U}^{n-1}, \boldsymbol{P}^{n-1}), \boldsymbol{D}^{n-1}). \tag{5.77}$$

After rescaling the single non-linear fluid and solid residuals (5.73) and (5.74), the final Nitsche-coupled finite-dimensional fluid-structure system of equations, which is to be solved for the current time level t^n, reads as follows: find discrete finite-dimensional vectors $\boldsymbol{U}^n, \boldsymbol{P}^n, \boldsymbol{D}^n$ such that

$$\begin{bmatrix} \boldsymbol{R}_{(U,P)} \\ \boldsymbol{R}_D \end{bmatrix}^n = \begin{bmatrix} \boldsymbol{C}^{\mathrm{fs}}((\boldsymbol{U}^n, \boldsymbol{P}^n), \boldsymbol{D}^n) + \sigma \boldsymbol{R}^{\mathrm{f}}(\boldsymbol{U}^n, \boldsymbol{P}^n) \\ \frac{1}{1-\alpha_f}\boldsymbol{R}^{\mathrm{s}}(\boldsymbol{D}^n) + \boldsymbol{C}^{\mathrm{sf}}((\boldsymbol{U}^n, \boldsymbol{P}^n), \boldsymbol{D}^n) - \frac{\alpha_f}{1-\alpha_f}\boldsymbol{F}^{\mathrm{s},n-1}_{\Gamma^{\mathrm{fs}}(t^{n-1})} \end{bmatrix}^n = \begin{bmatrix} \boldsymbol{0} \\ \boldsymbol{0} \end{bmatrix} \tag{5.78}$$

with given solid approximations $\boldsymbol{D}^{n-1}, \boldsymbol{V}^{n-1}, \boldsymbol{A}^{n-1}$ and fluid approximations $\boldsymbol{U}^{n-1}, \boldsymbol{P}^{n-1}$ from the previous time level t^{n-1} as well as projected fluid solutions $\tilde{\boldsymbol{U}}^{n-1}(\boldsymbol{U}^{n-1}), \tilde{\boldsymbol{A}}^{n-1}(\boldsymbol{A}^{n-1})$ with respect to the current interface location $\Gamma^{\mathrm{fs}}(t^n)$. Note, the fluid residual $\boldsymbol{R}_{(U,P)} = [\boldsymbol{R}_U, \boldsymbol{R}_P]^T$ can be further split into velocity and pressure residuals.

5.3.3 Monolithic Solution Algorithm for Unfitted Non-Linear Systems

In this subsection, a monolithic solution procedure for the non-linear coupled fluid-structure system is derived. For the sake of clarity, the overall final algorithm is split into two nested algorithms. The substantial solution procedure for non-linear FSI residuals is given by a Newton-Raphson-like iterative method and is presented in Algorithm 5.2. This main sub-algorithm is applicable to interface-fitted as well as unfitted mesh configurations as long as the fluid function space does not change while iterating. An extension of the classical time loop to the unfitted mesh case, which even allows to adapt the function space during the iterative procedure at a fixed time level, is summarized in Algorithm 5.1.

First, solution techniques which are well-established for full-implicitly coupled non-linear FSI systems will be examined. Afterwards, an overview of the overall algorithmic procedure, the final monolithic solution algorithm will be given. Therein, focus is directed to peculiarities of unfitted mesh configurations.

Newton-Raphson-like Approximation for Non-linear FSI Residuals. The solution approximation to the coupled fluid-solid system at a discrete time level t^n is given in terms of the finite-dimensional system of non-linear equations (5.78) for fluid velocities and pressure $(\boldsymbol{U}, \boldsymbol{P})^n$ and for structural displacements $\boldsymbol{D}^n$. Therein, non-linearities emanate from geometrical and material non-linear relations in the structural dynamics PDE on the one hand, and from the non-linear convective fluid term together with its occurrence in related fluid stabilizations on the other hand. Moreover, while structural equations are integrated in referential configuration, further non-obvious non-linearities are hidden in the change of the integration volume and surface area associated with the fluid subdomain, which depend on the non-linear interface motion.

Neglecting for a short term that due to the unfittedness of fluid and solid computational meshes the discrete fluid function space can change for structural/interfacial motions, the solution of the non-linear system (5.78) can be approximated iteratively by performing a Newton-Raphson-like method. The subsequent approximation procedure poses a mixture of fixed-point iterations for the fluid and a full Newton-Raphson method for the structural residual.

Algorithm 5.1 Monolithic solution algorithm for non-linear unfitted FSI-systems

INPUT: initial conditions $\boldsymbol{d}_0^{\mathrm{s}}, \dot{\boldsymbol{d}}_0^{\mathrm{s}}, \boldsymbol{u}_0^{\mathrm{f}}$ at T_0.
Initialize structural $\boldsymbol{A}_0^{\mathrm{s}}$ for G-α scheme and set fluid $\boldsymbol{A}_0^{\mathrm{f}}$ for OST or $\theta = 1.0$ for $n = 1$.
for time steps $1 \leqslant n \leqslant N$ **do**
  Update time level $t^n = T_0 + n\Delta t$. Reset cycle counter to $c = 1$.
  // cycle over fluid function space changes
  while (**not** converged) **do**
    if $(c > C_{\mathrm{max}})$ **then**
      Throw exception ("maximum number of function space changes at t^n exceeded!").
    end if
    if $(c = 1)$ **then**
      Structural Solver:
      Perform predictor $(\boldsymbol{D}, \boldsymbol{U}, \boldsymbol{A})_{c=1}^n \leftarrow P(\boldsymbol{D}, \boldsymbol{U}, \boldsymbol{A})^{n-1}$.
      Fluid Solver:
      Update interface position $(\Gamma_h)_{c=1}^n$ according to predicted $\boldsymbol{D}_{c=1}^n$, intersect $\widehat{\mathcal{T}}_h$ to obtain active mesh $(\mathcal{T}_h)_{c=1}^n$ and update face and element sets $(\mathcal{F}_\Gamma)_{c=1}^n$, $(\mathcal{T}_\Gamma)_{c=1}^n$.
      Perform Algorithm 2.1 to allocate DOFs and set up fluid function space $(\mathcal{W}_h^{\mathrm{f}})_{c=1}^n$.
      Perform Algorithm 3.1 and transcribe solution vectors between function spaces $(\mathcal{W}_h^{\mathrm{f}})^{n-1} \rightarrow (\mathcal{W}_h^{\mathrm{f}})_{c=1}^n$ between time levels s.t. $(\tilde{\boldsymbol{U}}, \tilde{\boldsymbol{P}}, \tilde{\boldsymbol{A}})_{c=1}^{n-1} \in (\mathcal{V}_h^{\mathrm{f}} \times \mathcal{Q}_h^{\mathrm{f}} \times \mathcal{V}_h)_{c=1}^n$.
      Perform fluid predictor, e.g., $(\boldsymbol{U}, \boldsymbol{P})_{c=1,i=1}^n = (\tilde{\boldsymbol{U}}, \tilde{\boldsymbol{P}})^{n-1} \in (\mathcal{W}_h^{\mathrm{f}})_{c=1,i=1}^n$.
    else // The fluid function space has changed within the last cycle $c-1$
      Perform Algorithm 3.1 and transcribe solution vectors between function spaces $(\mathcal{W}_h^{\mathrm{f}})^{n-1} \rightarrow (\mathcal{W}_h^{\mathrm{f}})_c^n$ between time levels s.t. $(\tilde{\boldsymbol{U}}, \tilde{\boldsymbol{P}}, \tilde{\boldsymbol{A}})_c^{n-1} \in (\mathcal{V}_h^{\mathrm{f}} \times \mathcal{Q}_h^{\mathrm{f}} \times \mathcal{V}_h^{\mathrm{f}})_c^n$.
      Use recent solution approximation from interrupted pass $c-1$ as initial guess for the following Newton-Raphson procedure. Note that $(\boldsymbol{U}, \boldsymbol{P})_{c,i=1}^n \in (\mathcal{W}_h^{\mathrm{f}})_c^n$.
    end if
    // previous time level solution available as: $(\boldsymbol{D}, \boldsymbol{V}, \boldsymbol{A})_c^{n-1}$ (solid), $(\tilde{\boldsymbol{U}}, \tilde{\boldsymbol{A}})_c^{n-1}$ (fluid)
    // prediction for current time level available as $((\boldsymbol{U}, \boldsymbol{P}), \boldsymbol{D})_{c,i=1}^n$
    Perform Algorithm 5.2. // (Re-)start NEWTON-RAPHSON-like iterations
    if (Newton-Raphson converged) **then**
      break while
    end if
    $c \leftarrow c + 1$
  end while
  // Inner Newton-Raphson loop converged with non-changing fluid function space
  Update structural vectors $\boldsymbol{A}^n, \boldsymbol{U}^n$ based on $\boldsymbol{D}^n$ for G-α scheme via (5.38)–(5.39).
  Update fluid acceleration approximation $\boldsymbol{A}^n$ for OST-scheme via (3.485), i.e. $\boldsymbol{a}_h^n(\boldsymbol{u}_h^n, \tilde{\boldsymbol{u}}_c^{n-1}, \tilde{\boldsymbol{a}}_c^{n-1})$ with $\tilde{\boldsymbol{u}}_c^{n-1}, \tilde{\boldsymbol{a}}_c^{n-1}$ the recent projections of $\boldsymbol{u}_c^{n-1}, \boldsymbol{a}_c^{n-1} \in \mathcal{V}_h^{n-1}$ to the fluid function space $\mathcal{V}_c^n$ belonging to the converged state.
  Store the structural force vector $\boldsymbol{F}_{\Gamma^{\mathrm{fs}}(t^n)}^{\mathrm{s},n}$ (5.77) for the next time level.
  Store final approximations: $(\boldsymbol{D}, \boldsymbol{U}, \boldsymbol{A})^n$ for the solid and $(\boldsymbol{U}, \boldsymbol{P}, \boldsymbol{A})^n$ for the fluid.
end for
OUTPUT: solid displacement and fluid velocity and pressure solution approximations $\{((\boldsymbol{U}, \boldsymbol{P}), \boldsymbol{D})^n\}_{1 \leqslant n \leqslant N}$ for discrete time levels $\{t^n\}_{1 \leqslant n \leqslant N}$. Note the possibly time-varying fluid approximation spaces $\{\mathcal{W}_h^{\mathrm{f}}\}_{1 \leqslant n \leqslant N}$.

Algorithm 5.2 Newton-Raphson-like solution procedure for non-linear FSI-system

INPUT: initial guess of structural displacements, fluid velocity and pressure $((\boldsymbol{U},\boldsymbol{P}),\boldsymbol{D})_{i=1}^{n}$ for iterative solution procedure. Previous time-step solutions for structure $(\boldsymbol{D},\boldsymbol{V},\boldsymbol{A})^{n-1}$, for fluid $(\tilde{\boldsymbol{U}},\tilde{\boldsymbol{A}})^{n-1}$, interfacial velocities $\boldsymbol{U}_{\Gamma}^{\mathrm{s},n-1}$ and structural forces $\boldsymbol{F}_{\Gamma^{\mathrm{fs}}(t^{n-1})}^{\mathrm{s},n-1}$.
for Newton-Raphson-like iterations $1 \leqslant i \leqslant N_{\max}$ **do**
  FSI Solver:
  Update structural interface velocity $(\boldsymbol{U}_{\Gamma}^{\mathrm{s}})_i^n$ based on $(\boldsymbol{D}_{\Gamma})_i^n$ with OST-scheme (5.72).
  Apply current iterations to structural solver and to CUTFEM fluid solver.
  Structural Solver:
  Evaluate structural contribution to matrix $\boldsymbol{L}_{DD}|_{\boldsymbol{D}_i^n}$ and to residual $\boldsymbol{R}_D|_{\boldsymbol{D}_i^n}$, see (5.79).
  Fluid Solver:
  if $(i > 1)$ **then**
    Update interface position to $(\Gamma_h)_i^n$ according to last iteration $\boldsymbol{D}_i^n$.
    Intersect the mesh $\widehat{\mathcal{T}}_h$ and obtain the active computational mesh $(\mathcal{T}_h)_i^n$ and construct updated face and element sets $(\mathcal{F}_{\Gamma})_i^n$, $(\mathcal{T}_{\Gamma})_i^n$.
    Perform Algorithm 2.1 to allocate DOFs and set up new fluid function spaces $(\mathcal{W}_h^{\mathrm{f}})_i^n$.
    Perform TRANSFER/COPY-PHASE of Algorithm 3.1 and transcribe solution vectors between function spaces $(\mathcal{W}_h^{\mathrm{f}})_{i-1}^n \rightarrow (\mathcal{W}_h^{\mathrm{f}})_i^n$ of previous and current iteration.
    if (TRANSFER/COPY-PHASE **not** successful) **then**
      // Change in fluid function space occurred, i.e. $(\mathcal{W}_h^{\mathrm{f}})_{i-1}^n \neq (\mathcal{W}_h^{\mathrm{f}})_i^n$.
      Perform EXTENSION-PHASE of Algorithm 3.1 and utilize the resulting approximation as initial guess for the next Newton-Raphson cycle $c+1$: $((\boldsymbol{U},\boldsymbol{P}),\boldsymbol{D})^n \in (\mathcal{W}_h^{\mathrm{f}})_{c+1,i=1}^n \times \mathcal{D}_h$
      return false.
    end if
  end if
  Evaluate fluid boundary conditions $\boldsymbol{g}_{\mathrm{D}}^{\mathrm{f}}(t^n)$, $\boldsymbol{h}_{\mathrm{N}}^{\mathrm{f}}(t^n)$ with respect to $(\Gamma_h)_i^n$.
  Evaluate stabilized fluid system, coupling matrices contributing to $\boldsymbol{L}_{xy}$ and to residuals $\boldsymbol{R}_U, \boldsymbol{R}_P, \boldsymbol{R}_D$, see (5.79).
  FSI Solver:
  Set up final linear fluid-structure system $\boldsymbol{L}^{\mathrm{fs}} \cdot \Delta((\boldsymbol{U},\boldsymbol{P}),\boldsymbol{D})_i^n = -\boldsymbol{R}^{\mathrm{fs}}$ (5.79).
  Apply strong Dirichlet boundary conditions from function spaces $\mathcal{W}_{h,\boldsymbol{g}_{\mathrm{D}}}^{\mathrm{f}}$ and $\mathcal{D}_{h,\boldsymbol{g}_{\mathrm{D}}}^{\mathrm{s}}$.
  Build block preconditioner and apply to (5.79).
  Solve preconditioned linearized fixed-point like system (5.79) for $\Delta((\boldsymbol{U},\boldsymbol{P}),\boldsymbol{D})_i^n$.
  Check convergence: $\|\Delta((\boldsymbol{U},\boldsymbol{P}),\boldsymbol{D})_i^n\| < TOL$ **and** $\|(\boldsymbol{R}^{\mathrm{fs}})_i^n\| < TOL$.
  if (FSI system converged) **then**
    return true
  end if
  Update Newton-Raphson iteration via (5.80) to $((\boldsymbol{U},\boldsymbol{P}),\boldsymbol{D})_{i+1}^n$.
end for
Throw exception ("maximum number of Newton-Raphson iterations reached!").
OUTPUT:
return false with iteration $((\boldsymbol{U},\boldsymbol{P}),\boldsymbol{D})_i^n \in (\mathcal{W}_h^{\mathrm{f}})_i^n \times \mathcal{D}_h^{\mathrm{s}}$ based on changed fluid function space $(\mathcal{W}_h^{\mathrm{f}})_i^n \neq (\mathcal{W}_h^{\mathrm{f}})_{i-1}^n$, or
return true with converged velocity, pressure and displacement solution approximations $((\boldsymbol{U}^n,\boldsymbol{P}^n),\boldsymbol{D}^n)$ for time level t^n.

The solution $((\boldsymbol{U},\boldsymbol{P}),\boldsymbol{D})^n$ is approximated iteratively for $i \geqslant 1$ by solving linear systems for increments $\Delta((\boldsymbol{U},\boldsymbol{P}),\boldsymbol{D})_i^n$ satisfying

$$\underbrace{\left[\begin{array}{c:c|c} \boldsymbol{L}_{UU} & \boldsymbol{L}_{UP} & \boldsymbol{L}_{UD} \\ \hdashline \boldsymbol{L}_{PU} & \boldsymbol{L}_{PP} & \boldsymbol{L}_{PD} \\ \hline \boldsymbol{L}_{DU} & \boldsymbol{L}_{DP} & \boldsymbol{L}_{DD} \end{array}\right]_i^n}_{\boldsymbol{L}^{\mathrm{fs}}} \cdot \left[\begin{array}{c} \Delta\boldsymbol{U} \\ \hdashline \Delta\boldsymbol{P} \\ \hline \Delta\boldsymbol{D} \end{array}\right]_i^n = -\underbrace{\left[\begin{array}{c} \boldsymbol{R}_U \\ \hdashline \boldsymbol{R}_P \\ \hline \boldsymbol{R}_D \end{array}\right]_i^n}_{\boldsymbol{R}^{\mathrm{fs}}} \tag{5.79}$$

followed by a Newton-Raphson incremental update step for the next iteration

$$\left[\begin{array}{c} \boldsymbol{U} \\ \hdashline \boldsymbol{P} \\ \hline \boldsymbol{D} \end{array}\right]_{i+1}^n = \left[\begin{array}{c} \boldsymbol{U} \\ \hdashline \boldsymbol{P} \\ \hline \boldsymbol{D} \end{array}\right]_i^n + \left[\begin{array}{c} \Delta\boldsymbol{U} \\ \hdashline \Delta\boldsymbol{P} \\ \hline \Delta\boldsymbol{D} \end{array}\right]_i^n . \tag{5.80}$$

Note that the subscript $()_i$ in matrix and right-hand side of the linear system (5.79) indicates sub-matrices and residuals being evaluated on basis of the current approximation $((\boldsymbol{U},\boldsymbol{P}),\boldsymbol{D})_i^n$. Therein, let $\boldsymbol{L}_{xy} = \frac{\partial \boldsymbol{R}_x}{\partial y}$ denote (pseudo)-directional derivatives of residuals $\boldsymbol{R}_x$ from (5.78) with respect to the finite dimensional solution approximation y, where $x, y \in \{\boldsymbol{U},\boldsymbol{P},\boldsymbol{D}\}$. Exemplarily, approximation $\boldsymbol{L}_{DD}$ for neglected Rayleigh damping is given as

$$\boldsymbol{L}_{DD}|_{((\boldsymbol{U},\boldsymbol{P}),\boldsymbol{D})_i^n} = \frac{1}{1-\alpha_f}\left(\boldsymbol{M}^{\mathrm{s}}\frac{1-\alpha_m}{\beta\Delta t^2} + \left.\frac{\partial \boldsymbol{F}_{\mathrm{int}}^{\mathrm{s},n}(\boldsymbol{D})}{\partial \boldsymbol{D}}\right|_{\boldsymbol{D}=\boldsymbol{D}_i^n}\right) + \boldsymbol{G}|_{((\boldsymbol{U},\boldsymbol{P}),\boldsymbol{D})_i^n}, \tag{5.81}$$

where

$$\begin{aligned} \boldsymbol{G}|_{((\boldsymbol{U},\boldsymbol{P}),\boldsymbol{D})_i^n} &\overset{\mathrm{def}}{=} \left.\frac{\partial \boldsymbol{C}^{\mathrm{sf}}((\boldsymbol{U},\boldsymbol{P}),\boldsymbol{D})}{\partial \boldsymbol{D}}\right|_{((\boldsymbol{U},\boldsymbol{P}),\boldsymbol{D})=((\boldsymbol{U},\boldsymbol{P}),\boldsymbol{D})_i^n} \\ \Leftrightarrow \quad &+ \langle \gamma(\mu/h)(-\partial_{\boldsymbol{D}}(\boldsymbol{u}_h^{\mathrm{s}})|_{\boldsymbol{D}_i^n}, (-\boldsymbol{z}_h)\rangle_{\Gamma^{\mathrm{fs}}(\boldsymbol{D}_i^n)} \\ &+ \langle \gamma(\rho^{\mathrm{f}}\sigma h + \rho^{\mathrm{f}}|\boldsymbol{u}_h^{\mathrm{f}}| + \mu/h)(-\partial_{\boldsymbol{D}}(\boldsymbol{u}_h^{\mathrm{s}})|_{\boldsymbol{D}_i^n})\cdot\boldsymbol{n}^{\mathrm{fs}}(\boldsymbol{D}_i^n), (-\boldsymbol{z}_h)\cdot\boldsymbol{n}^{\mathrm{fs}}(\boldsymbol{D}_i^n)\rangle_{\Gamma^{\mathrm{fs}}(\boldsymbol{D}_i^n)}, \end{aligned} \tag{5.82}$$

with $\partial_{\boldsymbol{D}}(\boldsymbol{u}_h^{\mathrm{s}})|_{\boldsymbol{D}_i^n} = \left.\frac{\partial \boldsymbol{u}_h^{\mathrm{s}}(\boldsymbol{D})}{\partial \boldsymbol{D}}\right|_{\boldsymbol{D}=\boldsymbol{D}_i^n} \Leftrightarrow \frac{1}{\theta_\Gamma \Delta t}\boldsymbol{D}_i^n$. Note that change of integration area and interface unit normal vectors are treated fixed-point-like. All other approximations $\boldsymbol{L}_{xy}$ can be derived by analogy but are not presented here.

Newton-Raphson-like Algorithmic Procedure for Non-changing Function Spaces. The solution procedure for the non-linear FSI residual (5.78) is summarized in Algorithm 5.2. It assumes that the fluid function space remains unchanged during the iteration loop. Relaxing this assumption will be addressed afterwards within a subsequent paragraph.

For starting the iterative solution procedure, an initial guess for the solution fields is required which is denoted with $((\boldsymbol{U},\boldsymbol{P}),\boldsymbol{D})_{i=1}^n$. These may be given, for instance, in terms of a predicted displacement field and the velocity solution of the previous time level as discussed, e.g., by Mayr *et al.* [185]. Furthermore, evaluating FSI residuals requires history from the previous time level for structural fields, i.e. $(\boldsymbol{D},\boldsymbol{V},\boldsymbol{A})^{n-1}$, as well as structural forces $\boldsymbol{F}_{\Gamma^{\mathrm{fs}}(t^{n-1})}^{\mathrm{s},n-1}$ as defined in (5.77). Note that due to unfitted approximation of the fluid field, approximations have to be first

projected onto the current function space $(\mathcal{W}_h^{\mathrm{f}})_{i=1}^n$ associated with the time level t^n by applying Algorithm 3.1, which provides approximations $(\tilde{\boldsymbol{U}}, \tilde{\boldsymbol{A}})^{n-1} \in (\mathcal{V}_h)_{i=1}^n \times (\mathcal{V}_h)_{i=1}^n$.

Newton-Raphson-like iterations are performed until convergence of residuals $(\boldsymbol{R}^{\mathrm{fs}})_i^n$ and of increments $\Delta((\boldsymbol{U}, \boldsymbol{P}), \boldsymbol{D})_i^n$ is achieved. For a current displacement iteration $\boldsymbol{D}_i^n$, structural interface velocities $(\boldsymbol{U}_\Gamma^{\mathrm{s}})_i^n$ can be updated via (5.72). After setting current approximations to the structural and the fluid solver, their contributions to matrices $(\boldsymbol{L}_{xy})_i^n$ and right-hand-side blocks $(\boldsymbol{R}_x)_i^n$ of the linearized FSI system (5.79) can be evaluated and finally assembled into the global system $\boldsymbol{L}^{\mathrm{fs}} \cdot \Delta((\boldsymbol{U}, \boldsymbol{P}), \boldsymbol{D})_i^n = -\boldsymbol{R}^{\mathrm{fs}}$. After applying strong Dirichlet constraints from $\mathcal{W}_{h,\boldsymbol{g}_{\mathrm{D}}}^{\mathrm{f}}$ and $\mathcal{W}_{h,\boldsymbol{g}_{\mathrm{D}}}^{\mathrm{s}}$ and setting up a block preconditioner, the linear FSI system can be solved for the Newton-Raphson increments. Finally, the approximations can be updated to $((\boldsymbol{U}, \boldsymbol{P}), \boldsymbol{D})_{i+1}^n$ via (5.80). If convergence checks fail, it has to be proceeded with the next iteration $i+1$. This procedure is summarized in Algorithm 5.2. Note that for unfitted fluid approximations their function spaces might change due to displacing the fluid-structure interface. This demands further measures as will be addressed later in Algorithm 5.1.

Solving Linear Matrix Systems. For approximating the incremental solution of each linear FSI iteration (5.79), a preconditioned GMRES solver is utilized. Building specific preconditioners is based on a unified framework recently proposed by Verdugo and Wall [256] which is applicable to different monolithically solved n-field coupled problems. Preconditioners used throughout this thesis use generic block Gauss–Seidel iterations for uncoupling the subproblems. For the decoupled structural and fluid blocks, any combination of either one-level domain decomposition preconditioners of incomplete factorization type, as developed by Sala and Heroux [224], or algebraic multigrid (AMG) methods, as proposed by Prokopenko *et al.* [211], is applicable. Both applied preconditioning techniques are developed under the Trilinos project conducted by Sandia National Laboratories.

Cycle over Possible Function Space Changes for Unfitted Fluid Approximations. Recalling the issue of applicability of iterative solution techniques for unfitted mesh methods, which consists in potentially varying fluid approximation spaces during the iterative procedure, the following generalization of the Newton-Raphson scheme for such problem settings is suggested:

As described in Algorithm 5.2, for each iteration the updated interface displacements are set to the CUTFEM fluid solver on which basis the computational mesh $\widehat{\mathcal{T}}_h^{\mathrm{f}}$ is intersected, associated face and element sets $(\mathcal{F}_\Gamma)_i^n$ and $(\mathcal{T}_\Gamma)_i^n$ are built and the fluid function space $(\mathcal{W}_h^{\mathrm{f}})_i^n$ is constructed. After updating the discrete function space via Algorithm 2.1, previous fluid iterations $(\boldsymbol{U}, \boldsymbol{P})_{i-1}^n \in (\mathcal{W}_h^{\mathrm{f}})_{i-1}^n$ have to be transcribed to $(\mathcal{W}_h^{\mathrm{f}})_i^n$. This can be carried out DOF-wise using the TRANSFER/COPY-PHASE of Algorithm 3.1 whenever $(\mathcal{W}_h^{\mathrm{f}})_{i-1}^n \equiv (\mathcal{W}_h^{\mathrm{f}})_i^n$. However, if $(\mathcal{W}_h^{\mathrm{f}})_{i-1}^n \neq (\mathcal{W}_h^{\mathrm{f}})_i^n$, the current Newton-Raphson cycle c has to be interrupted. Algorithm 3.1, that is including the EXTENSION-PHASE, can be applied to $(\boldsymbol{U}, \boldsymbol{P})_{c,i}^n \in (\mathcal{W}_h^{\mathrm{f}})_{c,i-1}^n$ to obtain a predicted approximation $((\boldsymbol{U}, \boldsymbol{P}), \boldsymbol{D})_{c+1,i=1}^n = (P_i^n(\boldsymbol{U}, \boldsymbol{P})_{c,i}^n, \boldsymbol{D})$ for the next pass $c+1$. These preparation steps for restarting the Newton-Raphson procedure in a new cycle are comprised in Algorithm 5.2.

As summarized in Algorithm 5.1, within a subsequent run, i.e. $c > 1$, the previous time level fluid solution has to be adapted according to the changed function space. For this purpose, a projection step as provided by Algorithm 3.1 can be performed such that $(\tilde{\boldsymbol{U}}, \tilde{\boldsymbol{P}}, \tilde{\boldsymbol{A}})_c^{n-1} \in (\mathcal{V}_h^{\mathrm{f}} \times$

$\mathcal{Q}_h^{\mathrm{f}} \times \mathcal{V}_h^{\mathrm{f}})_c^n$. Note that for unchanged DOFs the Newton-Raphson is interrupted just formally and the current solution approximation remains unmodified due to the DOF-wise copy-technique. However, theoretically it might happen that DOFs get repeatedly activated and deactivated for subsequent cycle runs $c, c+1, c+2, ...$ Together with continuously modified projected solutions $(\tilde{\boldsymbol{U}}, \tilde{\boldsymbol{P}}, \tilde{\boldsymbol{A}})_c^{n-1}$ such situations could worsen or even totally destroy convergence. As such behavior did not occur for the numerical simulations considered in this thesis, a precise description of counteracting measures was dispensed. However, straightforward techniques like freezing the fluid function space, i.e. $(\mathcal{W}_h^{\mathrm{f}})_i^n = (\mathcal{W}_h^{\mathrm{f}})_{i+1}^n = (\mathcal{W}_h^{\mathrm{f}})_{i+2}^n = ...$, could be simply realized and DOFs which are located outside of the integrated fluid domain can be sufficiently controlled by expanding the interface zone $\mathcal{F}_\Gamma$ for ghost-penalty-stabilization operators.

After achieving a converged solution from the proposed nested Newton-Raphson procedure, further time-stepping related quantities need to be updated. For an OST scheme in the fluid solver, an acceleration approximation $\boldsymbol{A}^n$ is obtained from (3.485), where $\boldsymbol{a}_h^n(\boldsymbol{u}_h^n, \tilde{\boldsymbol{u}}_c^{n-1}, \tilde{\boldsymbol{a}}_c^{n-1})$ incorporates projected velocity and acceleration approximations $\tilde{\boldsymbol{u}}_c^{n-1}, \tilde{\boldsymbol{a}}_c^{n-1}$ belonging to the converged cycle run c of the previous time level. For the structural field, acceleration and velocity fields $\boldsymbol{A}^n$ and $\boldsymbol{U}^n$ according to the G-α scheme are refreshed via (5.38)–(5.39). After storing the structural forces for the next time steps as specified in (5.77), all quantities required for proceeding with the next time level t^{n+1} are available, i.e. $(\boldsymbol{U}, \boldsymbol{P}, \boldsymbol{A})^n$ for the fluid and $(\boldsymbol{D}, \boldsymbol{U}, \boldsymbol{A})^n$ and $\boldsymbol{F}^{\mathrm{s},n}_{\Gamma^{\mathrm{fs}}(t^n)}$ for the solid.

5.3.4 Pulsating Flow over a Bending Flexible Flap

In the following, the proposed unfitted FSI solver is validated for a challenging three-dimensional test case which exhibits highly dynamic transient fluid-structure interaction. Robustness of the fluid solver and the ability to deal with large fluid domain changes has been already demonstrated in Section 3.6.4 for fluid-structure-interaction-like test examples. Therein, convective fluid flow induced by a moving cylinder and viscous flow around a moving beam-like structure are investigated, both were not compressible or deformable in fact, however, were subjected to large rigid body motions. In the following focus is directed to the full non-linear interaction between fluids and solids.

Problem Setup. The geometric setting of this problem is inspired by FSI test examples investigated in works by Gerstenberger and Wall [125] and Shahmiri [235]. While in the latter publications the considered fluid-solid interactions reach steady state, in the present work, material properties of the fluid and solid are weakened. This allows to demonstrate the performance of the proposed CutFEM-based FSI solver for highly dynamic interactions between a mainly convective-dominated flow and a flexible structure.

Initially inlet-driven fluid flow in a cuboid-shaped domain $\Omega = [0, 1.8] \times [0, 0.6] \times [-0.6, 0.6]$ around a rubbery flexible flap of initial dimensions $\Omega^{\mathrm{s}} = [0.49, 0.56] \times [0, 0.35] \times [-0.3, 0.3]$ is considered, which is clamped by the bottom wall of Ω_h at $x_2 = 0$. The top and the four side walls of the flap defines the interface Γ^{fs} at which fluid and solid interact. Fluid is periodically pushed into the domain Ω at the inlet $x_1 = 0$ where $\boldsymbol{u}_{\mathrm{in}} = (u_1, 0, 0) \cdot g(t)$ with $u_1(\boldsymbol{x}) = u^{\max}(81/2500)x_2(x_2 - 0.6)(x_3 + 0.6)(x_3 - 0.6)$ parabolic in directions x_2 and x_3. The peak

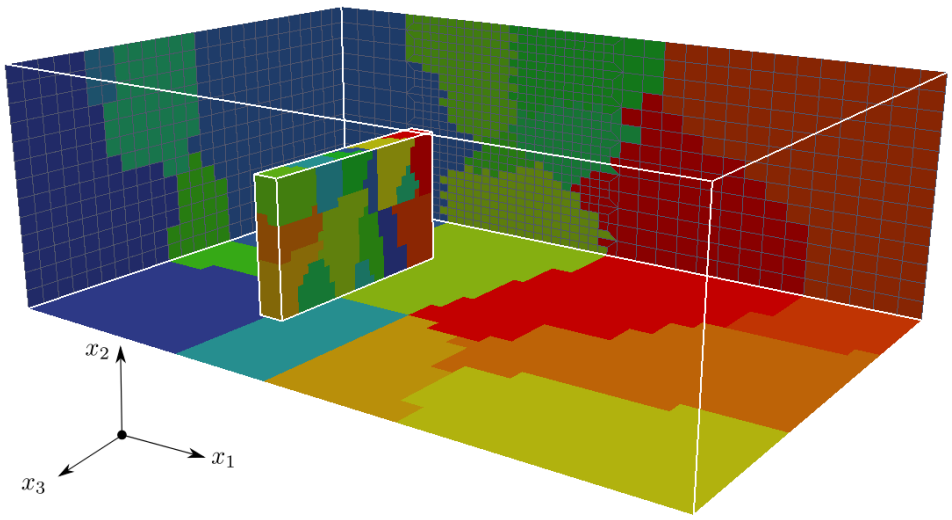

Figure 5.1: Pulsating flow over a bending flexible flap: geometric setup at $T_0 = 0$. Unfitted fixed-grid fluid mesh $\widehat{\mathcal{T}}_h^{\mathrm{f}}$ consisting of $\mathbb{Q}^1$-elements indicated at inlet side and side wall with partially refined middle block. A flexible structural flap is clamped by the bottom wall and interacts with the surrounding flow (colored by parallel distribution over 16 processors).

velocity is $u^{\max} = 2.0$ and varied by a temporal factor

$$g(t) = \begin{cases} \frac{1}{2}(1 - \cos(\pi t)) & \forall\, t \in [0, T_1], \\ 0 & \forall\, t \in (T_1, T], \end{cases} \tag{5.83}$$

where $T_1 = 10$ denotes the final time of the excitation phase and $T = 30.0$ the end of the simulation. This flow entering the domain excites the structural flap to initially bend and deform, while later its periodicity causes highly dynamic stimulations of fluid and solid to each other. No-slip wall boundary conditions at the four sides perpendicular to the inlet prevent the flow to escape. It is pushed outwards at the outlet at $x_1 = 1.8$ where a zero-traction Neumann condition $\boldsymbol{h}_{\mathrm{N}} = \mathbf{0}$ defines the pressure level. All boundary conditions for fluid velocity and structural displacements are enforced strongly and are incorporated into the respective fluid and solid trial and test function spaces $\mathcal{W}_{h,\boldsymbol{g}_{\mathrm{D}}}^{\mathrm{f}}$, $\mathcal{W}_{h,\mathbf{0}}^{\mathrm{f}}$ and $\mathcal{W}_{h,\boldsymbol{g}_{\mathrm{D}}}^{\mathrm{s}}$, $\mathcal{W}_{h,\mathbf{0}}^{\mathrm{s}}$. The material properties are chosen as follows: The flow is assumed incompressible with kinematic fluid viscosity $\nu^{\mathrm{f}} = 0.01$ and a density of $\rho^{\mathrm{f}} = 1.0$. Based on the maximum inflow velocity and the width of the flap, the Reynolds number Re ranges from 0–120. The structure exhibits a Neo-Hookean material with a Young's modulus of $E = 500$, a Poisson's ratio of $\nu^{\mathrm{s}} = 0.4$ and a density of $\rho^{\mathrm{s}} = 250$ for which large and dynamic deformations are expected. External volume loads are not present such that $\boldsymbol{f}^{\mathrm{f}} = \boldsymbol{f}^{\mathrm{s}} = \mathbf{0}$. A sketch of the problem setting is drawn in Figure 5.1.

Computational Approach. For the spatial approximation of the structural subdomain Ω^{s} a fluid-solid-interface fitted computational grid $\widehat{\mathcal{T}}_h^{\mathrm{s}}$ is used. It consists of 3720 8-node $\mathbb{Q}^1$-elements which in reference configuration are distributed in the three coordinate directions as $8 \times 15 \times 31$ such that $\Omega_{0,h} \equiv \Omega_{0,h}^* \equiv \Omega_0$. This mesh overlaps with a background fluid grid $\widehat{\mathcal{T}}_h^{\mathrm{f}}$ which fits to the

outer boundaries, however, does not fit to the fluid-solid interface Γ_h^{fs}, neither in the initial state nor when the structure displaces, i.e. $\Omega_h^{\mathrm{f}} \subsetneq \Omega_h^{\mathrm{f}*}$. The mesh $\widehat{\mathcal{T}}_h^{\mathrm{f}}$ is constructed as follows: a Cartesian grid consisting of $30 \times 13 \times 26$ elements covers the domain Ω and is subsequently refined in a middle block dimensioned by $[0.3, 0.9] \times [0, 0.6] \times [-0.6, 0.6]$ with one stage of element splitting in x_1 and x_2 direction. This increases the flow resolution in the region of main interest where the structure is expected to move and deform in. The final fluid mesh $\widehat{\mathcal{T}}_h^{\mathrm{f}}$ contains 21632 8-node $\mathbb{Q}^1$-elements. Note that its active computational mesh $\mathcal{T}_h^{\mathrm{f}}$ changes over time due to the displacing interface Γ_h^{fs}. For the approximation of fluid velocity and pressure the reduced volume-cell-composite enrichment strategy proposed in Section 2.2.5 is utilized. Temporal discretization for the fluid is based on a OST-scheme with $\theta = 1.0$. Similarly, the approximation of structural interface velocities from displacements (see equation (5.72)) uses $\theta_\Gamma = 1.0$. Moving fluid domains are treated as summarized in Algorithms 3.1 and 3.2. For structural time-stepping, the G-α scheme could be applied with characteristic parameters $\alpha_m = 1/2, \alpha_f = 1/2, \gamma = 1/2, \beta = 1/4$, i.e. $\rho_\infty = 1.0$ without numerical high-frequency dissipation (see also Table 5.1). Moreover, Rayleigh damping is neglected in this example, i.e. $c_M = c_K = 0$. The time-step length is chosen equal-sized as $\Delta t = 0.01$ resulting in 3000 time steps within $[0, T]$.

For the interface coupling of fluid and structural phase, the proposed monolithic CutFEM-based FSI solver developed in Sections 5.3.1–5.3.3 is applied. For the Nitsche-type coupling strategy, in this example, an adjoint-inconsistent formulation is studied (see sign choice in (5.67)). To sufficiently control mass conservation, the Nitsche penalty parameter in (5.68) and (5.69) is not neglected, however, chosen relatively small with $\gamma = 10.0$. Inf-sup stability in the vicinity of the intersected fluid mesh is ensured by different GP stabilization terms, whereas for efficiency reasons, the fluid formulation in the interior of its subdomain Ω_h^{f} is controlled by the RBVM technique, as summarized in Section 3.6.1.2. For each time step, the nonlinear FSI residuals (5.78) are approximated iteratively as outlined in Algorithm 5.1. Convergence checks for increments and residuals are performed separately for the distinct solution approximations, i.e. for $\boldsymbol{R}_U, \boldsymbol{R}_P, \boldsymbol{R}_D$ and $\Delta\boldsymbol{U}, \Delta\boldsymbol{P}, \Delta\boldsymbol{D}$ based on relative l^2- and l^∞-vector-norms with a uniform tolerance of $TOL = 10^{-8}$. Solutions to all involved global linear systems (5.79) are approximated by a block-preconditioned GMRES solver. For preconditioning, one block-Gauss–Seidel sweep is utilized with incomplete factorization type field preconditioners for the fluid and solid blocks. While for the solid a so-called fill-pattern (0) is sufficient, the fluid requires a fill-pattern (1) or even higher due to the enlarged bandwidth caused by GP terms; for details see documentation by Sala and Heroux [224] and advanced literature by, e.g., Verdugo and Wall [256]. The subsequent results have been computed with the fully parallelized code environment BACI (see [262]) based on $N_{\mathrm{core}} = 16$ cores. The parallel distribution over processors is visualized in Figure 5.1.

Results. Simulation results on the temporal evolution of the flap bending and its surrounding flow are shown in Figure 5.2 at different significant times. Flow entering the fluid domain at the inlet streams around the flap and forces acting on the structural front-surface cause bending in mean flow direction as depicted at times $T_1 = 0.5$ and $T_2 = 1.0$. When inflow is decreased to zero for the first time at $T_3 = 2.0$, the deformed structure tends to turn back to its undeformed initial state. At this stage, the flow is dominated by the structural motion and different swirls are induced as indicated by streamlines. Increasing again the mass flow rate at the inlet reaching

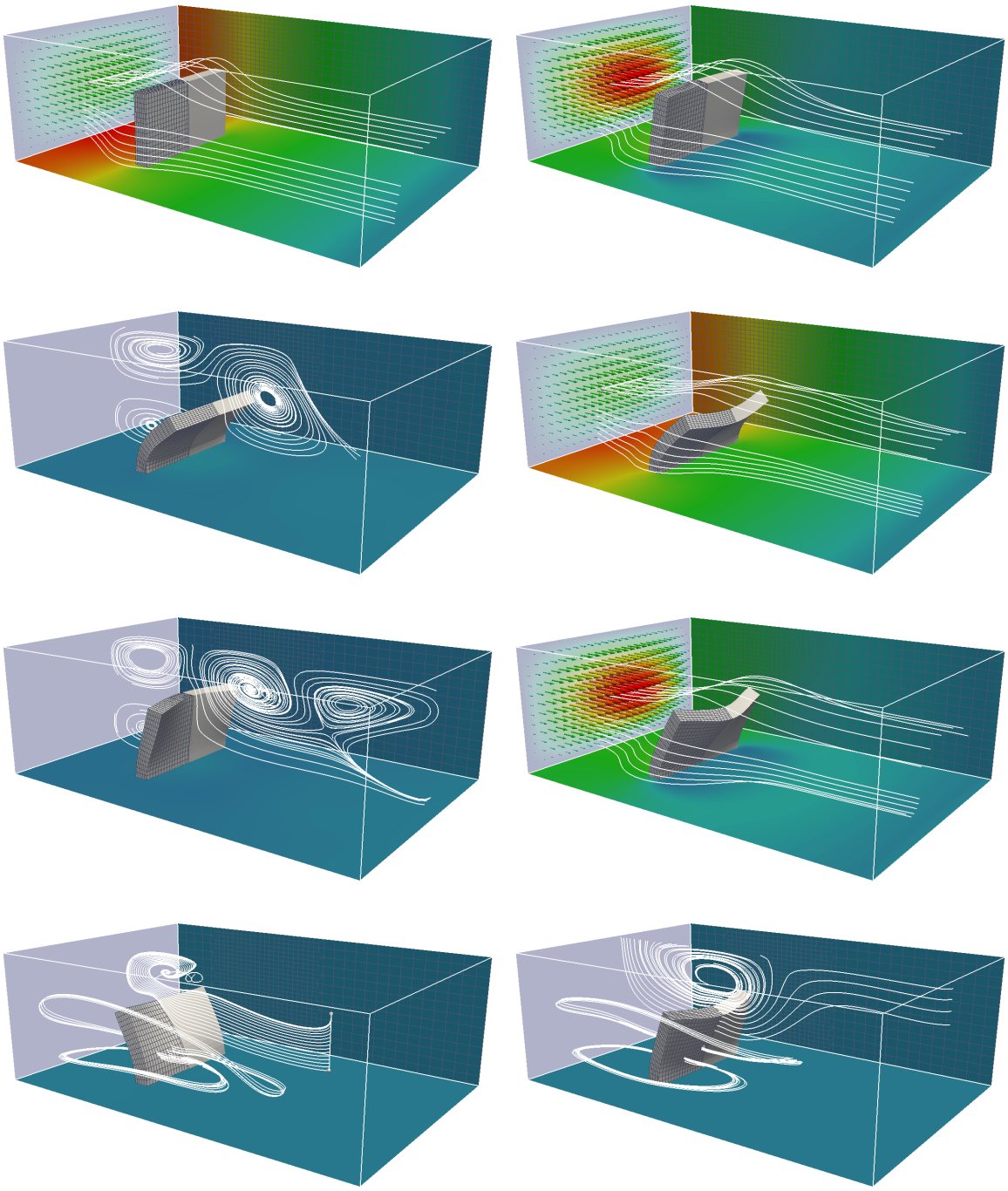

Figure 5.2: Pulsating flow over a bending flexible flap: visualization of the surrounding fluid flow and deformation of the bending rubbery flap at different times $T_1 = 0.5$, $T_2 = 1.0$, $T_3 = 2.0$, $T_4 = 2.5$, $T_5 = 6.0$, $T_6 = 9.0$ during the excitation phase when the pulsating inflow strongly affects the structural motion. When no fluid is entering the inlet anymore, flow and flap motion strongly influence each other as depicted at times $T_7 = 12.5$ and $T_8 = 16.0$ (times are ordered from top left to bottom right). The pulsating parabolic inlet is indicated by colored arrows. Streamlines visualize the evolution of the flow, which is strongly inflow-dominated when periodically increasing the inlet velocity, as well as swirls are creating and interacting with the flap for decreasing inflow rates. Side and bottom walls are colored by the pressure distribution.

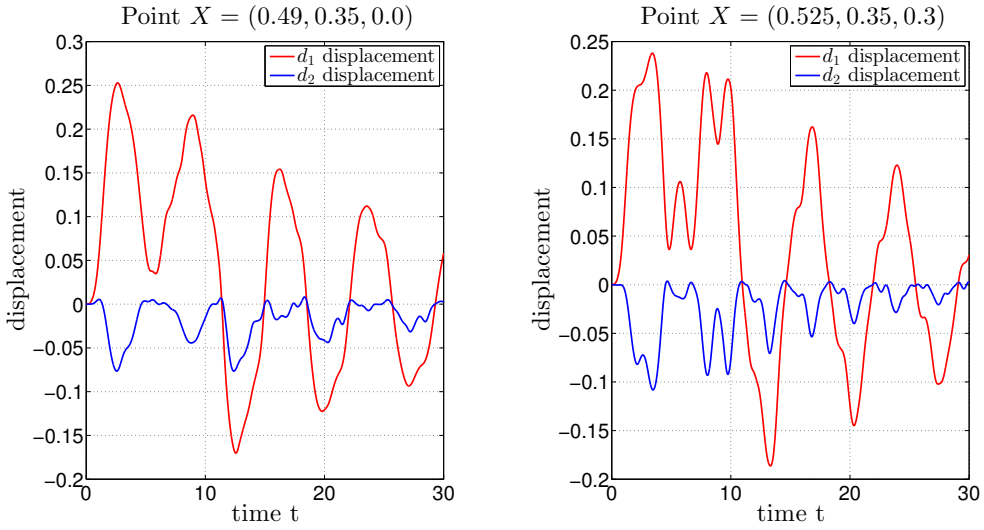

Figure 5.3: Pulsating flow over a bending flexible flap: history of displacement components d_1, d_2 of selected points located at top surface of the bending flap. Computed displacements for point $\boldsymbol{X} = (0.49, 0.35, 0.0)$ (left) and for point $\boldsymbol{X} = (0.525, 0.35, 0.3)$ (right) defined in referential configuration at $T_0 = 0$. Numerical results are computed with the RBVM/GP FSI solver based on $\Delta t = 0.01$ over $t \in [0, 30.0]$.

its peak at $T_4 = 2.5$, due to strong induced viscous and pressure forces acting on the flap this undergoes again deformations in mainly stream direction. Whenever, inflow is strong enough the structural motion is dominated by the flow and tries to minimize resistance in the surrounding flow. In contrast, when the structure is deformed and no flow is entering through the inlet anymore, its motion towards its undeformed configuration dominates the flow. States at later times during the excitation phase depict this highly dynamic fluid-structure interaction. The periodically recurring dominance of the pulsating inflow and the strongly deformed structural state is exemplarily shown at times $T_5 = 6.0$ and $T_6 = 9.0$. Upon the excitation phase, different low-velocity vortices are present in the fluid domain and continuously interact with the rubbery structure. Positive and negative deflections in x_1-direction occur as indicated at times $T_7 = 12.5$ and $T_8 = 16.0$. Due to the higher Poisson's ratio, even larger deformations perpendicular to the main stream direction arise. Due to the viscous effects, the amplitude of motion slowly decays over time. For two selected points located at the flap's top surface, the history of displacements in x_1- and x_2-directions is reported in Figure 5.3. Their coordinates are specified in initial configuration at $\boldsymbol{X} = (0.49, 0.35, 0.0)$ for the front top point and at $\boldsymbol{X} = (0.525, 0.35, 0.3)$ for the right top point.

Robustness of the proposed unfitted CUTFEM FSI solver is demonstrated for this challenging highly dynamic three-dimensional fluid-structure-interaction setting incorporating large motions and deformations of the compressible structure. The algorithmic treatment of time-changing fluid approximation spaces successfully works and convergence of the Newton-Raphson-like scheme applied to the non-linear residuals up to the specified tolerance was obtained during the overall simulation time. Moreover, due to the use of different ghost-penalty stabilization operators according to the RBVM/GP formulation, uniform well-conditioning of all linearized FSI systems could be achieved.

5.4 Unfitted Fluid-Structure Interaction Combined with Fluid Domain Decomposition

Particularly higher-Reynolds-number flows interacting with structures often exhibit high velocity gradients in the boundary layer of moving fluid-solid interfaces. Pure fixed-grid schemes usually lack accuracy when physics in the vicinity of the interface are not sufficiently captured, as might be also the case for the previously introduced unfitted CUTFEM FSI solver. While, in fact, in under-resolved situations weak constraint enforcement of FSI coupling conditions already highly improves quality of the flow solution and thus of the entire fluid-structure interaction compared to strong DOF-wise couplings, sufficient resolution of the flow characteristics in the vicinity of the interface is indispensable to capture physics appropriately. To avoid the need for finest mesh resolutions in the overall fluid domain and thereby to retain simplicity of mesh generation, if *a priori* knowledge on the approximate region of expected structural motion is given, a powerful FSI solver can be simply set up by combining the unfitted FSI solver with techniques of unfitted fluid domain decomposition as provided in Sections 4.2 and 4.3. Combining these two coupling techniques widens extensibility of existing fitted and unfitted approaches to a multitude of novel coupled FSI solvers. Possibly realizable composed discretization concepts based on the proposed fluid-solid and fluid-fluid couplings have been visualized in Figure 2.11 exemplarily for a single structural mesh and two overlapping fluid meshes. It has to be mentioned that further extensions to various fluid phases and structural bodies are straightforward from the coupling point of view. While the combination of fitted fluid-solid couplings with unfitted fluid domain decomposition (see Figure 2.11c) has been extensively studied in the thesis by Shahmiri [235], the following elaborations turn focus on a generalization of that which allows to utilize unfitted approximations at both interfaces, i.e. between fluid and solid subdomains as well as between the two fluid subdomains (see Figure 2.11b).

5.4.1 Nitsche-type Formulation of Coupled System

In the following, the semi-discrete Nitsche-type formulations for fluid-structure interaction from Section 5.3.1 and the fluid domain decompositions formulation for several fluid phases or subdomains from Section 4.2.1 are combined. In a first step, the final discrete coupled formulation is presented. Afterwards, in analogy to the fluid-structure coupling introduced in Section 5.3.3, the non-linear discrete residuals are formulated and the block matrix structure of resulting linear Newton-Raphson-like systems of equations are presented.

Extension of Nitsche-type Fluid-Structure Coupling to Several Fluid Phases. Let the space of admissible discrete solutions be denoted with $\mathcal{W}_{h,\boldsymbol{g}_\mathrm{D}} \overset{\text{def}}{=} (\oplus_{i=1}^{l} \mathcal{W}_h^{\mathrm{f}_i}) \oplus \mathcal{W}_{h,\boldsymbol{g}_\mathrm{D}}^{\mathrm{s}}$. This combined function space consists of $l \overset{\text{def}}{=} N_\mathrm{dom} - 1$ fluid subdomain spaces and, without loss of generality, one structural function space, which altogether are coupled in a fitted or an unfitted way. The subspaces are as defined in Section 4.2.1 and Section 5.1.3. The Nitsche-coupled stabilized formulation for this multidomain FSI problem setting reads as follows: for all $t \in (T_0, T]$, find fluid velocities and pressure approximations $U_h(t) = (\boldsymbol{u}_h(t), p_h(t)) \in (\oplus_{i=1}^{l} \mathcal{W}_h^{\mathrm{f}_i})$, where $U_h(t)|_{\Omega^i} = U_h^i(t) \in \mathcal{W}_h^{\mathrm{f}_i}$, and solid displacement and velocity $D_h(t) = (\boldsymbol{d}_h(t), \dot{\boldsymbol{d}}_h(t)) \in \mathcal{W}_{h,\boldsymbol{g}_\mathrm{D}}^{\mathrm{s}}$

such that for all $(V_h, W_h) \in (\oplus_{i=1}^{l} \mathcal{W}_h^{\mathrm{f}_i}) \oplus \mathcal{W}_{h,\mathbf{0}}^{\mathrm{s}}$

$$\widetilde{\mathcal{A}}_h((U_h, D_h), (V_h, W_h)) = \widetilde{\mathcal{L}}_h(U_h, (V_h, W_h)), \tag{5.84}$$

where

$$\begin{aligned}\widetilde{\mathcal{A}}_h((U_h, D_h), (V_h, W_h)) &\overset{\text{def}}{=} \sum_{1 \leqslant i \leqslant l} \Big(\mathcal{A}_h^{i,\mathrm{X}_i}(U_h, V_h) + \sum_{l \geqslant j > i} \mathcal{C}_h^{ij}(U_h, V_h) + \mathcal{C}_h^{i\mathrm{s}}((U_h, D_h), (V_h, W_h)) \Big) \\ &\quad + \mathcal{A}_h^{\mathrm{s}}(D_h, W_h), \end{aligned} \tag{5.85}$$

$$\begin{aligned}\widetilde{\mathcal{L}}_h(U_h, V_h) &\overset{\text{def}}{=} \sum_{1 \leqslant i \leqslant l} \Big(\mathcal{L}_h^{i,\mathrm{X}_i}(U_h, (V_h, W_h)) + \sum_{l \geqslant j > i} \mathcal{L}_h^{ij}(U_h, V_h) \Big) \\ &\quad + \mathcal{L}_h^{\mathrm{s}}(W_h) \end{aligned} \tag{5.86}$$

with operators for the single fluid phases $\mathcal{A}_h^{i,\mathrm{X}_i} - \mathcal{L}_h^{i,\mathrm{X}_i}$, see Sections 3.6.1.1 and 3.6.1.2, respective fluid-fluid Nitsche-type couplings $\mathcal{C}_h^{ij} - \mathcal{L}_h^{ij}$ from (4.34)–(4.45), and the structural variational form $\mathcal{A}_h^{\mathrm{s}} - \mathcal{L}_h^{\mathrm{s}}$ (5.24) which is coupled to the fluid phases with Nitsche-type couplings $\mathcal{C}_h^{i\mathrm{s}}$ as proposed in (5.66)–(5.69).

Non-linear Residuals. In analogy to (5.78), the final Nitsche-type coupled finite-dimensional system of equations consisting of l fluid blocks and one structure block for a discrete time level t^n reads: find discrete finite-dimensional vectors $((\boldsymbol{U}, \boldsymbol{P})^1, \ldots, (\boldsymbol{U}, \boldsymbol{P})^l, \boldsymbol{D}^{\mathrm{s}})^n$ such that

$$\begin{bmatrix} \boldsymbol{R}^1_{(U,P)} \\ \vdots \\ \boldsymbol{R}^l_{(U,P)} \\ \boldsymbol{R}_D \end{bmatrix}^n = \begin{bmatrix} \sigma \boldsymbol{R}^1((\boldsymbol{U}, \boldsymbol{P})^1) + \sum_{i=1}^{l} \boldsymbol{C}^{1i}((\boldsymbol{U}, \boldsymbol{P})^1, (\boldsymbol{U}, \boldsymbol{P})^i) + \boldsymbol{C}^{1\mathrm{s}}((\boldsymbol{U}, \boldsymbol{P})^1, \boldsymbol{D}^{\mathrm{s}}) \\ \vdots \\ \sigma \boldsymbol{R}^l((\boldsymbol{U}, \boldsymbol{P})^l) + \sum_{i=1}^{l} \boldsymbol{C}^{li}((\boldsymbol{U}, \boldsymbol{P})^i, (\boldsymbol{U}, \boldsymbol{P})^l) + \boldsymbol{C}^{l\mathrm{s}}((\boldsymbol{U}, \boldsymbol{P})^l, \boldsymbol{D}^{\mathrm{s}}) \\ \frac{1}{1-\alpha_f} \boldsymbol{R}^{\mathrm{s}}(\boldsymbol{D}^{\mathrm{s}}) + \sum_{i=1}^{l} \boldsymbol{C}^{\mathrm{s}i}((\boldsymbol{U}, \boldsymbol{P})^i, \boldsymbol{D}^{\mathrm{s}}) - \frac{\alpha_f}{1-\alpha_f} \boldsymbol{F}^{\mathrm{s},n-1}_{\Gamma^{\mathrm{fs}}(t^{n-1})} \end{bmatrix}^n = \mathbf{0} \tag{5.87}$$

where $\boldsymbol{C}^{i\mathrm{s}}, \boldsymbol{C}^{\mathrm{s}i}$ denote the splits of fluid-structure Nitsche couplings as defined in (5.75)–(5.76). Similar splits for Nitsche coupling terms (4.34)–(4.45) between fluid phases are denoted with $\boldsymbol{C}^{ij}, \boldsymbol{C}^{ji}$. Furthermore, $\boldsymbol{R}^{\mathrm{s}}$ denotes the structural residual and $\boldsymbol{R}^i$, $i = 1, \ldots, l$, the l fluid subdomain residuals without interface coupling terms.

Linearized Block Matrix Structure for Newton-Raphson Iterations. The algorithmic treatment of issues with regard to changing function spaces of unfitted mesh approximations proposed in Algorithm 5.1 and discussed in Section 5.3.3 can be straightforwardly adapted to a various number of unfitted computational meshes.

Following the procedure introduced in Section 5.3.3, the (pseudo-)linearized Newton-Raphson-like coupled system, which needs to be solved for each iteration step as described in Algorithm 5.2, becomes

$$\underbrace{\begin{bmatrix} \boldsymbol{L}_{UU}^{11} & \boldsymbol{L}_{UP}^{11} & \cdots & \boldsymbol{L}_{UU}^{1l} & \boldsymbol{L}_{UP}^{1l} & \boldsymbol{L}_{UD}^{1\mathrm{s}} \\ \boldsymbol{L}_{PU}^{11} & \boldsymbol{L}_{PP}^{11} & & \boldsymbol{L}_{PU}^{1l} & \boldsymbol{L}_{PP}^{1l} & \boldsymbol{L}_{PD}^{1\mathrm{s}} \\ \vdots & & \ddots & \vdots & & \vdots \\ \boldsymbol{L}_{UU}^{l1} & \boldsymbol{L}_{UP}^{l1} & \cdots & \boldsymbol{L}_{UU}^{ll} & \boldsymbol{L}_{UP}^{ll} & \boldsymbol{L}_{UD}^{l\mathrm{s}} \\ \boldsymbol{L}_{PU}^{l1} & \boldsymbol{L}_{PP}^{l1} & & \boldsymbol{L}_{PU}^{ll} & \boldsymbol{L}_{PP}^{ll} & \boldsymbol{L}_{PD}^{l\mathrm{s}} \\ \boldsymbol{L}_{DU}^{\mathrm{s}1} & \boldsymbol{L}_{DP}^{\mathrm{s}1} & \cdots & \boldsymbol{L}_{DU}^{\mathrm{s}l} & \boldsymbol{L}_{DP}^{\mathrm{s}l} & \boldsymbol{L}_{DD}^{\mathrm{ss}} \end{bmatrix}_i^n}_{\boldsymbol{L}} \cdot \begin{bmatrix} \Delta\boldsymbol{U}^1 \\ \Delta\boldsymbol{P}^1 \\ \vdots \\ \Delta\boldsymbol{U}^l \\ \Delta\boldsymbol{P}^l \\ \Delta\boldsymbol{D}^{\mathrm{s}} \end{bmatrix}_i^n = - \underbrace{\begin{bmatrix} \boldsymbol{R}_U^1 \\ \boldsymbol{R}_P^1 \\ \vdots \\ \boldsymbol{R}_U^l \\ \boldsymbol{R}_P^l \\ \boldsymbol{R}_D^{\mathrm{s}} \end{bmatrix}_i^n}_{\boldsymbol{R}} \tag{5.88}$$

with an incremental update step for the next iteration

$$\begin{bmatrix} \boldsymbol{U}^1 \\ \boldsymbol{P}^1 \\ \vdots \\ \boldsymbol{U}^l \\ \boldsymbol{P}^l \\ \boldsymbol{D}^{\mathrm{s}} \end{bmatrix}_{i+1}^n = \begin{bmatrix} \boldsymbol{U}^1 \\ \boldsymbol{P}^1 \\ \vdots \\ \boldsymbol{U}^l \\ \boldsymbol{P}^l \\ \boldsymbol{D}^{\mathrm{s}} \end{bmatrix}_i^n + \begin{bmatrix} \Delta\boldsymbol{U}^1 \\ \Delta\boldsymbol{P}^1 \\ \vdots \\ \Delta\boldsymbol{U}^l \\ \Delta\boldsymbol{P}^l \\ \Delta\boldsymbol{D}^{\mathrm{s}} \end{bmatrix}_i^n . \tag{5.89}$$

For details on the applied fixed-point-like treatment of stabilization scalings and geometric interface quantities in $\boldsymbol{L}_{xy}^{ij}$ as well as linearization of bulk and interface terms, the reader is referred to Section 5.3.3.

5.4.2 Vibrating of a Flexible Structure - Unfitted Fluid-Fluid-Structure Interaction

The test example of a tail-shaped flexible structure which is vibrating due to vortex-shedding induced by a surrounding higher-Reynolds-number flow is perfectly suited to demonstrate the high capabilities of the composed unfitted discretization concept for FSI. The considered problem setting has been originally introduced by Wall and Ramm [257] and extensively studied for a classical ALE-based interface-fitted moving mesh FSI solver in the thesis by Wall [258].

Problem Setup. The problem setting of this test example is taken unchanged from [258]. A schematic sketch is drawn in Figure 5.4. A two-dimensional flexible structure of length 4.0 and height 0.06 is clamped at its front end by a square-shaped obstacle of edge-length 1.0 which is assumed fixed. The rest of the tail can arbitrarily move in a surrounding fluid within a domain Ω of length 19.5 and height 12.0. The entire structural surface defines the fluid-structure interface Γ^{fs}. However, along the fixed head the fluid-solid interaction simplifies to a no-slip boundary condition for the fluid to be enforced weakly. The origin of the setting is set to the front end of the flexible structure. Constant inlet at $x_1 = -5.5$ with a fluid velocity of $u^{\max} = 51.3$ drives the flow around the fixed structural head. For higher Reynolds numbers, vortices detach in its backflow and strongly interact with the flexible structural tail. These excite the structure to vibrate which in return cause further creation and detachment of vortices

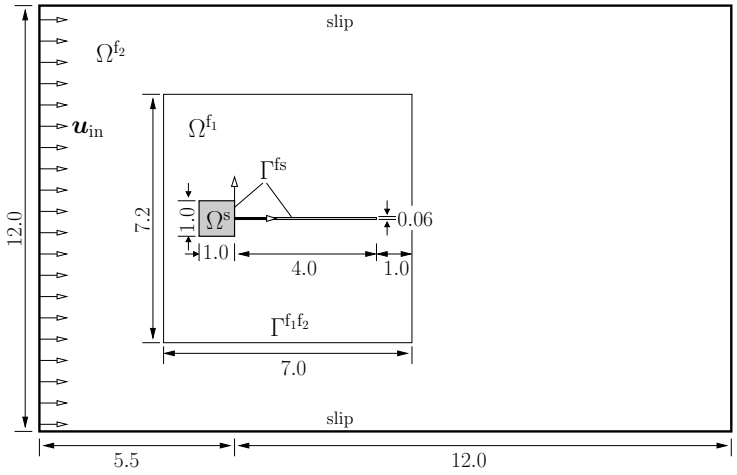

Figure 5.4: Vibrating of a flexible structure: geometric setup for unfitted fluid-fluid-solid interaction. A flexible tail is clamped by a fixed head and embedded into a surrounding flow fluid. Fluid domain is artificially decomposed into an inner domain Ω^{f_1} and outer template-shaped domain Ω^{f_2}.

from the structure. The flow velocity entering the domain is initially ramped up smoothly by a time curve factor $g(t) = \frac{1}{2}(1 - \cos(\pi t/0.1))$ within $t \in [0, 0.1]$ and kept constant afterwards. At the boarders perpendicular to the inlet, i.e. $x_2 = \pm 6.0$, slip-conditions prevent the flow to escape and a zero-traction Neumann boundary condition $\boldsymbol{h}_N = \boldsymbol{0}$ is enforced at $x_1 = 12.0$. The materials are chosen as follows: for the fluid, viscosity and density are set to $\mu^f = 1.82 \cdot 10^{-4}$ and $\rho^f = 1.18 \cdot 10^{-3}$ resulting in an approximate Reynold number of $\mathrm{Re} \approx 333$ based on the structural head dimension. For the structural tail, Neo-Hookean material is considered with a Poisson's ratio of $\nu^s = 0.35$ and two different characteristic material sets:

(A) a Young's modulus of $E = 2.5 \cdot 10^{-6}$ with a density $\rho^s = 0.1$ and

(B) a Young's modulus of $E = 2.0 \cdot 10^{-6}$ with a density $\rho^s = 2.0$.

Computational Approach. The structural tail is approximated by 20×2 two-dimensional 8-node $\mathbb{Q}^2$-elements. The fluid domain is decomposed at an artificial fluid-fluid interface $\Gamma^{f_1f_2}$ given by the boundary of the box $[-2.0, 5.0] \times [-3.6, 3.6]$ which defines $\Omega_h^{f_1} \cup \Omega_h^s$. In the current implementation of the applied fluid-fluid-structure solver the intersection of only one fluid mesh is enabled. For this reason, the inner fluid domain $\Omega_h^{f_1}$ is approximated unfitting by a fine-resolved fluid mesh consisting of 80×80 bilinearly-interpolated $\mathbb{Q}^1$-elements which covers a slightly enlarged fictitious domain $\Omega_h^{f_1 *} = [-2.05, 5.05] \times [-3.65, 3.65]$ and is unfitted to both interfaces, the fluid-solid interface Γ^{fs} and the fluid-fluid interface $\Gamma^{f_1f_2}$. The outer template-shaped fluid subdomain $\Omega_h^{f_2} = \Omega \backslash (\Omega_h^{f_1} \cup \Omega_h^s)$ is approximated by a mesh $\mathcal{T}_h^{f_2}$ which fits to its outer and inner subdomain boundary $\partial\Omega_h^{f_2}$. Note, the latter one is the fluid-fluid interface $\Gamma^{f_1f_2}$. The mesh $\mathcal{T}_h^{f_2}$ exhibits a mesh size of $h_1 = 0.1625$ in x_1-direction and $h_2 = 0.3$ in x_2-direction. This fluid mesh and the structural mesh overlap in an unfitted way with the inner fluid grid $\mathcal{T}_h^{f_1}$. The different approximations are visualized in Figure 5.5. As all meshes exhibit perfect symmetry with respect to the x_1-axis, the entire structure needs to be slightly displaced with a perturbation of $\epsilon = 0.001$ in positive x_2-direction to introduce a small imperfection to later cause vortex detachment. Otherwise, the flow would remain perfectly symmetric all over the time. It

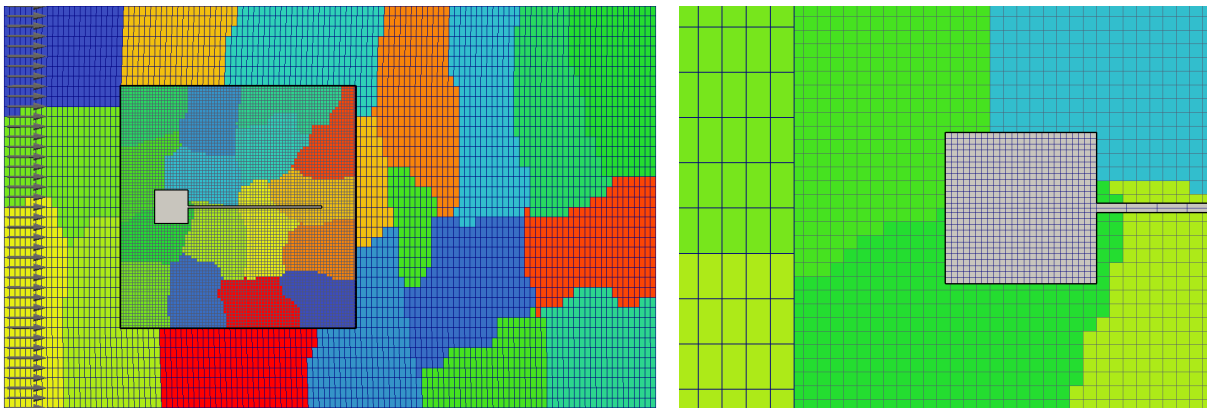

Figure 5.5: Vibrating of a flexible structure: (Left) Fitted mesh approximations $\mathcal{T}_h^{\mathrm{s}}, \mathcal{T}_h^{\mathrm{f}_2}$ for structural domain and outer fluid subdomain. Inner fluid domain is approximated with a finer computational grid $\mathcal{T}_h^{\mathrm{f}_1}$, which is unfitted to the fluid-solid interface Γ^{fs} as well as to the fluid-fluid interface $\Gamma^{\mathrm{f}_1\mathrm{f}_2}$ (colored by parallel distribution over 16 processors). Constant inlet indicated by arrows. (Right) Close-up view of overlapping meshes in the vicinity of the structural head and the fluid-fluid interface.

has to be mentioned that intersecting of multiple overlapped unfitted meshes would allow to simplify meshing of such a problem setting still more.

As a structural temporal discretization the G-α scheme without damping, i.e. $\rho_\infty = 1.0$, base on a trapezoidal-like approximation of internal and external forces is used. Furthermore, structural Rayleigh damping is neglected. To reduce numerical damping of the vortex shedding in the fluid field, the OST scheme is applied with a parameter $\theta = 0.55$. At the interface it is chosen $\theta_\Gamma = 1.0$ and the time-step length is set to $\Delta t = 0.001$.

Similar to the computational approach for the bending flap example in Section 5.3.4, an adjoint-inconsistent Nitsche method with low stabilization ($\gamma = 10$) for the fluid-solid as well as the fluid-fluid coupling is applied. To demonstrate robustness of the adjoint-inconsistent Nitsche formulation on cut meshes, the average weighting at the fluid-fluid interface is shifted to the finer inner intersected mesh $\mathcal{T}_h^{\mathrm{f}_1}$ equivalently to the weighting at the fluid-structure interface. Additionally, at the interface $\Gamma^{\mathrm{f}_1\mathrm{f}_2}$ an upwinding with $\gamma_{\mathrm{upw}} = 1/2$ is used (see Equations (4.39) and (4.45)). Within the fluid subdomain $\Omega_h^{\mathrm{f}_2}$ the classical RBVM formulation (see Section 3.1.3.1) is used, while for the intersected mesh $\mathcal{T}_h^{\mathrm{f}_1}$ the RBVM/GP method (see Section 3.6.1.2) is applied, supported by ghost-penalty operators in both interface zones $\mathcal{T}_\Gamma^{\mathrm{f}_1}$. Stabilization parameters are defined therein. Solving the non-linear residuals (5.87) is treated in analogy to the example from Section 5.3.4 with single-field tolerances $TOL = 10^{-8}$. For implementational reasons, a 2×2 block-Gauss–Seidel preconditioner for the linearized FSI systems (5.88) incorporating one single-field preconditioner for the entire fluid system and another single-field preconditioner for the structural block is applied. Splitting into 3×3 blocks is expected to further improve efficiency, see discussions in the work by Verdugo and Wall [256]. The final simulation has been performed with $N_{\mathrm{core}} = 16$ processors.

Results. Simulation results for the two different material settings (A) and (B) are visualized in Figure 5.6 and Figure 5.7 for different significant times, respectively. For both settings, the flow is driven by the inlet and fluid is convected from the inflow across the fluid-fluid interface. Accuracy of the fluid-fluid coupling is indicated by continuous streamlines crossing $\Gamma^{\mathrm{f}_1\mathrm{f}_2}$. Flow

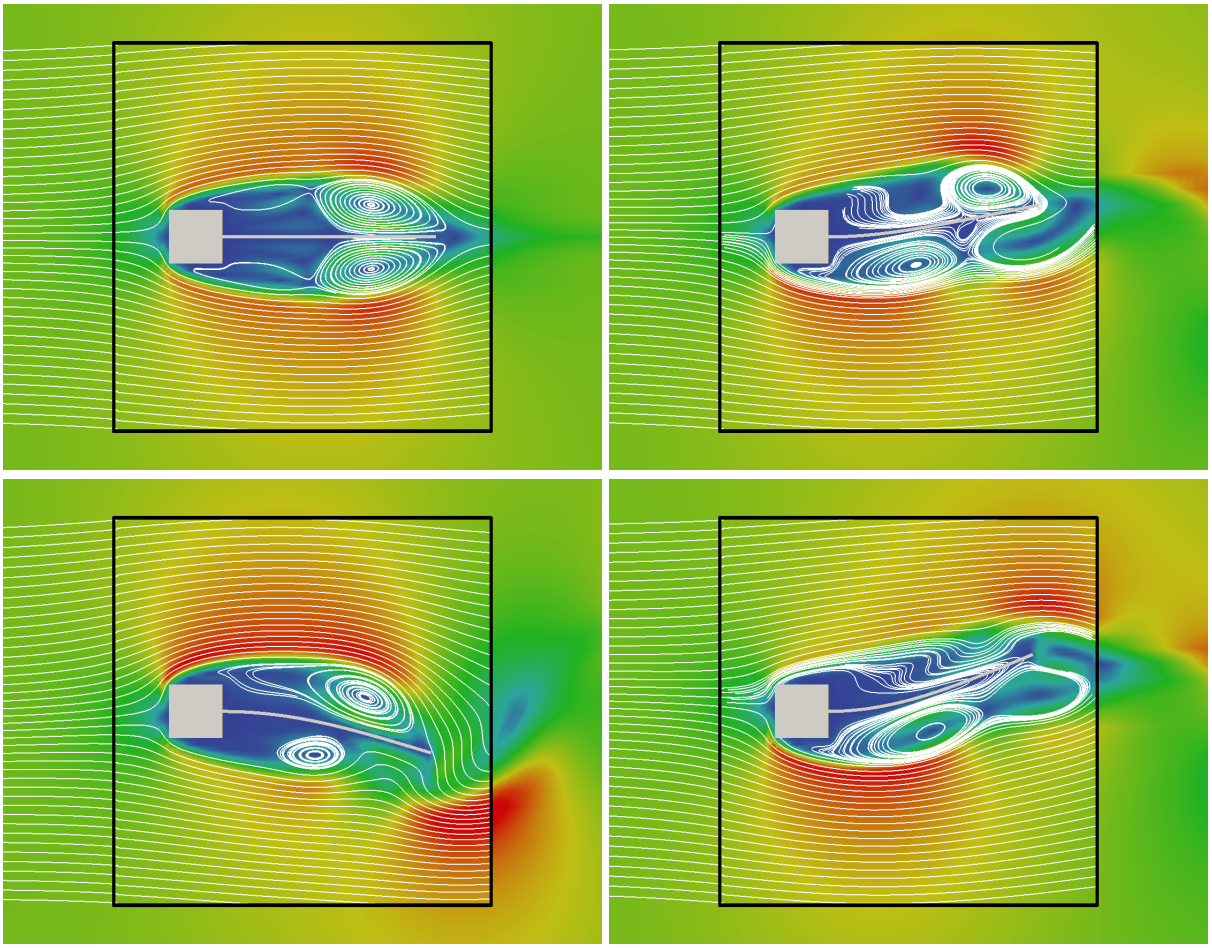

Figure 5.6: Vibrating of a flexible structure for setting (A): visualization of the surrounding fluid flow and deformation of the vibrating tail at different times $T_1 = 0.35$, $T_2 = 2.250$, $T_3 = 2.415$ and $T_4 = 2.560$. Streamlines indicate the flow field in the vicinity of the vibrating structure. Fluid is convected from inflow across the fluid-fluid interface (colored as black lines) and streams around the structural head. Due to the higher-Reynolds-number flow, vortices detach in its backflow and excite the tail to vibrate. Created swirls are again convected across the fluid-fluid interface. Vibration dominated by the first eigenfrequency is depicted.

streams around the structural head at which no-slip boundary conditions are enforced weakly using the Nitsche-type technique developed throughout this thesis. Due to the introduced small imperfection, flow develops slightly non-symmetric on the two sides of the flexible tail; see streamlines in Figure 5.6 at $T_1 = 0.35$. For this higher Reynolds number, vortices develop behind the structural step and are transported along the tail towards its end where they finally detach at slightly different times. As a result, the tail is excited to deform which further induces strong detaching vortices. The oscillation amplitude of the flexible tail increases and it starts to highly dynamically vibrate. Following elaborations in [258], for setting (A) vibration is expected to be dominated by the first structural eigenfrequency, whereas for setting (B) even higher modes are present. This can be clearly seen from the simulation results for the two different material settings in Figure 5.6 and Figure 5.7.

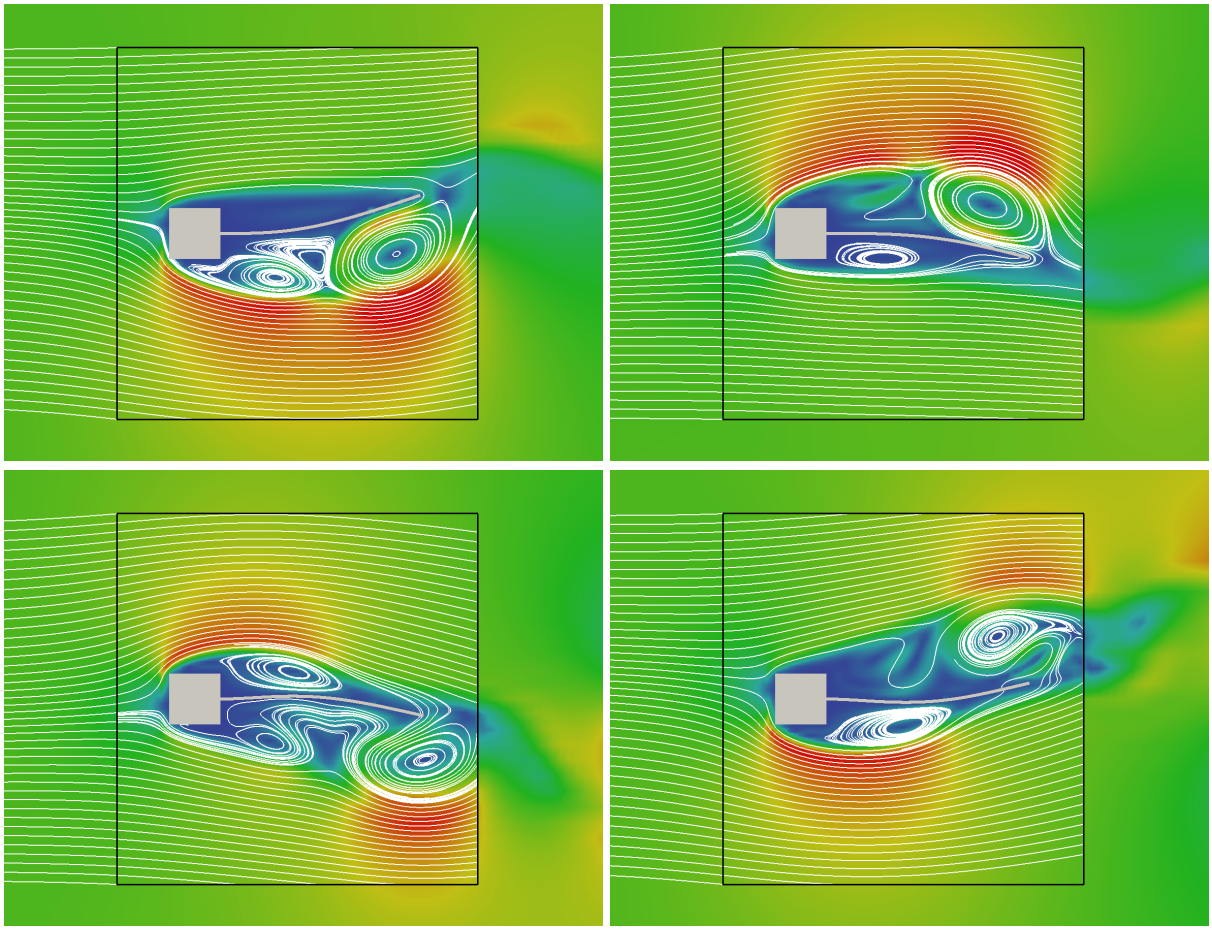

Figure 5.7: Vibrating of a flexible structure for setting (B): visualization of the surrounding fluid flow and deformation of the vibrating tail at different times $T_1 = 2.670$, $T_2 = 3.015$, $T_3 = 3.520$ and $T_4 = 3.880$. Streamlines indicate the flow field in the vicinity of the vibrating structure. Fluid is convected from inflow across the fluid-fluid interface (colored as black lines) and streams around the structural head. Due to the higher-Reynolds-number flow, vortices detach in its backflow and excite the tail to vibrate. Created swirls are again convected across the fluid-fluid interface. In contrast to setting (A), vibration exhibits even higher eigenfrequencies.

The great advantage of the proposed CUTFEM-based discretization concept is, on the one hand, to allow for large structural deformations and motions independent of the structural positioning within its surrounding fluid mesh. On the other hand, decomposing the fluid domain enables to utilize highly refined meshes in specific regions of interest, while computational costs can be kept at a minimum. Meshing is as simple as possible due to the fixed-grid character of the approximation and due to the possibility of unfittedness of the meshes with respect to boundaries and interfaces. In particular when motion of fluid meshes is taken into account, which can be easily realized by utilizing ALE techniques, this CUTFEM approximation concept allows for a multitude of further developments and adaption to different coupled problem settings in the future.

Chapter 6

Summary and Outlook

Summary. In this thesis, computational methodologies for simulating complex interface coupled flow problems are developed. The proposed methods aim at approximating multiphysics phenomena in which subdomains and interfaces are subjected to large deformations over time or even undergo topological changes. Novel composed non-interface-fitted discretization concepts based on the cut finite element methodology constitute the framework for various multiphysics applications considered in this work, which range from incompressible single-phase flow and mesh-tying techniques to incompressible two-phase flow up to advanced fluid-structure-interaction problem settings. The central focus of this thesis is a comprehensive mathematical and numerical investigation of selected cut-finite-element-based approaches existing to date, a detailed analysis of major issues arising from them and the development of novel stabilized cut finite element formulations for incompressible flows, which exhibit substantial improvements over a majority of existing methods with regard to numerical stability and accuracy.

Computational approximations of natural phenomena and various applications in engineering and physics have gained great attention over the last decades. However, the complexity of problem settings, which are of major interest nowadays, rapidly increases and goes far beyond the vast of single-field problems. As discussed in very detail throughout this thesis, many computational methods and approximation techniques which are in fact well-suited for single-field approximations are often limited in their applicability as part of a coupled multiphysics setting. In particular, when topological changes of the subdomains are involved, most if not all existing computational methods can not deal with such scenarios. As impressively demonstrated, cut finite element methodologies open up a great multitude of novel approximation techniques and provide accurate representations of geometry and the involved physical fields simultaneously. Even though not limited to those, in the present work, cut finite element methods were considered for incompressible flows and, moreover, for coupled problems in which fluid and solid phases mutually interact. All discretization concepts and finite-element-based formulations proposed and investigated throughout this thesis have been developed in consideration of their extensibility to more advanced multiphysics applications in the future. In the following, the various contributions of the present work are summarized in detail.

Most existing computational methodologies of coupled problems are based on the natural idea of decomposing the considered domain into subregions related to the different modeled physics.

Various approaches thereby mainly differ in approximations utilized for the single fields and their coupling strategies. After recalling common techniques for interface representations and general concepts of domain decomposition, the high capabilities of cut-finite-element-based composed discretizations were discussed and different aspects with regard to various flow problem settings considered in this thesis were highlighted. To ensure high accuracy of solution approximations even for topologically challenging scenarios, a generalized strategy of enriching function spaces in CUTFEMs was introduced. Throughout this work, all discrete variational formulations developed for flow problems rely on such unfitted FEM-based approximation spaces.

The major contribution of this thesis consists in the development of stabilized discrete formulations based on geometrically unfitted approximations for flow problems governed by the non-linear incompressible Navier-Stokes equations. As the majority of existing computational approaches lacks robustness and accuracy particularly for pathological intersections of the computational grids by boundaries or interfaces, different measures were taken. In a first step, a rigorous mathematical analysis corroborated by various numerical studies on established cut finite element methods for flow problems was provided. After introducing two classical fluid stabilization techniques for FEM-based fitted mesh approaches, that is the residual-based variational multiscale (RBVM) technique and the continuous interior penalty (CIP) method, fundamental concepts of establishing stability and *a priori* error estimates of FEMs were reviewed. Due to the unfittedness of geometry and computational mesh, weak constraint enforcement of boundary and interface coupling conditions is favored. For this purpose, different methodologies were compared and analogies and differences were pointed out. These preliminary analyses allowed to theoretically identify major difficulties of discrete cut finite element formulations which were observed in several numerical studies. Two major issues of most existing formulations can be summarized: first, discrete linearized systems of equations render in ill-conditioned and often almost singular matrix systems, which deteriorate the accuracy of the solutions as well as the solver performance. Second, due to the unfittedness of mesh and domain, inf-sup stability gets lost and yields uncontrolled error behavior for critical intersections of the finite elements. Mathematically, one major origin of such issues can be boiled down to suboptimal trace estimates for discrete polynomials in the vicinity of the subdomain boundary on intersected elements. An extremely effective counteracting measure is the usage of so-called ghost-penalty (GP) stabilizations, as originally introduced in the work by Burman [50]. In particular, its use in combination with a powerful Nitsche-type weak enforcement of boundary or coupling constraints emerged as a powerful approximation strategy. Discrete stability control and, as a result of this, optimal error estimates with respect to the entire computational mesh can be recovered. Furthermore, this enables to improve system conditioning and thus efficiency of the iterative solvers. A set of face-jump ghost-penalty stabilizations, which is activated in the interface region, was developed in this thesis and proven to ensure stability and optimality of error convergence for incompressible flow in the low- and the high-Reynolds-number regime independent of the positioning of interfaces within intersected elements. In summary, three ghost-penalty terms for velocity and pressure closely related to CIP-stabilizations, which have been originally developed for the interior of fluid domains, balance three major instabilities: one arising for convective-dominated flows, a second due to the use of equal-order approximations for velocity and pressure and a third caused by vanishing elliptic bulk control arising for small viscosities. Two further ghost-penalty terms sufficiently extend control of standard Galerkin formulations from the physical domain to the entire computational mesh: one for the

viscous elliptic part and another for the pseudo-reactive part of the formulation arising from discretizing the time derivative. Stability and optimal convergence for the Oseen problem were proven through a numerical analysis and corroborated by numerical convergence studies: a two-dimensional Taylor problem and a three-dimensional Beltrami flow at low and higher Reynolds numbers. An extension of the Nitsche-type CIP/GP formulation to the non-linear incompressible Navier-Stokes equations was proposed and, to reduce computational costs, an alternative RBVM/GP approach combining RBVM-techniques in the interior of the fluid domain with GP-operators in the boundary zone is suggested. The different formulations were validated for various challenging test examples in non-moving domains. These demonstrate robustness and point out the significant advantages of CUTFEMs with regard to simplified mesh generation. Considerable benefits of unfitted approximations are reaped for flows in moving domains: a mainly convective-dominated flow induced by a translationally moving cylinder and the viscous flow over a rotating beam-like structure. For such purposes, extensions of solution algorithms to moving domains were proposed.

Having established a stabilized CUTFEM flow solver for incompressible single-phase flows, extensions to coupled flow problems could be made. For problem settings in which fluid phases with equal or even high contrast in the fluid material parameters interact, focus needs to be turned to the interface coupling of the different subdomain solutions. Initially, fundamental modeling approaches towards interface coupled flow problems based on principles of conservation of mass and momentum were reviewed. Three applications of increasing complexity with regard to demands on representability of discontinuities in the flow fields were considered: mesh tying of an incompressible single-phase flow, two-phase flow exhibiting large density and viscosity ratios including surface-tension effects and modeling of premixed combustion. For all applications, enforcing coupling constraints can be realized within a unified unfitted computational framework. Independent of the choice of cut approximation spaces for the subdomain solutions, a Nitsche-type cut finite element method was utilized. By analogy to single-phase problems, stabilized formulations were developed and peculiarities of different applications were pointed out. The definition of average flux weighting plays a decisive role for the coupling of fields which exhibit high differences in material properties or in the respective mesh resolutions. For such problem settings, a harmonic weighting strategy accounting for these characteristics is suggested and its advantage was analyzed. Applying independent sets of ghost-penalty operators for all intersected subdomain-related approximation spaces ensures uniform inf-sup stability and optimality with respect to mesh intersections. Numerical examples for unfitted mesh-tying applications, which utilize overlapping fluid meshes, demonstrated the high capabilities of this discretization concept for the flow around obstacles and indicated its benefit in view of fluid-structure interaction to which this technique has been successfully extended by Shahmiri [235]. As an outlook, the analyzed formulation was validated for complex incompressible two-phase flows: different Rayleigh–Taylor instabilities with various material combinations including investigations of damping effects due to surface tension and the complex temporal flame-front evolution owing to a flame-vortex interaction. The latter example is strongly based on the work by Henke [147] to which the present work provides further developments on a more accurate cut approximation space, which is useful in situations of topological changes, and on discrete formulations with highly improved stability behavior for the respective single phases.

In a further step, the Nitsche-type coupling methodology introduced for two fluid phases was adapted to fluid-structure interaction (FSI), natural phenomena which are of high importance

for various industrial and biomedical applications. Unfitted approaches towards FSI are superior over classical moving mesh approaches as large structural motions and deformations are supported. Moreover, the extensibility to advanced related multiphysics problems like fluid-structure-fracture interaction, as considered in the work by Sudhakar [244], or fluid-structure-contact interaction, as addressed in parts by Mayer *et al.* [184], render such discretization techniques highly attractive. Besides a review of fundamentals on non-linear computational structural mechanics and a corresponding standard Galerkin finite element method, a stabilized Nitsche-type FSI formulation was developed. Stability issues of the fluid field are overcome by the proposed RBVM/GP and CIP/GP CUTFEM flow solvers. Unlike in previously mentioned works, monolithic solution algorithms which are able to treat difficulties arising from changes of the fluid approximation spaces were suggested and validated for a challenging transient highly dynamic three-dimensional pulsating flow over a bending flexible flap. Finally, advanced developments of composed discretization techniques, which combine unfitted fluid-structure-interaction approaches with the powerful tool of fluid domain decomposition, allow to easily realize locally increased resolutions of certain flow regions of interest. The high capabilities of such an advanced unfitted CUTFEM-based FSI solver were indicated by a challenging two-dimensional example, a higher-Reynolds-number flow surrounding a flexible structure at which vortices detach and excite the body to highly dynamically vibrate.

Outlook. As summarized before, a substantial progress towards unfitted approximation techniques for single-phase and interface coupled flow problems could be achieved in the present work. Fundamentals on a theoretical side were provided and the high potential of proposed methodologies for a variety of important applications could be demonstrated by challenging simulations. Nevertheless, to allow for further extensions to more complex practical scenarios, the following aspects should be considered in future.

From a numerical point of view, it seems to be worthwhile to put further effort in developing cut finite element approximations which ensure higher-order accuracy in space as well as in time. Fundamental issues are the low-order geometric approximation as well as the application of finite-difference based time-stepping schemes. First attempts on these topics are already available in literature as discussed within this thesis. From a stabilization point of view, for higher-order spatial approximations, the mentioned projection-based ghost-penalty stabilizations offer desired properties which can be developed in analogy to the face-jump penalty based terms utilized in this work. Moreover, an error analysis of the fully discretized scheme with respect to space and time and particular focus on moving domains is still outstanding. In a similar fashion, a numerical analysis of the RBVM/GP technique could be derived.

From an implementation point of view, the subsequent adaption should be made in future. Even though the current code framework is fully parallelized, more practical problem settings require very fine resolutions. As active parts of the computational mesh largely vary, dynamic load balancing is demanded for the fluid solver and continuous parallel redistribution seems necessary. Owing to permanent changes of the function spaces, matrix and vector data containers require clever memory management strategies to further reduce computational time for allocating memory and to reduce memory fragmentation during simulations. To increase flexibility in the coupling of approximation spaces for multiphysics, intersecting multiple overlapping meshes needs to be enabled. To fully exploit the benefit of fluid domain decomposition for capturing

boundary layer effects around structures, automated mesh generation of embedded body-fitted fluid patches would be desirable. According to this topic, further valuable extension with regard to efficiency and accuracy could be made in future when combining the proposed domain decomposition techniques with enrichment strategies for the function space of the embedded fluid patch. For instance, logarithmic enrichment functions which take into account the law-of-the-wall due to Spalding, as proposed in novel methodologies by Krank and Wall [166], would enable to efficiently capture high-gradient velocity profiles in turbulent boundary layers with relatively coarse resolved embedded body-fitted fluid patches. Potential industrial application fields for such computational approaches are the simulation of turbulent FSI. These occur, for instance, for rotating turbine blades of propellers, aircraft engines or wind and water power plants.

To fully reap the benefits of the high flexibility of the developed CutFEMs, which mainly consists in combining different fitted and unfitted discretizations independent of the actual subdomain geometry, various composed discretization methods for a variety of multifield applications are thinkable. The proposed unfitted monolithic FSI solver could be applied and algorithmically enhanced to aforementioned fluid-structure-contact interactions. Allowing for contact of submersed solids would enable computational modeling of, for example, tire hydroplaning or industrial pipe valves. In a biomedical setting, this would allow to simulate the reduced blood flow due to clamping a human artery during surgery or the opening and closing of cardiac valves in a pumping heart. The benefit for further inventions on prosthetic stents and heart valves seems obvious. Furthermore, incorporating algorithms for fluid-structure-fracture interaction enables the development of advanced methodologies which allow for making further progress in the computational modeling of biofilm architectures. Simulation of contacting biofilm streamers including growth and detachment processes caused by surrounding flow effects would be a potential application area. The versatility of introduced unfitted FSI solvers could be highly increased when unfitted fluid grids are allowed to arbitrarily move, which could be simply realized by incorporating ALE techniques. For instance, attaching fluid grids to structural motions would guarantee fine mesh resolutions in regions of interest and at the same time highly increase efficiency. Concerning the developed two-phase flow couplings, further extension of fluid-structure interaction to two-phase-structure interaction would open a new field of multiphysics applications, like the simulation of sailing boats or sloshing inside flexible tanks. For such applications, the Nitsche-type weak constraint enforcement can be adapted to allow for the imposition of more general Robin-type couplings, which enable reliable numerical modeling of contact lines between two fluid phases and a potential interacting solid. Furthermore, challenging multifield interactions of fluids with contacting structures and deformable porous media provide potential research directions.

The high versatility and capability of cut finite element methods demonstrated by computational approaches developed throughout this thesis gives rise to hope for further extensibility to important multiphysics problem settings in future. The variety of possible application fields in science and engineering seems unlimited and technological progress in many of these research areas are of considerable benefit to humankind.

Appendix A

Overview of Level-Set Representations

In this section, a review of level-set representations for simple-shaped basic geometric objects is given. For all objects considered in the following, the interior of the characterized point set is defined by points $\boldsymbol{x} \in \mathbb{R}^3$ which carry negative level-set values, i.e.

$$\Omega_{\text{Obj}} \stackrel{\text{def}}{=} \left\{ \boldsymbol{x} \in \mathbb{R}^3 \mid \phi_{\text{Obj}}(\boldsymbol{x}) < 0 \right\}, \tag{A.1}$$

where the function ϕ_{Obj} is specific for different objects. A selection of frequently used geometric shapes is proposed subsequently. All objects are defined at a certain reference location, mostly centered at the origin $\mathbf{0} \in \mathbb{R}^3$. However, using translational and rotational operations, these objects can be transformed to arbitrary positions and orientations, see Appendix A.2 below. In combination with Boolean operations, as proposed in (2.56)–(2.60), complex domains can be easily created without any meshing algorithm. Besides a classical static boundary representation, such an implicit definition can be simply adapted for dynamic boundaries by introducing a time-dependency in the definition of $\phi_{\text{Obj}}(\boldsymbol{x}, t)$. Furthermore, all subsequent definitions can be used as initial configurations for moving interface problems, where the motion is determined by solving evolution equations, as proposed for instance in (2.50).

A.1 Level-Set Functions for Basic Geometric Objects

Plane/Halfspace. An infinite space can be limited by a plane containing the origin $\mathbf{0} \in \mathbb{R}^3$. Defining its orthonormal unit vector $\boldsymbol{n}$ allows to describe a halfspace implicitly by

$$\phi_{\text{HSpace}}(\boldsymbol{x}; \boldsymbol{n}) \stackrel{\text{def}}{=} \boldsymbol{n} \cdot \boldsymbol{x}. \tag{A.2}$$

Applying a translational transformation $\boldsymbol{T} : \boldsymbol{x} \mapsto \boldsymbol{x} - \boldsymbol{x}_0$ yields

$$\phi_{\text{HSpace}}(\boldsymbol{x}; \boldsymbol{n}, \boldsymbol{x}_0) \stackrel{\text{def}}{=} \boldsymbol{n} \cdot (\boldsymbol{x} - \boldsymbol{x}_0), \tag{A.3}$$

which defines a parallel plane including a specified point $\boldsymbol{x}_0 \in \mathbb{R}^3$.

Cuboid. An axis-aligned cuboid is described by a variant of the l_∞-norm

$$\phi_{\text{Cuboid}}(\boldsymbol{x}; a_1, a_2, a_3) \overset{\text{def}}{=} \max\left(\frac{2|x_1|}{a_1}, \frac{2|x_2|}{a_2}, \frac{2|x_3|}{a_3}\right) - 1, \tag{A.4}$$

where $a_1, a_2, a_3 > 0$ are the lengths of the edges.

Sphere. A three-dimensional sphere with radius $r > 0$ is defined via the l_2-norm

$$\phi_{\text{Sphere}}(\boldsymbol{x}; r) \overset{\text{def}}{=} \sqrt{x_1^2 + x_2^2 + x_3^2} - r. \tag{A.5}$$

Ellipsoid. The sphere can be generalized to an ellipsoid by scaling along the main axes

$$\phi_{\text{Ellipsoid}}(\boldsymbol{x}; a_1, a_2, a_3) \overset{\text{def}}{=} \sqrt{(x_1/a_1)^2 + (x_2/a_2)^2 + (x_3/a_3)^2} - 1 \tag{A.6}$$

with radii $a_1, a_2, a_3 > 0$.

Infinite Cylinder. A cylinder infinitely extended along its mean axis, which is characterized by a unit normal vector $\boldsymbol{n}$, is described by

$$\phi_{\text{Cyl}_\infty}(\boldsymbol{x}; \boldsymbol{n}, r) \overset{\text{def}}{=} \sqrt{(x_1 - n_1(\boldsymbol{x}\cdot\boldsymbol{n}))^2 + (x_2 - n_2(\boldsymbol{x}\cdot\boldsymbol{n}))^2 + (x_3 - n_3(\boldsymbol{x}\cdot\boldsymbol{n}))^2} - r, \tag{A.7}$$

where $r > 0$ defines the radius of the cylinder. Hereby, the mean axis is crossing the origin $\mathbf{0}$.

Finite Cylinder. Using the Boolean set operation (2.57), an infinite cylinder can be limited by two cutting-off planes oriented to the mean axis of the cylinder

$$\phi_{\text{Cyl}}(\boldsymbol{x}; \boldsymbol{n}, r, h^+, h^-) \overset{\text{def}}{=} \max\left\{\phi_{\text{Cyl}_\infty}(\boldsymbol{x}; \boldsymbol{n}, r), \phi_{\text{HSpace}^+}(\boldsymbol{x}; \boldsymbol{n}, h^+\boldsymbol{n}), \phi_{\text{HSpace}^-}(\boldsymbol{x}; -\boldsymbol{n}, -h^-\boldsymbol{n})\right\} \tag{A.8}$$

defining $\Omega_{\text{Cyl}} = \Omega_{\text{Cyl}_\infty} \cap \Omega_{\text{HSpace}^+} \cap \Omega_{\text{HSpace}^-}$. Here, $\boldsymbol{n}$ is the unit vector defining the mean axis, $r > 0$ the radius and h^+, h^- the height of the cylinder in positive $(+)$ and negative $(-)$ normal direction.

Torus. A torus radially symmetric about the x_3-axis is represented implicitly by

$$\phi_{\text{Torus}}(\boldsymbol{x}; R, r) \overset{\text{def}}{=} \sqrt{(\sqrt{x_1^2 + x_2^2} - R)^2 + x_3^2} - r \tag{A.9}$$

with $r > 0$ the radius of the tube and $R > 0$ the radius measuring the distance from the center of the tube to the center of the torus. The latter is assumed being located at the origin $\mathbf{0}$.

Tube along Parametrized Curve. In general, a tube can be aligned along an arbitrary curve which is parametrized sufficiently smooth. Hereby, a parametrization of the curve $\boldsymbol{x}_{\text{curv}}(s)$ with $s \in \mathbb{R}$ is assumed, where $\frac{\partial \boldsymbol{x}_{\text{curv}}(s)}{\partial s}$ describes the tangential vector along the curve. The interior of a curve-aligned tube can be covered by moving an implicitly defined cross section ϕ_{cross} along the curve such that the cross section normal vector follows the curve tangential vector $\boldsymbol{t}(s)$ for $s \in \mathbb{R}$. Then, for any $s \in \mathbb{R}$ the cross-section lies in a plane which is defined by

$$\phi_{\text{Plane}}(\boldsymbol{x}; \frac{\partial \boldsymbol{x}_{\text{curv}}}{\partial s}(s), \boldsymbol{x}_{\text{curv}}(s)) = \frac{\partial \boldsymbol{x}_{\text{curv}}}{\partial s}(s) \cdot (\boldsymbol{x} - \boldsymbol{x}_{\text{curv}}(s)) = 0. \tag{A.10}$$

For a point $\boldsymbol{x} \in \Omega_{\text{Tube}}$ contained in the infinite tube, the closest point on the curve is defined by the minimizer $\tilde{s} \in \mathbb{R}$ of the euclidean distance

$$d(s) \overset{\text{def}}{=} \|\boldsymbol{x} - \boldsymbol{x}_{\text{curv}}(s)\| \overset{!}{=} \min. \tag{A.11}$$

This closest point can then be used as reference point for basic geometric objects defined in the sections before. In the following, we apply this concept to obtain a level-set description of an infinite helical pipe.

Infinite Helical Pipe. For a helical pipe, a circular cross section with unit normal $\boldsymbol{n}(s)$ and radius $r > 0$ is extended along a helical curve. A helix around the x_3-axis can be parametrized with $s \in \mathbb{R}$ as

$$\boldsymbol{x}_{\text{curv}}(s) = (R\cos(2\pi s), R\sin(2\pi s), \alpha s), \tag{A.12}$$

where $R > 0$ is the closest distance of all helical points to the mean axis and $\alpha > 0$ denotes the thread pitch. Following the concept introduced above, the minimal distance of a point $\boldsymbol{x}$ near the tube is formulated in terms of the minimization problem (A.11), which can be numerically approximated with the help of a method of descend in combination with an Armijo step-width control and a Newton descend search direction. For an introduction to basic optimization tools, the reader is referred to, e.g., the textbook by Jarre and Stoer [157].

For a point $\boldsymbol{x}$ being a minimizer, it is required that $d'(\tilde{s}) \overset{!}{=} 0$. This holds if

$$f(s;\boldsymbol{x}) = 2\pi R(x_1\sin(2\pi s) - x_2\cos(2\pi s)) + \alpha^2 s - \alpha x_3 \overset{!}{=} 0. \tag{A.13}$$

Then, the Newton search direction is given by

$$\Delta s = -\beta f(s;\boldsymbol{x})/f'(s;\boldsymbol{x}), \tag{A.14}$$

where the sign β is chosen to guarantee a descend direction

$$0 \overset{!}{>} \Delta s \cdot f'(s,\boldsymbol{x}) = -\beta f(s;\boldsymbol{x})/f'(s;\boldsymbol{x}) \cdot f'(s;\boldsymbol{x}) = -\beta f(s;\boldsymbol{x}). \tag{A.15}$$

This requires to define

$$\beta(s;\boldsymbol{x}) \overset{\text{def}}{=} \text{sign}\,(f(s;\boldsymbol{x})). \tag{A.16}$$

Moreover, to improve the convergence behavior of the optimization problem, the step width can be controlled by choosing the maximal step-width factor $\sigma \in \{0.5^k,\ k \in \mathbb{N}_0\}$ which still ensures a descend with respect to the objective function $d(s)$, i.e.

$$d(s + \sigma\Delta s) \overset{!}{<} d(s). \tag{A.17}$$

A start approximation for the iterative process can be chosen by setting $s_0 = x_3/\alpha$, which fulfills zero in the third component of $\boldsymbol{x} - \boldsymbol{x}_{\text{curv}}(s_0)$.

Then, each point $\boldsymbol{x}$ in the interior of an infinite helical pipe based on a circular cross section with tube radius $r > 0$ is characterized by

$$\|\boldsymbol{x} - \boldsymbol{x}_{\text{curv}}(s;\boldsymbol{x})\| \overset{!}{<} r \quad \forall\, \boldsymbol{x} \in \Omega_{\text{HelicalPipe}_\infty}, \tag{A.18}$$

which then leads to the implicit representation

$$\phi_{\text{HelicalPipe}_\infty}(\boldsymbol{x}) \overset{\text{def}}{=} \sqrt{(x_1 - R\cos(2\pi\tilde{s}(\boldsymbol{x})))^2 + (x_2 - R\sin(2\pi\tilde{s}(\boldsymbol{x})))^2 + (x_3 - \alpha\tilde{s}(\boldsymbol{x}))^2} - r \overset{!}{<} 0 \tag{A.19}$$

with $\tilde{s}(\boldsymbol{x})$ solution to the aforementioned distance optimization problem, which can be approximated at all nodes of the underlying computational mesh $\mathcal{T}_h$. In Figure A.1a, the level-set approximation of an infinite helical pipe is shown.

Finite Helical Pipe. Similar to the finite cylinder, also the infinite helical pipe can be cut-off by planes. Considering limitations which yield circular cross sections defined by the helical tangential vector $\boldsymbol{t}(s) = \frac{\partial \boldsymbol{x}_{\text{curv}}}{\partial s}(s)$ in the helical point $\boldsymbol{x}_{\text{curv}}(s)$, limiting halfspaces can be defined as

$$\phi_{\text{HSpace}}(\boldsymbol{x}; \pm\frac{\partial \boldsymbol{x}_{\text{curv}}(s)}{\partial s}, \boldsymbol{x}_{\text{curv}}(s)). \tag{A.20}$$

In addition to the cross-section planes, additional limitations in x_3-direction are required to cut the helical pipe not at all turns, but only at two specific heights. An example for an x_3-axis oriented helical pipe with a total height of 4 turns, based on a centerline range of $x_3 \in [-2\alpha, 2\alpha]$, is given by

$$\Omega_{\text{HelicalPipe}} = \Omega_{\text{HelicalPipe}_\infty} \setminus (\Omega_{\text{lim,bot}} \cup \Omega_{\text{lim,top}}), \tag{A.21}$$

$$\phi_{\text{HelicalPipe}} = \max\left\{\phi_{\text{HelicalPipe}_\infty}, -(\min\left\{\phi_{\text{lim,bot}}, \phi_{\text{lim,top}}\right\})\right\}. \tag{A.22}$$

The stairs-like limitations $\Omega_{\text{lim,bot}}$ and $\Omega_{\text{lim,top}}$ are defined as

$$\Omega_{\text{lim,bot}} = (\Omega_{\text{HSpace}_{x_3,1}} \cap \Omega_{\text{HSpace}_{\text{cross, bot}}}) \cup \Omega_{\text{HSpace}_{x_3,2}}, \tag{A.23}$$

$$\Omega_{\text{lim,top}} = (\Omega_{\text{HSpace}_{x_3,3}} \cap \Omega_{\text{HSpace}_{\text{cross, top}}}) \cup \Omega_{\text{HSpace}_{x_3,4}} \tag{A.24}$$

with respective level-set functions

$$\phi_{\text{lim,bot}} = \min\left\{\max\left\{\phi_{\text{HSpace}_{x_3,1}}, \phi_{\text{HSpace}_{\text{cross, bot}}}\right\}, \phi_{\text{HSpace}_{x_3,2}}\right\}, \tag{A.25}$$

$$\phi_{\text{lim,top}} = \min\left\{\max\left\{\phi_{\text{HSpace}_{x_3,3}}, \phi_{\text{HSpace}_{\text{cross, top}}}\right\}, \phi_{\text{HSpace}_{x_3,4}}\right\}. \tag{A.26}$$

The bounding halfspaces therein are defined as

$$\phi_{\text{HSpace}_{x_3,1}}(\boldsymbol{x}) = \phi_{\text{HSpace}}(\boldsymbol{x}; (0,0,1)^T, (R,0,-2\alpha + 1.1r)^T), \tag{A.27}$$

$$\phi_{\text{HSpace}_{x_3,2}}(\boldsymbol{x}) = \phi_{\text{HSpace}}(\boldsymbol{x}; (0,0,1)^T, (R,0,-2\alpha - 1.1r)^T), \tag{A.28}$$

$$\phi_{\text{HSpace}_{x_3,3}}(\boldsymbol{x}) = \phi_{\text{HSpace}}(\boldsymbol{x}; (0,0,-1)^T, (R,0,2\alpha - 1.1r)^T), \tag{A.29}$$

$$\phi_{\text{HSpace}_{x_3,4}}(\boldsymbol{x}) = \phi_{\text{HSpace}}(\boldsymbol{x}; (0,0,-1)^T, (R,0,2\alpha + 1.1r)^T), \tag{A.30}$$

$$\phi_{\text{HSpace}_{\text{cross, bot}}}(\boldsymbol{x}) = \phi_{\text{HSpace}}(\boldsymbol{x}; \boldsymbol{n}, (R,0,-2\alpha)^T), \tag{A.31}$$

$$\phi_{\text{HSpace}_{\text{cross, top}}}(\boldsymbol{x}) = \phi_{\text{HSpace}}(\boldsymbol{x}; -\boldsymbol{n}, (R,0,2\alpha)^T). \tag{A.32}$$

Hereby, the unit normal vector for the limiting cross section planes is given by

$$\boldsymbol{n} = 1/\sqrt{4\pi^2R^2 + \alpha^2} \cdot (0, 2\pi R, \alpha)^T \tag{A.33}$$

and is equal to the tangential vectors along the helix for $s = \pm 2$. In Figure A.1b, the finite helical pipe is exemplarily shown with a thread pitch of $\alpha = 0.6$, a helix radius $R = 0.2$ and a tube radius $r = 0.05$ discretized on a domain $\Omega = [-0.4, 0.4]^2 \times [-1.5, 1.5]$ with a regular mesh consisting of tri-linearly-interpolated hexahedral $\mathbb{Q}^1$-elements and a mesh size of $h = 0.8/75$.

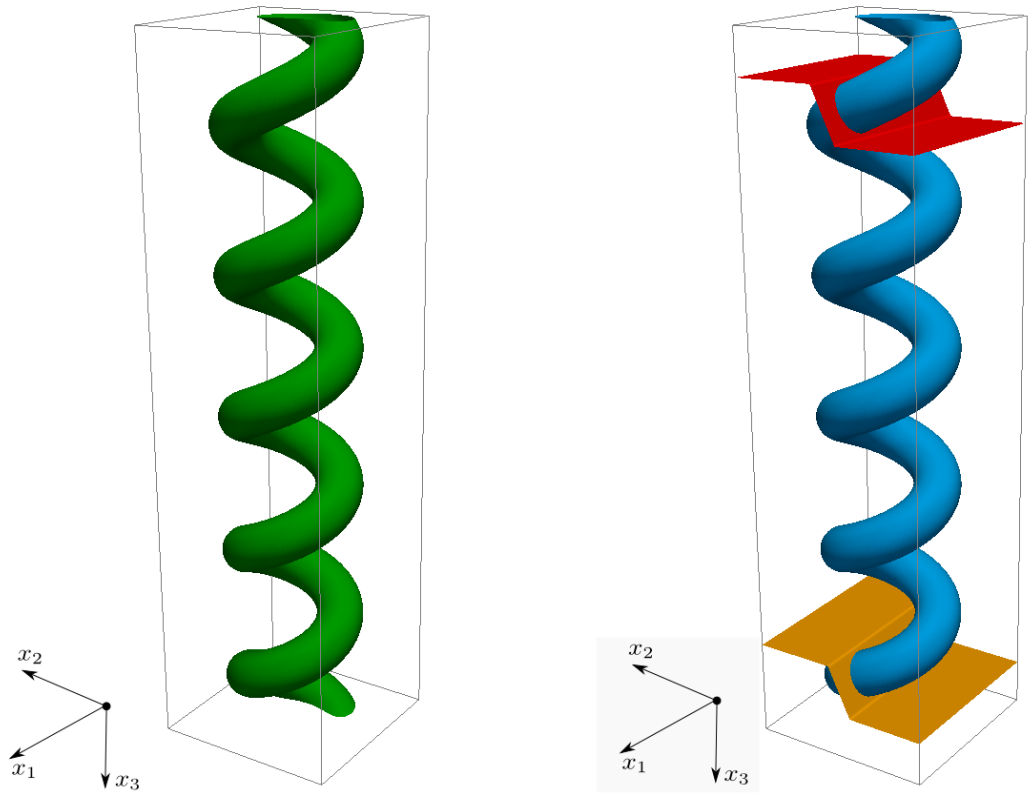

(a) (b)

Figure A.1: Level-set-boundary representation of an infinite and a finite helical pipe with circular cross section within a background domain $\Omega = [-0.4, 0.4]^2 \times [-1.5, 1.5]$: (a) Infinite helical pipe $\Omega_{\text{HelicalPipe}_\infty}$ with a thread pitch of $\alpha = 0.6$, a helix radius $R = 0.2$ and a tube radius $r = 0.05$ (colored in green). (b) Finite helical pipe constructed of an infinite helical pipe $\Omega_{\text{HelicalPipe}_\infty}$ (colored in blue) limited by two stairs-like half spaces $\Omega_{\text{lim,bot}}$ and $\Omega_{\text{lim,top}}$, which are implicitly described by functions $\phi_{\text{lim,bot}}$ (colored in red) and $\phi_{\text{lim,top}}$ (colored in orange) as defined in (A.25) and (A.26). The final pipe domain is defined as $\Omega_{\text{HelicalPipe}} = \Omega_{\text{HelicalPipe}_\infty} \setminus (\Omega_{\text{lim,bot}} \cup \Omega_{\text{lim,top}})$.

A.2 Translational and Rotational Mappings

All geometric objects Ω_{Obj} can be easily transformed by utilizing translational and rotational transformations $\boldsymbol{T} : \mathbb{R}^3 \to \mathbb{R}^3$, which can be defined as

$$\boldsymbol{T} : \begin{cases} \mathbb{R}^3 \to \mathbb{R}^3, \\ \boldsymbol{x} \mapsto \boldsymbol{R}^T \cdot (\boldsymbol{x} - \boldsymbol{c}) \end{cases} \tag{A.34}$$

consisting of a rotational and a translational part. Considering rotations in the reference configuration, $\boldsymbol{R} \in \mathbb{R}^{3\times3}$ denotes a orthonormal rotation matrix with column vectors $\boldsymbol{r}_1, \boldsymbol{r}_2, \boldsymbol{r}_3 \in \mathbb{R}^3$ which are the target vectors of the coordinate unit vectors. Furthermore, $\boldsymbol{c} \in \mathbb{R}^3$ defines the target position of the origin $\boldsymbol{0}$ when translating the object. Concatenation of the transformation and the level-set function in the form $\phi_{\text{Obj}} \circ \boldsymbol{T}$ yields an implicit representation of the translated and rotated object.

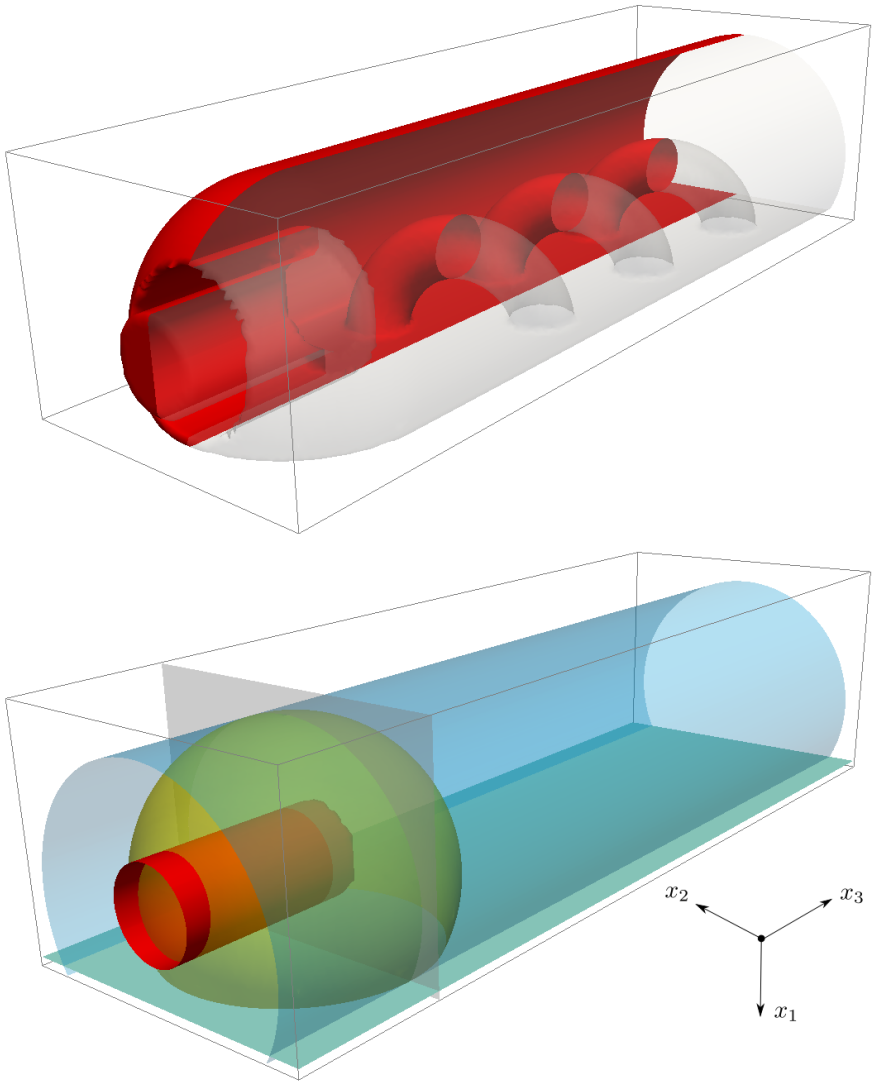

Figure A.2: Level-set-boundary representation of a complex composite fluid domain. (Top) Final fluid domain from (A.35) composed of different subdomains represented by level-set functions using Boolean set operations. The domain is approximated on an unfitted background mesh covering a cuboid $[0.7, 0.1] \times [0.5, 0.5] \times [1.5, 1.5]$ consisting of $\mathbb{Q}^1$-elements with $h = 0.02$. (Bottom) Composed subdomain $\Omega_{\text{outer surf}}$ from (A.41) consisting of a finite cylinder Ω_{Cyl} (colored in blue and gray), a spherical subdomain Ω_{Sphere} (colored in yellow), and a plane which limits the bottom side $\Omega_{\text{HSpace,bot}}$ (colored in green). Next, the domain is expanded by a finite cylinder $\Omega_{\text{Cyl,Fluid}}$ (colored in red), see (A.47).

A.3 Composed Level-Set Representation of Boundaries - An Example

In the following, an example is given how complex domains can be created by simply combining basic geometric objects as introduced in Appendix A.1. With the help of Boolean operations (2.56)-(2.60) and transformations (A.34), subdomains can be composed. In Figure A.2 a visualization of the considered final domain is given.

The overall domain Ω_{Fluid} is composed as the intersection of the exterior of a finite spiral and the interior of an outer limiting surface. The latter consists of cylinders, a sphere and several halfspaces. In addition, the inflow region is characterized by a hollow cylinder. The final domain can be composed as follows:

$$\Omega_{\text{Fluid}} = (((\Omega^c_{\text{Spiral}} \cap \Omega_{\text{outer surf}}) \cup \Omega_{\text{Cyl,Fluid}}) \backslash \Omega_{\text{Cyl,hollow}}) \cap \Omega_{\text{HSpace,in}}, \tag{A.35}$$

$$\phi_{\text{Fluid}} = \max\{\max\{\min\{\max\{-\phi_{\text{Spiral}}, \phi_{\text{outer surf}}\}, \phi_{\text{Cyl,Fluid}}\}, -\phi_{\text{Cyl,hollow}}\}, \phi_{\text{HSpace,in}}\}. \tag{A.36}$$

The interior of a finite spiral can be created with the help of an infinite helical pipe and limiting half spaces as

$$\Omega_{\text{Spiral}} = \Omega_{\text{HelicalPipe}_\infty} \cap (\Omega_{\text{lim,back}} \cap \Omega_{\text{lim,front}}), \tag{A.37}$$

$$\phi_{\text{Spiral}} = \max\left\{\phi_{\text{HelicalPipe}_\infty}, \max\{\phi_{\text{lim,back}}, \phi_{\text{lim,front}}\}\right\}, \tag{A.38}$$

with $\phi_{\text{HelicalPipe}_\infty}$ as defined in (A.19) based on a thread pitch of $\alpha = 0.6$, a helix radius $R = 0.2$ and a tube radius $r = 0.05$ and

$$\phi_{\text{lim,back}}(\boldsymbol{x}) = \phi_{\text{HSpace}}(\boldsymbol{x}; 1/\sqrt{2}(0,1,1)^T, (0,0,1.2)^T), \tag{A.39}$$

$$\phi_{\text{lim,front}}(\boldsymbol{x}) = \phi_{\text{HSpace}}(\boldsymbol{x}; -1/\sqrt{2}(0,1,1)^T, (0,0,-0.6)^T). \tag{A.40}$$

The outer surface is composed of a finite cylinder and a sphere limited in x_1- and x_3-direction by halfspaces as

$$\Omega_{\text{outer surf}} = ((\Omega_{\text{Cyl}} \cup \Omega_{\text{Sphere}}) \cap \Omega_{\text{HSpace,bot}}) \cap \Omega_{\text{HSpace,out}}, \tag{A.41}$$

$$\phi_{\text{outer surf}} = \max\{\max\{\min\{\phi_{\text{Cyl}}, \phi_{\text{Sphere}}\}, \phi_{\text{HSpace,bot}}\}, \phi_{\text{HSpace,out}}\} \tag{A.42}$$

with

$$\phi_{\text{Cyl}}(\boldsymbol{x}) = \phi_{\text{Cyl}}(\boldsymbol{T}_1\boldsymbol{x}; \boldsymbol{n} = (0,0,1)^T, r = 0.45, h^+ = 1.5, h^- = 1.0), \tag{A.43}$$

$$\phi_{\text{Sphere}}(\boldsymbol{x}) = \phi_{\text{Sphere}}(\boldsymbol{T}_1\boldsymbol{x}; r = 0.45), \tag{A.44}$$

$$\phi_{\text{HSpace,bot}}(\boldsymbol{x}) = \phi_{\text{HSpace}}(\boldsymbol{x}; \boldsymbol{n} = (1,0,0)^T, \boldsymbol{x}_0 = (0.05,0,0)), \tag{A.45}$$

$$\phi_{\text{HSpace,out}}(\boldsymbol{x}) = \phi_{\text{HSpace}}(\boldsymbol{x}; \boldsymbol{n} = (0,0,1)^T, \boldsymbol{x}_0 = (0,0,1.5)), \tag{A.46}$$

where $\boldsymbol{T}_1\boldsymbol{x} \overset{\text{def}}{=} \boldsymbol{x} + (0.15,0,0)^T$ shifts the cylinder and the sphere along the negative x_1-direction.

To construct the hollow-cylindrical inflow region, first, the fluid domain is expanded by a cylinder $\Omega_{\text{Cyl,Fluid}}$ given by

$$\phi_{\text{Cyl,Fluid}}(\boldsymbol{x}) = \phi_{\text{Cyl}}(\boldsymbol{T}_2\boldsymbol{x}; \boldsymbol{n} = (0,0,1)^T, r = 0.14, h^+ = -0.9, h^- = 1.5) \tag{A.47}$$

with a translation $\boldsymbol{T}_2\boldsymbol{x} \overset{\text{def}}{=} \boldsymbol{x} + (0.2,0,0)^T$. Second, an obstacle $\Omega_{\text{Cyl,hollow}}$ with the shape of a hollow cylinder is subtracted, which is constructed as

$$\Omega_{\text{Cyl,hollow}} = \Omega_{\text{Cyl}} \backslash \Omega_{\text{Cyl}_\infty}, \tag{A.48}$$

$$\phi_{\text{Cyl,hollow}} = \max\left\{\phi_{\text{Cyl}}, -\phi_{\text{Cyl}_\infty}\right\}, \tag{A.49}$$

with

$$\phi_{\text{Cyl}}(\boldsymbol{x}) = \phi_{\text{Cyl}}(\boldsymbol{T}_2\boldsymbol{x}; \boldsymbol{n} = (0,0,1)^T, r = 0.22, h^+ = -0.9, h^- = 1.5), \tag{A.50}$$

$$\phi_{\text{Cyl}_\infty}(\boldsymbol{x}) = \phi_{\text{Cyl}_\infty}(\boldsymbol{T}_2\boldsymbol{x}; \boldsymbol{n} = (0,0,1)^T, r = 0.14). \tag{A.51}$$

Third, the fluid domain is limited at the cylindrical inflow region in x_3-direction by a halfspace

$$\phi_{\text{HSpace,in}}(\boldsymbol{x}) = \phi_{\text{HSpace}}(\boldsymbol{x}; \boldsymbol{n} = (0,0,-1)^T, \boldsymbol{x}_0 = (0,0,-1.49)). \tag{A.52}$$

Combining all level-set fields as proposed in (A.36) defines the final fluid domain.

BIBLIOGRAPHY

[1] F. Alauzet, B. Fabrèges, M. A. Fernández, and M. Landajuela, Nitsche-XFEM for the coupling of an incompressible fluid with immersed thin-walled structures, *Computer Methods in Applied Mechanics and Engineering* **301**, 300–335, 2016.

[2] C. Annavarapu, M. Hautefeuille, and J. E. Dolbow, A robust Nitsche's formulation for interface problems, *Computer Methods in Applied Mechanics and Engineering* **225**, 44–54, 2012.

[3] D. N. Arnold, R. S. Falk, and R. Winther, Finite element exterior calculus, homological techniques, and applications, *Acta numerica* **15**, 1–155, 2006.

[4] I. Babuška, The finite element method with Lagrangian multipliers, *Numerische Mathematik* **20**, 179–192, 1973.

[5] I. Babuška and U. Banerjee, Stable Generalized Finite Element Method (SGFEM), *Computer Methods in Applied Mechanics and Engineering* **201-204**, 91–111, 2012.

[6] I. Babuška and J. M. Melenk, The Partition of Unity Method, *International Journal for Numerical Methods in Engineering* **40**, 727–758, 1997.

[7] S. Badia, F. Nobile, and C. Vergara, Fluid–structure partitioned procedures based on Robin transmission conditions, *Journal of Computational Physics* **227**, 7027–7051, 2008.

[8] S. Badia, A. Quaini, and A. Quarteroni, Splitting methods based on algebraic factorization for fluid-structure interaction, *SIAM Journal of Scientific Computing* **30**, 1778–1805, 2008.

[9] J. Baiges and R. Codina, The fixed-mesh ALE approach applied to solid mechanics and fluid-structure interaction problems, *International Journal for Numerical Methods in Engineering* **81**, 1529–1557, 2009.

[10] J. Baiges, R. Codina, F. Henke, S. Shahmiri, and W. A. Wall, A symmetric method for weakly imposing Dirichlet boundary conditions in embedded finite element meshes, *International Journal for Numerical Methods in Engineering* **90**, 636–658, 2012.

[11] R. E. Bank and L. R. Scott, On the Conditioning of Finite Element Equations with Highly Refined Meshes, *SIAM Journal on Numerical Analysis* **26**, 1383–1394, 1989.

[12] H. J. C. Barbosa and T. J. R. Hughes, The finite element method with Lagrange multipliers on the boundary: circumventing the Babuška-Brezzi condition, *Computer Methods in Applied Mechanics and Engineering* **85**, 109–128, 1991.

[13] H. J. C. Barbosa and T. J. R. Hughes, Boundary Lagrange multipliers in finite element methods: error analysis in natural norms, *Numerische Mathematik* **62**, 1–15, 1992.

[14] N. Barrau, R. Becker, E. Dubach, and R. Luce, A robust variant of NXFEM for the interface problem, *Comptes Rendus Mathématique* **350**, 789–792, 2012.

[15] Y. Bazilevs and T. J. R. Hughes, Weak imposition of Dirichlet boundary conditions in fluid mechanics, *Computers and Fluids* **36**, 12–26, 2007.

[16] Y. Bazilevs, M. Hsu, and M. A. Scott, Isogeometric Fluid–Structure Interaction Analysis with Emphasis on Non-Matching Discretizations, and with Application to Wind Turbines, *Computer Methods in Applied Mechanics and Engineering* **252**, 28–41, 2012.

[17] Y. Bazilevs, K. Takizawa, and T. E. Tezduyar, Challenges and directions in computational fluid–structure interaction, *Mathematical Models and Methods in Applied Sciences* **23**, 215–221, 2013.

[18] E. Béchet, N. Moës, and B. Wohlmuth, A stable Lagrange multiplier space for stiff interface conditions within the extended finite element method, *International Journal for Numerical Methods in Engineering* **78**, 931–954, 2009.

[19] R. Becker, P. Hansbo, and R. Stenberg, A finite element method for domain decomposition with non-matching grids, *ESAIM: Mathematical Modelling and Numerical Analysis* **37**, 209–225, 2003.

[20] R. Becker, E. Burman, and P. Hansbo, A Nitsche extended finite element method for incompressible elasticity with discontinuous modulus of elasticity, *Computer Methods in Applied Mechanics and Engineering* **198**, 3352–3360, 2009.

[21] T. Belytschko and T. Black, Elastic crack growth in finite elements with minimal remeshing, *International Journal for Numerical Methods in Engineering* **45**, 601–620, 1999.

[22] T. Belytschko and J. M. Kennedy, Computer models for subassembly simulation, *Nuclear Engineering and Design* **49**, 17–38, 1978.

[23] T. Belytschko, J. M. Kennedy, and D. F. Schoeberle, Quasi-Eulerian Finite Element Formulation for Fluid-Structure Interaction, *Journal of Pressure Vessel Technology* **102**, 62–69, 1980.

[24] T. Belytschko, N. Moës, S. Usui, and C. Parimi, Arbitrary discontinuities in finite elements, *International Journal for Numerical Methods in Engineering* **50**, 993–1013, 2001.

[25] D. Boffi, M. Fortin, and F. Brezzi, *Mixed finite element methods and applications*, Springer-Verlag, Berlin-Heidelberg, 2013.

[26] T. Boiveau, Fitted and unfitted domain decomposition using penalty free Nitsche method for the Poisson problem with discontinuous material parameters, *ArXiv e-prints*, http://arxiv.org/abs/1509.00542, 2015.

[27] T. Boiveau and E. Burman, A penalty-free Nitsche method for the weak imposition of boundary conditions in compressible and incompressible elasticity, *IMA Journal of Numerical Analysis* **36**, 770–795, 2016.

[28] M. Böl, R. B. Möhle, M. Haesner, T. R. Neu, H. Horn, and R. Krull, 3D finite element model of biofilm detachment using real biofilm structures from CLSM data, *Biotechnology and Bioengineering* **103**, 177–186, 2009.

[29] M. Böl, A. E. Ehret, A. Bolea Albero, J. Hellriegel, and R. Krull, Recent advances in mechanical characterisation of biofilm and their significance for material modelling, *Critical Reviews in Biotechnology* **33**, 145–171, 2013.

[30] R. Bouffanais, M. O. Deville, and E. Leriche, Large-eddy simulation of the flow in a lid-driven cubical cavity, *Physics of Fluids* **19**, 055108, 2007.

[31] M. Braack, E. Burman, V. John, and G. Lube, Stabilized finite element methods for the generalized Oseen problem, *Computer Methods in Applied Mechanics and Engineering* **196**, 853–866, 2007.

[32] J. U. Brackbill, D. B. Kothe, and C. Zemech, A continuum method for modeling surface tension, *Journal of Computational Physics* **100**, 335–354, 1992.

[33] D. Braess, *Finite Elemente: Theorie, schnelle Löser und Anwendungen in der Elastizitätstheorie*, Springer-Verlag, Berlin-Heidelberg, 2000.

[34] S. C. Brenner and L. R. Scott, *The mathematical theory of finite element methods*, Volume 15 of *Texts in Applied Mathematics*, Springer-Verlag, Berlin-Heidelberg, 3. Edition, 2008.

[35] F. Brezzi, On the Existence, Uniqueness and Approximation of Saddle-Point Problems Arising from Lagrangian Multipliers, *ESAIM: Mathematical Modelling and Numerical Analysis* **R–2**, 129–151, 1974.

[36] F. Brezzi and M. Fortin, *Mixed and hybrid finite element methods*, Volume 15 of *Springer Series in Computational Mathematics*, Springer-Verlag, New York, 1991.

[37] F. Brezzi, J. Douglas Jr., and L. D. Marini, Two families of mixed finite elements for second order elliptic problems, *Numerische Mathematik* **47**, 217–235, 1985.

[38] E. Burman, A unified analysis for conforming and nonconforming stabilized finite element methods using interior penalty, *SIAM Journal on Numerical Analysis* **43**, 2012–2033, 2005.

[39] E. Burman and M. A. Fernández, Stabilized explicit coupling for fluid–structure interaction using Nitsche's method, *Comptes Rendus Mathématique* **345**, 467–472, 2007.

[40] E. Burman and M. A. Fernández, Stabilization of explicit coupling in fluid–structure interaction involving fluid incompressibility, *Computer Methods in Applied Mechanics and Engineering* **198**, 766–784, 2009.

[41] E. Burman and M. A. Fernández, Continuous interior penalty finite element method for the time-dependent Navier–Stokes equations: space discretization and convergence, *Numerische Mathematik* **107**, 39–77, 2007.

[42] E. Burman and P. Hansbo, A unified stabilized method for Stokes' and Darcy's equations, *Journal of Computational and Applied Mathematics* **198**, 35–51, 2007.

[43] E. Burman and P. Hansbo, Interior-penalty-stabilized Lagrange multiplier methods for the finite-element solution of elliptic interface problems, *IMA Journal of Numerical Analysis* **30**, 870–885, 2010.

[44] E. Burman and P. Hansbo, Fictitious domain finite element methods using cut elements: I. A stabilized Lagrange multiplier method, *Computer Methods in Applied Mechanics and Engineering* **199**, 2680–2686, 2010.

[45] E. Burman and P. Hansbo, Fictitious domain finite element methods using cut elements: II. A stabilized Nitsche method, *Applied Numerical Mathematics* **62**, 328–341, 2012.

[46] E. Burman and P. Hansbo, Edge stabilization for Galerkin approximations of convection–diffusion–reaction problems, *Computer Methods in Applied Mechanics and Engineering* **193**, 1437–1453, 2004.

[47] E. Burman and P. Hansbo, Edge stabilization for the generalized Stokes problem: A continuous interior penalty method, *Computer Methods in Applied Mechanics and Engineering* **195**, 2393–2410, 2006.

[48] E. Burman, M. A. Fernández, and P. Hansbo, Continuous interior penalty finite element method for Oseen's equations, *SIAM Journal on Numerical Analysis* **44**, 1248–1274, 2006.

[49] E. Burman, Interior penalty variational multiscale method for the incompressible Navier–Stokes equation: Monitoring artificial dissipation, *Computer Methods in Applied Mechanics and Engineering* **196**, 4045–4058, 2007.

[50] E. Burman, Ghost penalty, *Comptes Rendus Mathématique* **348**, 1217–1220, 2010.

[51] E. Burman, Consistent SUPG-method for transient transport problems: stability and convergence, *Computer Methods in Applied Mechanics and Engineering* **199**, 1114–1123, 2010.

[52] E. Burman, A penalty-free nonsymmetric Nitsche-type method for the weak imposition of boundary conditions, *SIAM Journal on Numerical Analysis* **50**, 1959–1981, 2012.

[53] E. Burman, Projection stabilization of Lagrange multipliers for the imposition of constraints on interfaces and boundaries, *Numerical Methods for Partial Differential Equations* **30**, 567–592, 2014.

[54] E. Burman and A. Ern, Continuous interior penalty hp-finite element methods for advection and advection-diffusion equations, *Mathematics of Computation* **76**, 1119–1140, 2007.

[55] E. Burman and M. A. Fernández, Galerkin Finite Element Methods with Symmetric Pressure Stabilization for the Transient Stokes Equations: Stability and Convergence Analysis, *SIAM Journal on Numerical Analysis* **47**, 409–439, 2009.

[56] E. Burman and M. A. Fernández, Finite element methods with symmetric stabilization for the transient convection–diffusion–reaction equation, *Computer Methods in Applied Mechanics and Engineering* **198**, 2508–2519, 2009.

[57] E. Burman and M. A. Fernández, Analysis of the PSPG method for the transient Stokes' problem, *Computer Methods in Applied Mechanics and Engineering* **200**, 2882–2890, 2011.

[58] E. Burman and M. A. Fernández, An unfitted Nitsche method for incompressible fluid–structure interaction using overlapping meshes, *Computer Methods in Applied Mechanics and Engineering* **279**, 497–514, 2014.

[59] E. Burman and M. A. Fernández, Explicit strategies for incompressible fluid-structure interaction problems: Nitsche type mortaring versus Robin-Robin coupling, *International Journal for Numerical Methods in Engineering* **97**, 739–758, 2014.

[60] E. Burman and P. Hansbo, Fictitious domain methods using cut elements: III. A stabilized Nitsche method for Stokes' problem, *ESAIM: Mathematical Modelling and Numerical Analysis* **48**, 859–874, 2014.

[61] E. Burman and P. Zunino, A Domain Decomposition Method Based on Weighted Interior Penalties for Advection-Diffusion-Reaction Problems, *SIAM Journal on Numerical Analysis* **44**, 1612–1638, 2006.

[62] E. Burman and P. Zunino, Numerical approximation of large contrast problems with the Unfitted Nitsche method, In J. Blowey and M. Jensen (eds.), *Lecture Notes in Computational Science and Engineering*, Volume 85 LNCSE, pages 227–282, Springer-Verlag, Berlin-Heidelberg, 2012.

[63] E. Burman, S. Claus, P. Hansbo, M. G. Larson, and A. Massing, CutFEM: Discretizing geometry and partial differential equations, *International Journal for Numerical Methods in Engineering* **104**, 472–501, 2015.

[64] E. Burman, S. Claus, and A. Massing, A Stabilized Cut Finite Element Method for the Three Field Stokes Problem, *SIAM Journal on Scientific Computing* **37**, A1705–A1726, 2015.

[65] E. Burman, P. Hansbo, and M. G. Larson, A Cut Finite Element Method with Boundary Value Correction, *ArXiv e-prints*, http://arxiv.org/abs/1507.03096, 2015.

[66] E. Burman, P. Hansbo, M. G. Larson, and A. Massing, Cut Finite Element Methods for Partial Differential Equations on Embedded Manifolds of Arbitrary Codimensions, *ArXiv e-prints*, http://arxiv.org/abs/1610.01660v1, 2016.

[67] E. Burman, A. Ern, and M. A. Fernández, Fractional-step methods and finite elements with symmetric stabilization for the transient Oseen problem, *ESAIM: Mathematical Modelling and Numerical Analysis* **51**, 487–507, 2017.

[68] H. Carlos, L. Kleiser, and R. Friedrich, Subgrid-scale energy transfer in the near-wall region of turbulent flows, *Physics of Fluids* **6**, 3130–3143, 1994.

[69] P. Causin, J. F. Gerbeau, and F. Nobile, Added-mass effect in the design of partitioned algorithms for fluid-structure problems, *Computer Methods in Applied Mechanics and Engineering* **194**, 4506–4527, 2005.

[70] S. Chandrasekhar, *Hydrodynamic and Hydromagnetic Stability*, Dover Publ., New York, 1981.

[71] J. Chessa and T. Belytschko, An extended finite element method for two-phase fluids, *Journal of Applied Mechanics* **70**, 10–17, 2003.

[72] J. Chessa, P. Smolinski, and T. Belytschko, The extended finite element method (XFEM) for solidification problems, *International Journal for Numerical Methods in Engineering* **53**, 1959–1977, 2002.

[73] A. J. Chorin, Numerical solutions of the Navier-Stokes equations, *Mathematics of Computation* **22**, 745–762, 1968.

[74] J. Chung and G. M. Hulbert, A Time Integration Algorithm for Structural Dynamics With Improved Numerical Dissipation: The Generalized-α Method, *Journal of Applied Mechanics* **60**, 371–375, 1993.

[75] R. Codina, Analysis of a stabilized finite element approximation of the Oseen equations using orthogonal subscales, *Applied Numerical Mathematics* **58**, 264–283, 2008.

[76] R. Codina, G. Houzeaux, H. Coppola-Owen, and J. Baiges, The fixed-mesh ALE approach for the numerical approximation of flows in moving domains, *Journal of Computational Physics* **228**, 1591–1611, 2009.

[77] M. Coroneo, L. Yoshihara, and W. A. Wall, Biofilm growth: A multi-scale and coupled fluid-structure interaction and mass transport approach, *Biotechnology and Bioengineering* **111**, 1385–1395, 2014.

[78] R. Courant, Variational Methods for the Solution of Problems of Equilibrium and Vibrations, *Bulletin of the American Mathematical Society* **49**, 1–24, 1943.

[79] S. Court and M. Fournié, A fictitious domain finite element method for simulations of fluid-structure interactions: The Navier-Stokes equations coupled with a moving solid, *Journal of Fluids and Structures* **55**, 398–408, 2015.

[80] S. Court, M. Fournié, and A. Lozinski, A fictitious domain approach for the Stokes problem based on the extended finite element method, *International Journal for Numerical Methods in Fluids* **74**, 73–99, 2014.

[81] C. D'Angelo and P. Zunino, Numerical approximation with Nitsche's coupling of transient Stokes'/Darcy's flow problems applied to hemodynamics, *Applied Numerical Mathematics* **62**, 378–395, 2012.

[82] M. de Berg, O. Cheong, M. van Kreveld, and M. Overmars, *Computational Geometry: Algorithms and Applications*, Volume 40, Springer-Verlag, Berlin-Heidelberg, 2008.

[83] M. H. de Vaal, M. W. Gee, U. A. Stock, and W. A. Wall, Computational evaluation of aortic occlusion and the proposal of a novel, improved occluder: Constrained endo-aortic balloon occlusion (CEABO), *International Journal for Numerical Methods in Biomedical Engineering* **32**, n/a–n/a, 2016.

[84] W. Dettmer and D. Perić, An analysis of the time integration algorithms for the finite element solutions of incompressible Navier–Stokes equations based on a stabilised formulation, *Computer Methods in Applied Mechanics and Engineering* **192**, 1177–1226, 2003.

[85] D. A. Di Pietro and A. Ern, *Mathematical Aspects of Discontinuous Galerkin Methods*, Volume 69 of *Mathématiques et Applications*, Springer-Verlag, Berlin-Heidelberg, 2012.

[86] P. Diez, R. Cottereau, and S. Zlotnik, A stable extended FEM formulation for multi-phase problems enforcing the accuracy of the fluxes through Lagrange multipliers, *International Journal for Numerical Methods in Engineering* **96**, 303–322, 2013.

[87] J. E. Dolbow and I. Harari, An efficient finite element method for embedded interface problems, *International Journal for Numerical Methods in Engineering* **78**, 229–252, 2009.

[88] J. E. Dolbow, N. Moës, and T. Belytschko, Discontinuous enrichment in finite elements with a partition of unity method, *Finite Elements in Analysis and Design* **36**, 235–260, 2000.

[89] J. Donéa, P. Fasoli–Stella, and S. Giuliani, Lagrangian and Eulerian Finite Element Techniques for Transient Fluid–Structure Interaction Problems, In *Transactions of the 4th Int. Conference on SMIRT*, San Francisco, 1977.

[90] J. Donéa, S. Giuliani, and J. P. Halleux, An arbitrary Lagrangian-Eulerian finite element method for transient dynamic fluid-structure interactions, *Computer Methods in Applied Mechanics and Engineering* **33**, 689–723, 1982.

[91] J. Donéa and A. Huerta, *Finite Element Methods for Flow Problems*, John Wiley & Sons, Ltd, Chichester, 2003.

[92] R. M. Donlan, Biofilms and device-associated infections, In *Emerging Infectious Diseases*, pages 277–281, 7th Edition, 2001.

[93] J. Douglas and T. Dupont, Interior Penalty Procedures for Elliptic and Parabolic Galerkin Methods, In R. Glowinski and J. Lions (eds.), *Computing Methods in Applied Sciences, Lecture Notes in Physics*, pages 207–216, Springer-Verlag, Berlin-Heidelberg, 1976.

[94] C. Duarte, I. Babuška, and J. Oden, Generalized finite element methods for three-dimensional structural mechanics problems, *Computers & Structures* **77**, 215–232, 2000.

[95] R. Duddu, S. Bordas, D. Chopp, and B. Moran, A combined extended finite element and level set method for biofilm growth, *International Journal for Numerical Methods in Engineering* **74**, 848–870, 2008.

[96] R. Duddu, D. L. Chopp, and B. Moran, A two-dimensional continuum model of biofilm growth incorporating fluid flow and shear stress based detachment, *Biotechnology and Bioengineering* **103**, 92–104, 2009.

[97] C. D'Angelo and A. Scotti, A mixed finite element method for Darcy flow in fractured porous media with non-matching grids, *ESAIM: Mathematical Modelling and Numerical Analysis* **46**, 465–489, 2012.

[98] A. Ehrl, A. Popp, V. Gravemeier, and W. Wall, A dual mortar approach for mesh tying within a variational multiscale method for incompressible flow, *International Journal for Numerical Methods in Fluids* **76**, 1–27, 2014.

[99] A. Embar, J. E. Dolbow, and I. Harari, Imposing Dirichlet boundary conditions with Nitsche's method and spline-based finite elements, *International Journal for Numerical Methods in Engineering* **83**, 877–898, 2010.

[100] S. Erlicher, L. Bonaventura, and O. S. Bursi, The analysis of the Generalized-α method for non-linear dynamic problems, *Computational Mechanics* **28**, 83–104, 2002.

[101] A. Ern and J. L. Guermond, *Theory and Practice of Finite Elements*, Volume 159 of *Applied Mathematical Sciences*, Springer-Verlag, New York, 2004.

[102] A. Ern and J. L. Guermond, Weighting the Edge Stabilization, *SIAM Journal on Numerical Analysis* **51**, 1655–1677, 2013.

[103] C. R. Ethier and D. A. Steinman, Exact fully 3D Navier–Stokes solutions for benchmarking, *International Journal for Numerical Methods in Fluids* **19**, 369–375, 1994.

[104] C. Farhat and V. K. Lakshminarayan, An ALE formulation of embedded boundary methods for tracking boundary layers in turbulent fluid-structure interaction problems, *Journal of Computational Physics* **263**, 53–70, 2014.

[105] M. A. Fernández, Coupling schemes for incompressible fluid-structure interaction: implicit, semi-implicit and explicit, *SeMa Journal* **55**, 59–108, 2011.

[106] M. A. Fernández, M. Landajuela, and M. Vidrascu, Fully decoupled time-marching schemes for incompressible fluid/thin-walled structure interaction, *Journal of Computational Physics* **297**, 156–181, 2015.

[107] M. A. Fernández and M. Moubachir, A Newton method using exact jacobians for solving fluid–structure coupling, *Computers & Structures* **83**, 127–142, 2005.

[108] M. A. Fernández, J. Mullaert, and M. Vidrascu, Generalized Robin-Neumann explicit coupling schemes for incompressible fluid-structure interaction: stability analysis and numerics, *International Journal for Numerical Methods in Engineering* **101**, 199–229, 2015.

[109] S. Fernández-Méndez and A. Huerta, Imposing essential boundary conditions in mesh-free methods, *Computer Methods in Applied Mechanics and Engineering* **193**, 1257–1275, 2004.

[110] C. Förster, *Robust methods for fluid-structure interaction with stabilised finite elements*, Phd thesis, Universität Stuttgart, 2007.

[111] C. Förster, W. A. Wall, and E. Ramm, Artificial added mass instabilities in sequential staggered coupling of nonlinear structures and incompressible viscous flows, *Computer Methods in Applied Mechanics and Engineering* **196**, 1278–1293, 2007.

[112] L. P. Franca and S. L. Frey, Stabilized finite element methods: II. The incompressible Navier-Stokes equations, *Computer Methods in Applied Mechanics and Engineering* **99**, 209–233, 1992.

[113] S. Frei and T. Richter, A second order time-stepping scheme for parabolic interface problems with moving interfaces, *ESAIM: Mathematical Modelling and Numerical Analysis*, doi: 10.1051/m2an/2016072, 2016.

[114] T. P. Fries, Overview and comparison of different variants of the XFEM, *PAMM* **14**, 27–30, 2014.

[115] T. P. Fries and T. Belytschko, The extended/generalized finite element method: An overview of the method and its applications, *International Journal for Numerical Methods in Engineering* **84**, 253–304, 2010.

[116] T. P. Fries and S. Omerović, Higher-order accurate integration of implicit geometries, *International Journal for Numerical Methods in Engineering* **106**, 323–371, 2016.

[117] T. P. Fries and A. Zilian, On time integration in the XFEM, *International Journal for Numerical Methods in Engineering* **79**, 69–93, 2009.

[118] A. Fumagalli and A. Scotti, Numerical modelling of multiphase subsurface flow in the presence of fractures, *Communications in Applied and Industrial Mathematics* **3**, doi: 10.1685/journal.caim.380, 2011.

[119] P. Gamnitzer, *Residual-based variational multiscale methods for turbulent flows*, Phd thesis, Institute for Computational Mechanics, Technical University of Munich, 2010.

[120] P. Gamnitzer and W. A. Wall, An ALE-Chimera method for large deformation fluid-structure interaction, In *Proceedings of the European Conference on Computational Fluid Dynamics, ECCOMAS CFD, The Netherlands, TU Delft*, pages 1–14, 2006.

[121] M. W. Gee, U. Küttler, and W. A. Wall, Truly monolithic algebraic multigrid for fluid-structure interaction, *International Journal for Numerical Methods in Engineering* **85**, 987–1016, 2011.

[122] M. Germano, On the effect of torsion on a helical pipe flow, *Journal of Fluid Mechanics* **125**, 1–8, 1982.

[123] A. Gerstenberger, *An XFEM based fixed-grid approach to fluid-structure interaction*, Phd thesis, Institute for Computational Mechanics, Technical University of Munich, 2010.

[124] A. Gerstenberger and W. A. Wall, An eXtended Finite Element Method/Lagrange multiplier based approach for fluid-structure interaction, *Computer Methods in Applied Mechanics and Engineering* **197**, 1699–1714, 2008.

[125] A. Gerstenberger and W. A. Wall, An embedded Dirichlet formulation for 3D continua, *International Journal for Numerical Methods in Engineering* **82**, 537–563, 2010.

[126] V. Girault, B. Rivière, and M. F. Wheeler, A discontinuous Galerkin method with nonoverlapping domain decomposition for the Stokes and Navier-Stokes problems, *Mathematics of Computation* **74**, 53–84, 2005.

[127] V. Girault and P. A. Raviart, *Finite Element Methods for Navier-Stokes Equations*, Volume 5 of *Springer Series in Computational Mathematics*, Springer-Verlag, Berlin-Heidelberg, 1986.

[128] M. T. Goodrich and R. Tamassia, *Algorithm Design: Foundations, Analysis, and Internet Examples*, John Wiley & Sons, Inc., Chichester, 2002.

[129] V. Gravemeier and W. A. Wall, Variational multiscale methods for premixed combustion based on a progress-variable approach, *Combustion and Flame* **158**, 1160–1170, 2011.

[130] V. Gravemeier, M. W. Gee, M. Kronbichler, and W. A. Wall, An algebraic variational multiscale-multigrid method for large eddy simulation of turbulent flow, *Computer Methods in Applied Mechanics and Engineering* **199**, 853–864, 2010.

[131] P. M. Gresho and R. L. Sani, *Incompressible Flow and the Finite Element Method*, John Wiley & Sons, Chichester, 2000.

[132] M. Griebel and M. A. Schweitzer, A Particle-Partition of Unity Method Part V: Boundary Conditions, In *Geometric Analysis and Nonlinear Partial Differential Equations*, pages 519–542, Springer-Verlag, Berlin-Heidelberg, 2003.

[133] S. Groß and A. Reusken, *Numerical Methods for Two-phase Incompressible Flows, Springer Series in Computational Mathematics*, Volume 40, Springer-Verlag, Berlin-Heidelberg, 2011.

[134] S. Groß and A. Reusken, An extended pressure finite element space for two-phase incompressible flows with surface tension, *Journal of Computational Physics* **224**, 40–58, 2007.

[135] S. Groß and A. Reusken, Finite element discretization error analysis of a surface tension force in two-phase incompressible flows, *SIAM Journal on Numerical Analysis* **45**, 1679–1700, 2007.

[136] S. Groß, V. Reichelt, and A. Reusken, A finite element based level set method for two-phase incompressible flows, *Computing and Visualization in Science* **9**, 239–257, 2006.

[137] M. E. Gurtin, *An Introduction to Continuum Mechanics*, Volume 158 of *Mathematics in Science and Engineering*, Elsevier, New York, 1981.

[138] A. Hansbo and P. Hansbo, An unfitted finite element method, based on Nitsche's method, for elliptic interface problems, *Computer Methods in Applied Mechanics and Engineering* **191**, 5537–5552, 2002.

[139] A. Hansbo, P. Hansbo, and M. G. Larson, A finite element method on composite grids based on Nitsche's method, *ESAIM: Mathematical Modelling and Numerical Analysis* **37**, 495–514, 2003.

[140] P. Hansbo, Nitsche's method for interface problems in computational mechanics, *GAMM-Mitteilungen* **28**, 183–206, 2005.

[141] P. Hansbo, M. G. Larson, and S. Zahedi, A cut finite element method for a Stokes interface problem, *Applied Numerical Mathematics* **85**, 90–114, 2014.

[142] P. Hansbo, M. G. Larson, and S. Zahedi, Characteristic cut finite element methods for convection–diffusion problems on time dependent surfaces, *Computer Methods in Applied Mechanics and Engineering* **293**, 431–461, 2015.

[143] P. Hansbo, M. G. Larson, and S. Zahedi, A cut finite element method for coupled bulk-surface problems on time-dependent domains, *Computer Methods in Applied Mechanics and Engineering* **307**, 96–116, 2016.

[144] I. Harari and J. Dolbow, Analysis of an efficient finite element method for embedded interface problems, *Computational Mechanics* **46**, 205–211, 2010.

[145] D. Hartmann, M. Meinke, and W. Schröder, A level-set based adaptive-grid method for premixed combustion, *Combustion and Flame* **158**, 1318–1339, 2011.

[146] M. Hautefeuille, C. Annavarapu, and J. E. Dolbow, Robust imposition of Dirichlet boundary conditions on embedded surfaces, *International Journal for Numerical Methods in Engineering* **90**, 40–64, 2012.

[147] F. Henke, *An extended finite element method for turbulent premixed combustion*, Phd thesis, Institute for Computational Mechanics, Technical University of Munich, 2012.

[148] F. Henke, M. Winklmaier, V. Gravemeier, and W. A. Wall, A semi-Lagrangean time-integration approach for extended finite element methods, *International Journal for Numerical Methods in Engineering* **98**, 174–202, 2014.

[149] M. A. Heroux, E. T. Phipps, A. G. Salinger, H. K. Thornquist, R. S. Tuminaro, J. M. Willenbring, A. Williams, K. S. Stanley, R. A. Bartlett, V. E. Howle, R. J. Hoekstra, J. J. Hu, T. G. Kolda, R. B. Lehoucq, K. R. Long, and R. P. Pawlowski, An overview of the Trilinos project, *ACM Transactions on Mathematical Software* **31**, 397–423, 2005.

[150] C. W. Hirt, A. A. Amsden, and J. L. Cook, An arbitrary Lagrangian-Eulerian computing method for all flow speeds, *Journal of Computational Physics* **14**, 227–253, 1974.

[151] C. W. Hirt and B. D. Nichols, Volume of fluid (VOF) method for the dynamics of free boundaries, *Journal of Computational Physics* **39**, 201–225, 1981.

[152] G. A. Holzapfel, *Nonlinear Solid Mechanics: A Continuum Approach for Engineering*, John Wiley & Sons, Chichester, 2000.

[153] T. Horger, J. M. Melenk, and B. Wohlmuth, On optimal L2 and surface flux convergence in FEM, *Computing and Visualization in Science* **16**, 231–246, 2013.

[154] G. Houzeaux and R. Codina, A Chimera method based on a Dirichlet/Neumann(Robin) coupling for the Navier-Stokes equations, *Computer Methods in Applied Mechanics and Engineering* **192**, 3343–3377, 2003.

[155] T. J. R. Hughes, W. K. Liu, and T. K. Zimmermann, Lagrangian-Eulerian finite element formulation for incompressible viscous flows, *Computer Methods in Applied Mechanics and Engineering* **29**, 329–349, 1981.

[156] T. J. R. Hughes, G. Scovazzi, and L. P. Franca, Multiscale and Stabilized Methods, In *Encyclopedia of Computational Mechanics*, John Wiley & Sons, Chichester, 2007.

[157] F. Jarre and J. Stoer, *Optimierung*, Springer-Verlag, Berlin-Heidelberg, 2004.

[158] H. Ji and J. E. Dolbow, On strategies for enforcing interfacial constraints and evaluating jump conditions with the extended finite element method, *International Journal for Numerical Methods in Engineering* **61**, 2508–2535, 2004.

[159] H. Ji, D. Chopp, and J. E. Dolbow, A hybrid extended finite element/level set method for modeling phase transformations, *International Journal for Numerical Methods in Engineering* **54**, 1209–1233, 2002.

[160] A. Johansson and M. G. Larson, A high order discontinuous Galerkin Nitsche method for elliptic problems with fictitious boundary, *Numerische Mathematik* **123**, 607–628, 2013.

[161] M. Juntunen and R. Stenberg, Nitsche's method for general boundary conditions, *Mathematics of Computation* **78**, 1353–1374, 2009.

[162] J. Kim and P. Moin, Application of a Fractional-Step Method to Incompressible Navier-Stokes Equations, *Journal of Computational Physics* **59**, 308–323, 1985.

[163] T. Klöppel, *A Finite Element Model for the Human Red Blood Cell*, Phd thesis, Institute for Computational Mechanics, Technical University of Munich, 2012.

[164] T. Klöppel, A. Popp, U. Küttler, and W. A. Wall, Fluid–structure interaction for non-conforming interfaces based on a dual mortar formulation, *Computer Methods in Applied Mechanics and Engineering* **200**, 3111–3126, 2011.

[165] P. Knobloch and L. Tobiska, Improved stability and error analysis for a class of local projection stabilizations applied to the Oseen problem, *Numerical Methods for Partial Differential Equations* **29**, 206–225, 2013.

[166] B. Krank and W. A. Wall, A new approach to wall modeling in LES of incompressible flow via function enrichment, *Journal of Computational Physics* **316**, 94–116, 2016.

[167] R. Kruse, *Enforcing coupling conditions on embedded interfaces using stress-based Lagrange multipliers in the XFEM for incompressible flow*, Master's thesis, Technical University of Munich, 2013.

[168] U. Küttler, *Effiziente Lösungsverfahren für Fluid-Struktur-Interaktions-Probleme*, Phd thesis, Institute for Computational Mechanics, Technical University of Munich, 2009.

[169] U. Küttler, M. Gee, C. Förster, A. Comerford, and W. A. Wall, Coupling strategies for biomedical fluid-structure interaction problems, *International Journal for Numerical Methods in Biomedical Engineering* **26**, 305–321, 2010.

[170] U. Küttler and W. A. Wall, Fixed-point fluid-structure interaction solvers with dynamic relaxation, *Computational Mechanics* **43**, 61–72, 2008.

[171] P. Le Tallec and J. Mouro, Fluid-structure interaction with large structural displacements, *Computer Methods in Applied Mechanics and Engineering* **190**, 3039–3067, 2001.

[172] A. Legay, J. Chessa, and T. Belytschko, An Eulerian–Lagrangian method for fluid–structure interaction based on level sets, *Computer Methods in Applied Mechanics and Engineering* **195**, 2070–2087, 2006.

[173] A. Legay, A. Zilian, and C. Janssen, A rheological interface model and its space-time finite element formulation for fluid-structure interaction, *International Journal for Numerical Methods in Engineering* **86**, 667–687, 2011.

[174] C. Lehrenfeld, The Nitsche XFEM-DG Space-Time Method and its Implementation in Three Space Dimensions, *SIAM Journal on Scientific Computing* **37**, A245–A270, 2015.

[175] C. Lehrenfeld, High order unfitted finite element methods on level set domains using isoparametric mappings, *Computer Methods in Applied Mechanics and Engineering* **300**, 716–733, 2016.

[176] E. Leriche and S. Gavrilakis, Direct numerical simulation of the flow in a lid-driven cubical cavity, *Physics of Fluids* **12**, 1363–1376, 2000.

[177] J. H. Leung, A. R. Wright, N. Cheshire, J. Crane, S. A. Thom, A. D. Hughes, and Y. Xu, Fluid structure interaction of patient specific abdominal aortic aneurysms: a comparison with solid stress models, *BioMedical Engineering OnLine* **5**, 1–15, 2006.

[178] E. Marchandise and J. F. Remacle, A stabilized finite element method using a discontinuous level set approach for solving two phase incompressible flows, *Journal of Computational Physics* **219**, 780–800, 2006.

[179] A. Massing, M. G. Larson, and A. Logg, Efficient implementation of finite element methods on non-matching and overlapping meshes in 3D, *SIAM Journal of Scientific Computing* **35**, C23–C47, 2013.

[180] A. Massing, M. G. Larson, A. Logg, and M. E. Rognes, A stabilized Nitsche overlapping mesh method for the Stokes problem, *Numerische Mathematik* **128**, 73–101, 2014.

[181] A. Massing, M. G. Larson, A. Logg, and M. E. Rognes, A Stabilized Nitsche Fictitious Domain Method for the Stokes Problem, *Journal of Scientific Computing* **61**, 1–28, 2014.

[182] A. Massing, M. G. Larson, A. Logg, and M. E. Rognes, A Nitsche-based cut finite element method for a fluid-structure interaction problem, *Communications in Applied Mathematics and Computational Science* **10**, 97–120, 2015.

[183] A. Massing, B. Schott, and W. A. Wall, A stabilized Nitsche cut finite element method for the Oseen problem, *Computer Methods in Applied Mechanics and Engineering, ArXiv e-prints http://arxiv.org/abs/1611.02895v2*, submitted, 2017.

[184] U. M. Mayer, A. Popp, A. Gerstenberger, and W. A. Wall, 3D fluid-structure-contact interaction based on a combined XFEM FSI and dual mortar contact approach, *Computational Mechanics* **46**, 53–67, 2010.

[185] M. Mayr, T. Klöppel, W. A. Wall, and M. W. Gee, A Temporal Consistent Monolithic Approach to Fluid-Structure Interaction Enabling Single Field Predictors, *SIAM Journal on Scientific Computing* **37**, B30–B59, 2015.

[186] J. Melenk and I. Babuška, The partition of unity finite element method: Basic theory and applications, *Computer Methods in Applied Mechanics and Engineering* **139**, 289–314, 1996.

[187] R. Mittal and G. Iaccarino, Immersed Boundary Methods, *Annual Review of Fluid Mechanics* **37**, 239–261, 2005.

[188] N. Moës, J. E. Dolbow, and T. Belytschko, A finite element method for crack growth without remeshing, *International Journal for Numerical Methods in Engineering* **46**, 131–150, 1999.

[189] N. Moës, E. Béchet, and M. Tourbier, Imposing Dirichlet boundary conditions in the extended finite element method, *International Journal for Numerical Methods in Engineering* **67**, 1641–1669, 2006.

[190] S. E. Mousavi and N. Sukumar, Generalized Gaussian quadrature rules for discontinuities and crack singularities in the extended finite element method, *Computer Methods in Applied Mechanics and Engineering* **199**, 3237–3249, 2010.

[191] S. E. Mousavi, H. Xiao, and N. Sukumar, Generalized Gaussian quadrature rules on arbitrary polygons, *International Journal for Numerical Methods in Engineering* **82**, 99–113, 2010.

[192] C. J. Mueller, J. F. Driscoll, D. L. Reuss, M. C. Drake, and M. E. Rosalik, Vorticity generation and attenuation as vortices convect through a premixed flame, *Combustion and Flame* **112**, 342–358, 1998.

[193] B. Müller, F. Kummer, and M. Oberlack, Highly accurate surface and volume integration on implicit domains by means of moment-fitting, *International Journal for Numerical Methods in Engineering* **96**, 512–528, 2013.

[194] S. Nagrath, K. E. Jansen, and R. T. Lahey, Computation of incompressible bubble dynamics with a stabilized finite element level set method, *Computer Methods in Applied Mechanics and Engineering* **194**, 4565–4587, 2005.

[195] J. Nedelec, Mixed finite elements in R3, *Numerische Mathematik* **35**, 315–341, 1980.

[196] J. Nitsche, Über ein Variationsprinzip zur Lösung von Dirichlet-Problemen bei Verwendung von Teilräumen, die keinen Randbedingungen unterworfen sind, *Abhandlungen aus dem Mathematischen Seminar der Universität Hamburg* **36**, 9–15, 1971.

[197] W. Noh and P. Woodward, SLIC (Simple Line Interface Calculation), In *Lecture Notes in Physics, Proceedings of the Fifth International Conference on Numerical Methods for Fluid Dynamics*, Volume 59, pages 330–340, 1976.

[198] R. R. Nourgaliev, M. S. Liou, and T. G. Theofanous, Numerical prediction of interfacial instabilities: Sharp interface method (SIM), *Journal of Computational Physics* **227**, 3940–3970, 2008.

[199] J. T. Oden and L. Demkowicz, Advances in Adaptive Improvements: A Survey of Adaptive Finite Element Methods in Computational Mechanics, In *State of the Art Surveys in Computational Mechanics*, American Society of Mechanical Engineers (ASME), New York, 1986.

[200] J. T. Oden, I. Babuška, and C. E. Baumann, A Discontinuous hp Finite Element Method for Diffusion Problems, *Journal of Computational Physics* **146**, 491–519, 1998.

[201] C. S. Peskin, Flow patterns around heart valves: A numerical method, *Journal of Computational Physics* **10**, 252–271, 1972.

[202] C. S. Peskin, Numerical analysis of blood flow in the heart, *Journal of Computational Physics* **25**, 220–252, 1977.

[203] C. S. Peskin, The immersed boundary method, *Acta Numerica* **11**, 479–517, 2002.

[204] C. Picioreanu, M. van Loosdrecht, and J. Heinen, Discrete-differential modelling of biofilm structure, *Water Science and Technology* **39**, 115–122, 1999.

[205] J. Pitkäranta, Boundary subspaces for the finite element method with Lagrange multipliers, *Numerische Mathematik* **289**, 273–289, 1979.

[206] J. Pitkäranta, Local stability conditions for the Babuška method of Lagrange multipliers, *Mathematics of Computation* **35**, 1113–1129, 1980.

[207] F. Pochet, K. Hillewaert, P. Geuzaine, J. F. Remacle, and E. Marchandise, A 3D strongly coupled implicit discontinuous Galerkin level set-based method for modeling two-phase flows, *Computers and Fluids* **87**, 144–155, 2013.

[208] S. Popinet and S. Zaleski, A front-tracking algorithm for accurate representation of surface tension, *International Journal for Numerical Methods in Fluids* **30**, 775–793, 1999.

[209] A. Popp, *Mortar Methods for Computational Contact Mechanics and General Interface Problems*, Phd thesis, Institute for Computational Mechanics, Technical University of Munich, 2012.

[210] A. K. Prasad and J. R. Koseff, Reynolds number and end-wall effects on a lid-driven cavity flow, *Physics of Fluids A: Fluid Dynamics* **1**, 208–218, 1989.

[211] A. Prokopenko, J. J. Hu, T. A. Wiesner, C. M. Siefert, and R. S. Tuminaro, MueLu User's Guide 1.0, Technical report, Sandia National Labs, SAND2014-18874, 2014.

[212] E. G. Puckett, A. S. Almgren, J. B. Bell, D. L. Marcus, and W. J. Rider, A High-Order Projection Method for Tracking Fluid Interfaces in Variable Density Incompressible Flows, *Journal of Computational Physics* **130**, 269–282, 1997.

[213] S. Rand and C. E. Pearson, A computational method for viscous flow problems, *Journal of Fluid Mechanics* **21**, 611–622, 1966.

[214] U. Rasthofer, F. Henke, W. A. Wall, and V. Gravemeier, An extended residual-based variational multiscale method for two-phase flow including surface tension, *Computer Methods in Applied Mechanics and Engineering* **200**, 1866–1876, 2011.

[215] U. Rasthofer, *Computational Multiscale Methods for Turbulent Single and Two-Phase Flows*, Phd thesis, Institute for Computational Mechanics, Technical University of Munich, 2015.

[216] P. A. Raviart and J. M. Thomas, A mixed finite element method for 2nd order elliptic problems, In *Mathematical Aspects of the Finite Element Method, Lecture Notes in Mathematics 606*, Springer-Verlag, Berlin-Heidelberg, 1977.

[217] W. H. Reed and T. R. Hill, Triangluar mesh methods for the neutron transport equation, Technical report, Los Alamos Scientific Lab, New Mexico (USA), 1973.

[218] A. Reusken, Analysis of an extended pressure finite element space for two-phase incompressible flows, *Computing and Visualization in Science* **11**, 293–305, 2008.

[219] T. Richter, A Fully Eulerian formulation for fluid–structure-interaction problems, *Journal of Computational Physics* **233**, 227–240, 2013.

[220] B. Riviere, M. F. Wheeler, and V. Girault, A Priori Error Estimates for Finite Element Methods Based on Discontinuous Approximation Spaces for Elliptic Problems, *SIAM Journal on Numerical Analysis* **39**, 902–931, 2001.

[221] W. L. Roberts and J. F. Driscoll, A laminar vortex interacting with a premixed flame: Measured formation of pockets of reactants, *Combustion and Flame* **87**, 245–256, 1991.

[222] H. G. Roos, M. Stynes, and L. Tobiska, *Robust Numerical Methods for Singularly Perturbed Differential Equations*, Volume 24 of *Springer Series in Computational Mathematics*, Springer, Berlin-Heidelberg, 2008.

[223] E. Rothe, Zweidimensionale parabolische Randwertaufgaben als Grenzfall eindimensionaler Randwertaufgaben, *Mathematische Annalen* **102**, 650–670, 1930.

[224] M. Sala and M. Heroux, Robust Algebraic Preconditioners with IFPACK 3.0, Technical report, Sandia National Laboratories, SAND-0662, 2005.

[225] H. Sauerland and T. P. Fries, The extended finite element method for two-phase and free-surface flows: A systematic study, *Journal of Computational Physics* **230**, 3369–3390, 2011.

[226] H. Sauerland and T. P. Fries, The stable XFEM for two-phase flows, *Computers and Fluids* **87**, 41–49, 2013.

[227] M. Schäfer and S. Turek, Benchmark Computations of Laminar Flow Around a Cylinder, *Flow Simulation with High-Performance Computers II, Volume 52 of Notes on Numerical Fluid Mechanics, Vieweg* **52**, 547–566, 1996.

[228] P. J. Schneider and D. H. Eberly, *Geometric Tools for Computer Graphics*, Elsevier Science (USA), 2003.

[229] B. Schott, *Enforcing interface conditions with Nitsche's method in the XFEM*, Diploma thesis, Institute for Computational Mechanics, Technical University of Munich, 2010.

[230] B. Schott and W. A. Wall, A new face-oriented stabilized XFEM approach for 2D and 3D incompressible Navier-Stokes equations, *Computer Methods in Applied Mechanics and Engineering* **276**, 233–265, 2014.

[231] B. Schott, U. Rasthofer, V. Gravemeier, and W. A. Wall, A face-oriented stabilized Nitsche-type extended variational multiscale method for incompressible two-phase flow, *International Journal for Numerical Methods in Engineering* **104**, 721–748, 2015.

[232] B. Schott, S. Shahmiri, R. Kruse, and W. A. Wall, A stabilized Nitsche-type extended embedding mesh approach for 3D low- and high-Reynolds-number flows, *International Journal for Numerical Methods in Fluids* **82**, 289–315, 2016.

[233] J. A. Sethian, Curvature and the evolution of fronts, *Communications in Mathematical Physics* **101**, 487–499, 1985.

[234] J. Sethian, *Level Set Methods and Fast Marching Methods: Evolving interfaces in computational geometry, fluid mechanics, computer vision, and material science*, Cambridge University Press, New York, 1999.

[235] S. Shahmiri, *A Hybrid Fixed-Grid-ALE Approach for Fluid-Structure Interaction*, Phd thesis, Institute for Computational Mechanics, Technical University of Munich, 2014.

[236] S. Shahmiri, A. Gerstenberger, and W. A. Wall, An XFEM-based embedding mesh technique for incompressible viscous flows, *International Journal for Numerical Methods in Fluids* **65**, 166–190, 2011.

[237] P. Shankar and M. Deshpande, Fluid mechanics in the driven cavity, *Annual Review of Fluid Mechanics* **32**, 93–136, 2000.

[238] M. Shirtliff and J. G. Leid (eds.), *The Role of Biofilms in Device-Related Infections*, Volume 3 of *Springer Series on Biofilms*, Springer-Verlag, Berlin-Heidelberg, 2009.

[239] J. L. Steger, F. C. Dougherty, and J. A. Benek, A chimera grid scheme, *Advances in Grid Generation ASME FED5* **5**, 59–69, 1983.

[240] E. Stein, *Singular Integrals and Differentiability Properties of Functions*, Princeton University Press, Princeton, 1970.

[241] R. Stenberg, On some techniques for approximating boundary conditions in the finite element method, *Journal of Computational and Applied Mathematics* **63**, 139–148, 1995.

[242] P. Stoodley, Z. Lewandowski, J. D. Boyle, and H. M. Lappin-Scott, Oscillation characteristics of biofilm streamers in turbulent flowing water as related to drag and pressure drop, *Biotechnology and Bioengineering* **57**, 536–544, 1998.

[243] T. Strouboulis, K. Copps, and I. Babuška, The generalized finite element method: an example of its implementation and illustration of its performance, *International Journal for Numerical Methods in Engineering* **47**, 1401–1417, 2000.

[244] Y. Sudhakar, *An embedded interface finite element method for fluid-structure-fracture interaction*, Phd thesis, Institute for Computational Mechanics, Technical University of Munich, 2015.

[245] Y. Sudhakar and W. A. Wall, Quadrature schemes for arbitrary convex/concave volumes and integration of weak form in enriched partition of unity methods, *Computer Methods in Applied Mechanics and Engineering* **258**, 39–54, 2013.

[246] Y. Sudhakar, J. Moitinho de Almeida, and W. A. Wall, An accurate, robust, and easy-to-implement method for integration over arbitrary polyhedra: Application to embedded interface methods, *Journal of Computational Physics* **273**, 393–415, 2014.

[247] N. Sukumar, N. Moës, B. Moran, and T. Belytschko, Extended finite element method for three-dimensional crack modelling, *International Journal for Numerical Methods in Engineering* **48**, 1549–1570, 2000.

[248] M. Sussman, P. Smereka, and S. Osher, A level set approach for computing solutions to incompressible two-phase flow, *Journal of Computational Physics* **114**, 146–159, 1994.

[249] D. Taherzadeh, C. Picioreanu, U. Küttler, A. Simone, W. A. Wall, and H. Horn, Computational study of the drag and oscillatory movement of biofilm streamers in fast flows, *Biotechnology and Bioengineering* **105**, 600–610, 2010.

[250] D. Taherzadeh, C. Picioreanu, and H. Horn, Mass Transfer Enhancement in Moving Biofilm Structures, *Biophysical Journal* **102**, 1483–1492, 2012.

[251] F. Tanios, M. Gee, J. Pelisek, S. Kehl, J. Biehler, V. Grabher-Meier, W. A. Wall, H.-H. Eckstein, and C. Reeps, Interaction of Biomechanics with Extracellular Matrix Components in Abdominal Aortic Aneurysm Wall, *European Journal of Vascular and Endovascular Surgery* **50**, 167–174, 2015.

[252] C. A. Taylor, T. J. R. Hughes, and C. K. Zarins, Finite element modeling of blood flow in arteries, *Computer Methods in Applied Mechanics and Engineering* **158**, 155–196, 1998.

[253] T. E. Tezduyar, S. Sathe, R. Keedy, and K. Stein, Space–time finite element techniques for computation of fluid–structure interactions, *Computer Methods in Applied Mechanics and Engineering* **195**, 2002–2027, 2006.

[254] C. Truesdell and W. Noll, *The Non-Linear Field Theories of Mechanics*, Springer-Verlag, Berlin-Heidelberg, 2004.

[255] F. van der Bos and V. Gravemeier, Numerical simulation of premixed combustion using an enriched finite element method, *Journal of Computational Physics* **228**, 3605–3624, 2009.

[256] F. Verdugo and W. A. Wall, Unified framework for the efficient solution of n-field coupled problems with monolithic schemes, *Computer Methods in Applied Mechanics and Engineering* **310**, 335–366, 2016.

[257] W. A. Wall and E. Ramm, Fluid–Structure Interaction Based upon a Stabilized (ALE) Finite Element Method, Computational Mechanics – New Trends and Applications, In S. R. Idelsohn, E. Oñate, and E. N. Dvorkin (eds.), *Proc. 4th World Congress on Computational Mechanics*, Buenos Aires, 1998, CIMNE, Barcelona.

[258] W. A. Wall, *Fluid-Struktur-Interaktion mit stabilisierten Finiten Elementen*, Dissertation, Universität Stuttgart, 1999.

[259] W. A. Wall, A. Gerstenberger, P. Gamnitzer, C. Förster, and E. Ramm, Large deformation fluid-structure interaction–advances in ALE methods and new fixed grid approaches, In *Fluid-structure interaction*, pages 195–232, Springer-Verlag, Berlin-Heidelberg, 2006.

[260] W. A. Wall, P. Gamnitzer, and A. Gerstenberger, Fluid–structure interaction approaches on fixed grids based on two different domain decomposition ideas, *International Journal of Computational Fluid Dynamics* **22**, 411–427, 2008.

[261] W. A. Wall, L. Wiechert, A. Comerford, and S. Rausch, Towards a comprehensive computational model for the respiratory system, *International Journal for Numerical Methods in Biomedical Engineering* **26**, 807–827, 2010.

[262] W. A. Wall, C. Ager, M. Grill, M. Kronbichler, A. Popp, B. Schott, and A. Seitz, BACI: A multiphysics simulation environment, Technical report, Institute for Computational Mechanics, Technical University of Munich, 2017.

[263] C. Y. Wang, On the low-Reynolds-number flow in a helical pipe, *Journal of Fluid Mechanics* **108**, 185–194, 1981.

[264] X. Wang and W. K. Liu, Extended immersed boundary method using FEM and RKPM, *Computer Methods in Applied Mechanics and Engineering* **193**, 1305–1321, 2004.

[265] Z. J. Wang and V. Parthasarathy, A fully automated Chimera methodology for multiple moving body problems, *International Journal for Numerical Methods in Fluids* **33**, 919–938, 2000.

[266] C. H. Whiting, *Stabilized finite element methods for fluid dynamics using a hierarchical basis*, Phd thesis, Rensselaer Polytechnic Institute, 1999.

[267] C. H. Whiting and K. E. Jansen, A stabilized finite element method for the incompressible Navier-Stokes equations using a hierarchical basis, *International Journal for Numerical Methods in Fluids* **35**, 93–116, 2001.

[268] T. Wick, Fully Eulerian fluid–structure interaction for time-dependent problems, *Computer Methods in Applied Mechanics and Engineering* **255**, 14–26, 2013.

[269] L. Wiechert, *Computational Modeling of Multi-Field and Multi-Scale Phenomena in Respiratory Mechanics*, PhD thesis, Technical University of Munich, 2011.

[270] F. A. Williams, *Combustion Theory*, Westview Press, 2nd Edition, 1985.

[271] B. Wohlmuth, *Discretization Methods and Iterative Solvers Based on Domain Decomposition*, Volume 17 of *Lecture Notes in Computational Science and Engineering*, Springer-Verlag, Berlin-Heidelberg, 2001.

[272] P. Wriggers, *Nonlinear Finite Element Methods*, Springer-Verlag, Berlin-Heidelberg, 2008.

[273] L. Yoshihara, C. J. Roth, and W. A. Wall, Fluid-structure interaction including volumetric coupling with homogenized subdomains for modeling respiratory mechanics, *International Journal for Numerical Methods in Biomedical Engineering* **33**, doi: 10.1002/cnm.2812, 2017.

[274] L. Zabielski and A. J. Mestel, Steady flow in a helically symmetric pipe, *Journal of Fluid Mechanics* **370**, 297–320, 1998.

[275] Y. Zang, R. L. Street, and J. R. Koseff, A dynamic mixed subgrid-scale model and its application to turbulent recirculating flows, *Physics of Fluids A: Fluid Dynamics* **5**, 3186–3196, 1993.

[276] L. Zhang, A. Gerstenberger, X. Wang, and W. K. Liu, Immersed finite element method, *Computer Methods in Applied Mechanics and Engineering* **193**, 2051–2067, 2004.

[277] O. C. Zienkiewicz and R. L. Taylor, *The Finite Element Method: Solid mechanics*, Butterworth-Heinemann, Oxford, 5th Edition, 2000.

[278] A. Zilian and A. Legay, The enriched space–time finite element method (EST) for simultaneous solution of fluid–structure interaction, *International Journal for Numerical Methods in Engineering* **75**, 305–334, 2008.

[279] P. Zunino, Analysis of backward Euler/extended finite element discretization of parabolic problems with moving interfaces, *Computer Methods in Applied Mechanics and Engineering* **258**, 152–165, 2013.

VERZEICHNIS DER BETREUTEN STUDIENARBEITEN

Im Rahmen dieser Dissertation entstanden am Lehrstuhl für Numerische Mechanik (LNM) in den Jahren von 2011 bis 2016 unter wesentlicher wissenschaftlicher, fachlicher und inhaltlicher Anleitung des Autors die im Folgenden aufgeführten studentischen Arbeiten. Der Autor dankt allen Sudierenden für Ihr Engagement bei der Unterstützung dieser wissenschaftlichen Arbeit.

Studierende(r)	**Studienarbeit**
Raffaela Kruse	*Enforcing coupling conditions on embedded interfaces using stress-based Lagrange multipliers in the XFEM for incompressible flow*, Masterarbeit, 2013